Department of Engineering

A Time Accurate Computational Analysis of Two-Dimensional Wakes

by

William P. Bennett

Thesis submitted to the University of Leicester in accordance with the requirements for the degree of Doctor of Philosophy

Supervisor: Dr. Aldo Rona

Co-supervisor: Prof. J.P. Gostelow

May 2005

A Time Accurate Computational Analysis of Two-Dimensional Wakes

William P. Bennett
Department of Engineering,
University of Leicester,
Leicester, LE1 7RH, UK.

Abstract

The unsteady transport of large-scale coherent vortices can induce a redistribution in the stagnation temperature and pressure relative to the free stream flow. The time averaged result of this redistribution is the Eckert-Weise effect, by which a cooled region is defined along the wake centre. The time accurate characteristics of this mechanism for bluff body near wake flows are, however, sparsely documented at low transonic Mach numbers. For example, no available published research has, to date, studied the time resolved energy separation characteristics in the transonic near wake flow of a circular cylinder using a time accurate numerical model.

A novel time accurate computational analysis is developed of the near wake energy separation characteristics downstream of a circular cylinder in a low transonic cross-flow at high Reynolds number. This circular cylinder analysis is extended to a novel time accurate computational study of energy separation in an asymmetric turbine cascade wake at a low transonic exit Mach number. Energy separation is reported to primarily be a convective flow effect. A structured inviscid and turbulent test program examines the extent to which an inviscid model is able to predict energy separation.

Results from this study indicate a good correlation of the time accurate and time mean flow statistics with published work. These results demonstrate that an inviscid model is able to capture the basic energy separation mechanism. However, inviscid models are shown to over-predict the stagnation temperature and pressure redistribution. The inviscid prediction suggests that air compressibility modifies the incompressible energy separation mechanism. Turbulence diffusion reduces the stagnation temperature and pressure extrema to demonstrate a better comparison with experimental data. A relationship between the energy separation and vortex strength is highlighted. This is shown in the turbine cascade prediction to be dependent on the boundary layer separation characteristics.

Contents

Acknowledgements vi

Nomenclature vii

1. Introduction 1

1.1 Aims & Objectives 3

1.2 Thesis Overview 4

2. Literature Review 6

2.1 Introduction 6

2.2 Boundary Layer Development in Turbine Cascades 7

2.3 Cascade Boundary Layer/Vortex Shedding Interaction 16

2.4 Compressibility Effects 20

2.5 The Flow Around Circular Cylinders 30

2.6 Energy Separation in Vortex Dominated Wake Flows 33

3. The Numerical Solution Procedure 41

3.1 Implementation Overview 41

3.1.1 Introduction 41

3.1.2 Dominant Flow Physics Overview 41

3.1.3 Numerical Method Overview 43

3.2 Governing Equations 47

3.3 The Euler Equations 48

3.3.1 Introduction 48

3.3.2 Quasi-Linear Form 51

3.4 The Short-Time Averaged Navier-Stokes Equations 52

3.4.1 Introduction 52
3.4.2 The Two-Equation $k-\omega$ Turbulence Model of Wilcox 53
3.4.3 Closure Approximations 55
3.4.4 Quasi-Linear Form 60
3.5 Estimation of the Convective Fluxes 62
3.5.1 Introduction 62
3.5.2 Godunov-Type Riemann Solvers 63
3.5.3 The Approximate Riemann Solver of Roe 64
3.5.4 $k-\omega$ Formulation of the Approximate Riemann Solver of Roe 67
3.5.5 Entropy Preservation 69
3.5.6 Higher Order Spatial Accuracy - MUSCL Extrapolation 74
3.5.7 Total Variation Diminishing (TVD) Schemes 76
3.5.8 The Minmod Flux Limiter 76
3.6 Estimation of the Turbulent Fluxes 82
3.7 Estimation of the Turbulent Source Terms 84
3.8 Time Integration Method 85
3.9 Boundary Conditions 87
3.9.1 Subsonic Inlet 88
3.9.2 Supersonic Inlet 90
3.9.3 Subsonic Outlet 91
3.9.4 Supersonic Outlet 92
3.9.5 Inter-Domain Boundary 92
3.9.6 Periodic Boundary 93
3.9.7 Inviscid Wall Boundary 93
3.9.8 Adiabatic No-slip Surface Boundary 95
3.10 The Adaptive Mesh Refinement (AMR) Method 96
3.10.1 Introduction 96
3.10.2 The AMR Flagging and Grouping Procedure 99
3.10.3 A Two-Dimensional Coarse-Fine Interpolation Procedure 100
3.10.4 Integrating the Flow Field 109

3.10.5 AMR Boundary Conditions 111
3.10.6 The Conservative Fine-Coarse Solution Projection 112

4. AMR Method Validation 116
4.1 Introduction 116
4.2 One-Dimensional Shock Tube Problem 116
4.2.1 Test Case Description 116
4.2.2 Results & Discussion 118
4.3 Two-Dimensional Acoustic Pulse Problem 125
4.3.1 Test Case Description 125
4.3.2 Results & Discussion 129
4.4 Turbulent Boundary Layer - Zero Pressure Gradient 144
4.4.1 Test Case Description 144
4.4.2 Results & Discussion 150

5. Circular Cylinder Prediction 160
5.1 Introduction 160
5.2 Inviscid Circular Cylinder Flow Prediction 161
5.2.1 Numerical Model Specifications 161
5.2.2 The Initial Transient Flow Field Development 163
5.2.3 The Self-Sustained Vortex Shedding Development 166
5.2.4 Inviscid Prediction Validation 171
5.2.5 Compressibility and the Inviscid Vortex Shedding Cycle 176
5.2.6 Energy Separation in the Inviscid Vortex Shedding Cycle 185
5.2.7 Summary 201
5.3 Turbulent Circular Cylinder Flow Prediction 202
5.3.1 Numerical Model Specifications 202
5.3.2 Turbulent Circular Cylinder Validation 204
5.3.3 Compressibility and the Turbulent Vortex Shedding Cycle 214
5.3.4 Energy Separation in the Turbulent Vortex Shedding Cycle 224
5.3.5 Summary 245

6. Turbine Cascade Prediction **247**

6.1 Introduction 247

6.2 Inviscid Turbine Cascade Flow Prediction 248

6.2.1 Numerical Model Specifications 248

6.2.2 Time Averaged Isentropic Mach Number Distribution 252

6.2.3 Vortex Shedding Characteristics 256

6.2.4 Energy Separation in the Turbine Cascade Wake 265

6.2.5 Summary 278

6.3 Turbulent Turbine Cascade Flow Prediction 280

6.3.1 Numerical Model Specifications 280

6.3.2 Time Accurate Base Pressure Analysis 281

6.3.3 Turbine Blade Boundary Layer Analysis 284

6.3.4 Time Averaged Isentropic Mach Number Distribution 288

6.3.5 Turbulent Vortex Shedding Characteristics 290

6.3.6 Energy Separation in the Turbulent Cascade Wake 300

6.3.7 Summary 314

7. Conclusions & Further Research **317**

7.1 Overview 317

7.2 Circular Cylinder Flow 318

7.3 Turbine Cascade Flow 321

7.4 Further Research Recommendations 322

A. Appendices **326**

A.1 Short-Time Averaging 326

A.2 Circular Cylinder Laminar Sublayer Height Estimation 329

A.3 Energy Separation In The Relative Reference Frame 332

Bibliography **340**

Acknowledgements

I would firstly like to thank Dr. Aldo Rona for all the advice, motivation, guidance and support given in the realisation of this thesis. I would also like to thank Prof. J. P. Gostelow for his resolute support and promotion of this research. Special thanks are also due to Jon Ackerman at the University of Leicester for allowing uninhibited access to his experimental data.

The support of an EPSRC research studentship grant is acknowledged. I would also like to thank the IMechE for the receipt of a Thomas Andrew common grant. This work was partially performed using the University of Leicester Mathematical Modelling Centre's supercomputer, which was purchased through the EPSRC strategic equipment initiative.

Thanks also to Ed, Denver, Jon, Mark, Richard, Andrew, Mohammed and John Twiddle for all those incidental discussions that made my time as a postgraduate student so enjoyable. Thanks also go to Tom Robotham, Jason Palmer, Andrew Norman and all the other support staff at the University of Leicester.

Finally, I would like to thank my family for their constant motivation and support.

Nomenclature

English Symbols

a	Speed of sound
$\boldsymbol{A}$	Conservative variable Jacobian matrix for the Euler equations
$\boldsymbol{A_t}$	Conservative variable Jacobian matrix for the Navier-Stokes equations
b	AMR scaling parameter
c	Turbine blade chord
c_1	Turbine blade axial chord
c_p	Specific heat at constant pressure
c_v	Specific heat at constant volume
C_d	Coefficient of drag
C_f	Skin friction coefficient
C_p	Coefficient of pressure
C_{pb}	Coefficient of base pressure
C_l	Coefficient of lift
D	Circular cylinder diameter
D_t	Turbine blade trailing edge diameter
e	Specific energy
$\boldsymbol{e}$	Eigenvector
$f_{\beta^\star}$	Dimensionless cross-diffusion parameter
$\boldsymbol{F}$	Conservative flux vector
$\boldsymbol{F}_c$	Convective flux vector
$\boldsymbol{F}_t$	Turbulent flux vector
h	Specific enthalpy
$\boldsymbol{I}$	Unit tensor

k	Specific turbulence kinetic energy
k^*	Wavenumber
K	Kinetic energy
$\mathcal{K}$	Thermal conductivity
$\mathcal{K}_t$	Thermal eddy conductivity
L	Adaptive Mesh Refinement level
$\mathcal{L}_2$	Convergence residual
M	Mach number
M_t	Turbulence Mach number
M_{t_o}	Compressibility correction closure coefficient
$\boldsymbol{n}$	Unit normal vector
N_f	Number of faces in a unit control volume
$\mathcal{O}$	Order of accuracy for a given expression
p	Pressure
Pr	Prandtl number
Pr_t	Turbulent Prandtl number
$\boldsymbol{q}$	Molecular heat flux vector
$\boldsymbol{q_t}$	Turbulent heat flux vector
rI_f, rJ_f	AMR spatial refinement factors
rt_f	AMR temporal refinement factor
R	Gas constant
Re	Reynolds number
s	Specific entropy
Str	Strouhal number
$\mathcal{S}$	Control volume surface area
$\boldsymbol{S}$	Turbulent source terms vector
t	Time
T	Temperature
Tu	Turbulence intensity
$\boldsymbol{u}$	Velocity vector

u^+	Dimensionless boundary layer velocity
u_τ	Friction velocity
$\boldsymbol{U}$	Conservative variables vector
V	Volume
x_1, x_2	Physical space Cartesian coordinates
x_n	Surface normal distance
y^+	Dimensionless surface normal coordinate

Greek Symbols

α	Characteristic wave strength
β	$k-\omega$ model closure coefficient
$\beta^\star$	$k-\omega$ model closure coefficient
β_o, $\beta_o^\star$	$k-\omega$ dissipation term closure coefficients
γ	Specific heat ratio, c_p/c_v
δ_1	Boundary layer displacement thickness
δ_2	Boundary layer momentum thickness
δ_{99}	Boundary layer thickness (to 99% of the boundary layer edge velocity)
ϵ	Specific dissipation
ε	MUSCL extrapolation parameter to determine the local spatial accuracy
$\varepsilon^\star$	Entropy modification parameter
η	MUSCL extrapolation parameter to determine the local spatial accuracy
κ	Karman constant, 0.41
λ	Eigenvalue of Jacobian matrix
μ_l	Dynamic or laminar viscosity
μ_t	Turbulent (eddy) viscosity
$\xi^\star$	$k-\omega$ dissipation term compressibility correction coefficient
ρ	Density
σ	$k-\omega$ model closure coefficient for turbulent transport of ω
$\sigma^\star$	$k-\omega$ model closure coefficient for turbulent transport of k
$\boldsymbol{\tau}$	Viscous stress tensor

$\boldsymbol{\tau_r}$	Reynolds stress tensor
τ_w	Surface (wall) shear stress
$\mathbf{\Phi}$	Non-linear limiting function
φ	$k-\omega$ model closure coefficient
χ_k	Dimensionless cross-diffusion parameter
ψ	Runge-Kutta coefficient
ω	Specific turbulence dissipation rate
Ω	Minmod limiting function coefficient

Other Symbols

$\otimes$	Tensor product
:	Double scalar product

Subscripts

1, 2	Cartesian components
e	Turbine cascade discharge (exit) condition
i, j	Cell indices
s	Stagnation condition
w	Boundary layer surface (wall) value
∞	Free stream condition

Superscripts

T	Transpose operator
$\prime$	Large scale fluctuating component
$\prime\prime$	Turbulent fluctuating component

Accents

$\wedge$	Roe averaged variable
$-$	Short-time averaged variable
$\sim$	Time mean component

Chapter 1

Introduction

The unsteady wake downstream of a bluff body can have a significant impact on the structural, financial and environmental performance of many practical engineering applications. Unsteady wakes can lead to stagnation pressure losses, fatigue inducing vibrations and noise pollution. A fundamental analysis of the underlying flow physics for a specific wake flow can lead to significant beneficial increases in component performance, suppression of destructive vibration modes, and a decreased environmental impact.

One engineering discipline in which significant practical benefits have resulted from the analysis of wake flows is that of turbomachinery aerodynamics. Strategic developments in the design of turbomachinery blading have lead to increases in aerodynamic efficiency, significant reductions in fuel consumption, reduced blade numbers, increased reliability and lower emitted levels of acoustic radiation.

The flow downstream of a turbine blade may comprise of a wide range of loss producing flow features. These include, for example, unsteady shock waves, shock wave-boundary layer interactions and high frequency vortex shedding characteristics. Each of these flow features constitutes a significant source of entropy production, leading to an overall decrease in turbine stage efficiency.

This study is concerned with one unsteady loss producing phenomenon that has received relatively minor attention in published research. Energy separation describes the time accurate redistribution of stagnation enthalpy in a wake flow due to the action of downstream moving coherent vortices. The result, for a von Kármán street of convecting vortex cores, is a redistribution of the stagnation temperature

and pressure to increase locally above the free stream condition along the edges of the wake and decrease below the free stream condition along the centre of the wake. On a time resolved basis, these stagnation temperature and pressure extrema are defined locally at each convecting vortex. The time averaged result, however, is a decrease in stagnation temperature and pressure along the centre of a wake. This time averaged effect was first discovered at the base of a thermally insulated cylinder in a uniform cross-flow by Eckert & Weise (1943). The time resolved stagnation temperature and pressure redistribution was initially predicted downstream of a circular cylinder by Kurosaka et al. (1987) in incompressible flow.

A renewed interest in this phenomenon has emerged with regard to the flow downstream of turbine blade rows. The requirement for internal cooling of high-pressure stage turbine blades, due to high stage loading and high operating temperature requirements, has lead to a number of turbine blade designs with thick trailing edges. Increases in trailing edge thickness can lead to the presence of vortex shedding downstream of each turbine blade row. A number of vortex shedding effects are documented for one such turbine nozzle guide vane in transonic flow by Carscallen & Gostelow (1994) at $M_e = 1.16$. High speed stagnation temperature and pressure measurements on this blade have identified significant time dependent energy separation effects associated with vortex shedding at an exit Mach number of $M_e = 0.95$, as reported by Carscallen et al. (1998, 1999) and Hogg et al. (1997).

From these transonic turbine cascade wake measurements and the subsonic circular cylinder analysis of Kurosaka et al. (1987), a new study is undertaken on factors influencing the energy separation mechanism in the near wake region. Such factors may include the boundary layer development and separation characteristics, asymmetric pressure distribution effects and compressibility. For example, established circular cylinder research at low transonic Mach numbers and high Reynolds numbers report that the boundary layer development and vortex shedding characteristics are highly influenced by transient radial shock waves, which oscillate circumferentially over the cylinder surface. To the authors knowledge, no significant time accurate computational fluid dynamics research on the energy separation mechanism

in the circular cylinder near wake flow has been undertaken within this intermittent shock wave regime. Similarly, little time accurate research is documented on the energy separation mechanism in a turbine blade near wake flow at low transonic Mach numbers below, for example, $M_e = 0.8$.

1.1 Aims & Objectives

A fundamental analysis of the near wake energy separation effects in the low transonic, high Reynolds number wake of a circular cylinder and a thick trailing edge turbine cascade is undertaken in this study. This represents a novel and original extension to the time averaged transonic circular cylinder analysis of Eckert & Weise (1943), Ryan (1951) and Thomann (1959), and the time accurate subsonic circular cylinder analysis of Kurosaka et al. (1987). The turbine blade of choice for this study is the highly loaded turbine nozzle guide vane of Carscallen et al. (1996, 1998, 1999). This study also represents a novel extension to the energy separation research documented for this turbine cascade at high transonic Mach numbers.

A computational analysis of the near wake flow field is adopted in this study. The use of a numerical approach in studying the near wake flow is justified as non-intrusive measurements in this region, at the range of sampling frequencies required, would prove difficult to perform and expensive to fund. Also, the proposed energy separation mechanism put forward by Kurosaka et al. (1987) is primarily a convective flow effect. A structured inviscid and turbulent computational analysis is chosen to examine the ability for an inviscid numerical method to accurately predict energy separation in a high Reynolds number wake flow. This study should highlight any small-scale turbulence effects or secondary effects due to compressibility.

The free stream conditions imposed in the circular cylinder and turbine blade models are chosen to match a concurrent experimental research program by J.R. Ackerman at the University of Leicester. This concurrent experimental research program, documented in Ackerman (2005), supplies crucial validation data for the current numerical method and provides supporting evidence for the energy separation characteristics further downstream of the circular cylinder. The current study

should, in turn, supply a more complete overview of the flow field development leading up to the measurements of Ackerman (2005). The circular cylinder is modelled at uniform free stream conditions of $M_\infty = 0.6$ and $Re_D = 6.87 \times 10^5$, based on the circular cylinder diameter D. The turbine cascade is modelled at exit conditions of $M_e = 0.6$ and $Re_{D_t} = 7.48 \times 10^4$, based on a turbine blade trailing edge diameter of $D_t = 6.35 \times 10^{-3} m$.

1.2 Thesis Overview

This thesis is divided into the following chapters:

Chapter 2: This chapter provides a concise overview of the available published literature, to date, on the unsteady compressible flow past a circular cylinder and turbine cascade at high Reynolds numbers. This chapter introduces the reader to the underlying motivation for this study and provides a wider context for the current research.

Chapter 3: The numerical solution procedure used to model the circular cylinder and turbine cascade is described in this chapter. This chapter places the numerical method into context with the modelled flow and highlights improvements made to the existing numerical method over the course of this study.

Chapter 4: An Adaptive Mesh Refinement (AMR) method is implemented into the existing numerical method to increase the computational efficiency. The AMR method is described in Chapter 3. This chapter presents and discusses selected results from a structured AMR validation test case procedure.

Chapter 5: The compressible, high Reynolds number circular cylinder model flow is introduced in this chapter and results are presented and discussed. The chapter is divided into two main sections. The first half of this chapter presents and discusses results from the inviscid circular cylinder prediction. This analysis is extended in

the second half to a turbulent circular cylinder prediction.

Chapter 6: This chapter introduces the compressible flow past the model turbine cascade. The first half of this chapter presents and discusses results from the inviscid turbine cascade prediction, placing these results into context with published work. The second half of this chapter introduces the development of a turbulent cascade prediction, discussing the results in light of published research and the turbulent circular cylinder model.

Chapter 7: This chapter discusses the current study and draws conclusions based on the research presented in this thesis. From these conclusions, suggested further developments to this research are then discussed.

Chapter 2

Literature Review

2.1 Introduction

This chapter provides a concise overview of published literature, available to the author, on the high Reynolds number, compressible flow past circular cylinders and turbine blades. This review is intended to place the current study into context and to provide a source of reference for further research. The literature review is divided into the following sections:

1. The development of boundary layers on turbine blades;
2. Cascade boundary layer/vortex shedding interaction;
3. Compressibility in turbine cascade flows;
4. The flow around circular cylinders;
5. Energy separation in vortex dominated wake flows.

Sections 2.2 to 2.5 present a physical review concerning flow features that can influence the performance of turbine blades and circular cylinders. Published research on energy separation in vortex dominated wakes is then reviewed in Section 2.6. This review is supplemented by an overview of numerical modelling issues affecting the prediction of these flow features, based on the numerical method described in Chapter 3. Particular attention is given to the performance of the two-equation $k-\omega$ turbulence model of Wilcox (1988) and the requirement for an enhanced turbulence closure method to tackle this class of flows. Turbulence closure modifications are

described in Section 3.4.3.

Throughout this review, sources of 'loss' are highlighted. Denton (1993), defines a 'loss' as *any flow feature that reduces the efficiency of a turbomachine*, from which a similar definition can be made for circular cylinder flows. Broadly stated, turbine cascade losses are categorised according to three groups, *profile losses*, *secondary/endwall losses* and *tip leakage losses*. *Endwall losses* and *tip leakage losses*, which have analogues for a circular cylinder sited in a wind tunnel, are not present in a two-dimensional model and are therefore not addressed in this work. The interested reader is referred to Denton (1993) or Dunham (1995). *Profile loss*, as defined in this study, comprises all two-dimensional losses associated with the boundary layer development, separation and wake induced or shock induced losses. Losses are quantified by Denton (1993) in terms of entropy production, as entropy is independent of the relative frame of reference, unlike stagnation pressure or stagnation enthalpy losses, which are calculated along streamlines. Entropy production as a measure of loss creation is convenient for the present work and is used in the work of Carscallen et al. (1998, 1999) for measurements on the same cascade flow.

2.2 Boundary Layer Development in Turbine Cascades

Turbine blade passages are subjected to a periodic ingestion of trailing edge wakes, caused by the relative rotation of the rotors and stators in a turbine stage. Rotor blades pass downstream of the stators during each rotation of the turbine. Turbulent wakes therefore convect from the upstream row of stator blades causing a periodic turbulent inflow to the downstream rotor row. Convected turbulent wakes are interleaved by regions of more uniform flow, emanating from between the adjacent blade wakes. The situation is reversed as the rotor blades from the upstream stage pass upstream of the stator blades, resulting in cyclic inflow conditions to each stator blade. The investigation of rotor-stator wake interactions is particularly active at the present time, producing a rapidly increasing body of published literature drawn from experiments and computational predictions.

Past research indicates that an increase in the upstream turbulence intensity cor-

responds to an upstream movement of transition onset in turbine blade boundary layers, as correlated by Abu-Ghannam & Shaw (1980), Mayle (1991) and Mayle & Schulz (1997). An increased upstream turbulence intensity also corresponds to a decrease in the transition length as correlated, for instance, by Narasimha (1985). High turbulence intensity shortens the length of any separation bubbles, eventually resulting in by-pass transition of the boundary layer ahead of the laminar separation. This is reported by Mayle (1991), Roberts & Denton (1996) and Stieger (2002). Experimental research into the mechanism by which transition occurs under cyclic inflow conditions and an adverse pressure gradient indicates the presence of a *calmed region*, which, follows the transit of a turbulent wake in time. This locally reduces viscous dissipation to a level representative of laminar conditions and is resistant to laminar separation. These observations are reported in Gostelow et al. (1997), Stieger (2002) and other references cited therein. As reported in Stieger (2002), cyclic, long duration calmed regions, together with short duration turbulent strips and short duration separation bubble formation, can significantly reduce the time averaged viscous dissipation with respect to steady upstream conditions. A detailed review of the literature concerning the influence of periodic wakes past turbine blades is beyond the scope of the present study. The interested reader is referred to reviews by Stieger (2002) and Gostelow (2003). Accurate numerical predictions of the flow around a turbine blade under cyclic upstream conditions would ideally require solving the Navier-Stokes equations over all turbulence length scales by the application of a Direct Numerical Simulation (DNS) approach. Alternatively, the use of an experimental correlation combined with a conventional turbulence model can be used, as in Vicedo et al. (2004). A fundamental analysis of the flow physics around a turbine blade is however possible using the simplified case of a steady upstream flow condition. In the present study, the flow around a highly loaded turbine blade is modelled in order to analyse the physics underlying energy separation at transonic flow conditions in a vortex dominated wake flow. For the purposes of the present study, therefore, the assumption of a steady upstream flow condition is considered a justifiable simplification of a practical turbine cascade flow.

With a steady upstream flow, the fluid impinges on the turbine blade leading edge. The location of the upstream stagnation point depends on the geometry and loading of the turbine blade, as well as on the exit flow angle of the upstream blade row. Roberts & Denton (1996) investigate the precession of the upstream stagnation point with turbine blade loading at a low subsonic exit condition of $M_e < 0.05$. Roberts & Denton (1996) simulate a turbine blade using a flat plate in a wind tunnel with a contoured floor and ceiling. Increasing the loading on the plate, by contouring of the pitch-wise exit boundaries, increases the mass flow over the simulated suction surface. The upstream stagnation point is shown to move around the leading edge to assume a position further along the simulated pressure surface. The standard two-equation $k - \omega$ turbulence model of Wilcox (1988) is reported to over-predict the turbulence kinetic energy level approaching the leading edge stagnation point. This is due to the invalidity of the Boussinesq hypothesis in regions with high strain rates. The failure of the Boussinesq hypothesis under such conditions is documented by Kato & Launder (1993), Larsson (1998), Medic & Durbin (2002), Wilcox (2002) and other references therein. A number of modifications to standard two-equation turbulence models are proposed in the cited literature. The present implementation locally limits the production of turbulence kinetic energy, based on the local dissipation of turbulence kinetic energy.

The initial development of the boundary layer over the leading edge of the turbine blade significantly influences its downstream state. In turn, the level of turbulence in the boundary layer at separation from the trailing edge has a significant influence on the downstream wake flow, as discussed in Section 2.3. The difficulty associated with accurately measuring the boundary layer around the leading edge of a turbine blade is addressed by Hodson (1985). The thin boundary layer in this region prevents the use of Pitot probes to measure the local dynamic pressure profile, as such measurements can cause significant blockage effects and may lack adequate spatial resolution, normal to the surface. The fundamental physics of separation and transition in the leading edge region are therefore often aided by research using a flat plate or curved surface with an imposed stream-wise pressure gradient. Such

an approach is documented, for example, in Gostelow & Blunden (1989), D'Ovidio et al. (2001a, 2001b), Schobeiri et al. (2002), Talan (2002) and in further references therein. As reported in Stieger (2002), extending flat plate or curved plate results to turbine blade flows requires an adequate account of loading, circulation and curvature effects.

As the laminar boundary layer develops over the leading edge surface, an adverse pressure gradient of sufficient strength may reduce the wall shear stress to zero, resulting in a separated flow region. Transition of the separated shear layer and its subsequent reattachment to the surface defines the length of the laminar separation bubble. The influence of the upstream turbulence intensity on the length of a separation bubble follows from the introduction to cyclic upstream conditions at the start of this section. Laminar separation bubbles are categorised by Owen & Klanfer (1953) according to their stream-wise extent. The separation length is normalised by δ_{1s}, the displacement thickness of the laminar boundary layer at separation. This choice for the normalising parameter is based on the understanding that the separation length is related to the location of transition in the separated shear layer, which, is determined by the stability of the laminar boundary layer at separation. *Short* laminar separation bubbles are defined as having a normalised stream-wise length, l_s, of order $l_s/\delta_{1s} \approx \mathcal{O}(10^2)$. *Long* separation bubbles are defined as having a normalised stream-wise length in the range $\mathcal{O}(10^3) \leq l_s/\delta_{1s} \leq \mathcal{O}(10^5)$. Owen & Klanfer (1953) also categorise the influence of the Reynolds number on the length of the laminar separation bubble. The general trend is confirmed in a number of experiments, including Hodson (1985) and Smolny & Blaszczak (1995). Owen & Klanfer (1953) define a reference Reynolds number, $(R_{\delta_1})_s$, as

$$(R_{\delta_1})_s = \frac{\rho_s u_s \delta_{1s}}{\mu_s}, \tag{2.1}$$

where, ρ_s, u_s and μ_s are the boundary layer edge density, velocity and molecular viscosity respectively at separation. A *critical* Reynolds number range is defined by Owen & Klanfer (1953) as $400 \leq (R_{\delta_1})_s \leq 500$. For $(R_{\delta_1})_s < 400$, a *long* laminar separation bubble is expected. *Short* separation bubbles are therefore expected for

$(R_{\delta_1})_s > 500$. Smolny & Blaszczak (1995) indicate that the stream-wise starting location for a laminar separation bubble demonstrates an independence on the free stream Reynolds number. Positioning of a small diameter trip wire close to the leading edge decreases the length of the separation bubble, as reported by Smolny & Blaszczak (1995). This locally increases the turbulence intensity, which, when convected downstream to the separation bubble, acts in a similar manner to increasing the turbulence intensity upstream of the leading edge. Placing the trip wire further downstream is reported to cause by-pass transition of the boundary layer and the complete suppression of the separation bubble. Owen & Klanfer (1953) report that *long* separation bubbles are associated with an upstream velocity peak closer to the leading edge, corresponding to a small radius of leading edge curvature and to a small thickness to chord ratio. Placing this brief review of laminar separation bubbles into context with the present study, Brooksbank (2001) reports the possibility of a laminar separation bubble along the suction surface leading edge from wind tunnel measurements of the turbine blade modelled in the present study at $M_e = 1.16$. From this brief physical review, the location of separation of a laminar boundary layer, along a turbine blade profile appears to be primarily a function of the stream-wise pressure gradient. The length of separation is, however, related to the onset of transition and the amplification of disturbances in the separated shear layer. The $k - \omega$ turbulence model used in the present study may therefore be able to reasonably approximate the location of the pressure induced boundary layer separation. The transition in the separated shear layer is, however, a highly complex, three-dimensional phenomenon, which depends on the upstream flow history. As documented in Wilcox (1994, 2002), the $k - \omega$ turbulence model is only capable of modelling the turbulence intensity of any convecting boundary layer disturbances and its average frequency. It is not surprising, therefore, that many flow predictions report erroneous values for the location of reattachment, or the onset of a turbulent boundary layer ahead of the measured laminar separation point. This inaccuracy is compounded by an over production of k approaching stagnation points, as well as a sensitivity of the standard $k - \omega$ model to the free stream ω value, as reported in

Menter (1992, 1993, 1994), Larsson (1997), Kok (2000) and Wilcox (2002). Under-predicting a short laminar separation bubble, close to a turbine blade leading edge, may not significantly affect the downstream flow providing a turbulent boundary layer with equivalent integral parameters is predicted downstream of the reattachment point. To this end, the location of the turbulent boundary layer onset is often 'fixed' to ensure the correct boundary layer integral parameters are predicted, as documented in Wilcox (1993, 1994, 2002).

Under the influence of a sufficiently mild adverse pressure gradient, the laminar boundary layer may remain attached to the surface of a turbine blade. Transition of the attached boundary layer occurs as the laminar boundary layer reaches a *critical* Reynolds number. Two main categories of transition are identified. Natural transition is defined by Van Hest (1996) as the *amplification and subsequent breakdown to turbulence of boundary layer instabilities*. By-pass transition occurs in boundary layers with a high turbulence intensity or strong adverse pressure gradient. Bypass transition is defined by Van Hest (1996) as a *direct nonlinear breakdown* of the boundary layer. The process of natural transition is documented in established literature on viscous fluid flows, including Schlichting (1979) and White (1991), only a brief outline is therefore given here. Natural transition begins with the amplification of small-scale disturbances in the laminar boundary layer at the critical Reynolds number, to form Tollmein-Schlichting waves. Constructive interference of unstable Tollmein-Schlichting waves form 'wave-packets' of disturbed flow, as detailed in Van Hest (1996). The specific breakdown of the wave packets to a fully developed turbulent flow remains the subject of ongoing research, but can occur via the presence of localised turbulent spots. Coalescence of the turbulent spots occurs as they move downstream until all wavenumber values of the turbulence kinetic energy spectrum are continuously populated and a fully developed turbulent boundary layer is defined. The precise route to turbulence depends on the upstream turbulence level. As the upstream turbulence level increases, transition occurs via different mechanisms. At higher upstream turbulence levels, the amplification of the upstream disturbances results in the formation of two-dimensional Tollmein-Schlichting waves,

which develop into hairpin vortices. The span-wise alignment of the hairpin vortices changes as the upstream disturbance level increases. A number of breakdown mechanisms have been identified and categorised, as described in White (1991) and Van Hest (1996). The coalescence of the turbulent spots form the fully developed turbulent flow. At high upstream turbulence levels, or under the influence of a strong stream-wise adverse pressure gradient, turbulent spots are triggered directly, leading to a by-pass type transition. The physical mechanism by which transition occurs is sensitive to a number of flow parameters. Stieger (2002) lists these as including Reynolds number, Mach number, acoustic radiation, surface roughness, surface temperature, surface curvature and flow history effects. A detailed description of recent developments regarding transition research is documented by Van Hest (1996) and Stieger (2002). The influence of the stream-wise pressure gradient on the physical mechanism of transition is discussed in Van Hest (1996) and Gostelow (2003). The $k-\omega$ model simulates the boundary layer transition process based on the relative increase in the k and ω production and dissipation terms. Wilcox (1994, 2002) provides a description of the mechanism by which transition is modelled in the $k-\omega$ model. In a turbine blade or circular cylinder flow, the flow curvature at the leading edge stagnation point gives a localised increase in k just at the onset of the laminar boundary layer. Further downstream, the reduced flow curvature and strain rate leads to the dissipation being greater in the k and ω transport equations and the boundary layer remains laminar. As fluid with a higher turbulence kinetic energy is entrained into the boundary layer, a *critical* Reynolds number is reached, at which the production of k exceeds the dissipation. The level of turbulence kinetic energy in the boundary layer continues to increase with downstream distance until the production term in the ω transport equation starts to exceed the dissipation term. This increases the magnitude of the turbulence kinetic energy dissipation term. The start of the turbulent boundary layer is then defined at the stream-wise location where the production and dissipation of k become approximately equal in magnitude. The stream-wise location for the onset of a fully turbulent boundary layer is therefore sensitive to the free stream turbulence kinetic energy and the asymptotic value of ω

approaching the surface. Wilcox (1994, 2002) advocates the use of this sensitivity as a method to explicitly define the onset of the turbulent boundary layer to match experimental measurements, as used by Chima (1996) and Larsson (1997).

Turbulent flow is characterised by an increase in diffusion and heat transfer. Standard texts on turbulent boundary layers document the presence of three main layers. Briefly, these comprise of an inner layer of fluid close to the surface which is dominated by molecular viscosity, an outer layer of fluid at the boundary layer edge which is dominated by turbulence motion, and a region of overlap. In the overlap region, both molecular viscosity and the turbulence motion are influential. Denton (1993), provides a thorough overview of entropy production in turbulent boundary layers. From this work, the following statements are drawn. Dawes (1990), reports that approximately 90% of the entropy generated in a turbulent boundary layer is generated by the inner layer due to the large velocity gradient close to the surface. The influence of boundary layer thickness on the production of entropy is approximated by Truckenbrodt (1952) and Schlichting (1979) for laminar and turbulent boundary layers respectively. The development of boundary layers under favourable pressure gradients are shown by Denton (1993) to generally reduce boundary layer dissipation losses. Conversely, an adverse pressure gradient is shown to increase dissipation loss. The total entropy produced in the boundary layer from the leading edge to a specific downstream location is defined by Denton (1993) through the definition of an *entropy thickness*. Assuming the flow remains attached to separation from the trailing edge, the entropy thickness can be used to estimate the total entropy production along the entire surface of the turbine blade, as detailed in Denton (1993).

Quantifying the boundary layer separation characteristics at the trailing edge is an important aspect in turbomachinery aerodynamics. The boundary layer separation characteristics can determine the exit flow angle, the thickness of the separating shear layers, the downstream wake characteristics and therefore the potential for work output. Simpson (2002) expresses an opinion that the criterion for separation of a turbulent boundary layer is not adequately described by a zero wall shear stress or by the presence of flow reversal alone. Simpson (1989, 2002) cate-

gorises turbulent boundary layer separation into a number of levels of detachment. These levels of detachment are based on the fraction of time the attached flow is directed upstream. The categories are defined as *incipient detachment*, *intermittent transitory detachment* and *transitory detachment*. The *detachment* point is then defined where the time averaged surface shear stress τ_w is zero. Oscillatory separation is also reported in, for example, Sieverding & Heinemann (1989, 1990), Carscallen & Gostelow (1994), Cicatelli & Sieverding (1995, 1996, 1997) and Ubaldi & Zunino (2000). Upstream of the incipient detachment point, Simpson (2002) reports that the incompressible Ludwieg-Tillmann skin friction equation, for example, and the log layer velocity profile approximations remain satisfactory. Relations between incompressible and compressible skin friction, documented for example in White (1991), should also remain satisfactory upstream of the incipient detachment point. Turbulent boundary layer separation and the influence of the upstream boundary layer on the vortex shedding characteristics from a thick trailing edge turbine blade are discussed further in Section 2.3.

Other unsteady boundary layer features present in turbine cascades include Görtler vortices and shock wave-boundary layer interaction. Görtler vortices appear in boundary layers flowing over concave surfaces. Pairs of adjacent, contra-rotating vortices are defined with a stream-wise axis of rotation. These are often observed along the pressure surface of turbine blades and are considered to contribute significantly to the transition of laminar boundary layers on concave surfaces. As Görtler vortices are not reported in past literature concerning the turbine blade modelled in the present study, this phenomenon is not detailed further in this review. Details concerning the physics of Görtler vortices are available in White (1991), Schlichting (1979) and Gostelow (1984). At supersonic free stream conditions, shock waves from adjacent blades, or from upstream blade rows, may interact with the developing boundary layer. This is observed for the turbine blade modelled in the present study at supersonic exit conditions by Carscallen & Gostelow (1994), Carscallen et al. (1999) and Gostelow (2003). A detailed discussion of literature concerning the physics of shock wave-boundary layer interaction is given in Section 2.4.

2.3 Cascade Boundary Layer/Vortex Shedding Interaction

Reviews detailing early research of vortex shedding in turbine cascades and the influence of the upstream boundary layer are provided by Sieverding & Heinemann (1989, 1990) and Cicatelli & Sieverding (1995). Experimental flow visualisations, cited in these reviews, provide a qualitative insight into the near wake flow downstream of a thick trailing edge. These include high-speed Schlieren visualisation by Bryanston-Cross & Camus (1982), Lawaczeck & Heinemann (1976), Lawaczeck, Bütefisch & Heinemann (1976) and Carscallen & Gostelow (1994); interferometry by Bryanston-Cross et al. (1981) and Desse & Pegneaux (1991), as well as smoke visualisation by Han & Cox (1982) and Sieverding et al. (2003). These flow visualisations confirm the presence of vortex shedding at subsonic, transonic and supersonic Mach numbers. Periodic vortex shedding patterns of pitch-wise asymmetry are often observed downstream of thick trailing edge turbine blades at subsonic and transonic Mach numbers, with stronger vortices observed towards the pressure surface side of the wake. This is observed, for example, by Lawaczeck et al. (1976) from a frequency analysis of a photomultiplier signal and is evident by a tighter rolling of the pressure side vortices in smoke visualisations by Han & Cox (1982) and Roberts & Denton (1996). Arnone & Pacciani (1997) show that the difference in strength of vortices shed from the suction and pressure surfaces is also associated to a greater downstream duration of the pressure surface vortices. This is based on a comparison of a turbulent prediction of the flow past a turbine blade with measurements by Cicatelli & Sieverding (1996). Schlieren visualisations by Cicatelli & Sieverding (1996, 1997) document the growth and convection of successive vortices from the suction and pressure surfaces of a turbine blade at $M_e = 0.4$ and $Re_c = 2 \times 10^6$, over the period of one vortex shedding cycle.

At supersonic Mach numbers, the near wake flow is characterised by a convergence of the separated shear layers from the pressure and suction surfaces, forming a confluence region downstream of the trailing edge. The convergence of these separated shear layers is indicative of the low static pressure on both sides of the turbine blade in this region. Shock waves are generated at the confluence region

and propagate into the flow either side of the wake, at smaller angles to the mean flow direction with increasing Mach number. The supersonic near wake flow is detailed further in Section 2.4 and is described by Sieverding et al. (1983), Denton & Xu (1989) and Brooksbank (2002). A similar confluence region downstream of an aerofoil is described by Benelmouffok & Beretta-Piccoli (1986), as cited by Cicatelli & Sieverding (1995). Schlieren visualisation by Carscallen & Gostelow (1994) indicates a replacement of the periodic vortex shedding pattern observed in subsonic and low transonic flows by a number of complex, transient vortex shedding patterns originating from the confluence region. The results of a statistical analysis by Carscallen & Gostelow (1994) on the average fraction of time dedicated to each vortex pattern is reported in Section 2.4. The frequency of vortex shedding, given by the non-dimensional Strouhal number $Str = fD_t/u_e$, varies significantly with Reynolds number and Mach number. Lawaczeck et al. (1976) report Strouhal numbers covering the range $0.25 \leq Str \leq 0.4$ over the Mach and Reynolds number ranges $0.2 < M_e < 1.1$ and $1.5 \times 10^4 < Re_{D_t} < 5 \times 10^4$. Cicatelli & Sieverding (1995) collate measured Strouhal numbers from Heinemann & Bütefisch (1977), Bryanston-Cross et al. (1981), Sieverding & Heinemann (1989) and Carscallen & Gostelow (1994). These are compared as a function of cascade exit Mach number by Cicatelli & Sieverding (1995) in Figure 2.1. As documented in Cicatelli & Sieverding (1995), the Reynolds number varies with Mach number for all measurements in Fig. 2.1 except those of Bryanston-Cross et al. (1981). The variation of Strouhal number in Figure 2.1 highlights the influence of the turbine blade geometry and loading on the frequency of vortex shedding, indicating a relationship between the boundary layer separation characteristics and the strength and frequency of the vortex shedding. From the analysis of Sieverding & Heinemann (1989, 1990), using flat plates and turbine blades with round and square trailing edges, it is suggested that the turbulence level in the separated shear layers downstream of the trailing edge largely determines the frequency of vortex shedding. This hypothesis is further substantiated by the experimental measurements of Roberts & Denton (1996). Cicatelli & Sieverding (1995) use the hypothesis of Sieverding & Heinemann (1989, 1990) and

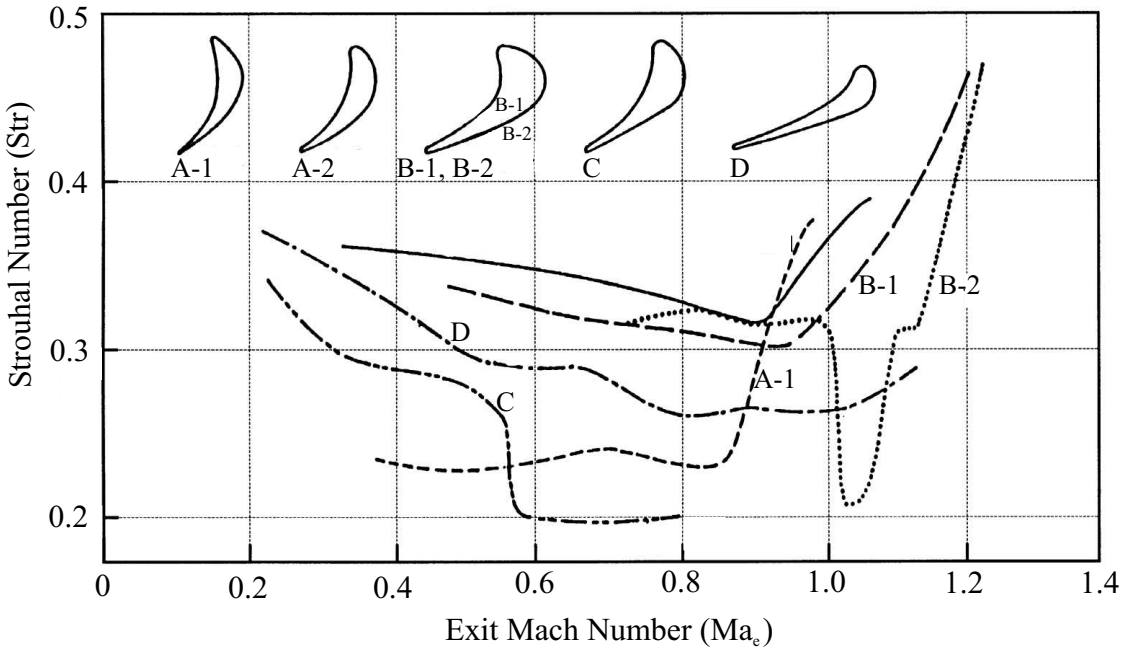

Figure 2.1: Strouhal number variation with Mach number for various turbine blade geometries, from Cicatelli & Sieverding (1995). A-1, A-2: Heinemann & Bütefisch (1977), B-1, B-2: Bryanston-Cross et al. (1981), C: Sieverding & Heinemann (1989), D: Carscallen & Gostelow (1994).

the collated results in Figure 2.1 to categorise turbine blade Strouhal numbers at exit Mach numbers up to sonic conditions according to the turbulent state of the boundary layer at separation from the trailing edge. In general, Strouhal numbers above $Str \approx 0.35$ indicate laminar boundary layers on both surfaces at separation; Strouhal numbers in the range $0.23 \leq Str \leq 0.35$ indicate a transitional boundary layer on one or both surfaces and Strouhal numbers below $Str \approx 0.2 - 0.23$ indicate transitional or turbulent boundary layers at separation on both surfaces. This categorisation indicates that turbine blades with properties favouring boundary layer transition upstream of the trailing edge, such as high blade loading close to the leading edge or high surface friction, tend to shed vortices at a lower Strouhal number. Sieverding & Heinemann (1989, 1990) postulate that it is the turbulent state and thickness of the separated shear layers rather than the turbulent state of the boundary layer that is most influential in determining the Strouhal number. Square trailing edges are observed to initiate transition of the separated shear layers for lam-

inar boundary layers. This results in a narrower Strouhal number range between wakes from a confluence of laminar boundary layers and wakes from a confluence of transitional or turbulent boundary layers, in comparison with separation from a rounded trailing edge. A physical explanation for the influence of the separated shear layer thickness and turbulence level on the vortex shedding frequency is given by Cicatelli & Sieverding (1995, 1996, 1997) for turbine blades, using an incompressible circular cylinder near wake analysis by Gerrard (1966). Gerrard (1966) proposes that the stream-wise length taken by a growing vortex, and the vortex shedding frequency, are dependent on how quickly a growing vortex can entrain sufficient fluid from the far side shear layer to cancel the near side shear layer vorticity. The cessation in circulation supply from the near side shear layer sheds the growing vortex and a new vortex with opposite vorticity forms on the other side of the wake. The increased diffusion in turbulent shear layers increases the time required to entrain sufficient fluid from the far side shear layer. As the Reynolds number increases, Gerrard (1966) proposes a balance for circular cylinders between a shortening of the formation region, defined from the cylinder to the location of entraining fluid, and the increase in entrainment time. For circular cylinders, this balance leads to a consistency of the Strouhal number for Reynolds numbers below $Re_D \approx 2 \times 10^5$. Further details on the variation of Strouhal number with Reynolds number around circular cylinders are provided in Section 2.5. Cicatelli & Sieverding (1996, 1997) propose that the increased loading and asymmetric geometry for turbine blades tend towards an earlier transition and an increased thickness of the suction surface shear layer. The difference in the turbulent state and thickness of the suction and pressure surface shear layers may destabilise the vortex shedding balance proposed by Gerrard (1966), resulting in the wide range of vortex shedding frequencies observed in Figure 2.1. The difference in shear layer thickness may therefore be responsible for the increase in strength and duration of the pressure surface vortices observed in Arnone & Pacciani (1997), and the better resolved pressure side vortices observed in Han & Cox (1982) and Roberts & Denton (1996). From an analysis of the wake, Roberts & Denton (1996) report that over three quarters of the wake stagnation

pressure loss is created in the first ten trailing edge diameters. After this point, the rate of mixing in the wake is reported to be relatively low. The reliance of vortex shedding on the separated shear layer thickness holds potential issues for the accuracy of numerical predictions. The standard $k-\omega$ turbulence model of Wilcox (1988) is known to over-predict spreading rates in free shear layers. This is documented, for example, in Menter (1992, 1994), Kok (2000) and Wilcox (2002). For this reason, a cross-diffusion term has been incorporated into the $k-\omega$ turbulence model for this study. This is described further in Section 3.4.3. Currie & Carscallen (1998) report a grid resolution sensitivity of the vortex shedding frequency downstream of the turbine blade modelled in the present study. Currie & Carscallen (1998) also cite excessive numerical dissipation in this region as the most probable cause of an inaccurate prediction of base pressure. Denton & Xu (1989), Denton (1993), Dunham (1995) and Roberts & Denton (1996) state that, for subsonic exit trailing edge conditions, approximately a third of the profile loss in a two-dimensional turbine cascade is caused by wake induced mixing losses. However, results from Mee et al. (1992), as cited in Denton (1993), indicate that this proportion increases significantly as the trailing edge Mach number rises above unity. The reasons for this are evident from the compressibility analysis in the following section.

2.4 Compressibility Effects

Compressibility is generally accepted as affecting air flows above a Mach number of 0.3. This is the Mach number at which the isentropic static density is around 95% of the stagnation density, as described in Anderson (1985). For increasing transonic Mach numbers, over the range $0.3 \leq M_e \leq 1.2$, turbine cascade flows are increasingly influenced by compressible effects such as the presence of shock waves around the trailing edge and near wake regions. Compressible flow features are similarly observed on the downstream side of circular cylinders in transonic cross-flows. Zdravkovich (1997) divides the free stream transonic Mach number range $0.4 \leq M_\infty \leq 1.2$ into a number of separate regimes for circular cylinders, based on the strength and location of shock wave behaviour. These are:

1) An *intermittent shock wave* regime ($0.4 \leq M_\infty \leq 0.65$);
2) A *permanent shock wave* regime ($0.65 \leq M_\infty \leq 0.8$);
3) A *wake shock wave* regime ($0.8 \leq M_\infty \leq 1.0$);
4) A *detached bow shock wave* regime ($1.0 \leq M_\infty < 1.2$).

A review of compressible effects in a circular cylinder flow is given, based on the Mach number modelled in this study, in Section 2.5. Similar Mach number flow regimes can be defined for turbine cascade flows from experimental and numerical flow visualisations. These include Lawaczeck & Heinemann (1976), Carscallen & Gostelow (1994), Cicatelli & Sieverding (1995), Moustapha et al. (1993), Carscallen et al. (1996, 1999), Currie et al. (1998), Pieringer et al. (2001) and Gostelow (2002). These flows exhibit compressible effects that are specific to the turbine cascade under study and depend on the blade geometry and loading. General trends may, however, be noted.

At low transonic discharge Mach numbers, local regions of supersonic flow are defined, which form very weak shock waves as the flow undergoes recompression. Outward propagating pressure waves, from vortex shedding and oscillatory boundary layer separation at rounded trailing edges, propagate upstream through the subsonic flow region. Cicatelli & Sieverding (1996, 1997) observe that pressure waves from an oscillating boundary layer separation propagate a significant distance upstream of the trailing edge at $M_e = 0.4$. Schlieren visualisation of the turbine cascade modelled in the present study, at $M_e = 0.71$, is reproduced from Gostelow (2002) in Figure 2.2. This shows a periodic vortex shedding pattern, typical of other thick trailing edge turbine cascades at similar Mach number. Pressure waves are highlighted travelling upstream, as described in Cicatelli & Sieverding (1996, 1997). These waves are observed to impinge on the suction surface of the adjacent blade and are reflected back towards the pressure surface. Shock waves are observed in the near wake region as the Mach number increases. These shock waves are observed to fluctuate in a series of Schlieren photographs in Cicatelli & Sieverding (1995), taken over the

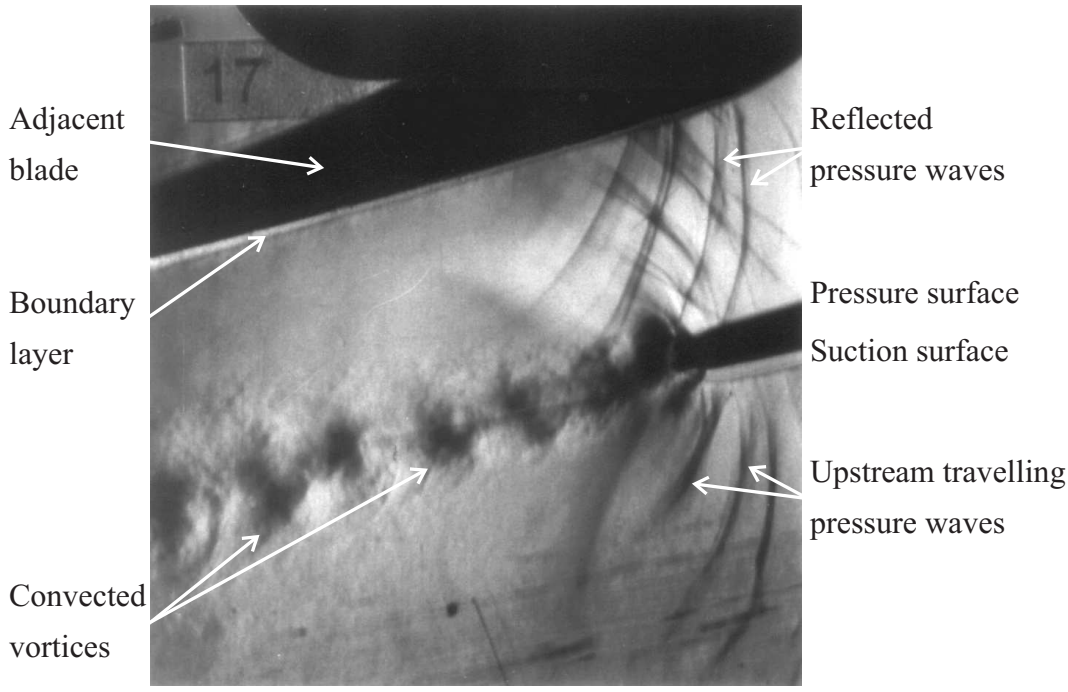

Figure 2.2: Schlieren visualisation of a turbine cascade at a discharge Mach number of $M_e = 0.71$, from Gostelow (2002).

period of half a complete vortex shedding cycle. In the time dependent visualisation of Cicatelli & Sieverding (1995), shock waves oriented at shallow angles to the mean flow normal direction stem from the centre of the growing vortices. These shock waves are reported to travel downstream for a short distance with each convecting vortex, until a new vortex of sufficient circulation is formed at the trailing edge. The shock wave front is then observed to shift to the location of the new vortex in the formation region. Unsteady, oscillatory shock wave movement is reported by Denton (1993) to increase the entropy generation with respect to stationary shock waves. The increase in entropy generated during the upstream movement of a shock wave is considered to be greater than the corresponding decrease as the shock moves downstream. Therefore, the overall entropy production increases.

Carscallen & Gostelow (1994) propose that, above a discharge Mach number of $M_e = 0.96$, the formation and shedding of vortices is no longer associated with the trailing edge surface of the turbine blade but migrates downstream with the interaction of the trailing edge shock waves. Embedded shock waves are also observed in

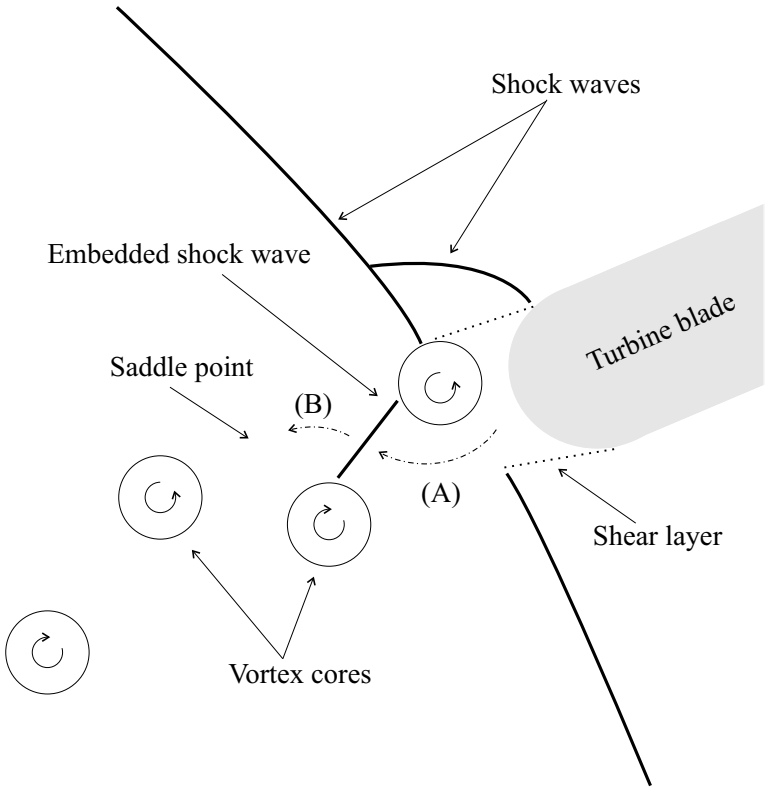

Figure 2.3: Representation of the instantaneous near wake flow under transonic discharge conditions. $- \cdot -$ local flow direction, (A) flow accelerated to local supersonic conditions in channel between vortices, (B) recompression of flow to local subsonic conditions across the embedded shock wave.

the near wake region, as shown in the Schlieren visualisations of Cicatelli & Sieverding (1995). The origin of these shock waves can be explained using Figure 2.3. Cicatelli & Sieverding (1995) define a channel of accelerated fluid travelling between adjacent vortices. Close to the trailing edge, this channel flow can be accelerated to local supersonic conditions. This is defined by the region labelled (A) in Figure 2.3. As the local supersonic flow approaches the local *saddle point*, of irrotational flow between successive vortices on the same side of the wake, the local flow undergoes a compression back to subsonic conditions. The subsonic flow immediately following this recompression is labelled (B) in Figure 2.3. An embedded shock wave forms at the recompression location.

A Schlieren photograph of the turbine blade modelled in the present study, tested at a discharge Mach number of $M_e = 0.97$, is reproduced from Gostelow (2002) in

Figure 2.4. Shock waves can be observed originating from the near wake region. These shock waves propagate normal to the mean flow direction, across the turbine blade throat, leading to choked conditions. In Figure 2.4, the pressure surface shock wave impinges on the suction surface of the adjacent blade. At certain flow regimes, shock wave impingement on a turbine blade suction surface can cause the boundary layer to separate. As the separation point has a significant influence on the base flow and near wake development, the flow conditions leading to a shock induced boundary layer separation are investigated further. Inger & Mason (1976) describe the impact of a normal shock wave on a developing laminar or turbulent boundary layer. For impingement of a very weak shock, defined by Inger & Mason (1976) as shock waves with a peak supersonic upstream Mach number below $M_{peak} = 1.05$, even a laminar boundary layer may not necessarily separate from the surface. However, transition of the boundary layer is expected downstream of the shock impingement. As the shock wave strength increases, laminar boundary layers are more susceptible to separation than turbulent boundary layers, due to a greater sensitivity to local changes in the adverse pressure gradient. Inger & Mason (1976) define an approximate condition for separation of a turbulent boundary layer due to impingement of a normal shock wave as requiring a peak upstream Mach number in excess of $M_{peak} = 1.3$. This threshold closely matches the value of $M_{peak} \geq 1.4$ reported in Atkin & Squire (1992), as cited by Denton (1993). The analytical results of Inger & Mason (1976) and the physical description of oblique shock waves in Délery & Bur (2000) imply that a number of changes occur as a turbulent boundary layer approaches an impinging shock wave. The increase in static pressure downstream of the shock wave is transmitted through the subsonic region of the boundary layer, close to the surface. This causes a thickening of the boundary layer ahead of the shock wave position, resulting in local curvature of the streamlines in this region. In addition to direct stagnation pressure losses across a shock wave, caused by high viscous stresses and heat conduction, indirect losses also occur, as reported in Denton (1993). These additional losses are created from a number of sources, such as increased dissipation in shock-induced separation bubbles, or premature shock-

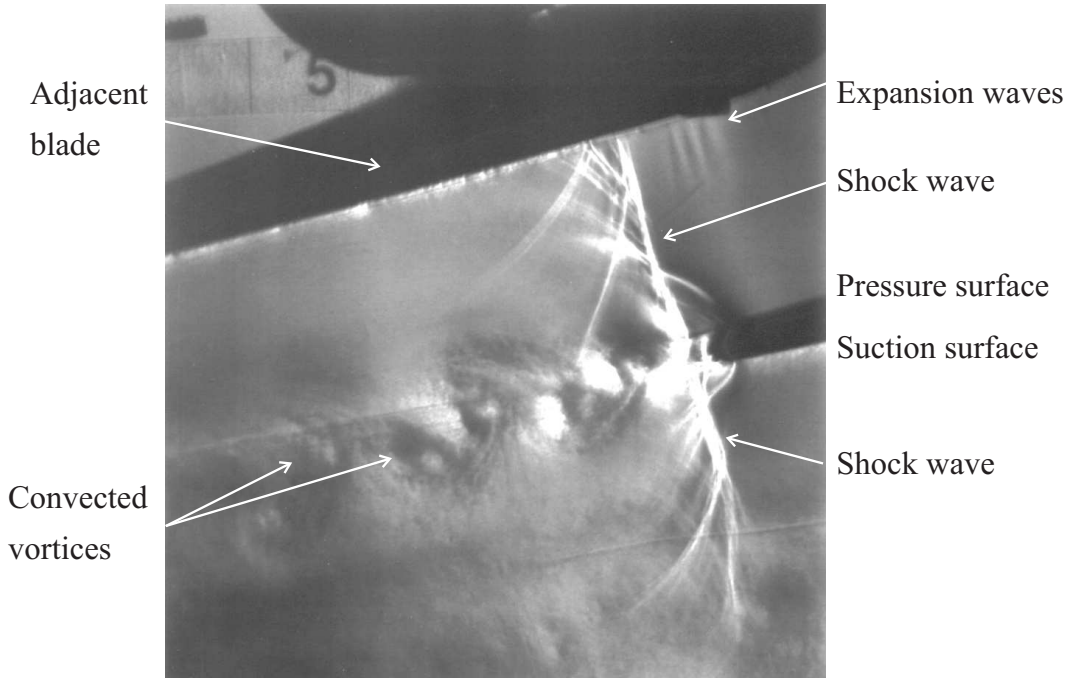

Figure 2.4: Schlieren visualisation of a turbine cascade at a discharge Mach number of $M_e = 0.97$, from Gostelow (2002).

induced transition of laminar boundary layers. The physics of shock wave-boundary layer interaction are described in a range of literature, including Shapiro (1953), Inger & Mason (1976), Atkin & Squire (1992) and Délery & Bur (2000).

Above a sonic discharge Mach number, a change in the near wake flow structure is observed. This change has a significant impact on the downstream vortex shedding characteristics. Denton & Xu (1989) describe the flow for supersonic trailing edge conditions. The turbine blade geometry dictates that a supersonic flow at the trailing edge should initially appear on the suction surface. If both surfaces are supersonic at the trailing edge, the separated shear layers on both sides turn towards the opposite surface generating expansion waves. These are shown in Figure 2.5. A confluence region is defined at the convergence of these two shear layers. Denton & Xu (1989) define the origin of the two wake shock waves in Figure 2.5, as the point at which the two shear layers turn towards the common downstream mean flow direction. Denton (1993) reports that the major source of entropy production within a supersonic near wake region originates from viscous dissipation

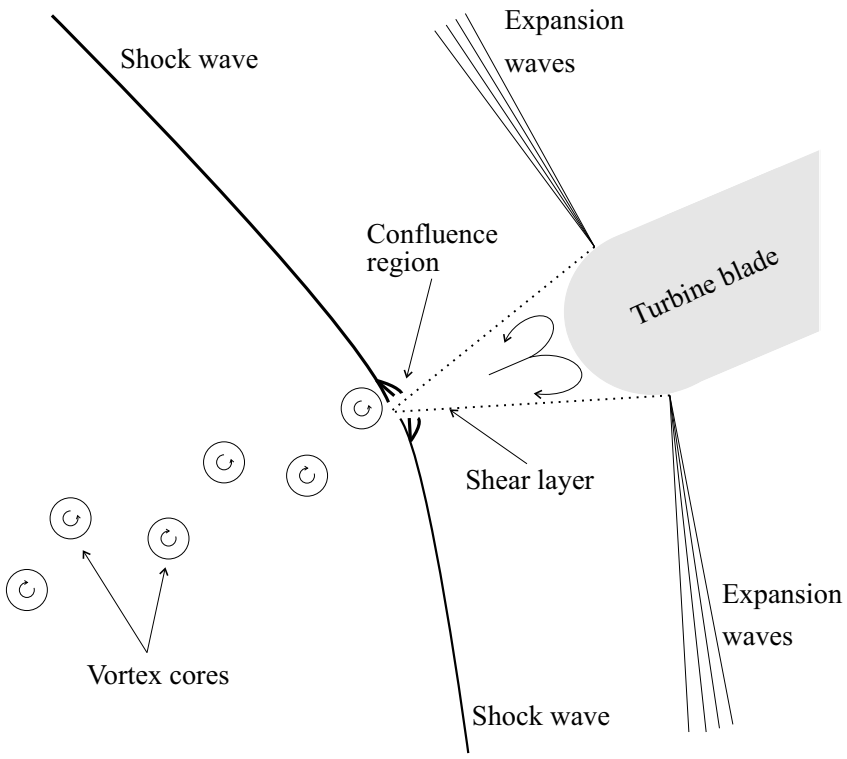

Figure 2.5: Representation of the confluence region downstream of a turbine blade at supersonic exit Mach numbers, based on Denton & Xu (1989).

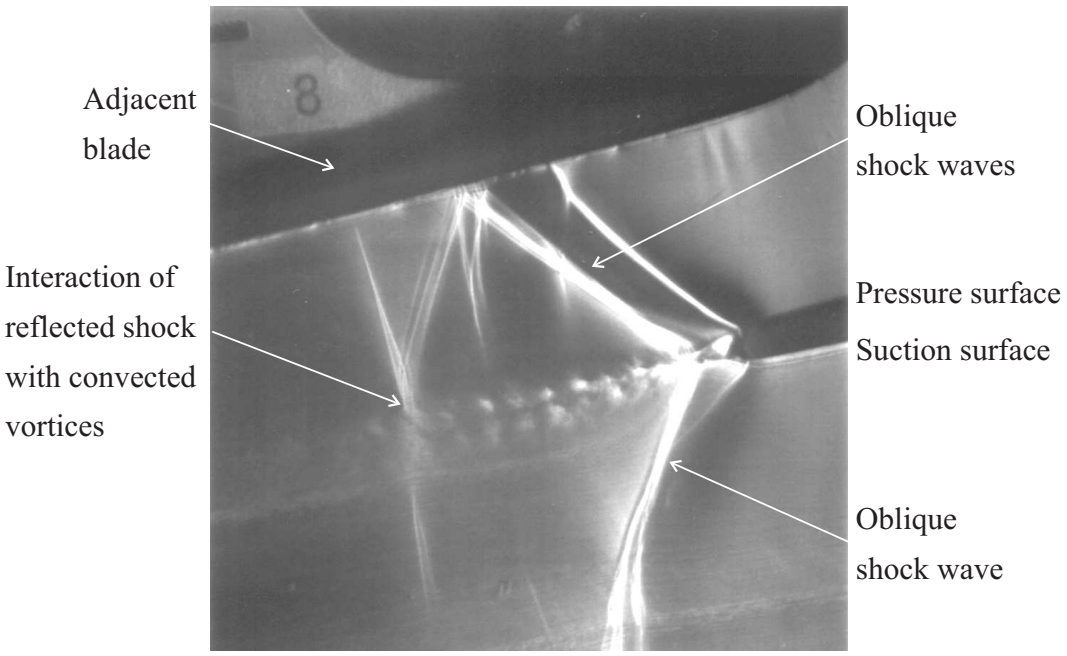

Figure 2.6: Schlieren visualisation of a turbine cascade at a discharge Mach number of $M_e = 1.09$, from Gostelow (2002).

in the converging shear layers and the strong trailing edge shock waves. As the Mach number increases further, the entropy produced by these trailing edge shock waves decreases as the shock waves become increasingly oblique to the mean flow direction. This is supported by Mee et al. (1992), who demonstrate an increasing proportion of the profile loss in a turbine blade is caused by shock losses up to $M_e = 1.0$. At $M_e > 1.0$, this proportion gradually decreases with further increases in discharge Mach number. The wake at supersonic discharge Mach numbers is unsteady and may be dominated by transient, multi-mode vortex shedding patterns that originate from the confluence region. Schlieren visualisation of the flow downstream of the turbine blade modelled in the present study, at a discharge Mach number of $M_e = 1.09$, is shown in Figure 2.6, from Gostelow (2002). Carscallen & Gostelow (1994) and Carscallen et al. (1996) have undertaken a statistical analysis of the transient vortex shedding patterns, downstream of this turbine cascade, at $M_e = 1.16$. A number of vortex shedding patterns are identified and the average percentage occurrence of each vortex pattern is reported. The patterns observed in Carscallen & Gostelow (1994) and Carscallen et al. (1996) are represented dia-

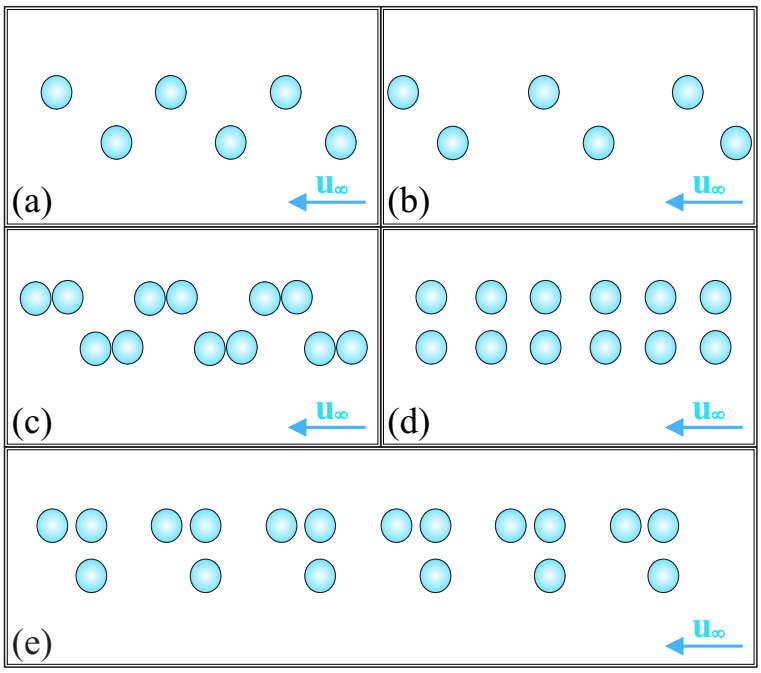

Figure 2.7: Vortex shedding patterns in a supersonic turbine blade wake, from Carscallen et al. (1996). (a) Classic von Kármán vortex street, (b) leaning von Kármán vortex street, (c) doublets, (d) couples, (e) hybrid.

grammatically in Figure 2.7. The percentage occurrence of each pattern is given in Table 2.1. The influence of compressibility on the turbine blade base pressure at increasing transonic Mach numbers is discussed in Cicatelli & Sieverding (1995) over the range $0.7 \leq M_e \leq 1.4$ based on graphical data from Michel & Kost (1982). The base pressure p_b is reported to decrease as the Mach number increases, within the transonic region, from $p_b \approx 0.59 p_{s\infty}$ at $M_e = 0.8$ to $p_b \approx 0.38 p_{s\infty}$ at $M_e = 1.0$, where $p_{s\infty}$ is the upstream stagnation pressure. This decrease may be due to an increase in the strength of the periodic vortex shedding in this region. Above $M_e = 1.0$, the base pressure remains constant and displays an insensitivity to further increases in Mach number up to $M_e \approx 1.1$. This insensitivity may result from the migration of vortex shedding from the trailing edge to the confluence region. Above $M_e \approx 1.1$, the base pressure is shown to decrease once more due to an increasing expansion around the trailing edge.

Measurements on the same blade profile modelled in the present study confirm a decrease in base pressure with increasing Mach number, approaching sonic trailing

Vortex shedding pattern	Label in Figure 2.7	Occurrence in wake (%)
No definable pattern	n/a	35.5
Classic von Kármán vortex street	(a)	30.5
Leaning von Kármán vortex street	(b)	16.0
No coherent structure	n/a	9.0
Doublets	(c)	4.0
Couples	(d)	3.5
Hybrid	(e)	1.5

Table 2.1: Percentage occurrence of transient wake flow patterns, from Carscallen et al. (1996).

edge conditions. This is also attributed by Carscallen et al. (1996) to an increase in vortex shedding strength. A partial recovery of the base pressure is however noted between $0.95 \leq M_e \leq 1.0$ by Carscallen et al. (1996). This is attributed to the migration of the vortex shedding origin downstream, resulting in an intermittent vortex shedding pattern. In contrast to the insensitivity of base pressure to increases in Mach number at $M_e > 1$ reported in Cicatelli & Sieverding (1995), from Michel & Kost (1982), Carscallen et al. (1996) report a gradual increase in the base pressure with increasing Mach number. As well as the reported change in base pressure approaching $M_e = 1.0$, Carscallen et al. (1996) also observe changes caused by the redistribution of stagnation temperature and pressure in the wake. This is further addressed in Section 2.6.

Placing this physical review of compressibility effects into context with the turbulence model used in this study, Wilcox (2002) reports that two-equation turbulence models should be capable of reasonably predicting shock wave/turbulent boundary layer interactions. Currie & Carscallen (1998) and Carscallen et al. (1998, 1999) report results from a numerical prediction, using the $k - \omega$ model, on the turbine blade used in the present study. From the numerical Schlieren provided, reflection of an oblique shock wave is observed from the suction surface of the adjacent blade. No adverse effects from the shock wave-boundary layer interaction are documented and a good overall comparison with the experimental Schlieren visualisation is observed.

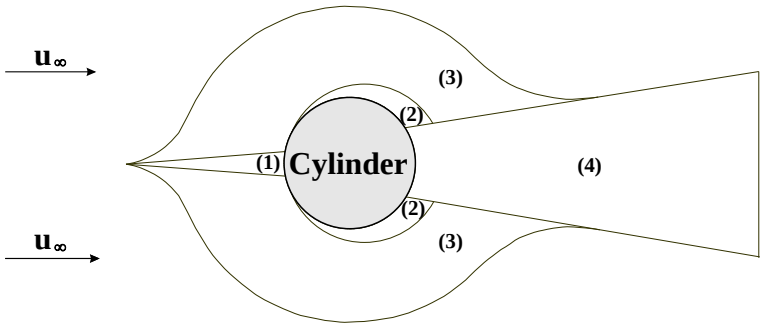

Figure 2.8: Flow regions around a cylinder in cross-flow. (1) Stagnation region, (2) boundary layer development, (3) disturbed and accelerated flow, (4) wake region.

2.5 The Flow Around Circular Cylinders

The combination of complex, unsteady flow physics and a simple geometry makes the flow around a circular cylinder popular as a test case to validate numerical prediction methods. Recent examples include Shang (1982), Salas (1983), Pandolfi & Larrocca (1989), Song & Yuan (1990), Behr et al. (1991), Botta (1995), Breuer (1998, 2000), and de With et al. (2003).

Comprehensive reviews on the physics of the flow around a circular cylinder are available in Morkovin (1964) and Zdravkovich (1997). From Zdravkovich (1997), the flow around a circular cylinder, at typical engineering scale Reynolds numbers ($Re_D > 200$), can be divided into four separate regions, as shown in Figure 2.8. These are:

(1) A narrow *stagnation* region of retarded flow approaching the cylinder;
(2) Boundary layer development on the surface of the cylinder;
(3) Disturbed and accelerated flow outside of the boundary layer;
(4) A separated wake region downstream of the circular cylinder.

The flow features around a circular cylinder in a cross-flow share similarities with those around a turbine blade, as reviewed in Sections 2.2 to 2.4. In a very large aspect ratio cylinder (span $\gg$ diameter), the boundary layer development, separation and wake characteristics display a similar dependency on the free stream

Reynolds number, turbulence intensity, surface roughness and compressibility. Consider a circular cylinder in cross-flow with low free stream turbulence intensity and a hydraulically smooth surface. A series of Reynolds number regimes are defined, based on the stream-wise location of transition downstream of the forward stagnation point. The low Reynolds number regimes are described in detail in a number of publications, including Morkovin (1964), Williamson (1996), Zdravkovich (1997) and Fey et al. (1998).

The Reynolds number regimes of interest to the present study are the *critical*, *super-critical* and *post-critical* regimes, which apply to Reynolds numbers above $Re_D \approx (3.8 \sim 4.0) \times 10^5$:

(1) The *two-bubble* regime: $(3.8 \sim 4.0) \times 10^5 \leq Re_D \leq (0.5 \sim 1.0) \times 10^6$,
(2) The *super-critical* regime: $(0.5 \sim 1.0) \times 10^6 \leq Re_D \leq (3.4 \sim 6.0) \times 10^6$,
(3) The *post-critical* regime: $Re_D \geq (3.4 \sim 6.0) \times 10^6$.

These regimes give flow patterns that are equivalent to those observed in the thick trailing edge turbine blade analysis of Carscallen et al. (1999). At the *two-bubble* critical regime, laminar boundary layers develop from the cylinder upstream stagnation point over the windward surface. Outside of the boundary layer, the flow accelerates around the cylinder to a maximum induced velocity at $\Delta\theta \approx 60^\circ$ from the leading edge. Further along the cylinder, the adverse pressure gradient induced by the outer flow causes a boundary layer separation. At $(3.8 \sim 4.0) \times 10^5 \leq Re_D \leq (0.5 \sim 1) \times 10^6$, the separated boundary layer undergoes transition and reattaches as a turbulent boundary layer, terminating a laminar separation bubble on both sides of the cylinder. Hence, the *two-bubble* regime. Subsequent increases in the Reynolds number moves transition further upstream to a location ahead of the laminar boundary layer separation. This is reported to occur intermittently along the span of the cylinder at first (super-critical regime), eventually occurring uniformly along the cylinder span (post-critical regime) at higher Reynolds numbers. Further increases in Reynolds number cause incrementally ear-

lier transition of the laminar boundary layers. Published measurements, including Weiselsberger (1922), Achenbach (1968), James et al. (1979) and numerical predictions by Ishii et al. (1985) and Wang et al. (2001), in the *critical*, *super-critical* and *post-critical* regimes, show a rapid decrease of the drag coefficient, followed by a plateau with increasing Reynolds number. This is caused by a downstream movement of the final separation point. The overall result is a pitch-wise narrowing of the wake. The base pressure displays a plateau in this regime, as plotted by Williamson (1996) from data by Flaschbart (1929), Bearman (1969) and Shih et al. (1992).

The Reynolds number of the flow modelled in the present study, $Re_D = 6.87 \times 10^5$, falls between the *two-bubble* and *super-critical* regimes. The two-dimensional flow prediction is, however, unable to reproduce the three-dimensional span-wise variation in transition associated to the super-critical regime. The current prediction is therefore expected to predict either symmetric laminar separation bubbles, an onset of turbulence ahead of the boundary layer separation points, or remain laminar to separation. The specific flow details are, of course, dependent on the free stream turbulence intensity and the compressible flow features at the present transonic Mach number. A review of published data on the influence of the free stream turbulence intensity at $Re_D \approx 6 \times 10^5$ is available in Zdravkovich (1997). This includes proposals for the replacement of the individual Reynolds number and turbulence intensity variables by a common variable, combining both Re_D and Tu_∞. Data from Kiya et al. (1982) indicates that $Re_D^{1.34} Tu_\infty$ yields a reasonable data collapse for drag and base pressure coefficients.

Compressible effects largely dominate in the boundary layer separation and vortex shedding characteristics at transonic Mach numbers. Mach number regimes exist for a circular cylinder in cross-flow that are analogous to those for a turbine blade with a thick trailing edge. The latter is described in Section 2.4. At $M_\infty > 0.4$, the circular cylinder flow exhibits an intermittent shock wave regime ($0.4 \leq M_\infty \leq 0.65$), a permanent shock wave regime ($0.65 \leq M_\infty \leq 0.8$), a wake shock wave regime ($0.8 \leq M_\infty \leq 1.0$) and a detached bow shock regime ($M_\infty \geq 1.0$).

The circular cylinder modelled in the present study lies within the *intermittent shock wave* regime. Zdravkovich (1997) reproduces a series of Schlieren photographs from Dyment & Gryson (1979) at a transonic Mach number of $M_\infty = 0.64$ and super-critical Reynolds number of $Re_D = 1.35 \times 10^6$. These show a shock wave moving along the surface of the cylinder in the upstream direction during the formation of each vortex. The upstream moving shock wave is located on the same pitch-wise side as the growing vortex. No corresponding shock wave is observed on the opposite side until the vortex is shed and a new vortex, with opposite vorticity, begins to grow from the other pitch-wise side of the cylinder. From Denton (1993), the upstream movement of the shock wave should increase the entropy production with respect to a stationary shock wave. At $M_\infty = 0.6$, the surface pressure distribution, drag coefficient and Strouhal number are reported to display a moderate independence to the free stream Reynolds number. This is evident in surface pressure distributions by Murthy & Rose (1978) at $M_\infty = 0.6$, $Re_D = 1.66 \times 10^5$ and $Re_D = 5 \times 10^5$, drag coefficients collated by Zdravkovich (1997), as well as Strouhal number variations with Reynolds number and Mach number by Murthy & Rose (1978). These are collectively reported by Zdravkovich (1997). This Reynolds number independence initially appears at odds with the Reynolds number variation reported at the start of this section. This Reynolds number independence, however, is attributed to the presence of radial surface shock waves. The radial shock waves fix the boundary layer separation location and induce the onset of transition in laminar separated shear layers. This is similar to the influence of a square trailing edge on the shear layer thickness and turbulence level, as documented in Section 2.3.

2.6 Energy Separation in Vortex Dominated Wake Flows

The earliest acknowledged measurements of energy separation behind a bluff body are reported in Eckert & Weise (1943), after observing a drop in temperature of approximately $20°C$ at the base of a circular cylinder, with respect to the free stream conditions. The time averaged static temperature records in Eckert & Weise (1943) come from a surface embedded thermocouple, at the base of a hollow rubber cylinder.

The measurements reported in Eckert & Weise (1943) are substantiated by the report of Ryan (1951), in which an extension to this analysis incorporates other blunt bodies. Ryan (1951) concludes that energy separation can occur behind any blunt body subjected to a periodic vortex shedding. The link between energy separation and vortex shedding is further substantiated in two analytical models of a vortex street by Schultz-Grunow (1951) and Ackeret (1954). Thomann (1959) documents the relationship between vortex shedding strength and the time averaged stagnation temperature decrease downstream of a circular cylinder and a triangular wedge. Using a splitter plate to suppress vortex shedding, Mach numbers in the range $0.5 \leq M_\infty \leq 3.0$ are considered. A recovery factor R can be defined as

$$R = \frac{T_b - T_\infty}{T_s - T_\infty}, \tag{2.2}$$

where, T_b is the surface temperature measured at the base of the cylinder or wedge. T_s is the free stream stagnation temperature. T_∞ is the free stream static temperature, calculated using T_s and the free stream Mach number M_∞. Thomann (1959) records a decrease in the recovery factor at low transonic Mach numbers, which falls to $R \approx -0.2$ at $M_\infty \approx 0.65$. Above $M_\infty \approx 0.65$, an increase in the recovery factor continues to $0.8 \leq R \leq 1.0$ at $1.0 \leq M_\infty \leq 3.0$. The increase in the recovery factor approaching $M_\infty = 1.0$ is attributed by Thomann (1959) to a decrease in the strength of the vortex shedding, due to increasing compressibility effects. Above $M_\infty = 1.0$, a similar trailing edge structure to Figure 2.5 defines the near wake region for the cylinder and triangular wedge. The downstream movement of the vortex formation region to the confluence region results in a decrease in the recovery temperature deficit.

Deich et al. (1976) report condensation in the wake region of a steam cascade, which is attributed to the periodic vortex shedding. Vortex shedding, as a mechanism for the measured reduction in stagnation temperature at the centre of a wake, is investigated further by Kurosaka et al. (1987). Kurosaka et al. (1987) document the use of acoustic resonance to enhance the vortex shedding in a circular cylinder flow. The objective is to establish whether a relationship exists between the vortex

shedding intensity and the wake temperature recovery. Results from Kurosaka et al. (1987) support the existence of such a relationship. Comparison of the span-wise velocity, base pressure and temperature recovery distribution over the Mach number range confirms the propositions of Schultz-Grunow (1951), Ackeret (1954), Ryan (1951), Thomann (1959) and Deich (1976). A time accurate numerical study using an explicit finite difference method shows local regions of flow with an instantaneous stagnation temperature higher than the free stream value, as well as localised regions lower in stagnation temperature than the free stream condition. Furthermore, localised regions of higher and lower than free stream stagnation pressure are predicted at stream-wise locations corresponding to those of the instantaneous stagnation temperature extrema. Kurosaka et al. (1987) provide an explanation for the energy separation mechanism using a hypothetical fluid particle flowing around a vortex, which is convected in the downstream direction. Depending on the relative velocity of the vortex and the particle, three particle paths are defined. A *curtate* particle path is defined for a downstream fluid velocity, u_1, greater than that of the angular particle velocity, u_θ. A *cycloidal* particle path is defined for $u_1 = u_\theta$, and a *prolate* path is defined for $u_1 < u_\theta$.

A graphical representation of a fluid particle travelling along a curtate pathline, at a fixed radius from the centre of a downstream moving vortex, is given in Figure 2.9. The fluid particle is represented at constant time intervals along the pathline by solid red circles in this figure. The downstream moving vortex is represented at five equi-spaced locations by dotted black circles. The vortex at intermediate times is represented by solid grey circles. The vortex moves downstream at a constant velocity in Figure 2.9. The fluid particle proceeds around the vortex at a constant rotational speed. The direction of rotation is highlighted by arrows within the vortex.

Figure 2.9 shows a deceleration of the fluid particle over the first half of the cycle, as the particle passes downstream of the vortex centre. The particle deceleration over the course of this movement is highlighted by the particle spacing at (i) and (ii) in this figure. The deceleration between (i) and (ii) in Figure 2.9 is due to the

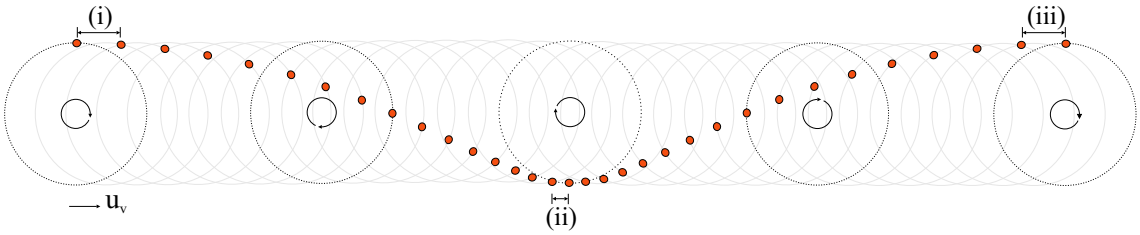

Figure 2.9: Representation of a fluid particle travelling a curtate pathline around a downstream moving vortex. The vortex is moving at a constant downstream velocity. The solid circles represent the progress of the fluid particle, at a constant angular velocity, travelling around the vortex. The vortex is represented, at five equi-spaced intervals, by dotted circles. Arrows within each of these vortices highlight the direction of rotation. At intermediate times, the vortex progress is shown by solid grey lines. (i)-(iii) Distance between successive particle positions. These lengths, (i)-(iii), illustrate the change in particle velocity along the pathline with respect to the constant vortex velocity.

centripetal force, which acts on the particle in the direction of the vortex centre. A component of the centripetal force can be resolved along the particle pathline. This component of the centripetal force opposes the downstream motion of the particle. The stagnation temperature of the fluid particle can be represented as:

$$T_s = T + \frac{(u_1^2 + u_2^2)}{2c_p}, \tag{2.3}$$

where T_s is the particle stagnation temperature. T is the particle static temperature. u_1 and u_2 are Cartesian components of the particle velocity. From Eqn. 2.3, the deceleration of the fluid particle between (i) and (ii) in Figure 2.9 is shown to result in a local decrease of the particle stagnation temperature. A decrease in the local stagnation pressure also occurs between (i) and (ii).

As the particle travels from the bottom of the vortex to the top, upstream of the vortex centre, a local acceleration of the particle occurs. This acceleration is evident in Figure 2.9 by comparing the particle spacing at (ii) and (iii). The fluid particle acceleration between (ii) and (iii) results from a component of the centripetal force, which acts in the downstream direction along the particle pathline. From Eqn. 2.3, a local increase in the stagnation temperature occurs between (ii) and (iii). A similar increase in the local stagnation pressure occurs over this interval.

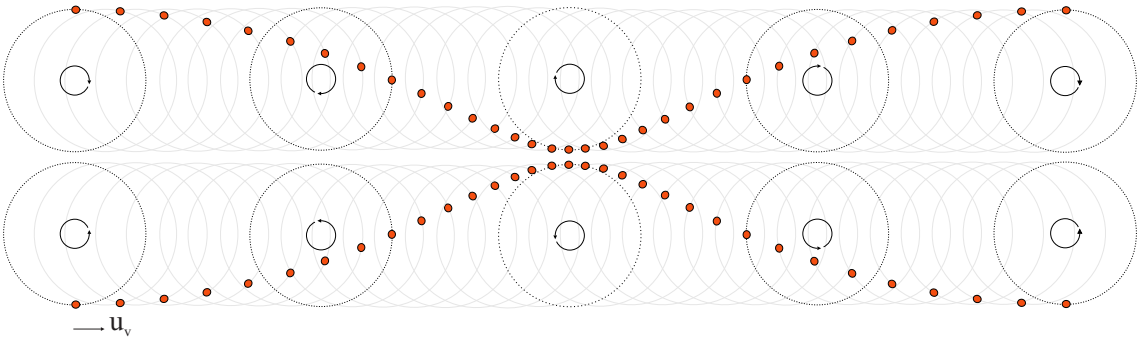

Figure 2.10: Diagrammatical representation of two fluid particles travelling curtate pathlines in a von Kármán vortex street. The von Kármán vortex street is approximated as two isolated vortex rows. Each vortex is moving at a constant downstream velocity. Each fluid particle is rotating around a vortex at a constant angular velocity. The solid red circles represent the fluid particles travelling around the downstream moving vortices.

The overall result of the relative movement of the vortex and the fluid particle is a redistribution of T_s and p_s, to increase on one side of the vortex and decrease on the opposite side. For example, the instantaneous velocity of a particle directly above the centre of the vortex, at (i) or (iii) in Figure 2.9, is a combination of the vortex velocity and the local tangential velocity. As both components of velocity are directed downstream, the local velocity and stagnation properties of the particle are able to rise above the free stream condition. Conversely, for a particle directly below the centre of the vortex, at (ii) in Figure 2.9, the instantaneous velocity of the particle is a combination of the downstream directed vortex velocity and the upstream directed tangential velocity. The opposition of the two velocity components results in a particle velocity, and stagnation properties, below the free stream condition.

In summary, the downstream movement of the vortex causes an effective 'exchange of work', from fluid particles moving downstream of the vortex centre, to fluid particles moving upstream of the vortex centre. Kurosaka et al. (1987) draw an analogy between this process and that of a 'compressor-turbine' cycle.

Figure 2.10 highlights this energy separation mechanism in the context of an idealised von Kármán vortex street. The von Kármán vortex street in Figure 2.10 is approximated as two isolated vortices, of opposing rotation, moving downstream at a constant velocity in the downstream direction. Figure 2.10 highlights the overall

reduction in velocity, T_s and p_s that occurs at the centre of the wake, along with the increase in velocity, T_s and p_s that occurs locally along the outer edges of the wake. The idealised situation in Figure 2.10 is, however, complicated in physical flows by the presence of additional 'cross-over' particle pathlines, as reported by Kurosaka et al. (1987). Cross-over pathlines occur as a fluid particle enters on one side of the vortex street and exits on the opposite side of the vortex street. These pathlines are highlighted by Kurosaka et al. (1987) through the injection of a dye into water, downstream of a circular cylinder in a uniform cross-flow.

The stagnation temperature and pressure distribution of Kurosaka et al. (1987) is supported by Ng et al. (1990) through temperature and pressure measurements on a cylinder at $M_\infty = 0.4$ and $Re_D = 2.3 \times 10^5$. Ng et al. (1990) report a maximum in the stagnation temperature and pressure fluctuations at a distance of two cylinder diameters downstream of the cylinder base. This indicates that $2D$ downstream of the cylinder is close to the point of maximum circulation of the growing vortices in this case. The hypothesis of Kurosaka et al. (1987) is also applied to a shear layer in a channel by O'Callaghan & Kurosaka (1993). O'Callaghan & Kurosaka (1993) conclude that the magnitude of the total temperature separation is approximately proportional to the square of the difference in Mach number between the fast and slow moving fluid streams. This may possibly be extended to the difference between the free stream flow and the mean wake flow downstream of a circular cylinder or turbine blade.

Carscallen & Oosthuizen (1989) extend this research to include thick trailing edge turbine blades, at Mach numbers of $0.7 \leq M_e \leq 1.16$. A Mach number dependency in the energy separation characteristics is measured, and peaks at $M_e = 0.95$. Energy separation is then reported to decrease for $M_e \geq 1.0$. These results lead to the statistical analysis and high speed Schlieren visualisation reported in Section 2.4. Carscallen et al. (1998, 1999) and Hogg et al. (1997) have subsequently extended this research to a time accurate analysis using a specifically designed fast response stagnation temperature probe. The pitch-wise asymmetric vortex shedding discussed in Section 2.3 is reported to cause a pitch-wise asymmetry in stagnation temperature

and pressure. This difference in stagnation temperature, between the suction and pressure surface sides of the wake, is quantified by Carscallen et al. (1998, 1999) and Hogg et al. (1997). The instantaneous hot spots on the pressure side are approximately $8°K$ above the free stream stagnation temperature. In contrast, the suction side hot spots are approximately $6°K$ above the free stream stagnation temperature. The wake centre is approximately $16°K$ lower than the free stream stagnation temperature. Instantaneous entropy contours show the maximum entropy value is around 28% lower on the suction side of the wake, although this is spread over a larger area of flow. The change in the turbine blade wake, from a continuous vortex street at subsonic exit Mach numbers to a transient wake pattern at supersonic exit Mach numbers, results in a decrease of the stagnation temperature and pressure redistribution at $M_e > 1$.

Time accurate numerical predictions of the energy separation behind this turbine cascade are reported by Currie & Carscallen (1998) and Carscallen et al. (1998, 1999). These predictions are computed using an implicit, unstructured numerical method, which solves the Navier-Stokes equations using a second order MUSCL implementation of Roe's flux difference splitting scheme. Turbulence is modelled using the zonal $k - \omega/k - \epsilon$ Shear Stress Transport (SST) formulation of Menter (1993). Results from this modelling compare favourably with the turbine blade predictions of Arnone & Pacciani (1997). Recent work includes a detailed time accurate inviscid prediction of a simulated turbine blade at $M_e = 1.16$ by Brooksbank (2001). This work, summarised in Gostelow (2002), proposes that Kelvin-Helmholtz instabilities in the separated shear layers may provide a secondary source of energy separation. The Kelvin-Helmholtz instabilities are also thought to contribute to the generation of the transient vortex shedding at the confluence region at this Mach number.

Sieverding et al. (2003) document the near wake development and energy separation characteristics downstream of a similar thick trailing edge turbine blade at $M_e = 0.79$ and $Re_{D_t} = 1.487 \times 10^5$. Measurements include boundary layer profiles on the suction and pressure surfaces at the trailing edge, smoke visualisation and holographic/white light interferometry of the near wake development. These

results indicate turbulent boundary layer separation from both sides of the trailing edge and an asymmetric vortex shedding pattern downstream of the turbine blade. The shed vortices are reported to travel downstream at non equi-spaced intervals. Time mean and time accurate stagnation temperature and pressure measurements are also reported at $2.5D_t$ downstream of the trailing edge. A complete traverse of the wake is not reported for the stagnation temperature due to the probe head proving too fragile. The stagnation temperature field over half of the wake, and the complete stagnation pressure wake traverse, indicate a redistribution in these properties on a time accurate and time mean basis. These results further substantiate the time accurate stagnation temperature and pressure measurements of Carscallen et al. (1998, 1999).

Ackerman (2005) extends the time accurate circular cylinder research of Kurosaka et al. (1987) to the transonic Mach number regime. Surface pressure, drag and Strouhal number measurements are documented at $0.5 \leq M_\infty \leq 0.95$ and $6.75 \times 10^5 \leq Re_D \leq 8.95 \times 10^5$. In addition, Ackerman (2005) reports phase-lock averaged stagnation temperature and pressure measurements downstream of the circular cylinder at $M_\infty = 0.6$ and $Re_D = 6.86 \times 10^5$. These results are detailed further in this thesis as predictions from the current study are compared with those of Ackerman (2005).

Chapter 3

The Numerical Solution Procedure

3.1 Implementation Overview

3.1.1 Introduction

This chapter details the numerical method used in the present study to model the compressible, turbulent flow of air past a circular cylinder and a turbine cascade. This section provides an overview of the structure and rationale underlying the implementation of the numerical method. This is intended to be a self contained overview, providing a level of insight that is adequate to allow the CFD conversant reader to proceed to the subsequent chapters. The remainder of this chapter provides further details on each constituent component of the numerical method, including specification of the boundary conditions used in the inviscid and turbulent predictions.

By examining the physics of the flow under consideration, the numerical solution procedure may be tailored through the application of reasonable simplifying assumptions, to satisfy the research objectives while minimising the computational expense. This section therefore begins with a brief review of the dominant characteristics in the transonic flow past circular cylinders and turbine blades, from which simplifying arguments for the numerical procedure are developed.

3.1.2 Dominant Flow Physics Overview

Compressible and incompressible circular cylinder flows are reviewed in Chapter 2, on the basis of the available literature. The high transonic regime considered in

this study, $M_\infty \geq 0.6$, is characterised by the appearance of compressible flow features as the local Mach number approaches unity over the cylindrical surface. The boundary layer development and separation is influenced by the presence of weak shock waves close to the surface of the cylinder. These manifest as intermittent, unsteady shock waves over the free stream Mach number range $0.4 \geq M_\infty \geq 0.7$. As the free stream Mach number approaches unity, $0.7 \geq M_\infty \geq 1.0$, the shock waves increase in strength. They are present close to the cylinder surface and in the near wake region throughout the vortex shedding cycle. At supersonic free stream Mach numbers, a bow shock forms upstream of the circular cylinder and 'fishtail' shocks appear in the near wake region. Strong adverse pressure gradients induced by shock waves close to the cylinder surface can cause boundary layer separation, irrespective of whether the boundary layer is laminar or turbulent. This is different with respect to the incompressible regime, in which the development of turbulence in the boundary layer influences the location of separation, the subsequent development of the separated shear layers and the wake characteristics further downstream. At the free stream conditions considered in this study, previous experimental and numerical research indicates that the flow downstream of the cylinder is dominated by large scale vorticity. Vortices periodically appear, increase in size and circulation and are shed from the leeward surface of the cylinder, forming the distinct downstream pattern of the von Kármán vortex street.

This brief summary highlights the dominance of compressibility and convection effects over viscous diffusion in the transonic, turbulent flow past a circular cylinder at high Reynolds numbers. Past research on highly loaded turbine blades, including published experimental results by Carscallen et al. (1996, 1998), suggest that similar flow features dominate the discharge from a thick trailing edge cascade. With respect to the present study, this implies that an inviscid circular cylinder or turbine cascade model should adequately capture many of the main wake characteristics, such as energy separation. Inviscid models are therefore developed in this study as a first approximation to the compressible, turbulent flow field. These models use approximate solutions to the short-time averaged Euler equations. The fully de-

veloped quasi-stationary inviscid flow solution is subsequently used as the starting conditions for a turbulent computation, using the short-time averaged Navier-Stokes equations. The short-time averaged Euler and Navier-Stokes equations are defined in Sections 3.3.1 and 3.4.1 respectively. Subsection 3.1.3 provides a brief overview of the solution procedure employed for the inviscid and turbulent predictions. Further details of the solution procedure are provided in Sections 3.3 to 3.9.

3.1.3 Numerical Method Overview

A finite volume method is used to integrate the two-dimensional form of the short-time averaged Euler and Navier-Stokes equations over the computational domain. Finite volume methods, finite difference methods and finite element methods are reviewed in Hoffman & Chiang (1995), and in Versteeg & Malalasekera (1995). In the finite volume method, the governing equations are integrated over a series of control volumes. Applying Gauss' divergence theorem to the integral form of the governing equations allows the convective and diffusive terms to be solved through a summation of the convective and diffusive fluxes across each cell interface, as detailed in Sections 3.3 and 3.4. The solution of the governing equations is thereby decoupled into separate spatial and temporal integration stages. The convective fluxes are calculated using the asymmetric stencil, Flux Difference Splitting (FDS) approximate Riemann solver of Roe (1981). Asymmetric stencil methods provide greater accuracy and stability than central difference methods in regions of discontinuity by accounting for the direction of wave propagation in the approximate Riemann solver. The approximate Riemann solver of Roe (1981) uses the difference in the flow variables across each cell interface as the initial conditions to a Riemann problem. The convective flux at each cell interface is then calculated by solving a linear approximation to the Riemann problem. The approximate Riemann problem is defined by replacing the Jacobian matrix in the quasi-linear form of the governing equations by a local linear approximation. Roe (1981) used the approximate Riemann problem to reduce the computational effort required to estimate the intercell fluxes with respect to solving the exact Riemann problem, as discussed in Section 3.5.3.

The stability of Roe's approximate Riemann solver at flow discontinuities and the accuracy with which shock waves can be resolved are desirable properties for the current compressible flow study. In the present study, the entropy modification of Harten & Hyman (1983) is added to eliminate the presence of expansion shocks in the numerical prediction. The original one-dimensional scheme of Roe (1981) is extended to two dimensions by considering wave propagation normal to each cell interface. Using simple trigonometric transformations, the Cartesian velocity components are transformed to normal and tangential velocities at each cell interface, and an interface-normal Riemann problem is solved in this reference system.

The approximate Riemann solver of Roe (1981) is monotone and conservative, but only first order accurate. Second order spatial accuracy is achieved by replacing the piece-wise constant conservative variable distribution in each cell by a linear piece-wise approximation, after Van Leer (1979). This involves extrapolation of the volume averaged flow variables to the cell interfaces. The MUSCL approach (Monotone Upstream-centred Schemes for Conservation Laws) is used in this study. This is based on a Taylor series expansion of the volume averaged variables in each cell and provides a conservative method that is up to second order accurate in space. The MUSCL approach alone does not however retain the monotonicity of the first order method of Roe. Indeed, Godunov's theorem establishes that all linear, monotone methods can be at most first order accurate in space, as discussed in Roe (1986). An appropriate level of monotonicity is reinstated in the scheme by rendering it Total Variation Diminishing. The Total Variation Diminishing (TVD) condition provides a less stringent condition to that of monotonicity. The TVD condition ensures that no new extrema are created in a flow solution and that the magnitude of local maxima and minima are non-increasing. This ensures the preservation of monotonicity for an initially monotone flow field. A TVD scheme is therefore 'monotonicity preserving', as discussed in Section 3.5.7. The TVD condition is satisfied in the MUSCL approach through the addition of non-linear limiting functions. Limiters allow higher order spatial accuracy in regions of smooth flow, while ensuring the TVD condition is satisfied in regions with shock waves and shear flows. The

minmod limiter, defined in Section 3.5.8, is used in the present study. Therefore, for an initially monotone flow field, the application of the TVD satisfying MUSCL scheme with the minmod limiter should ensure that a monotone solution of higher than first order accuracy is obtained throughout the computation.

The flow field is integrated in time using the explicit, low storage Runge-Kutta method detailed in Hu et al. (1995). The standard Runge-Kutta coefficients, 0.5 and 1.0, are used to achieve a second order formal accuracy in time. Further details on the time integration method are provided in Section 3.8.

Short time averaging of the compressible Navier-Stokes equations introduces additional second and third order flow statistics in the momentum and energy equations. These higher-order terms are modelled using the standard two-equation $k-\omega$ turbulence model of Wilcox (1988), as given in Wilcox (1993), with the subsequent improvements detailed in this chapter. This model defines two additional transport equations. These are the specific turbulence kinetic energy, k, and the specific turbulence dissipation rate, ω. Time accurate values of k and ω are combined in an 'eddy viscosity', which is used to close the short-time averaged Navier-Stokes equations through the Boussinesq approximation. The $k-\omega$ turbulence model of Wilcox (1993) has been validated in published literature over a significant range of flows, as discussed in Wilcox (2002). Wilcox (1993, 1994) demonstrates that non-trivial solutions can be obtained by using the $k-\omega$ model for laminar boundary layers. Through the specification of appropriate free stream or surface conditions, the $k-\omega$ model may also be used to model transition in certain boundary layers. This is a particularly desirable property for the present study, as past research indicates that boundary layers remain laminar for a significant portion of the model circular cylinder surface and over the pressure side of the modelled turbine blade. The original $k-\omega$ turbulence model is shown by Wilcox (2002) to be prone to over-production of the turbulence kinetic energy, k, in free shear flows. This leads to predicted mixing rates that are significantly greater than those measured experimentally, Wilcox (2002). To remedy this problem, the present $k-\omega$ model implementation includes the cross-diffusion modification of Wilcox (2002). A dimensionless parameter is introduced into the

dissipation term of the turbulence kinetic energy transport equation. For free shear flows, the dimensionless parameter becomes significantly large. This increases dissipation in the specific turbulence kinetic energy transport equation, thereby reducing the specific turbulence kinetic energy in free shear flows. The result is a reduction of the free shear flow spreading rate to physically acceptable values. Conversely, for boundary layers, the dimensionless parameter decreases to extremely small values thereby having negligible influence on the turbulence kinetic energy. This is an important property, as the original $k-\omega$ model of Wilcox provides a good correlation between numerical predictions and experimental measurements for boundary layers. Finally, the compressibility modification of Wilcox (2002) is implemented into the $k-\omega$ model. This modification accounts for the turbulence Mach number, improving the predicted spreading rates in compressible free shear flows. These modifications are intended to improve the turbulent circular cylinder and turbine cascade predictions along the separated shear layers and in the downstream wake region.

Using the numerical method described in this section, the convective and viscous fluxes of the short-time averaged Navier-Stokes equations, including the $k-\omega$ model transport equations, are computed. In each computational cell, the resultant fluxes are combined with a volume integral of the turbulent source terms. These turbulent source terms are detailed further in Section 3.7. The resulting solution in each cell is then integrated in time using the Runge-Kutta method described in Section 3.8.

The efficiency of this numerical method is improved in the current study through the implementation of the Adaptive Mesh Refinement (AMR) algorithm of Quirk (1991). The flow model is predicted on a hierarchy of nested levels, of increasing spatial and temporal refinement. Local regions of rapidly developing flow or large density differences are computed on a fine resolution mesh, defined locally around the flow feature. Slow developing or uniform flow regions are then computed on a relatively coarse grid using a larger time step. At each level, the flow field is developed using the numerical method described in Sections 3.2 to 3.8. The current implementation of the AMR algorithm of Quirk (1991) is detailed in Section 3.10.

3.2 Governing Equations

The governing equations for mass, momentum and energy conservation are

$$\frac{\partial \rho}{\partial t} + \nabla \cdot (\rho \boldsymbol{u}) = 0, \tag{3.1}$$

$$\frac{\partial}{\partial t}(\rho \boldsymbol{u}) + \nabla \cdot (\rho \boldsymbol{u} \otimes \boldsymbol{u} + p\boldsymbol{I} - \boldsymbol{\tau}) = 0, \tag{3.2}$$

$$\frac{\partial}{\partial t}(\rho e_s) + \nabla \cdot (\rho \boldsymbol{u} h_s + \boldsymbol{q} - \boldsymbol{\tau} \cdot \boldsymbol{u}) = 0. \tag{3.3}$$

The variables e_s, h_s, $\boldsymbol{\tau}$ and $\boldsymbol{q}$ are the specific stagnation energy, the specific stagnation enthalpy, the viscous stress tensor and the heat flux vector respectively. These are given by the following auxiliary relationships:

$$e_s = \frac{p}{\rho(\gamma - 1)} + \frac{\boldsymbol{u} \cdot \boldsymbol{u}}{2}, \tag{3.4}$$

$$h_s = e_s + \frac{p}{\rho}, \tag{3.5}$$

$$\boldsymbol{\tau} = \mu_l \left(\nabla \boldsymbol{u} + \boldsymbol{u} \nabla - \frac{2}{3} \boldsymbol{I} \nabla \cdot \boldsymbol{u} \right), \tag{3.6}$$

$$\boldsymbol{q} = -\frac{\mu_l c_p}{P_r} \nabla T, \tag{3.7}$$

where c_p is the specific heat coefficient at constant pressure and Pr is the Prandtl number, which, for the present study takes the value 0.726. The molecular viscosity, μ_l, is estimated using Sutherlands law:

$$\mu_l = 1.458 \times 10^{-6} \frac{T^{3/2}}{(T + 110.4)}. \tag{3.8}$$

The perfect gas equation of state, per unit mass, completes the governing equations:

$$p = \rho R T, \tag{3.9}$$

where $R = c_p - c_v$ and c_v is the specific heat coefficient at constant volume. The equations given in this section assume air to be an ideal gas. The viscous stress tensor, Eqn. 3.6, assumes a Newtonian fluid. At the transonic Mach numbers and Reynolds numbers considered in this study these assumptions are justified.

3.3 The Euler Equations

3.3.1 Introduction

The Euler equations are a simplification of the Navier-Stokes equations. Assuming the flow under consideration is inviscid and adiabatic, the compressible form of the governing equations, Eqns. 3.1-3.3, reduce to

$$\frac{\partial \rho}{\partial t} + \nabla \cdot (\rho \boldsymbol{u}) = 0, \tag{3.10}$$

$$\frac{\partial}{\partial t}(\rho \boldsymbol{u}) + \nabla \cdot (\rho \boldsymbol{u} \otimes \boldsymbol{u} + p\boldsymbol{I}) = 0, \tag{3.11}$$

$$\frac{\partial}{\partial t}(\rho e_s) + \nabla \cdot (\rho \boldsymbol{u} h_s) = 0, \tag{3.12}$$

where the stagnation energy, e_s, and the stagnation enthalpy, h_s, are given by Eqns. 3.4 and 3.5 respectively. The equation of state, Eqn. 3.9, completes the Euler equations. The Euler equations, Eqns. 3.10-3.12, are written in conservative form using the density, the specific momentum vector and the specific stagnation energy as the state variables. A number of alternative forms for the Euler equations are possible as detailed, for instance, in Manna (1992). These include the primitive form of the Euler equations, written in terms of the density, velocity vector and static pressure, and the characteristic form, in which the flow state is evaluated along characteristic lines, surfaces or hyper-surfaces. The primitive form of the Euler equations is non-differentiable across flow discontinuities, such as shock waves and thin mixing layers. For the transonic circular cylinder and turbine blade flows, the conservative form of the Euler equations therefore represents a more suitable choice as the governing equations are differentiable in the presence of these flow features. Eqns. 3.10-3.12 make use of instantaneous flow variables. This implies that throughout the flow domain, all disturbance wavelengths are resolved by the numerical scheme. In practical computations, the shortest resolvable wavelength is limited by the spacing of the computational mesh. To acknowledge this, the governing equations are short-time averaged, as described in Appendix A.1. Short-time averaging separates an instantaneous flow scalar variable, ζ, into a short-time averaged com-

ponent, $\bar{\zeta}$, and a turbulent fluctuating component, ζ''. The short-time averaged component includes both the time mean component and all large scale fluctuations resolved by the computational time step. Therefore, after short-time averaging Eqns. 3.10-3.12 and neglecting the unresolved small scale fluctuations, the Euler equations become

$$\frac{\partial \bar{\rho}}{\partial t} + \nabla \cdot (\bar{\rho}\bar{\boldsymbol{u}}) = 0, \tag{3.13}$$

$$\frac{\partial}{\partial t}(\bar{\rho}\bar{\boldsymbol{u}}) + \nabla \cdot (\bar{\rho}\bar{\boldsymbol{u}} \otimes \bar{\boldsymbol{u}} + \bar{p}\boldsymbol{I}) = 0, \tag{3.14}$$

$$\frac{\partial}{\partial t}(\bar{\rho}\bar{e}_s) + \nabla \cdot \left(\bar{\rho}\bar{\boldsymbol{u}}\bar{h}_s\right) = 0. \tag{3.15}$$

The short-time averaged stagnation energy, $\bar{e}_s$, and stagnation enthalpy, $\bar{h}_s$, are given by

$$\bar{e}_s = \frac{\bar{p}}{\bar{\rho}(\gamma - 1)} + \frac{\bar{\boldsymbol{u}} \cdot \bar{\boldsymbol{u}}}{2}, \tag{3.16}$$

$$\bar{h}_s = \bar{e}_s + \frac{\bar{p}}{\bar{\rho}}. \tag{3.17}$$

The conservative form of the compressible Euler equations can be written in the alternative compact form of the transport equations, which is a vector formulation. This is

$$\frac{\partial \boldsymbol{U}}{\partial t} + \nabla \cdot \boldsymbol{F}(\boldsymbol{U}) = 0, \tag{3.18}$$

where $\boldsymbol{U}$ is the vector of conserved variables and $\boldsymbol{F}(\boldsymbol{U})$ is the conservative flux vector. These are given by

$$\boldsymbol{U} = \begin{pmatrix} \bar{\rho} \\ \bar{\rho}\bar{\boldsymbol{u}} \\ \bar{\rho}\bar{e}_s \end{pmatrix}, \qquad \boldsymbol{F}(\boldsymbol{U}) = \begin{pmatrix} \bar{\rho}\bar{\boldsymbol{u}} \\ \bar{\rho}\bar{\boldsymbol{u}} \otimes \bar{\boldsymbol{u}} + \bar{p}\boldsymbol{I} \\ \bar{\rho}\bar{\boldsymbol{u}}\bar{h}_s \end{pmatrix}. \tag{3.19}$$

The coupled system of Equations 3.18 is non-linear and differential. To obtain numerical solutions to Equation 3.18, it is convenient to rewrite it in integral form. The integral form of the Euler equations is obtained by integrating Eqn. 3.18 over

an arbitrary control volume, V, giving

$$\frac{\partial}{\partial t}\int_V \boldsymbol{U}\ dV + \int_V \nabla \cdot \boldsymbol{F}\left(\boldsymbol{U}\right)\ dV \ = \ 0. \tag{3.20}$$

The volume integral of the inviscid fluxes in Eqn. 3.20 can be transformed by the application of the Gauss divergence theorem, from which

$$\int_V \nabla \cdot \boldsymbol{F}\left(\boldsymbol{U}\right)\ dV \ \equiv \ \oint_{\mathcal{S}} \boldsymbol{F}\left(\boldsymbol{U}\right)\ \cdot \boldsymbol{n}\, d\mathcal{S}, \tag{3.21}$$

where $\boldsymbol{n}$ is the outward unit vector normal to the surface $\mathcal{S}$ that bounds V. Equation 3.21 states that the net mass, momentum and energy flow out of the control volume is equivalent to the sum of the respective normal fluxes across the closed boundary $\mathcal{S}$. Upon application of the Gauss divergence theorem to Eqn. 3.20, the integral form of the Euler equations becomes

$$\frac{\partial}{\partial t}\int_V \boldsymbol{U}\ dV + \oint_{\mathcal{S}} \boldsymbol{F}\left(\boldsymbol{U}\right)\ \cdot \boldsymbol{n}\ d\mathcal{S} \ = \ 0. \tag{3.22}$$

To solve the integral form of the Euler equations numerically, Eqn. 3.22 is discretised using volume averaged variables, defined for a cell of index, i, as

$$\boldsymbol{U}_i V_i \ \equiv \ \int_{V_i} \boldsymbol{U}\, dV, \tag{3.23}$$

where $\boldsymbol{U}_i$ is the volume averaged state variables vector and V_i is the volume of the i^{th} computational cell. The finite volume formulation defined in this work is based on a polyhedron, which is bound by a finite number of surfaces, $\mathcal{S}_{i,k}$. The surface integral of the inviscid fluxes in Equation 3.22 is therefore replaced by a summation of the surface averaged normal fluxes, over the faces of the cell.

$$\oint_{\mathcal{S}} \boldsymbol{F}\left(\boldsymbol{U}\right)\ \cdot \boldsymbol{n}\ d\mathcal{S} \ \equiv \ \sum_{k=1}^{N_f} \left(\boldsymbol{F}\left(\boldsymbol{U}\right)_{i,k} \cdot \boldsymbol{n}_{i,k}\right) \mathcal{S}_{i,k}, \tag{3.24}$$

where N_f is the total number of faces in the computational cell. $\mathcal{S}_{i,k}$ is the surface area of face k. $\boldsymbol{n}_{i,k}$ is the vector normal to the surface $\mathcal{S}_{i,k}$. The resulting semi-discrete form of the Euler equations, found by dividing Eqn. 3.22 throughout by V_i,

is

$$\frac{\partial}{\partial t}\boldsymbol{U}_i \;=\; -\frac{1}{V_i}\sum_{k=1}^{N_f}\left(\boldsymbol{F}\left(\boldsymbol{U}\right)_{i,k}\;\cdot\boldsymbol{n}_{i,k}\right)\mathcal{S}_{i,k}. \tag{3.25}$$

This form of the Euler equations divides the numerical solution procedure into separate spatial and temporal integration stages. These stages are described in Sections 3.5 and 3.8 respectively.

3.3.2 Quasi-Linear Form

The quasi-linear form of the Euler equations allows numerical prediction methods based on the propagation of characteristic waves to be developed. This form of the Euler equations can be derived from Eqn. 3.18 through the introduction of a Jacobian matrix, $\boldsymbol{A}$, to relate the inviscid fluxes to the conservative variables. Considering the flow in the direction normal to each cell interface, the Jacobian matrix is defined as

$$\boldsymbol{A} \;=\; \frac{\partial\boldsymbol{F}\left(\boldsymbol{U_n}\right)\cdot\boldsymbol{n}}{\partial\boldsymbol{U_n}}, \tag{3.26}$$

where $\boldsymbol{U_n} = \left(\bar{\rho}, \bar{\rho}\bar{u}_n, \bar{\rho}\bar{u}_t, \bar{\rho}\bar{e}_s\right)^T$, with $\bar{u}_n = \bar{u}_1 n_1 + \bar{u}_2 n_2$ and $\bar{u}_t = \bar{u}_2 n_1 - \bar{u}_1 n_2$. Substituting Eqn. 3.26 in Eqn. 3.18, the quasi-linear form of the Euler equations is

$$\frac{\partial\boldsymbol{U}}{\partial t} + \boldsymbol{M}\left(\boldsymbol{An}\cdot\nabla\boldsymbol{U_n}\right) \;=\; 0, \tag{3.27}$$

where $\boldsymbol{M}$ is a $|\boldsymbol{n}| = 1$ transformation matrix used to recover the Cartesian conservation variables:

$$\boldsymbol{M} \;=\; \begin{bmatrix} 1 & 0 & 0 & 0 \\ 0 & n_1 & -n_2 & 0 \\ 0 & n_2 & n_1 & 0 \\ 0 & 0 & 0 & 1 \end{bmatrix}. \tag{3.28}$$

This form of the Euler equations is used in Section 3.5 to compute the inviscid fluxes.

3.4 The Short-Time Averaged Navier-Stokes Equations

3.4.1 Introduction

The Navier-Stokes equations, Eqns. 3.1-3.3, provide a time accurate description of the flow for a viscous, Newtonian fluid. The high Reynolds numbers considered in this study are associated with turbulent flows. Turbulence is three dimensional, unsteady and is spread over a wide range of time and length scales (Wilcox, 2002). The Direct Numerical Simulation (DNS) of a high Reynolds number, turbulent flow therefore requires modelling of the fluid motion over all relevant time and length scales. The length scales of turbulence present in the test cases predicted in this study range from the largest, energy containing vortices of order $\Delta x \sim \mathcal{O}\left(10^{-1}m\right)$, to the smallest, Kolmogorov length scales of order $\Delta x \sim \mathcal{O}\left(10^{-6}m\right)$, associated with viscous dissipation of turbulence kinetic energy into heat. For a turbulent circular cylinder and turbine blade flow, an accurate prediction of the turbulence kinetic energy cascade over such a wide range of length scales represents an unfeasible task with the available computational resources. In this study, therefore, short-time averaging of the Navier-Stokes equations is employed to reduce this range. Appendix A.1 describes the derivation of the short-time averaged Navier-Stokes equations from 3.1-3.3. This gives

$$\frac{\partial \bar{\rho}}{\partial t} + \nabla \cdot \left(\bar{\rho}\bar{\boldsymbol{u}}\right) = 0, \tag{3.29}$$

$$\frac{\partial}{\partial t}\left(\bar{\rho}\bar{\boldsymbol{u}}\right) + \nabla \cdot \left(\bar{\rho}\bar{\boldsymbol{u}} \otimes \bar{\boldsymbol{u}} + \bar{p}\boldsymbol{I}\right) = \nabla \cdot \left(\bar{\boldsymbol{\tau}} - \bar{\rho}\overline{\boldsymbol{u}'' \otimes \boldsymbol{u}''}\right), \tag{3.30}$$

$$\begin{aligned}\frac{\partial}{\partial t}\bar{\rho}\left(\bar{e}_s + \bar{k}\right) + \nabla \cdot \bar{\rho}\bar{\boldsymbol{u}}\left(\bar{h}_s + \bar{k}\right) = \nabla \cdot \Big(&-\bar{\boldsymbol{q}} - \bar{\rho}\overline{\boldsymbol{u}''h''} + \bar{\boldsymbol{\tau}} \cdot \bar{\boldsymbol{u}} + \\ &\overline{\boldsymbol{\tau}'' \cdot \boldsymbol{u}''} - \bar{\rho}\overline{\boldsymbol{u}'' \otimes \boldsymbol{u}''} \cdot \bar{\boldsymbol{u}} - \\ &\bar{\rho}\overline{\boldsymbol{u}'' \otimes \boldsymbol{u}'' \cdot \boldsymbol{u}''/2}\Big).\end{aligned} \tag{3.31}$$

In the short-time averaging procedure, the contributions to the short-time averaged mass, momentum and energy balance from the turbulent density fluctuations, ρ'', and the turbulent static temperature fluctuations, T'', are omitted in the heat conduction term on the basis that they are negligibly small in comparison to the

short-time averaged contributions. Short-time averaging introduces the Reynolds stress tensor $\bar{\rho}\overline{\boldsymbol{u}'' \otimes \boldsymbol{u}''}$ into the momentum conservation equation, Eqn. 3.30. In the energy equation, Eqn. 3.31, a number of additional terms are created. From the analysis of Wilcox (2002), these terms are:

$$\begin{aligned}
\bar{\rho}\overline{\boldsymbol{u}''h''} &: \text{Turbulent heat flux;} \\
\overline{\boldsymbol{\tau}'' \cdot \boldsymbol{u}''} &: \text{Molecular diffusion;} \\
\bar{\rho}\overline{\boldsymbol{u}'' \otimes \boldsymbol{u}''} \cdot \bar{\boldsymbol{u}} &: \text{Work done by the Reynolds stresses;} \\
\bar{\rho}\overline{\boldsymbol{u}'' \otimes \boldsymbol{u}'' \cdot \boldsymbol{u}''/2} &: \text{Turbulent transport of the turbulence kinetic energy.}
\end{aligned}$$

These additional terms are grouped together with the molecular heat flux on the right hand side of the energy equation. The short-time averaged specific turbulence kinetic energy, $\bar{k}$, adds to the short time averaged stagnation energy, $\overline{e}_s$, and stagnation enthalpy, $\overline{h}_s$, in the total energy balance. The short-time averaged turbulence kinetic energy is defined as:

$$\bar{k} = \frac{\overline{\boldsymbol{u}'' \cdot \boldsymbol{u}''}}{2}. \tag{3.32}$$

The additional terms defined in the short-time averaged momentum and energy conservation equations are not explicitly defined using the resolved flow state variables $(\overline{\rho}, \overline{\rho\boldsymbol{u}}, \overline{\rho e}_s)$. Deriving an explicit model for these terms solves this 'turbulence closure problem'. In this study, turbulence closure is provided by the two-equation $k-\omega$ turbulence model outlined in Wilcox (1993), with the subsequent developments outlined in Wilcox (2002).

3.4.2 The Two Equation $k-\omega$ Turbulence Model of Wilcox

A number of turbulence models have been developed to solve the turbulence closure problem. These models include algebraic models, 1/2-equation models, one-equation models, two-equation models and Large Eddy Simulations (LES). A detailed introduction and critical review of turbulence modelling is given in Wilcox (2002). In common with all two-equation turbulence models, the $k-\omega$ model of Wilcox (1993)

is based on the Boussinesq eddy-viscosity approximation. This approximation centres around estimating the Reynolds stresses using an analogy between turbulent motion and the viscous stresses. This analogy allows the Reynolds stresses to be computed through multiplication of an 'eddy viscosity', μ_t, with the mean flow strain rate tensor. This gives

$$\bar{\boldsymbol{\tau}}_{\boldsymbol{r}} = -\bar{\rho}\overline{\boldsymbol{u}'' \otimes \boldsymbol{u}''} = \bar{\mu_t}\left(\nabla\bar{\boldsymbol{u}} + \bar{\boldsymbol{u}}\nabla - \frac{2}{3}\boldsymbol{I}\nabla\cdot\bar{\boldsymbol{u}}\right) - \frac{2}{3}\boldsymbol{I}\bar{\rho}\bar{k}. \tag{3.33}$$

Two-equation turbulence models compute the eddy viscosity by combining the turbulence kinetic energy with a characteristic turbulence length scale. Flow history effects are included in the eddy viscosity by defining two transport equations for the specific turbulence kinetic energy, k, and an additional variable. The Wilcox $k-\omega$ turbulence model uses the specific turbulence dissipation rate, ω, as the dependent variable in the second transport equation. Alternative choices for the second turbulent closure variable include the turbulence dissipation, ϵ, and the turbulence dissipation time, τ_t. These alternatives are discussed in Wilcox (2002). The compressible k and ω transport equations of Wilcox (1993) are Favre-averaged, following the compressible Favre-averaged conservation equations for mass, momentum and energy balance. An adapted form of the k and ω transport equations of Wilcox are therefore defined to close the short-time averaged Navier-Stokes equations. The transport equation for $\bar{k}$ is derived using the instantaneous momentum conservation equation, Eqn. 3.2. The instantaneous momentum conservation equation is multiplied by $\boldsymbol{u}''$ and the resulting equation is short-time averaged. A similar approach is described in detail in Wilcox (2002) for the Favre-averaged turbulent kinetic energy transport equation. Recalling that $\overline{\boldsymbol{u}''\cdot\boldsymbol{u}''} = 2\bar{k}$, the short-time averaged specific turbulence kinetic energy transport equation is thus obtained as

$$\begin{aligned}\frac{\partial}{\partial t}\left(\bar{\rho}\bar{k}\right) + \nabla\cdot\left(\bar{\rho}\bar{\boldsymbol{u}}\bar{k}\right) &= \bar{\boldsymbol{\tau}}_{\boldsymbol{r}} : \nabla\bar{\boldsymbol{u}} - \overline{\boldsymbol{\tau}''} : \overline{\nabla\boldsymbol{u}''} + \overline{p''\nabla\cdot\ \boldsymbol{u}''} + \\ &\quad \nabla\cdot\left(\overline{\boldsymbol{\tau}''\cdot\ \boldsymbol{u}''} - \bar{\rho}\overline{\boldsymbol{u}''\otimes\boldsymbol{u}''\cdot\boldsymbol{u}''/2} - \overline{p''\ \boldsymbol{u}''}\right).\end{aligned} \tag{3.34}$$

This form of the short-time averaged turbulent kinetic energy transport equation differs from the Favre averaged turbulent kinetic energy transport equation by the omission of the pressure work term. The omission of the pressure work term results from the definition $\bar{\boldsymbol{u}}'' = 0$. Conversely, the Favre averaging procedure defines that, for compressible flows, the time average of the turbulent velocity fluctuation is non-zero when the density fluctuation is appreciable. However, the pressure work term is taken as zero in the Favre averaged turbulent kinetic energy transport equation by Wilcox (1993), due to the scarcity of established physical relations for this term. The corresponding transport equation for the short-time averaged specific turbulence dissipation rate, $\bar{\omega}$, originates from a differential equation postulated for ω by Kolmogorov (1942). In formulating the transport equations for k and ω, Wilcox (1988) has added a production term using the Reynolds stress tensor defined in Eqn. 3.33. Wilcox (1988) also added a molecular diffusion term for application to laminar flow regions, such as within the viscous sublayer of turbulent boundary layers. The short-time averaged specific dissipation rate transport equation used in the present study is given in Eqn. 3.43.

3.4.3 Closure Approximations

Numerical models for the second and third order flow statistics are sought in the short-time averaged Navier-Stokes equations, based on the short-time averaged conservation variables. The closure approximation for the Reynolds stress tensor is defined in Eqn. 3.33. The work done against the Reynolds stresses in the energy conservation equation $\bar{\rho}\overline{\boldsymbol{u}'' \otimes \boldsymbol{u}''} \cdot \bar{\boldsymbol{u}}$ is simply defined as the product of the Reynolds stresses, $\bar{\boldsymbol{\tau}}_{\boldsymbol{r}}$, and the short-time averaged velocity, $\bar{\boldsymbol{u}}$. The remaining closure approximations are defined, following the closure approximations of Wilcox (1993), by the following relations.

The *turbulent heat flux* $\left(\bar{\rho}\overline{\boldsymbol{u}''h''}\right)$ represents the transport of heat by the action of the turbulent motion. Using the analogy of Reynolds (1874), between heat and momentum transfer, Wilcox (1993) defines the turbulent heat flux as being proportional

to the temperature gradient. For the short-time averaged Navier-Stokes equations, this leads to

$$\bar{\rho}\overline{\boldsymbol{u}''h''} \;=\; \boldsymbol{q_t} = -\frac{\mu_t c_p}{Pr_t}\nabla T, \tag{3.35}$$

where the turbulent Prandtl number $Pr_t = \mu_t c_p/\mathcal{K}_t$ and $\mathcal{K}_t$ is the thermal eddy conductivity. In this study, $Pr_t = 0.9$, as suggested by Wilcox (2002).

The *turbulent transport of specific turbulence kinetic energy* $\left(\overline{\bar{\rho}\boldsymbol{u}'' \otimes \boldsymbol{u}'' \cdot \boldsymbol{u}''/2}\right)$ represents the transport of the specific turbulence kinetic energy by the turbulent velocity fluctuations. Turbulent flows are characterised by a greater transport of momentum and kinetic energy by the motion of turbulence than by molecular diffusion, as discussed by Tennekes & Lumley (1972). A closure approximation is derived by Wilcox (1993) through analogy with the modelling of molecular transport effects. This yields an expression for the turbulent transport of specific turbulence kinetic energy in terms of the eddy viscosity, μ_t, the $k-\omega$ model closure coefficient $\sigma^\star$ and the spatial gradient of the turbulence kinetic energy, which, for the short-time averaged Navier-Stokes equations, is $\nabla\bar{k}$. Therefore:

$$\overline{\bar{\rho}\boldsymbol{u}'' \otimes \boldsymbol{u}'' \cdot \boldsymbol{u}''/2} \;=\; \sigma^\star \mu_t \nabla\bar{k}. \tag{3.36}$$

The *molecular diffusion* $\left(\overline{\boldsymbol{\tau}'' \cdot\; \boldsymbol{u}''}\right)$ accounts for the mixing and transport of the turbulence kinetic energy by the molecular motion of the fluid. This term is modelled using the spatial gradient of the short-time averaged turbulence kinetic energy as in Wilcox (1993). For the short-time averaged equations, this gives

$$\overline{\tau'' \cdot\; \boldsymbol{u}''} \;=\; \mu_l \nabla\bar{k}. \tag{3.37}$$

The *short-time averaged dissipation rate* $\left(\overline{\boldsymbol{\tau}'' : \nabla \boldsymbol{u}''}\right)$ in the $\bar{k}$ transport equation, Eqn. 3.34, accounts for the viscous dissipation of turbulence through the action of the viscous shear stresses. Dissipation is responsible for the conversion of turbulent kinetic energy into heat, resulting in a local increase in temperature. Wilcox (1993)

defines dissipation as 'equal to the mean rate at which work is done by the fluctuating part of the strain rate against the fluctuating viscous stresses'. Following the analysis of Wilcox (1993), $\overline{\boldsymbol{\tau}'' : \nabla \boldsymbol{u}''}$ can be re-written in terms of the dissipation term $\overline{\rho\epsilon}$. The specific dissipation $\bar{\epsilon}$ is approximately proportional to the square of the fluctuating strain-rate tensor. Following Kolmogorov (1942), the specific dissipation $\bar{\epsilon}$ is related by Wilcox (1993) to the specific dissipation rate $\bar{\omega}$, by $\bar{\epsilon} = \beta^\star \bar{k}\bar{\omega}$. The short-time averaged dissipation rate is therefore written as

$$\overline{\boldsymbol{\tau}'' : \nabla \boldsymbol{u}''} \;=\; \bar{\rho}\beta^\star \bar{k}\bar{\omega}. \tag{3.38}$$

The *pressure dilatation* $\left(\overline{p''\nabla \cdot \ \boldsymbol{u}''}\right)$, and the *pressure diffusion* $\left(\overline{p''\ \boldsymbol{u}''}\right)$ terms are omitted in the present $k-\omega$ model formulation as widely accepted models for these equations are not currently available. Further details on the characteristics of the pressure dilatation and pressure diffusion terms, as well as the contribution of recent Direct Numerical Simulation (DNS) in the further development of closure approximations for these terms, are available in Wilcox (2002).

Using these closure approximations, the short-time averaged Navier Stokes equations, along with the transport equations for $\bar{k}$ and $\bar{\omega}$, become

$$\frac{\partial \bar{\rho}}{\partial t} + \nabla \cdot (\bar{\rho}\bar{\boldsymbol{u}}) \;=\; 0, \tag{3.39}$$

$$\frac{\partial}{\partial t}(\bar{\rho}\bar{\boldsymbol{u}}) + \nabla \cdot (\bar{\rho}\bar{\boldsymbol{u}} \otimes \bar{\boldsymbol{u}} + \bar{p}\boldsymbol{I}) \;=\; \nabla \cdot \left(\bar{\boldsymbol{\tau}} + \bar{\boldsymbol{\tau}}_{\boldsymbol{r}}\right), \tag{3.40}$$

$$\begin{aligned} \frac{\partial}{\partial t}\bar{\rho}\left(\bar{e}_s + \bar{k}\right) + \nabla \cdot \bar{\rho}\bar{\boldsymbol{u}}\left(\bar{h}_s + \bar{k}\right) \;=\; & \nabla \cdot \left[-\left(\bar{\boldsymbol{q}} + \bar{\boldsymbol{q}}_{\boldsymbol{t}}\right) + \left(\bar{\boldsymbol{\tau}} + \bar{\boldsymbol{\tau}}_{\boldsymbol{r}}\right) \cdot \bar{\boldsymbol{u}} + \right. \\ & \left. \left(\mu_l + \sigma^\star \mu_t\right) \nabla \bar{k}\right], \end{aligned} \tag{3.41}$$

$$\begin{aligned} \frac{\partial}{\partial t}\left(\bar{\rho}\bar{k}\right) + \nabla \cdot \left(\bar{\rho}\bar{\boldsymbol{u}}\bar{k}\right) \;=\; & \bar{\boldsymbol{\tau}}_{\boldsymbol{r}} : \nabla \bar{\boldsymbol{u}} - \beta^\star \bar{\rho}\bar{k}\bar{\omega} + \\ & \nabla \cdot \left[\left(\mu_l + \sigma^\star \mu_t\right) \nabla \bar{k}\right], \end{aligned} \tag{3.42}$$

$$\begin{aligned} \frac{\partial}{\partial t}\left(\bar{\rho}\bar{\omega}\right) + \nabla \cdot \left(\bar{\rho}\bar{\boldsymbol{u}}\bar{\omega}\right) \;=\; & \frac{\varphi\bar{\omega}}{\bar{k}}\bar{\boldsymbol{\tau}}_{\boldsymbol{r}} : \nabla \bar{\boldsymbol{u}} - \beta\bar{\rho}\bar{\omega}^2 + \\ & \nabla \cdot \left[\left(\mu_l + \sigma\mu_t\right) \nabla \bar{\omega}\right]. \end{aligned} \tag{3.43}$$

The Reynolds stress tensor $\boldsymbol{\tau}_{\boldsymbol{r}}$ is given by Eqn. 3.33. The following auxiliary equa-

tions and closure coefficients are defined for the present $k-\omega$ model implementation:

$$\varphi = \frac{13}{25}, \qquad \sigma = \frac{1}{2}, \qquad \sigma^\star = \frac{1}{2}, \tag{3.44}$$

$$\mu_t = \frac{\bar{\rho}\bar{k}}{\bar{\omega}}. \tag{3.45}$$

The cross-diffusion modification of Wilcox (2002) is applied to the $k-\omega$ model to improve the prediction of spreading rates for free shear flows over the original $k-\omega$ model of Wilcox (1988). The cross-diffusion modification increases the level of dissipation in the $\bar{k}$ transport equation through modification of the $\beta^\star$ closure coefficient. By comparing the $\bar{\omega}$ transport equation with the $\bar{k}-\bar{\epsilon}$ model transport equation for $\bar{\epsilon}$, which has better shear flow spreading rate characteristics, Wilcox (2002) introduces two dimensionless parameters, χ_k and $f_{\beta^\star}$. The closure coefficient $\beta^\star$ is made to be dependent on χ_k and $f_{\beta^\star}$, which are defined as

$$\chi_k = \frac{1}{\bar{\omega}^3}\nabla\bar{k}\nabla\bar{\omega}, \tag{3.46}$$

$$f_{\beta^\star} = \begin{cases} 1 & \forall\, \chi_k \leq 0 \\ \left(1+680\chi_k^2\right)/\left(1+400\chi_k^2\right) & \forall\, \chi_k > 0 \end{cases}, \tag{3.47}$$

To allow for the weakly compressible turbulence in the modelled flows, the compressibility correction of Wilcox (1992) is added to the current $k-\omega$ model implementation. This correction scales $\beta^\star$ and β as

$$\beta^\star = \beta_o^\star f_{\beta^\star}\left[1+\xi^\star\mathcal{F}\left(M_t\right)\right], \tag{3.48}$$

$$\beta = \beta_o - \beta_o^\star f_{\beta^\star}\xi^\star\mathcal{F}\left(M_t\right), \tag{3.49}$$

where

$$\beta_o^\star = \frac{9}{100}, \qquad \beta_o = \frac{9}{125}, \qquad \xi^\star = \frac{3}{2}, \tag{3.50}$$

$$M_{t_o} = \frac{1}{4}, \tag{3.51}$$

$$\mathcal{F}\left(M_t\right) = \left[M_t^2 - M_{t_o}^2\right]\mathcal{H}\left(M_t - M_{t_o}\right). \tag{3.52}$$

In Eqn. 3.52, $\mathcal{H}$ is the heaviside step function. The variable M_t is defined as the

turbulence Mach number. This is a function of $\bar{k}$ and of the local speed of sound:

$$M_t^2 = \frac{2\bar{k}}{a^2}. \tag{3.53}$$

The short-time averaged governing equations with the $k-\omega$ turbulence closure model, Eqns. 3.39-3.43, can be expressed in the compact vector form

$$\frac{\partial \boldsymbol{U}}{\partial t} + \nabla \cdot \left(\boldsymbol{F_c}\left(\boldsymbol{U}\right) + \boldsymbol{F_t}\left(\boldsymbol{U}\right)\right) + \boldsymbol{S} = 0. \tag{3.54}$$

In Eqn. 3.54, the conservative vector, $\boldsymbol{U}$, and the convective flux vector, $\boldsymbol{F_c}\left(\boldsymbol{U}\right)$, are

$$\boldsymbol{U} = \begin{pmatrix} \bar{\rho} \\ \bar{\rho}\bar{\boldsymbol{u}} \\ \bar{\rho}\left(\bar{e}_s + \bar{k}\right) \\ \bar{\rho}\bar{k} \\ \bar{\rho}\bar{\omega} \end{pmatrix}, \qquad \boldsymbol{F_c}\left(\boldsymbol{U}\right) = \begin{pmatrix} \bar{\rho}\bar{\boldsymbol{u}} \\ \bar{\rho}\bar{\boldsymbol{u}} \otimes \bar{\boldsymbol{u}} + \bar{p}\boldsymbol{I} \\ \bar{\rho}\bar{\boldsymbol{u}}\left(\bar{h}_s + \bar{k}\right) \\ \bar{\rho}\bar{\boldsymbol{u}}\bar{k} \\ \bar{\rho}\bar{\boldsymbol{u}}\bar{\omega} \end{pmatrix}. \tag{3.55}$$

The turbulent flux vector, $\boldsymbol{F_t}\left(\boldsymbol{U}\right)$, is

$$\boldsymbol{F_t}\left(\boldsymbol{U}\right) = \begin{pmatrix} 0 \\ -\left(\bar{\boldsymbol{\tau}} + \bar{\boldsymbol{\tau}}_{\boldsymbol{r}}\right) \\ \bar{\boldsymbol{q}} + \bar{\boldsymbol{q}}_{\boldsymbol{t}} - \left(\bar{\boldsymbol{\tau}} + \bar{\boldsymbol{\tau}}_{\boldsymbol{r}}\right) \cdot \bar{\boldsymbol{u}} - \left(\mu_l + \sigma^\star \mu_t\right) \nabla \bar{k} \\ -\left(\mu_l + \sigma^\star \mu_t\right) \nabla \bar{k} \\ -\left(\mu_l + \sigma \mu_t\right) \nabla \bar{\omega} \end{pmatrix}. \tag{3.56}$$

Finally, the turbulent source terms vector, $\boldsymbol{S}$, is

$$\boldsymbol{S} = \begin{pmatrix} 0 \\ 0 \\ 0 \\ \beta^\star \bar{\rho}\bar{k}\bar{\omega} - \bar{\boldsymbol{\tau}}_{\boldsymbol{r}} : \nabla \bar{\boldsymbol{u}} \\ \beta \bar{\rho}\bar{\omega}^2 - \frac{\varphi\bar{\omega}}{\bar{k}} \bar{\boldsymbol{\tau}}_{\boldsymbol{r}} : \nabla \bar{\boldsymbol{u}} \end{pmatrix}. \tag{3.57}$$

The compact differential form of the short-time averaged Navier-Stokes equations, Eqn. 3.54, is integrated in space over an arbitrary control volume V. Applying Gauss' divergence theorem to the combined convective and viscous fluxes normal to the closed surface $\mathcal{S}$ that bounds V, the integral form of the short-time averaged Navier-Stokes equations are obtained as

$$\frac{\partial}{\partial t}\int_V \boldsymbol{U}\, dV + \oint_{\mathcal{S}} \left(\boldsymbol{F_c}\left(\boldsymbol{U}\right) + \boldsymbol{F_t}\left(\boldsymbol{U}\right)\right)\cdot \boldsymbol{n}\, d\mathcal{S} + \int_V \boldsymbol{S}\, dV \;=\; 0, \tag{3.58}$$

where $\mathbf{n}$ is the unit vector normal to the surface $\mathcal{S}$. The semi-discrete form of the short-time averaged Navier-Stokes equations are obtained from the integral form by substituting into Eqn. 3.58 the volume averaged variables, $\boldsymbol{U}_i$, defined in Eqn. 3.23. The surface integral of the convective and turbulent fluxes are then replaced with a summation over N_f discrete surfaces, bounding the computational volume V_i of the i^{th} computational cell:

$$\sum_{k=1}^{N_f} \left[\left(\boldsymbol{F_c}\left(\boldsymbol{U_i}\right) + \boldsymbol{F_t}\left(\boldsymbol{U_i}\right)\right)\cdot \boldsymbol{n}\right]_k \mathcal{S}_{i,k} \;\equiv\; \oint_{\mathcal{S}} \left(\boldsymbol{F_c}\left(\boldsymbol{U}\right) + \boldsymbol{F_t}\left(\boldsymbol{U}\right)\right)\cdot \boldsymbol{n}\, d\mathcal{S}. \tag{3.59}$$

Dividing Eqn. 3.58 throughout by V_i, the semi-discrete form of the short-time averaged Navier-Stokes equations are therefore obtained as

$$\frac{\partial}{\partial t}\boldsymbol{U}_i \;=\; -\frac{1}{V_i}\sum_{k=1}^{N_f} \left[\left(\boldsymbol{F_c}\left(\boldsymbol{U}\right) + \boldsymbol{F_t}\left(\boldsymbol{U}\right)\right)\cdot \boldsymbol{n}\right]_{i,k} \mathcal{S}_{i,k} \;-\; \boldsymbol{S}_i. \tag{3.60}$$

3.4.4 Quasi-Linear Form

The quasi-linear form of the short-time averaged Navier-Stokes equations with application of the $k-\omega$ turbulence model is defined by differentiating the convective flux with respect to the conservative variables vector. This defines the Jacobian matrix for the short-time averaged Navier-Stokes equations, which is

$$\boldsymbol{A_t} \;=\; \frac{\partial \boldsymbol{F_c}\left(\boldsymbol{U_n}\right)\cdot \boldsymbol{n}}{\partial \boldsymbol{U_n}}, \tag{3.61}$$

where $\boldsymbol{U_n} = \left(\bar{\rho}, \bar{\rho}\bar{u}_n, \bar{\rho}\bar{u}_t, \bar{\rho}\left(\bar{e}_s + \bar{k}\right), \bar{\rho}\bar{k}, \bar{\rho}\bar{\omega}\right)^T$, with $\bar{u}_n = \bar{u}_1 n_1 + \bar{u}_2 n_2$ and $\bar{u}_t = \bar{u}_2 n_1 - \bar{u}_1 n_2$. Substituting Eqn. 3.61 into Eqn. 3.54, the quasi-linear form of Eqn. 3.54 is

$$\frac{\partial \boldsymbol{U}}{\partial t} + \boldsymbol{M}_t \left(\boldsymbol{A_t}\, \boldsymbol{n} \cdot \nabla \boldsymbol{U_n}\right) + \nabla \cdot \boldsymbol{F_t}\left(\boldsymbol{U}\right) + \boldsymbol{S} = 0. \tag{3.62}$$

where $\boldsymbol{M}_t$ is a $|\boldsymbol{n}| = 1$ transformation matrix used to recover the Cartesian conservation variables:

$$\boldsymbol{M}_t = \begin{bmatrix} 1 & 0 & 0 & 0 & 0 & 0 \\ 0 & n_1 & -n_2 & 0 & 0 & 0 \\ 0 & n_2 & n_1 & 0 & 0 & 0 \\ 0 & 0 & 0 & 1 & 0 & 0 \\ 0 & 0 & 0 & 0 & 1 & 0 \\ 0 & 0 & 0 & 0 & 0 & 1 \end{bmatrix}. \tag{3.63}$$

The quasi-linear form of the short-time averaged Euler equations (Eqn. 3.27) and the $k - \omega$ equations (Eqn. 3.62) are used in the next section to define characteristic based methods for estimating the convective fluxes.

3.5 Estimation of the Convective Fluxes

3.5.1 Introduction

In this study, the approximate Riemann solver of Roe (1981) is used to estimate the convective fluxes. Second order formal accuracy is achieved through the MUSCL (Monotone Upstream-centred Schemes for Conservation Laws) variable extrapolation method. Generally, two main types of numerical scheme are available for calculating convective fluxes, namely central difference schemes and asymmetric stencil schemes, that can be either upstream or downstream biased. Central difference schemes estimate the cell interface flux based on a symmetric stencil of cells either side of the interface. For non-smooth flow regions with large, near-discontinuous flow gradients, central difference schemes can develop numerical instabilities. The deficiency of central difference schemes in such regions is caused by a lack of sensitivity to the physical direction of propagation of the flow. The oscillatory behaviour of central difference schemes around discontinuities is improved by the addition of damping functions (artificial viscosity) or by the introduction of high order, low-pass filters.

Asymmetric stencil schemes comprise of two main types, *Flux Vector Splitting (FVS)* and *Flux Difference Splitting (FDS)* methods. Flux vector splitting schemes divide the flux Jacobian, Eqn. 3.26, into positive and negative contributions by determining the sign of the corresponding eigenvalues. The positive and negative contributions are then evaluated through forward or backward differences depending on the direction of the local characteristic. The sum of the two contributions is then used to compute the interface flux. Further details regarding central difference schemes and flux vector splitting techniques are provided in, for example, Hirsch (1990). A flux difference splitting method is used in this study. Flux difference splitting methods are introduced in section 3.5.2 by consideration of one specific group of methods, Godunov-type Riemann solvers.

3.5.2 Godunov-Type Riemann solvers

In finite volume Godunov-type methods, a continuous flow is discretised into a number of finite volumes, in which the flow state is constant in each elementary volume and is discontinuous between neighbouring volumes. This gives a piece-wise-constant approximation to the physical flow field. Godunov-type Riemann solvers use the discontinuity in flow variables across each cell interface as the initial conditions to a Riemann problem. The flux across each cell interface is then evaluated by computing the solution to the Riemann problem. A general introduction to the application of characteristic based methods to the Riemann problem is available in Toro (1999) and Hirsch (1990). Godunov-type Riemann solvers comprise of two main types, *exact Riemann solvers* and *approximate Riemann solvers*. Godunov's original, (1959), and revised, (1976), upwind schemes are examples of *exact* Riemann solvers. Considering the one-dimensional case, Godunov's (1976) method evaluates the interface flux by initially sampling the Riemann problem at each cell interface to determine the characteristic wave pattern. Once the identity of the left and right propagating waves have been established, the flux at the interface is computed using appropriate physical relations. To determine the pressure at the cell interface, an iterative procedure is required, such as a Newton-Raphson scheme. After computing the interface fluxes for each cell in the one dimensional scheme, the flux difference is integrated in time using a time step small enough to ensure that waves propagating from the two interfaces do not interact. This method is applied to multi-dimensional problems by dimensionally splitting the problem into a summation of one-dimensional problems. Computing the exact solution to the Riemann problem using the method of Godunov (1959, 1976) in this manner is computationally expensive. The computational cost is incurred in determining the wave pattern and in the iterative solution procedure required to calculate the pressure. The high cost of calculating the exact solution to the Riemann problem has prompted the development of approximate Riemann solvers; this includes the method used in the present study, the approximate Riemann solver of Roe (1981).

3.5.3 The Approximate Riemann Solver of Roe

Roe (1981) argues that the computational effort required to compute the exact solution to the Riemann problem is only justified if the accuracy of the solution is maintained in the remainder of the computational procedure. Roe (1981) proposes that an approximate solution to the Riemann problem may be sufficient, providing the solution still satisfactorily describes the non-linear behaviour of the Riemann problem. This section describes the approximate Riemann solver of Roe applied to the Euler equations. The $k-\omega$ formulation of the Roe approximate Riemann solver is described in Section 3.5.4. In the approximate Riemann solver of Roe, the Jacobian matrix, $\boldsymbol{A}$ in Eqn. 3.26, is replaced by a constant matrix $\hat{\boldsymbol{A}}$. This constant matrix is a function of the flow states either side of the finite volume interface and linearises the Euler equations. In order for the constant matrix to satisfactorily approximate the Jacobian matrix, the constant matrix must satisfy three properties, collectively termed 'property U'. These are:

1) The hyperbolic nature of the non-linear system of Euler equations should be maintained. The approximation must therefore possess a set of m real eigenvalues, $(\lambda_1, \ldots, \lambda_m)$, and a complete set of linearly independent eigenvectors, $(\boldsymbol{e_1}, \ldots, \boldsymbol{e_m})$.

2) The constant matrix $\hat{\boldsymbol{A}}$ should be consistent with the Jacobian $\boldsymbol{A}$.
In the limit as $\boldsymbol{U^L} \rightarrow \boldsymbol{U^R} \rightarrow \boldsymbol{U}$, then, $\hat{\boldsymbol{A}}\left(\boldsymbol{U^L}, \boldsymbol{U^R}\right) \rightarrow \boldsymbol{A}\left(\boldsymbol{U}\right)$.

3) The constant matrix $\hat{\boldsymbol{A}}$ should be conservative.
$\hat{\boldsymbol{A}}\left(\boldsymbol{U^L} - \boldsymbol{U^R}\right) = \boldsymbol{F}\left(\boldsymbol{U^R}\right)$ - $\boldsymbol{F}\left(\boldsymbol{U^L}\right)$.

In stating 'property U', L and R denote the variable state respectively to the left and to the right of a cell interface. Later in this section, Eqn. 3.73 presents an appropriate averaging technique for $\hat{\boldsymbol{A}}$, which satisfies property U.

A number of characteristic waves propagate away from the cell interface. Consider one such interface, located at $i+\frac{1}{2}$, separating two cells, i and $i+1$, to the left (L) and right (R) of the interface respectively. The flux is determined through a summation of the negative and positive travelling characteristic waves, either extrapolating from the left or from the right state:

$$\boldsymbol{F}_{i+\frac{1}{2}}\left(\boldsymbol{U^L},\boldsymbol{U^R}\right)\cdot\boldsymbol{n} \;=\; \boldsymbol{F}\left(\boldsymbol{U^L}\right)\cdot\boldsymbol{n}+\sum_{k}^{-}\hat{\alpha}_k\,\hat{\lambda}_k\,\hat{\boldsymbol{e}}_{\boldsymbol{k}}, \tag{3.64}$$

$$\boldsymbol{F}_{i+\frac{1}{2}}\left(\boldsymbol{U^L},\boldsymbol{U^R}\right)\cdot\boldsymbol{n} \;=\; \boldsymbol{F}\left(\boldsymbol{U^R}\right)\cdot\boldsymbol{n}-\sum_{k}^{+}\hat{\alpha}_k\,\hat{\lambda}_k\,\hat{\boldsymbol{e}}_{\boldsymbol{k}}, \tag{3.65}$$

or by interpolating from both states. Specifically, the arithmetic mean of Eqns. 3.64 and 3.65 gives

$$\boldsymbol{F}_{i+\frac{1}{2}}\left(\boldsymbol{U^L},\boldsymbol{U^R}\right)\cdot\boldsymbol{n} \;=\; \frac{1}{2}\left[\left(\boldsymbol{F}\left(\boldsymbol{U^L}\right)+\boldsymbol{F}\left(\boldsymbol{U^R}\right)\right)\cdot\boldsymbol{n}-\sum_{k=1}^{m}\hat{\alpha}_k|\hat{\lambda}_k|\hat{\boldsymbol{e}}_{\boldsymbol{k}}\right], \tag{3.66}$$

where m is the number of propagating characteristic waves. In a two-dimensional flow field there are four characteristic waves. These comprise of two acoustic waves, a shear wave and an entropy wave. The eigenvalues of the approximate Jacobian matrix quantify the speeds of the characteristic waves. These are computed by solving the characteristic equation, which is obtained from the determinant

$$|\hat{\boldsymbol{A}}-\hat{\lambda}\boldsymbol{I}| \;=\; 0. \tag{3.67}$$

The resulting eigenvalues for a two-dimensional inviscid flow are (Quirk, 1991):

$$\begin{aligned}
\hat{\lambda}_1 &= \hat{u}_n-\hat{a},\\
\hat{\lambda}_2 &= \hat{u}_n,\\
\hat{\lambda}_3 &= \hat{u}_n,\\
\hat{\lambda}_4 &= \hat{u}_n+\hat{a},
\end{aligned} \tag{3.68}$$

where $\hat{u}_n=(\hat{u}_1n_1+\hat{u}_2n_2)$ is the velocity normal to the cell interface. The corresponding eigenvectors can be found by substituting these eigenvalues into

$\left(\hat{\boldsymbol{A}} - \hat{\lambda}_k \boldsymbol{I}\right) \hat{\boldsymbol{e}}_{\boldsymbol{k}} = 0$, and solving for $\hat{\boldsymbol{e}}_{\boldsymbol{k}}$. Finally, the characteristic variables can be determined by considering the initial flow state discontinuity across the cell interface as the summation of wave strengths:

$$\boldsymbol{U^R} - \boldsymbol{U^L} = \sum_{k=1}^{m} \hat{\alpha}_k \, \hat{\boldsymbol{e}}_{\boldsymbol{k}}, \tag{3.69}$$

and solving for $\hat{\alpha}_k$. Similarly, the flux difference through the cell interface can be expressed as

$$\boldsymbol{F}\left(\boldsymbol{U^R}\right) - \boldsymbol{F}\left(\boldsymbol{U^L}\right) = \sum_{k=1}^{m} \hat{\alpha}_k \, |\hat{\lambda}_k| \hat{\boldsymbol{e}}_{\boldsymbol{k}}. \tag{3.70}$$

The conservative variable eigenvectors are therefore defined as

$$\begin{aligned}
\hat{\boldsymbol{e}}_{\mathbf{1}} &= \left[1, \hat{u}_n - \hat{a}, \hat{u}_t, \hat{h}_s - \hat{u}_n \hat{a}\right]^T, \\
\hat{\boldsymbol{e}}_{\mathbf{2}} &= \left[1, \hat{u}_n, \hat{u}_t, \frac{(\hat{u}_n^2 + \hat{u}_t^2)}{2}\right]^T, \\
\hat{\boldsymbol{e}}_{\mathbf{3}} &= \left[0, 0, 1, \hat{u}_t\right]^T, \\
\hat{\boldsymbol{e}}_{\mathbf{4}} &= \left[1, \hat{u}_n + \hat{a}, \hat{u}_t, \hat{h}_s + \hat{u}_n \hat{a}\right]^T,
\end{aligned} \tag{3.71}$$

where $\hat{u}_n = (\hat{u}_1 n_1 + \hat{u}_2 n_2)$ is the cell interface normal velocity and $\hat{u}_t = (\hat{u}_2 n_1 - \hat{u}_1 n_2)$ is the cell interface tangential velocity. The corresponding wave strengths are

$$\begin{aligned}
\hat{\alpha}_1 &= \frac{\Delta p - \hat{\rho}\hat{a}\Delta u_n}{2\hat{a}^2}, \\
\hat{\alpha}_2 &= \Delta\rho - \frac{\Delta p}{\hat{a}^2}, \\
\hat{\alpha}_3 &= \hat{\rho}\Delta u_t, \\
\hat{\alpha}_4 &= \frac{\Delta p + \hat{\rho}\hat{a}\Delta u_n}{2\hat{a}^2}.
\end{aligned} \tag{3.72}$$

In Eqn. 3.72, the symbol Δ represents the difference in the flow variables across the cell interface, for instance $\Delta p = p^R - p^L$. The form of the eigenvalues, eigenvectors and wave speeds defined in this section are derived using the exact quasi-linear form of the Euler equations. These are made to satisfy property U by the use of 'Roe

averaged variables', (Roe & Pike, 1984). The Roe averaged variables are denoted in Eqns. 3.68, 3.71 and 3.72 by the 'hat' (ˆ) symbol. These are

$$\begin{aligned}
\chi &= \sqrt{\frac{\rho^R}{\rho^L}}, \\
\hat{\rho} &= \chi\rho^L, \\
\hat{u}_n &= \frac{\chi u_n^R + u_n^L}{1+\chi}, \\
\hat{u}_t &= \frac{\chi u_t^R + u_t^L}{1+\chi}, \\
\hat{h}_s &= \frac{\chi h_s^R + h_s^L}{1+\chi}, \\
\hat{p} &= \frac{\chi p^R + p^L}{1+\chi}, \\
\hat{a} &= \sqrt{\frac{\gamma\hat{p}}{\hat{\rho}}}.
\end{aligned} \tag{3.73}$$

In summary, the flux at each cell interface is calculated by initially computing the Roe averaged variables to the left and right of the cell interface, Eqn. 3.73. The Roe averaged variables are then substituted into the equations for the eigenvalues, Eqn. 3.68, the eigenvectors, Eqn. 3.71, and the wave strengths, Eqn. 3.72. The interface flux is finally computed through a summation of the fluxes across each characteristic wave, Eqn. 3.66.

3.5.4 $k-\omega$ Formulation of the Approximate Riemann Solver of Roe

The approximate Riemann solver of Roe is used to estimate the convective fluxes in the short-time averaged Navier-Stokes equations. Introducing the $k-\omega$ turbulence closure of Wilcox (1993) in the short-time averaged Navier-Stokes equations modifies Eqn. 3.68 and Eqns. 3.71-3.73 by the addition of the specific turbulence kinetic energy (k) and of the specific dissipation rate (ω). The Roe averaged variables used

in the turbulent prediction are redefined as

$$\begin{aligned}
\chi &= \sqrt{\frac{\rho^R}{\rho^L}}, \\
\hat{\rho} &= \chi\rho^L, \\
\hat{u}_n &= \frac{\chi u_n^R + u_n^L}{1+\chi}, \\
\hat{u}_t &= \frac{\chi u_t^R + u_t^L}{1+\chi}, \\
\hat{h}_s &= \frac{\chi h_s^R + h_s^L}{1+\chi}, \\
\hat{p} &= \frac{\chi p^R + p^L}{1+\chi}, \\
\hat{k} &= \frac{\chi k^R + k^L}{1+\chi}, \\
\hat{\omega} &= \frac{\chi \omega^R + \omega^L}{1+\chi}, \\
\hat{a}_t &= \sqrt{\left(\frac{\gamma\hat{p}}{\hat{\rho}} + \frac{2}{3}\gamma\hat{k}\right)}.
\end{aligned} \tag{3.74}$$

In Eqn. 3.74, $u_n = (u_1 n_1 + u_2 n_2)$ and $u_t = (u_2 n_1 - u_1 n_2)$ are the normal and tangential components of velocity with respect to the computational cell boundary. $\hat{a}_t$ is the numerical speed of sound, which, with the $k-\omega$ turbulence closure becomes greater than the conventional isentropic relationship for a perfect gas, $a = \sqrt{\gamma p/\rho}$. The eigenvalues for the turbulent prediction are

$$\begin{aligned}
\hat{\lambda}_1 &= \hat{u}_n - \hat{a}_t, \\
\hat{\lambda}_2 &= \hat{u}_n, \\
\hat{\lambda}_3 &= \hat{u}_n, \\
\hat{\lambda}_4 &= \hat{u}_n + \hat{a}_t, \\
\hat{\lambda}_5 &= \hat{u}_n, \\
\hat{\lambda}_6 &= \hat{u}_n.
\end{aligned} \tag{3.75}$$

In Eqn. 3.75, $\hat{\lambda}_5$ and $\hat{\lambda}_6$ are the eigenvalues associated to the $\hat{k}$ and $\hat{\omega}$ transport equations. The corresponding eigenvectors are

$$\begin{aligned}
\hat{\boldsymbol{e}}_{\mathbf{1}} &= \left[1, \hat{u}_n - \hat{a}_t, \hat{u}_t, \left(\hat{h}_s + \frac{2}{3}\hat{k}\right) - \hat{u}_n\hat{a}_t, \hat{k}, \hat{\omega}\right]^T, \\
\hat{\boldsymbol{e}}_{\mathbf{2}} &= \left[1, \hat{u}_n, \hat{u}_t, \left(\hat{h}_s + \frac{2}{3}\hat{k}\right) - \frac{\hat{a}_t^2}{(\gamma-1)}, \hat{k}, \hat{\omega}\right]^T, \\
\hat{\boldsymbol{e}}_{\mathbf{3}} &= [0, 0, 1, \hat{u}_t, 0, 0]^T, \\
\hat{\boldsymbol{e}}_{\mathbf{4}} &= \left[1, \hat{u}_n + \hat{a}_t, \hat{u}_t, \left(\hat{h}_s + \frac{2}{3}\hat{k}\right) + \hat{u}_n\hat{a}_t, \hat{k}, \hat{\omega}\right]^T, \\
\hat{\boldsymbol{e}}_{\mathbf{5}} &= \left[0, 0, 0, \frac{3\gamma - 5}{3(\gamma-1)}, 1, 0\right]^T, \\
\hat{\boldsymbol{e}}_{\mathbf{6}} &= [0, 0, 0, 0, 0, 1]^T.
\end{aligned} \tag{3.76}$$

The characteristic wave strengths are defined as

$$\begin{aligned}
\hat{\alpha}_1 &= \frac{1}{2\hat{a}_t^2}\left[\Delta p + \frac{2}{3}\left(\hat{\rho}\Delta k + \hat{k}\Delta\rho\right) - \hat{\rho}\hat{a}_t\Delta u_n\right], \\
\hat{\alpha}_2 &= \Delta\rho - \frac{1}{\hat{a}_t^2}\left[\Delta p + \frac{2}{3}\left(\hat{\rho}\Delta k + \hat{k}\Delta\rho\right)\right], \\
\hat{\alpha}_3 &= \hat{\rho}\Delta\hat{u}_t, \\
\hat{\alpha}_4 &= \frac{1}{2\hat{a}_t^2}\left[\Delta p + \frac{2}{3}\left(\hat{\rho}\Delta k + \hat{k}\Delta\rho\right) + \hat{\rho}\hat{a}_t\Delta u_n\right], \\
\hat{\alpha}_5 &= \hat{\rho}\Delta k, \\
\hat{\alpha}_6 &= \hat{\rho}\Delta\omega.
\end{aligned} \tag{3.77}$$

The interface flux is estimated from the procedure outlined in Section 3.5.3, using Eqns. 3.74-3.77.

3.5.5 Entropy Preservation

A well-documented problem with the approximate Riemann solver of Roe is that non-physical discontinuities are permitted in regions of expansion. Although expansion shocks are one possible mathematical solution to the Riemann problem, these are associated with negative increases in entropy. This contravenes the second law of thermodynamics and does not represent a physical solution to the governing equa-

tions. Expansion shocks occur as the local velocity in the expansion wave achieves the sonic velocity. At the sonic velocity, one of the acoustic eigenvalues takes a value of zero and a discontinuity is propagated as an expansion shock. A detailed introduction to the characteristic properties of expansion shocks, contact surfaces and compression shocks is provided by Toro (1999). Expansion shocks are eliminated in this study using the entropy modification of Harten & Hyman (1983). This modifies the eigenvalues around the sonic point to include localised differentiable gradients. The Harten & Hyman (1983) modification used in this study defines

$$\left|\hat{\lambda}_m\right| = \begin{cases} \left|\hat{\lambda}_m\right| & \forall \left|\hat{\lambda}_m\right| \geq \varepsilon_m^\star \\ \varepsilon_m^\star & \forall \left|\hat{\lambda}_m\right| < \varepsilon_m^\star \end{cases}, \tag{3.78}$$

where, $\varepsilon_m^\star$ is defined as

$$\varepsilon_m^\star = \max\left[0,\, \left(\hat{\lambda}_m - \lambda_m^L\right),\, \left(\lambda_m^R - \hat{\lambda}_m\right)\right]. \tag{3.79}$$

The eigenvalue to be modified is defined by $\hat{\lambda}_m$. λ_m^L and λ_m^R are the corresponding eigenvalues computed using the variables stored in the contiguous cells to the left and right of the interface. The positive direction is taken as being from left to right. This formulation distinguishes expansion waves from compression waves by a zero in the $\varepsilon_m^\star$ equation. By definition, the speed of characteristics behind a compression shock are greater in magnitude than those leading the shock. Conversely, in a region of expansion, $\lambda_m^L < \lambda_m < \lambda_m^R$. Therefore, $\varepsilon_m^\star > 0$. Equation 3.78 ensures that $\lambda_m^L < \varepsilon_m^\star < \lambda_m^R$, inhibiting the formation of expansion shocks. As $\varepsilon_m^\star = 0$ for compression shock waves, where $\lambda_m^L > \lambda_m > \lambda_m^R$, these remain unmodified by Eqn. 3.78 while expansion shocks are eliminated. The current implementation of the Harten & Hyman modification is validated by predicting a one dimensional Riemann problem test case with a transonic expansion fan. A detailed description of this test case, which is a modified form of the shock-tube problem of Sod (1978), is available in Toro (1999). A rectangular computational domain of length l defines the length of the tube along x_1. The initial flow field is divided into two contiguous regions, extending over the range $0 \leq x_1 \leq l/3$ and $l/3 \leq x_1 \leq l$ respectively. These two flow

regions are initially separated by a diaphragm at $x_1 = l/3$. The initial conditions to the left and right of this diaphragm are defined in Table 3.1.

Variable	Left	Right
ρ/ρ_r	8.0	1.0
u_1/a_∞	0.75	0.0
p/p_r	10	1.0

Table 3.1: Riemann problem initial conditions.

The computational domain extends $0 \leq x_2 \leq l/8$ in the flow normal direction. Periodic boundary conditions, of the type described in Section 3.9.6, are imposed at $x_2 = 0$ and $x_2 = l/8$. Extrapolation outlet boundary conditions, as described in Section 3.9.4, are imposed at the flow normal boundaries $x_1 = 0$ and $x_1 = l$. The computational domain is discretised by a uniform mesh of 250×32 cells. The numerical solution is time marched from the initial conditions in Table 3.1 to a final time of $t = 0.25l/a_\infty$ seconds, in constant time steps of $\Delta t = 1.0 \times 10^{-4} l/a_\infty$ seconds. The resulting density profile after $t = 0.25l/a_\infty$ seconds, computed using the first order approximate Riemann solver of Roe without the Harten & Hyman (1983) entropy modification, is given in Figure 3.1. The stream-wise distance is normalised using the computational domain length l. The density in Figure 3.1 is normalised by the density to the right of the diaphragm, at time $t = 0$, given in Table 3.1. A benchmark analytical solution for this problem is obtained from the shock-tube analysis in Hirsch (1990) and is overlaid on the numerical prediction in Figure 3.1. An expansion fan extends over the region, $0.23l \leq x_1 \leq 0.41l$; a contact discontinuity is located at $x_1 = 0.67l$ and a compression shock wave is evident at $x_1 = 0.87l$. The location and magnitude of these flow features are correctly predicted by the first order scheme, in comparison to the analytical solution. A significant expansion shock is however evident in Figure 3.1, at $x_1 = l/3$.

A comparative prediction of the Riemann problem, with application of the entropy modification of Harten & Hyman (1983), is shown in Figure 3.2. This density profile is computed from identical initial conditions, and uses the same first order approximate Riemann solver of Roe, as for Figure 3.1. Figure 3.2 shows the density profile

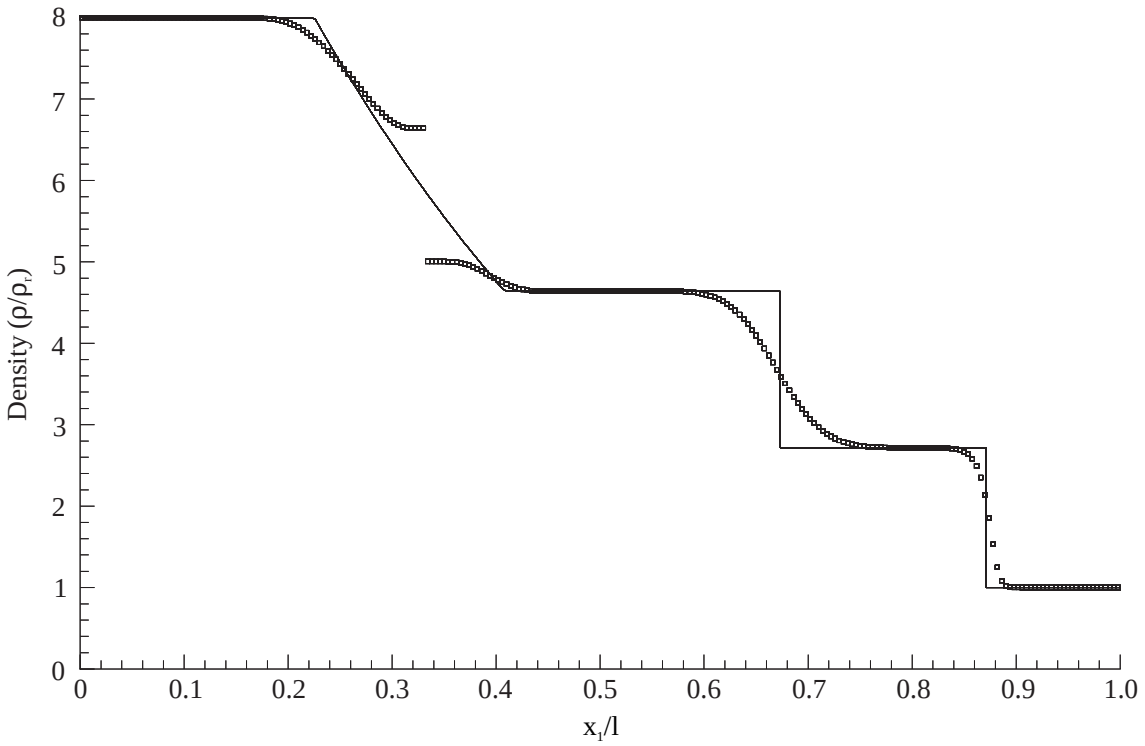

Figure 3.1: Riemann problem density profile at $t = 0.25l/a_\infty$ seconds. First order Roe approximate Riemann solver without entropy modification. □ numerical prediction, — analytical solution.

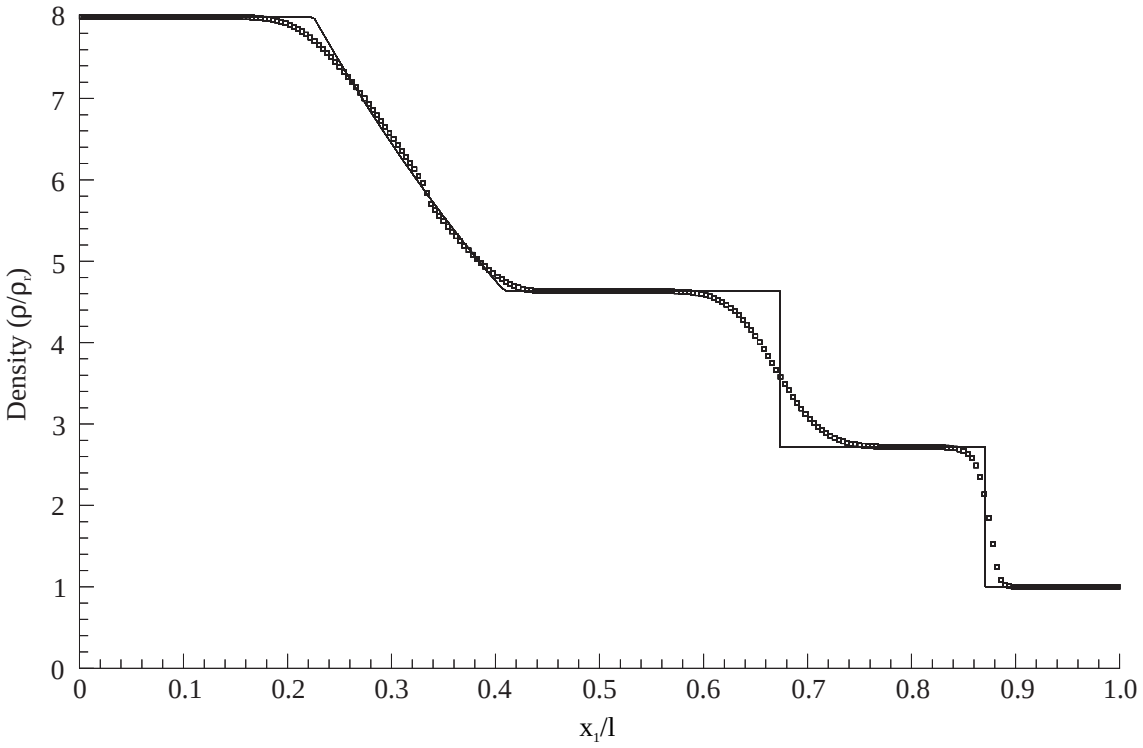

Figure 3.2: Riemann problem density profile at $t = 0.25l/a_\infty$ seconds. First order Roe approximate Riemann solver with the Harten & Hyman (1983) entropy modification. □ numerical prediction, — analytical solution.

after $t = 0.25l/a_\infty$ seconds. The entropy modification of Harten & Hyman (1983) significantly reduces the influence of the expansion shock in Figure 3.2. Only a small region, of differentiable gradient, remains at $x_1 = l/3$. The significant reduction of the expansion shock justifies the use of the Harten & Hyman (1983) entropy modification in this study. Further justification of the Harten & Hyman (1983) entropy modification to higher order accurate solutions, through a MUSCL extrapolation with the approximate Riemann solver of Roe (1981), is presented in Section 3.5.8.

3.5.6 Higher Order Spatial Accuracy - MUSCL Extrapolation

The approximate Riemann solver of Roe (1981) is monotone and conservative but only first order accurate in space. Numerical predictions based on this first order method contain excessive diffusion. In the present study, a higher order extension to the numerical method is considered using the MUSCL (Monotone Upstream-centred Schemes for Conservation Laws) approach. The MUSCL approach, introduced by Van Leer (1979), achieves high order spatial accuracy by replacing the piece-wise constant data in each cell by linear or quadratic approximations, as diagrammatically shown in Figure 3.3. The redistributed volume averaged flow states at the cell interfaces are then used as the initial conditions to the Riemann problem. The approximate Riemann solver of Roe is then used in the present study to solve the Riemann problem at each cell interface. The variable extrapolation at each cell interface can be derived based on a Taylor series expansion in each cell, as described in Hirsch (1990). Following the transformation of the Taylor series expansion to volume average variables, and introducing the parameter η for convenience, the extrapolated variables to the left and right of an interface located at $i + \frac{1}{2}$ are defined by

$$\boldsymbol{U}^L_{i+\frac{1}{2}} = \boldsymbol{U}_i + \frac{\varepsilon}{4}\left[(1-\eta)\,\Delta\boldsymbol{U}_{i-\frac{1}{2}} + (1+\eta)\,\Delta\boldsymbol{U}_{i+\frac{1}{2}}\right], \tag{3.80}$$

$$\boldsymbol{U}^R_{i+\frac{1}{2}} = \boldsymbol{U}_{i+1} - \frac{\varepsilon}{4}\left[(1-\eta)\,\Delta\boldsymbol{U}_{i+\frac{3}{2}} + (1+\eta)\,\Delta\boldsymbol{U}_{i+\frac{1}{2}}\right]. \tag{3.81}$$

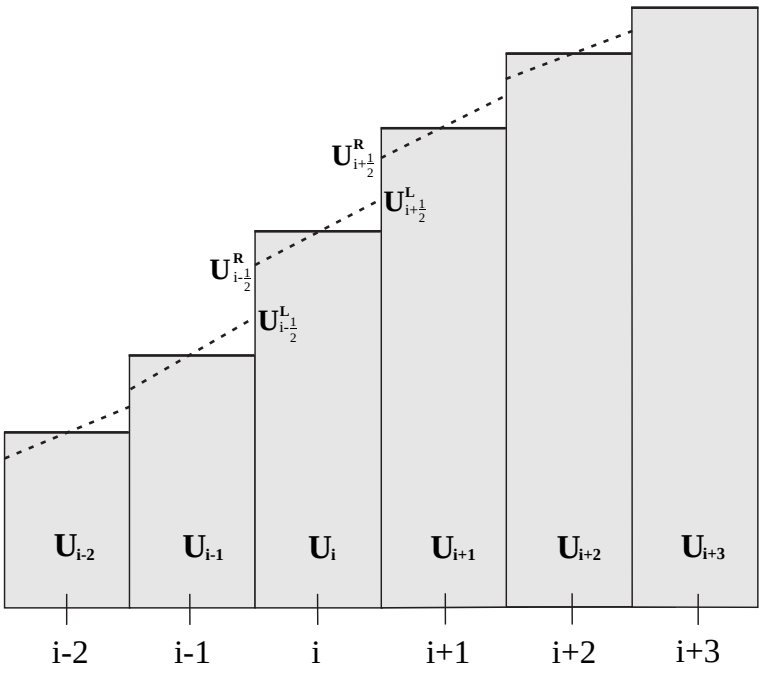

Figure 3.3: Discrete variable approximation. (—) Piece-wise constant approximation, (- - -) piece-wise linear approximation.

In Eqns. 3.80 and 3.81, the volume averaged flow state differences, $\Delta \boldsymbol{U}$, are:

$$\Delta \boldsymbol{U}_{i-\frac{1}{2}} = \boldsymbol{U}_i - \boldsymbol{U}_{i-1}, \tag{3.82}$$

$$\Delta \boldsymbol{U}_{i+\frac{1}{2}} = \boldsymbol{U}_{i+1} - \boldsymbol{U}_i, \tag{3.83}$$

$$\Delta \boldsymbol{U}_{i+\frac{3}{2}} = \boldsymbol{U}_{i+2} - \boldsymbol{U}_{i+1}. \tag{3.84}$$

The parameter η is introduced to allow the spatial accuracy of the MUSCL scheme to be defined explicitly. In the present study, $\eta = \frac{1}{3}$. Alternative values for η are given in Table 3.2. For the present study, $\varepsilon = 1$. For $\varepsilon = 0$, the first order piece-wise

η	**Description**
-1	Asymmetric biased stencil method.
0	Fromm scheme.
1/2	'QUICK' method of Leonard.
1/3	Second order asymmetric biased method.
1	Three point central difference method.

Table 3.2: Selection of MUSCL 'η' parameter values, from Manna (1992).

constant distribution is recovered.

3.5.7 Total Variation Diminishing (TVD) Schemes

The high order MUSCL approach introduced in section 3.5.6 provides a conservative method for increasing the spatial accuracy of the numerical scheme through variable extrapolation. High order accurate methods are susceptible to numerical instabilities across discontinuities, leading to non-monotone flow predictions. To prevent oscillatory behaviour at discontinuities, the variable gradients estimated by the MUSCL scheme are limited. By definition, Hirsch (1990), a numerical method is monotone if it results in a non-oscillatory solution that satisfies the entropy condition, which is defined in Hirsch (1990). Godunov's theorem states that all *linear* monotone schemes are at most first order accurate. The proof underlying Godunov's theorem is reported in Roe (1986). The concept of the Total Variation Diminishing (TVD) scheme provides a less stringent condition to that of a monotone scheme and preserves monotonicity in an initially monotone flow field. The TVD condition ensures that no new extrema are created in the flow field and that the absolute magnitude of local maxima and minima are decreasing as the solution progresses. The Total Variation (TV) of the conservative variable vector $\boldsymbol{U}$ is defined as

$$TV\left(\boldsymbol{U}^n\right) \;=\; \sum_{i=1}^{N_i} |\boldsymbol{U}_{i+1}^n - \boldsymbol{U}_i^n|, \tag{3.85}$$

where N_i is the total number of cells in the computational domain. n represents the solution time stage. The condition for a TVD scheme therefore requires that the total variation decreases as the flow field develops over time:

$$TV\left(\boldsymbol{U}^{n+1}\right) \;\leq\; TV\left(\boldsymbol{U}^n\right). \tag{3.86}$$

3.5.8 The Minmod Flux Limiter

To ensure the higher order extension to the flux estimation satisfies the TVD criterion of Eqn. 3.86, limiting functions are added to the MUSCL extrapolation. These

additional terms prevent new local extrema from appearing in the flow prediction. Since Godunov's theorem applies to TVD schemes, these limiting functions must be non-linear. The limited MUSCL extrapolation for the cell interface, $i+\frac{1}{2}$, is defined as

$$\boldsymbol{U}^L_{i+\frac{1}{2}} = \boldsymbol{U}_i + \frac{\varepsilon}{4}\left[(1-\eta)\,\boldsymbol{\Phi}^R_{i-\frac{1}{2}}\Delta\boldsymbol{U}_{i-\frac{1}{2}} + (1+\eta)\,\boldsymbol{\Phi}^L_{i+\frac{1}{2}}\Delta\boldsymbol{U}_{i+\frac{1}{2}}\right], \tag{3.87}$$

$$\boldsymbol{U}^R_{i+\frac{1}{2}} = \boldsymbol{U}_{i+1} - \frac{\varepsilon}{4}\left[(1-\eta)\,\boldsymbol{\Phi}^L_{i+\frac{3}{2}}\Delta\boldsymbol{U}_{i+\frac{3}{2}} + (1+\eta)\,\boldsymbol{\Phi}^R_{i+\frac{1}{2}}\Delta\boldsymbol{U}_{i+\frac{1}{2}}\right]. \tag{3.88}$$

Each limiting term $\boldsymbol{\Phi}$ is a function of r. The variable r is defined as the ratio of the local to the upwind wave strength, where the upwind direction may be denoted by the superscript in $\boldsymbol{\Phi}$, for instance, $\boldsymbol{\Phi}^R_{i-\frac{1}{2}}$ represents a limiter for a right going wave. Therefore:

$$\begin{aligned}
\boldsymbol{\Phi}^R_{i-\frac{1}{2}} &= \boldsymbol{\Phi}\left(\frac{\boldsymbol{U}_{i+1}-\boldsymbol{U}_i}{\boldsymbol{U}_i-\boldsymbol{U}_{i-1}}\right) = \boldsymbol{\Phi}\left(r^L\right),\\
\boldsymbol{\Phi}^L_{i+\frac{1}{2}} &= \boldsymbol{\Phi}\left(\frac{\boldsymbol{U}_i-\boldsymbol{U}_{i-1}}{\boldsymbol{U}_{i+1}-\boldsymbol{U}_i}\right) = \boldsymbol{\Phi}\left(\frac{1}{r^L}\right),\\
\boldsymbol{\Phi}^L_{i+\frac{3}{2}} &= \boldsymbol{\Phi}\left(\frac{\boldsymbol{U}_{i+1}-\boldsymbol{U}_i}{\boldsymbol{U}_{i+2}-\boldsymbol{U}_{i+1}}\right) = \boldsymbol{\Phi}\left(r^R\right),\\
\boldsymbol{\Phi}^R_{i+\frac{1}{2}} &= \boldsymbol{\Phi}\left(\frac{\boldsymbol{U}_{i+2}-\boldsymbol{U}_{i+1}}{\boldsymbol{U}_{i+1}-\boldsymbol{U}_i}\right) = \boldsymbol{\Phi}\left(\frac{1}{r^R}\right),
\end{aligned} \tag{3.89}$$

where:

$$\boldsymbol{\Phi}(r) = \text{minmod}(1,r) = \max\left[0,\min(1,r)\right]. \tag{3.90}$$

The minmod limiter satisfies the symmetry property

$$\boldsymbol{\Phi}(r) = r\boldsymbol{\Phi}\left(\frac{1}{r}\right). \tag{3.91}$$

This ensures that forward and backward differences are treated in the same manner. The non-linear limiting function $\boldsymbol{\Phi}$ is constrained to lie within defined parameters, to satisfy the TVD condition. The constraints introduced by Sweby (1984) for

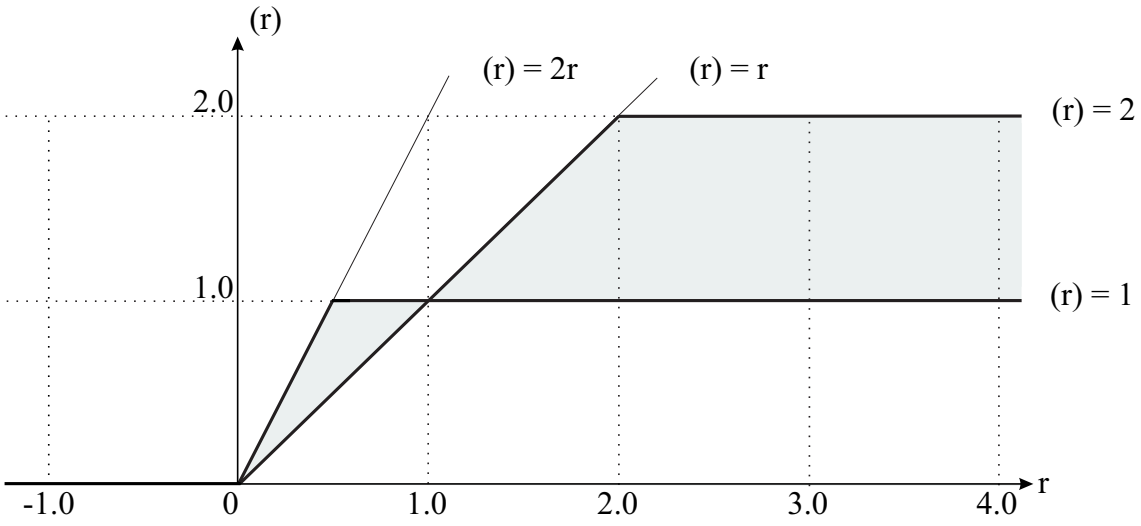

Figure 3.4: TVD limiter region, after Sweby (1984).

second-order, explicit schemes using limiters that satisfy Eqn. 3.91 are

$$\begin{aligned} \boldsymbol{\Phi}(r) &= 0 && \forall\ r \leq 0, \\ r \leq \boldsymbol{\Phi}(r) &\leq \min(1, 2r) && \forall\ 0 < r \leq 1, \\ 1 \leq \boldsymbol{\Phi}(r) &\leq \min(2, r) && \forall\ r > 1. \end{aligned} \tag{3.92}$$

The limiting region provided by Eqn. 3.92 is shown graphically in Figure 3.4. The minmod limiter follows the lower bounds of the TVD region in Figure 3.4 and is shown graphically in Figure 3.5. For two adjacent flow state gradients ($\Delta \boldsymbol{U}$), of the same sign ($r > 0$), the minmod limiter imposes the minimum of the two gradients. For adjacent gradients of opposite sign ($r < 0$), the limiter assumes a value of zero. The minmod limited gradients for the MUSCL extrapolation are given by

$$\begin{aligned} \Delta\overline{\overline{\boldsymbol{U}}}_{i-\frac{1}{2}} &= \boldsymbol{\Phi}^R_{i-\frac{1}{2}}\, \Delta \boldsymbol{U}_{i-\frac{1}{2}}, \\ \Delta\overline{\overline{\boldsymbol{U}}}_{i+\frac{1}{2}} &= \boldsymbol{\Phi}^L_{i+\frac{1}{2}}\, \Delta \boldsymbol{U}_{i+\frac{1}{2}}, \\ \Delta\overline{\overline{\boldsymbol{U}}}_{i+\frac{3}{2}} &= \boldsymbol{\Phi}^L_{i+\frac{3}{2}}\, \Delta \boldsymbol{U}_{i+\frac{3}{2}}, \\ \Delta\overline{\overline{\boldsymbol{U}}}'_{i+\frac{1}{2}} &= \boldsymbol{\Phi}^R_{i+\frac{1}{2}}\, \Delta \boldsymbol{U}_{i+\frac{1}{2}}. \end{aligned} \tag{3.93}$$

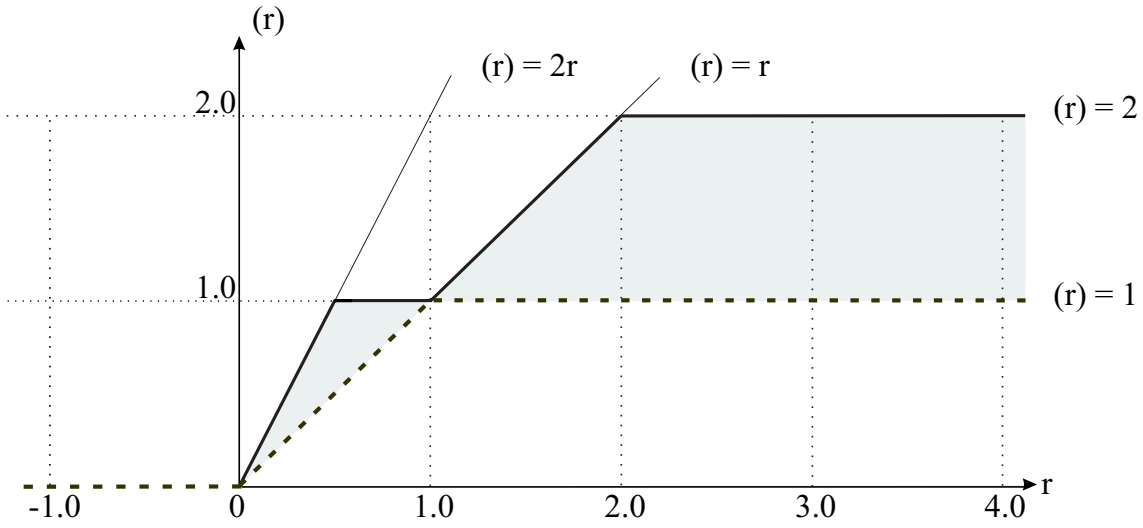

Figure 3.5: Minmod limiter, Eqn. 3.90, (—) TVD region boundary, (- - -) minmod limiter function.

In regions of near uniform flow, $\Delta \boldsymbol{U} \rightarrow 0$. To prevent numerical underflow when evaluating r, Eqn. 3.93 is recast as

$$\begin{aligned}
\Delta\overline{\overline{\boldsymbol{U}}}_{i-\frac{1}{2}} &= \operatorname{sign}\left(\Delta \boldsymbol{U}_{i-\frac{1}{2}}\right) \cdot \max\left[0, \min\left(|\Delta \boldsymbol{U}_{i-\frac{1}{2}}|, \Delta \boldsymbol{U}_{i+\frac{1}{2}} \cdot \operatorname{sign}\left(\Delta \boldsymbol{U}_{i-\frac{1}{2}}\right)\right)\right], \\
\Delta\overline{\overline{\boldsymbol{U}}}_{i+\frac{1}{2}} &= \operatorname{sign}\left(\Delta \boldsymbol{U}_{i+\frac{1}{2}}\right) \cdot \max\left[0, \min\left(|\Delta \boldsymbol{U}_{i+\frac{1}{2}}|, \Delta \boldsymbol{U}_{i-\frac{1}{2}} \cdot \operatorname{sign}\left(\Delta \boldsymbol{U}_{i+\frac{1}{2}}\right)\right)\right], \\
\Delta\overline{\overline{\boldsymbol{U}}}_{i+\frac{3}{2}} &= \operatorname{sign}\left(\Delta \boldsymbol{U}_{i+\frac{3}{2}}\right) \cdot \max\left[0, \min\left(|\Delta \boldsymbol{U}_{i+\frac{3}{2}}|, \Delta \boldsymbol{U}_{i+\frac{1}{2}} \cdot \operatorname{sign}\left(\Delta \boldsymbol{U}_{i+\frac{3}{2}}\right)\right)\right], \\
\Delta\overline{\overline{\boldsymbol{U}}}'_{i+\frac{1}{2}} &= \operatorname{sign}\left(\Delta \boldsymbol{U}_{i+\frac{1}{2}}\right) \cdot \max\left[0, \min\left(|\Delta \boldsymbol{U}_{i+\frac{1}{2}}|, \Delta \boldsymbol{U}_{i+\frac{3}{2}} \cdot \operatorname{sign}\left(\Delta \boldsymbol{U}_{i+\frac{1}{2}}\right)\right)\right].
\end{aligned} \tag{3.94}$$

The final form of the minmod limited MUSCL extrapolation is

$$\boldsymbol{U}^{L}_{i+\frac{1}{2}} = \boldsymbol{U}_i + \frac{\varepsilon}{4}\left[(1-\eta)\,\Delta\overline{\overline{\boldsymbol{U}}}_{i-\frac{1}{2}} + (1+\eta)\,\Delta\overline{\overline{\boldsymbol{U}}}_{i+\frac{1}{2}}\right], \tag{3.95}$$

$$\boldsymbol{U}^{R}_{i+\frac{1}{2}} = \boldsymbol{U}_{i+1} - \frac{\varepsilon}{4}\left[(1-\eta)\,\Delta\overline{\overline{\boldsymbol{U}}}_{i+\frac{3}{2}} + (1+\eta)\,\Delta\overline{\overline{\boldsymbol{U}}}'_{i+\frac{1}{2}}\right]. \tag{3.96}$$

Equations 3.95 and 3.96 are mathematically identical to Equations 3.87 and 3.88, but eliminate the requirement to evaluate $r = \lim_{\Delta U \rightarrow 0}\left(\frac{\Delta \boldsymbol{U}}{\Delta \overline{\boldsymbol{U}}}\right)$ for uniform flows, in their numerical implementation.

The Harten & Hyman (1983) entropy modification, validated for the first order approximate Riemann solver of Roe (1981) in Section 3.5.5, is further validated for the

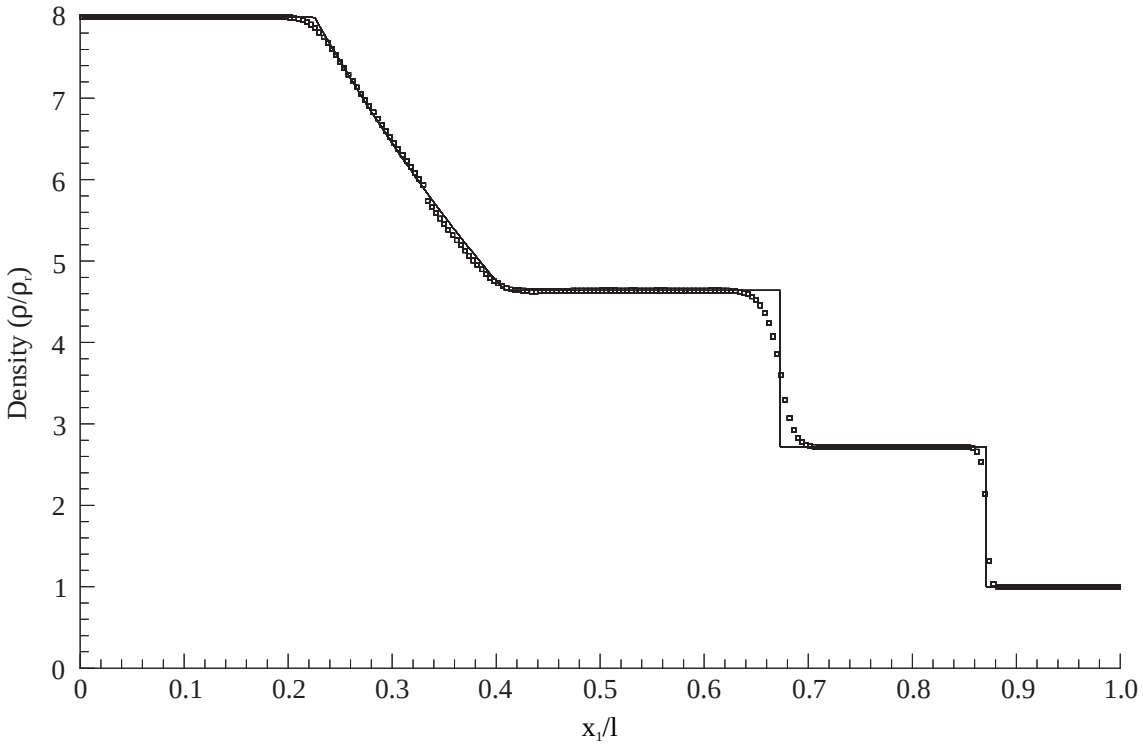

Figure 3.6: Riemann problem normalised density profile at $t = 0.25l/a_\infty$ seconds. Second order MUSCL scheme using the Roe approximate Riemann solver with the minmod flux limiter. No entropy modification. □ numerical prediction, (—) analytical solution.

second order MUSCL scheme with application of the minmod flux limiter. Increasing the formal accuracy of the spatial integration method to second order and applying the minmod flux limiter further reduces the influence of the expansion shock, even without entropy modification. The Riemann problem, predicted using the second order MUSCL scheme with the minmod flux limiter, is shown in Figure 3.6 without application of the Harten & Hyman entropy modification. The location of the expansion shock is unaltered and is sited at $x_1 = l/3$. The entropy modification of Harten & Hyman (1983) further reduces the expansion shock, as shown in Figure 3.7. The resulting prediction follows the analytical profile closely across the expansion fan, thereby justifying the application of the Harten & Hyman (1983) entropy modification to the second order extension of Roe's approximate Riemann solver.

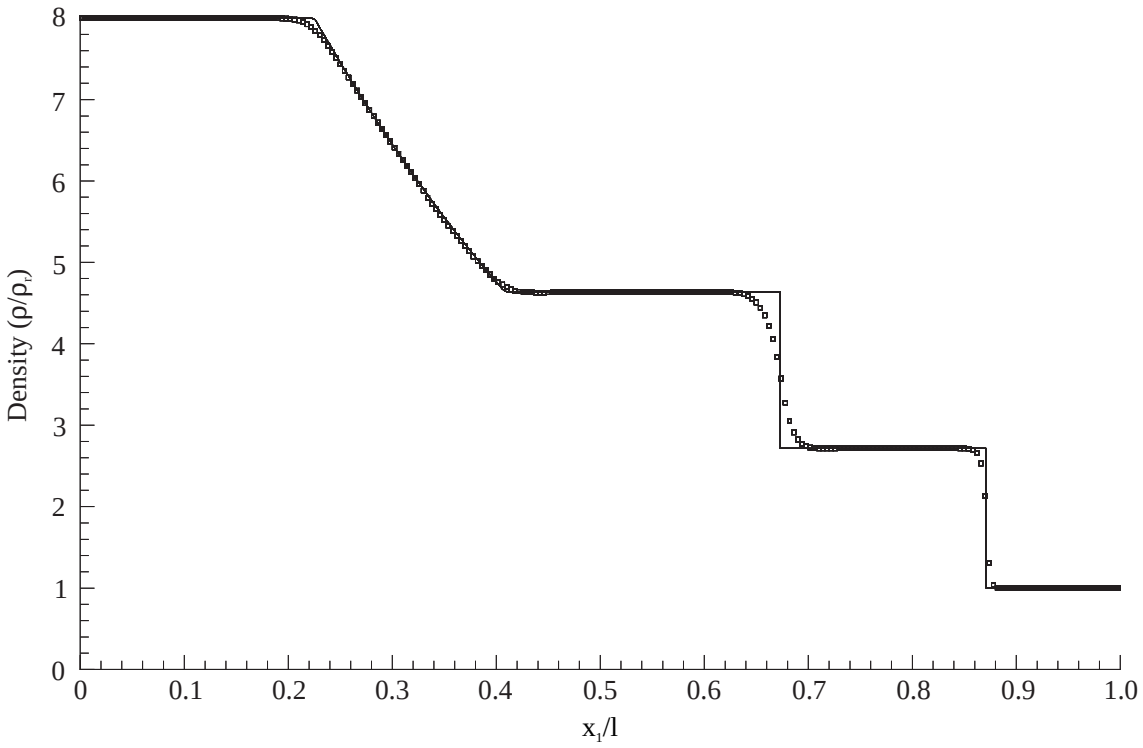

Figure 3.7: Riemann problem normalised density profile at $t = 0.25l/a_\infty$ seconds. Second order MUSCL scheme using the Roe approximate Riemann solver with the minmod flux limiter. Entropy modification of Harten & Hyman (1983). □ numerical prediction, (—) analytical solution.

3.6 Estimation of the Turbulent Fluxes

The turbulent flux vector $\boldsymbol{F_t}(\boldsymbol{U})$ in the short-time averaged Navier-Stokes equations is defined by Eqn. 3.56. The addition of the turbulent flux to the convective flux $\boldsymbol{F_c}(\boldsymbol{U})$ defines the 'total flux' crossing each unit cell interface. Consider the interface $\left(i+\frac{1}{2},j\right)$ connecting the cells (i,j) and $(i+1,j)$ in the section of grid outlined in Figure 3.8. The turbulent flux vector is estimated using a symmetric stencil of cells across the interface. The short-time averaged velocity vector, $\bar{\boldsymbol{u}}$, at $\left(i+\frac{1}{2},j\right)$ is interpolated as

$$\bar{\boldsymbol{u}}_{i+\frac{1}{2},j} = \frac{1}{2}\left(\bar{\boldsymbol{u}}_{i+1,j}+\bar{\boldsymbol{u}}_{i,j}\right), \tag{3.97}$$

Similar expressions define $\boldsymbol{q}$, $\boldsymbol{q_t}$, μ_l and μ_t in Eqn. 3.56. The spatial gradients of $\bar{\boldsymbol{u}}$, $\bar{T}$, $\bar{k}$ and $\bar{\omega}$ at $\left(i+\frac{1}{2},j\right)$ are determined from Gauss' divergence theorem. First, a trapezoidal frame is described across $\left(i+\frac{1}{2},j\right)$. The perimeter of this trapezoidal frame is defined using dashed red lines in Figure 3.8. The four corners of the quadrilateral $ABCD$ are located at the midpoints of the surrounding cell interfaces. In the present numerical implementation, the spatial coordinates of the lower left-hand vertex are stored for each cell. For example, the coordinate vector $\boldsymbol{x}_{i,j}$ is defined as the cell vertex joining cells (i,j), $(i,j-1)$, $(i-1,j-1)$ and $(i-1,j)$, where $\boldsymbol{x}=(x_1,x_2)^T$. The spatial coordinate vector, $\boldsymbol{x}^A_{i,j}$ in Figure 3.8 is therefore defined as

$$\boldsymbol{x}^A = \frac{1}{2}\left(\boldsymbol{x}_{i+1,j+1}+\boldsymbol{x}_{i,j+1}\right). \tag{3.98}$$

Similar expressions define the remaining three corners. Next, the flow state along each side of the trapezoidal frame is estimated. The velocity vectors $\bar{\boldsymbol{u}}^{\boldsymbol{N}}$, $\bar{\boldsymbol{u}}^{\boldsymbol{E}}$, $\bar{\boldsymbol{u}}^{\boldsymbol{S}}$

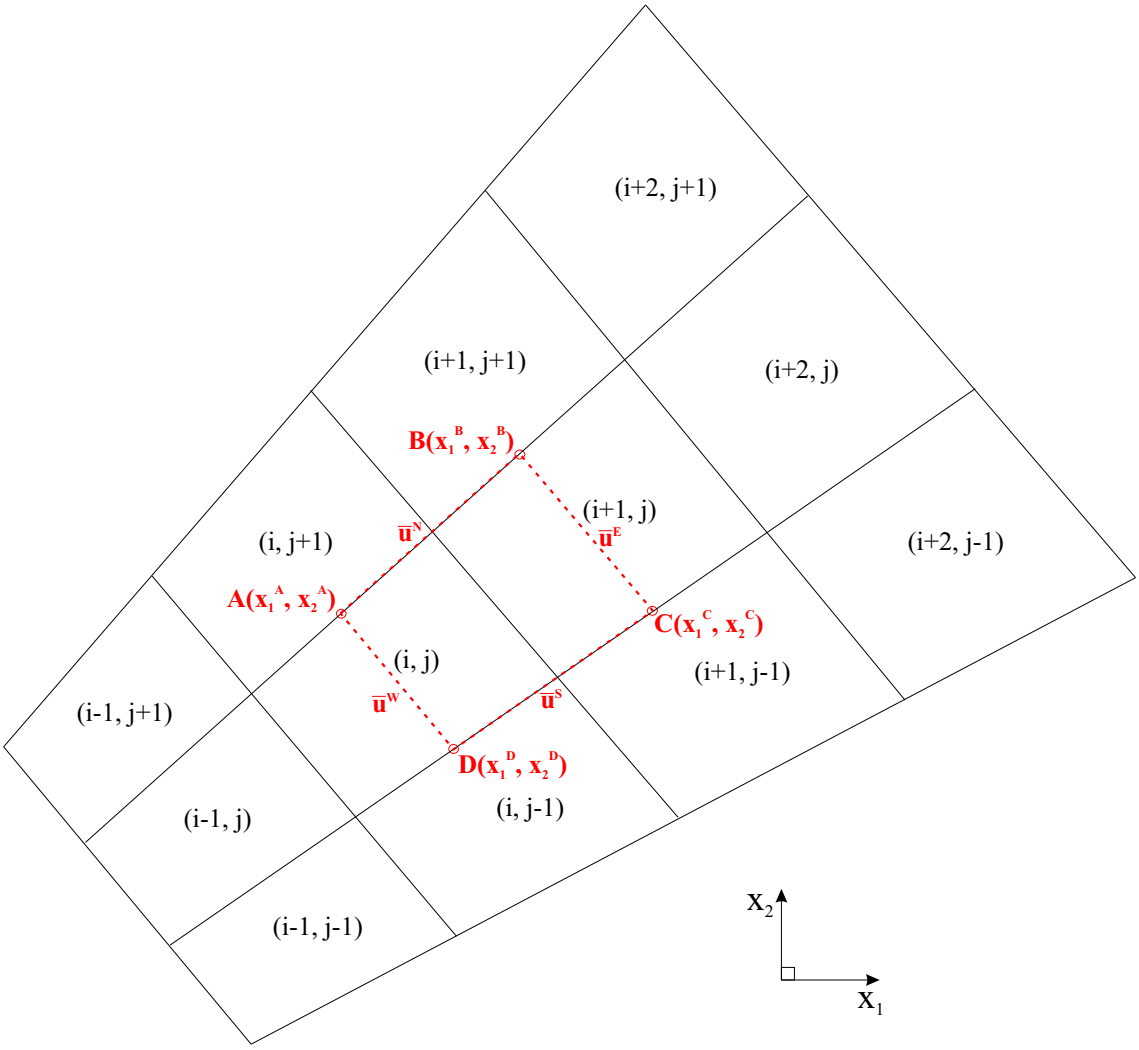

Figure 3.8: Turbulent flux central difference stencil for $i + \frac{1}{2}$. (—) Computational cell boundary, (- - -) turbulent flux boundary for $\left(i + \frac{1}{2}, j\right)$.

and $\bar{\boldsymbol{u}}^{\boldsymbol{W}}$ in Figure 3.8 are defined by

$$\begin{aligned}
\bar{\boldsymbol{u}}^{\boldsymbol{N}} &= \frac{1}{4}\left(\bar{\boldsymbol{u}}_{i,j} + \bar{\boldsymbol{u}}_{i+1,j} + \bar{\boldsymbol{u}}_{i+1,j+1} + \bar{\boldsymbol{u}}_{i,j+1}\right), \\
\bar{\boldsymbol{u}}^{\boldsymbol{E}} &= \bar{\boldsymbol{u}}_{i+1,j} \\
\bar{\boldsymbol{u}}^{\boldsymbol{S}} &= \frac{1}{4}\left(\bar{\boldsymbol{u}}_{i,j} + \bar{\boldsymbol{u}}_{i+1,j} + \bar{\boldsymbol{u}}_{i+1,j-1} + \bar{\boldsymbol{u}}_{i,j-1}\right), \\
\bar{\boldsymbol{u}}^{\boldsymbol{W}} &= \bar{\boldsymbol{u}}_{i,j}.
\end{aligned} \tag{3.99}$$

Similar equations are defined for $\bar{T}$, $\bar{k}$ and $\bar{\omega}$. Applying Gauss divergence theorem, the gradients for $\bar{u}_1$ with respect to x_1 and x_2 are

$$\begin{aligned}
\frac{\partial \bar{u}_1}{\partial x_1} &= \frac{1}{V}\left[\bar{u}_1^S\left(x_2^C - x_2^D\right) + \bar{u}_1^E\left(x_2^B - x_2^C\right) + \bar{u}_1^N\left(x_2^A - x_2^B\right) + \bar{u}_1^W\left(x_2^D - x_2^A\right)\right], \\
\frac{\partial \bar{u}_1}{\partial x_2} &= -\frac{1}{V}\left[\bar{u}_1^S\left(x_1^C - x_1^D\right) + \bar{u}_1^E\left(x_1^B - x_1^C\right) + \bar{u}_1^N\left(x_1^A - x_1^B\right) + \bar{u}_1^W\left(x_1^D - x_1^A\right)\right],
\end{aligned} \tag{3.100}$$

where V is the area of ABCD, defined as

$$V = \frac{1}{2}\left[x_1^A\left(x_2^D - x_2^B\right) + x_1^B\left(x_2^A - x_2^C\right) + x_1^C\left(x_2^B - x_2^D\right) + x_1^D\left(x_2^C - x_2^A\right)\right]. \tag{3.101}$$

Similar derivatives define the gradients of the $\bar{u}_2$ velocity component, the static temperature, specific turbulence kinetic energy and the specific dissipation rate. Using this approach, the turbulent flux vector of Eqn. 3.56 is estimated at each cell interface. Similar expressions define the turbulent fluxes in the j-direction.

3.7 Estimation of the Turbulent Source Terms

The source terms vector $\boldsymbol{S}$ in the short-time averaged Navier-Stokes equations is defined by Eqn. 3.57. This vector contains the production and destruction terms for the $\bar{k}$ and $\bar{\omega}$ equations. Volume averaged variables in each cell are used to construct Eqn. 3.57. The compressibility correction of Wilcox (1992) is applied through the modification of $\beta^\star$ and β by Eqns. 3.48 to 3.53. The divergence of $\bar{\boldsymbol{u}}$

in Eqn. 3.57, as well as the divergence of $\bar{k}$ and $\bar{\omega}$ in Eqn. 3.56, are computed from Gauss' divergence theorem applied to individual cell boundaries. An upper limit to the turbulence kinetic energy production, $\bar{\boldsymbol{\tau}}_{\boldsymbol{r}} : \nabla \bar{\boldsymbol{u}}$, is applied to prevent over-production of $\bar{k}$ around stagnation regions. The local production of $\bar{k}$ is therefore limited to a maximum value of twenty times the $\bar{k}$ dissipation, which is estimated as $\beta^{\star} \bar{\rho} \bar{k} \bar{\omega}$ from Eqn. 3.57. This upper limit to the production of $\bar{k}$ remains inactive for fully developed turbulent boundary layers and free shear layers. The source terms vector $\boldsymbol{S}$ is added to the discrete integration, according to Eqn. 3.60, to estimate the right-hand side of the quasi-linear Navier-Stokes equations, Eqn. 3.62. From the resulting value for $\partial \boldsymbol{U} / \partial t$, the flow state vector $\boldsymbol{U}$ is obtained by integrating in time.

3.8 Time Integration Method

This section introduces the temporal integration stage for the short-time averaged Euler and Navier-Stokes equations. In this study, the two-step, explicit Runge-Kutta method of Hu et al. (1995) is used. To simplify the notation in the Runge-Kutta expression, the inviscid fluxes in the semi-discrete Euler equations, Eqn. 3.25, are replaced by the symbol, $\mathcal{R}_i(\boldsymbol{U})$, giving

$$\mathcal{R}_i(\boldsymbol{U}) = -\frac{1}{V_i} \sum_{k=1}^{N_f} \left(\boldsymbol{F}(\boldsymbol{U})_{i,k} \cdot \boldsymbol{n}_{i,k} \right) \mathcal{S}_{i,k}. \tag{3.102}$$

Similarly, the combined total flux and source terms in the semi-discrete form of the short-time averaged Navier-Stokes equations, Eqn. 3.60, are replaced by $\mathcal{R}_t(\boldsymbol{U})$, defined as

$$\mathcal{R}_t(\boldsymbol{U}) = -\frac{1}{V_i} \sum_{k=1}^{N_f} \left[\left(\boldsymbol{F_c}(\boldsymbol{U}) + \boldsymbol{F_t}(\boldsymbol{U}) \right) \cdot \boldsymbol{n} \right]_{i,k} \mathcal{S}_{i,k} - \boldsymbol{S_i}. \tag{3.103}$$

The Runge-Kutta time integration method used in this study is common to the inviscid and turbulent flow computations. The symbols $\mathcal{R}_i(\boldsymbol{U})$ and $\mathcal{R}_t(\boldsymbol{U})$ can therefore be generalised using the symbol $\mathcal{R}(\boldsymbol{U})$. Runge-Kutta methods obtain

high order accuracy by dividing the temporal integration over m steps. Consider the integration of $\mathcal{R}(\boldsymbol{U})$ from an initial time n to a time of $n+1$. The Runge-Kutta method is defined at each step as

$$\begin{aligned} \boldsymbol{U}^0 &\equiv \boldsymbol{U}^n, \\ \boldsymbol{U}^z &= \boldsymbol{U}^0 - \psi_z \Delta t \mathcal{R}\left(\boldsymbol{U}^{(z-1)}\right), \quad 1 \leq z \leq m \\ \boldsymbol{U}^{n+1} &\equiv \boldsymbol{U}^m. \end{aligned} \tag{3.104}$$

The Runge-Kutta coefficients ψ_z and the time step Δt in Eqn. 3.104 are chosen to obtain a numerically stable solution. A detailed analysis of the constraints underlying the choice of ψ_z is given in Hu et al. (1995) and Manna (1992). The coefficients used in this study, for the two step Runge-Kutta method, are $\psi_1 = 0.5$ and $\psi_2 = 1.0$. These coefficients give a second order formal accuracy for the temporal integration procedure, as detailed in Hu et al. (1995).

The time step is chosen to satisfy the Courant-Freidrich-Lewy (CFL) condition. For the inviscid prediction, the maximum permitted time step is estimated from the volume averaged variables as:

$$(\Delta t)_c = \frac{CFL}{\left[\sum_{k=1}^{Nf} (u_1 n_2 + u_2 n_1 + a)\, \mathcal{S}_k\right]_{\max}}, \tag{3.105}$$

where $[]_{\max}$ represents the maximum value over the computational domain.

The maximum permitted time step for a turbulent computation is estimated as:

$$(\Delta t)_t = \min\left((\Delta t)_c, \frac{CFL}{[2(\nu + \nu_t) V_i / \mathcal{S}_{\min}^2]_{\max}}\right), \tag{3.106}$$

where $\mathcal{S}_{\min}$ is the minimum control volume surface area for the subject cell. ν is the kinematic viscosity, defined as $\nu = \mu/\rho$. ν_t is the kinematic eddy viscosity, defined as $\nu_t = \mu_t/\rho$. $[]_{\max}$ represents the maximum value over the computational domain.

3.9 Boundary Conditions

The computational domain used to model the flow past a circular cylinder and a turbine blade is decomposed into a number of topologically orthogonal blocks. External and inter-block boundary conditions are defined using a perimetrical frame of unit cell depth around each block.

The conservative variables at these boundaries are updated by upwinding along characteristic lines. Characteristic waves travel into and out from the interior of each block. Each wave direction is identified by the sign of the associated eigenvalue. Characteristics travelling into a block require the definition of external *physical* boundary conditions. Outward travelling characteristics carry the influence of the interior flow towards the boundary. In this case *numerical* boundary conditions, based on extrapolation or characteristic procedures, are imposed. The formulation of inlet and outlet boundaries exploits the hyperbolicity of the Euler equations. For the short-time averaged Navier-Stokes equations, this characteristic based method is considered an acceptable approximation for high Reynolds number flows, in which the hyperbolic convection terms dominate. Numerical errors introduced through other ill-posed boundary conditions, particularly for unsteady aeroacoustic applications, are described in a number of publications, including Giles (1990) and Poinsot & Lele (1992).

Boundary conditions used in this study include subsonic and supersonic inlet and outlet boundaries, periodic boundaries, inviscid surface boundaries and an adiabatic no-slip surface condition. These are detailed in Subsections 3.9.1 to 3.9.8. The following symbology is defined to distinguish between internal, external (imposed) and computed boundary flow states. $[\,]_{Interior}$ denotes the flow state on the unit cell adjacent to the boundary cell, inside the computational domain. $[\,]_{Exterior}$ denotes an exterior flow variable imposed on a boundary cell. The resultant flow state assigned to the boundary cell is defined by $[\,]_{Boundary}$. This is a function of $[\,]_{Interior}$ and $[\,]_{Exterior}$, the final form depending on the boundary condition imposed.

3.9.1 Subsonic Inlet

In a two-dimensional inviscid flow prediction, four characteristics waves are defined. For a local subsonic inlet flow, the sign of the eigenvalues indicate that three characteristic waves are directed into the computational domain. The remaining characteristic, an outgoing acoustic wave, is directed away from the interior of the domain. Accordingly, one extrapolated and three imposed flow properties are used to define the flow state along a subsonic inlet boundary. For turbulent predictions, the complement of characteristic waves increases by the number of additional turbulent transport equations. For the $k-\omega$ turbulence model, two additional state variables are imposed at a subsonic inlet. The three imposed state variables for an inviscid flow are chosen as the short-time averaged stagnation temperature $\bar{T}_s$, the stagnation pressure $\bar{p}_s$ and the inlet flow angle, defined as $\phi = \tan(u_2/u_1)$, where u_1 and u_2 are the imposed inlet velocity components. This choice for the imposed state variables is convenient for matching with experimental measurements and is reputed by Manna (1992) to possess improved convergence properties over alternative choices. The additional imposed state variables for a turbulent prediction are the upstream values of the short-time averaged turbulence kinetic energy $\bar{k}$ and the specific dissipation rate $\bar{\omega}$. The extrapolated state variable is calculated by equating the interior cell Mach number to the required inlet Mach number. This is achieved through consideration of the Van Leer flux splitting method, to yield

$$\left[\frac{\bar{\rho}\bar{a}}{4}\left(1+\bar{M}_n\right)^2\right]_{Interior} = \left[\frac{\bar{\rho}\bar{a}}{4}\left(1+\bar{M}_n\right)^2\right]_{Boundary}, \tag{3.107}$$

where $\bar{M}_n$ is the short-time averaged Mach number component normal to the inlet boundary, defined as

$$\bar{M}_n = \frac{\bar{u}_n}{\sqrt{\gamma R\bar{T}}}. \tag{3.108}$$

The velocity component normal to the inlet boundary in Eqn. 3.108 is given by $\bar{u}_n = (\bar{u}_1 n_1 + \bar{u}_2 n_2)$. Equation 3.107 therefore relates the known properties in the interior domain to the required properties at the boundary. To simplify the number

of unknowns on the right hand side of Eqn. 3.107, isentropic equations relating the density $\bar{\rho}$ and sound speed $\bar{a}$ to the imposed state variables $\bar{T}_s$ and $\bar{p}_s$, and the boundary Mach number M_n are defined as

$$\bar{\rho} = \frac{\bar{p}_s}{R\bar{T}_s}\left(1+\frac{\gamma-1}{2}\bar{M}_n^2\right)^{-\frac{1}{\gamma-1}}, \tag{3.109}$$

$$\bar{a} = \sqrt{\gamma R\bar{T}_s}\left(1+\frac{\gamma-1}{2}\bar{M}_n^2\right)^{-\frac{1}{2}}. \tag{3.110}$$

Substituting Eqns. 3.109 and 3.110 into the right hand side of Eqn. 3.107 and rearranging to bring the unknown variable $\bar{M}_n$ to the left-hand side gives the following expression for $\bar{M}_n$ at the boundary:

$$\left[\left(1+\bar{M}_n\right)^2\left(1+\frac{\gamma-1}{2}\bar{M}_n{}^2\right)^{\frac{-(\gamma+1)}{2(\gamma-1)}}\right]_{Boundary} = \frac{\left[\bar{\rho}\bar{a}\left(1+\bar{M}_n\right)^2\right]_{Interior}}{\left[\bar{p}_s\sqrt{\frac{\gamma}{R\bar{T}_s}}\right]_{Exterior}}. \tag{3.111}$$

The unknown boundary Mach number on the left of Eqn. 3.111 is computed using an iterative Newton-Raphson method. An initial estimate for $\left[\overline{M}_n\right]_{Boundary}$ is required for the Newton-Raphson algorithm. This is provided by the local interior Mach number. Once the Mach number at the boundary is known, the boundary values of static density, temperature, pressure and the normal velocity are computed from Eqn. 3.109 and 3.110, along with

$$\bar{T} = \bar{T}_s\left(1+\frac{\gamma-1}{2}\bar{M}_n^2\right)^{-1}, \tag{3.112}$$

$$\bar{p} = \bar{p}_s\left(\frac{\bar{T}_s}{\bar{T}}\right)^{-\frac{\gamma}{\gamma-1}}, \tag{3.113}$$

$$\bar{u}_n = \bar{a}\sqrt{\gamma R\bar{T}}. \tag{3.114}$$

Using the flow variables at the boundary, the conservative variables vector $[\boldsymbol{U}]_{Boundary}$ is then obtained. For the Euler equations, this is given by Eqn. 3.19. The boundary values of $\bar{k}$ and $\bar{\omega}$ required for the turbulent conservative variables vector, Eqn. 3.55, are defined as the imposed values of $\bar{k}$ and $\bar{\omega}$.

3.9.2 Supersonic Inlet

At supersonic velocities, all characteristic eigenvalues are of the same sign. Specifically, only characteristics travelling into the computational domain are present at a supersonic inlet. Therefore, the interior flow variables have no influence on $[\boldsymbol{U}]_{Boundary}$. Four imposed flow properties are required at a supersonic inlet boundary for an inviscid computation. In this study, the stagnation temperature $\bar{T}_s$, the stagnation pressure $\bar{p}_s$ and the two Cartesian components of the inlet Mach number, $\bar{M}_1$ and $\bar{M}_2$, are imposed. The conservative variables vector $[\boldsymbol{U}]_{Boundary}$ for the Euler equations, Eqn. 3.19, is therefore estimated from

$$\begin{aligned}
\bar{M} &= \sqrt{(\bar{M}_1^2 + \bar{M}_2^2)}, \\
\bar{T} &= \bar{T}_s \left(1 + \frac{\gamma - 1}{2}\bar{M}^2\right)^{-1}, \\
\bar{p} &= \bar{p}_s \left(\frac{\bar{T}_s}{\bar{T}}\right)^{-\frac{\gamma}{\gamma-1}}, \\
\bar{\rho} &= \frac{\bar{p}}{R\bar{T}}, \\
\bar{u}_1 &= M_1\sqrt{\gamma R\bar{T}}, \\
\bar{u}_2 &= M_2\sqrt{\gamma R\bar{T}}, \\
\bar{e}_s &= \frac{\bar{p}}{\bar{\rho}\,(\gamma - 1)} + \frac{\bar{\boldsymbol{u}} \cdot \bar{\boldsymbol{u}}}{2}.
\end{aligned} \tag{3.115}$$

Additional boundary conditions are required in the turbulent prediction. This is satisfied by imposing boundary values for $\bar{k}$ and $\bar{\omega}$. The stagnation energy $\bar{e}_s$ for the turbulent prediction is re-defined as

$$\bar{e}_s = \frac{\bar{p}}{\bar{\rho}\,(\gamma - 1)} + \frac{\bar{\boldsymbol{u}} \cdot \bar{\boldsymbol{u}}}{2} + \bar{k}. \tag{3.116}$$

The conservative variables vector for the short-time averaged Navier-Stokes equations, Eqn. 3.55, is defined at the supersonic inlet boundary from Eqns. 3.115 and 3.116.

3.9.3 Subsonic Outlet

As with the subsonic inlet boundary of subsection 3.9.1, the characteristics associated with the subsonic outlet boundary have both positive and negative eigenvalues. For the two-dimensional Euler prediction, three characteristics are directed out of the computational domain and require the extrapolation of three flow state variables based on the interior flow field. The remaining state variable is defined by imposing the external static pressure $\bar{p}$. The density, $\bar{\rho}$, and the velocity components, $\bar{u}_1$ and $\bar{u}_2$, are obtained by a zeroth order extrapolation from the interior domain. The Mach number normal to the outlet boundary M_n, defined by Eqn. 3.108, is computed using an iterative Newton-Raphson algorithm. As with the subsonic inlet boundary, the expression for the outlet boundary Mach number is obtained from a flux vector splitting analysis, leading to

$$c_1 \bar{M}_n^3 + c_2 \bar{M}_n^2 + c_3 \bar{M}_n + c_4 \;=\; 0, \tag{3.117}$$

where the coefficients c_1 to c_4 are given by

$$\begin{aligned} c_1 &= \gamma - 1, \\ c_2 &= 2\gamma, \\ c_3 &= \gamma + 3, \\ c_4 &= 2 - \frac{1}{\gamma \bar{p}} \left[\bar{\rho}\bar{a} \left(1 + \bar{M}_n\right)^2 \left(2\bar{a} + (\gamma - 1)\, \bar{u}_n\right) \right]_{Interior}. \end{aligned} \tag{3.118}$$

The velocity normal to the boundary is $\bar{u}_n = (\bar{u}_1 n_1 + \bar{u}_2 n_2)$. The initial estimate of $\bar{M}_n$ for the Newton-Raphson algorithm is taken as the interior Mach number. Once the Mach number at the boundary has been determined, the speed of sound at the boundary is calculated using a rearranged form of Eqn. 3.107, along with the imposed static pressure $\bar{p}$, leading to

$$\bar{a} \;=\; \frac{\left[\gamma \bar{p} \left(1 + \bar{M}_n\right)^2 \right]_{Boundary}}{\left[\bar{\rho}\bar{a} \left(1 + \bar{M}_n\right)^2 \right]_{Interior}}, \tag{3.119}$$

The primitive variables at the boundary are therefore calculated as

$$\begin{aligned} \bar{\rho} &= \frac{\gamma \bar{p}}{\bar{a}^2}, \\ \bar{u}_n &= \bar{M}_n \bar{a}, \\ \bar{u}_1 &= [\bar{u}_1]_{Interior}, \\ \bar{u}_2 &= [\bar{u}_2]_{Interior}, \\ \bar{p} &= [\bar{p}]_{Exterior}, \end{aligned} \tag{3.120}$$

where $\bar{a}$ is the local speed of sound at the boundary, estimated from Eqn. 3.119. $\bar{M}_n$ is the local Mach number normal to the outlet boundary, estimated from Eqn. 3.117. The conservative variables vector for the Euler equations, Eqn. 3.19, is therefore constructed using the flow variables given in Eqn. 3.120 with the stagnation energy $\bar{e}_s$ estimated by Eqn. 3.115. Two additional numerical boundary conditions are defined for the turbulent prediction, these are $\left[\bar{k}\right]_{Interior}$ and $[\bar{\omega}]_{Interior}$. The stagnation energy $\bar{e}_s$ for the turbulent case is estimated from Eqn. 3.116.

3.9.4 Supersonic Outlet

As for the supersonic inlet condition, all flow characteristics have the same eigenvalue sign at a supersonic outlet. All characteristics travel out of the computational domain. Therefore, only extrapolated boundary conditions, based on the interior flow states, are required. In the present study, the boundary flow state is determined by a zeroth order extrapolation of the interior conservative variables.

3.9.5 Inter-Domain Boundary

A seamless transition of the flow field variables across neighbouring topologically orthogonal blocks is achieved by overlapping the interior and exterior cells (ghost cells) of adjacent blocks along the common interface, as shown in Figure 3.9. The perimetrical ghost cells are updated by copying the conservative variables from the underlying interior cells.

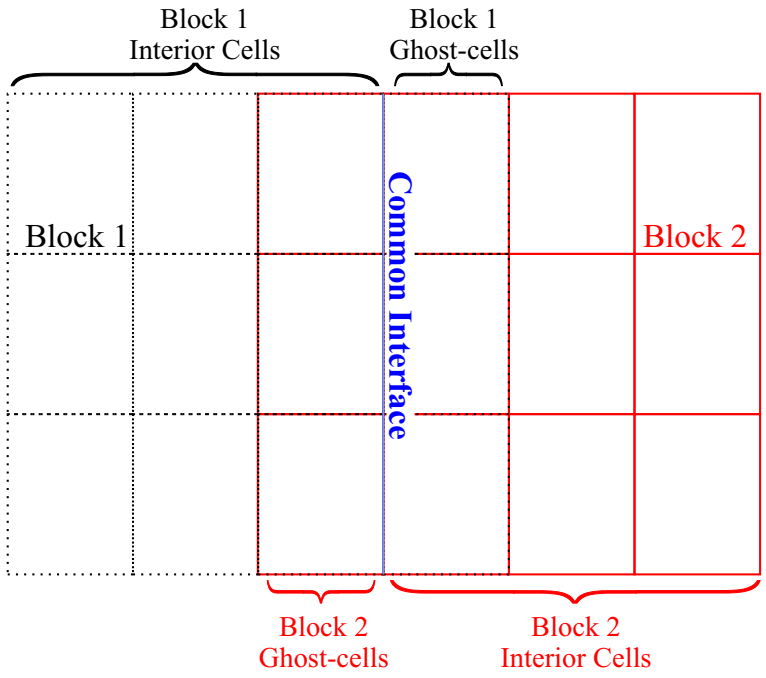

Figure 3.9: Schematic showing the location of the inter-domain boundary between two adjacent blocks.

3.9.6 Periodic Boundary

The periodic boundary condition is an extension of the inter-domain boundary condition. Periodic boundaries are used in the present study to reduce the computational domain required to model a pitch-wise periodic turbine cascade geometry to a region surrounding a single turbine blade. Figure 3.10 shows the basis of this boundary condition applied to the boundaries of a single block. Arrows indicate the direction of information exchange between the periodic cells and the associated interior cells. The periodic cells are updated by copying across the flow state from the associated interior cells.

3.9.7 Inviscid Wall Boundary

A number of boundary conditions are used in the present study to describe solid surfaces. The inviscid wall (or 'slip' wall) condition defines a solid surface in which no mass flux crosses the boundary. This is also known as a 'no-penetration' boundary condition. The velocity component normal to the boundary, $\bar{u}_n$, is defined as zero

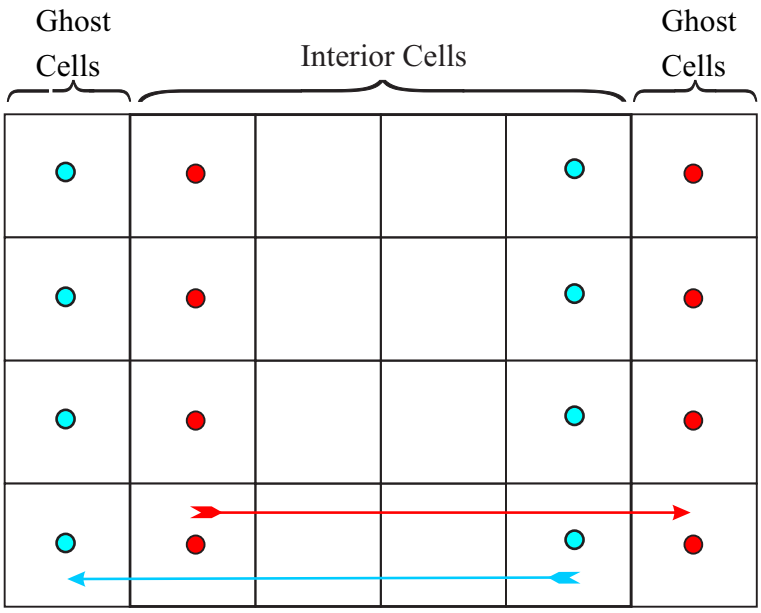

Figure 3.10: Schematic showing the information exchange between ghost cells and the associated interior cells at a periodic boundary.

at the surface. The surface value for the tangential velocity component $\bar{u}_t$ remains unchanged from the interior value. Therefore

$$\begin{aligned} [\bar{u}_n]_{Boundary} &= 0, \\ [\bar{u}_t]_{Boundary} &= [\bar{u}_t]_{Interior}\,, \end{aligned} \tag{3.121}$$

where, $\bar{u}_n = \bar{u}_1 n_1 + \bar{u}_2 n_2$, and $\bar{u}_t = \bar{u}_2 n_1 - \bar{u}_1 n_2$. The Cartesian components of velocity at the external cells are therefore defined as

$$\begin{aligned} \bar{u}_1 &= -\bar{u}_t n_2, \\ \bar{u}_2 &= \bar{u}_t n_1. \end{aligned} \tag{3.122}$$

The cell normal components n_1 and n_2 are defined as $(n_1, n_2)^T = \boldsymbol{n}$, where $\boldsymbol{n}$ is the surface unit normal to the boundary $\mathcal{S}$. The boundary values of density $\bar{\rho}$ and static pressure $\bar{p}$ are set equal to the interior cell values. The stagnation energy $\bar{e}_s$, defined in Eqn. 3.115 for the Euler equations, is subsequently re-calculated with the updated velocities. For turbulent predictions, the values of $\bar{k}$ and $\bar{\omega}$ are determined from a zeroth order extrapolation of the interior cell values. The stagnation energy

$\bar{e}_s$ for the turbulent computation is then updated using Eqn. 3.116.

3.9.8 Adiabatic No-slip Surface Boundary

The 'no-slip' surface condition represents an improved approximation to surfaces bounding viscous flows, permitting the development of surface boundary layers. For turbulent computations, five imposed boundary conditions and one extrapolated boundary condition are required. The imposed no-slip velocity provides two physical boundary conditions for the surface. The zero velocity condition at the surface implies an imposed zero value for $\bar{k}$. Menter (1993) provides a limiting value for $\bar{\omega}$ close to a hydraulically smooth surface. These conditions are

$$\begin{aligned} \bar{u}_1 &= 0, \\ \bar{u}_2 &= 0, \\ \bar{k} &= 0, \\ \bar{\omega} &= \frac{60\bar{\mu}_{l_w}}{\beta_o \left(\Delta x_2\right)_1}, \end{aligned} \tag{3.123}$$

where $\left(\Delta x_2\right)_1$ is the surface normal height between the physical surface and the centre of the first interior cell. $\bar{\mu}_{l_w}$ is the laminar viscosity at the wall, estimated by a zeroth-order extrapolated from the first interior cell. β_o is defined in Eqn. 3.50. The final imposed boundary condition is defined from the adiabatic condition:

$$\bar{\boldsymbol{q}}_w = 0. \tag{3.124}$$

This condition indicates a boundary value for the static temperature equal to that of the adjacent interior cell. The static temperature is therefore estimated by a zeroth-order extrapolation from the interior cells. The extrapolated condition is found by assuming a zero pressure gradient normal to the wall, therefore, $\left[\overline{p}\right]_{Boundary} = \left[\overline{p}\right]_{Interior}$ and $\left[\overline{T}\right]_{Boundary} = \left[\overline{T}\right]_{Interior}$. This condition provides a satisfactory approximation for attached boundary layer flows with adequate grid resolution in the laminar flow region. As noted in Manna (1992), the assumption of a zero pressure gradient normal to the wall is strictly limited to attached boundary

layer flows at high Reynolds numbers.

A summary of the numerical solution procedure documented in this chapter is outlined in Figure 3.11.

3.10 The Adaptive Mesh Refinement (AMR) Method

3.10.1 Introduction

The high Reynolds number flows predicted in this study require the satisfactory resolution of turbulent boundary layers to the laminar sublayer region. Resolving this region requires a high resolution grid, with a high degree of grid stretching in the surface normal direction. The current explicit method imposes an upper limit on the time step for numerical stability, based on the minimum cell size. Any decrease in the length of the smallest cell, in order to resolve the laminar sublayer, causes an associated decrease in the maximum permitted time step Δt. Integrating over a highly stretched grid with a uniform time step can lead to slow developing flow features, which could be more efficiently computed with a lower spatial and temporal resolution.

The Adaptive Mesh Refinement (AMR) method represents one strategy for overcoming this inefficiency. A hierarchy of nested mesh levels, with increasing spatial and temporal resolution, are defined at the start of the computation. Regions of slow developing flow, or regions with shallow flow gradients, are computed using a relatively coarse spatial and temporal resolution on a low-level grid. Other regions, which require a better level of resolution, are computed at higher mesh levels with an increased spatial and temporal resolution.

The AMR method used in the present study is based on the method of Quirk and a detailed description of the AMR method is provided in Quirk (1991). A brief outline, highlighting modifications introduced in the current implementation, is given in this Chapter. A diagrammatical overview of the current AMR procedure, showing the flow of information through one time step at the lowest mesh level, is shown in Figure 3.12. The lowest level mesh, which covers the entire computational

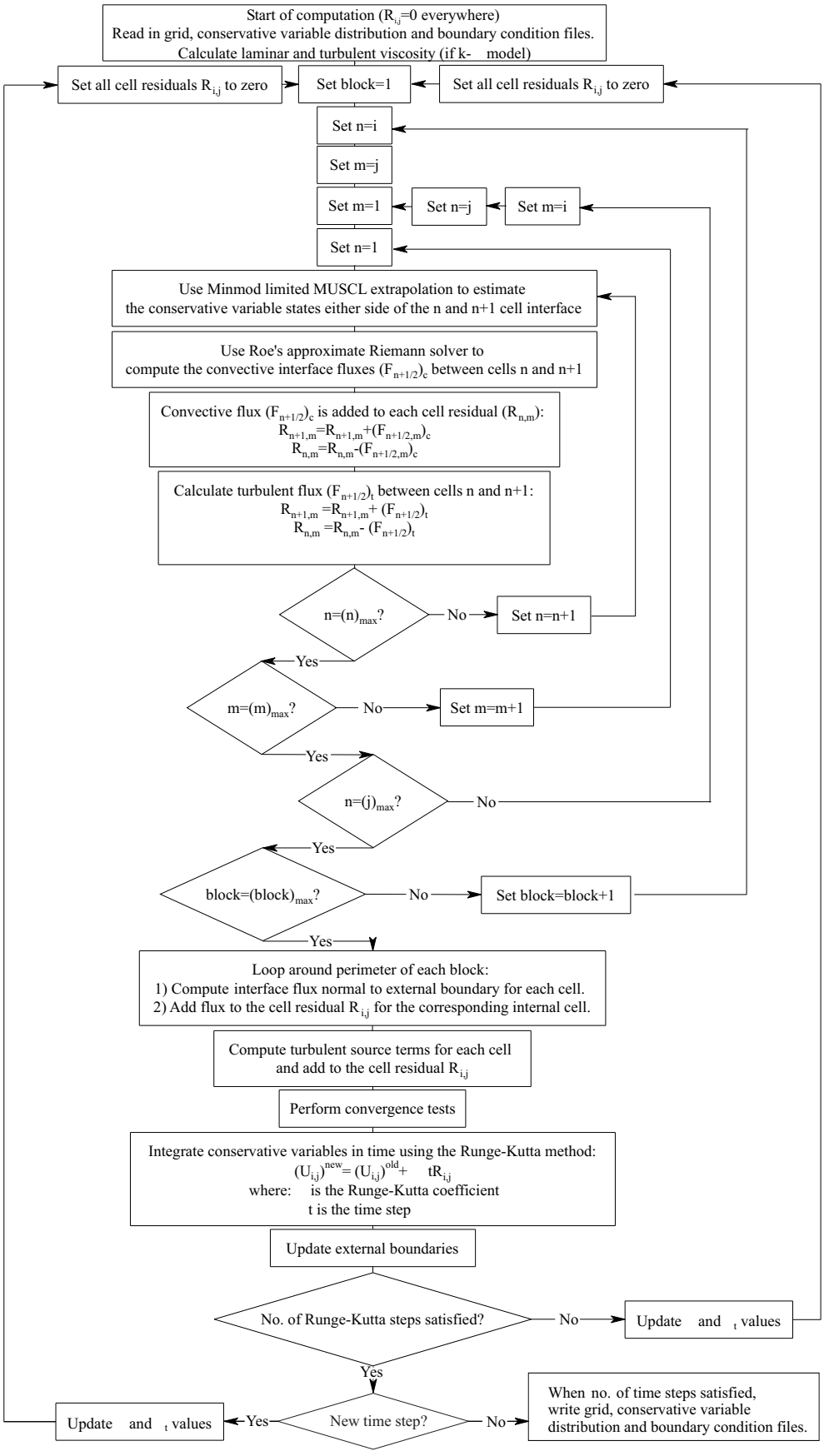

Figure 3.11: Numerical solution procedure flowchart. (i,j) is a general cell index.

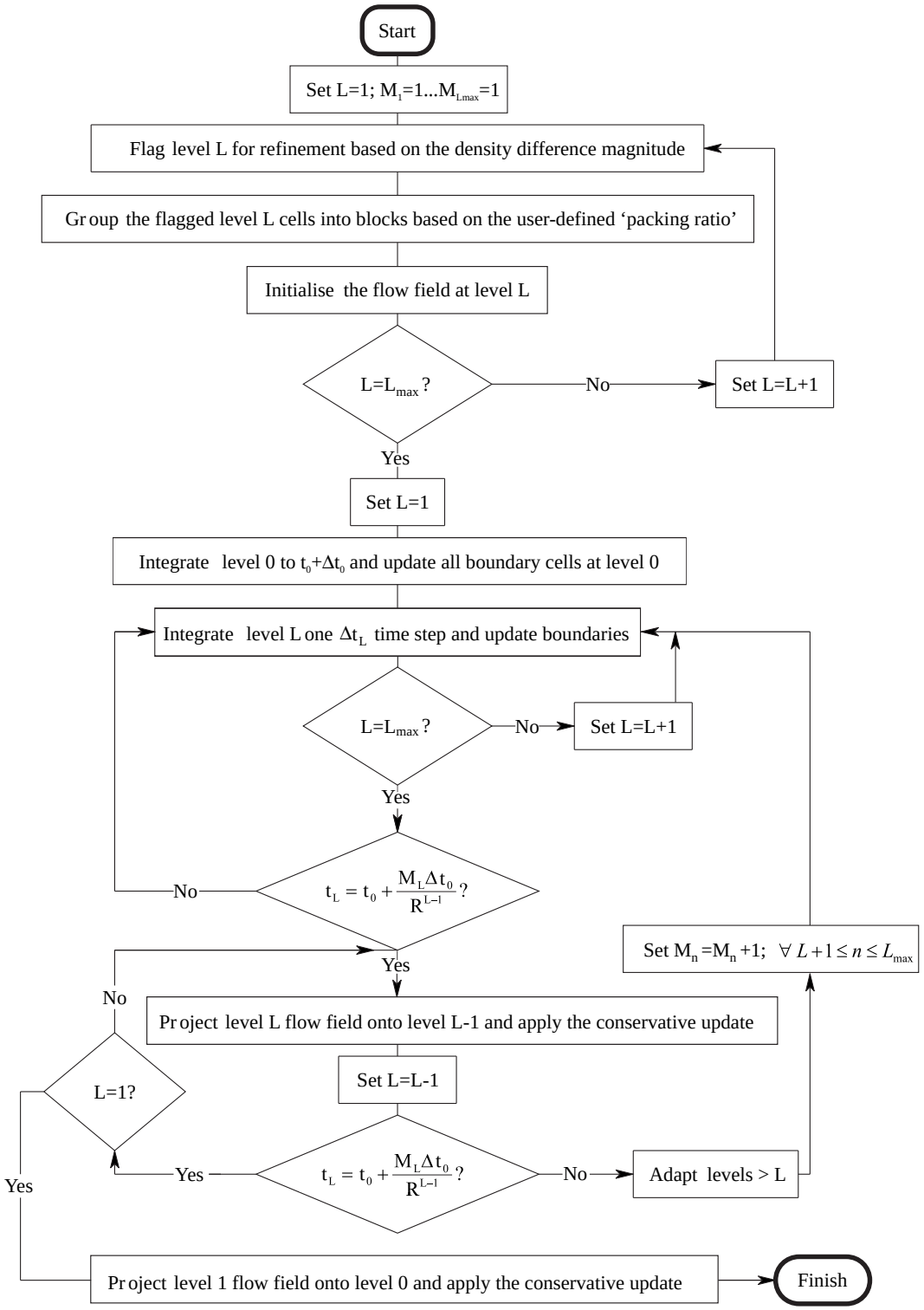

Figure 3.12: Flowchart showing the creation and integration of levels 1 to L_{max} for one level 0 time step. L is the current AMR level ($1 \leq L \leq L_{max}$), t_L is the current time at level L. t_0 is the time at level 0, at the start of the flowchart. Δt_0 is the time step at level 0, R is the user-defined spatial and temporal resolution between AMR levels. M_L is a variable representing the number of level L grid adaptions for each level 0 time step (i.e., for levels 0 to 2, M_1 and M_2 are defined).

domain, is designated as level 0. An incremental increase in the level index is used for subsequent levels. A three level AMR prediction, for example, is defined with levels 0, 1 and 2. Each separate stage in the AMR algorithm of Figure 3.12 is described in the remainder of this Chapter.

3.10.2 The AMR Flagging and Grouping Procedure

The computation starts with a coarse discretisation at level 0. Regions of level 0 are then flagged for refinement based on the density difference. This choice of flagging parameter refines, for example, shock waves and thin compressible shear layers in inviscid predictions. In a turbulent compressible prediction, the density variation through the boundary layer triggers a mesh refinement close to the surface.

The refinement procedure begins with an initial survey of level 0, to establish the maximum density difference $|\Delta\rho_{\max}|$, between contiguous cells, at level 0. A user defined 'AMR scaling parameter' b is multiplied by $|\Delta\rho_{\max}|$ and contiguous cells with density difference $|\Delta\rho_{i,j}| > b|\Delta\rho_{\max}|$ are flagged for refinement. In this study $0.02 \leq b \leq 0.10$. The influence of the AMR scaling parameter b is discussed, through a series of test cases, in Chapter 4. As discussed in Quirk (1991), discontinuities that cross the boundary between different levels of refinement can lead to numerical vorticity. The current explicit scheme ensures that discontinuities cannot travel further than the length of any one cell over a single time step. To prevent flow discontinuities from travelling out of the refined region, a perimetrical layer one cell deep is flagged for refinement around each cell with $|\Delta\rho_{i,j}| > b|\Delta\rho_{\max}|$. This additional flagging ensures that all refined discontinuities remain within the bounds of the refined region for each time step of the underlying level. After developing over a length of time equal to one time step of the underlying level, each level $L > 0$ is recreated from the updated flow field of the underlying level, thereby tracking moving discontinuities.

Once a level has been flagged for refinement, the refined cells are grouped into a series of contiguous rectangular blocks. A user-defined 'packing criterion', defined between 0 and 1.0, determines the permitted ratio of *flagged* to *unflagged* cells for

each refined block. For example, a user-defined packing criterion of 0.75 dictates that the proportion of *flagged* cells in each newly refined block is at least 75%. The procedure used in the current AMR grouping stage is identical to the procedure outlined by Quirk (1991). Initially, a single rectangular block is defined, which covers the entire refined region. This block is then recursively divided into two separate regions, along the longest side, until a series of contiguous blocks are defined which satisfy the packing criterion. A perimetrical frame, two refined cells deep, is defined around each refined block for implementation of boundary conditions. The initialisation of these cells, along with the interior cells of each refined block, is discussed in Section 3.10.3. The subsequent updating of these boundaries, between integrations, is discussed in Section 3.10.5.

A user-defined refinement ratio determines the increment in spatial and temporal resolution between successive levels. In this study, a common refinement ratio is used for the i and j directions, termed rI_f and rJ_f respectively. Each coarse level L cell is therefore divided into $(rI_f)^2$ cells at level $L+1$ and $(rI_f)^4$ cells at level $L+2$. Numerical stability is satisfied at all levels through division of the time step at the underlying level by the user-defined refinement ratio. The choice of refinement ratio for practical applications is discussed in Chapter 4.

3.10.3 A Two-Dimensional Coarse-Fine Interpolation Procedure

At the start of the AMR computation, or in newly refined regions at successive adaptions, an initial estimate of the state variables for each refined cell is obtained through a two-dimensional interpolation of the piece-wise constant state variables in the underlying coarse level. This interpolation must locally conserve the mass, momentum and energy of the coarse level L flow field. In addition, the monotonicity of the coarse level L flow field must be preserved at higher levels, in the presence of rapidly changing flow gradients such as shock waves and thin shear layers, to satisfy the TVD condition at all refined levels. The minmod-limited MUSCL procedure, described in Sections 3.5.6 to 3.5.8, defines a one-dimensional variation in state variables across each cell that is conservative and which preserves the monotonicity

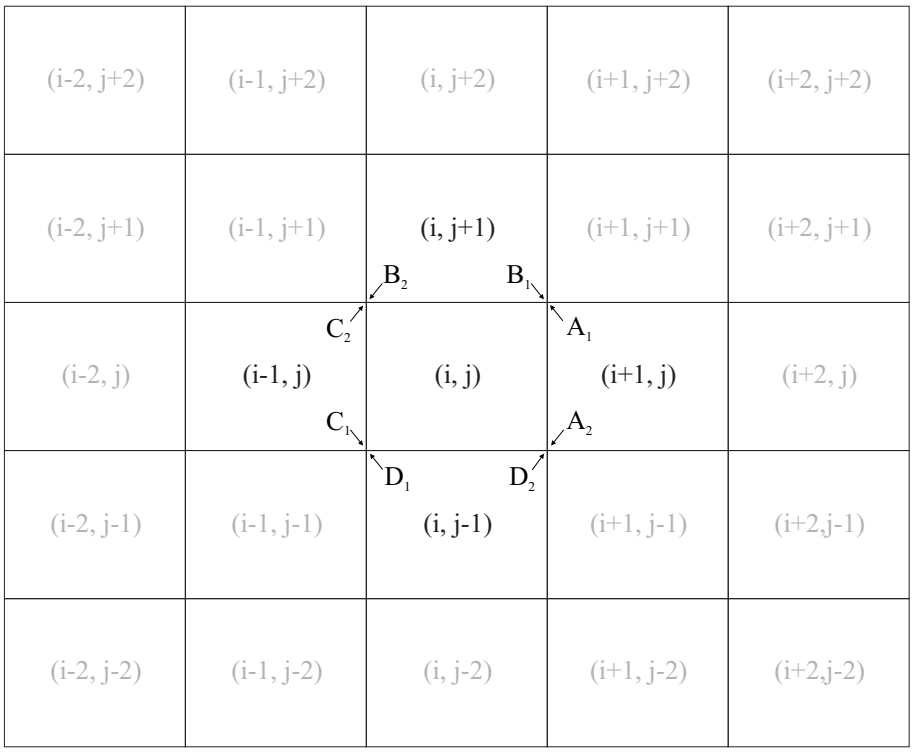

Figure 3.13: Representation of the coarse level L grid used to initialise the fine level $L+1$ flow field. A_1-D_2: Difference in the state variables vector, between the piece-wise linear variation at the corner of the neighbouring cells and the piece-wise constant state in cell (i,j), Eqns 3.133-3.140.

of the piece-wise constant flow distribution. Directly applying this one-dimensional MUSCL extrapolation procedure to two-dimensions, through simple linear addition of the one-dimensional gradients, does not guarantee a monotone variation of the interpolated flow field. Additional limiting of the state variables gradients is required to ensure a conservative two-dimensional interpolation procedure, which preserves monotonicity between AMR levels.

The two-dimensional AMR interpolation procedure used in this study defines a flow field gradient across an arbitrary cell of index (i,j), by considering the variation of the conservative variables across the four neighbouring cells: $(i+1,j)$, $(i-1,j)$, $(i,j+1)$ and $(i,j-1)$. A diagrammatical representation of a section of the coarse level L mesh, around the cell (i,j), is shown in Figure 3.13. The two-dimensional interpolation procedure used in this study comprises of five main stages. These stages are described, for an arbitrary level L cell of index (i,j), in

the remainder of this section.

Stage 1: A one-dimensional linear distribution of the conservative variables across each cell is initially estimated in the i and j directions using a form of the minmod-limited MUSCL procedure described in Section 3.5.6. Consider a coarse level L cell at (i, j). To ensure a monotone variation in the conservative variables across this cell, a form of the MUSCL procedure is applied to cells (i, j), $(i-1, j)$, $(i+1, j)$, $(i, j-1)$ and $(i, j+1)$. As a common method is used to calculate the change in the state variables across these cells, a generalised cell index (n, m) can be defined to condense the notation. The state variables variation in cell (n, m) is initially computed as

$$\Delta \boldsymbol{U}^{i}_{n,m} = \frac{\alpha_{n,m}}{2}\left[(1-\eta)\Delta\overline{\overline{\boldsymbol{U}}}_{n-\frac{1}{2},m} + (1+\eta)\Delta\overline{\overline{\boldsymbol{U}}}_{n+\frac{1}{2},m}\right], \tag{3.125}$$

$$\Delta \boldsymbol{U}^{j}_{n,m} = \frac{\alpha_{n,m}}{2}\left[(1-\eta)\Delta\overline{\overline{\boldsymbol{U}}}_{n,m-\frac{1}{2}} + (1+\eta)\Delta\overline{\overline{\boldsymbol{U}}}_{n,m+\frac{1}{2}}\right], \tag{3.126}$$

where

$$\begin{aligned}
\Delta\overline{\overline{\boldsymbol{U}}}_{n-\frac{1}{2},m} &= \text{sign}\left(\Delta \boldsymbol{U}_{n-\frac{1}{2}}\right)\cdot\max\left[0, \min\left(|\Delta \boldsymbol{U}_{n-\frac{1}{2}}|, \Delta \boldsymbol{U}_{n+\frac{1}{2}}\cdot\text{sign}\left(\Delta \boldsymbol{U}_{n-\frac{1}{2}}\right)\right)\right], \\
\Delta\overline{\overline{\boldsymbol{U}}}_{n+\frac{1}{2},m} &= \text{sign}\left(\Delta \boldsymbol{U}_{n+\frac{1}{2}}\right)\cdot\max\left[0, \min\left(|\Delta \boldsymbol{U}_{n+\frac{1}{2}}|, \Delta \boldsymbol{U}_{n-\frac{1}{2}}\cdot\text{sign}\left(\Delta \boldsymbol{U}_{n+\frac{1}{2}}\right)\right)\right], \\
\Delta\overline{\overline{\boldsymbol{U}}}_{n,m-\frac{1}{2}} &= \text{sign}\left(\Delta \boldsymbol{U}_{m-\frac{1}{2}}\right)\cdot\max\left[0, \min\left(|\Delta \boldsymbol{U}_{m-\frac{1}{2}}|, \Delta \boldsymbol{U}_{m+\frac{1}{2}}\cdot\text{sign}\left(\Delta \boldsymbol{U}_{m-\frac{1}{2}}\right)\right)\right], \\
\Delta\overline{\overline{\boldsymbol{U}}}_{n,m+\frac{1}{2}} &= \text{sign}\left(\Delta \boldsymbol{U}_{m+\frac{1}{2}}\right)\cdot\max\left[0, \min\left(|\Delta \boldsymbol{U}_{m+\frac{1}{2}}|, \Delta \boldsymbol{U}_{m-\frac{1}{2}}\cdot\text{sign}\left(\Delta \boldsymbol{U}_{m+\frac{1}{2}}\right)\right)\right].
\end{aligned} \tag{3.127}$$

The constant η is defined in Table 3.2. In this study, $\eta = 1/3$. The superscripts i and j in Eqns. 3.125 and 3.126 denote variations in the i and j directions respectively. The differences $\Delta \boldsymbol{U}_{n-\frac{1}{2}}$, $\Delta \boldsymbol{U}_{n+\frac{1}{2}}$, $\Delta \boldsymbol{U}_{m-\frac{1}{2}}$ and $\Delta \boldsymbol{U}_{m+\frac{1}{2}}$ are given by

$$\Delta \boldsymbol{U}_{n-\frac{1}{2}} = \boldsymbol{U}_{n,m} - \boldsymbol{U}_{n-1,m}, \tag{3.128}$$

$$\Delta \boldsymbol{U}_{n+\frac{1}{2}} = \boldsymbol{U}_{n+1,m} - \boldsymbol{U}_{n,m}, \tag{3.129}$$

$$\Delta \boldsymbol{U}_{m-\frac{1}{2}} = \boldsymbol{U}_{n,m} - \boldsymbol{U}_{n,m-1}, \tag{3.130}$$

$$\Delta \boldsymbol{U}_{m+\frac{1}{2}} = \boldsymbol{U}_{n,m+1} - \boldsymbol{U}_{n,m}. \tag{3.131}$$

The coefficient $\alpha_{n,m}$ in Eqns. 3.125 and 3.126 ensures that the variation in $\boldsymbol{U}_{n,m}$ remains within the bounds of the piece-wise constant neighbouring cell states. The coefficient $\alpha_{n,m}$ is defined as

$$\alpha_{n,m} = \frac{\min\left[|\Delta \boldsymbol{U}^i_{n,m}| + |\Delta \boldsymbol{U}^j_{n,m}|,\, 2|\Delta \boldsymbol{U}_{n-\frac{1}{2}}|,\, 2|\Delta \boldsymbol{U}_{n+\frac{1}{2}}|,\, 2|\Delta \boldsymbol{U}_{m-\frac{1}{2}}|,\, 2|\Delta \boldsymbol{U}_{m+\frac{1}{2}}|\right]}{\left(|\Delta \boldsymbol{U}^i_{n,m}| + |\Delta \boldsymbol{U}^j_{n,m}|\right)}, \tag{3.132}$$

where the differences $\Delta \boldsymbol{U}_{n-\frac{1}{2}}$, $\Delta \boldsymbol{U}_{n+\frac{1}{2}}$, $\Delta \boldsymbol{U}_{m-\frac{1}{2}}$ and $\Delta \boldsymbol{U}_{m+\frac{1}{2}}$ are defined in Eqns. 3.128 - 3.131. $\Delta \boldsymbol{U}^i_{n,m}$ and $\Delta \boldsymbol{U}^j_{n,m}$ are given by Eqns. 3.125 and 3.126 from an initial estimate of $\alpha_{n,m} = 1$.
$\Delta \boldsymbol{U}^i_{n,m}$ and $\Delta \boldsymbol{U}^j_{n,m}$ are then updated before stage 2 using the value of $\alpha_{n,m}$ computed from Eqn. 3.132. $\alpha_{n,m}$ is defined in the range $0 \leq \alpha_{n,m} \leq 1$.

Stage 2: The variation of $\boldsymbol{U}$ in cell (i, j) is further restricted by the change in state variables across each neighbouring cell. Given that a piece-wise linear variation is imposed in each cell, the greatest departure from the volume averaged value occurs at the vertices of each cell. Common vertices, between the subject cell (i, j) and the neighbouring cells, are highlighted in Figure 3.13 by the labelled differences A_1 to D_2. The variables A_1 to D_2 are formally defined as the difference in the conservative state variables, between the piece-wise linear gradient at the vertex of each neighbouring cell and the piece-wise constant state variables in cell (i, j). A_1 to D_2 are thus defined as

$$\begin{aligned} A_1 = \max\Bigg[0, \Bigg(&\boldsymbol{U}_{i+\mathrm{sign}\left(\Delta U^i_{i,j}\right),j} - \frac{1}{2}\mathrm{sign}\left(\Delta \boldsymbol{U}^i_{i,j}\right) \Delta \boldsymbol{U}^i_{i+\mathrm{sign}\left(\Delta U^i_{i,j}\right),j} + \\ &\frac{1}{2}\mathrm{sign}\left(\Delta \boldsymbol{U}^j_{i,j}\right) \Delta \boldsymbol{U}^j_{i+\mathrm{sign}\left(\Delta U^i_{i,j}\right),j} - \boldsymbol{U}_{i,j}\Bigg)\Bigg], \end{aligned} \tag{3.133}$$

$$A_2 = \max\left[0, \left(\boldsymbol{U}_{i+\text{sign}\left(\Delta U^i_{i,j}\right),j} - \frac{1}{2}\text{sign}\left(\Delta \boldsymbol{U}^i_{i,j}\right)\Delta \boldsymbol{U}^i_{i+\text{sign}\left(\Delta U^i_{i,j}\right),j} - \frac{1}{2}\text{sign}\left(\Delta \boldsymbol{U}^j_{i,j}\right)\Delta \boldsymbol{U}^j_{i+\text{sign}\left(\Delta U^i_{i,j}\right),j} - \boldsymbol{U}_{i,j}\right)\right], \tag{3.134}$$

$$B_1 = \max\left[0, \left(\boldsymbol{U}_{i,j+\text{sign}\left(\Delta U^j_{i,j}\right)} + \frac{1}{2}\text{sign}\left(\Delta \boldsymbol{U}^i_{i,j}\right)\Delta \boldsymbol{U}^i_{i,j+\text{sign}\left(\Delta U^j_{i,j}\right)} - \frac{1}{2}\text{sign}\left(\Delta \boldsymbol{U}^j_{i,j}\right)\Delta \boldsymbol{U}^j_{i,j+\text{sign}\left(\Delta U^j_{i,j}\right)} - \boldsymbol{U}_{i,j}\right)\right], \tag{3.135}$$

$$B_2 = \max\left[0, \left(\boldsymbol{U}_{i,j+\text{sign}\left(\Delta U^j_{i,j}\right)} - \frac{1}{2}\text{sign}\left(\Delta \boldsymbol{U}^i_{i,j}\right)\Delta \boldsymbol{U}^i_{i,j+\text{sign}\left(\Delta U^j_{i,j}\right)} - \frac{1}{2}\text{sign}\left(\Delta \boldsymbol{U}^j_{i,j}\right)\Delta \boldsymbol{U}^j_{i,j+\text{sign}\left(\Delta U^j_{i,j}\right)} - \boldsymbol{U}_{i,j}\right)\right], \tag{3.136}$$

$$C_1 = \min\left[0, \left(\boldsymbol{U}_{i-\text{sign}\left(\Delta U^i_{i,j}\right),j} + \frac{1}{2}\text{sign}\left(\Delta \boldsymbol{U}^i_{i,j}\right)\Delta \boldsymbol{U}^i_{i-\text{sign}\left(\Delta U^i_{i,j}\right),j} - \frac{1}{2}\text{sign}\left(\Delta \boldsymbol{U}^j_{i,j}\right)\Delta \boldsymbol{U}^j_{i-\text{sign}\left(\Delta U^i_{i,j}\right),j} - \boldsymbol{U}_{i,j}\right)\right], \tag{3.137}$$

$$C_2 = \min\left[0, \left(\boldsymbol{U}_{i-\text{sign}\left(\Delta U^i_{i,j}\right),j} + \frac{1}{2}\text{sign}\left(\Delta \boldsymbol{U}^i_{i,j}\right)\Delta \boldsymbol{U}^i_{i-\text{sign}\left(\Delta U^i_{i,j}\right),j} + \frac{1}{2}\text{sign}\left(\Delta \boldsymbol{U}^j_{i,j}\right)\Delta \boldsymbol{U}^j_{i-\text{sign}\left(\Delta U^i_{i,j}\right),j} - \boldsymbol{U}_{i,j}\right)\right], \tag{3.138}$$

$$D_1 = \min\left[0, \left(\boldsymbol{U}_{i,j-\text{sign}\left(\Delta U^j_{i,j}\right)} - \frac{1}{2}\text{sign}\left(\Delta \boldsymbol{U}^i_{i,j}\right)\Delta \boldsymbol{U}^i_{i,j-\text{sign}\left(\Delta U^j_{i,j}\right)} + \frac{1}{2}\text{sign}\left(\Delta \boldsymbol{U}^j_{i,j}\right)\Delta \boldsymbol{U}^j_{i,j-\text{sign}\left(\Delta U^j_{i,j}\right)} - \boldsymbol{U}_{i,j}\right)\right], \tag{3.139}$$

$$D_2 = \min\left[0, \left(\boldsymbol{U}_{i,j-\text{sign}\left(\Delta U^j_{i,j}\right)} + \frac{1}{2}\text{sign}\left(\Delta \boldsymbol{U}^i_{i,j}\right)\Delta \boldsymbol{U}^i_{i,j-\text{sign}\left(\Delta U^j_{i,j}\right)} + \frac{1}{2}\text{sign}\left(\Delta \boldsymbol{U}^j_{i,j}\right)\Delta \boldsymbol{U}^j_{i,j-\text{sign}\left(\Delta U^j_{i,j}\right)} - \boldsymbol{U}_{i,j}\right)\right]. \tag{3.140}$$

$\boldsymbol{U}_{i,j}$ is the volume averaged state variables vector in cell (i,j). $\boldsymbol{U}_{i-\text{sign}\left(\Delta U^i_{i,j}\right),j}$,

$\boldsymbol{U}_{i+\text{sign}\left(\Delta U^i_{i,j}\right),j}$, $\boldsymbol{U}_{i,j-\text{sign}\left(\Delta U^j_{i,j}\right)}$ and $\boldsymbol{U}_{i,j+\text{sign}\left(\Delta U^j_{i,j}\right)}$ are the volume averaged state variables vectors in the neighbouring cells. The variation in the state variables in each neighbouring cell is calculated from Eqns. 3.125 and 3.126.

Equations 3.133 to 3.140 define the difference between each interpolated neighbouring cell vertex value and cell (i, j), independent of the rotational orientation of the flow field gradient. A_1, A_2, B_1 and B_2 always have positive or zero values and C_1, C_2, D_1 and D_2 are always negative or zero. The orientation of A_1 to D_2 in Figure 3.13 assumes positive gradients for the positive i and j directions. The current two-dimensional interpolation scheme assumes that 'sign(0)' is positive. This condition is satisfied in the Fortran 90 programming language used for the current implementation.

Stage 3: Monotonicity is preserved by further limiting $\frac{1}{2}\left(|\Delta\boldsymbol{U}^i_{i,j}| + |\Delta\boldsymbol{U}^j_{i,j}|\right)$ using the values of A_1 to D_2. This is achieved by introducing three new variables, O, P and Q, defined as

$$O = \min\left[A_1,\, B_1,\, -C_1,\, -D_1,\, \frac{1}{2}\left(|\Delta\boldsymbol{U}^i_{i,j}| + |\Delta\boldsymbol{U}^j_{i,j}|\right)\right], \tag{3.141}$$

$$P = \max\left[D_2,\, -B_2,\, \min\left(\text{sign}\left(\Omega\right) D_2, \Omega\right), -2O\right], \tag{3.142}$$

$$Q = \min\left[A_2,\, -C_2,\, \max\left(-\text{sign}\left(\Omega\right) A_2, \Omega\right), 2O\right], \tag{3.143}$$

where

$$\Omega = \frac{1}{2}\left(|\Delta\boldsymbol{U}^i_{i,j}| - |\Delta\boldsymbol{U}^j_{i,j}|\right). \tag{3.144}$$

These values of $\Delta\boldsymbol{U}^i_{i,j}$ and $\Delta\boldsymbol{U}^j_{i,j}$ are computed from stage 1.

Stage 4: The values of O, P and Q are used to determine the final i and j variation across cell (i, j), defined as $\Delta\check{\boldsymbol{U}}^i_{i,j}$ and $\Delta\check{\boldsymbol{U}}^j_{i,j}$. These are given by

$$\Delta\check{\boldsymbol{U}}^i_{i,j} = \text{sign}\left(\Delta\boldsymbol{U}^i_{i,j}\right)\left(O + W\right), \tag{3.145}$$

$$\Delta\check{\boldsymbol{U}}^j_{i,j} = \text{sign}\left(\Delta\boldsymbol{U}^j_{i,j}\right)\left(O - W\right), \tag{3.146}$$

where W is defined as

$$W = \frac{(P+Q)}{2}. \tag{3.147}$$

Stage 5: The interpolated fine level state variables vector in each fine cell, overlying the coarse cell (i, j), is finally calculated as

$$\boldsymbol{U}_{i_f,j_f} = \boldsymbol{U}_{i_c,j_c} + \Delta\check{\boldsymbol{U}}^{i}_{i_c,j_c}\left[\left(i_f - \frac{1}{2}\right)/rI_f - \frac{1}{2}\right] + \Delta\check{\boldsymbol{U}}^{j}_{i_c,j_c}\left[\left(j_f - \frac{1}{2}\right)/rJ_f - \frac{1}{2}\right]. \tag{3.148}$$

rI_f and rJ_f are the increment in resolution between successive AMR levels in the i and j directions respectively. In this study $rI_f = rJ_f$. i_f and j_f are indices for the fine level L+1 cells that lie within each coarse level L cell. For each coarse level L cell, $1 \leq i_f \leq rI_f$ and $1 \leq j_f \leq rJ_f$. i_c and j_c are indices for the coarse level L cell. $\Delta\check{\boldsymbol{U}}^{i}_{i_c,j_c}$ and $\Delta\check{\boldsymbol{U}}^{j}_{i_c,j_c}$ are the i and j directed variation in state variables across the coarse cell (i_c, j_c), calculated from Eqns. 3.145 and 3.146. $\boldsymbol{U}_{i_c,j_c}$ is the volume averaged level L state variables vector for the coarse cell (i_c, j_c). Given that the variation in the state variables across each cell is piece-wise linear, conservation is maintained between levels in Eqn. 3.148.

To ensure monotonicity in cell (i_c, j_c) at level L is preserved, neighbouring level L cells with 'imposed' level L+1 flow states (those carried over between adaptions, Section 3.10.4) are taken into consideration. Consider the coarse grid at level L in Figure 3.13. Values for A_1 to D_2 surrounding the cell (i_c, j_c) are computed from stage 2. Now assume cell $(i_c + 1, j_c)$ underlies a portion of the level L+1 grid that is common between level L+1 adaptions. To maintain the accuracy of the level L+1 flow field, the level L+1 flow states in these common cells are simply copied between adaptions. To account for these 'imposed' states, an additional stage is defined, between stages 2 and 3. In this sub-stage, the value of A_1 to D_2 from stage 2 is replaced by the difference between the level L+1 cells overlying A_1 to D_2 and the volume averaged level L state variables in cell (i_c, j_c).

The i and j gradients are further limited for neighbouring cells that have an odd increase in resolution between AMR levels, and have 'imposed' level $L+1$ states. As a linear gradient is imposed in cell (i_c, j_c) at level L, the variation of the imposed level L+1 flow states are accommodated by redefining $\Delta\check{\boldsymbol{U}}^i_{i,j}$ and $\Delta\check{\boldsymbol{U}}^j_{i,j}$, from stage 4, as

$$\Delta\check{\boldsymbol{U}}^i_{i,j} = \text{sign}\left(\Delta\boldsymbol{U}^i_{i,j}\right) \cdot \min\left(O+W, 2A_3, -2C_3\right), \tag{3.149}$$

$$\Delta\check{\boldsymbol{U}}^j_{i,j} = \text{sign}\left(\Delta\boldsymbol{U}^j_{i,j}\right) \cdot \min\left(O-W, 2B_3, -2D_3\right). \tag{3.150}$$

A_3, B_3, C_3 or D_3 is the difference in state, between the imposed level L+1 cell at $\left[i_c + \frac{1}{2}\text{sign}\left(\Delta\boldsymbol{U}^i_{i_c,j_c}\right), j_c\right]$, $\left[i_c, j_c + \frac{1}{2}\text{sign}\left(\Delta\boldsymbol{U}^j_{i_c,j_c}\right)\right]$, $\left[i_c - \frac{1}{2}\text{sign}\left(\Delta\boldsymbol{U}^i_{i_c,j_c}\right), j_c\right]$, $\left[i_c, j_c - \frac{1}{2}\text{sign}\left(\Delta\boldsymbol{U}^j_{i_c,j_c}\right)\right]$ respectively, and the volume averaged state variables in cell (i_c, j_c). A_3, B_3, -C_3 and -D_3 are assumed positive for a monotonically varying flow distribution. The location of the fine level $L+1$ cells used to compute A_3 to D_3 are shown in Figure 3.14, for an increase in resolution of three between levels L and $L+1$. The orientation of A_3 to D_3 in Figure 3.14 assumes positive state variable gradients in the positive i and j directions respectively.

In summary, the interpolation procedure described in this section ensures a monotonic two-dimensional variation of the flow field. This is achieved by firstly ensuring that the final gradient in the coarse grid cell (i_c, j_c), i.e., $\frac{1}{2}\left[|\Delta\check{\boldsymbol{U}}^i_{i_c,j_c}| + |\Delta\check{\boldsymbol{U}}^j_{i_c,j_c}|\right]$, is less than or equal to the combined minmod limited i and j variation in each of the neighbouring cells, along each common interface. This can be written mathematically as

$$\frac{1}{2}\left[|\Delta\check{\boldsymbol{U}}^i_{i_c,j_c}| + |\Delta\check{\boldsymbol{U}}^j_{i_c,j_c}|\right] \leq \max\left(\Gamma_1, \Gamma_2, \Gamma_3, \Gamma_4\right), \tag{3.151}$$

where

$$\Gamma_1 = |\boldsymbol{U}_{i_c+1,j_c} - \boldsymbol{U}_{i_c,j_c}| - \frac{1}{2}\left(|\Delta\boldsymbol{U}^i_{i_c+1,j_c}| + |\Delta\boldsymbol{U}^j_{i_c+1,j_c}|\right), \tag{3.152}$$

$$\Gamma_2 = |\boldsymbol{U}_{i_c-1,j_c} - \boldsymbol{U}_{i_c,j_c}| - \frac{1}{2}\left(|\Delta\boldsymbol{U}^i_{i_c-1,j_c}| + |\Delta\boldsymbol{U}^j_{i_c-1,j_c}|\right), \tag{3.153}$$

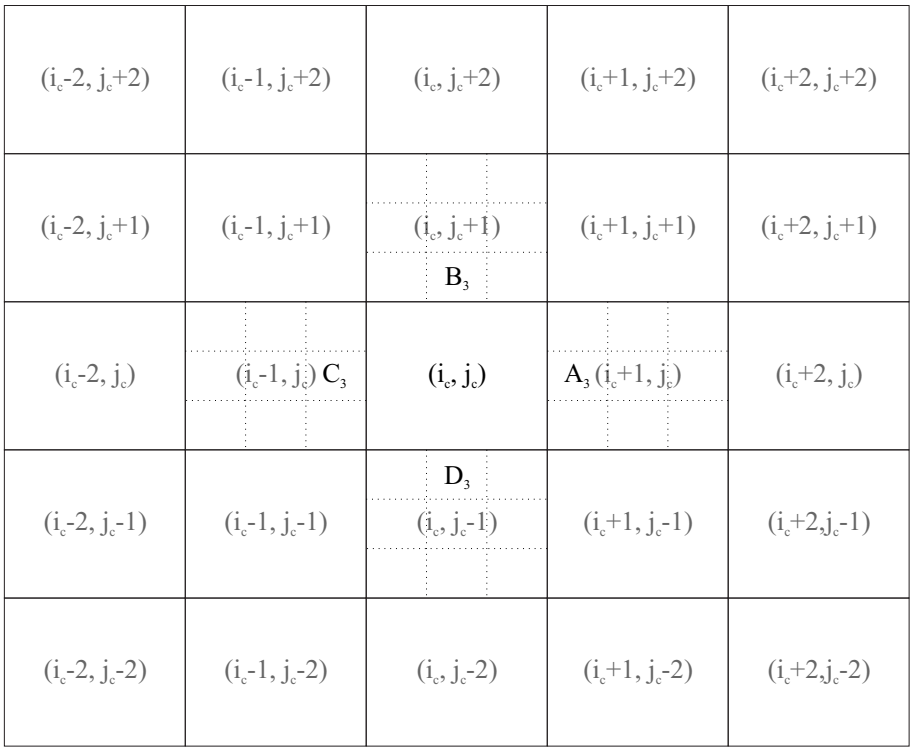

Figure 3.14: Representation of the coarse level L grid used to initialise the fine level $L+1$ flow field. A_3-D_3: Difference in the piece-wise constant state variables, between the imposed level $L+1$ cells and cell (i_c, j_c) at level L. (—) Level L cell boundary. $(\cdots)$ Level $L+1$ cell boundaries within one level L cell.

$$\Gamma_3 = |\boldsymbol{U}_{i_c,j_c+1} - \boldsymbol{U}_{i_c,j_c}| - \frac{1}{2}\left(|\Delta\boldsymbol{U}^i_{i_c,j_c+1}| + |\Delta\boldsymbol{U}^j_{i_c,j_c+1}|\right), \tag{3.154}$$

$$\Gamma_4 = |\boldsymbol{U}_{i_c,j_c-1} - \boldsymbol{U}_{i_c,j_c}| - \frac{1}{2}\left(|\Delta\boldsymbol{U}^i_{i_c,j_c-1}| + |\Delta\boldsymbol{U}^j_{i_c,j_c-1}|\right). \tag{3.155}$$

Monotonicity is then guaranteed by ensuring that these combined minmod limited i and j gradients are not exceeded after applying stages 1-5 at each of the neighbouring coarse grid cells, $(i_c \pm 1, j_c)$ and $(i_c, j_c \pm 1)$. This can be written mathematically, for an arbitrary cell $(n, m) = (i_c + 1, j_c)$, $(i_c - 1, j_c)$, $(i_c, j_c + 1)$, $(i_c, j_c - 1)$, as

$$\frac{1}{2}\left[|\Delta\check{\boldsymbol{U}}^i_{n,m}| + |\Delta\check{\boldsymbol{U}}^j_{n,m}|\right] \leq \frac{1}{2}\left[|\Delta\boldsymbol{U}^i_{n,m}| + |\Delta\boldsymbol{U}^j_{n,m}|\right]. \tag{3.156}$$

Equations 3.151-3.156 ensure the preservation of a monotonically varying flow field between successive levels.

3.10.4 Integrating the Flow Field

Following the initial creation of all AMR levels and the priming of each level with an initial flow distribution, through the procedures described in Sections 3.10.2 and 3.10.3, the flow field at each level is advanced in time. Each level is time marched using the baseline numerical method described in Sections 3.2 to 3.9.

The time step at each level is estimated by recursively dividing the level 0 time step by the inter-level increment in resolution:

$$\Delta t_L = \frac{\Delta t_0}{(rt_f)^L}. \tag{3.157}$$

Where Δt_0 is the time step at level 0, Δt_L is the calculated time step at a general level L and rt_f is the increment in resolution between levels. rt_f is defined constant on all levels in the current implementation. To advance the flow field at a general level L by one time step of the underlying level, rt_f successive integrations are performed. $(rt_f)^L$ successive integrations of level L are therefore required to satisfy one time step of the baseline level 0 flow field.

Starting with level 0, one Δt_L time step at each level is initially performed. After each integration, the ghost cells around the perimeter of each block are updated.

This boundary update stage is important, as these external cells are used for interpolating state variables for the perimetrical ghost cells at higher levels. Strategies for updating perimetrical ghost cells at each AMR level ($L > 0$) are detailed in Section 3.10.5. After each level has progressed one Δt_L time step and the boundaries have been updated, the most refined level ($L_{\max}$) is integrated in time a further $rt_f - 1$ times for temporal synchronisation with the underlying level. After this synchronisation with level L, levels $L+1$ to $L_{\max}$ are adapted to ensure that flow discontinuities remain within the refined meshes. The adaption process begins by an area weighted projection of the state variables of each level onto the level below. A conservation updating algorithm is then applied around the perimeter of the projected region. The back-projection and conservative updating procedure, which is carried out in descending level of refinement starting with level $L_{\max}$, is detailed in Section 3.10.6. Following the back-projection and conservation update, down to the general level L, levels $L+1$ to $L_{\max}$ are then redefined by the flagging and grouping procedure outlined in Section 3.10.2. To ensure each level remains properly nested within the bounds of its underlying level at $t > 0$, each level is flagged in descending order of refinement, starting with level $L_{\max -1}$. Following the flagging of levels $L_{\max} - 1$ to L, the flagged cells are grouped into a series of contiguous blocks and each newly created block is primed with an initial flow field distribution.

The priming of adapted regions at $t > 0$ is carried out by two main methods. Those adapted regions at a common spatial location between adaptions are primed by directly copying the volume averaged state variables from the coincident cells stored before the adaption stage. Carrying over the state variables between adaptions maintains the solution accuracy in those commonly refined regions. Newly refined regions are primed through interpolation from the underlying level, using the conservative two-dimensional interpolation procedure outlined in Section 3.10.3. Each refined level $L > 0$ is re-created and primed $(rt_f)^{L-1}$ times for each level 0 time step.

3.10.5 AMR Boundary Conditions

At $t_L > 0$, three main types of AMR boundaries are defined, *fine-fine* boundaries, *fine-coarse* boundaries and *external* boundaries.

Fine-fine boundaries are defined as those ghost cells that overlie interior cells of a different block, at the same hierarchical level L. Boundaries of this type are treated in the same manner as for the inter-domain boundary condition in Section 3.9.5. The ghost cells are updated by directly copying the state variables from the coincident interior cells.

Fine-coarse boundaries are defined as those ghost cells that only overlie interior cells of the level below. To update ghost cells of this type, an interpolation of the time synchronous volume averaged state variables in the interior cells of the level below is required. After each temporal integration, however, two successive levels may not be time synchronous. For example, after the first integration of all levels, the flow field at a general level $L+1$ is developed to a time of $t_0 + \frac{\Delta t_0}{\left(rt_f\right)^{L+1}}$. The underlying level (level L) is, however, at a time of $t_0 + \frac{\Delta t_0}{\left(rt_f\right)^{L}} \equiv t_0 + \frac{rt_f \Delta t_0}{\left(rt_f\right)^{L+1}}$. To update the fine-coarse boundaries of level $L+1$, a linear interpolation in time of the interior cell state variables of level L is performed. From this linear interpolation, an estimation of the level L interior state variables at $t_0 + \frac{\Delta t_0}{\left(rt_f\right)^{L+1}}$ is obtained. The fine-coarse ghost cells are then interpolated using the two-dimensional interpolation method of Section 3.10.3. In addition, the ghost cells are updated after each Runge-Kutta stage. The Runge-Kutta algorithm is described in Section 3.8. For the current study, of second order temporal accuracy, the conservation equations are integrated twice for each increment in time step. A linear interpolation in time of the intermediate state variables, after each Runge-Kutta stage of level L, are therefore used to interpolate values for the level $L+1$ ghost cells, between each level $L+1$ Runge-Kutta stage.

External boundaries are defined as those ghost cells that overlie ghost cells at level 0. At the start of the computation, and at each successive adaption, any external boundaries are primed by interpolating from the updated ghost cells of the level below. Between adaptions, these external boundaries are updated after

each integration using the appropriate boundary conditions defined in Section 3.9. The interior variables required for these boundary conditions are provided by the updated internal cells, on the same AMR level, adjacent to the external boundary.

3.10.6 The Conservative Fine-Coarse Solution Projection

After synchronising two or more levels to a common time, the updated fine level solution is imposed onto the underlying coarse level through an area weighted back-projection. The numerical procedure outlined in Sections 3.2 to 3.9 ensures the flow field is conservative within each level. After the back-projection stage, contiguous coarse cells with back-projected state variables should therefore remain conservative within the area defined by each fine block. Conservation is not however maintained between successive levels. The back-projected region will therefore not be conservative with the surrounding coarse grid, across the fine-coarse interface. The flux imbalance that exists across the fine-coarse interface is remedied after the back-projection stage by applying a conservation update to the coarse level cells, which underlie the fine level ghost cells. Figure 3.15 shows a representation of a fine-coarse boundary interface, between two successive levels. The area weighted back-projection for cell (i_c+1, j_c) in Figure 3.15 is defined as

$$\boldsymbol{U}^t_{L,i_c+1,j_c} = \frac{1}{V^t_{L,i_c+1,j_c}} \sum_{m=0}^{rJ_f-1} \sum_{n=0}^{rI_f-1} \boldsymbol{U}^t_{L+1,i_f+n,j_f+m} V^t_{L+1,i_f+n,j_f+m}, \tag{3.158}$$

where V^t_{L+1,i_f+n,j_f+m} and $\boldsymbol{U}^t_{L+1,i_f+n,j_f+m}$ are the area and state variables matrix for each fine level $L+1$ cell at time t. V^t_{L,i_c+1,j_c} and $\boldsymbol{U}^t_{L,i_c+1,j_c}$ are the area and state variables matrix for the cell (i_c+1, j_c) at level L. (i_f, j_f) is the index of the level $L+1$ fine cell sharing the bottom left hand vertex with the level L cell (i_c, j_c).

The conservative update uses the flux crossing the fine-coarse interface at level L and level $L+1$ to evaluate the total mass, momentum and energy crossing the interface over one coarse level time step Δt_L. The difference in total mass, momentum and energy crossing the fine-coarse interface at levels L and $L+1$ is then used to compensate each level L cell lying along the fine-coarse boundary interface.

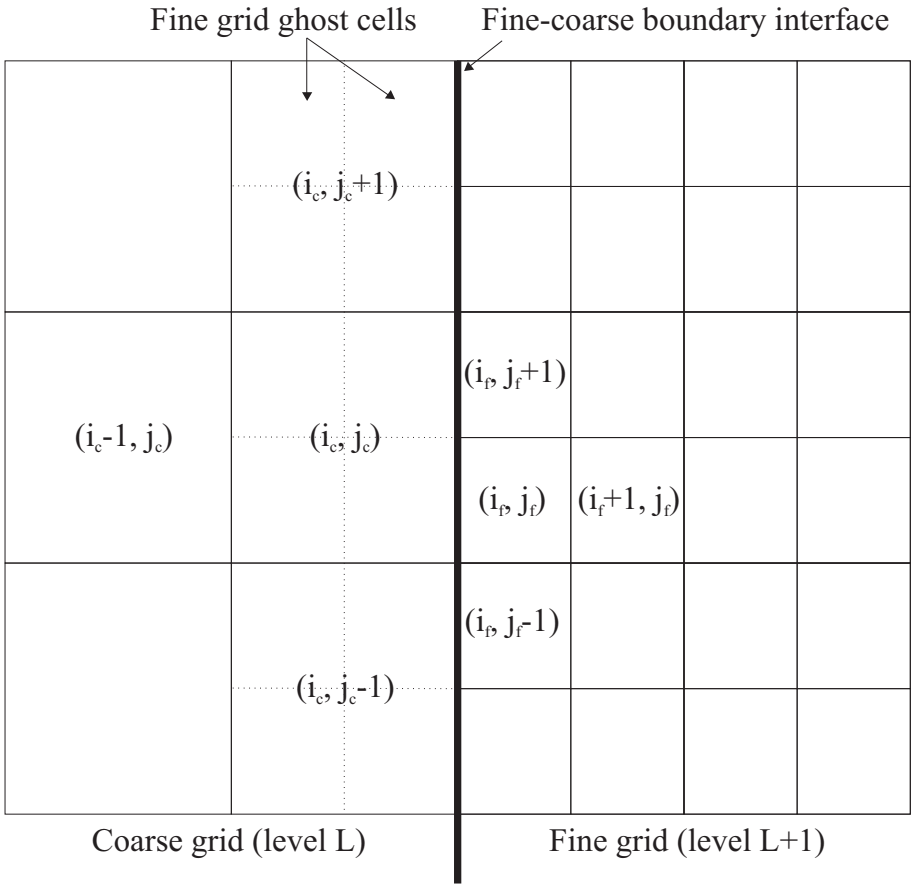

Figure 3.15: Diagrammatical representation of a fine-coarse boundary interface between level L and level $L+1$. (i_c, j_c) is the coarse level cell index. (i_f, j_f) is the fine level cell index. $(\cdots)$ Outline of the fine level ghost cells.

The total mass, momentum and energy crossing the fine-coarse interface at level L, between cells (i_c, j_c) and $(i_c + 1, j_c)$, is:

$$\left(\boldsymbol{U}^t_{vol}\right)_L = \Delta t_L \boldsymbol{F}\left(\boldsymbol{U}\right)^t_{L,i_c+\frac{1}{2},j_c} A^t_{L,i_c+\frac{1}{2},j_c}. \tag{3.159}$$

Where $\boldsymbol{F}\left(\boldsymbol{U}\right)^t_{L,i_c+\frac{1}{2},j_c}$ is the flux crossing the fine-coarse interface at level L. $A^t_{L,i_c+\frac{1}{2},j_c}$ is the length of the fine-coarse interface, between cells (i_c, j_c) and $(i_c + 1, j_c)$. The total mass, momentum and energy crossing an equivalent interface length at level $L + 1$ is given by

$$\left(\boldsymbol{U}^t_{vol}\right)_{L+1} = \frac{\Delta t_L}{rt_{L+1}} \sum_{m=1}^{rt_f} \sum_{n=0}^{rJ_f-1} \boldsymbol{F}\left(\boldsymbol{U}\right)^{(t-1)+m\Delta t_{L+1}}_{L+1,i_f-\frac{1}{2},j_f+n} A^t_{L+1,i_f-\frac{1}{2},j_f+n}. \tag{3.160}$$

Therefore, the conservative update applied to cell (i_c, j_c) in Figure 3.15 is:

$$\left(\boldsymbol{U}^t\right)_{L,i_c,j_c} = \left(\boldsymbol{U}^t\right)_{L,i_c,j_c} + \frac{\left(\boldsymbol{U}^t_{vol}\right)_L - \left(\boldsymbol{U}^t_{vol}\right)_{L+1}}{V^t_{L,i_c,j_c}}. \tag{3.161}$$

Due to sign convention, the conservative update in Eqn. 3.161 is valid for western facing fine-coarse interfaces only, as in Figure 3.15. For an eastern facing fine-coarse interface, with the coarse cell (i_c, j_c) underlying the fine level ghost cells, Eqns. 3.159-3.161 are redefined as:

$$\left(\boldsymbol{U}^t_{vol}\right)_L = \Delta t_L \boldsymbol{F}\left(\boldsymbol{U}\right)^t_{L,i_c-\frac{1}{2},j_c} A^t_{L,i_c-\frac{1}{2},j_c}, \tag{3.162}$$

$$\left(\boldsymbol{U}^t_{vol}\right)_{L+1} = \frac{\Delta t_L}{rt_{L+1}} \sum_{m=1}^{rt_f} \sum_{n=0}^{rJ_f-1} \boldsymbol{F}\left(\boldsymbol{U}\right)^{(t-1)+m\Delta t_{L+1}}_{L+1,i_f+\frac{1}{2},j_f+n} A^t_{L+1,i_f+\frac{1}{2},j_f+n}, \tag{3.163}$$

$$\left(\boldsymbol{U}^t\right)_{L,i_c,j_c} = \left(\boldsymbol{U}^t\right)_{L,i_c,j_c} - \frac{\left(\boldsymbol{U}^t_{vol}\right)_L - \left(\boldsymbol{U}^t_{vol}\right)_{L+1}}{V^t_{L,i_c,j_c}}. \tag{3.164}$$

Similarly, for a southern facing fine-coarse interface, Eqns. 3.159-3.161 are redefined as:

$$\left(\boldsymbol{U}^t_{vol}\right)_L = \Delta t_L \boldsymbol{F}\left(\boldsymbol{U}\right)^t_{L,i_c,j_c+\frac{1}{2}} A^t_{L,i_c,j_c+\frac{1}{2}}, \tag{3.165}$$

$$\left(\boldsymbol{U}^t_{vol}\right)_{L+1} = \frac{\Delta t_L}{rt_{L+1}} \sum_{m=1}^{rt_f} \sum_{n=0}^{rI_f-1} \boldsymbol{F}\left(\boldsymbol{U}\right)^{(t-1)+m\Delta t_{L+1}}_{L+1,i_f+n,j_f-\frac{1}{2}} A^t_{L+1,i_f+n,j_f-\frac{1}{2}}, \tag{3.166}$$

$$\left(\boldsymbol{U}^t\right)_{L,i_c,j_c} = \left(\boldsymbol{U}^t\right)_{L,i_c,j_c} + \frac{\left(\boldsymbol{U}^t_{vol}\right)_L - \left(\boldsymbol{U}^t_{vol}\right)_{L+1}}{V^t_{L,i_c,j_c}}. \tag{3.167}$$

Finally, for a northern facing fine-coarse interface, Eqns. 3.159-3.161 are redefined as:

$$\left(\boldsymbol{U}^t_{vol}\right)_L = \Delta t_L \boldsymbol{F}\left(\boldsymbol{U}\right)^t_{L,i_c,j_c-\frac{1}{2}} A^t_{L,i_c,j_c-\frac{1}{2}}, \tag{3.168}$$

$$\left(\boldsymbol{U}^t_{vol}\right)_{L+1} = \frac{\Delta t_L}{rt_{L+1}} \sum_{m=1}^{rt_f} \sum_{n=0}^{rI_f-1} \boldsymbol{F}\left(\boldsymbol{U}\right)^{(t-1)+m\Delta t_{L+1}}_{L+1,i_f+n,j_f+\frac{1}{2}} A^t_{L+1,i_f+n,j_f+\frac{1}{2}}, \tag{3.169}$$

$$\left(\boldsymbol{U}^t\right)_{L,i_c,j_c} = \left(\boldsymbol{U}^t\right)_{L,i_c,j_c} - \frac{\left(\boldsymbol{U}^t_{vol}\right)_L - \left(\boldsymbol{U}^t_{vol}\right)_{L+1}}{V^t_{L,i_c,j_c}}. \tag{3.170}$$

With the AMR numerical procedure described in Sections 3.10.1 to 3.10.6, the predicted flow field at each level should be as accurate as a single level non-AMR prediction, of equivalent spatial and temporal resolution. The accuracy of the current AMR implementation is analysed through a series of test cases in Chapter 4.

Chapter 4

AMR Method Validation

4.1 Introduction

Selected results from a structured validation program for the Adaptive Mesh Refinement (AMR) numerical method are presented in this chapter. The AMR scheme provides a computationally efficient method for locally increasing the resolution of the numerical mesh in areas of large density gradient. In the current study, these regions constitute flow features of direct interest. Predictions using the AMR method should provide a close approximation to predictions that use a uniformly refined single mesh, of equivalent spatial and temporal resolution. The results presented in this chapter are therefore validated against available analytical or experimental correlations, as well as predictions using a non-adapted uniformly refined mesh. The latter is obtained from the baseline numerical procedure described in Sections 3.2 to 3.9.

4.2 One-Dimensional Shock Tube Problem

4.2.1 Test Case Description

The first AMR test case is an inviscid prediction of the one-dimensional flow in a shock tube. The flow problem is diagrammatically represented in Figure 4.1. A diaphragm initially separates air of different densities and pressures at rest in a rigid walled tube, Figure 4.1(a). The initial fluid properties, to the left and right of this diaphragm, are given in Table 4.1. These properties are denoted l and r in Figure 4.1(a). After removing the diaphragm, a shock wave and a contact

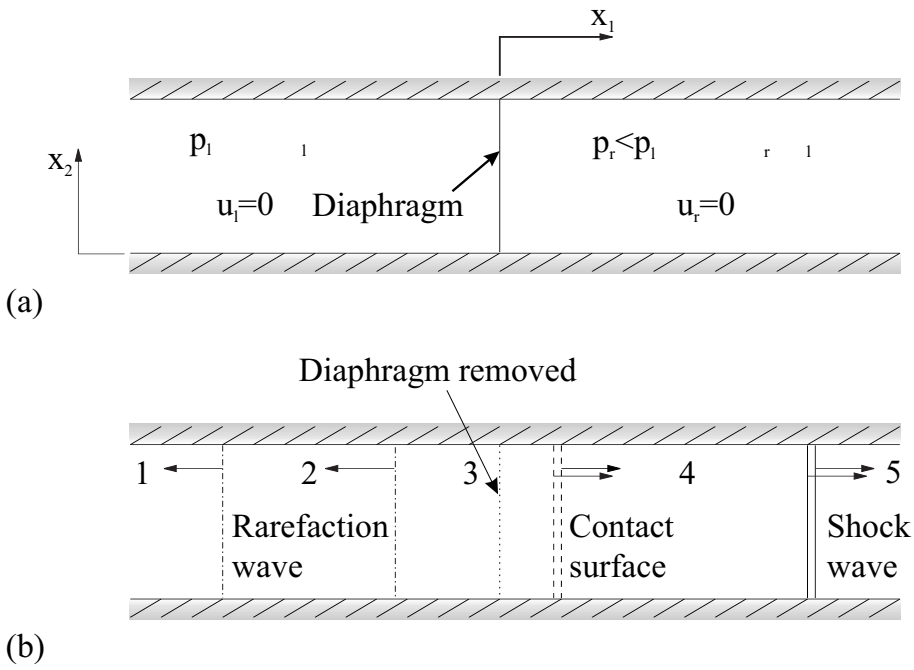

Figure 4.1: Shock tube flow geometry. (a) Initial flow condition before removal of the diaphragm. (b) Flow field at time t seconds after the diaphragm removal.

Variable	Left	Right
ρ/ρ_r	2.881	1.0
u_1/u_{shock}	0.0	0.0
p/p_r	4.4	1.0

Table 4.1: Shock tube initial flow conditions

discontinuity travel from $x_1 = 0$, through the low pressure fluid p_r. A rarefaction wave travels from $x_1 = 0$, through the high pressure fluid p_l. The instantaneous flow field at $t > 0$ is divided into 5 separate regions. These are defined in Figure 4.1(b). Regions 1 and 5 are undisturbed by the compression and rarefaction waves and maintain the initial flow states to the left and right of the diaphragm, given in Table 4.1. The flow properties in regions 1-5 at time $t > 0$ are given in Hixon (1999), following the analytical solution development in Hirsch (1990). These flow properties are listed in Table 4.2. The shock wave has a constant velocity of $u_{shock} = 1.486a_\infty$. The rarefaction wave leading and trailing edge velocities are $u_{le} = -1.297a_\infty$ and $u_{te} = -0.551a_\infty$ respectively. These velocities highlight the increase in stream-wise length of the rarefaction wave with time. The shock tube computational domain

Variable	Region 1	Region 2	Region 3	Region 4	Region 5
ρ/ρ_r	2.881	$\frac{\rho_\infty \gamma p_2}{\rho_r \left(u_2 - \frac{x_1}{t}\right)^2}$	1.741	1.718	1.0
u_1/u_{shock}	0.0	$\frac{2a_\infty}{(\gamma+1)u_{shock}} \left(\frac{x_1}{t} + \sqrt{\frac{\gamma p_1}{\rho_1}}\right)$	0.418	0.418	0.0
p/p_r	4.4	$\frac{\rho_\infty a_\infty^2 p_1}{p_r} \left(\frac{u_2 - \frac{x_1}{t}}{\sqrt{\frac{\gamma p_1}{\rho_1}}}\right)^{\left(\frac{2\gamma}{\gamma-1}\right)}$	2.174	2.174	1.0

Table 4.2: Analytical shock tube flow properties at $t > 0$.

extends $-l/2 \leq x_1 \leq l/2$ in the stream-wise direction and $0 \leq x_2 \leq l/8$ in the cross-stream direction, where l is the computational domain stream-wise length. The diaphragm separating the initial left and right flow states is located at $x_1 = 0$. The periodic boundary condition described in Section 3.9.6 is imposed at $x_2 = 0$ and $x_2 = l/8$. The extrapolated outlet condition described in Section 3.9.4 is imposed at the flow normal boundaries, $x_1 = -l/2$ and $x_1 = l/2$.

Three separate shock tube predictions are presented in this section. The first models the shock tube using one level of AMR refinement (level 1), in addition to the uniform baseline grid (level 0). The second prediction models the shock tube using two levels of AMR refinement (levels 1 and 2), in addition to the baseline grid (level 0). These two predictions use an AMR scaling parameter of $b = 0.02$. The third prediction highlights the importance of a suitable choice for this scaling parameter. As in the first prediction, a baseline (level 0) grid is defined with one additional level of AMR refinement (level 1). A scaling parameter of $b = 0.05$ is defined for this prediction. A common level 0 grid of 125×16 cells in the x_1 and x_2 directions is defined in all three predictions. Level 1 constitutes an increase in the spatial resolution by a factor of two from the level 0 grid. A further increase in the spatial resolution by a factor of two from level 1 defines level 2.

4.2.2 Results & Discussion

The flow field develops from the initial conditions listed in Table 4.1, at time $t = 0$, to a time of $t = 0.1906 l/a_\infty$ seconds. A constant time step of $\Delta t = 1.906 \times 10^{-3} l/a_\infty$ seconds is used at level 0. This time step is reduced by a factor of two for each

successive AMR level. Additional benchmarking of the level 1 and level 2 predictions is achieved using non-refined predictions with 250×32 cells and 500×64 cells respectively. These benchmark predictions use equivalent time steps to levels 1 and 2, i.e. $\Delta t = 9.53 \times 10^{-4} l/a_\infty$ seconds and $\Delta t = 4.765 \times 10^{-4} l/a_\infty$ seconds respectively.

The adapted AMR computational grids from the three cases at a time of $t = 0.1906 l/a_\infty$ seconds are shown in Figure 4.2(a-c). The AMR scheme locally refines the level 0 grid around the shock wave, the contact surface and the rarefaction wave. Changing the scaling parameter from $b = 0.02$ to $b = 0.05$ results in an absence of AMR refinement across the contact surface, Figure 4.2(c).

A cross-section of the flow field along $x_2 = l/16$ from the first prediction, with $b = 0.02$, is given in Figure 4.3(a-c). This figure shows the static density profile (a), the static pressure profile (b) and the velocity profile (c). Two isolated frames within this figure detail the shock wave (i) and the contact surface (ii) from the density profile. The analytical solution is defined in this figure by a blue line; the benchmark prediction is defined by a black line. The most refined level AMR prediction is defined using square symbols.

A good correlation in the alignment of the shock wave, the contact discontinuity and the rarefaction wave is evident between the AMR prediction, the benchmark prediction and the analytical solution. Some numerical dissipation is evident in the prediction of these features, identified by a finite spatial spread of the discontinuous shock wave and contact surface over a number of cells, and by a rounding of the rarefaction wave leading and trailing edges. No discernable differences are evident between the AMR prediction and the non-refined benchmark prediction. The same level of dissipation is evident at the shock wave, the contact surface and the rarefaction wave in the two predictions, indicating the AMR scheme retains the dissipative and dispersive properties of the original numerical scheme.

The effect of an additional level of mesh refinement is shown in Figure 4.4. Three AMR levels (levels 0, 1 and 2) are specified, with a baseline (level 0) grid of 125×16 cells. The non-refined benchmark prediction is computed using a uniform computational grid of 500×64 cells. A decrease in the dissipation error is evident in

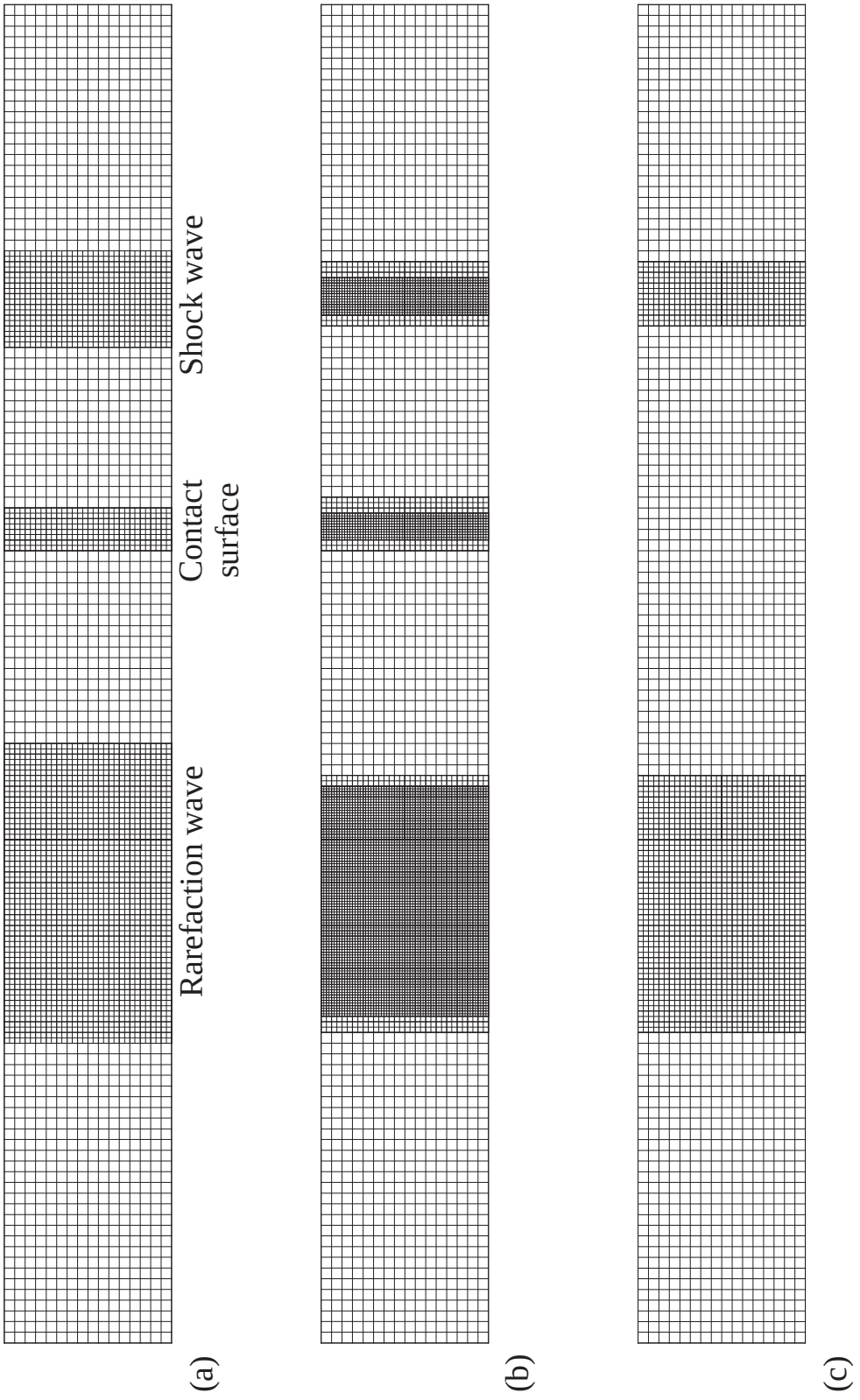

Figure 4.2: Shock tube computational grid. Adaptive levels shown at $t = 0.1906l/a_\infty$ seconds. (a) Baseline grid (level 0) with one additional level of multigrid refinement, $b = 0.02$. (b) Baseline grid (level 0) with two additional levels of multigrid refinement, $b = 0.02$. (c) Baseline grid (level 0) with one additional level of multigrid refinement, $b = 0.05$.

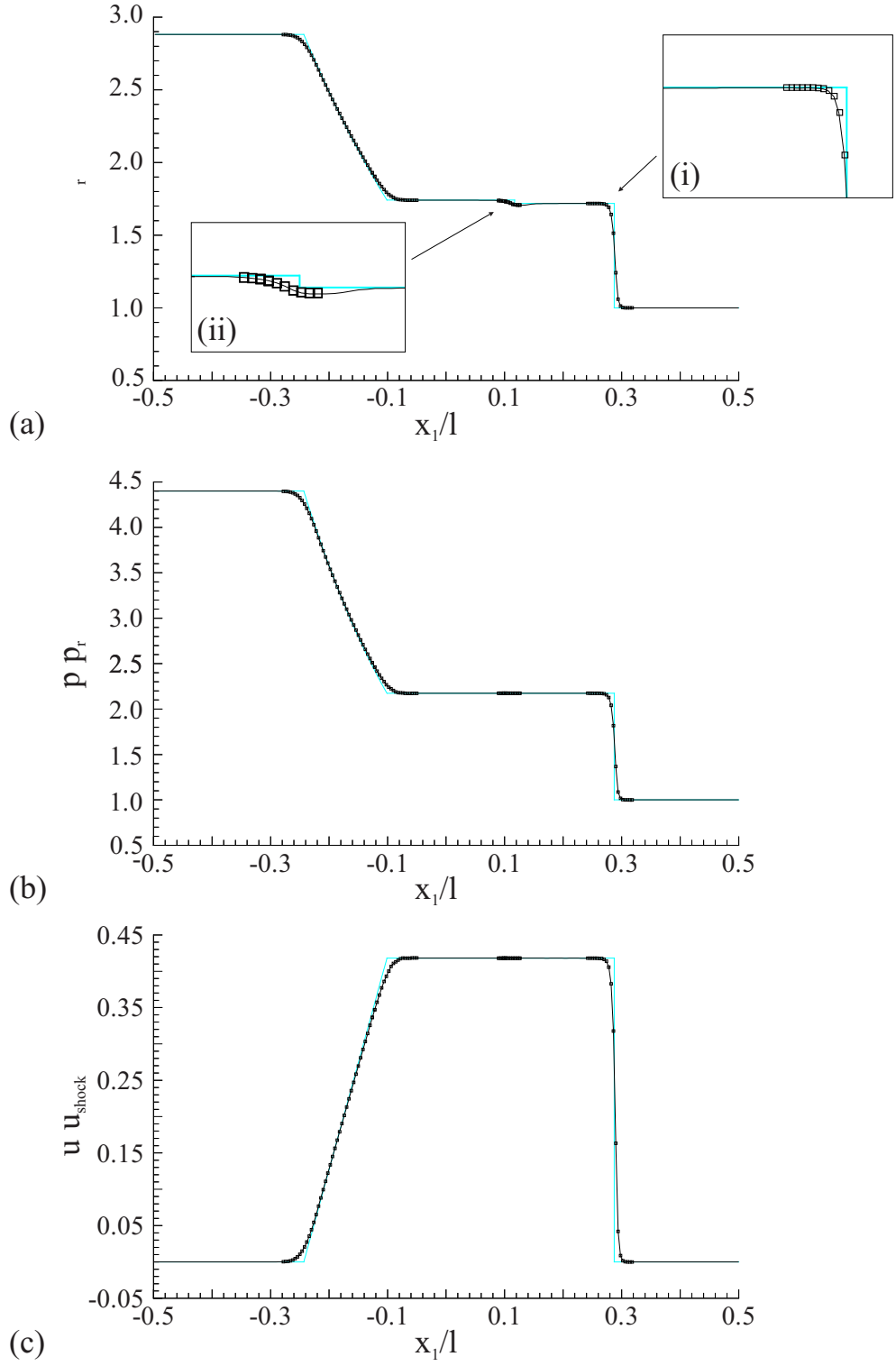

Figure 4.3: Shock tube cross-section at $t = 0.1906 l/a_\infty$ seconds, along $x_2 = l/16$. Two levels of multigrid refinement (levels 0 and 1). (a) Static density distribution, $\rho_r = 1.272\rho_\infty$, (i) detail in the shock wave region, (ii) detail across the contact surface. (b) Static pressure distribution, $p_r = 1.0\rho_\infty a_\infty^2$. (c) Velocity distribution, $u_{shock} = 1.486 a_\infty$. (—) Analytical solution. (—) Non refined benchmark prediction. ☐ AMR level 1 prediction, $b = 0.02$.

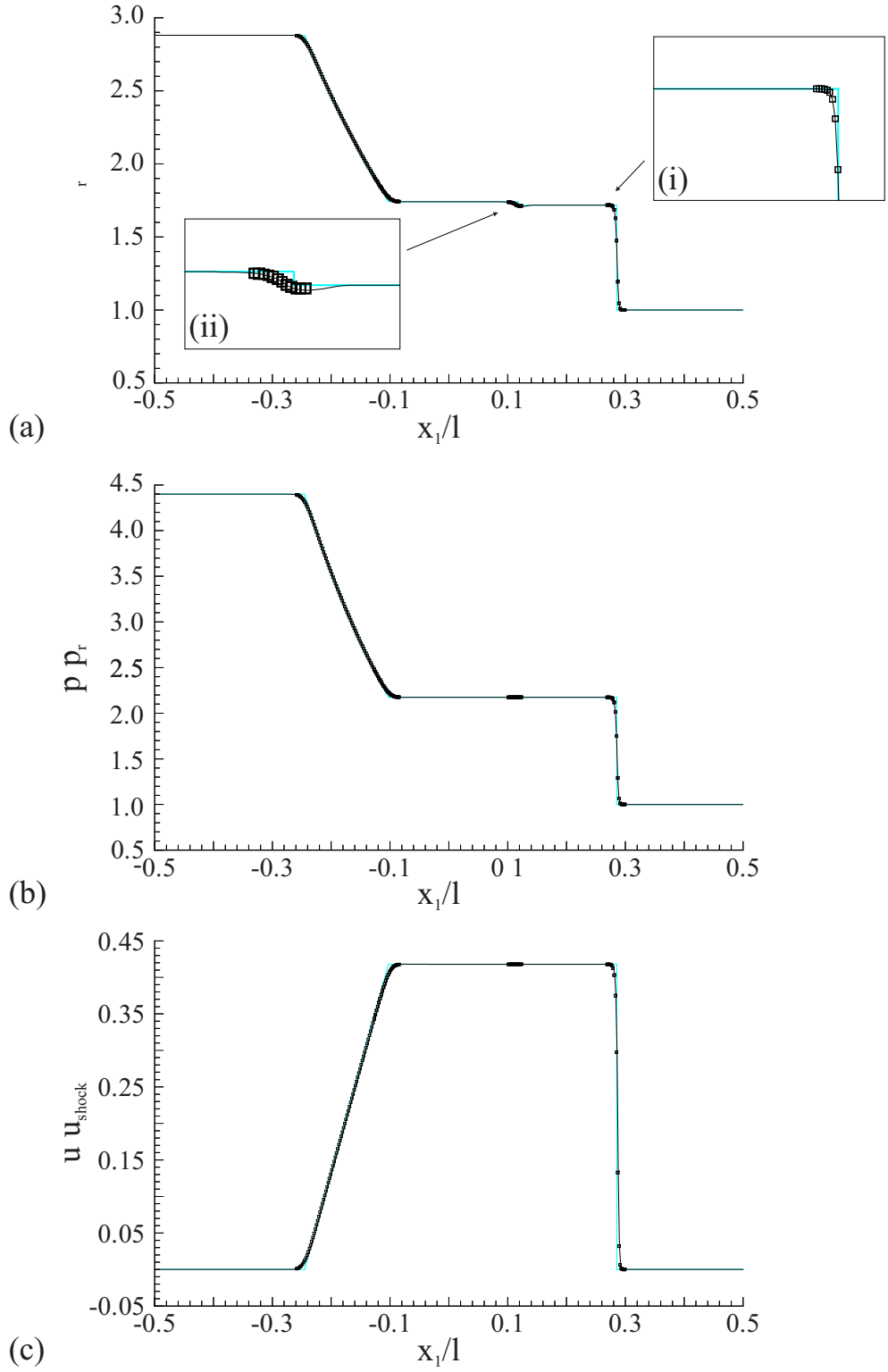

Figure 4.4: Shock tube cross-section at $t = 0.1906 l/a_\infty$ seconds, along $x_2 = l/16$ with three levels of multigrid refinement (levels 0, 1 and 2). (a) Static density distribution, $\rho_r = 1.272\rho_\infty$, (i) detail in the shock wave region, (ii) detail across the contact surface. (b) Static pressure distribution, $p_r = 1.0\rho_\infty a_\infty^2$. (c) Velocity distribution, $u_{shock} = 1.486 a_\infty$. (—) Analytical solution. (—) Non refined benchmark prediction. □ AMR level 2 prediction, $b = 0.02$.

Figure 4.4, with respect to Figure 4.3. Accompanying the increase in the resolution of the flow features is an associated decrease in the width of refined grid required to cover each feature. This is evident in Figure 4.2 as a reduction in the number of cells required at level 1 in Figure 4.2(b). The predicted flow features are again well placed, and the magnitude of the shock wave, contact surface and rarefaction wave show a close agreement with the analytical solution. The agreement between the AMR prediction and the benchmark prediction is good, indicating no discernable deterioration of the prediction occurs from using the AMR method in this case.

The AMR method demonstrates a significant increase in computational speed over the non-refined benchmark prediction. The difference in computational time required to advance the flow field from the starting conditions (t=0) to the flow field in Figure 4.3, between the two levels AMR prediction and the non-AMR benchmark prediction, is 51.9%. This decrease in computational time from the use of the AMR method is further indicated in the second prediction. The decrease in computational time required to compute the three levels AMR prediction, with respect to the non-AMR benchmark prediction, is 88.3%. These predictions demonstrate the advantages that can be gained through localised grid refinement using the AMR method.

The influence of the AMR scaling parameter b on the prediction accuracy and efficiency is shown in Figure 4.5. A baseline grid of 125×16 cells with two AMR levels of refinement (levels 0 and 1) is compared against the non-refined benchmark prediction of 250×32 cells, and against the analytical solution. For this prediction, the AMR scaling parameter is changed from $b = 0.02$ to $b = 0.05$. Increasing this parameter asserts that a greater density gradient between two adjacent cells is required before the region is refined. The result of this change is evident by comparing Figure 4.2(a) with Figure 4.2(c), and by comparing Figure 4.3(a) with Figure 4.5. In addition to the absence of any grid refinement around the contact surface, fewer level 1 cells are defined around the shock wave and the rarefaction wave in the $b = 0.05$ prediction. This results in less of the shock wave and rarefaction wave being covered by the refined grid in Figure 4.5. Further significant increases

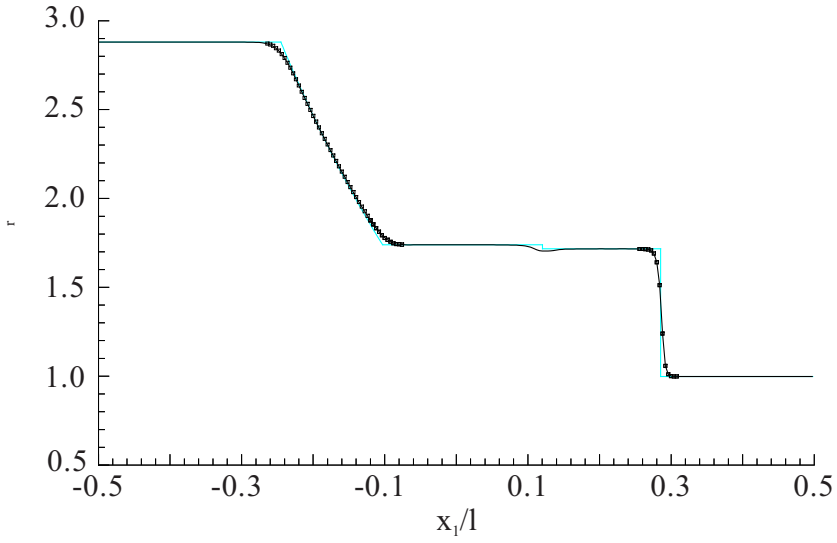

Figure 4.5: Shock tube cross-section at $t = 0.1906l/a_\infty$ seconds, along $x_2 = l/16$, with two levels of AMR refinement. Static density, $\rho_r = 1.272\rho_\infty$. (—) Analytical solution. (—) Non-refined benchmark prediction. □ AMR level 1 prediction, $b = 0.05$.

in b may result in problems of preserving monotonicity across the fine-coarse level boundaries, due to the higher variable gradients in this region.

Increasing b from $b = 0.02$ to $b = 0.05$ gives a further reduction of 13% in the time required to compute the shock tube prediction in Figure 4.5. This case highlights the inherent conflict in choosing the AMR scaling parameter b, between ensuring an accurate, well resolved flow field prediction and the efficient utilisation of the available computational resources.

Overall, an engineering accurate prediction is achieved in the one-dimensional shock tube problem from the application of the AMR method. No significant deterioration of the prediction is evident with respect to the non-refined benchmark prediction, indicating that the numerical characteristics of the original baseline scheme are preserved.

4.3 Two-Dimensional Acoustic Pulse Problem

4.3.1 Test Case Description

The second AMR test case is a two-dimensional acoustic pulse, which propagates outwards from the centre of the domain. This test case is chosen to highlight some inherent limitations in the monotonicity preserving interpolation method used to initialise the flow field at each AMR level. The computational domain, with an initial Gaussian distribution, is represented diagrammatically in Figure 4.6(a-b). The computational domain is of square topology with length l. The origin, as indicated in Figure 4.6(a), is located at the centre of the computational domain. The computational domain is therefore defined over the region $-l/2 \leq x_1 \leq l/2$ and $-l/2 \leq x_2 \leq l/2$. An extrapolated pressure boundary condition, described in Section 3.9.4, is defined at the boundaries $b1 - b4$. Ambient conditions are defined at time $t = 0$. Imposed onto these ambient conditions is a two dimensional Gaussian distribution, centred at $x_1 = x_2 = 0$. The initial static pressure and density fields are defined by

$$p/\rho_\infty a_\infty^2 = 1.0 + 0.01 \exp\left(-(\ln 2)\left(\frac{(200x_1/l)^2 + (200x_2/l)^2}{9}\right)\right) \quad (4.1)$$

$$\rho/\rho_\infty = 1.0 + \frac{0.01}{\gamma} \exp\left(-(\ln 2)\left(\frac{(200x_1/l)^2 + (200x_2/l)^2}{9}\right)\right) \quad (4.2)$$

where $\gamma = 1.4$ is the specific heat ratio. A cross-section of the initial Gaussian density distribution is shown diagrammatically in Figure 4.6(b). The computational domain is truncated in this figure to $-l/2 \leq x_1 \leq l/2$, $0 \leq x_2 \leq l/2$, to show half of the Gaussian pulse. From the initial conditions, the flow field is time marched to $t = 30l/118a_\infty$ seconds. The acoustic pulse at time $t > 0$ seconds is shown diagrammatically in Figure 4.7(a-b). The computational domain is again truncated in Figure 4.7(b) to $-l/2 \leq x_1 \leq l/2$, $0 \leq x_2 \leq l/2$ to show a cross-section of the propagating acoustic pulse, along $x_2 = 0$. An analytical solution to the acoustic pulse flow field at $t > 0$ is available, based on the linear form of the Euler equations,

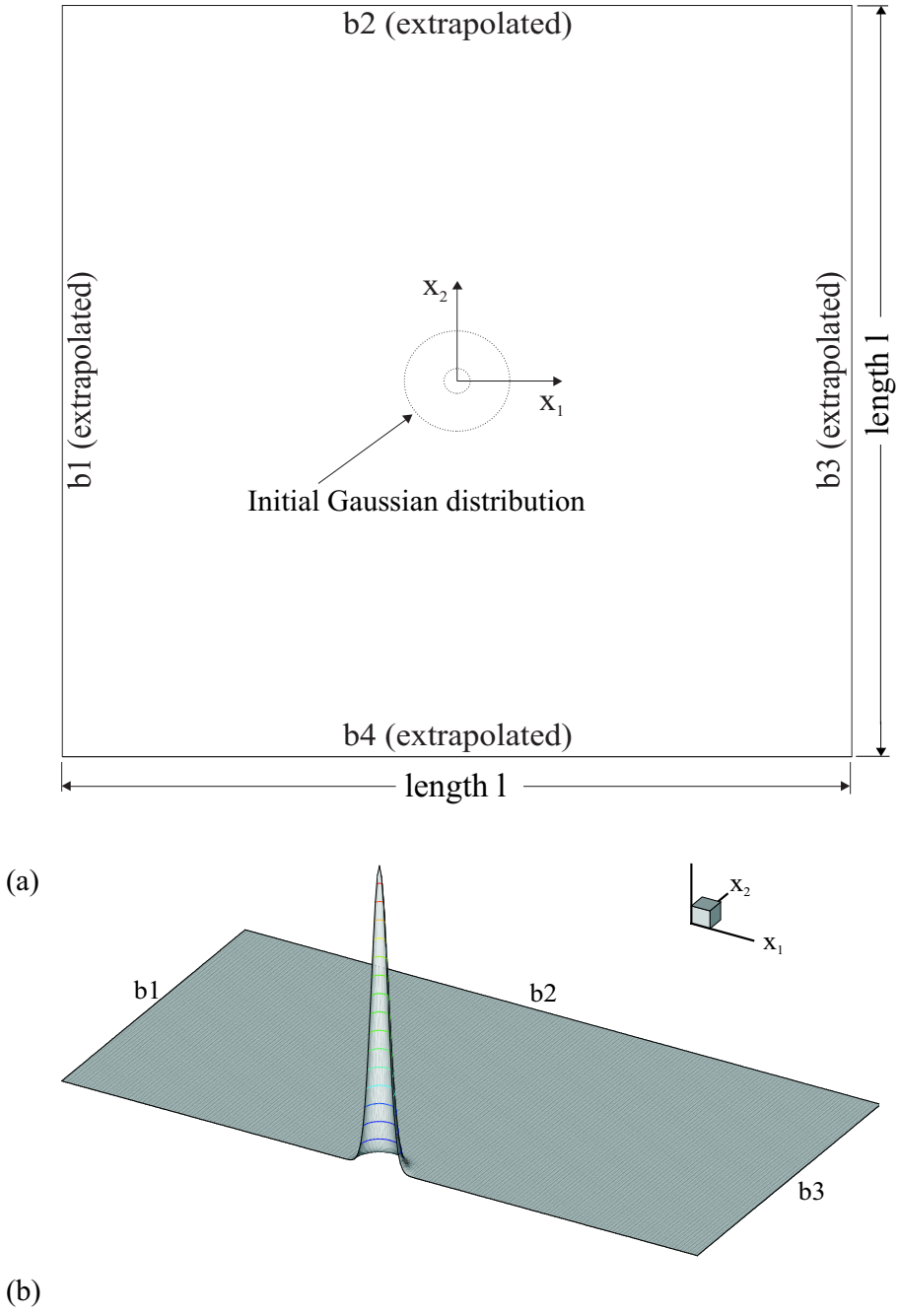

Figure 4.6: Acoustic pulse geometry. (a) Plan view of the computational domain. (b) Representation of initial Gaussian distribution in cross-section along $x_2 = 0$. The extent of the flow domain shown in (b) is $-l/2 \leq x_1 \leq l/2$, $0 \leq x_2 \leq l/2$.

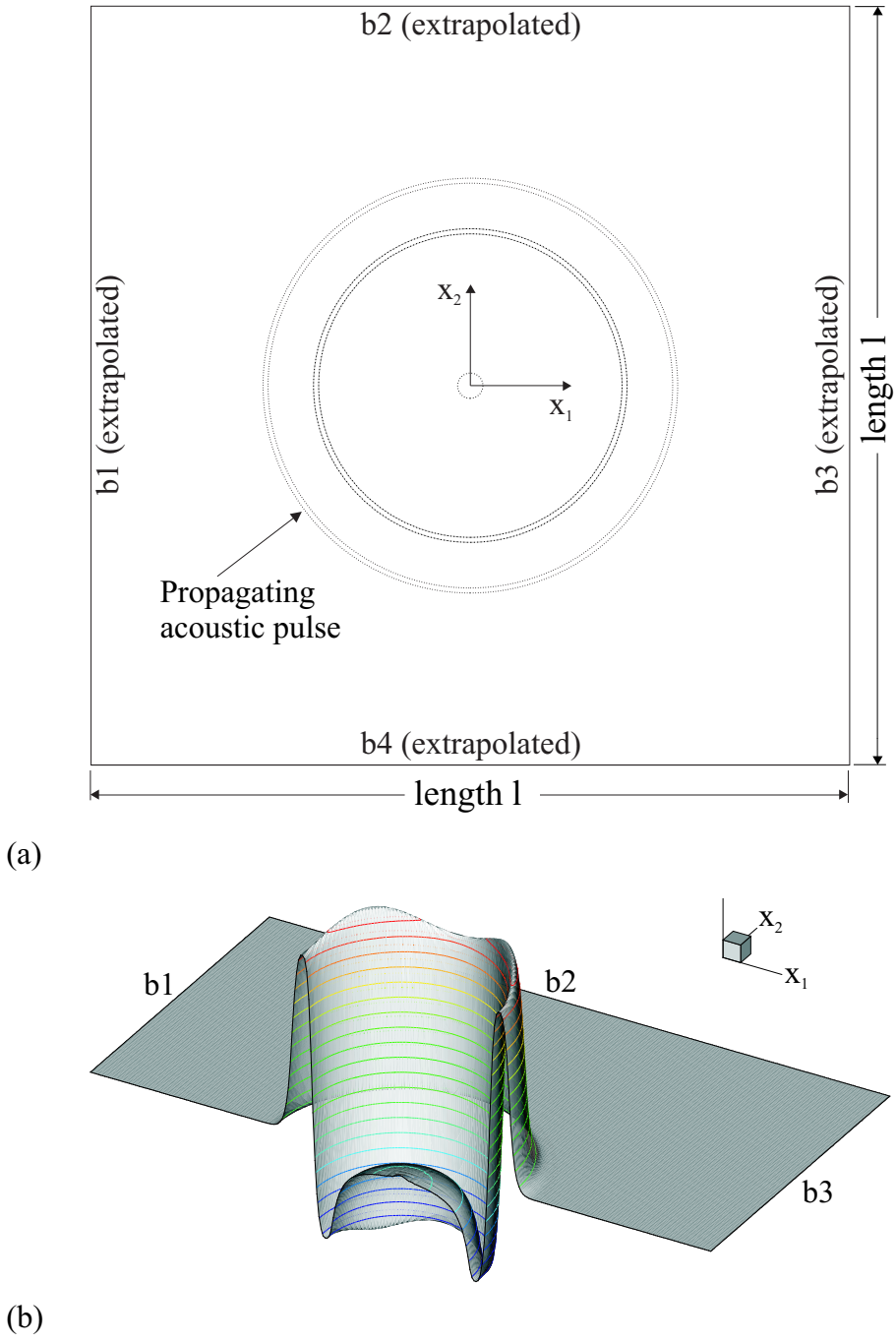

Figure 4.7: Acoustic pulse geometry. (a) Plan view of the computational domain. (b) Representation of propagating acoustic pulse in cross-section along $x_2 = 0$. The extent of the flow domain shown in (b) is $-l/2 \leq x_1 \leq l/2$, $0 \leq x_2 \leq l/2$.

in Tam & Webb (1993). The analytical solution used in the present study is

$$p/\rho_\infty a_\infty^2 = 1.0 + \frac{0.01}{2\alpha_1} \int_0^\infty e^{-\frac{\xi^2}{4\alpha_1}} \cos(\xi t)\, J_0(\xi\eta)\, \xi d\xi \tag{4.3}$$

$$\rho/\rho_\infty = 1.0 + \frac{0.01}{2\alpha_1\gamma} \int_0^\infty e^{-\frac{\xi^2}{4\alpha_1}} \cos(\xi t)\, J_0(\xi\eta)\, \xi d\xi \tag{4.4}$$

$$u_1/a_\infty = \frac{2x_1/l}{2\alpha_1\eta} \int_0^\infty e^{-\frac{\xi^2}{4\alpha_1}} \sin(\xi t)\, J_1(\xi\eta)\, \xi d\xi \tag{4.5}$$

$$u_2/a_\infty = \frac{2x_2/l}{2\alpha_1\eta} \int_0^\infty e^{-\frac{\xi^2}{4\alpha_1}} \sin(\xi t)\, J_1(\xi\eta)\, \xi d\xi \tag{4.6}$$

where $\eta = \sqrt{\left[(200x_1/l)^2 + (200x_2/l)^2\right]}$. J_0 and J_1 are Bessel functions of zeroth order and first order respectively. α_1 is related to the half-width of the Gaussian pulse b_1 by the relationship, $\alpha_1 = \ln(2/b_1^2)$. A Gaussian pressure pulse half-width of $b_1 = 3.0$ is used in Tam & Webb (1993) and in the present study. $\gamma = 1.4$ is the specific heat ratio.

The present test case is based on, but differs from, problem 1 (Category 3) in the first CAA Workshop on benchmark problems by Tam & Webb (1993) in three main respects. Firstly, only the acoustic pulse is considered, specified at the centre of the computational domain. The entropy and vorticity pulses, present in Tam & Webb (1993), are therefore eliminated in the current test case. Secondly, no free stream velocity is specified. The initial Gaussian pulse is therefore specified in a quiescent fluid. Thirdly, no interaction of the acoustic pulse with the computational domain boundaries occurs. This prevents numerical wave reflections from complicating the prediction. The analytical solution given by Eqns. 4.3-4.6 is accordingly altered from the analytical solution given in Tam & Webb (1993).

A rectangular baseline (level 0) grid of 101×101 cells discretises the computational domain. A constant time step of $\Delta t = 3l/708a_\infty$ seconds is used to advance the flow prediction on the baseline grid. Two separate AMR models of the acoustic pulse test case are discussed in this section. Starting from the baseline (level 0) grid of

101×101 cells, one additional AMR level (level 1) is defined in the first model. This is compared in the second model with three AMR levels (levels 0, 1 and 2), from a 101×101 cells level 0 mesh. A refinement ratio of three is defined between successive AMR levels. Each level 0 cell is therefore divided into nine cells at level 1 and eighty-one cells at level 2. An odd number is chosen for the refinement ratio in order to resolve the Gaussian distribution peak at the computational domain centre on all refined levels.

In addition to the analytical solution, the prediction from each AMR model is compared against a benchmark non-refined prediction from a model of equivalent resolution to the most refined AMR level. The level 1 prediction is compared against a single mesh benchmark prediction with 303×303 cells. The time step used to develop this benchmark prediction is $\Delta t = 3l/2124a_\infty$ seconds. The second model level 2 prediction is compared against a non-refined benchmark prediction of 909×909 cells, developed in constant time steps of $\Delta t = 3l/6372a_\infty$ seconds.

4.3.2 Results & Discussion

A preliminary assessment of grid dependency in the benchmark numerical scheme is given in Figure 4.8. This shows a cross-section of the acoustic pulse density field, along $x_2 = 0$. The symmetry of the acoustic pulse about $x_1 = 0$ allows half of the acoustic pulse, between $x_1 = -l/2$ and $x_1 = 0$, to be omitted from these figures without loss of information. For reference, the analytical solution given by Eqns. 4.3-4.6 is also shown. A significant level of dissipation error is evident from the lower amplitude of the 101×101 prediction, with respect to the analytical solution. A significant level of dispersion error is also noted in the spatial location of the density field extrema. As the resolution of the grid is increased, the level of dissipation and dispersion decreases. Even with a 909×909 grid, however, amplitude and phase differences between the prediction and the analytical solution are still evident. Differences, between the analytical solution and the prediction, may always remain due to the use of the non-linear form of the Euler equations, Eqns. 3.10-3.12, in the current predictions. The dependency of the developing prediction on the local flow

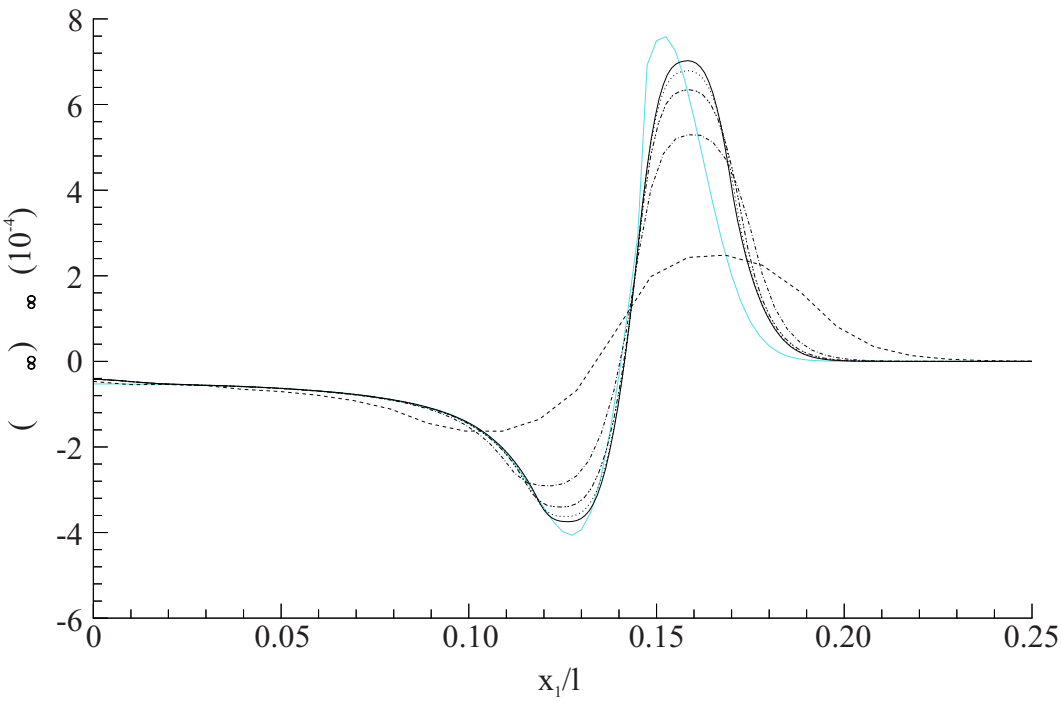

Figure 4.8: Acoustic pulse grid sensitivity comparison for the non-AMR baseline scheme. Cross-section of the acoustic pulse along $x_2 = 0$. (—) Analytical solution based on the linearised Euler equations. Predictions using (- - -) 101×101 cells, $(- \cdot -)$ 303×303 cells, $(\cdot \cdot -)$ 505×505 cells, $(\cdot \cdot \cdot)$ 707×707 cells, (—) 909×909 cells.

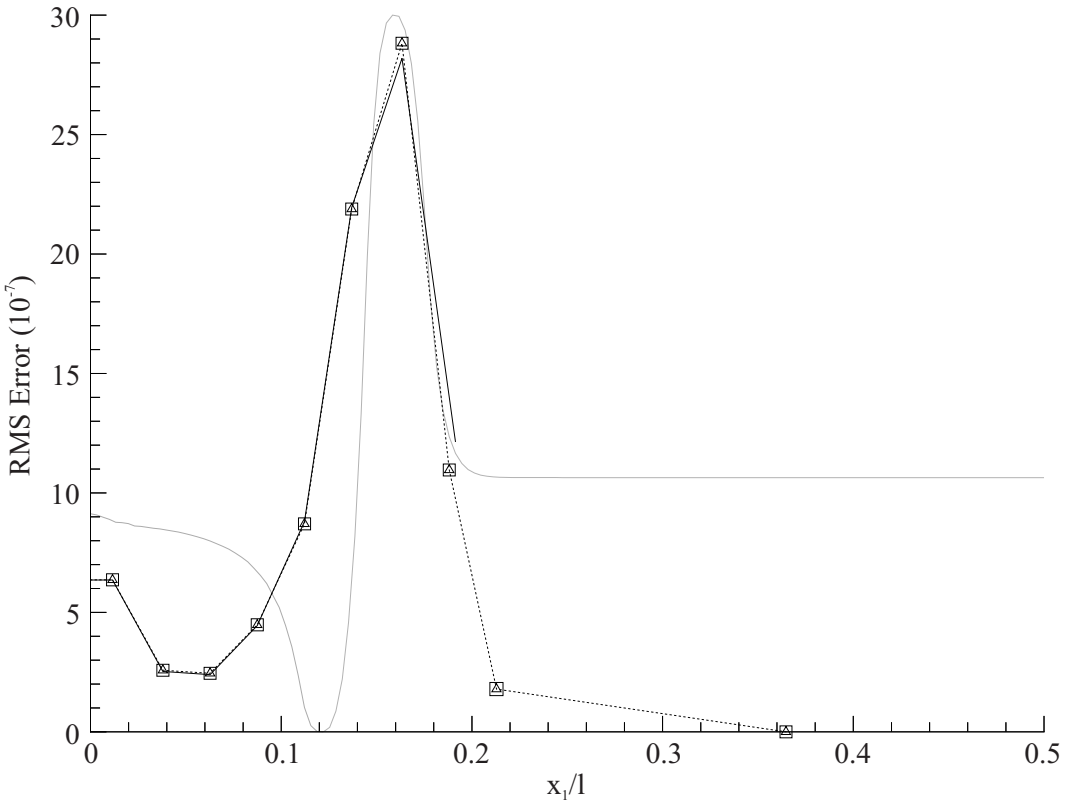

Figure 4.9: Root Mean Square (RMS) error profiles. (—) RMS error between an AMR level 1 prediction ($b = 0.05$) and a non-refined benchmark prediction. ($-\Box-$) RMS error between a non-adaptive ($b = 0$) AMR level 1 prediction and the benchmark prediction (identical alignment with $\triangle$ symbols). ($-\triangle-$) RMS error between the benchmark prediction and a non-AMR prediction with the initial $b = 0$ AMR flow field imposed at $t = 0$. (—) Representation of the density profile along $x_2 = 0$, used for RMS error placement.

velocity is not reflected in the analytical solution, which is based on the linearised Euler equations. These differences are, however, considered to be less than those indicated between the 909×909 case and the analytical solution, indicating a level of grid sensitivity remains. The AMR predictions in this section are therefore primarily compared against the non-refined benchmark predictions. As the refined AMR levels should maintain the accuracy of an equivalently resolved single level prediction, this remains a satisfactory term of comparison.

An AMR prediction of the acoustic pulse with 2 levels of refinement (levels 0 and 1), from a level 0 mesh of 101×101 cells, is compared with a non-refined prediction of 303×303 cells in Figure 4.9. The Root Mean Square (RMS) difference between the

adapted AMR level 1 prediction and the non-refined benchmark prediction, at $t = 30l/118a_\infty$, is represented by a solid black line. This extends over the range $-0.19l \leq x_1 \leq 0.19l$ as the AMR scheme refines only regions of significant density gradient. The remaining flow field is developed on the coarse level 0 grid. A diagrammatical representation of the density distribution along $x_2 = 0$ is shown as a solid gray line. This is defined for placement of the RMS error profiles along the acoustic pulse cross-section. RMS error maxima occur at the centre of the computational domain ($-0.01l \leq x_1 \leq 0.01l$) and at the density perturbation peak, $x_1 = \pm 0.163l$. As the peak RMS error in Figure 4.9 is several orders of magnitude greater than the current level of machine zero (10^{-16}), two further predictions are defined to source the origin of this error. The first, a two level AMR prediction (levels 0 and 1) with a global $b = 0$ refinement of level 1, is represented in Figure 4.9 by a dashed line with solid square symbols. The second, a non-AMR single level benchmark prediction with 303×303 cells, has the initial interpolated level 1 flow distribution imposed at the start of the computation. This is represented in Figure 4.9 by a dashed line with hollow triangular symbols. An exact overlap of these RMS error profiles occurs, indicating the source of the error as the initial interpolation of the level 1 flow field at $t = 0$.

The close match among all RMS errors in Figure 4.9 indicates that, although slight differences occur due to the refined grid adaption, these errors represent relatively minor sources of error. This secondary error is caused by the flow field interpolation from level 0 to level 1 in the newly refined regions around the outer edges of the acoustic pulse.

The primary source of error in the AMR prediction, the initial flow field interpolation at level 1, is analysed using the initial Gaussian distribution along $x_2 = 0$ at $t = 0$. This is given in Figure 4.10. The initial Gaussian distribution is interpolated at level 1 from the baseline (level 0) grid using a two-dimensional interpolation algorithm, with a second order formal accuracy. The level 1 density distribution along $x_2 = 0$ is defined in Figure 4.10 by a solid line with square symbols. A non-refined reference distribution with 303×303 cells, initialised by the analytical Gaussian dis-

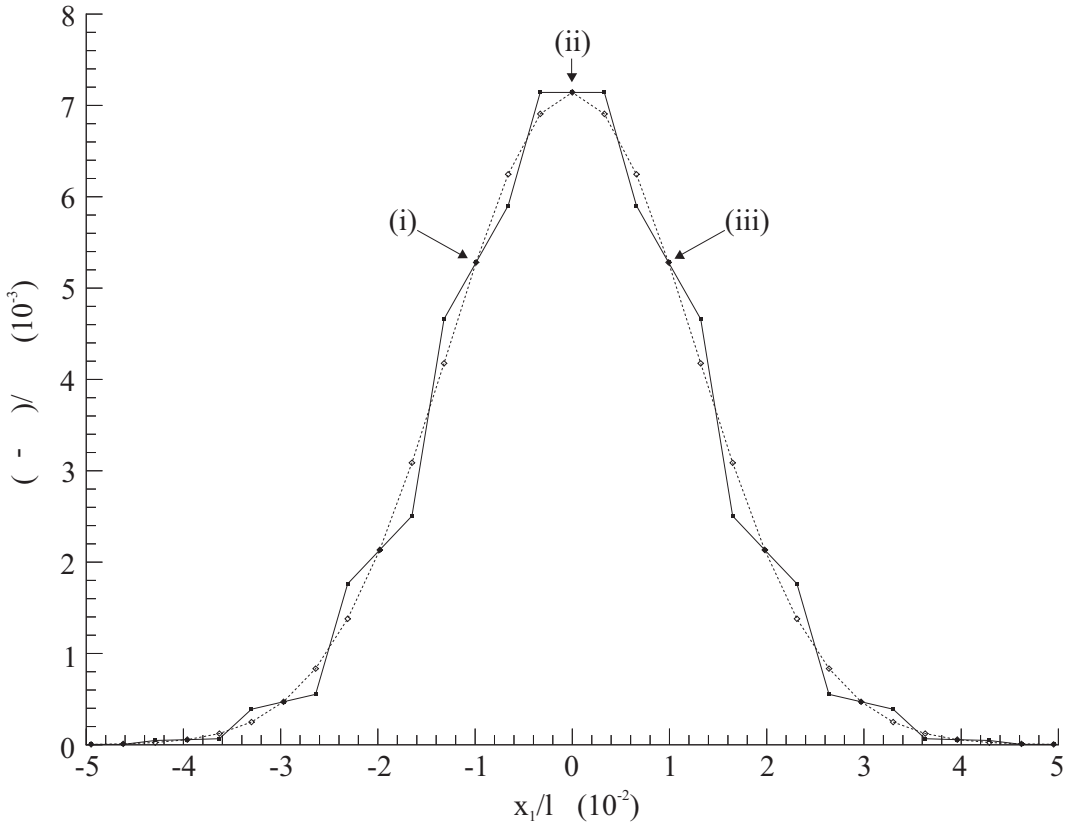

Figure 4.10: Comparison between the AMR and the non-AMR initial Gaussian distribution. Density field cross-section at $x_2 = 0$ $(t = 0)$. $(-\Box-)$ Initial AMR density distribution at level 1, interpolated from the level 0 (101×101) density field. $(-\diamond-)$ Non-refined 303×303 density field cross-section.

tribution of Eqns. 4.1-4.2, is represented by a dashed line with hollow diamond shape symbols. Each symbol along the density distributions in Figure 4.10 represents the density in one computational cell. The symbols on level 1 of the interpolated AMR prediction form groups of three across the Gaussian pulse. Each group of three symbols represents the refinement of a coarse level 0 cell. The centre symbol in each group of three is observed to precisely overlap a symbol on the non-refined benchmark prediction, for example at (i), (ii) and (iii) in Figure 4.10. This overlap occurs as a result of the interpolation procedure. The interpolation procedure defines a flow field gradient across each coarse cell. Fine cells that overlie the centre of the coarse cell are initialised with a direct copy of the coarse cell conservative variables vector. These cells are therefore indirectly initialised using the analytical Gaussian distribution of Eqns. 4.1 and 4.2. The variable state gradient in each coarse cell is limited using the minmod flux limiter described in Section 3.5.8. This flux limiting stage is an essential stage in the interpolation procedure, in order to maintain the monotonicity of the level 0 flow field at all refined levels. The application of the minmod flux limiter, however, results in a departure of the interpolated level 1 flow field from the initial reference flow field, as observed in Figure 4.10. The influence of the minmod limiter is further evident at $x_1 = 0$, where it results in a zero gradient interpolation at (ii). This zero density gradient replaces the density gradients, with opposing sign, defined between (i) and (ii) and between (iii) and (ii) in the level 0 profile.

The shape of the error waveform, defined by subtracting one density profile in Figure 4.10 from the other, is a wave centred at zero with alternate positive and negative peaks. A Fourier analysis of this short wavelength 'sawtooth' type waveform yields the wavenumber distribution in Figure 4.11. The short wavelength 'sawtooth' waveform has a wavenumber distribution dominated by high wavenumber contributions. Two dominant peaks are evident in Figure 4.11, at $k^*\Delta x_1 = 0.597\pi$ and $k^*\Delta x_1 = 0.748\pi$. A small, low wavenumber peak is also located at $k^*\Delta x_1 = 0.203\pi$. The amplitude of this peak is however less than 1% of the amplitude of the two high wavenumber peaks. Relating this wavenumber distribution to the dispersion

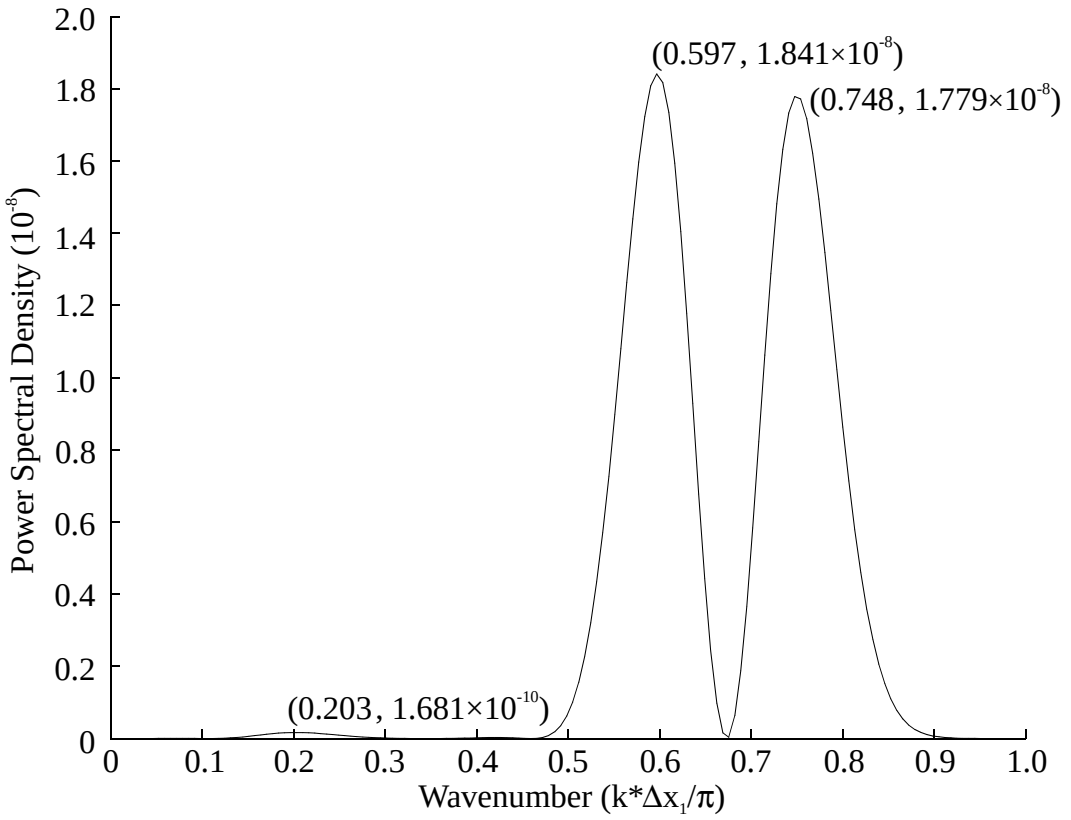

Figure 4.11: Wavenumber distribution of the difference in the initial density profile, along $x_2 = 0$, between an AMR level 1 prediction and an equivalent non-AMR benchmark prediction with 303×303 cells.

characteristics of the second order asymmetric stencil method used in this study highlights the transport characteristics of the numerical error. The group velocity for dispersive waves in the current numerical method will be zero at some wavenumber close to $k^*\Delta x_1 = \pi/2$. This provides a possible explanation for the RMS error peak observed in Figure 4.9 at $-0.01l \leq x_1 \leq 0.01l$. The high proportion of high wavenumber error indicates that the majority of the initial interpolation error may travel with a range of negative velocities, i.e. in a direction opposing the acoustic pulse propagation direction. The broad-band spread observed at high wavenumbers explains the large spatial spread in the RMS error profile of Figure 4.9.

To confirm the initial interpolation error as the primary cause of the RMS error in Figure 4.9 and to assess the error transport characteristics, the interpolation error is time marched in isolation to the acoustic pulse on a non-refined 303×303 grid. The resulting error at $t = 30l/118a_\infty$ seconds is shown in cross-section along $x_2 = 0$ in Figure 4.12. This is represented in Figure 4.12 using a solid black line with square shaped symbols. The RMS error profile for the non-adapted level 1 prediction, previously shown in Figure 4.9, is repeated for reference. The similarity of the two profiles is strong. The RMS peak at the centre, caused by the stationary wave component, and the peak around $x_1 = \pm 0.163l$ are common to both RMS error profiles. These results confirm the initial interpolation error as the major source of additional error in the AMR prediction, and substantiate the dispersion characteristics previously described. Differences between the two predictions in Figure 4.12 are expected as the interpolation error travels as a superposition of the acoustic pulse in the former prediction.

The application of the minmod flux limiter in the interpolation procedure as a source of error in the AMR method has not, to the authors knowledge, been previously documented in the available published literature. The analysis in this section therefore represents an original contribution to the future development of AMR methods of the present type. Potential remedies to the problems highlighted in this section, through low-pass filtering of the interpolated initial solution, are complicated by the presence of additional low wavenumber components

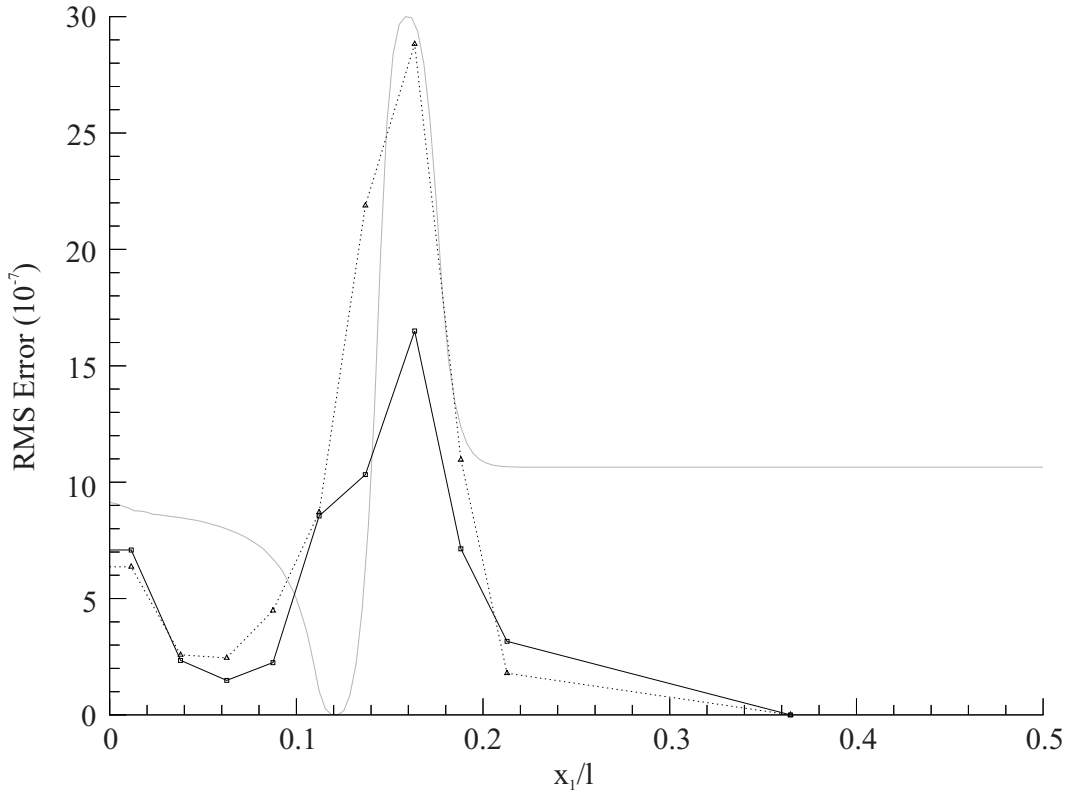

Figure 4.12: Comparison of the RMS error at $t = 30l/118a_\infty$ seconds, between the isolated initial error distribution and a globally refined level 1 AMR prediction, along $x_2 = 0$. (—) Representation of the density profile along $x_2 = 0$, used for RMS error placement. $(-\square-)$ RMS error of the time evolved AMR level 1 interpolation error distribution, developed in isolation to the acoustic pulse. $(-\triangle-)$ RMS error in the non-adaptive, globally refined AMR level 1 prediction ($b = 0$).

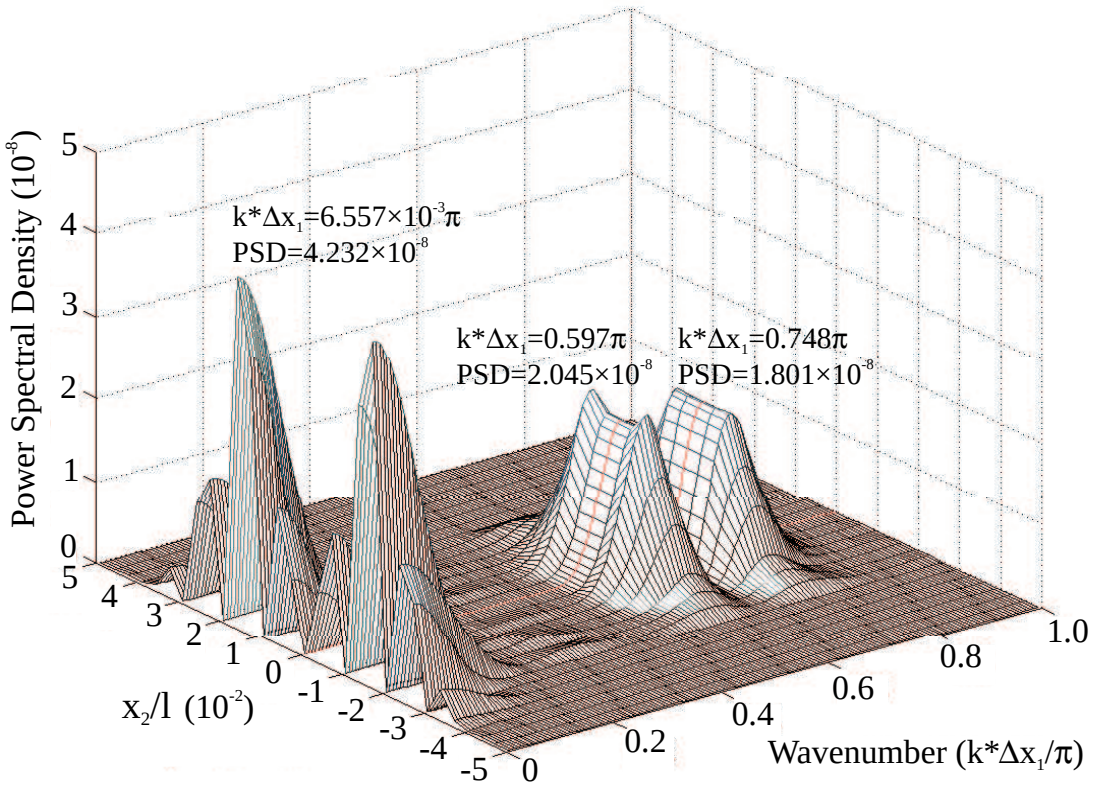

Figure 4.13: Wavenumber distribution of the difference in the initial density profile, along constant lines of x_2 in the range $-0.05l \leq x_2 \leq 0.05$l, between an AMR level 1 prediction and an equivalent non-AMR prediction with 303×303 cells. (—) Wavenumber distribution along $x_2 = 0$, highlighted for reference with Figure. 4.11

in the two-dimensional Gaussian pulse error distribution. These low wavenumber components are evident by collectively plotting the wavenumber distributions of the initial interpolation error, along cell rows of constant x_2, over the initial distribution. This is given in Figure 4.13, which is a plot of the Power spectral Density (PSD) against wavenumber along each cell row in the range $-0.05l \leq x_2 \leq 0.05l$. For reference with Figure 4.11, the wavenumber distribution of the interpolation error at $x_2 = 0$ is highlighted by a red line. The red line shows the two high wavenumber peaks, at $k^*\Delta x_1 = 0.597\pi$ and $k^*\Delta x_1 = 0.748\pi$, identified in Figure 4.11. These high wavenumber peaks extend in the x_2 direction, covering the range $-2.67 \times 10^{-2}l \leq x_2 \leq 2.67 \times 10^{-2}l$. Each line parallel to the wavenumber axis represents a row of cells with constant x_2. Additional low wavenumber peaks

are defined at $x_2 = \pm 6.67 \times 10^{-3} l$, $x_2 = \pm 1.67 \times 10^{-2} l$, $x_2 = \pm 2.33 \times 10^{-2} l$ and $x_2 = \pm 3.33 \times 10^{-2} l$. No significant low wavenumber contribution is evident at $x_2 = 0$, $x_2 = \pm 1.0 \times 10^{-2} l$, $x_2 = \pm 2.0 \times 10^{-2} l$ and $x_2 = \pm 3.0 \times 10^{-2} l$.

The low wavenumber distribution may be explained by analysing the difference in density between the interpolated level 1 distribution and the equivalent non-refined distribution, over the interval $6.67 \times 10^{-3} l \leq x_2 \leq 1.33 \times 10^{-2} l$. This is given in Figure 4.14. The three density profiles refer to three adjacent rows of computational cells, whose combined x_2 extent cover one level 0 row of cells. The centre of this level 0 cell row lies at $x_2 = 1.0 \times 10^{-2} l$. The fine level 1 density profile at this x_2 location is shown in Figure 4.14(b). Figures 4.14(a,c) therefore represent level 1 cells which lie off-centre in the x_2 direction, with respect to the underlying level 0 cell centreline. The density profile in Figure 4.14(b), which crosses the underlying cell centres, has a similar profile to Figure 4.10. The square symbols, which each represent one level 1 cell in the x_1 direction, are grouped into three. The centre symbol overlies the non-refined benchmark prediction. The two outer symbols in each group of three symbols have a density magnitude respectively greater than, and less than the non-refined benchmark profile. The difference in density between the two profiles in Figure 4.14(b) produces the familiar short wavelength 'sawtooth' type error waveform. This waveform leads to a similar wavenumber spectrum as Figure 4.11, which is dominated by high wavenumber contributions. The interpolated density profiles in Figures 4.14(a,c), however, lack the same overlap in density with the non-refined profile evident in Figure 4.14(b) at the centre of each group of three symbols. The resulting difference in density, between the level 1 prediction and the non-refined benchmark prediction, produces a waveform with larger amplitude peaks and a greater proportion of low wavenumber components. This explains the repeating pattern in Figure 4.13, of a negligible low wavenumber contribution in every third row of cells (with constant x_2) interleaved by two rows with significant low wavenumber contributions.

The interpolation error is compounded as the number of refined levels increase. In a further test case, an additional level of refinement is added. Three levels of AMR

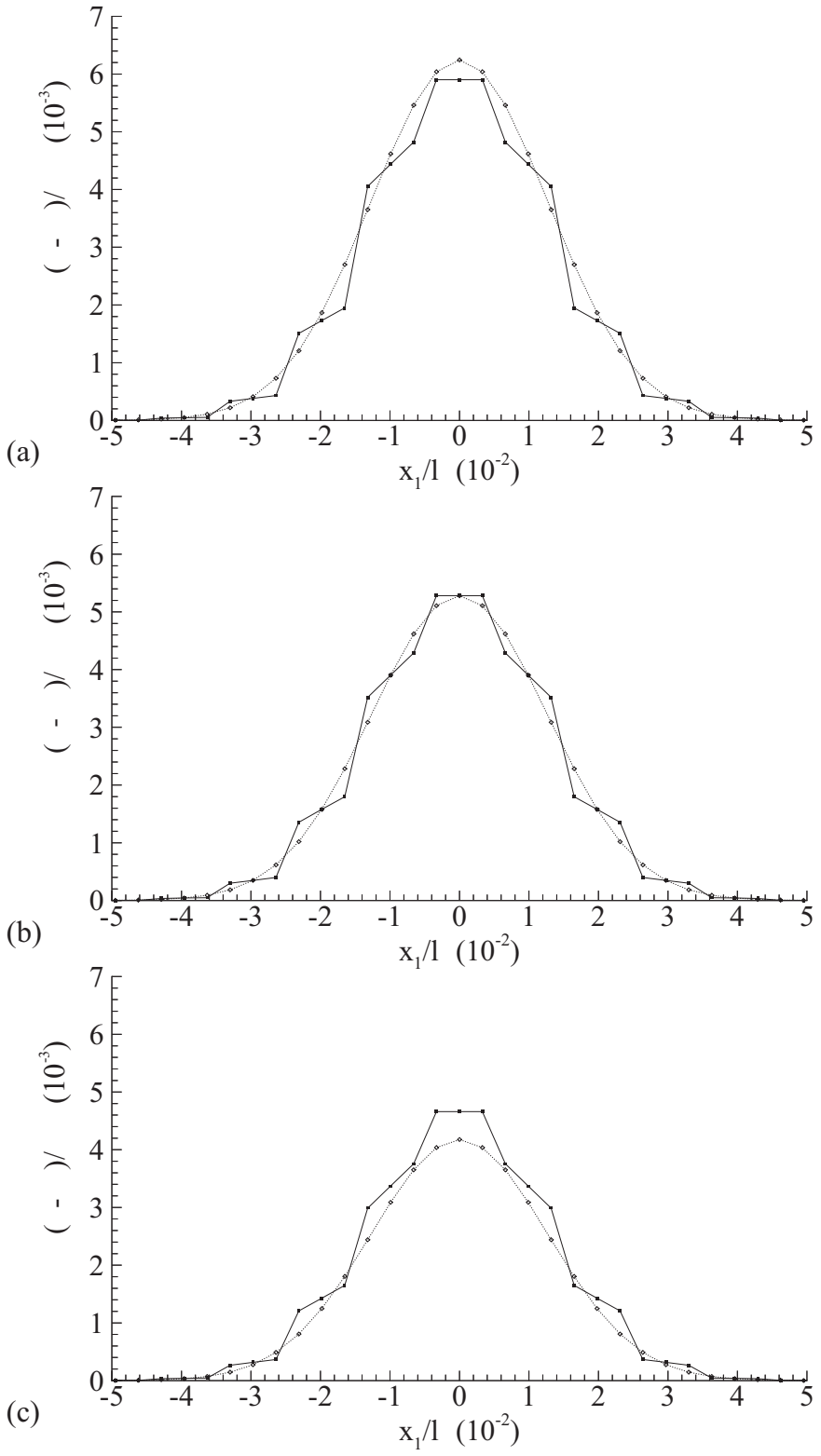

Figure 4.14: Comparison between the AMR and non-AMR initial Gaussian distribution ($t = 0$). $(-\square-)$ Initial AMR density distribution at level 1, interpolated from the level 0 (101×101) density field. $(-\diamond-)$ Non-AMR 303×303 benchmark prediction. (a) Density field cross-section at $x_2 = 6.67 \times 10^{-3} l$. (b) Density field cross-section at $x_2 = 1.0 \times 10^{-2} l$. (c) Density field cross section at $x_2 = 1.33 \times 10^{-2} l$.

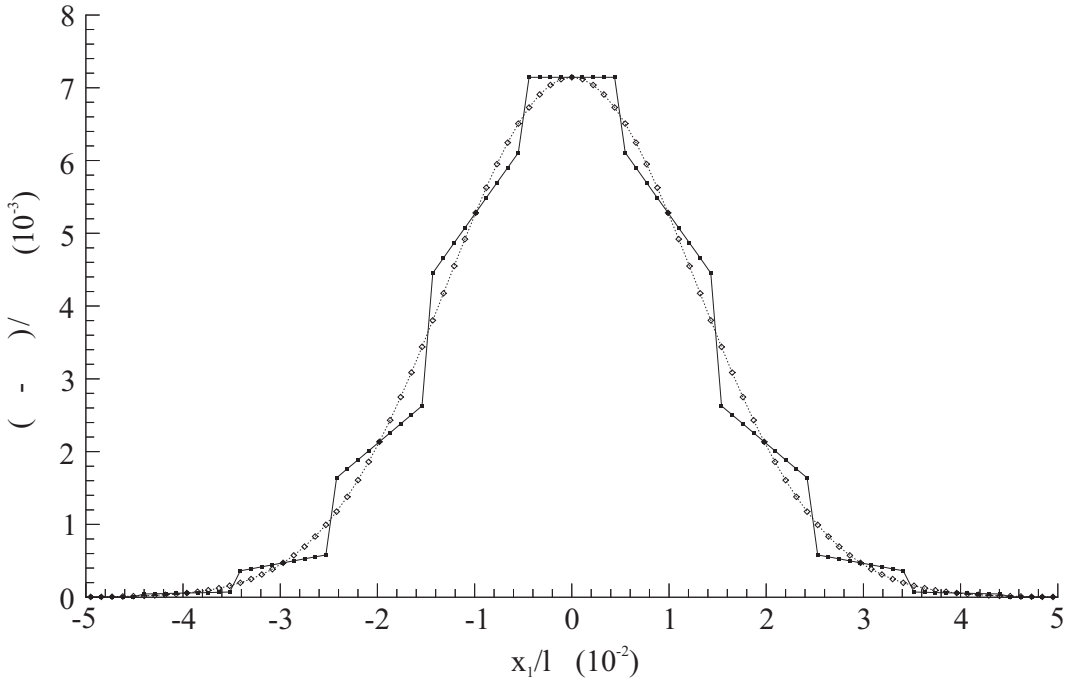

Figure 4.15: Comparison between the AMR and the non-AMR initial Gaussian distribution. Density field cross-section at $x_2 = 0$ $(t = 0)$. $(-\Box-)$ Initial AMR density distribution at level 2, interpolated from the level 1 (303×303) density field. $(-\diamond-)$ Non-refined 909×909 benchmark prediction.

refinement (levels 0, 1 and 2) are defined from a level 0 grid of 101×101 cells. The most refined level (level 2) has an equivalent spatial resolution to a non-refined grid of 909×909 cells. A comparison of the initial density cross-section at $x_2 = 0$, between the AMR level 2 prediction and the non-refined benchmark prediction, is given in Figure 4.15. The level 2 flow field is initialised through interpolation of the level 1 flow field, given in Figure 4.10. Each symbol represents the density in a single cell along $x_2 = 0$. The interpolated level 2 profile is similar in form to the level 1 profile of Figure 4.10. The minmod limiting stage is responsible for producing the lines of constant gradient in the level 1 interpolation. Interpolation from the level 1 flow field to level 2 simply follows the lines of constant gradient at level 1. An associated increase occurs in the number of level 2 cells that lie between points of overlap with the non-refined predictions. In the level 1 prediction, two cells lie between points of overlap. At level 2, this is increased to eight cells. A Fourier analysis on the difference in density between the two profiles demonstrates an associated increase in the low

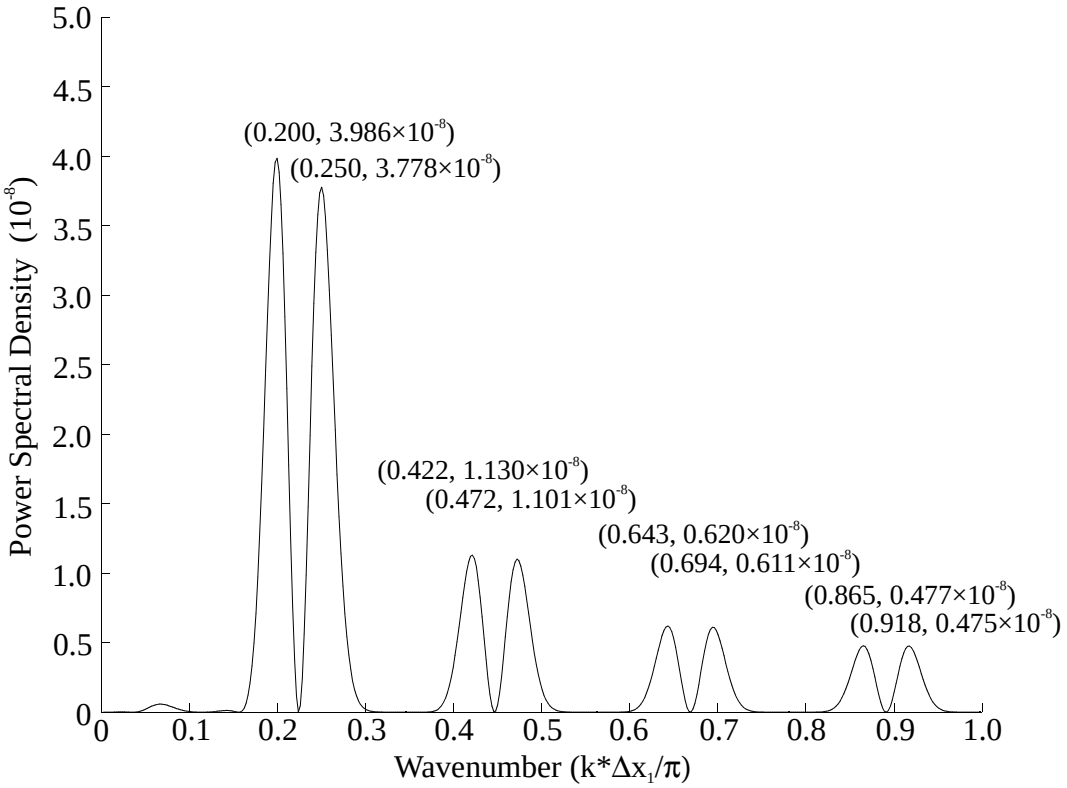

Figure 4.16: Wavenumber distribution of the difference in the initial density profile, along $x_2 = 0$, between an AMR level 2 prediction and an equivalent non-AMR prediction with 909×909 cells.

wavenumber contributions, as shown in Figure 4.16. A repeating pattern of double peaks, spread over a large range of wavenumbers, characterises this wavenumber distribution. The largest amplitude peaks in Figure 4.16 are now associated with wavenumbers below $k^*\Delta x_1 = 0.3\pi$. Specifically, $k^*\Delta x_1 = 0.2\pi$ and $k^*\Delta x_1 = 0.25\pi$. The maximum wavenumber contribution between $k^*\Delta x_1 = 0.5\pi$ and $k^*\Delta x_1 = 0.9\pi$, which represents the region of dominant contribution in Figure 4.11, is less than 15.6% of the Power Spectral Density at $k^*\Delta x_1 = 0.2\pi$ in Figure 4.16. This further complicates any potential remedies through low-pass filtering. The trend towards a greater spread in wavenumber, and an increased amplitude, of the interpolation error as further levels of refinement are added is expected to continue for additional levels of refinement, i.e. for four and five levels of AMR refinement.

The inclusion of the minmod limiting stage in the interpolation procedure reduces the AMR prediction accuracy to below machine accuracy (10^{-16}), with respect to

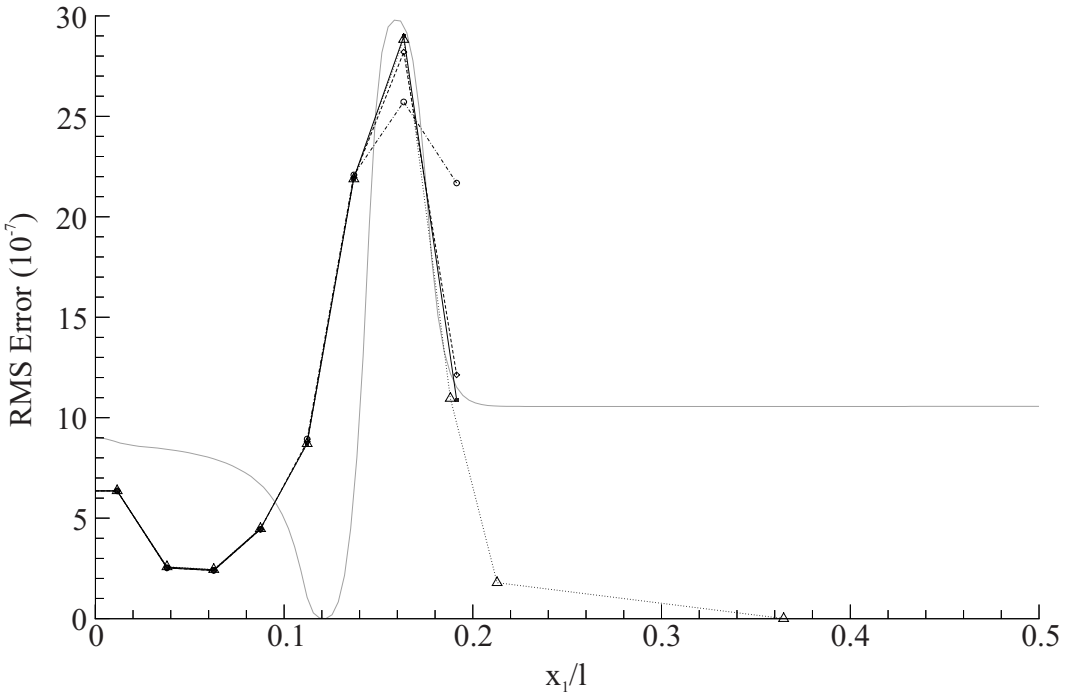

Figure 4.17: Root Mean Square (RMS) difference between three AMR predictions and a non-AMR, single level prediction of equivalent spatial and temporal resolution to level 1. Comparison of the AMR scaling parameter, b. (—) Representation of density profile along $x_2 = 0$, used for RMS error placement. ($-\triangle-$) RMS error in a non-adaptive AMR level 1 prediction, along $x_2 = 0$, $b = 0$. ($-\square-$) RMS error in an AMR level 1 prediction along $x_2 = 0$, $b = 0.02$. ($-\diamond-$) RMS error in an AMR level 1 prediction along $x_2 = 0$, $b = 0.05$. ($-\circ-$) RMS error in an AMR level 1 prediction along $x_2 = 0$, $b = 0.10$.

an equivalent single level prediction. The current interpolation procedure does, however, preserve the conservation and monotonicity of the baseline level 0 flow field at all refined levels.

The influence of the AMR scaling parameter, b, on the transported interpolation error is quantified in Figure 4.17. The level 1 density field from four separate AMR predictions are compared with a non-AMR benchmark prediction with 303×303 cells. The AMR scaling parameter is incrementally increased between the first three predictions, from $b = 0.02$ to $b = 0.10$. In addition, the non-adapted AMR prediction ($b = 0$) shown in Figure 4.9 is repeated for reference. Also given is a spatial representation of the acoustic pulse density perturbation, to discuss the RMS error in the context of the time accurate acoustic pulse. Recall that the flow is symmetric

about $x_1 = 0$. All predictions show a common level of RMS error, within a spread of 1%, over the range $-0.137l \leq x_1 \leq 0.137l$. Between $x_1 = \pm 0.137l$ and the edge of the refined region, a deviation of the adaptively refined AMR predictions from the non-adaptively refined AMR prediction is observed, which increases with the AMR scaling parameter b. The RMS error in the adaptively refined AMR predictions, with $b = 0.02$ and $b = 0.05$, continue to follow the general alignment of the non-adaptive ($b = 0$) AMR prediction. The adaptively refined prediction, with $b = 0.02$ remains within 12% of the non-adaptive reference prediction, over the extent of level 1. As the AMR scaling parameter is increased to $b = 0.05$, a larger deviation is noted. Specifically, the adaptively refined AMR prediction remains within 25% of the non-adaptive AMR prediction throughout the extent of level 1. The deterioration in the adaptive AMR prediction increases significantly between $b = 0.05$ and $b = 0.10$, as the outer edge of level 1 falls into regions of higher density gradient. Further increases in the AMR scaling parameter results in a level 1 grid defined as a 'ring' covering only the large gradient density perturbation. As with the shock tube test case, a comprise is therefore sought in the choice of the AMR scaling parameter, between maintaining a satisfactory level of accuracy and reducing the computational effort.

4.4 Turbulent Boundary Layer - Zero Pressure Gradient

4.4.1 Test Case Description

The third AMR test case documented in this chapter is the development of a turbulent compressible boundary layer under a zero stream-wise pressure gradient. This test case is used to verify the AMR method, applied to the short-time averaged Navier-Stokes equations with the $k - \omega$ turbulence model. This test case models the turbulent $M_\infty = 2.5$ boundary layer development under a zero pressure gradient in Mabey & Sawyer (1976). Boundary layer profile measurements are tabulated in Mabey & Sawyer (1976) at a number of stream-wise locations, downstream of the leading edge. For the purposes of the present test case, two stream-wise locations

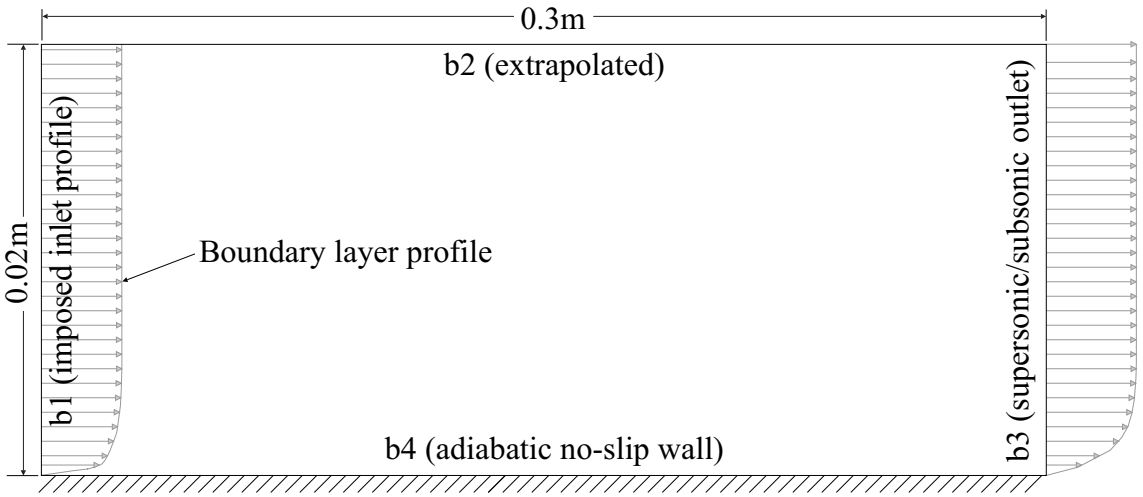

Figure 4.18: Turbulent boundary layer computational domain.

are considered. These locations are $x_1 = 0.368m$ (profile 43) and $x_1 = 0.623m$ (profile 58) from the leading edge. An estimation of the boundary layer profile at $x_1 = 0.368m$ is imposed at the computational domain inlet boundary. The boundary layer develops from this profile over a distance of $\Delta x_1 = 0.255m$ in the stream-wise direction. The predicted boundary layer profile at $x_1 = 0.623m$ is then compared against the measured profile, of corresponding stream-wise location, in Mabey & Sawyer (1976).

A diagrammatical representation of the computational domain is shown in Figure 4.18. The computational domain extends $0.3m$ in the stream-wise direction and $0.02m$ in the cross-stream direction. The inlet profile imposed at $b1$ is estimated in a separate computation, in which a turbulent boundary layer is developed from a laminar Blasius profile using the 'numerical roughness strip' method described in Wilcox (2002). This method involves locally specifying a surface value for ω in order to simulate a rough wall condition over a predefined stream-wise surface length. In the current prediction, the roughness height specified is based on the height of the 'ballotini' used by Mabey & Sawyer (1976) to fix the boundary layer transition location in the experiment. A detailed introduction to using the numerical roughness strip method to develop a numerical turbulent boundary layer profile is given in Wilcox (2002). The resulting boundary layer profile at $x_1 = 0.368m$ from the

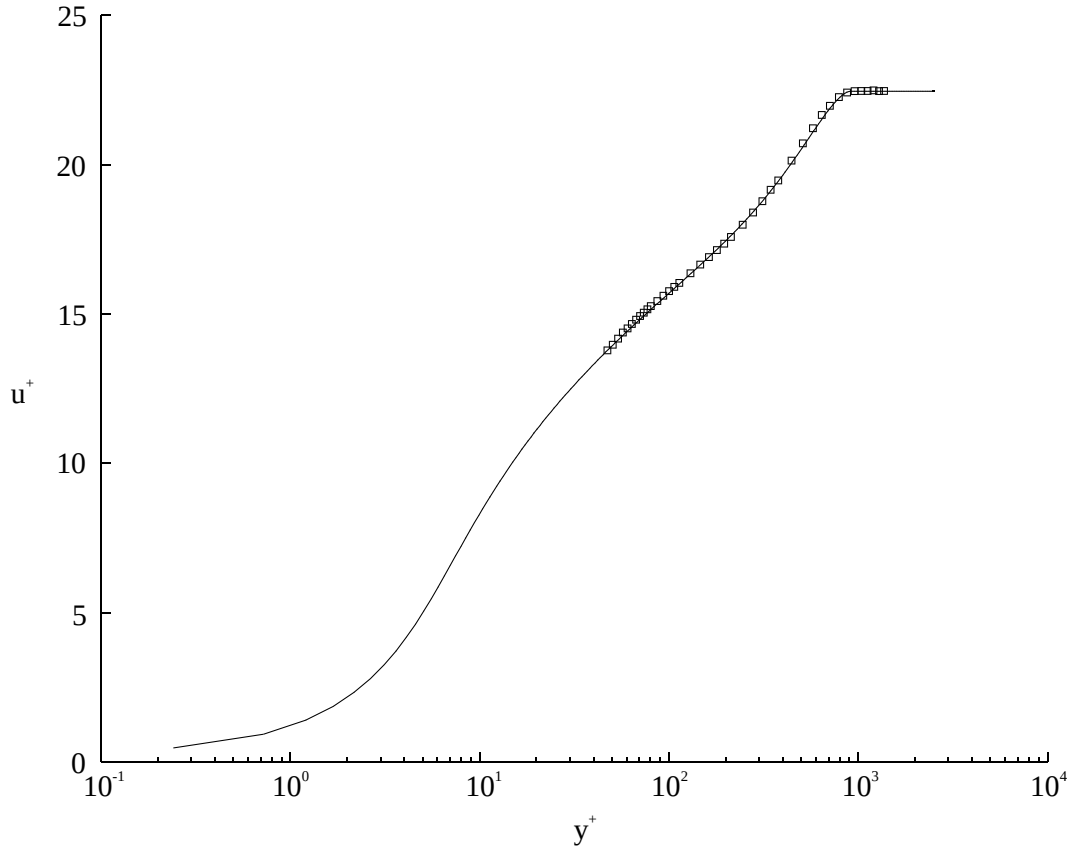

Figure 4.19: Comparison of the predicted boundary layer profile at $0.368m$, against profile 43 from Mabey & Sawyer (1976). (—) Numerical prediction. □ Measurements of Mabey & Sawyer (1976).

leading edge is compared against the measurements of Mabey & Sawyer (1976) in Figure 4.19. A good overall estimation of the boundary layer is observed. The integral parameters from the measured and predicted boundary layer profiles, at a stream-wise location of $x_1 = 0.368m$ from the leading edge, are compared in Table 4.3. A satisfactory overall agreement of the integral parameters from the current prediction and the measurements of Mabey & Sawyer (1976) is observed. Specifically, the predicted parameters fall within 2.6% of the measured values.

For reference, the dimensionless specific turbulence kinetic energy k profile at $x_1 = 0.368m$ is given in Figure 4.20. k, in Figure 4.20, is normalised using the square of the free stream velocity $u_{1\infty}$. The predicted specific turbulence kinetic energy dissipation rate ω profile at $x_1 = 0.368m$ is given in Figure 4.21. ω, in Figure 4.21, is normalised using the flat plate total length $L = 1.6m$ and the free

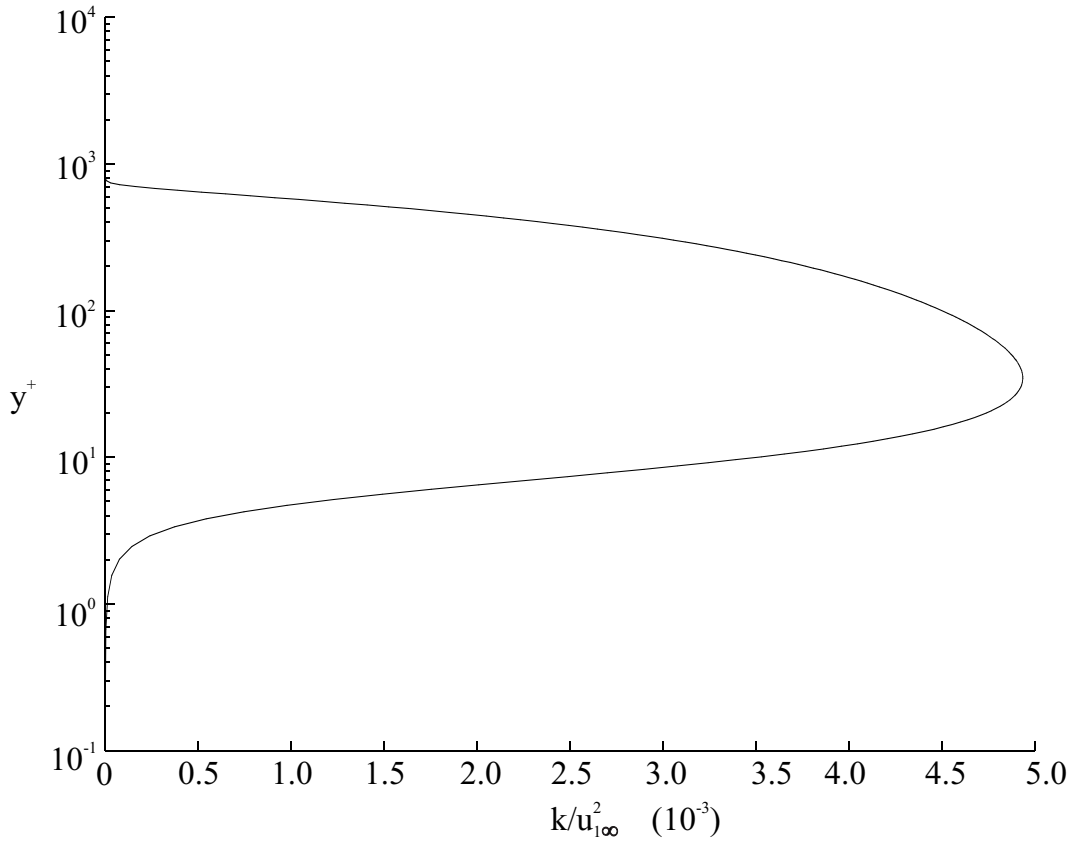

Figure 4.20: Dimensionless specific turbulence kinetic energy k prediction at $x_1 = 0.368m$ (profile 43 in Mabey & Sawyer (1976)). k is normalised using the free stream velocity $u_{1\infty}$.

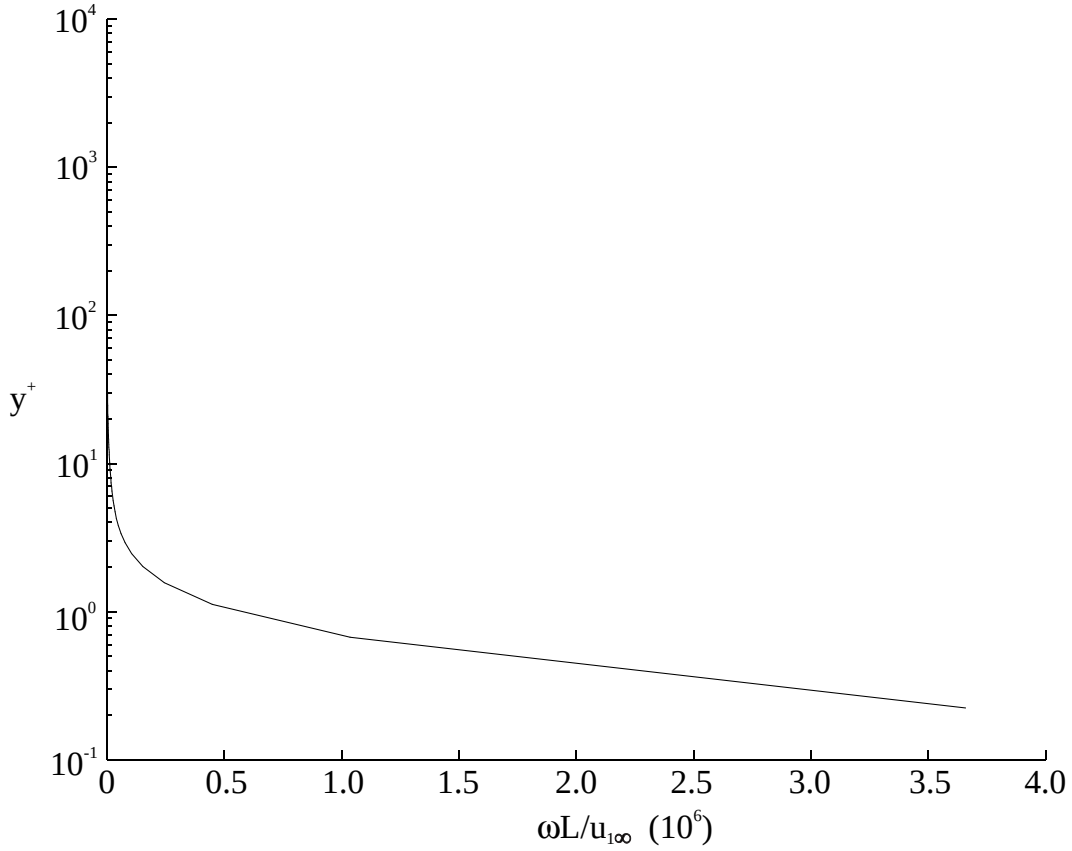

Figure 4.21: Specific turbulence kinetic energy dissipation rate ω prediction at $x_1 = 0.368m$ (profile 43 in Mabey & Sawyer (1976)). ω is normalised using the flat plate length $L = 1.6m$, and the free stream velocity $u_{1\infty}$.

Result	$\delta_1\ (m)$	$\delta_2\ (m)$	Re_{δ_2}
Mabey & Sawyer (1976)	1.96×10^{-3}	5.0×10^{-4}	5.97×10^{3}
Prediction	2.01×10^{-3}	4.97×10^{-4}	5.92×10^{3}

Table 4.3: Integral parameters comparing the measurements of Mabey & Sawyer (1976) against the current prediction at $0.368m$ from the leading edge (profile 43 in Mabey & Sawyer (1976)). δ_1 Boundary layer displacement thickness, δ_2 momentum thickness, Re_{δ_2} Reynolds number based on the momentum thickness.

stream velocity $u_{1\infty}$. The flat plate length L is given by Mabey & Sawyer (1976).

An extrapolated boundary condition is applied at the upper boundary $b2$, as shown in Figure 4.18. This boundary is defined within a region of uniform cross-stream flow, above the boundary layer edge. A composite subsonic/supersonic outlet is defined at the downstream boundary $b3$. The local Mach number of the flow is estimated from each internal cell neighbouring the outlet boundary $b3$. External cells along $b3$ that are on a stream-wise alignment with internal cells of supersonic flow are updated based on the supersonic outlet boundary condition, detailed in Section 3.9.4. External cells that are on a stream-wise alignment with internal subsonic flow cells are updated using the subsonic outlet boundary procedure detailed in Section 3.9.3. The no-slip wall condition detailed in Section 3.9.8 is defined at $b4$.

The computational domain is discretised using a benchmark grid of 36×198 cells in the x_1 and x_2 directions respectively. A further row of ghost cells is defined around the perimeter of the computational domain to impose the boundary conditions. This grid resolution is used to compare the most refined level of each subsequent AMR prediction. Linear grid stretching is applied normal to the surface to achieve a y^+ value of $y^+ = 0.25$ at the first cell. The first AMR prediction is a two levels AMR prediction (levels 0 and 1). This prediction uses a level 0 grid of 12×66 cells in the x_1 and x_2 directions respectively. An increase in spatial and temporal resolution of three is defined between each successive AMR level. The level 1 grid therefore comprises of 36×198 internal cells and is compared directly against the non-AMR prediction with an equivalent resolution. The second AMR prediction is defined over three AMR levels (levels 0, 1 and 2). The level 0 computational domain is

discretised by 4×22 internal cells. Level 1 comprises an equivalent resolution to a single mesh of 12×66 cells. Level 2 therefore comprises an equivalent resolution to a single mesh of 36×198 internal cells. A constant time step of $\Delta t = 6 \times 10^{-8}$ seconds is defined at the most refined level in each AMR prediction, as well as in the single level benchmark prediction. The time step is decreased by a factor three for the 12×66 cell grid and by a factor of nine at the 4×22 cell grid. The flow field is time marched to a final time of $t = 0.12$ seconds. This time is based on a convergence of the prediction to an $\mathcal{L}_2$ norm value of $\mathcal{L}_2 = 6.3 \times 10^{-5}$. The $\mathcal{L}_2$ norm value is defined as:

$$\mathcal{L}_2 = \sqrt{\frac{\sum_{i=1}^{(i)_{\max}} \sum_{j=1}^{(j)_{\max}} \left[\mathcal{R}\left(\rho\right)_{i,j}^2 \right]}{(i)_{\max} (j)_{\max}}}, \tag{4.7}$$

where, $(i)_{\max}$ and $(j)_{\max}$ are the maximum number of cells in the i and j directions respectively. $\mathcal{R}\left(\rho\right)_{i,j}$ is the mass flux residual for cell (i, j).

4.4.2 Results & Discussion

The predicted boundary layer benchmark profile at $x_1 = 0.623m$ from the flat plate leading edge is compared against the measurements of Mabey & Sawyer (1976) in Figure 4.22. A reasonable overlap with the measured profile is shown in Figure 4.22. A slight divergence of the two profiles is shown in the range $100 \leq y^+ \leq 1000$. The stream-wise velocity and the static density profiles at $x_1 = 0.623m$, from the single level benchmark prediction, are shown in Figures 4.23 and 4.24 respectively. A reasonable approximation to the measured profile of Mabey & Sawyer (1976) is again observed throughout the boundary layer. The integral parameters from the prediction and measurements are compared in Table 4.4. These integral parameters from the prediction demonstrate a reasonable agreement with the measured values, remaining within 6% of the measurements of Mabey & Sawyer (1976).

For reference with Figure 4.20, the dimensionless specific turbulence kinetic energy k profile at $x_1 = 0.623m$, profile 58 in Mabey & Sawyer (1976), is given in Figure 4.25. k, in Figure 4.25, is normalised using the square of the free stream

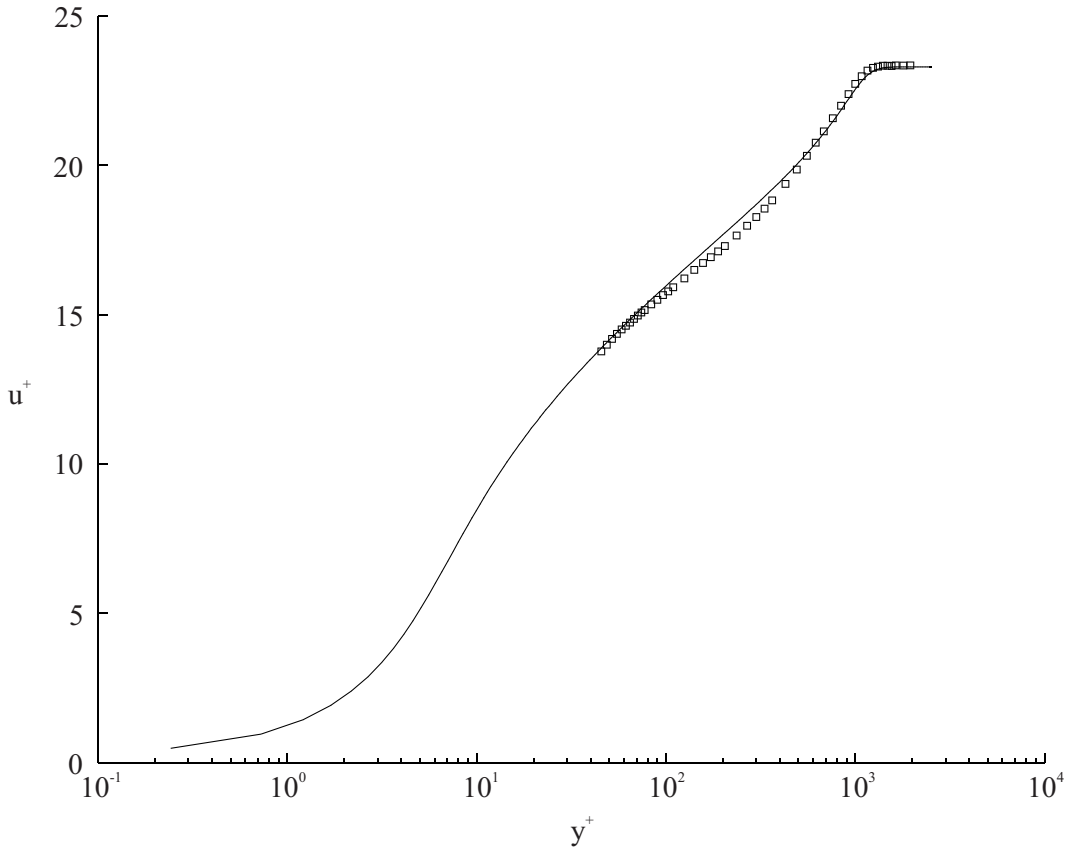

Figure 4.22: Comparison of the predicted boundary layer profile at $0.623m$, against profile 58 from Mabey & Sawyer (1976). (—) Numerical prediction. □ Measurements from Mabey & Sawyer (1976).

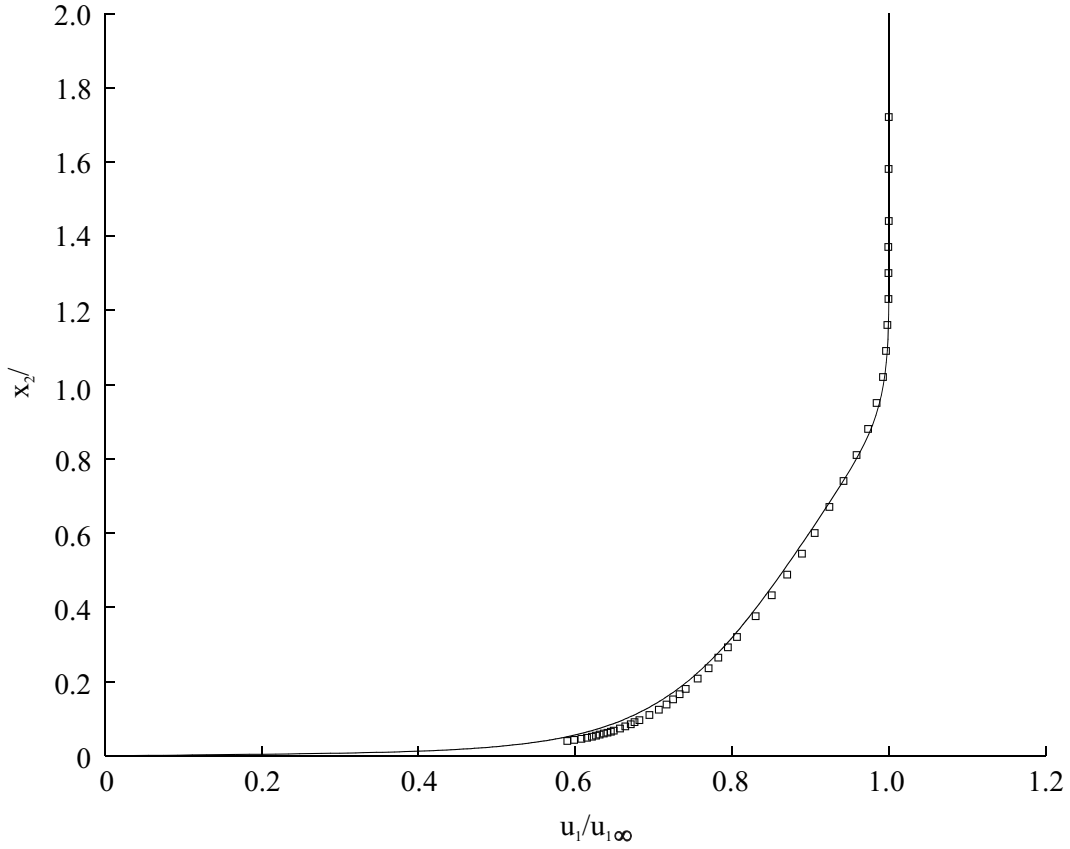

Figure 4.23: Stream-wise velocity profile normalised by the free stream velocity $u_{1\infty}$. x_2, surface normal distance. δ_{99} surface normal distance to 99% of the free stream velocity. □ Measurements from Mabey & Sawyer (1976), profile 58.

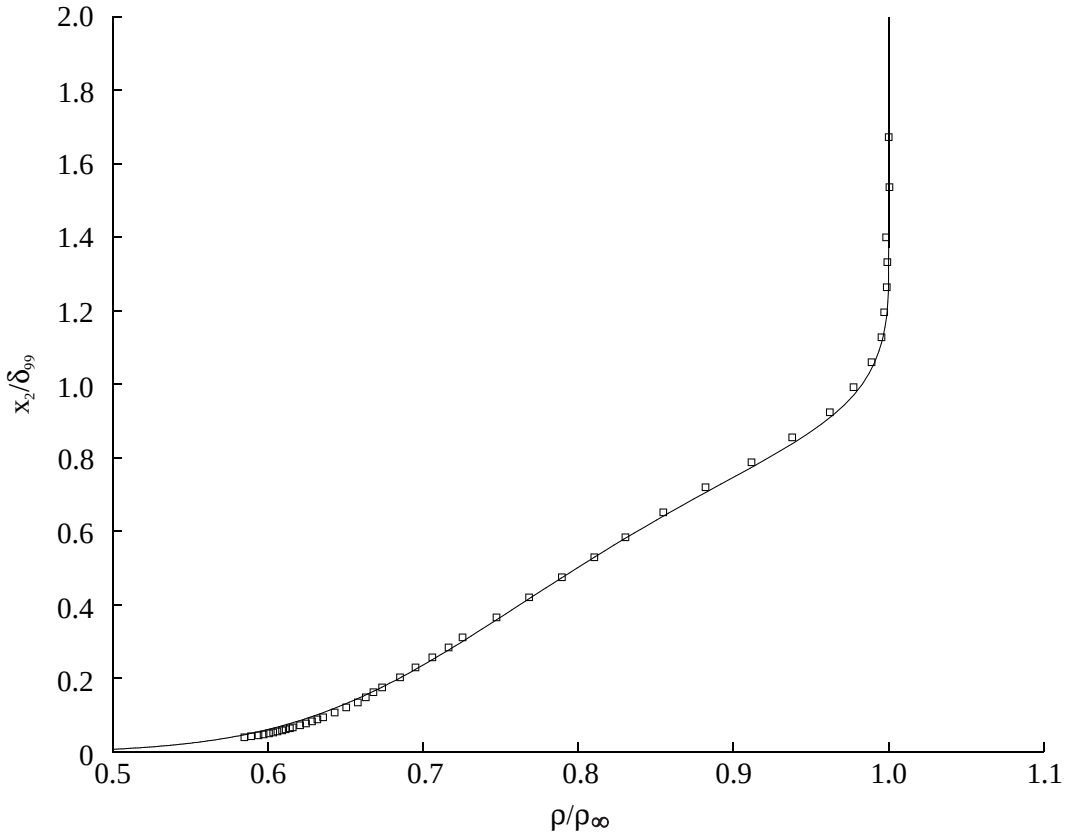

Figure 4.24: Static density profile normalised by the free stream density ρ_∞. x_2 Surface normal distance, δ_{99} surface normal distance to 99% of the free stream velocity. □ Measurements from Mabey & Sawyer (1976), profile 58.

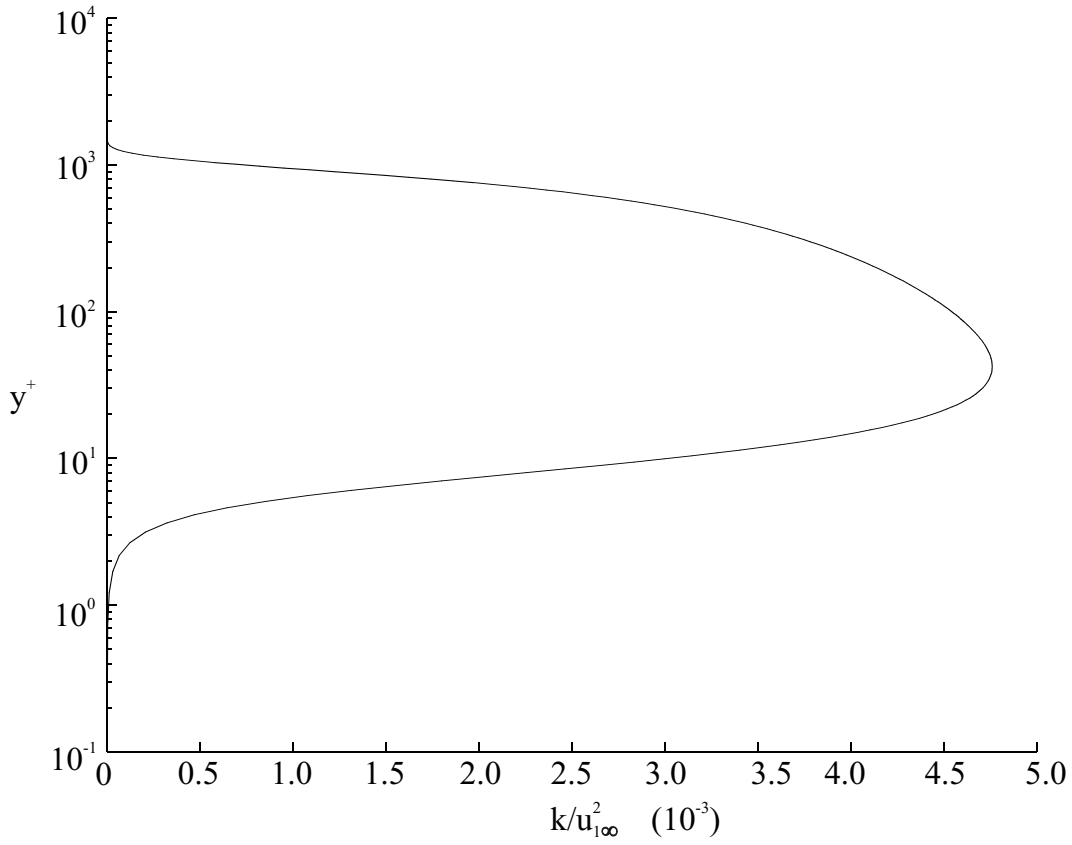

Figure 4.25: Dimensionless specific turbulence kinetic energy k prediction at $x_1 = 0.623m$ (profile 58 in Mabey & Sawyer (1976)). k is normalised using the free stream velocity $u_{1\infty}$.

Result	$\delta_1\ (m)$	$\delta_2\ (m)$	Re_{δ_2}
Mabey & Sawyer (1976)	2.98×10^{-3}	7.50×10^{-4}	9.0×10^3
Prediction	3.0×10^{-3}	7.94×10^{-4}	9.53×10^3

Table 4.4: Integral parameters comparing the measurements of Mabey & Sawyer (1976) against the single level benchmark prediction at $0.623m$ from the leading edge (profile 58 in Mabey & Sawyer (1976)). δ_1 Boundary layer displacement thickness, δ_2 momentum thickness, Re_{δ_2} Reynolds number based on the momentum thickness.

velocity $u_{1\infty}$. The predicted specific turbulence kinetic energy dissipation rate ω profile at $x_1 = 0.623m$ is given in Figure 4.26. ω, in Figure 4.26, is normalised using the flat plate total length $L = 1.6m$ and the free stream velocity $u_{1\infty}$.

The single level boundary layer profile at $x_1 = 0.623m$ from the leading edge shows little significant variation against the AMR predictions, of two and three levels refinement respectively. The three predictions are overlaid in Figure 4.27. The two AMR predictions follow the profile of the single level benchmark prediction closely. Minor differences are, however, observed. In particular, differences are evident in the outer region of the boundary layer, at $y^+ \geq 100$. These differences are more clearly defined in Figure 4.28, which is a detailed view of the boundary layer profile at $y^+ \geq 50$. A number of different values for the AMR scaling parameter b have been tested. At all scaling parameters tested below $b = 0.15$ the boundary layer is completely covered by the refined AMR levels. The observed differences in the boundary layer profile may therefore be primarily due to the initial interpolation of the boundary layer, at the start of the computation. This proposition is further substantiated by the increased magnitude in this error as further AMR levels are added, i.e. between the two levels AMR prediction and the three levels AMR prediction. This test case demonstrates an extension of the interpolation error documented for the inviscid acoustic pulse test case in Section 4.3 to turbulent flow. This source of error is expected to exist in any AMR prediction in which a finite gradient flow feature is interpolated between successive levels. Providing the number of AMR levels specified in a prediction is limited, this source of error appears to remain at a reasonably low level.

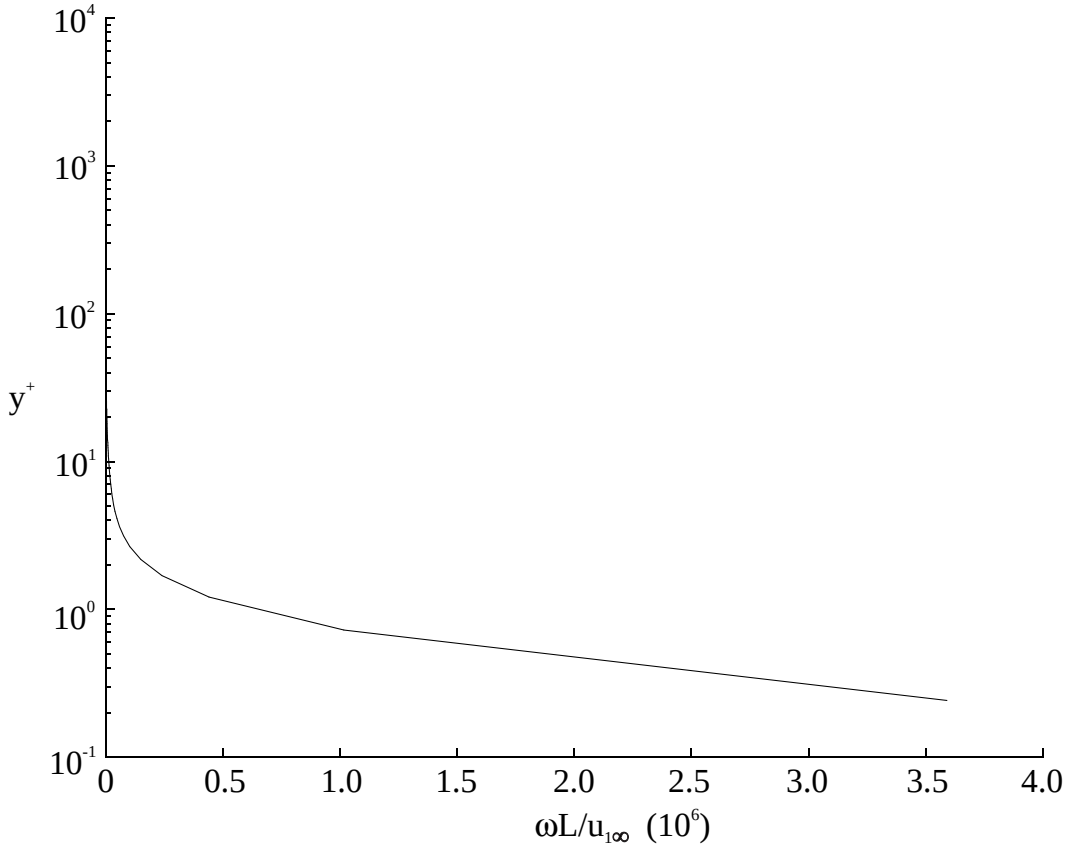

Figure 4.26: Specific turbulence kinetic energy dissipation rate ω prediction at $x_1 = 0.623m$ (profile 58 in Mabey & Sawyer (1976)). ω is normalised using the flat plate length $L = 1.6m$, and the free stream velocity $u_{1\infty}$.

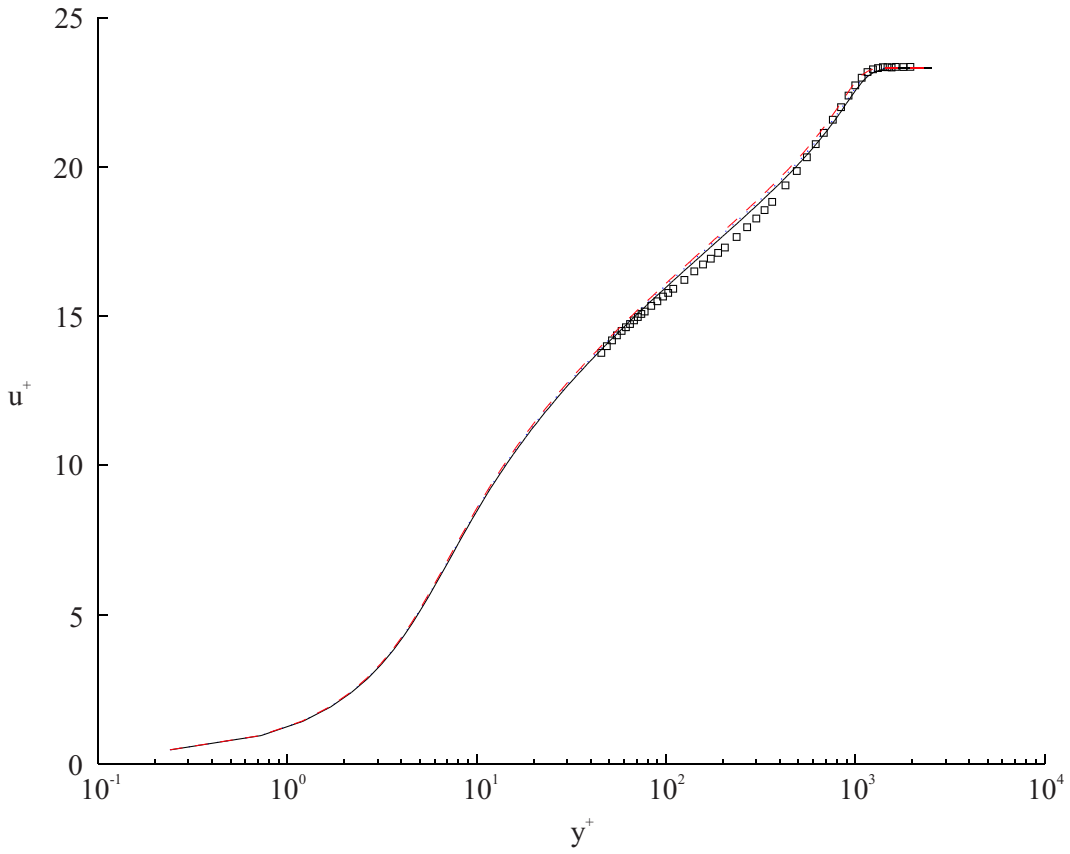

Figure 4.27: Comparison of the single level benchmark prediction against the AMR predictions of respectively two and three levels of multigrid refinement. (—) non-AMR single level prediction. (· · ·) Two levels AMR prediction (level 1 profile). (– – –) Three levels AMR prediction (level 2 profile). □ Measurements from Mabey & Sawyer (1976), profile 58.

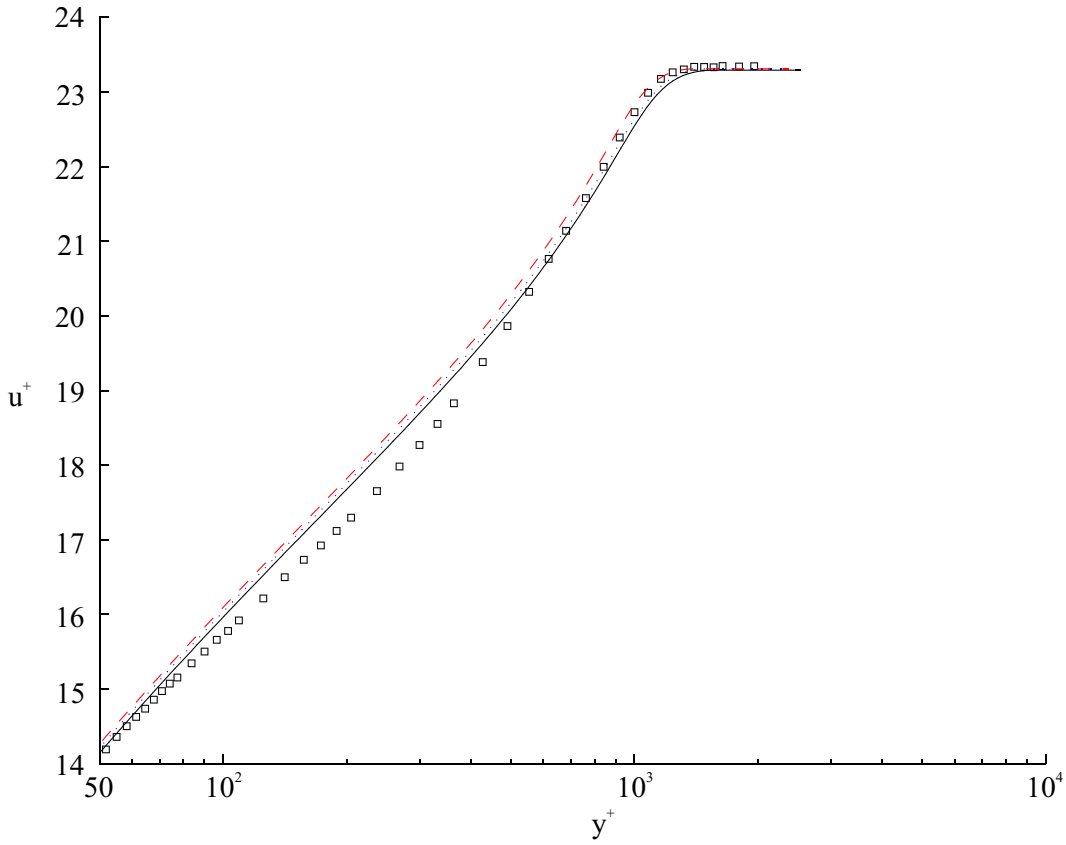

Figure 4.28: Detail of the single level benchmark prediction and the two AMR predictions. (—) non-AMR single level prediction. (· · ·) Two levels AMR prediction (level 1 profile). (– – –) Three levels AMR prediction (level 2 profile). □ Measurements from Mabey & Sawyer (1976), profile 58.

Overall, a reasonable prediction of a compressible turbulent boundary layer development under a zero stream-wise pressure gradient is documented in this section. Discrepancies in the AMR prediction, in comparison with a single level benchmark prediction, are observed and an explanation for these discrepancies is proposed. Even with the interpolation error, the AMR boundary layer prediction is considered satisfactory for the purposes of the current study.

Chapter 5

Circular Cylinder Prediction

5.1 Introduction

The time accurate compressible flow around a circular cylinder in a uniform $M_\infty = 0.6$ free stream flow is modelled in this chapter. An inviscid model of the flow is initially developed by locally solving the short-time averaged Euler equations. A turbulent prediction at a free stream Reynolds number of $Re_D = 6.87 \times 10^5$, based on the cylinder diameter, is then developed by computing the short-time averaged Navier-Stokes equations. These predictions are used to study the separation of stagnation temperature and pressure in a compressible, vortex dominated wake flow on a time resolved basis. The time averaged result of this energy separation is the Eckert-Weise effect described in Section 2.6. An overview of past research concerning transonic turbulent cylinder flows and the Eckert-Weise effect is given, based on the available literature, in Section 2.6. As suggested in Section 3.1.2, the presence of a high Reynolds number flow, dominated by large scale vortical and compressible wake features, should enable a reasonable flow field prediction from a time resolved inviscid prediction. This approach is analysed in Section 5.2. The inviscid prediction is then used to initialise the flow field for the turbulent prediction. The inviscid and turbulent predictions are compared with published numerical and experimental results, including wind tunnel measurements from a concurrent program of research by Ackerman (2005). Section 5.3 discusses results from the turbulent prediction using the numerical solution procedure described in Sections 3.4 to 3.9. Introducing the $k-\omega$ turbulence model should improve the prediction by accounting for bound-

ary layer development and separation, as well as introducing turbulence diffusion in the separated shear layers and vortex shedding mechanism. This study extends the time accurate energy separation predictions of Kurosaka et al. (1987) to transonic circular cylinder flows and extends the time averaged transonic measurements of Eckert & Weise (1943), Ryan (1951) and Thomann (1959) to a time accurate flow analysis. These developments are novel and original contributions in the context of the literature known to the author. The symmetrical flow development around a circular cylinder also provides comparative data for the asymmetric flow development in the transonic turbine cascade predictions of Chapter 6.

5.2 Inviscid Circular Cylinder Flow Prediction

5.2.1 Numerical Model Specifications

A diagrammatical representation of the computational domain used for the inviscid and turbulent predictions is given in Figure 5.1. The stagnation pressure and stagnation temperature at the inlet boundary $b1$ are chosen to model an unheated, blow down wind tunnel. The free stream conditions modelled at the inlet boundary are listed in Table 5.1. A rectangular computational domain extends $30.2D$ in the

Variable	Value
M_∞	0.6
$T_{s\infty}$	300 K
T_∞	280 K
$p_{s\infty}$	129.24 kN/m^2
p_∞	101.325 kN/m^2
ρ_∞	1.261 kg/m^3
$u_{1\infty}$	201.25 m/s

Table 5.1: Circular cylinder free stream flow conditions

stream-wise direction and $25.3D$ in the transverse direction. A cylinder of diameter $D = 40 \times 10^{-3}m$ is located $10.1D$ downstream of the inlet $b1$ and $12.65D$ from the constant pressure boundaries $b2$ and $b4$. The cylinder diameter is changed to $D = 47.41 \times 10^{-3}m$ in the turbulent predictions of Section 5.3, to match the free stream Reynolds number in the experimental measurements of Ackerman (2005).

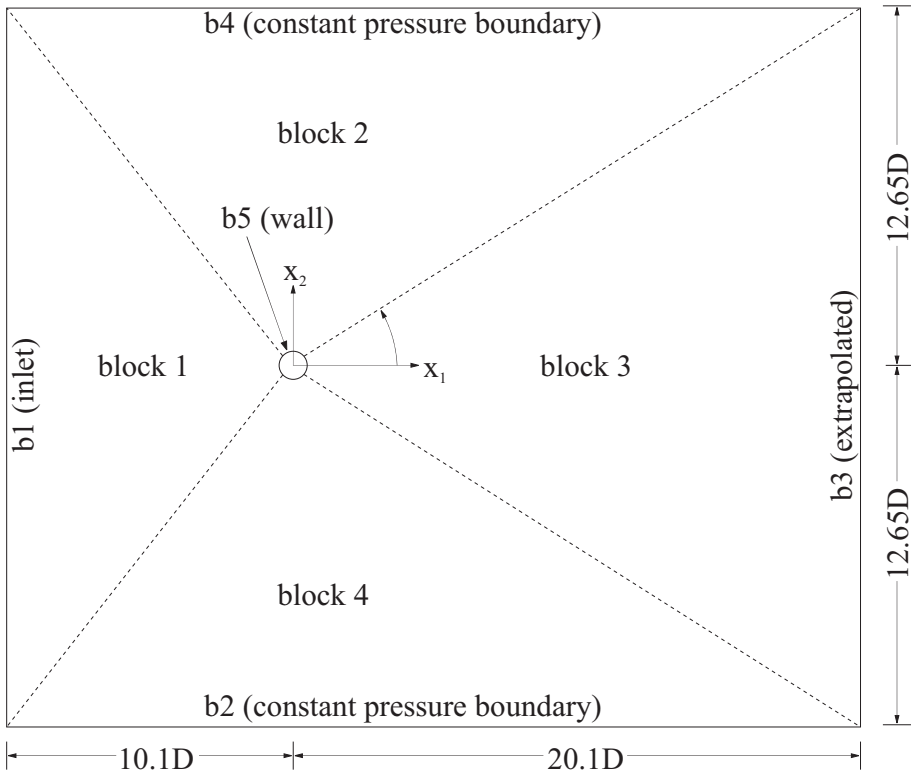

Figure 5.1: Circular cylinder computational domain.

The same $30.2D \times 25.3D$ computational domain shown in Figure 5.1 is used for the inviscid and turbulent predictions; all results in this chapter are presented using dimensionless units, with lengths scaled by the cylinder diameter D. The distance of the outer computational boundaries from the surface of the cylinder in Figure 5.1 is approximately equal to that of the finest computational grid used by Shang (1982) to model the viscous flow past a circular cylinder at $M_\infty = 0.6$ and $Re_D = 1.67 \times 10^5$. As reported in Rona & Bennett (2001), no strong wave reflection is observed at the inlet boundary $b1$ in the current prediction. The boundary therefore seems to be sufficiently far upstream of the cylinder to allow for a satisfactory convective decay of the upstream propagating pressure fluctuations. The subsonic boundary condition of Section 3.9.1 is specified at boundary $b1$. At $b2$ and $b4$, the constant pressure boundary condition described in Section 3.9.3 is specified. Downstream of the cylinder, along the boundary $b3$, the flow is extrapolated in the downstream direction as described in Section 3.9.4. An inviscid wall condition is imposed at the cylinder surface. The computational domain is divided into four separate blocks.

Each block is connected using the inter-domain boundary condition described in Section 3.9.5. These inter-block boundaries are defined by dashed lines in Figure 5.1. The interior of each block is discretised using a body-fitted grid of 100×200 cells. The four contiguous blocks give a combined mesh of 400×200 cells, covering the interior of the computational domain. The boundary conditions are imposed by creating a further rim, of one cell depth, around the perimeter of each block as described in Section 3.9. Linear grid stretching is defined normal to the circular cylinder for increased resolution close to the cylinder surface. A Gauss-Seidel iterative smoothing method, described in Hoffman & Chiang (1995), is applied to the grid to reduce cell skewness. The computational grid comprises of cells with aspect ratios in the range $1.60 \leq A \leq 6.81$. Computational cell sizes (length, height) vary from $(3.54 \times 10^{-3}D,\ 5.66 \times 10^{-3}D)$ to $(0.16D,\ 1.09D)$. The computational grid is defined such that the largest area and largest aspect ratio cells are located away from the region of interest, at the corners of the computational domain. The smallest cells with almost square topology are located at the surface of the cylinder. The grid resolution close to the surface and the surface normal grid stretching at the base of the circular cylinder ($\theta = 0°$) is shown in Figure 5.2.

5.2.2 The Initial Transient Flow Field Development

The free stream flow conditions in Table 5.1 are defined uniformly throughout the flow field at the start of the computation. The flow solution is time marched from these initial conditions to a self-sustained, periodic vortex shedding pattern in time steps of $\Delta t = 0.001D/u_\infty$. This time step corresponds to a Courant number of $a_\infty \Delta t/\Delta x = 0.366$. The initial transient flow development is represented in a series of annotated diagrams in Figure 5.3. Initially, a bow shock wave develops along the upstream surface of the circular cylinder. This is caused by the imposed uniform flow conditions rebounding against the cylinder surface condition. Downstream, an expansion wave is observed at the base of the cylinder. A representation of the flow field at this time is shown in Figure 5.3(a).

As the flow field develops, the upstream bow pressure wave propagates radially

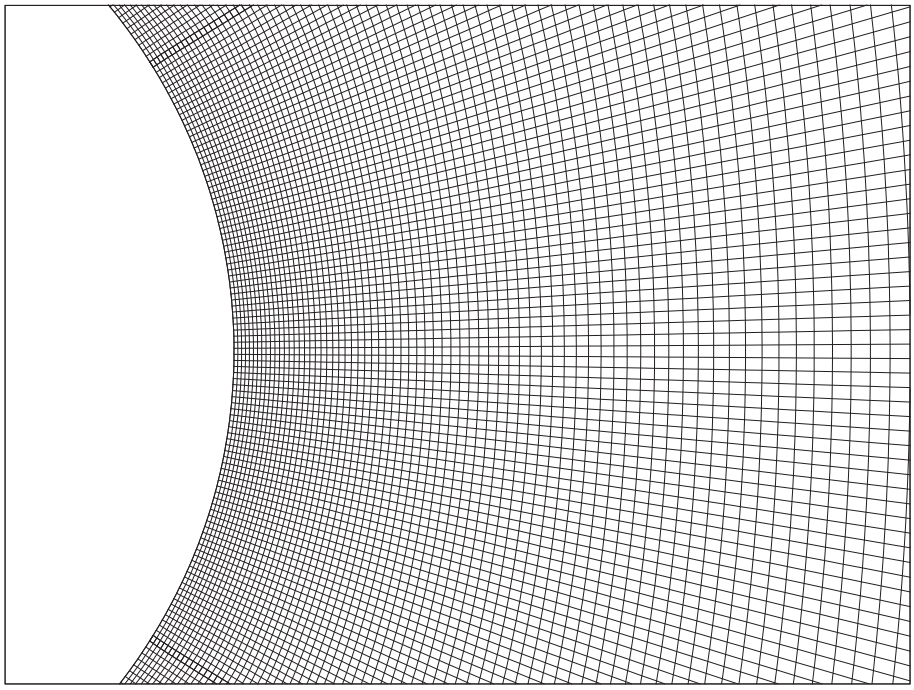

Figure 5.2: Computational grid detail around the circular cylinder base region.

away from the cylinder in the upstream direction, it decays in strength with upstream distance and eventually exits the domain. Radial shock waves appear on the upper and lower surfaces, close to the rear stagnation point ($\theta = 0°$). Two contra-rotating vortices form immediately downstream of these shock waves, as represented in Figure 5.3(b). The two radial shock waves gradually increase in strength and move upstream along the surface of the cylinder. This upstream movement ceases at around $\theta \approx \pm 60°$. The contra-rotating vortices gradually increase in size and strength during this time. As the radial shock waves form a stationary presence at $\theta \approx \pm 60°$, the two contra-rotating vortices start to elongate in the stream-wise direction. This is represented by Figure 5.3(c).

After a significant stream-wise elongation of the contra-rotating vortices, a breakdown of the cross-stream symmetry begins. Initially, this occurs as an asymmetric elongation of one vortex, as shown in Figure 5.3(d). This imbalance causes a cross-wake migration and subsequent rotation of the outer shear layers, close to the downstream extent of the vortices. The cross-wake migration of the outer shear layer divides the stream-wise length of the vortices, gradually leading to the dominance

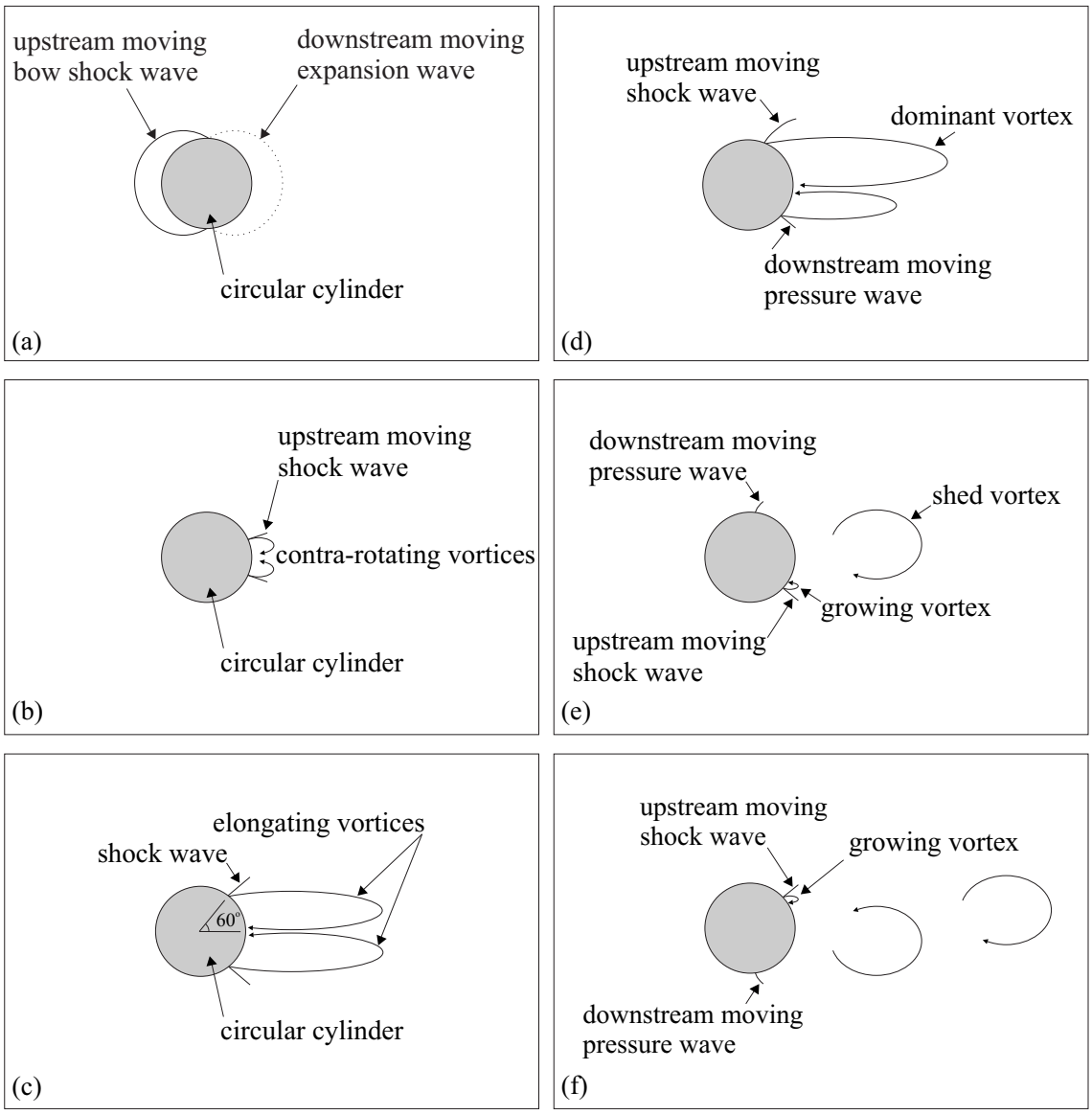

Figure 5.3: Representation of the initial transient flow past a circular cylinder. (a) A bow shock wave appears upstream of the cylinder and moves away from the cylinder surface. An expansion wave appears on the downstream surface and moves in the downstream direction. (b) Two short radial shock waves appear on the downstream surface close to the rear stagnation point. Contra-rotating vortices appear downstream of the radial shock waves. (c) The contra-rotating vortices elongate in the downstream direction and the radial shock waves move upstream, along the cylinder surface. (d) An asymmetry of the two contra-rotating vortices occurs. The radial shock wave on the dominant vortex side continues to move upstream. The other radial shock wave moves in the downstream direction. (e) The dominant vortex eventually sheds from the cylinder. The radial shock wave on this side then moves downstream along the cylinder surface. The vortex on the opposite side grows and is eventually shed from the other side of the cylinder. (f) Onset of the von Kármán vortex street.

of one vortex over the other at the base of the cylinder. The dominant vortex grows until sufficient strength is gained to entrain the far side shear layer. The vortex is then shed from the cylinder. During this period, the radial shock wave on the dominant vortex side of the wake increases in strength and slowly continues to propagate upstream to around $\theta \approx 90°$. The shock wave on the other side loses strength and gradually moves downstream towards the rear stagnation point. This shock wave movement is indicated in Figure 5.3(d).

After the dominant vortex is shed, the vortex with opposite rotation starts to increase in size and strength on the other side of the wake, as represented in Figure 5.3(e). This vortex subsequently increases in size and strength until sufficient fluid from the shear layer on the opposite side of the wake is entrained for the vortex to shed from the cylinder. The vortex then convects downstream, marking the onset of a von Kármán vortex street. This is represented in Figure 5.3(f).

As a numerical study of the circular cylinder flow development at very short times is not a direct objective of this study, further details are not supplied in this work. An in-depth analysis of this flow regime at transonic Mach numbers is reported in Botta (1995).

5.2.3 The Self-Sustained Vortex Shedding Development

After the initial transient development described in Section 5.2.2, the circular cylinder flow settles into a self-excited regime in which vortices are alternately shed from the downstream surface. As reported in Rona & Bennett (2001), the von Kármán vortex street initially passes through a *transient* vortex shedding regime as the phase-locking feedback in the vortex shedding develops. During this transient regime, subtle differences in the near wake flow are observed between each vortex formation and shedding event. This variation is most evident in the time accurate pressure at the rear stagnation point, $\theta = 0°$. The time accurate base pressure history over a portion of the *transient* vortex shedding regime is shown in Figure 5.4. The base pressure coefficient in Figure 5.4 is defined as

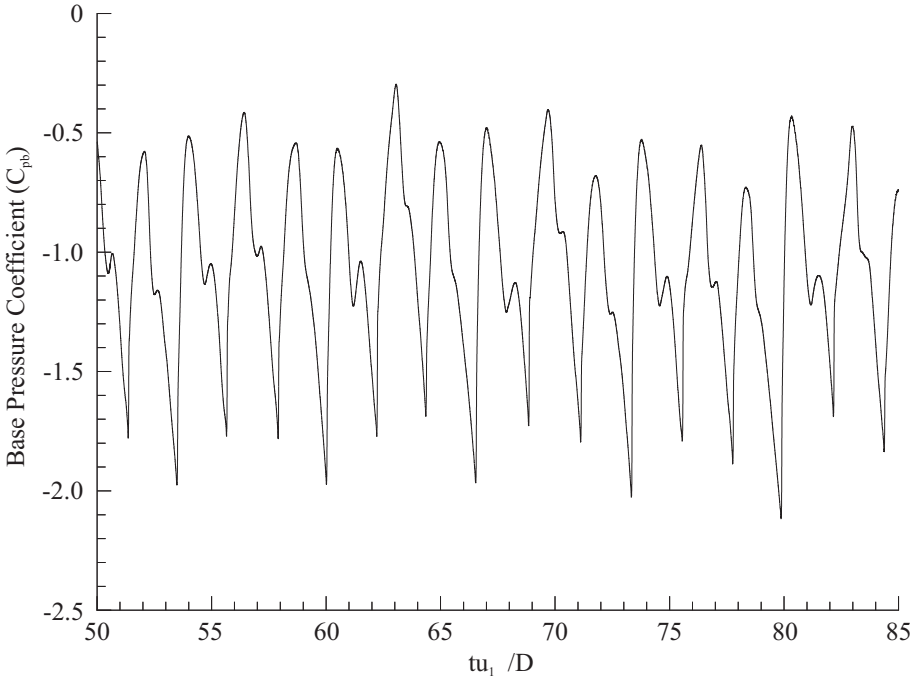

Figure 5.4: Base pressure coefficient in the transient vortex shedding regime.

$$C_{pb} = \frac{p_b - p_\infty}{p_{s\infty} - p_\infty}, \tag{5.1}$$

where, p_b defines the static pressure at the rear stagnation point ($\theta = 0°$). p_∞ and $p_{s\infty}$ are the free stream static pressure and stagnation pressure respectively.

The surface pressure at $\theta = 0°$ is equally affected by the vortex shedding events on the upper and lower surfaces of the cylinder. The time interval between successive local maxima or minima in Figure 5.4 represents the time between the formation or shedding of successive vortices from each side of the cylinder. This therefore represents half of the vortex shedding cycle, or twice the vortex shedding frequency. Consider, for example, the vortex shedding half cycle between $tu_{1\infty}/D = 60$ and $tu_{1\infty}/D \approx 62.3$ in Figure 5.4. A local minimum in the base pressure occurs as the strength of the vortex in the formation region approaches its maximum value. This occurs just before the vortex cuts off the circulation supply from the near side shear layer. As the vortex is shed from the cylinder and begins to convect downstream, the base pressure reaches a local maximum, at around $tu_{1\infty}/D \approx 60.6$. As the vortex on the opposite side of the wake then starts to increase in size and strength,

the base pressure is observed to decrease again. This decrease is non-monotonic; a short interval of increasing pressure is observed at approximately halfway along this pressure decrease. For example, the decreasing base pressure between $tu_{1\infty}/D \approx 60.6$ and $tu_{1\infty}/D \approx 62.3$ is interrupted by two additional local extrema, at $tu_{1\infty}/D \approx 61.2$ and $tu_{1\infty}/D \approx 61.5$. The temporal location and magnitude of this feature appears to vary on a cycle-to-cycle basis. A detailed study of the time accurate Mach number and static pressure contours, not shown here, associates this feature to an interaction between the cross-wake migration of the far side shear layer and a newly formed radial shock wave. This radial shock wave extends between the growing vortex and the cylinder surface. The shock wave is transient, appearing in addition to the two primary radial shock waves during the formation of each vortex. Further details on the vortex formation and shedding cycle, including the formation and decay of the transient shock wave, is given in Section 5.2.5.

As reported in Rona & Bennett (2001), the cycle-to-cycle variation in amplitude and shape of the base pressure trace decreases at later times as the vortex shedding develops a phase-locked periodicity. The base pressure coefficient over the period $115 \leq (tu_{1\infty}/D) \leq 150$ is shown in Figure 5.5. A significantly lower cycle-to-cycle variation is observed in Figure 5.5, which is defined in Rona & Bennett (2001) as the *quasi-stationary* vortex shedding regime. The amplitude and phase of this waveform appears be more invariant on a cycle-to-cycle basis. In Figure 5.5, the pressure coefficient fluctuations are made up from two identifiable waveforms. A dominant waveform is shown, with a peak-to-peak amplitude of approximately $\Delta C_{pb} = 1.5$. This wave displays rounded maxima at $C_{pb} \approx -0.75$ and sharp minima at $C_{pb} \approx -1.9$. A second wave, of lower amplitude and lower frequency, is shown to modulate the base pressure fluctuations in Figure 5.5. This second wave appears to phase-lead the dominant waveform throughout Figure 5.5. Constructive interference of the waveforms occur at certain times, increasing the cycle amplitude. At other times, the waveforms appear out of phase, leading to additional inflexion points in the normalised pressure trace. An observation of the base pressure variation at later times reveals little significant reduction of the cycle-to-cycle variation in amplitude and shape.

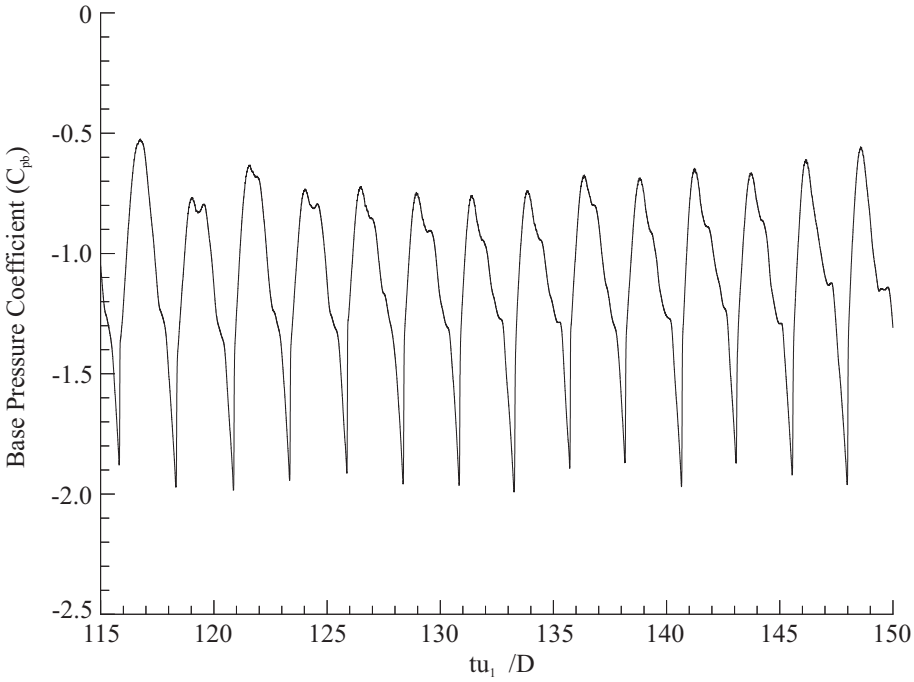

Figure 5.5: Base pressure coefficient in the quasi-stationary vortex shedding regime.

Botta (1995) shows a similar cycle-to-cycle variation of the flow characteristics at $M_\infty = 0.6$, in an inviscid prediction of the lift and drag coefficients. As described in Rona & Bennett (2001) and in Section 5.2.4, a similar cycle-to-cycle variation occurs in the time accurate drag coefficient and, to a lesser degree, in the lift coefficient. The lower cycle-to-cycle variation in the normalised pressure fluctuations of Figure 5.5, compared to Figure 5.4, is further evident from a Fourier analysis of the two waveforms. Digital Fourier transforms of Figure 5.5 and Figure 5.4 have been computed over an integer number of fourteen cycles. The resulting non-dimensional Power Spectral Density (PSD) distributions are given in Figure 5.6 and Figure 5.7 respectively. A significant reduction in the frequency content of the normalised base pressure during the quasi-stationary regime is observed in Figure 5.7, compared to Figure 5.6. Specifically, Figure 5.6 shows that the fluctuations in the normalised base pressure occur essentially at twice the vortex shedding frequency. A 10% shift in the dominant frequency is also observed between Figures 5.6 and 5.7. The reduction in C_{pb} as the flow becomes quasi-stationary is quantified by comparing the Root Mean Square (RMS) values of the two waveforms over an integer number of

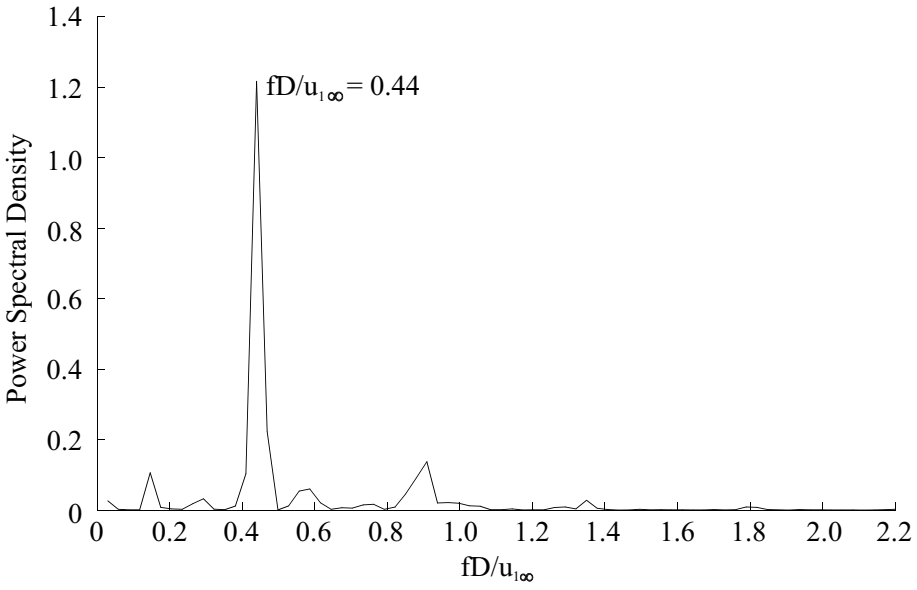

Figure 5.6: Frequency analysis of the base pressure coefficient at $\theta = 0°$ in the transient vortex shedding regime.

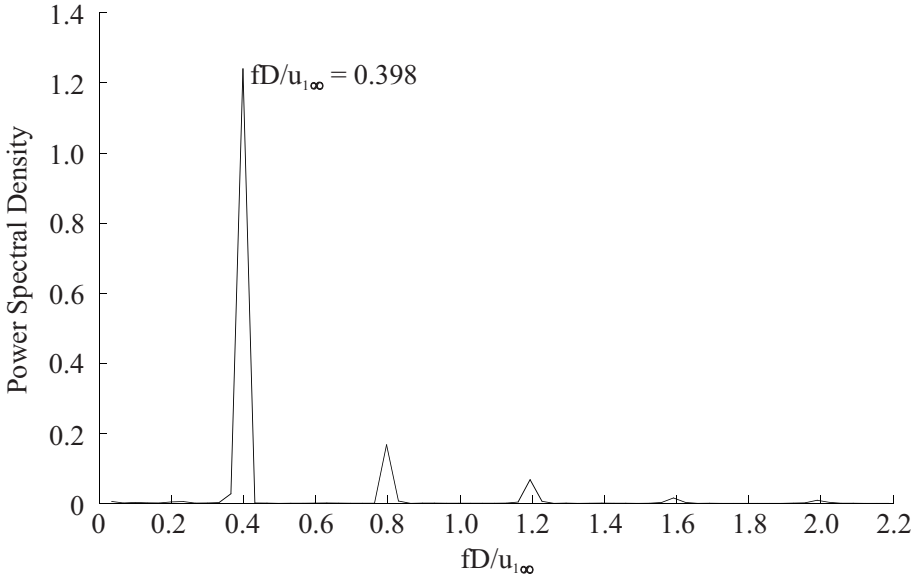

Figure 5.7: Frequency analysis of the base pressure at $\theta = 0°$ in the quasi-stationary vortex shedding regime.

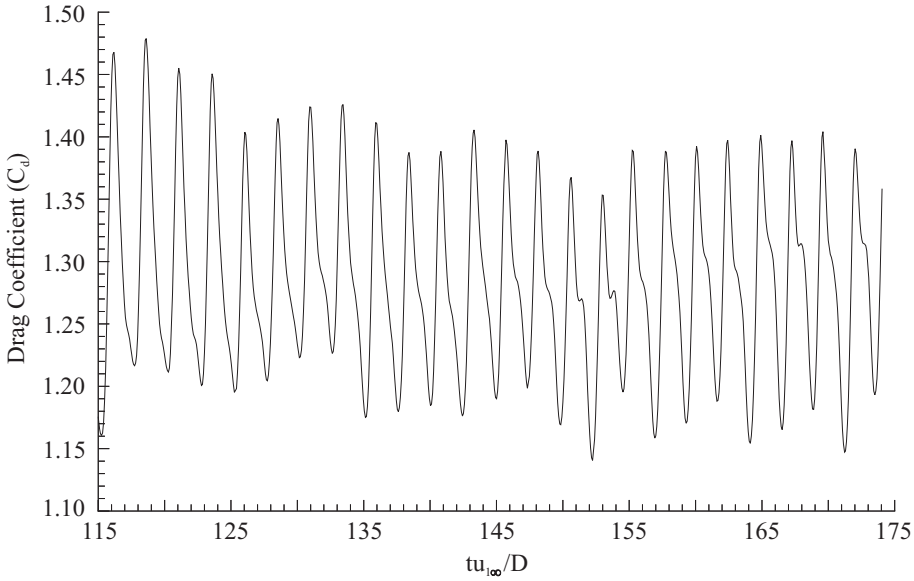

Figure 5.8: Drag coefficient history in the quasi-stationary vortex shedding regime.

cycles, as reported in Rona & Bennett (2001). The predicted RMS base pressure coefficients are 0.38 and 0.34 for Figures 5.4 and 5.5 respectively. At $tu_{1\infty}/D \geq 150$, the base pressure coefficient dominant frequency settles to the same value reported for Figure 5.7. This is twice the vortex shedding frequency reported in Table 5.4, as discussed in the following section.

5.2.4 Inviscid Prediction Validation

Analysis of the current prediction against the inviscid predictions of Pandolfi & Larocca (1989) and Botta (1995) at $M_\infty = 0.6$ are reported in Rona & Bennett (2001) and are detailed in this section. Tentative comparisons with the viscous prediction of Shang (1982) and with the concurrent experimental research program of Ackerman (2005) are also reported. A coarse quantitative agreement is found with the experimental measurements. This is likely to be due to the neglect of the boundary layer flow in the inviscid computation. An improved comparison is anticipated through the introduction of the $k - \omega$ turbulence model and no-slip surface condition. These results are presented in Section 5.3.

Figure 5.8 shows a time accurate trace of the pressure drag coefficient in the quasi-stationary vortex shedding regime. The pressure drag coefficient is calculated

by integrating the surface pressure coefficient C_p around the cylinder:

$$C_d = -\frac{1}{2}\int_0^{2\pi} C_p \, d(\sin\theta), \tag{5.2}$$

A maximum in the drag coefficient occurs at each vortex shedding event. Drag coefficient minima occur during the early formation of each vortex at the downstream surface of the cylinder. This is clarified in Section 5.2.5, from a time accurate analysis of the static density contours over one vortex shedding cycle. The dominant drag coefficient frequency is therefore twice the vortex shedding frequency. The cycle-to-cycle variations observed in the base pressure traces in Section 5.2.3 are also present in the drag coefficient. Unsteady variations in the drag coefficient peak-to-peak amplitude are also reported at $M_\infty = 0.6$ in Pandolfi & Larocca (1989) and Botta (1995). The drag coefficient maxima and minima from Figure 5.8, and their variation, are compared against Pandolfi & Larocca (1989) and Botta (1995) in Table 5.2. The average drag coefficient for the current prediction in Table 5.2 is

Source	Max. C_d	Average C_d	Min. C_d
Current prediction	1.41 ± 0.06	1.284	1.18 ± 0.05
Botta (1995)	1.5 ± 0.05	1.3 ± 0.05	1.1 ± 0.05
Pandolfi & Larocca (1989)	1.5 ± 0.03	1.38 ± 0.03	1.25 ± 0.03

Table 5.2: Circular cylinder drag coefficient fluctuations.

calculated as the arithmetic mean of the time accurate drag coefficient history over 30 complete cycles. The average drag coefficients of Botta (1995) and Pandolfi & Larocca (1989) in Table 5.2 are computed from the respective maxima and minima. The current prediction is within 6% of the prediction of Botta (1995), and within 10% of Pandolfi & Larocca (1989). The peak-to-peak amplitude of the current prediction is lower than both reference predictions, but compares more favourably with that of Pandolfi & Larocca (1989). The level of fluctuation in the peak-to-peak drag coefficient amplitude is greater in the current prediction than in either Botta (1995) or Pandolfi & Larocca (1989). The differences observed between the current prediction and the referenced predictions may result from the different radial

and circumferential grid resolutions used in these studies, as proposed in Rona & Bennett (2001). These differences may also be caused by the different numerical solution procedures employed.

The average drag coefficients in Table 5.2 also compare favourably with the measured pressure drag coefficient of Ackerman (2005) at $M_\infty = 0.6$ and $Re_D = 6.75 \times 10^5$. The measured mean value, $C_d = 1.36$, is approximately 6% from the current prediction. This correlation indicates the dominance of compressibility and the kinematic flow features over viscous effects at the modelled flow conditions. The total drag for a practical cylinder of assumed infinite span also includes the skin friction drag and the wave drag from the unsteady radial shock waves on the surface of the cylinder. The presence of radial shock waves are detailed further in Section 5.2.5. Skin friction drag for circular cylinders is discussed in Section 5.3.2.

The aerodynamic loading of the circular cylinder in the transverse direction, due to the self-sustained vortex shedding, is quantified by the lift coefficient C_l. This is computed for the current prediction as

$$C_l = \frac{1}{2}\int_0^{2\pi} C_p \, d(\cos\theta), \tag{5.3}$$

where C_p is the time accurate surface pressure coefficient. The time history of the lift coefficient in the quasi-stationary regime is given in Figure 5.9. For a pitchwise symmetric body in a uniform free stream flow, the lift coefficient oscillates about its zero mean value. As noted in Rona & Bennett (2001), a positive peak in the lift coefficient corresponds to the shedding of a vortex from the lower half of the cylinder. A negative peak in the lift coefficient similarly corresponds to the shedding of a vortex from the upper surface of the cylinder. The fundamental frequency of oscillation in the lift coefficient therefore corresponds to the vortex shedding frequency and to half the drag coefficient fundamental frequency. The time resolved lift coefficient maxima and minima are compared with corresponding results by Botta (1995) and Pandolfi & Larocca (1989) in Table 5.3. As with the drag coefficient, significant cycle-to-cycle variations are displayed by all three lift coefficient predictions. The peak-to-peak amplitude of C_l in the current prediction

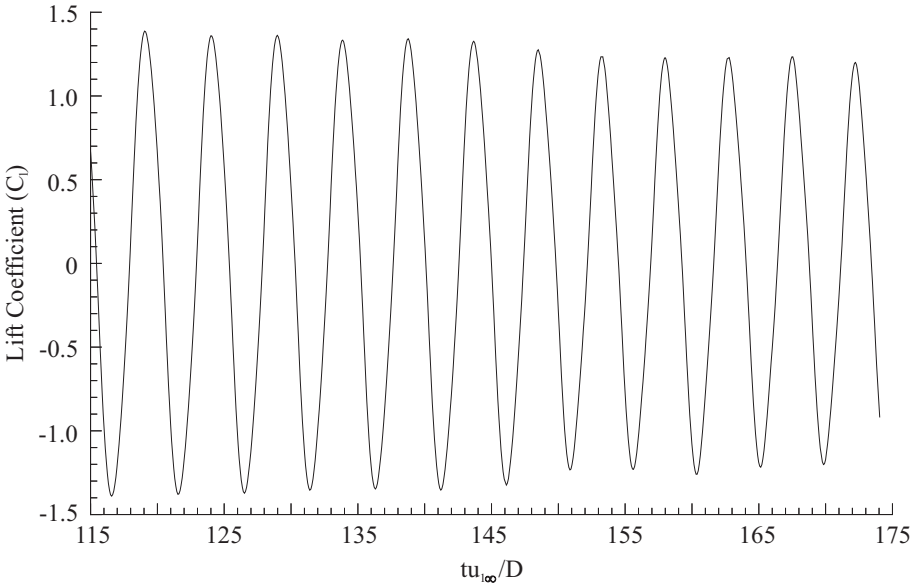

Figure 5.9: Lift coefficient history in the quasi-stationary vortex shedding regime.

Source	Max. C_l	Min. C_l
Current prediction	1.3 ± 0.1	-1.3 ± 0.1
Botta (1995)	1.2 ± 0.15	-1.2 ± 0.15
Pandolfi & Larocca (1989)	1.5 ± 0.15	-1.5 ± 0.15

Table 5.3: Circular cylinder lift coefficient fluctuations.

lies between the predicted values of Botta (1995) and of Pandolfi & Larocca (1989). Specifically, a difference of 8% is computed between the current prediction and that of Botta (1995). A difference of 14.3% separates the current prediction from that of Pandolfi & Larocca (1989). The difference between the two referenced predictions is 22.2%. The magnitude of the cycle-to-cycle fluctuations, as a proportion of the peak-to-peak lift amplitude, is smaller for the current prediction than for both referenced predictions. The non-stationary fluctuation in the current C_l prediction is approximately 7.7% of the average peak-to-peak lift coefficient amplitude. This compares with 12.5% for Botta (1995) and 10% for Pandolfi & Larocca (1989). The non-stationary fluctuation in the current lift coefficient, normalised by the peak-to-peak C_l amplitude, is significantly lower than the corresponding value for the drag coefficient. This indicates that a large proportion of the cyclic unsteadiness generates close to the downstream stagnation point ($\theta = 0^\circ$) in the present results.

The vortex shedding frequency in the quasi-stationary flow regime is estimated by a digital Fourier transform of the time accurate lift coefficient. The result ties in with the vortex shedding period estimated from the average distance between successive minima in the time accurate near wake pressure history. The vortex shedding frequency f is tabulated as a non-dimensional Strouhal number ($Str = fD/u_{1\infty}$) in Table 5.4, using the cylinder diameter D and the free stream velocity $u_{1\infty}$. The current prediction is compared with the inviscid predictions of Botta (1995) and Pandolfi & Larocca (1989) in Table 5.4. Also reported in this table are the vortex shedding Strouhal numbers measured at $M_\infty = 0.6$ by Ackerman (2005) and Murthy & Rose (1978), as well as a viscous prediction by Shang (1982). The measurements

Source	Strouhal no.
Current prediction	0.199
Botta (1995)	0.2
Pandolfi & Larocca (1989)	0.198
Ackerman (2005) (2000 series)	0.175
Ackerman (2005) (2002 series)	0.176
Murthy & Rose (1978)	0.181
Shang (1982)	0.21

Table 5.4: Strouhal number comparison. Measurements of Ackerman (2005): $M_\infty = 0.6$, $Re_D = 6.86 \times 10^5$ (2000 series) and $M_\infty = 0.6$, $Re_D = 6.75 \times 10^5$ (2002 series). Measurements of Murthy & Rose (1978) at $M_\infty = 0.6$, $Re_D = 0.83 \times 10^5 - 5 \times 10^5$. Prediction of Shang (1982) at $M_\infty = 0.6$, $Re_D = 1.67 \times 10^5$.

of Murthy & Rose (1978) demonstrate that at $M_\infty = 0.6$, the fundamental vortex shedding Strouhal number approximates a constant value of around $Str = 0.181$ over the Reynolds number range $0.83 \times 10^5 \leq Re_D \leq 5 \times 10^5$. This Strouhal number is close to the measurements of Ackerman (2005) at $Re_D = 6.75 \times 10^5 - 6.86 \times 10^5$. These measurements show that the dominant vortex shedding Strouhal number is relatively insensitive to the free stream Reynolds number at $M_\infty = 0.6$. The current prediction compares well with the inviscid predictions of Botta (1995) and Pandolfi & Larocca (1989), falling between the two values, at 0.5% from each. The measured Strouhal numbers, which correlate well ($< 3.5\%$) with each other, are $\leq 12.1\%$ from the current prediction and $\leq 16.7\%$ lower than the viscous prediction

of Shang (1982). The lower measured Strouhal numbers in Table 5.4 indicate that these vortices take longer to shed from the cylinder, with respect to the current inviscid prediction. This is reconcilable with the physical vortex formation mechanism proposed by Gerrard (1966), as described in Section 2.3. Briefly, Roshko (1954) and Gerrard (1966) suggest that the vortex formation region length at the rear of a circular cylinder relates to the length of time taken for the vortex to entrain fluid from the far side shear layer. In the tabulated measurements, the increased diffusion in the turbulent shear layer increases the length of time taken for the growing vortex to entrain sufficient opposing vorticity from the far side shear layer to cancel the vorticity in the near side shear layer. After sufficient vorticity has been entrained, the vortex is shed from the cylinder and convects downstream. Gerrard (1966) suggests that an increase in shear layer thickness, or 'diffusion length', balances the decrease in formation region length as the free stream Reynolds number increases, leading to a consistency of the vortex shedding Strouhal number. The inviscid predictions, which lack turbulence diffusion, represent the limiting case of a very high Reynolds number flow and may be expected to yield a slightly higher Strouhal number. The vortex shedding frequency in the inviscid predictions may therefore be determined predominantly by the vorticity of the separated shear layers and by the numerical diffusion in the vortex formation region, which is linked to the local grid resolution.

5.2.5 Compressibility and the Inviscid Vortex Shedding Cycle

The time accurate base pressure, lift and drag coefficients indicate a self sustained, periodic vortex shedding pattern downstream of the circular cylinder at the modelled free stream conditions. Unsteady radial shock waves are reported in Dyment & Gryson (1979), Pandolfi & Larocca (1989), Botta (1995) and in Rona & Bennett (2001). These shock waves oscillate circumferentially around the cylinder at $M_\infty = 0.6$, in phase with the vortex formation and shedding cycle. The relationship between the precession of shock waves on the cylinder surface and the vortex shedding cycle can be analysed further using the instantaneous density contour plot sequence from the current prediction shown in Figures 5.10 and 5.11. Figure 5.10 doc-

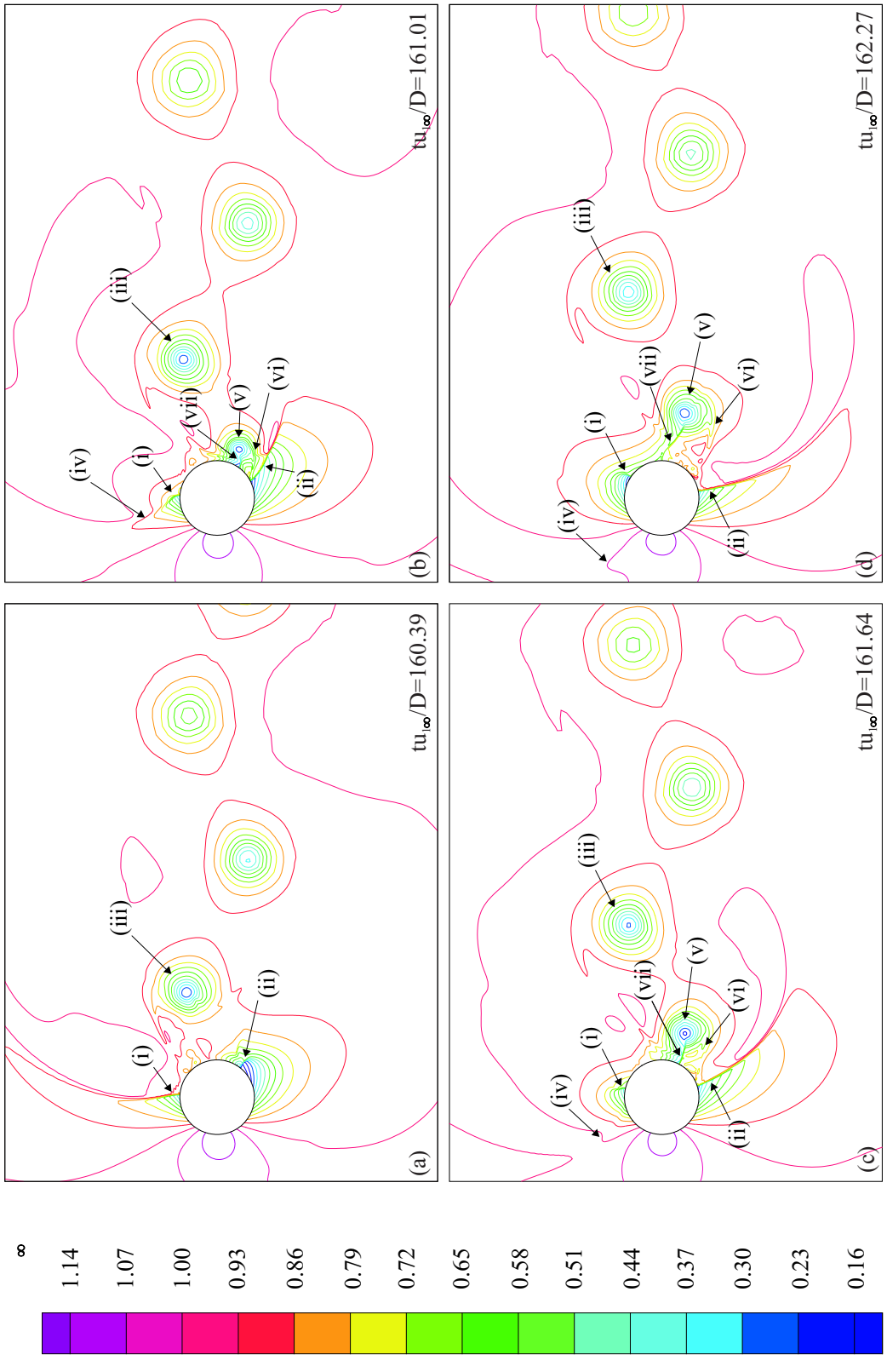

Figure 5.10: Instantaneous density contours over the first half of the vortex shedding cycle: $160.39 \leq tu_{1\infty}/D \leq 162.27$. $\rho_{\max} = 1.14\rho_\infty$, $\rho_{\min} = 0.16\rho_\infty$, $\Delta\rho = 0.07\rho_\infty$. (i)-(viii) labelled flow features.

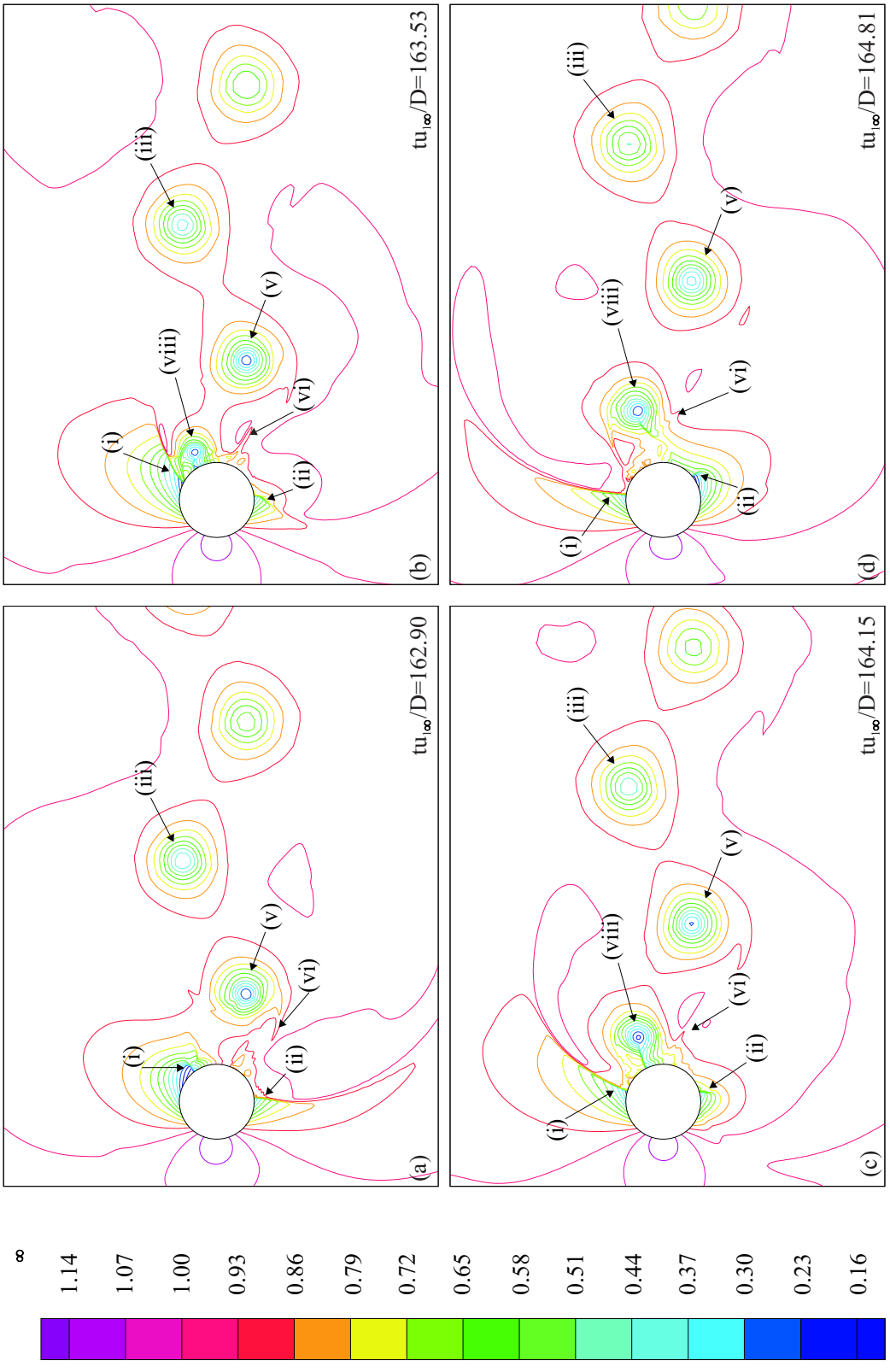

Figure 5.11: Instantaneous density contours over the second half of the vortex shedding cycle: $162.90 \leq tu_{1\infty}/D \leq 164.81$. $\rho_{\max} = 1.14\rho_\infty$, $\rho_{\min} = 0.16\rho_\infty$, $\Delta\rho = 0.07\rho_\infty$. (i)-(viii) labelled flow features.

uments the formation of an anti-clockwise rotating vortex at the lower downstream side of the cylinder, over the time interval $160.39 \leq tu_{1\infty}/D \leq 162.27$. Figure 5.11 documents the shedding of this vortex and the formation of a new clockwise rotating vortex on the upper surface over the time period $162.90 \leq tu_{1\infty}/D \leq 164.81$. Figures 5.10 and 5.11 therefore document the static density field development in the circular cylinder near wake over one complete vortex shedding cycle. Figures 5.10 and 5.11 cover a small portion of the computational domain. Specifically, these figures detail an area close to the cylinder extending approximately $\Delta x_1 = 7.8D$ in the stream-wise direction and $\Delta x_2 = 5.8D$ in the stream-wise normal direction. This allows a greater resolution of the unsteady flow features close to the surface of the cylinder. These figures represent approximately 25.8% of the stream-wise extent and 22.9% of the transverse extent for the actual computational domain. The density contours clearly show radial shock waves on the upper and lower surfaces. These shock waves, labelled (i) and (ii) respectively in Figures 5.10 and 5.11, fluctuate about a time mean circumferential position over the vortex shedding period. The two radial shock waves demonstrate a pitch-wise asymmetry in strength and circumferential location. Figure 5.10(a) shows the radial shock wave on the upper surface (i) at its furthest upstream position, at approximately $\theta = 90°$. The shock wave on the lower surface (ii) is located further downstream. This location represents the furthest downstream position either shock wave takes over the vortex shedding cycle. The upper (i) and lower (ii) radial shock waves oscillate between these two circumferential locations over the course of each vortex shedding event. The clockwise rotating vortex, labelled (iii) in Figure 5.10(a), is at the point of being shed from the cylinder in this figure. Two further vortices, one with an anti-clockwise rotation and the other with a clockwise rotation, are located downstream of this vortex in Figure 5.10(a-d). These two vortices are the product of the previous vortex shedding cycle. The vortex shedding aspect ratio is defined as the ratio of the stream-wise length l, between successive vortices on the same row, to the cross-wake width between the two vortex rows w. The mean aspect ratio in the current prediction, calculated over three separate shedding events in the region $1.2D \leq x_1 \leq 7.4D$, is

$w/l = 0.278$. This value is within 1.1% of the analytical value of von Kármán, given as $w/l = 0.281$ in Schlichting (1979) and Douglas (1995). However, as reported in Rona & Bennett (2001), this value is observed to vary by up to 25% due to the cycle-to-cycle flow variations highlighted in Section 5.2.3.

As the flow field progresses from Figure 5.10(a) a new vortex forms on the lower surface of the cylinder. This anti-clockwise rotating vortex is labelled (v) in Figure 5.10(b-d). Over the course of Figure 5.10(b-d), the outer portion of the upper surface shock wave (i) continues to move upstream as a finite gradient pressure fluctuation through the subsonic flow region. This upstream moving pressure fluctuation is labelled (iv) in Figure 5.10(b-d). The lower portion of this shock wave (i) defines the downstream limit of a local supersonic acceleration along the cylinder surface. This shock wave is constrained by the upstream limit of the adverse pressure gradient, remaining at approximately the same circumferential location over the period $160.39 \leq tu_{1\infty}/D \leq 161.01$. The anti-clockwise rotating vortex (v) is fed by the separated shear layer at the lower surface of the cylinder. This shear layer is labelled (vi) in Figure 5.10(b) and is shown as a deviation in the iso-density contours along a line almost tangential to the cylinder surface. As the strength of this vortex (v) increases, a channel of fluid between the vortex core and the cylinder surface accelerates to supersonic velocities. This local supersonic region terminates with a radial shock wave that extends between the cylinder surface and the vortex core. This secondary shock wave, labelled (vii), first appears in Figure 5.10(b) and increases in strength with the vortex growth in Figure 5.10(c). The increased peripheral pressure from the formation of the vortex (v) increases the strength of the primary radial shock wave (ii) on this side. This shock wave responds by moving circumferentially upstream, slowing the incoming flow to lower supersonic velocities. The increase in strength of the vortex (v) in Figure 5.10(c) is evident by the identification of iso-density contours darker blue in colour, close to the centre of this vortex. The weakened shock wave (i), on the opposite pitch-wise side of the cylinder, gradually moves downstream circumferentially over the interval $161.01 \leq tu_{1\infty}/D \leq 162.90$. The fluid upstream of this shock wave gradually accelerates to higher supersonic

velocities before recompressing. The period $160.39 \leq tu_{1\infty}/D \leq 162.90$ corresponds to a gradual increase in the lift coefficient, which crosses $C_l = 0$ at approximately $tu_{1\infty}/D = 161.64$. The instantaneous density contour plot at $tu_{1\infty}/D = 161.64$ in Figure 5.10(c) shows an approximate pitch-wise symmetry in the location of the two primary radial shock waves (i) and (ii). The low pressure supersonic fluid travelling around the vortex (v), ahead of the secondary shock wave (vii), is located close to the base pressure location ($x_2/D = 0$) in this figure. This secondary shock wave (vii) moves anti-clockwise around the surface of the cylinder in Figure 5.10(d) as the vortex approaches separation from the cylinder. The primary shock wave on the upper surface (i) moves clockwise resulting in lower pressure fluid over a significant proportion of the upper surface. Together with the clockwise movement of the supersonic region ahead of the secondary shock wave (vii), and the shortening of the supersonic region upstream of (ii), a resultant force in the positive x_2 direction and a positive lift coefficient is observed. The lift coefficient continues to increase in magnitude, reaching a maximum positive value at $tu_{1\infty}/D \approx 162.90$ in Figure 5.11(a). A similar sequence of events to those described for Figure 5.10(a-d) occurs over the course of Figure 5.11(a-d), for the formation of a clockwise rotating vortex (viii). Figure 5.11(a-d) corresponds to a decreasing lift coefficient, which reaches a minimum value at $tu_{1\infty}/D \approx 165.41$.

A static pressure history of the primary radial shock wave movement over the upper and lower surfaces of the cylinder is documented at three surface locations in Figure 5.12. Specifically, the three surface locations are $\theta = 60°$ and $\theta = 80°$, shown in Figure 5.12(a), and $\theta = -60°$, as shown in Figure 5.12(b). These surface locations are taken with respect to the base pressure location, which is defined as $\theta = 0°$ as shown in Figure 5.1. From the two pressure traces in Figure 5.12(a), four primary regions can be defined over each cycle. In the range $138 \leq tu_{1\infty}/D \leq 143$ these are:

1. An upstream movement of the radial shock wave circumferentially along the upper surface to cross $\theta = 60°$ at $tu_{1\infty}/D = 139.4$. The passing of the shock wave

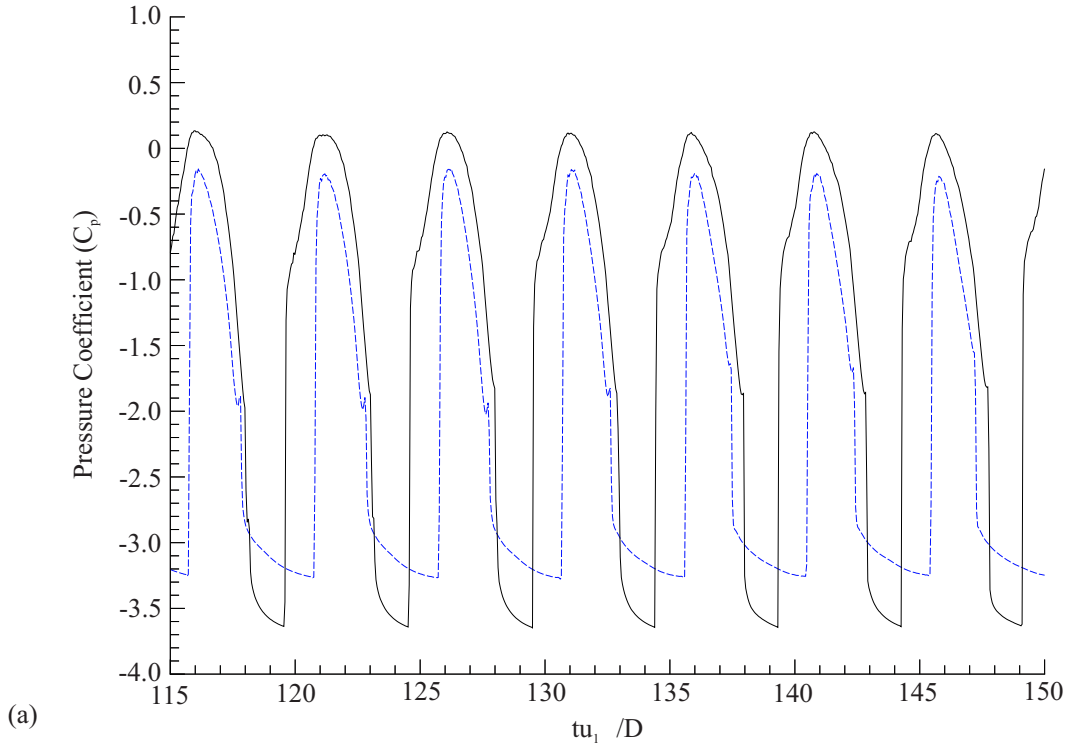

(a)

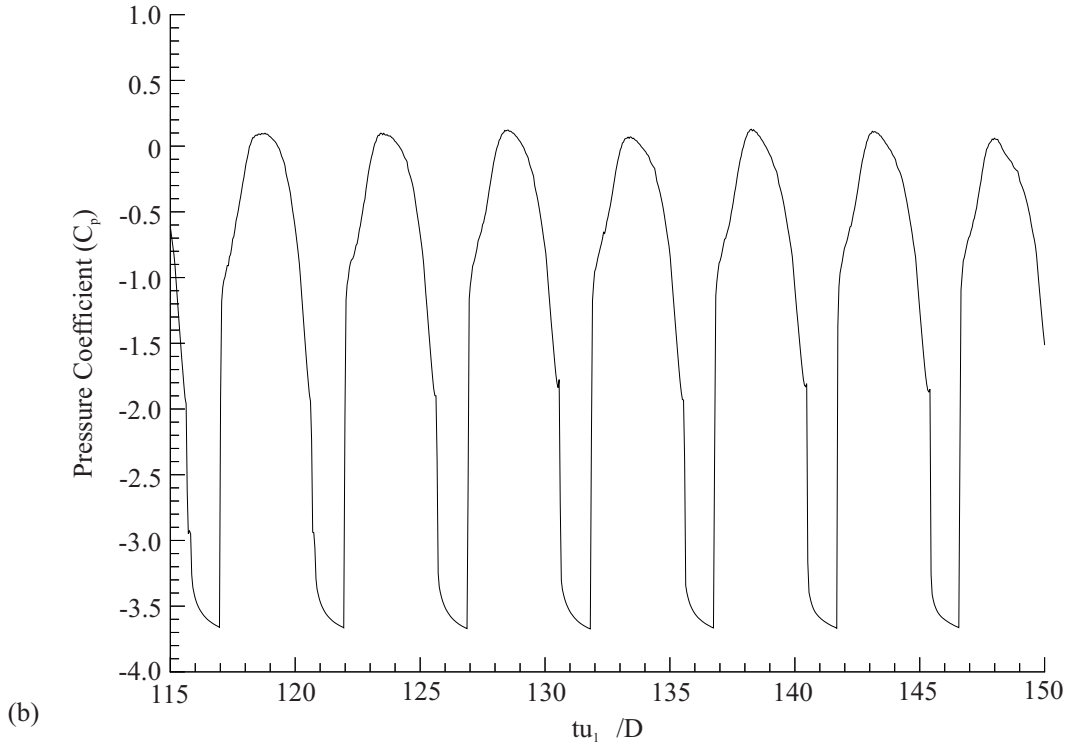

(b)

Figure 5.12: Surface pressure history: (a) (—) $\theta = 60°$, (- - -) $\theta = 80°$, (b) (—) $\theta = -60°$.

over the $\theta = 60°$ location causes a sharp increase in the pressure coefficient at $tu_{1\infty}/D = 139.4$.

2. An upstream movement of the shock wave on the upper surface of the cylinder between $\theta = 60°$ and $\theta = 80°$, over the period $139.4 \leq tu_{1\infty}/D \leq 140.5$. At $tu_{1\infty}/D = 140.5$ the shock wave passes over the $\theta = 80°$ location causing a sudden pressure rise at this monitoring point.

3. Movement of the shock wave along the upper surface of the cylinder at $80° \leq \theta \leq 90°$, over the interval $140.5 \leq tu_{1\infty}/D \leq 142.4$. During this time interval both $\theta = 60°$ and $\theta = 80°$ remain above their time mean values.

4. A downstream movement of the weak shock wave along the upper surface of the cylinder, between $\theta = 60$ and $\theta = 80°$, over the time interval $142.4 \leq tu_{1\infty}/D \leq 142.9$. This movement causes a sharp drop in the pressure coefficient as the shock wave moves over the $\theta = 80°$ location, at $tu_{1\infty}/D = 142.4$. The shock wave then passes over the $\theta = 60°$ location at $tu_{1\infty}/D = 142.9$.

The greater amplitude of the discontinuity at $tu_{1\infty}/D = 139.4$ in the $\theta = 60°$ pressure trace, with respect to the discontinuity at $tu_{1\infty}/D = 142.9$, confirms the earlier suggestion that the shock wave is stronger during the upstream movement. The time difference between the shock wave passing over the 60° location at $tu_{1\infty}/D = 139.4$ and the $\theta = 80°$ location at $tu_{1\infty}/D = 140.5$ determines the average shock wave propagation speed, relative to the cylinder, for an upstream travelling shock wave. Specifically, from Figure 5.12(a), the shock wave is computed to travel over the distance, $60° \leq \theta \leq 80°$, at an average angular velocity of $u_\theta = 18.2° u_{1\infty}/D$ in the upstream direction. The corresponding angular velocity of the shock wave travelling in the downstream direction, between $\theta = 80°$ and $\theta = 60°$, is $u_\theta = 40° u_{1\infty}/D$. The forward and backward shock wave speeds, relative to the cylinder, differ. This gives a variable phase difference between the $\theta = 60°$ and $\theta = 80°$ waveforms, which

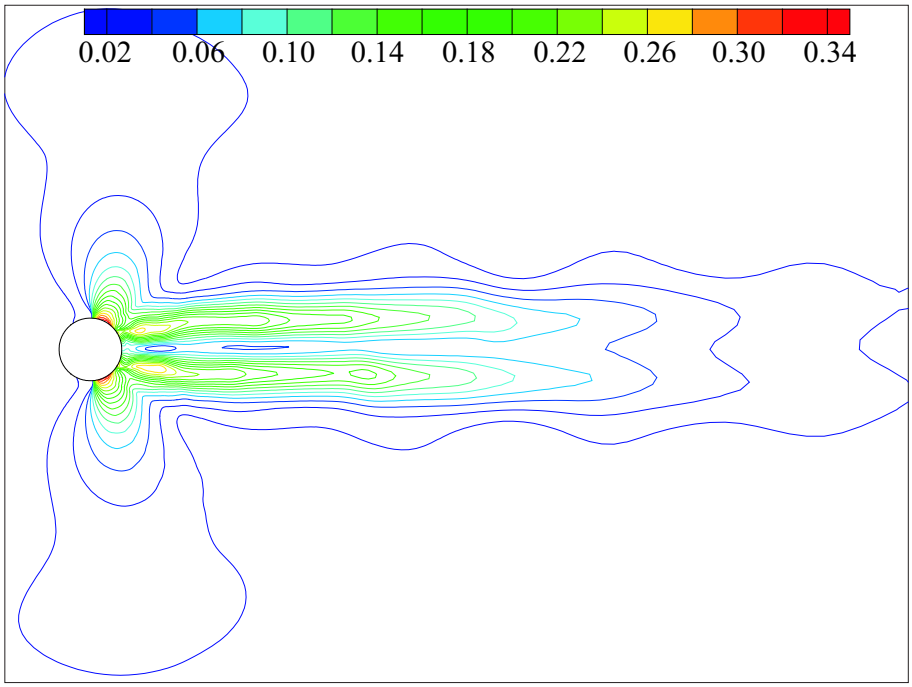

Figure 5.13: Root mean square density field. $(\rho_{\max})_{rms} = 0.34\rho_\infty$, $(\rho_{\min})_{rms} = 0.02\rho_\infty$, $\Delta\rho = 0.02\rho_\infty$.

changes the shape of the $\theta = 80°$ with respect to the $\theta = 60°$ wave during one vortex shedding cycle.

Waveforms of similar shape define the surface pressure at $\theta = 60°$ in Figure 5.12(a) and the surface pressure at $\theta = -60°$ in Figure 5.12(b). The waveform in Figure 5.12(b) is however shifted by approximately $tu_{1\infty}/D = 2.51$ with respect to Figure 5.12(a). This is half the mean vortex shedding period. The Root Mean Square (RMS) pressure coefficient at $\theta = 60°$ is 1.45. The RMS pressure coefficient at $\theta = -60°$ is 1.42. The 2% difference in these two RMS values is due to the transient cycle-to-cycle variations in the quasi-stationary vortex shedding regime. The upstream extent of the radial shock wave fluctuations is highlighted in the root mean square iso-density contours of Figure 5.13. A slight asymmetry is observed across the wake due to the transient cycle-to-cycle fluctuations. Also highlighted in Figure 5.13 are the paths taken by the vortices as they are shed and convect downstream. A gradual decrease in the magnitude of the rms density fluctuation occurs with stream-wise distance along these paths. This is due to the decrease in vortex

strength with increasing distance from the cylinder by numerical dissipation as the computational grid cell size increases. The precessing primary radial shock waves and the transient secondary radial shock waves described in this section are expected to locally increase the entropy. As cited in Chapter 2, Denton (1993) reports that a circumferential shock wave oscillation increases the time averaged entropy with respect to fixed radial shock waves. The radial shock waves cause the presence of 'wave drag', in addition to the pressure drag documented in Section 5.2.4.

5.2.6 Energy Separation in the Inviscid Vortex Shedding Cycle

A further source of entropy production arises from the redistribution of stagnation temperature and stagnation pressure in a vortex dominated wake flow, the time averaged result of which is the Eckert-Weise effect. The numerical time accurate analysis of this phenomenon at compressible Mach numbers is novel in the context of circular cylinder flows, based on the body of literature available to the author. Specifically, the current prediction extends the results of Kurosaka et al. (1987) at $M_\infty = 0.35$ to compressible circular cylinder flows. A further novel aspect of this analysis is the use of time accurate predictions to give an enhanced insight into the compressible Eckert-Weise effect, with respect to the time averaged experimental investigations of Eckert & Weise (1943) and Thomann (1959). The development of the stagnation temperature field in the near wake region is documented over one typical vortex shedding period $160.39 \leq tu_{1\infty}/D \leq 164.81$ in Figures 5.14 and 5.15. The stagnation temperature T_s is normalised using the free stream stagnation temperature $T_{s\infty}$. The non-dimensional stagnation temperature field in Figures 5.14 and 5.15 is phase synchronous with the density field development in Figures 5.10 and 5.11. Specifically, Figure 5.14 documents the growth of the anti-clockwise rotating vortex on the lower surface of the cylinder, over half of the vortex shedding cycle. Figure 5.15 then documents the shedding of this vortex and the development of a new vortex with clockwise rotation over the second half of the cycle. Localised regions of fluid with stagnation temperatures higher than the free stream condition are observed at the outer shear layer of each convecting vortex. One example region

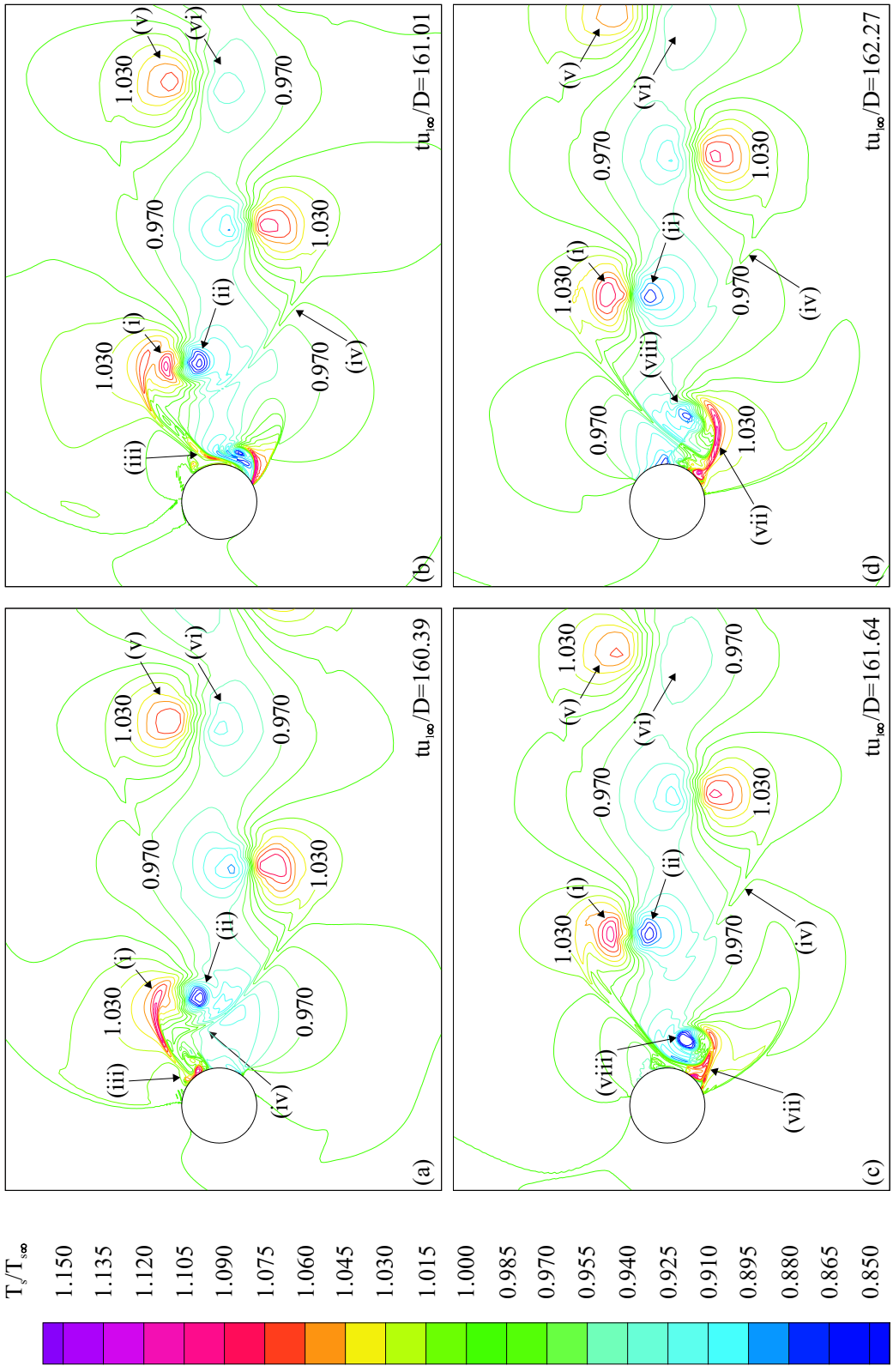

Figure 5.14: Instantaneous stagnation temperature contours over the first half of the vortex shedding cycle: $160.39 \leq tu_{1\infty}/D \leq 162.27$. $T_{s\,\max} = 1.150T_{s\infty}$, $T_{s\,\min} = 0.850T_{s\infty}$, $\Delta T_s = 0.015T_{s\infty}$. (i)-(ix) labelled flow features.

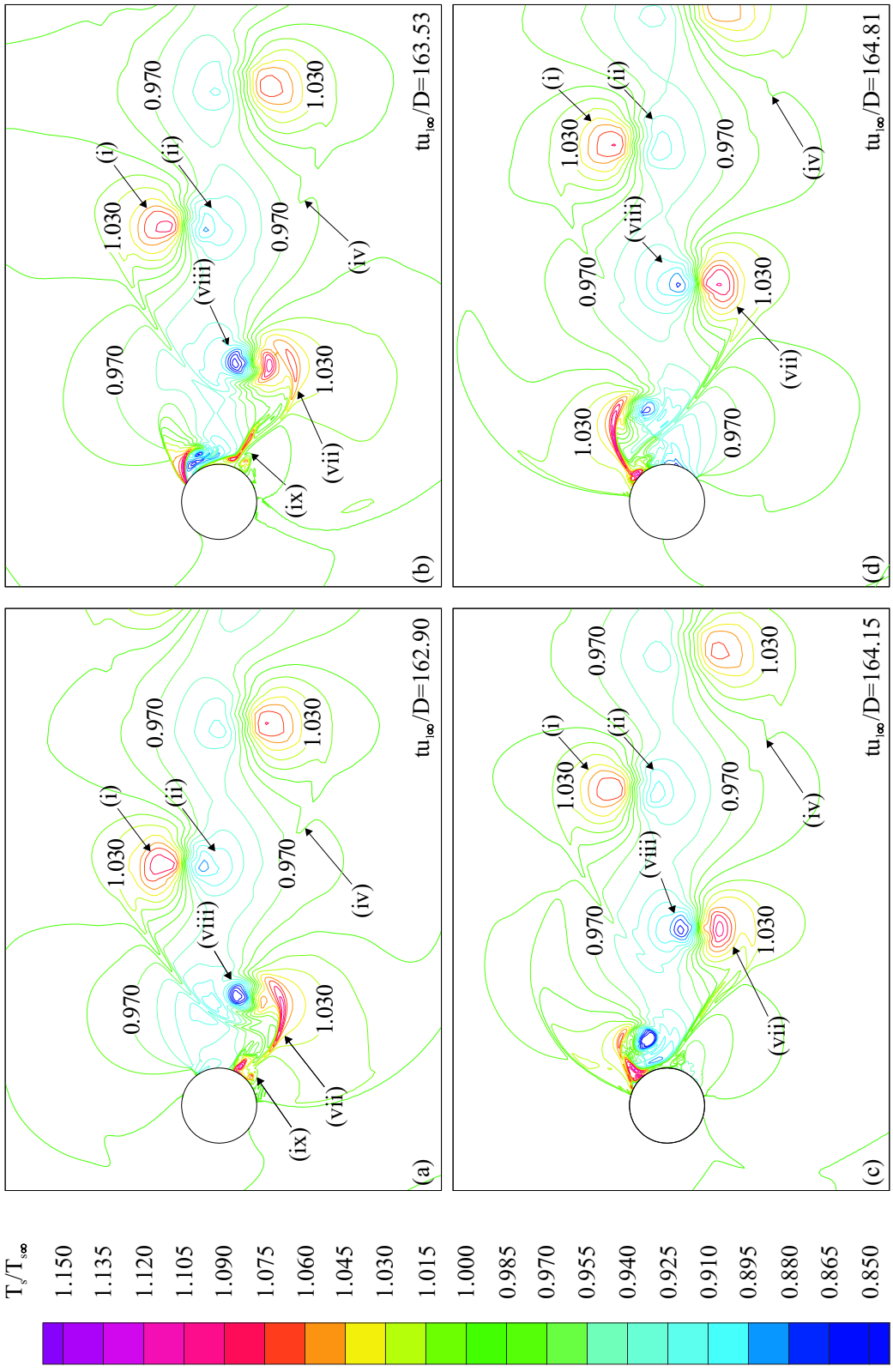

Figure 5.15: Instantaneous stagnation temperature contours over the second half of the vortex shedding cycle: $162.90 \leq tu_{1\infty}/D \leq 164.81$. $T_{s\,\max} = 1.150T_{s\infty}$, $T_{s\,\min} = 0.850T_{s\infty}$, $\Delta T_s = 0.015T_{s\infty}$. (i)-(ix) labelled flow features.

is labelled (i) in Figures 5.14 and 5.15. Localised regions of fluid with stagnation temperatures lower than the free stream condition are observed towards the centre of the wake with local minima located at each vortex, close to the wake centreline. An example region is labelled (ii) in Figures 5.14 and 5.15. These maxima (i) and minima (ii) are termed *hot spots* and *cold spots* respectively by Kurosaka et al. (1987) and Rona & Bennett (2001). The hot and cold spots pair either side of each vortex, along a stream-wise normal plane. These occur over both the vortex formation and vortex shedding phases, convecting downstream with each vortex. The location of the hot spots (i) and cold spots (ii) in Figure 5.14, relative to the convecting vortex cores in Figure 5.10, are consistent with the energy separation mechanism proposed by Kurosaka et al. (1987), as described in Section 2.6. The maximum stagnation temperature reported in Figures 5.14 and 5.15 is $T_{s\,\max} = 1.15T_{s\infty}$. The T_s minimum value is $T_{s\,\min} = 0.85T_{s\infty}$. The difference between the local T_s maximum and minimum varies over the vortex shedding period. The maximum stagnation temperature contour level in Figure 5.14(a) is, for example, $T_{s\,\max} = 1.105T_{s\infty}$. This hot spot, labelled (i) in Figure 5.14(a), is located in the outer shear layer of the clockwise rotating vortex being shed from the cylinder. For reference, the instantaneous stagnation temperatures reported in Kurosaka et al. (1987) vary between $T_{s\,\max} = 1.05T_{s\infty}$ and $T_{s\,\min} = 0.85T_{s\infty}$. A further local region of fluid with $T_{s\,\max} = 1.105T_{s\infty}$ is observed close to the surface of the cylinder in Figure 5.14(a). This region is labelled (iii). The two separated hot spots, (i) and (iii), are caused by the separation of a single hot spot at the entrainment of the far side shear layer (iv). The time resolved flow physics leading up to this situation can be interpreted from the end of the vortex shedding cycle in Figure 5.15(b-d), and is detailed later in this section.

A slight decay in the vortex induced heating and cooling occurs with stream-wise distance. The hot spot labelled (v) in Figure 5.14(a) has a maximum stagnation temperature of $T_s = 1.075T_{s\infty}$, displaying a temperature drop of under 3% from the hot spots labelled (i) and (iii) in this figure. The cold spot associated with this vortex, labelled as (vi) in Figure 5.14(a), has a minimum stagnation temperature of $T_s = 0.925T_{s\infty}$. This value is around 8.8% higher than the value of $T_s = 0.85T_{s\infty}$

observed in the cold spot labelled (ii) in this figure. A shear layer of fluid stretches between the clockwise rotating vortex, located between (i) and (ii), and the anti-clockwise rotating vortex immediately downstream. This shear layer is labelled (iv) in Figure 5.14(a). The shear layer is produced by a competing entrainment between the successive clockwise and anti-clockwise rotating vortices and constitutes a region of entropy production. The shear layer (iv) stretches as the two vortices continue to rotate in opposite directions with downstream distance.

As the flow progresses in time from Figure 5.14(a), a new vortex of anti-clockwise rotation grows at the cylinder surface. This anti-clockwise rotating vortex eventually starts to entrain fluid from the separated shear layer on the upper surface of the cylinder, as documented in Figure 5.14(b). A significant separation of the stagnation temperature is observed around the growing vortex, even in the early stages of the vortex formation. The maximum stagnation temperature contour level in Figure 5.14(b) is $T_{s\,\max} = 1.15T_{s\infty}$. This is located in the outer shear of the growing vortex. The cold spot associated with this vortex has a stagnation temperature of $T_s = 0.865T_{s\infty}$. The lowest stagnation temperature in Figure 5.14(b) ($T_{s\,\min} = 0.85T_{s\infty}$) is located at (ii). The stagnation temperature in Figure 5.14(b-c) shows an increase close to the shock induced shear layer separation. This implies an influence of the radial shock wave on the magnitude and location of heating around the growing vortex. As documented in Rona & Bennett (2001), the supersonic region upstream of the radial shock wave on the lower surface of the cylinder in Figure 5.14(b) restricts the transport of heat from the outer shear layer of the growing vortex. It is stressed that this stagnation temperature rise is not caused by the air compression across the shock wave but rather to a reduction in heat transport due to the oncoming supersonic region. A large stagnation temperature gradient therefore exists across this radial shock wave. This is evident in Figure 5.14(b) by the close spacing of the stagnation temperature contours at this radial shock wave. The partial insulation of the hot spot (vii) by the upstream shock wave is further compounded by the appearance of the transient secondary radial shock wave that forms between the growing vortex and the cylinder surface. This secondary shock

wave, which is labelled (vii) in Figure 5.10(b-d), further insulates the hot spot from the cross-wake transport of heat. This is evident at (vii) in Figure 5.14(c). Heating in this region is also aided by the cross-wake convection of the hot spot labelled (iii) in Figure 5.14(a-b). This region, which is transported across the wake with the entrainment of the far side shear layer, cools slightly approaching the growing vortex and is transported between the vortex and the cylinder into the region insulated by the radial shock waves. As the far side shear layer is entrained by the vortex, the region of raised stagnation temperature (vii) at the anti-clockwise rotating vortex is stretched, as shown in Figure 5.14(d). The entrainment of the far side shear layer divides this hot region into two separate hot spots. These two isolated hot spots are labelled (vii) and (ix) in Figure 5.15(a-b). The first hot spot (vii) is convected with the vortex in the outer shear layer. The second hot spot (ix) is cut off from the vortex by the entrained shear layer and remains close to the surface of the cylinder. This mechanism, which occurs as each vortex is shed from the cylinder, is also responsible for the two hot spots observed at (i) and (iii) in Figure 5.14(a).

This mechanism, which is studied for the first time in the compressible regime using a time accurate CFD approach, may be responsible for the double hot spot evident at around the same location in the subsonic prediction of Kurosaka et al. (1987). The presence of shock waves in the current prediction appears to be responsible for an enhancement in the magnitude of this hot spot, with respect to the subsonic prediction of Kurosaka et al. (1987). The development of the new clockwise rotating vortex in Figure 5.15(a-d) follows a similar pattern to the flow field development described for Figure 5.14(a-d).

Time averaging the near wake stagnation temperature field over an integer number of vortex shedding cycles yields the time averaged stagnation temperature field given in Figure 5.16. A region of reduced stagnation temperature is observed along the centre of the wake. The minimum stagnation temperature in this region is $T_{s\,\min} = 0.941 T_{s\infty}$. This local minimum, labelled (i) in Figure 5.16, corresponds to a stagnation temperature decrease of $17.7K$ with respect to the free stream condition. This region is located a distance of $x_1 = 0.15D$ from the rear surface of the cylinder.

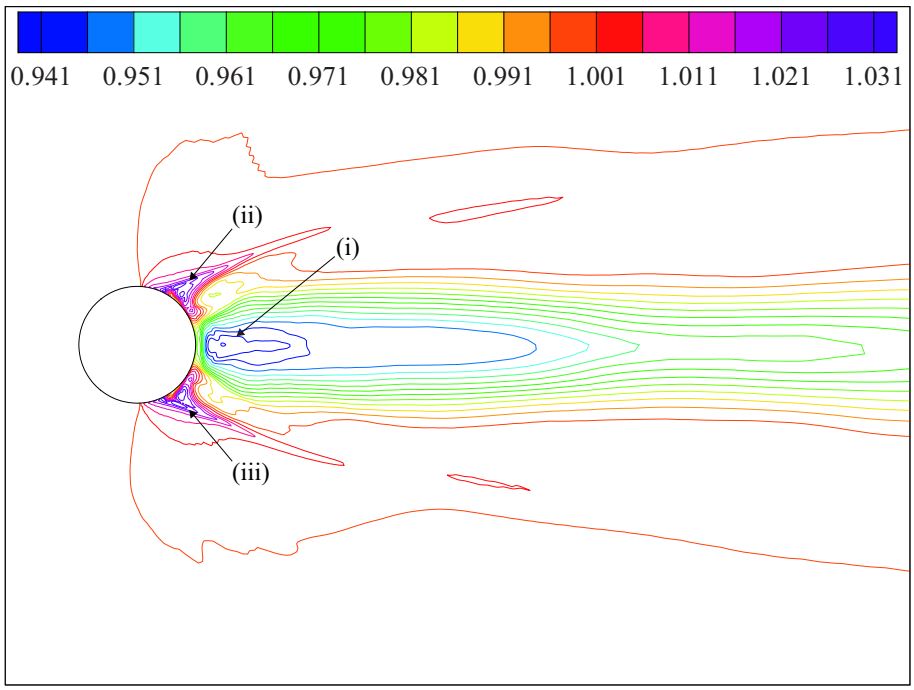

Figure 5.16: Time averaged stagnation temperature contours. $T_{s\,\max} = 1.031T_{s\infty}$, $T_{s\,\min} = 0.941T_{s\infty}$, $\Delta T_s = 0.005T_{s\infty}$.

Approaching the surface of the cylinder from this point, the stagnation temperature increases from $T_{s\,\min} = 0.941T_{s\infty}$ to $T_s = 0.981T_{s\infty}$. This increase is partly due to the cross-wake movement of the isolated hot spots, labelled (iii) and (ix) in Figures 5.14 and 5.15, as the far side shear layer is entrained. The downstream increase in stagnation temperature along the centre of the wake from (i) correlates well with the time averaged measurements of Thomann (1959).

The maximum stagnation temperature in Figure 5.16 is $T_{s\,\max} = 1.031T_{s\infty}$. This stagnation temperature maximum occurs close to the surface of the cylinder, at (ii) and (iii) in Figure 5.16, and equates to an increase of $9.3K$ above the free stream stagnation temperature. Extending around the base of the cylinder to $\theta = \pm 18°$, these regions are absent from the time averaged prediction of Kurosaka et al. (1987) at $M_\infty = 0.35$. These high stagnation temperature regions may therefore be augmented by the thermal shielding of the shear layers by the primary and transient shock waves. This effect is, however, thought to be enhanced by the inviscid surface condition and the absence of turbulence diffusion in the separated

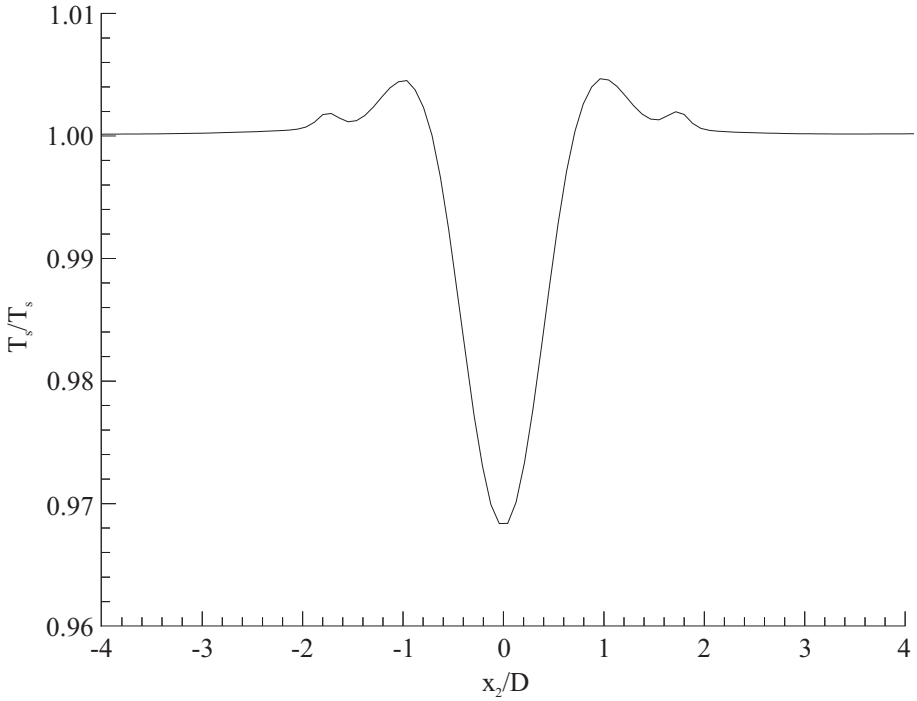

Figure 5.17: Stream-wise normal cross-section of the stagnation temperature in the wake of a circular cylinder at $x_1 = 6.5D$.

shear layers. This issue is investigated further in Section 5.3, where time dependent short-time averaged Navier-Stokes predictions are compared to these results.

Further downstream, regions of fluid with time averaged stagnation temperatures T_s greater than $T_{s\infty}$ remain at the outer edges of the wake. This is shown in the wake cross-section at $x_1 = 6.5D$ in Figure 5.17. The time averaged stagnation temperature rise along the edges of the wake remains significantly lower than the stagnation temperature in the time resolved hot spots of Figures 5.14 and 5.15. This decrease is due to the alternate convection of hot spots and cooler regions along the wake edges. These hot spots and cooler regions are associated with the passing of each near-side and far-side vortex respectively. The maximum stagnation temperature in Figure 5.17 is $T_{s\,\max} = 1.004T_{s\infty}$. Located at $x_2 = \pm 0.962D$, this corresponds to an increase of $1.2K$ above the free stream stagnation temperature. Secondary peaks are observed further away from the wake centreline at $x_2 = \pm 1.72D$. These secondary peaks result from the intense shearing of fluid between successive vortices. A time averaged region of stagnation temperature below the free stream condition is also

shown, falling to around $T_s = 0.968T_{s\infty}$ at $x_2 = 0$. This represents a local cooling of around $9.6K$ from the free stream condition.

Kurosaka et al. (1987) suggest that the stagnation pressure field in the incompressible wake downstream of a circular cylinder exhibits a pattern analogous to the stagnation temperature field. This study extends the proposal of Kurosaka et al. (1987) to the time accurate stagnation pressure field in a $M_\infty = 0.6$ circular cylinder wake. These predictions are shown in Figures 5.18 and 5.19. Eight contour plots document the development of the stagnation pressure field over one complete vortex shedding cycle, in the range $160.39 \leq tu_{1\infty}/D \leq 164.81$. The phases of flow development reported in Figures 5.18 and 5.19 correspond to the stagnation temperature and static density field development given in Figures 5.14-5.15 and Figures 5.10-5.11. The predicted stagnation pressure field shows a similar pattern to that of the stagnation temperature field. Regions of stagnation pressure higher than the free stream condition occur in localised regions at the edges of the wake, for example (i) and (iii). Localised regions of stagnation pressure lower than the free stream condition are located close to the wake centreline, for example (ii) and (iv). A close examination of the stagnation pressure field indicates that the stagnation pressure minima occur close to the vortex cores. The low pressure vortex cores augment the vortex-induced stagnation pressure redistribution. Shock waves also act to locally decrease the stagnation pressure. The high p_s regions at the edges of the wake, where $p_s > p_{s\infty}$, exhibit a maximum of $p_s = 1.2p_{s\infty}$ at the regions labelled (i) and (iii). The increase in stagnation pressure during the formation of new vortices, close to the surface of the cylinder, is limited by a decrease in the stagnation pressure as the fluid passes through the radial shock waves. This results in a stagnation pressure gradient across the shock wave, which may locally increase the vorticity of the shock-induced separated shear layers.

Time averaging the unsteady stagnation pressure field over an integer number of cycles gives the low stagnation pressure wake in Figure 5.20. Stagnation pressure minima occur either side of the wake centreline, close to the surface of the cylinder. These stagnation pressure minima result from the formation and growth of vortices

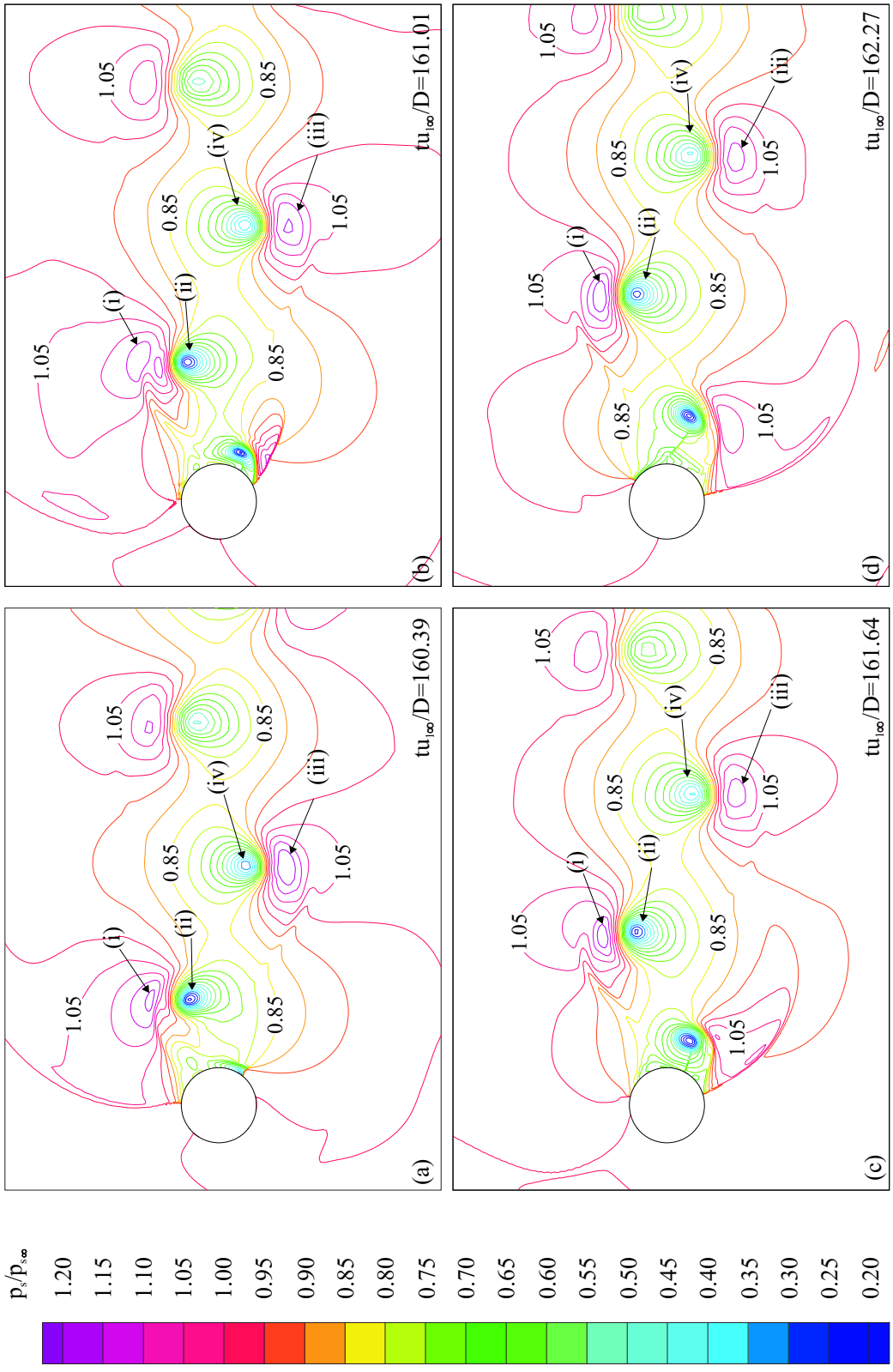

Figure 5.18: Instantaneous stagnation pressure contours over the first half of the vortex shedding cycle: $160.39 \leq tu_{1\infty}/D \leq 162.27$. $p_{s\,\max} = 1.2p_{s\infty}$, $p_{s\,\min} = 0.2p_{s\infty}$, $\Delta p_s = 0.05p_{s\infty}$. (i)-(iv) labelled flow features.

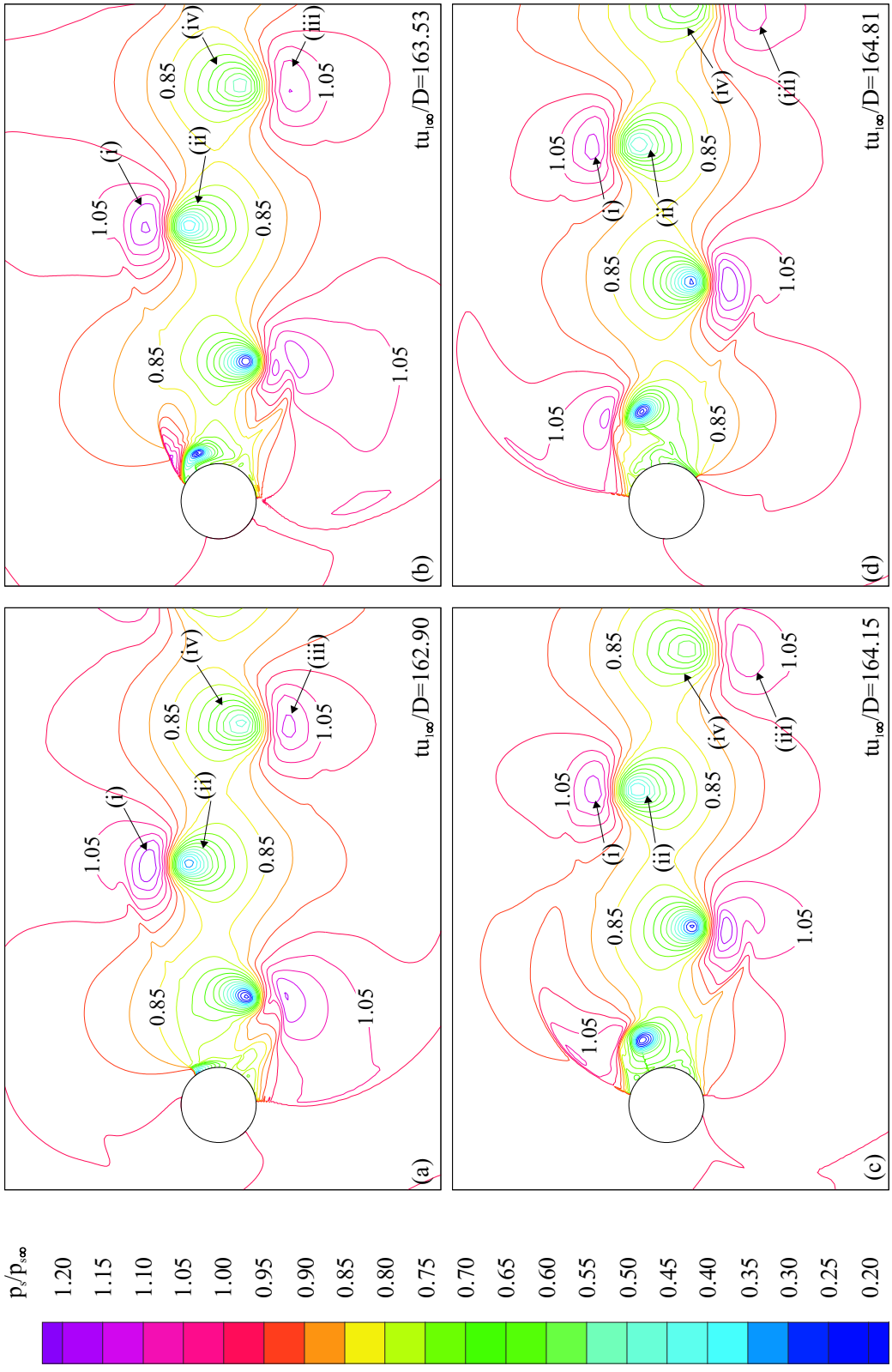

Figure 5.19: Instantaneous stagnation pressure contours over the second half of the vortex shedding cycle: $162.90 \leq tu_{1\infty}/D \leq 164.81$. $p_{s\,\max} = 1.2p_{s\infty}$, $p_{s\,\min} = 0.2p_{s\infty}$, $\Delta p_s = 0.05p_{s\infty}$. (i)-(iv) labelled flow features.

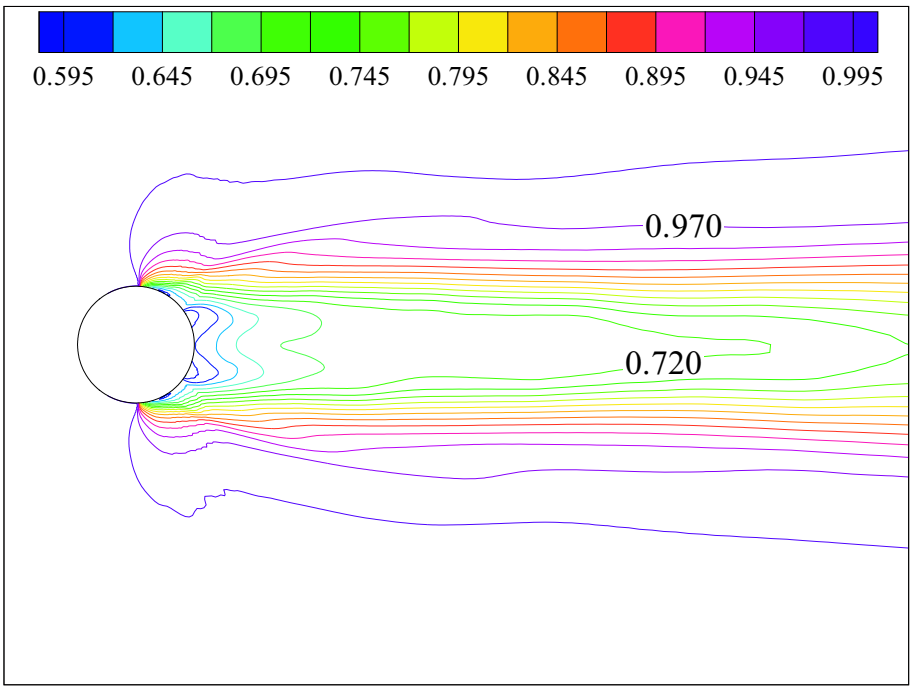

Figure 5.20: Time averaged stagnation pressure contours. $p_{s\,\max} = 0.995p_{s\infty}$, $p_{s\,\min} = 0.595p_{s\infty}$, $\Delta p_s = 0.025p_{s\infty}$.

from each side of the cylinder over each vortex shedding cycle. The alignment of the vortex centres during the formation and initial shedding phases are identified in the stagnation pressure contours either side of the wake centreline in Figure 5.20. Further downstream, numerical diffusion decreases the strength of the vortices and a gradual recovery of the stagnation pressure is observed with downstream distance. The time averaged stagnation pressure then falls to a local minimum at the wake centreline, $x_1 = 0$. The time averaged stagnation pressure deficit in the wake covers a significantly wider transverse distance with respect to the time averaged stagnation temperature field. The augmented stagnation temperature regions along the edges of the wake are observed as regions of stagnation pressure deficit in Figure 5.20. These time averaged results highlight the influence of the low stagnation pressure regions along the edges of the time resolved wake, between the local stagnation pressure maxima at each vortex.

A cross-section of the time averaged stagnation pressure wake distribution at a stream-wise distance of $x_1 = 6.5D$ is shown in Figure 5.21. The low pressure wake

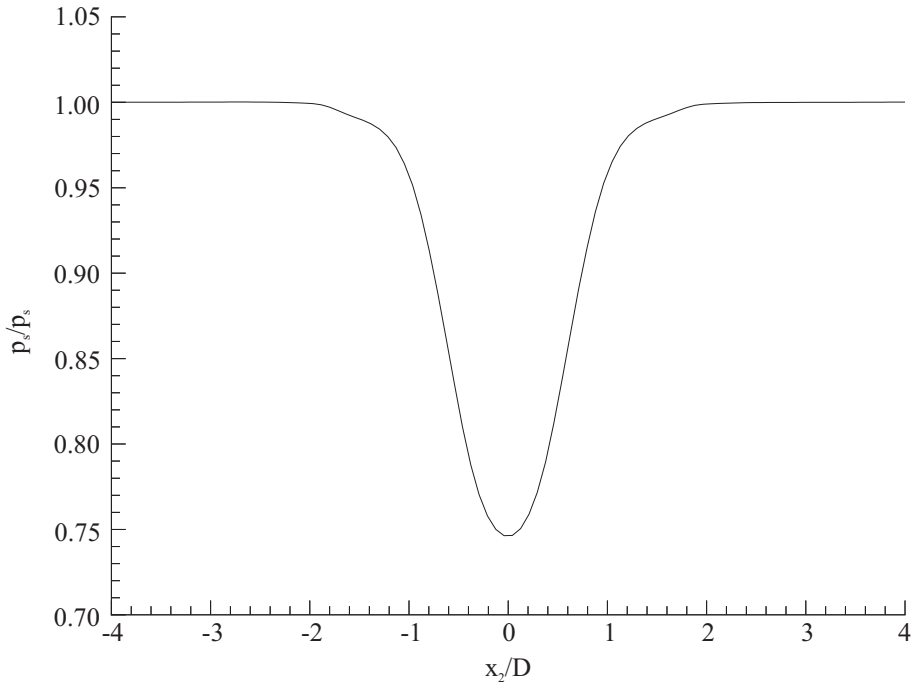

Figure 5.21: Stream-wise normal cross-section of the time averaged stagnation pressure across a circular cylinder wake at $x_1 = 6.5D$.

centre falls to a time averaged minimum of around $p_s = 0.745 p_{s\infty}$ at $x_2 = 0$. The absence of a time averaged stagnation pressure rise above the free stream condition is evident in this figure, as is the wide stagnation pressure deficit, which covers the region $-2D \leq x_2 \leq 2D$.

While the stagnation temperature field exhibits a central low T_s wake sided by two higher temperature bands, the stagnation pressure field shows only a wide wake of reduced p_s with no augmented side bands. Local differences in the T_s and p_s fields constitute regions of entropy production. The specific entropy is estimated as

$$s \;=\; c_p \ln\left(\frac{T_s}{T_{s\infty}}\right) - R \ln\left(\frac{p_s}{p_{s\infty}}\right), \tag{5.4}$$

where c_p is the specific heat at constant pressure, $c_p = 1005 J/kgK$, R is the specific gas constant, $R = 287 J/kgK$, and $s_\infty = 0$. A time sequence of eight entropy contour plots, equally spaced over the vortex shedding cycle, are given in Figures 5.22 and 5.23. Specific entropy s is normalised using the specific gas constant, $R = 287 J/kgK$. Increases in entropy occur as the local supersonic fluid is

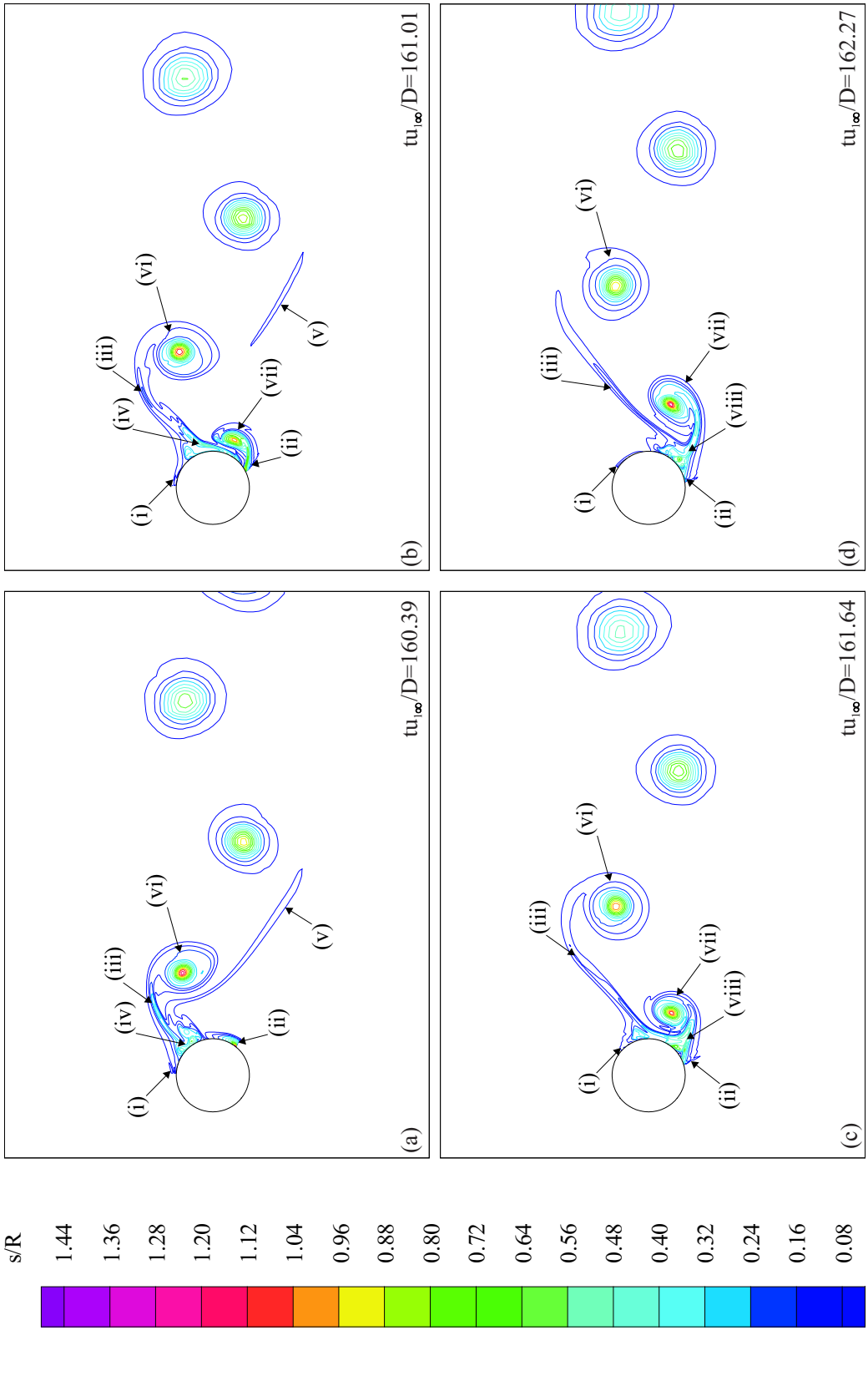

Figure 5.22: Instantaneous entropy contours over the first half of the vortex shedding cycle: $160.39 \leq tu_{1\infty}/D \leq 162.27$. $s_{\max} = 1.44R$, $s_{\min} = 0.08R$, $\Delta s = 0.08R$, $s_\infty = 0$. (i)-(viii) labelled flow features.

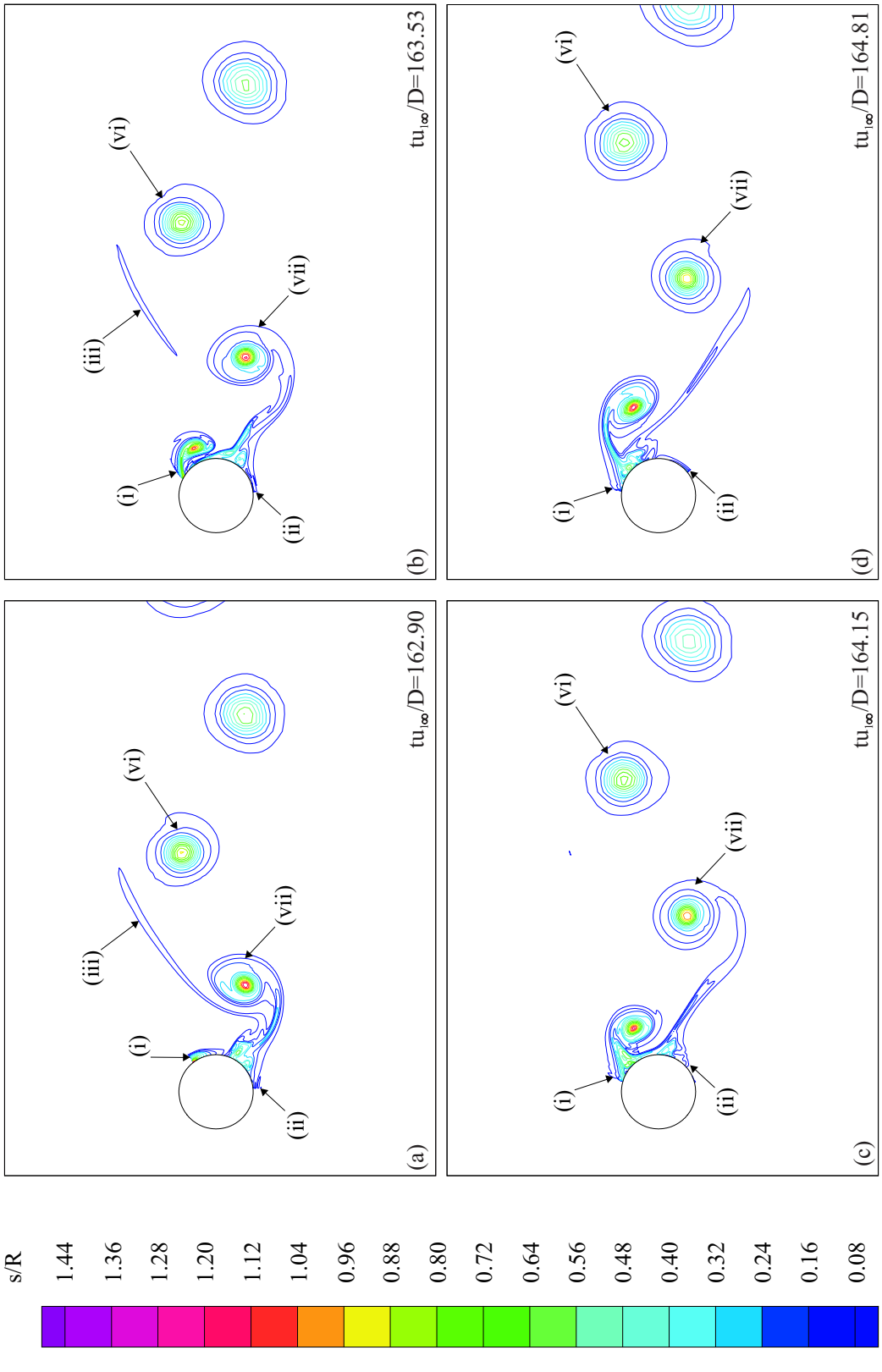

Figure 5.23: Instantaneous entropy contours over the second half of the vortex shedding cycle: $162.90 \leq tu_{1\infty}/D \leq 164.81$. $s_{\max} = 1.44R$, $s_{\min} = 0.08R$, $\Delta s = 0.08R$, $s_\infty = 0$. (i)-(viii) labelled flow features.

recompressed by the unsteady radial shock waves. The recompressed fluid immediately downstream of each shock wave is labelled (i) and (ii) respectively for the upper and lower radial shock waves in Figures 5.22 and 5.23. This increase in entropy determines the upstream extent of the specific entropy contours on the upper (i) and lower (ii) surfaces in Figures 5.22 and 5.23. The strong upstream moving radial shock waves and the weaker downstream moving radial shock waves are qualitatively evident from the relative radial extent of the specific entropy contours at (i) and (ii) over the vortex shedding cycle. Downstream of the cylinder, the low pressure vortex cores are highlighted as regions of entropy production. The low stagnation pressure in these vortex cores is not similarly highlighted as a region of stagnation temperature minimum. The entropy contours therefore clearly define the distinct alternating pattern of the von Kármán vortex street. From an analysis of these convecting vortex cores over the vortex shedding cycle, an approximate vortex convection velocity of $u_{1v} = 0.69u_{1\infty}$ is calculated. In Figure 5.22(a), a further region of increased specific entropy is highlighted between the radial shock wave at (i) and the clockwise rotating vortex (vi). This entropy producing region is defined along the thin shearing layer of fluid between the cylinder surface and the outer edge of the growing vortex. Two distinct regions of localised specific entropy maxima are evident in this shear layer. These regions, labelled (iii) and (iv) in Figure 5.22(a), correspond approximately to the two isolated stagnation temperature maxima labelled (i) and (iii) in Figure 5.14(a). Similar regions of shearing flow extend between each downstream pair of successive vortices, for example (v) in Figure 5.22(a). The iso-entropy lines in Figure 5.22(a-c) clearly document the cross-wake entrainment of the separated shear layer, labelled (iii), to the opposite side of the wake by the anti-clockwise rotating vortex (vii). Also evident in Figure 5.22(a-b) is the cross-wake transport of the hot spot labelled (iii) in Figure 5.14(a-b) by the entrainment of the shear layer. This is evident by following the local specific entropy maximum (iv) over Figure 5.22(a-c). The transient radial shock wave, extending between the surface of the cylinder and the anti-clockwise rotating vortex (vii), then appears as a source of additional entropy in Figure 5.22(c). The recompressed fluid behind this

transient shock wave is labelled (viii) in Figure 5.22(c-d). Figure 5.23(a-d) documents the shedding of this vortex (vii) and the roll up of the shear layer entrained from the far side, creating a stretched shearing layer of fluid between the convecting vortices labelled (vi) and (vii).

5.2.7 Summary

The results presented in this section document the development of an inviscid, compressible model flow around a circular cylinder, from a uniform $M_\infty = 0.6$ flow field condition, to a self-sustained, periodic vortex shedding condition. The current prediction shows a satisfactory correlation with published inviscid predictions at the same free stream Mach number. Possible areas for improvement of the current correlation with published measurements, through the subsequent introduction of a turbulence model, are highlighted. Energy separation in the von Kármán vortex street, evident as a redistribution of the stagnation enthalpy, temperature and pressure, is predicted by the inviscid numerical model on a time accurate and time averaged basis. This further substantiates the hypothesis that energy separation is predominantly a convective phenomenon. The prediction highlights hot spots of stagnation temperature greater than the free stream condition at the edges of the wake. Localised cold spots, of lower stagnation temperature than the free stream condition, are predicted at the wake centre. The stagnation temperature maxima and minima show a good overall correlation with the subsonic predictions of Kurosaka et al. (1987). Additional compressible effects are highlighted in the current prediction. A similar redistribution of the stagnation pressure is predicted in the time resolved and time averaged wake. Localised regions of stagnation pressure higher than the free stream condition are observed at the outer shear layer of each downstream moving vortex. Localised regions of stagnation pressure lower than the free stream condition are also predicted close to the wake centreline at each vortex. The stagnation pressure rise at the outer edge of each convecting vortex in the time accurate prediction is absent in the time mean prediction. This is attributed to the stagnation pressure deficit between each convecting vortex, reducing the overall stag-

nation pressure at the edges of the wake on a time averaged basis. Energy separation in the near wake flow is highlighted as increasing the overall entropy downstream of the circular cylinder. Additional regions of entropy production are highlighted in the vortex cores, along the shear layers and downstream of the fluctuating radial shock waves.

5.3 Turbulent Circular Cylinder Flow Prediction

5.3.1 Numerical Model Specifications

A turbulent circular cylinder prediction at a free stream Mach number of $M_\infty = 0.6$ and a Reynolds number, based on the cylinder diameter D, of $Re_D = 6.87 \times 10^5$ is presented in this section. The initial flow field for the turbulent prediction is primed using the self-sustained inviscid vortex shedding prediction documented in Section 5.2. To match the Reynolds number regime in concurrent tests by Ackerman (2005) at $M_\infty = 0.6$, the cylinder model diameter is increased to $D = 47.41 \times 10^{-3} m$. This increase in cylinder diameter is achieved by uniformly scaling the computational domain defined in the inviscid prediction. By uniformly scaling the computational domain, the relative dimensions in Figure 5.1 are preserved and the relative computational cell sizes are maintained. The volume averaged state variables vector ($\boldsymbol{U}$ in Equation 3.19) is a vector of intensive properties, independent of cell volume. By preserving the relative computational cell dimensions, the volume averaged state variables from the inviscid prediction can be directly imposed onto the updated mesh. The inviscid prediction is then time marched for a short number of vortex shedding cycles. This is carried out to identify any change in the inviscid flow prediction, resulting from minor rounding errors in the scaling process. The current inviscid prediction, however, demonstrates no appreciable flow change after implementing the scaled grid.

In addition to priming the turbulent field with the inviscid prediction, initial estimates for the specific turbulence kinetic energy k and the specific turbulence dissipation rate ω are required. Free stream values of $k_\infty = 0.1 m^2/s^2$ and $\omega_\infty = 5221 Hz$

are imposed uniformly throughout the domain at the start of the turbulent computation. These free stream values give a turbulence intensity, $Tu = \sqrt{2k_\infty/3u_\infty^2}$, of $Tu = 0.13\%$, which models a quiet wind tunnel. The value of ω_∞ gives a ratio of free stream laminar viscosity μ_∞ to eddy viscosity, $\mu_{t\infty} = \rho_\infty k_\infty/\omega_\infty$, of $\mu_\infty/\mu_{t\infty} = 0.725$. As a guideline, this value for $\mu_\infty/\mu_{t\infty}$ is within the range of free stream values used in the transonic RAE 2822 aerofoil prediction of Bardina et al. (1997) using the $k-\omega$ turbulence model. This value for $\mu_\infty/\mu_{t\infty}$ is also within the range used in the transonic turbine cascade prediction of Currie & Carscallen (1998), for an estimated turbulence intensity of $Tu = 0.1\%$.

From the circular cylinder literature review in Section 2.5, the modelled free stream Reynolds number $Re_D = 6.87 \times 10^5$ places the turbulent prediction in the low super-critical Reynolds number regime. This regime extends over the range $(0.5 \sim 1.0) \times 10^6 \leq Re_D \leq (3.4 \sim 6.0) \times 10^6$. At low Mach numbers, the flow is characterised by an upstream movement of the boundary layer transition location with increasing Reynolds number and free stream turbulence intensity, as discussed in Zdravkovich (1997).

A frequency analysis of the time resolved circular cylinder surface pressure measurements by Ackerman (2005) at $M_\infty = 0.6$ and $Re_D = 6.86 \times 10^5$, however, indicates a shock induced separation of the boundary layer before the onset of transition. To accommodate laminar boundary layers in the current prediction, the no-slip boundary condition of Section 3.9.8 is defined at the cylinder surface. All other boundary conditions for the turbulent prediction are defined as in Figure 5.1.

In the absence of published boundary layer measurements at the current free stream conditions, a compressible laminar boundary layer analysis has been undertaken for the circular cylinder using the integral method of Gruschwitz (1950) to estimate the boundary layer height. This integral method is described in a number of standard texts, including Schlichting (1979) and White (1991). In the integral method of Gruschwitz (1950), the distribution of density, velocity, viscosity and static temperature are required at the boundary layer edge. These are satisfied in the present circular cylinder analysis by sixth order polynomial approximations to

the time averaged inviscid cylinder surface distribution, computed on the turbulent cylinder scale grid. From the method of Gruschwitz (1950), estimates for the boundary layer integral parameters, the skin friction coefficient and the surface normal velocity profiles are obtained along the upstream facing cylinder surface. This preliminary boundary layer analysis, which is not documented here, indicates a possible under-resolution of the laminar boundary layer by the 400×200 grid used in the inviscid prediction.

Based on this analysis, the Adaptive Mesh Refinement (AMR) method is used to increase the grid resolution with two levels of AMR refinement (levels 0 and 1). The level 0 grid, which covers the whole computational domain, is the grid of 400×200 internal cells scaled up from the inviscid prediction. Level 1 locally increases the grid resolution by a factor of three from this level 0 grid. Level 1 is adaptively defined around flow features of significant density gradient and is of equivalent resolution to a single grid of 1200×600 internal cells. To ensure the boundary layer is resolved by level 1 at all points around the cylinder, the first 25 cell rows above the cylinder surface at level 0 are explicitly flagged for refinement around the circumference of the cylinder. This distance is considered sufficient to completely resolve the attached boundary layer to separation, based on the preliminary laminar boundary layer analysis. The remaining cells at level 0 are autonomously flagged by the AMR scheme based on the density gradient between contiguous cells, as described in Section 3.10.2. The AMR scheme adaptively refines the fluctuating shock waves, the separated shear layers and the growing vortices in the near wake region.

5.3.2 Turbulent Circular Cylinder Validation

The turbulent flow field at level 0 is time marched from the initial conditions described in this section in constant time steps of $\Delta t = 2.15 \times 10^{-4} D/u_{1\infty}$. The level 1 flow field is therefore time marched in constant time steps of $\Delta t = 7.2 \times 10^{-5} D/u_{1\infty}$. An initial transient period of flow develops at the start of the computation as the specific turbulence kinetic energy k and the specific turbulence dissipation rate ω fields develop from the uniformly imposed free stream conditions.

After the initial transient period, a self sustained vortex shedding is again defined downstream of the cylinder. The boundary layer displacement thickness increases the effective diameter of the cylinder. In addition to the pressure drag and wave drag that are present in the inviscid prediction, the development of the boundary layer momentum thickness leads to a further drag contribution, that of skin friction drag. The relative contribution of skin friction to the total drag represents a small proportion at high Reynolds numbers. For example, measurements by Achenbach (1968) are used to document the proportion of skin friction drag to the total drag for a circular cylinder in cross-flow at $6 \times 10^4 \leq Re_D \leq 5 \times 10^6$, $Tu = 0.7\%$ and $M_\infty \leq 0.1$. Achenbach (1968) shows that the skin friction drag constitutes less than 2% of the total drag over this Reynolds number range. The wave drag contribution, which is caused by the sudden increase in static pressure across each shock wave, is considered at the current free stream conditions to be significantly lower than the contribution of pressure drag. The contribution of wave drag increases significantly at higher Mach numbers and constitutes the largest contribution at supersonic free stream Mach numbers, as reported in Douglas et al. (1995).

The time resolved pressure drag coefficient, which represents the largest contribution to total drag at the modelled free stream conditions, is documented for the turbulent prediction in Figure 5.24. The drag coefficient is computed by integrating the surface pressure coefficient around the cylinder using Equation 5.2. Eleven complete cycles of a coherent pressure drag fluctuation are documented over the interval $275 \leq tu_{1\infty}/D \leq 305$. As in the inviscid prediction of Figure 5.8, the drag coefficient rises to a maximum value immediately preceding the shedding of vortices from each side of the cylinder. The introduction of turbulence and the presence of a no-slip surface condition alters the drag coefficient waveform in Figure 5.24 from the inviscid prediction of Figure 5.8. The inviscid drag coefficient history is characterised by a single maximum at each vortex shedding event. A further transient contribution leads to the presence of additional localised extrema within each vortex shedding cycle. The relative location and magnitude of these local extrema change on a cycle-to-cycle basis. The single peak maxima in the inviscid drag coefficient

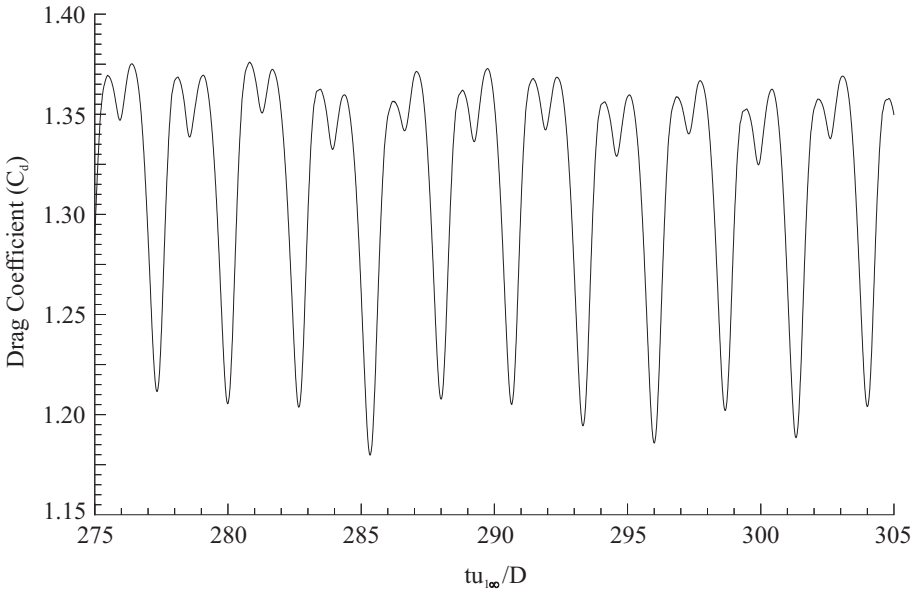

Figure 5.24: Turbulent pressure drag coefficient history over the time interval $275 \leq tu_{1\infty}/D \leq 305$.

are replaced in Figure 5.24 by double peaked maxima, synchronised to each vortex shedding event. The relative magnitude and temporal spacing between these two peaks also varies on a cycle-to-cycle basis. This variation follows a similar unsteady fluctuation in the drag coefficient amplitude over the documented time interval. A similar unsteady drift in the inviscid drag coefficient and base pressure traces is documented in Sections 5.2.3 and 5.2.4. A reduction in the drag coefficient amplitude fluctuation is however observed in the turbulent drag coefficient with respect to the inviscid prediction of Figure 5.8. This peak-to-peak fluctuation is quantified, along with the maximum, minimum and time averaged drag coefficients in Table 5.5.

Comparing the average drag coefficient from the turbulent prediction with the previous inviscid prediction shows that an increase of 2.57% accompanies the introduction of turbulence modelling and the no-slip surface condition. A similar increase is observed in the minimum C_d average value, which increases by 1.36%. A decrease of 3.26% is observed in the turbulent C_d maximum. Table 5.5 also lists time averaged experimental drag coefficients by Ackerman (2005) and Murthy & Rose (1978), as well as the viscous prediction by Shang (1982). For comparison, the inviscid predictions of Botta (1995) and Pandolfi & Larocca (1989) are also

Source	Max. C_d	Average C_d	Min. C_d
Current $k-\omega$ prediction	1.364 ± 0.012	1.317	1.196 ± 0.015
Ackerman (2005) (2000 case)	–	1.67	–
Ackerman (2005) (2002 case)	–	1.36	–
Murthy & Rose (1978)	–	$1.37 - 1.56$	–
Shang (1982)	–	1.27	–
Current inviscid prediction	1.41 ± 0.06	1.284	1.18 ± 0.05
Botta (1995)	1.5 ± 0.05	1.3 ± 0.05	1.1 ± 0.05
Pandolfi & Larocca (1989)	1.5 ± 0.03	1.38 ± 0.03	1.25 ± 0.03

Table 5.5: Circular cylinder drag coefficient comparison. Measurements of Ackerman (2005): $M_\infty = 0.6$, $Re_D = 6.86 \times 10^5$ (2000 case), $M_\infty = 0.6$, $Re_D = 6.75 \times 10^5$ (2002 case). Measurements of Murthy & Rose (1978) at $M_\infty = 0.6$, $Re_D = 0.83 \times 10^5$, 1.66×10^5 and 5×10^5. Prediction of Shang (1982) at $M_\infty = 0.6$, $Re_D = 1.67 \times 10^5$.

tabulated.

The tabulated measurements of Ackerman (2005) and Murthy & Rose (1978) are defined at a common free stream Mach number of $M_\infty = 0.6$. The free stream Reynolds number in these experiments, however, vary between $Re_D = 0.83 \times 10^5$ and $Re_D = 6.86 \times 10^5$. At $M_\infty = 0.6$, the drag coefficient is less sensitive to the free stream Reynolds number and free stream turbulence intensity than at lower Mach numbers. This insensitivity arises from the presence of intermittent radial shock waves. As documented in Section 2.5, these shock waves fix the separation location of laminar boundary layers, induce transition in separating laminar shear layers and can significantly shorten the attached length of turbulent boundary layers, downstream of the shock wave. This shock induced boundary layer separation prevents the 'drag crisis' that is documented in Zdravkovich (1997) at lower free stream Mach numbers.

A substantial variation is still evident, however, in the measured drag coefficients in Table 5.5. The time averaged C_d measurements of Ackerman (2005) change between two separate wind tunnel runs at similar free stream Reynolds numbers. Ackerman (2005) reports that these changes are caused by a change in the arrangement of surface pressure transducers around the cylinder. A single pressure transducer is used in the 2000 series measurements. This is replaced in the 2002 series mea-

surements by four pressure transducers, of larger diameter, equi-spaced around the circumference of the cylinder. Ackerman (2005) proposes that the increase in diameter of the pressure transducer is responsible for inducing transition upstream of the shock induced separation point. In short, Ackerman (2005) proposes that the 2000 series of experiments measure the development and shock induced separation of a laminar boundary layer at $M_\infty = 0.6$. The 2002 series therefore measure a transition of the boundary layer upstream the separation point and the shock induced separation of a transitional or turbulent boundary layer. The time averaged drag coefficient range reported in Murthy & Rose (1978) indicates a variation in C_d between three free stream Reynolds numbers of $Re_D = 0.83 \times 10^5,\ 1.66 \times 10^5$ and 5×10^5. The drag coefficient/Reynolds number correlation is not discernable at $M_\infty = 0.6$ from the graph provided by Murthy & Rose (1978). However, the drag coefficient variation in Murthy & Rose (1978) may also be attributable to a similar change in the boundary layer turbulence level upstream of the separation point. As expected, the change in drag coefficient with free stream Reynolds number in Murthy & Rose (1978) is significantly lower than is documented over the same Reynolds number range at subsonic Mach numbers by, for example, Zdravkovich (1997). The mean drag coefficient in the current turbulent prediction ($C_d = 1.317$) is below the tabulated measurements. Specifically, the turbulent prediction is 3.16% lower than the 2002 series measurements of Ackerman (2005) and 3.87% lower than the estimated minimum C_d value of Murthy & Rose (1978). As the average drag coefficient ($C_d = 1.317$) from the turbulent prediction is closer to the cited measurements ($1.37 \leq C_d \leq 1.67$) than the inviscid drag coefficient ($C_d = 1.284$), the turbulent prediction represents an improved approximation. In comparison with the laminar boundary layer measurements of Ackerman (2005) and the possible laminar boundary layer in Murthy & Rose (1978), the low predicted drag coefficient may indicate an under-resolution of the laminar boundary layer on the upstream facing cylinder surface.

To determine whether the close proximity of the turbulent prediction to the turbulent boundary layer drag coefficient of Ackerman (2005) and the lower bound of Murthy & Rose (1978) may result from the prediction of a turbulent boundary layer,

a posteriori turbulent boundary layer analysis is developed. As a minimum criterion, the laminar sublayer of a turbulent boundary layer must be resolved by at least ten computational cells in the surface normal direction. By calculating an approximate height for the laminar sublayer at the modelled free stream conditions, a coarse estimation of whether the laminar sublayer may be resolved by the AMR level 1 grid is possible. To the authors knowledge, no published compressible, turbulent boundary layer measurements of the laminar sublayer height are currently available for a circular cylinder at the modelled free stream conditions. In the absence of published measurements, a coarse approximation is computed from the incompressible circular cylinder boundary layer measurements of Patel (1969) at $Re_D = 5.01 \times 10^5$. In the experiment of Patel (1969), turbulent boundary layers develop from two surface mounted trip wires, of diameter $D_w = 6.67 \times 10^{-3} D$, placed at $\Delta\theta = \pm 45^\circ$ from the upstream stagnation point. Boundary layer integral parameters and surface normal velocity profiles are documented at a number of circumferential stations between $\Delta\theta = \pm 60^\circ$ and $\Delta\theta = \pm 100^\circ$ from the upstream stagnation point. The skin friction coefficient C_f is estimated in the current analysis based on the integral parameters documented in Patel (1969), along with the incompressible momentum integral equation. The skin friction is adjusted for compressibility through the general 'van Driest II' relation, according to Spalding & Chi (1964), and is used to compute the surface normal distance of $y^+ = 1$ for the current prediction. For this estimate, the state variable distribution along the cylinder surface from the inviscid prediction is used to approximate the boundary layer edge distribution. An outline of this analysis is presented in Appendix A.2. It is recognised that this analysis is based on a number of assumptions, including the application of the 'van Driest II' correlation to the circular cylinder flow, and is therefore of limited accuracy. This analysis also neglects the effects of pressure diffusion, which occurs upstream of each radial shock wave through the subsonic boundary layer region. This pressure gradient is expected to increase the actual laminar sublayer height with respect to the estimation. However, based on this analysis, at a circumferential distance of $\Delta\theta = 60^\circ$ from the upstream stagnation point, the surface normal height of the laminar sublayer edge

(assumed to be $y^+ = 10$) is approximately $x_n = 2.8 \times 10^{-4} D$. To resolve the laminar sublayer below $y^+ = 10$ with at least ten cells, assuming equi-spaced grid points in the laminar sublayer, the height of the first cell above the surface is required to be $x_n \leq 2.8 \times 10^{-5} D$. To resolve down to this level using the AMR scheme, six levels of refinement are required (levels 0 to 5) with a resolution increment of three between each level. Even with the AMR scheme efficiency, resolving down to this level represents a computationally demanding task with the current explicit scheme and is not possible within the time constraint of the current turbulent prediction.

The under-prediction of the mean drag coefficient to the turbulent boundary layer (2002) case of Ackerman (2005) is therefore thought to be caused by an under-resolution of a laminar boundary layer. An under-resolution of the laminar boundary layer would imply fewer surface normal cells falling within the subsonic region of the boundary layer. The pressure diffusion through the subsonic region of the laminar boundary layer, upstream of each shock wave, is therefore under-predicted. The result is a lower local static pressure and a higher predicted velocity, with respect to the measured boundary layer, upstream of each shock wave. The higher velocity predicted in the laminar boundary layer approaching the radial shock waves may also result in the laminar boundary layer supporting a greater static pressure rise across the shock wave before separating.

The lower static pressure approaching the shock wave and the delayed boundary layer separation would result in a surface pressure distribution and mean drag coefficient closer in form to the turbulent boundary layer measurements. For example, the pressure diffusion through the subsonic region of a boundary layer, upstream of an incident shock wave, is observed further upstream of the shock wave in a laminar boundary layer than in a turbulent boundary layer. Schlichting (1979) reports typical values for the length of boundary layer, upstream of an incident shock wave, effected by the shock wave presence as $100\delta_{99}$ for a laminar boundary layer and $10\delta_{99}$ for a turbulent boundary layer, where δ_{99} is the boundary layer thickness. Turbulent boundary layers can also support a greater pressure rise across an incident shock wave before separating, due to the enhanced diffusivity in the turbulent boundary

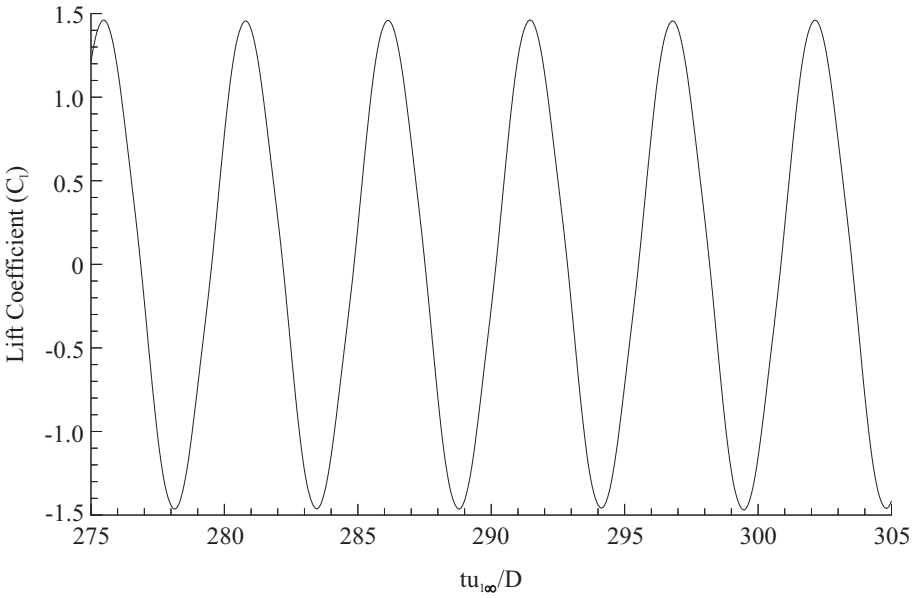

Figure 5.25: Lift coefficient history in the quasi-stationary vortex shedding regime.

layer. The result is a delay in the separation location of the turbulent boundary layer, downstream of the shock wave, with respect to a laminar boundary layer. To improve the boundary layer prediction, additional AMR levels are required. Due to the limited computational resources available to the author, a further refinement of the boundary layer with additional AMR levels is unfortunately not possible.

The primary objective of the turbulent circular cylinder prediction is an analysis of the redistribution of stagnation temperature and pressure in a turbulent cylinder wake. At the current compressible free stream Mach number, the vortex shedding mechanism in the near wake is relatively insensitive to the free stream Reynolds number and the boundary layer characteristics before separation for a circular cylinder. A time accurate study on the influence of turbulence production, turbulent heat transfer and small scale turbulence diffusion on the vortex shedding and energy separation mechanism, downstream of this cylinder, remains a feasible and valid objective.

The time accurate lift coefficient history from the turbulent prediction, over the time interval $275 \leq tu_{1\infty}/D \leq 305$, is shown in Figure 5.25. The lift coefficient is less sensitive to the transient cycle-to-cycle fluctuation observed in the time accurate drag coefficient over the same time interval. Approximately five and a half cycles of

a sinusoidal oscillation are documented. Each cycle corresponds to the shedding of a vortex from the upper and lower surfaces of the circular cylinder. The maximum and minimum lift coefficients, along with the associated cycle-to-cycle fluctuation, are quantified in Table 5.6. Maximum and minimum values for C_l are also tabu-

Source	Max. C_l	Min. C_l
Current $k-\omega$ prediction	1.46 ± 0.005	-1.46 ± 0.005
Current inviscid prediction	1.3 ± 0.1	-1.3 ± 0.1
Botta (1995)	1.2 ± 0.15	-1.2 ± 0.15
Pandolfi & Larocca (1989)	1.5 ± 0.15	-1.5 ± 0.15

Table 5.6: Circular cylinder lift coefficient comparison.

lated for the inviscid cylinder prediction of Section 5.2 and the inviscid predictions of Botta (1995) and Pandolfi & Larocca (1989). The average peak-to-peak amplitude in the turbulent prediction is 12.31% greater than the inviscid prediction of Section 5.2 and 21.67% greater than the inviscid prediction of Botta (1995). The peak-to-peak C_l amplitude in the turbulent prediction also remains 0.67% lower than the inviscid prediction of Pandolfi & Larocca (1989). The peak-to-peak fluctuation (± 0.005) for the turbulent prediction is significantly lower than all three inviscid predictions, mirroring the lower peak-to-peak drag coefficient fluctuation. Comparing the fluctuations in peak-to-peak lift and drag amplitude yields a significantly lower unsteady fluctuation for the lift coefficient. Specifically, the unsteady fluctuation in the turbulent lift coefficient is approximately 0.34% of the peak-to-peak lift coefficient amplitude. This compares with 16.07% for the drag coefficient waveform. The lower relative fluctuation in the lift coefficient highlights the most likely source of the unsteady cycle-to-cycle fluctuation as originating from the base of the circular cylinder, confirming the source of the unsteady fluctuation as the vortex shedding mechanism.

A Fourier analysis of the time accurate lift coefficient over an integer number of cycles yields a value for the vortex shedding frequency. The resulting Strouhal number for the turbulent prediction is compared with published measurements by Ackerman (2005) and Murthy & Rose (1978) in Table 5.7. The turbulent prediction

Source	Strouhal no.
Current $k-\omega$ prediction	0.187
Ackerman (2005) (2000 series)	0.175
Ackerman (2005) (2002 series)	0.176
Murthy & Rose (1978)	0.181
Shang (1982)	0.21
Current inviscid prediction	0.199
Botta (1995)	0.2
Pandolfi & Larocca (1989)	0.198

Table 5.7: Strouhal number comparison. Measurements of Ackerman (2005): $M_\infty = 0.6$, $Re_D = 6.86 \times 10^5$ (2000 series), $M_\infty = 0.6$, $Re_D = 6.75 \times 10^5$ (2002 series). Measurements of Murthy & Rose (1978) at $M_\infty = 0.6$, $Re_D = 0.83 \times 10^5 - 5 \times 10^5$. Prediction of Shang (1982) at $M_\infty = 0.6$, $Re_D = 1.67 \times 10^5$.

is also compared against the viscous prediction of Shang (1982), inviscid predictions by Botta (1995) and Pandolfi & Larocca (1989), and against the current inviscid prediction of Section 5.2. The introduction of a turbulence model and no-slip boundary condition in the numerical model improves the Strouhal number correlation with the cited measurements. The decrease in Strouhal number from $Str = 0.199$ in the inviscid prediction to $Str = 0.187$ in the turbulent prediction represents a reduction of 6.03%. This decrease accompanies an increase in the separated shear layer thickness due to the additional contribution of molecular and turbulence diffusion.

As discussed in Sections 2.3 and 5.2.4, Gerrard (1966) proposes that a balance exists between increases in shear layer thickness, or 'diffusion length', and the reduction in formation region length as the free stream Reynolds number or turbulence intensity is increased. This balance is proposed to result in an insensitivity of the Strouhal number to changes in these free stream parameters. This insensitivity is observed in the measured Strouhal numbers of Murthy & Rose (1978), which remain constant over the Reynolds number range $0.83 \times 10^5 \leq Re_D \leq 5 \times 10^5$. The decrease in Strouhal number between the current inviscid and turbulent predictions may therefore result from a relative imbalance between these two opposing mechanisms as the turbulence model is introduced. The resulting turbulent prediction is closer to the measured Strouhal numbers of Ackerman (2005) and Murthy & Rose (1978)

than for the current inviscid prediction. Specifically, the turbulent prediction is within 6.9% of the cited measurements, which vary by less than 3.5% with respect to each other.

5.3.3 Compressibility and the Turbulent Vortex Shedding Cycle

The drag coefficient, lift coefficient and Strouhal number indicate that introducing the $k-\omega$ turbulence model and imposing a no-slip surface condition provides a better physical approximation to the measured flow field development, with respect to the inviscid prediction. Time resolved static density iso-contours document the turbulent cylinder near wake development over one typical vortex shedding cycle in Figures 5.26(a-d) and 5.27(a-d). A series of eight instantaneous density iso-contour plots document the static density field over the normalised time interval $294.09 \leq tu_{1\infty}/D \leq 298.76$. Figure 5.26(a-d) documents the formation of an anti-clockwise rotating vortex from the lower surface of the cylinder. Figure 5.27(a-d) documents the shedding of this vortex and the formation of a new vortex, with clockwise rotation, from the upper surface of the cylinder. The turbulent density field development in these figures is approximately phase synchronous over the vortex shedding cycle with the inviscid density field development in Figures 5.10(a-d) and 5.11(a-d). The inviscid near wake density field development over a typical vortex shedding cycle is discussed in Section 5.2.5. The current discussion highlights modifications to this inviscid prediction through the introduction of the $k-\omega$ turbulence model and no-slip surface condition.

Figure 5.26(a) documents a stage in the vortex shedding cycle at the initial formation of an anti-clockwise rotating vortex, labelled (iii), from the lower side of the cylinder. Two radial shock waves close to the surface of the cylinder are labelled (i) and (ii) in this figure. These shock waves are similar in form to the radial shock waves described in the inviscid prediction. However, the radial shock wave labelled (i) on the upper surface of the cylinder is located upstream of $\theta = 90°$. In contrast, the radial shock waves do not appear upstream of $\theta = \pm 90°$ along the surface of the cylinder in the inviscid prediction. The precession of the radial shock waves

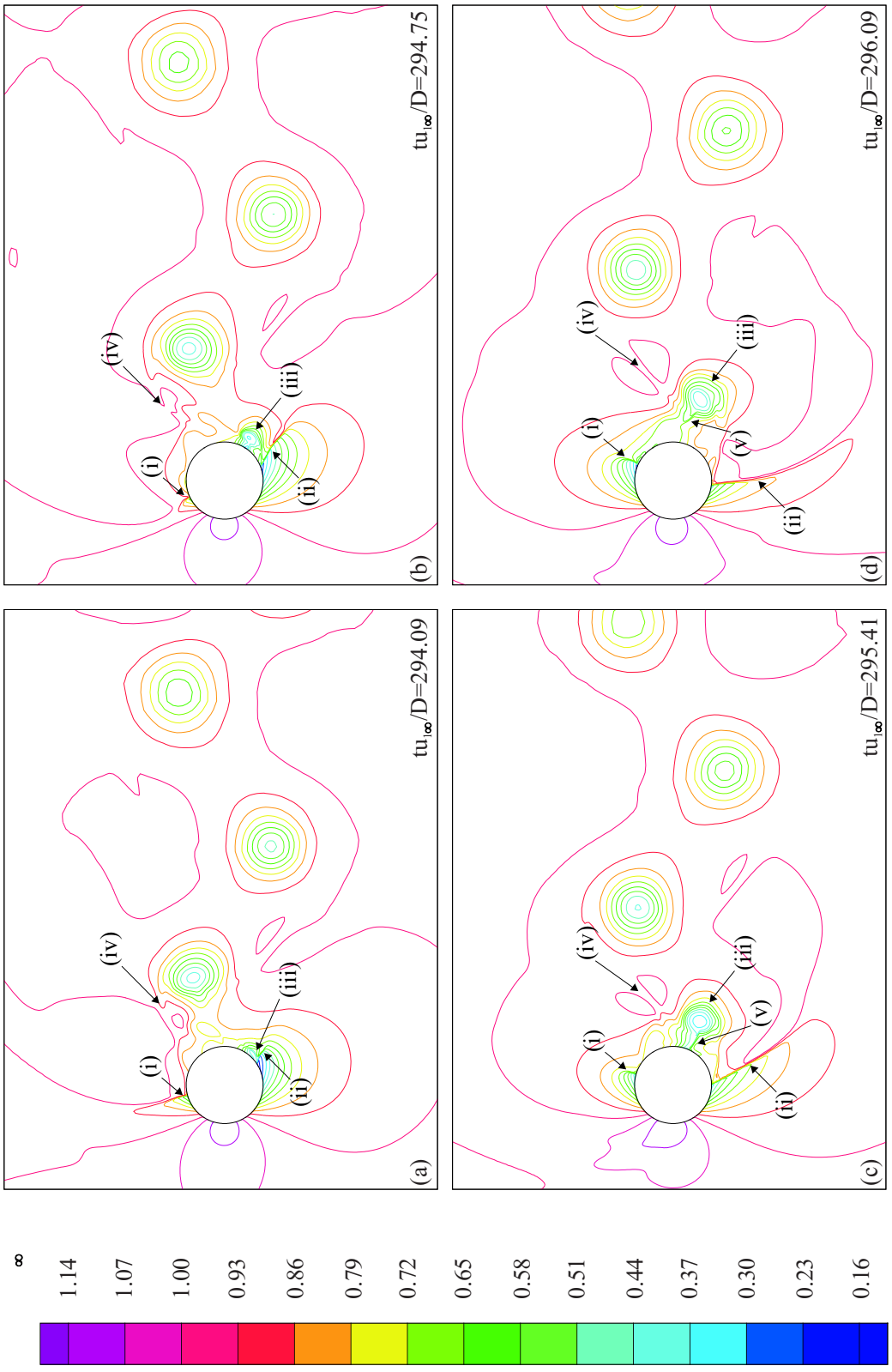

Figure 5.26: Time resolved density field development over the first half of a typical turbulent vortex shedding cycle: $294.09 \leq tu_{1\infty}/D \leq 296.09$. $\rho_{\max} = 1.14\rho_\infty$, $\rho_{\min} = 0.16\rho_\infty$, $\Delta\rho = 0.07\rho_\infty$. (i)-(v) labelled flow features.

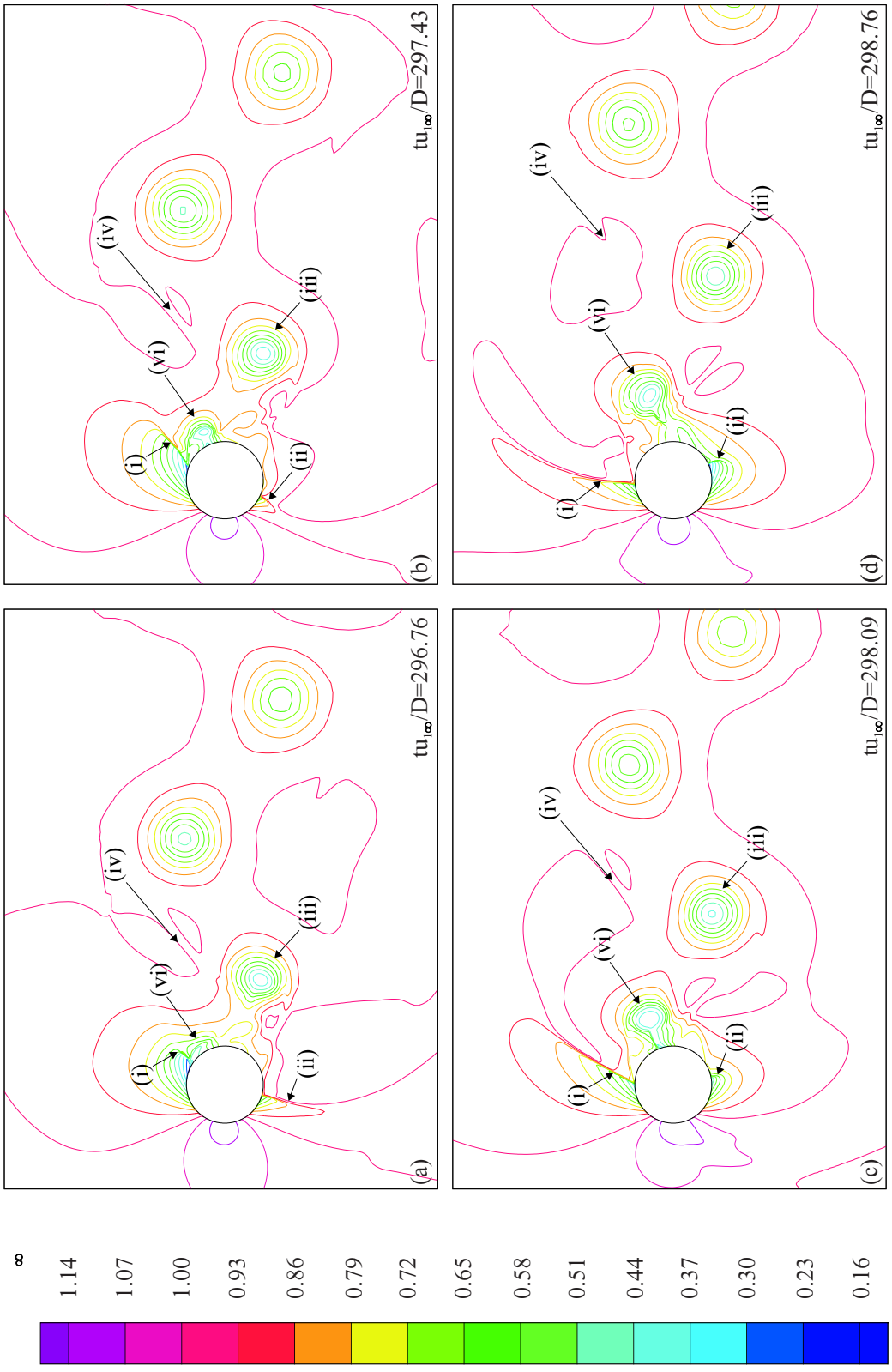

Figure 5.27: Time resolved density field development over the second half of a typical turbulent vortex shedding cycle: $296.76 \leq tu_{1\infty}/D \leq 298.76$. $\rho_{\max} = 1.14\rho_\infty$, $\rho_{\min} = 0.16\rho_\infty$, $\Delta\rho = 0.07\rho_\infty$. (i)-(v) labelled flow features.

to a surface location further upstream in the turbulent prediction is indicative of the transverse widening of the wake, which results from the introduction of turbulence diffusion. The outer region of the radial shock wave, located at (i), continues upstream as a pressure wave at subsequent times after Figure 5.26(a). The short radial shock wave that remains at the surface and terminates a local supersonic region, for example (i) in Figure 5.26(b), is defined over a significantly shorter radial length in the turbulent prediction. The boundary layer does not appear to separate following this radial shock wave, but indicates a subsequent re-acceleration shortly downstream. This subsequent acceleration terminates without a radial shock wave, indicating that only a local subsonic acceleration is defined. As an anti-clockwise rotating vortex develops at the far side of the wake in Figure 5.26(b-d), the fluid travelling along the upper surface is accelerated to higher supersonic velocities, resulting in a gradual downstream movement and increase in radial extent of this shock wave (i).

The radial shock wave labelled (ii) on the opposite side of the cylinder is located close to its downstream limit in Figure 5.26(a). The initial formation of the anti-clockwise rotating vortex (iii) is just visible close to the base of this shock wave. As the anti-clockwise rotating vortex (iii) increases in size and circulation in Figure 5.26(b-d) an additional transient shock wave (v) appears between the growing vortex and the cylinder surface. A similar transient radial shock wave is described in the inviscid prediction as the far side shear layer is entrained by each vortex and accelerates to supersonic velocities at the base of the cylinder. The definition of a no-slip surface condition creates an additional shear stress on the fluid travelling across this shock wave, which is expected to result in additional vorticity in the near side shear layer and a local increase in the turbulence kinetic energy production.

Chen (1972) reports that, as the vortices grow downstream of the cylinder, a reduction in the cross-stream distance from the vortex centre to the wake centreline occurs up to the end of the formation region. Downstream of the end of the vortex formation region, the shed vortices initially move further from the wake centreline. A constant cross-stream distance between each vortex row is then maintained further

downstream in the 'stable region'. The initial narrowing of the wake, the subsequent widening after each vortex is shed and the downstream convection of the vortex cores are evident by tracking the anti-clockwise rotating vortex labelled (iii) over the course of Figures 5.26(a-d) and 5.27(a-d). A similar development of a clockwise rotating vortex (vi) is then observed over the course of Figure 5.27(a-d).

The production and convection of small-scale turbulence kinetic energy in the near wake region is highlighted in Figures 5.28(a-d) and 5.29(a-d). The rate of dissipation of turbulence kinetic energy, to increase the internal energy of the near wake region, is then documented in Figures 5.30(a-d) and 5.31(a-d). Figures 5.28(a-d) and 5.29(a-d) document the development of the specific turbulence kinetic energy k over the same time interval as the static density field in Figures 5.26(a-d) and 5.27(a-d). The k field is normalised by the square of the free stream velocity $u_{1\infty}$. The specific turbulence dissipation rate ω is documented in phase with the density and k fields over the same time interval. ω is normalised using the free stream velocity $u_{1\infty}$ and the cylinder diameter D.

The peak turbulence kinetic energy at the start of this sequence, in Figure 5.28(a), is located downstream of the radial shock wave on the lower surface. This region, labelled (i), is the initial location of the anti-clockwise rotating vortex. The vortex formation locally represents a region of high strain rate of the fluid as the boundary layer separates at the shock wave and the resulting shear layer is stretched around the growing vortex. The centre of this vortex (ii) remains a region of high k, partly through the entrainment of fluid from the shock wave region and partly due to the shearing of fluid by the vortex motion. The onset of the secondary transient shock wave, between the growing vortex and the cylinder surface (vii), then constitutes an additional region of turbulence kinetic energy production. Upstream of the radial shock waves, a thin layer of fluid with a high level of turbulence kinetic energy is observed within the attached boundary layer at (iii). The turbulence kinetic energy increases with downstream development of the laminar boundary layer as the $k-\omega$ model simulates the selective amplification of the free stream disturbances in the laminar boundary layer by increasing the production of k in this region of stream-

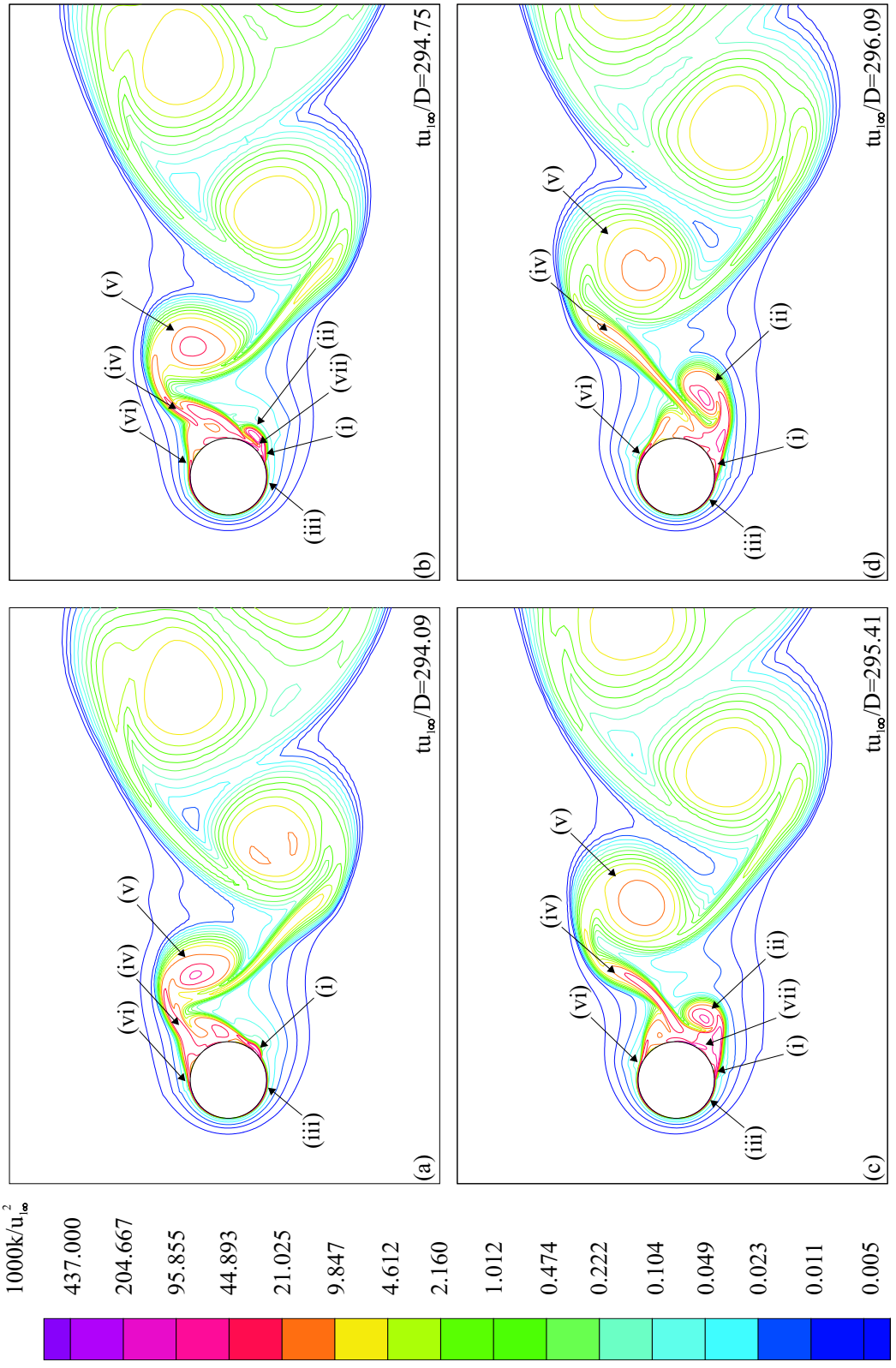

Figure 5.28: Specific turbulence kinetic energy k contours over the first half of the vortex shedding cycle: $294.09 \leq tu_{1\infty}/D \leq 296.09$. $k_{\max} = 0.437u_{1\infty}^2$, $k_{\min} = 5 \times 10^{-6}u_{1\infty}^2$, exponential contour distribution. (i)-(viii) labelled flow features.

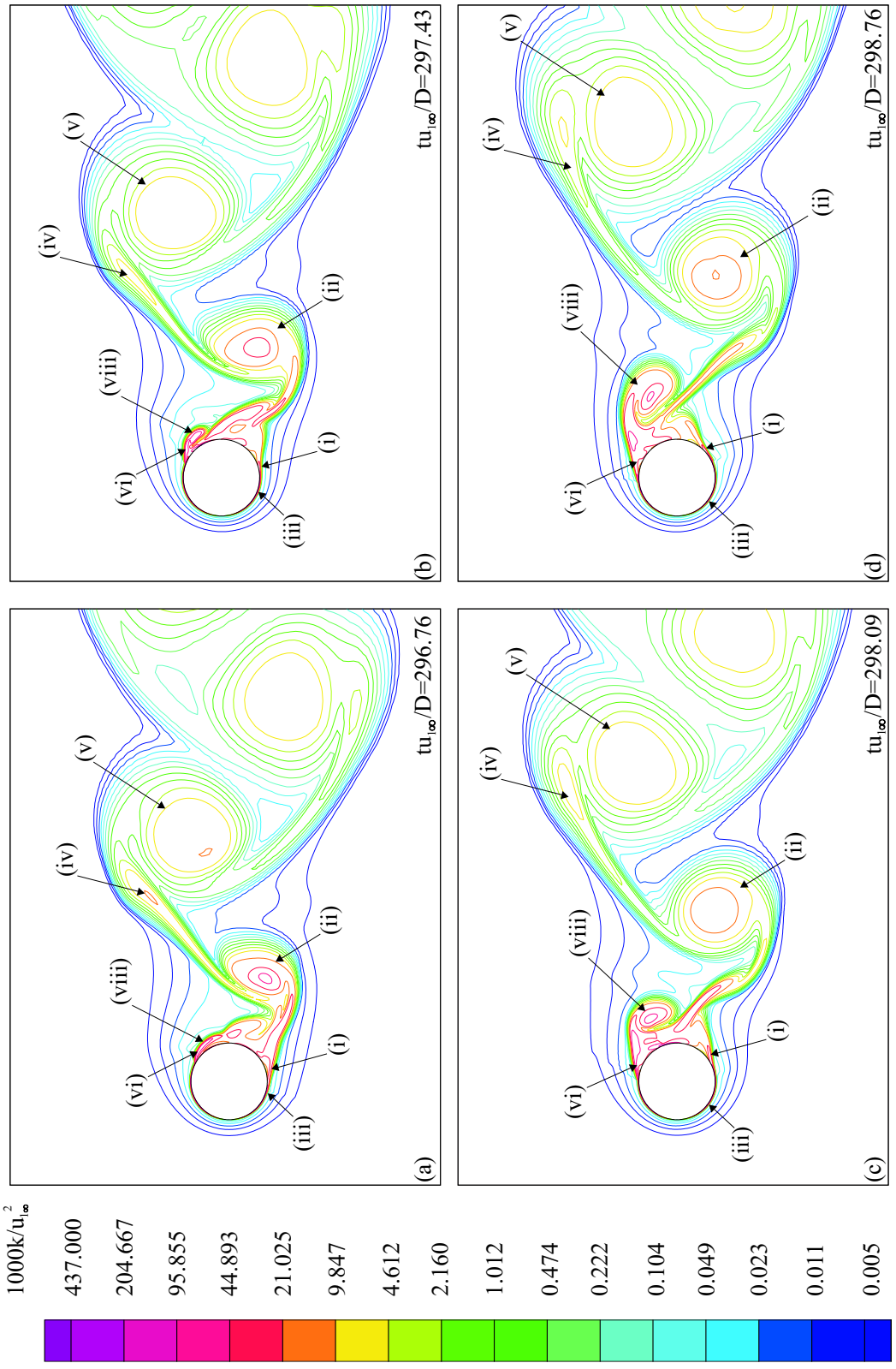

Figure 5.29: Specific turbulence kinetic energy k contours over the second half of the vortex shedding cycle: $296.76 \leq tu_{1\infty}/D \leq 298.76$. $k_{\max} = 0.437u_{1\infty}^2$, $k_{\min} = 5 \times 10^{-6}u_{1\infty}^2$, exponential contour distribution. (i)-(viii) labelled flow features.

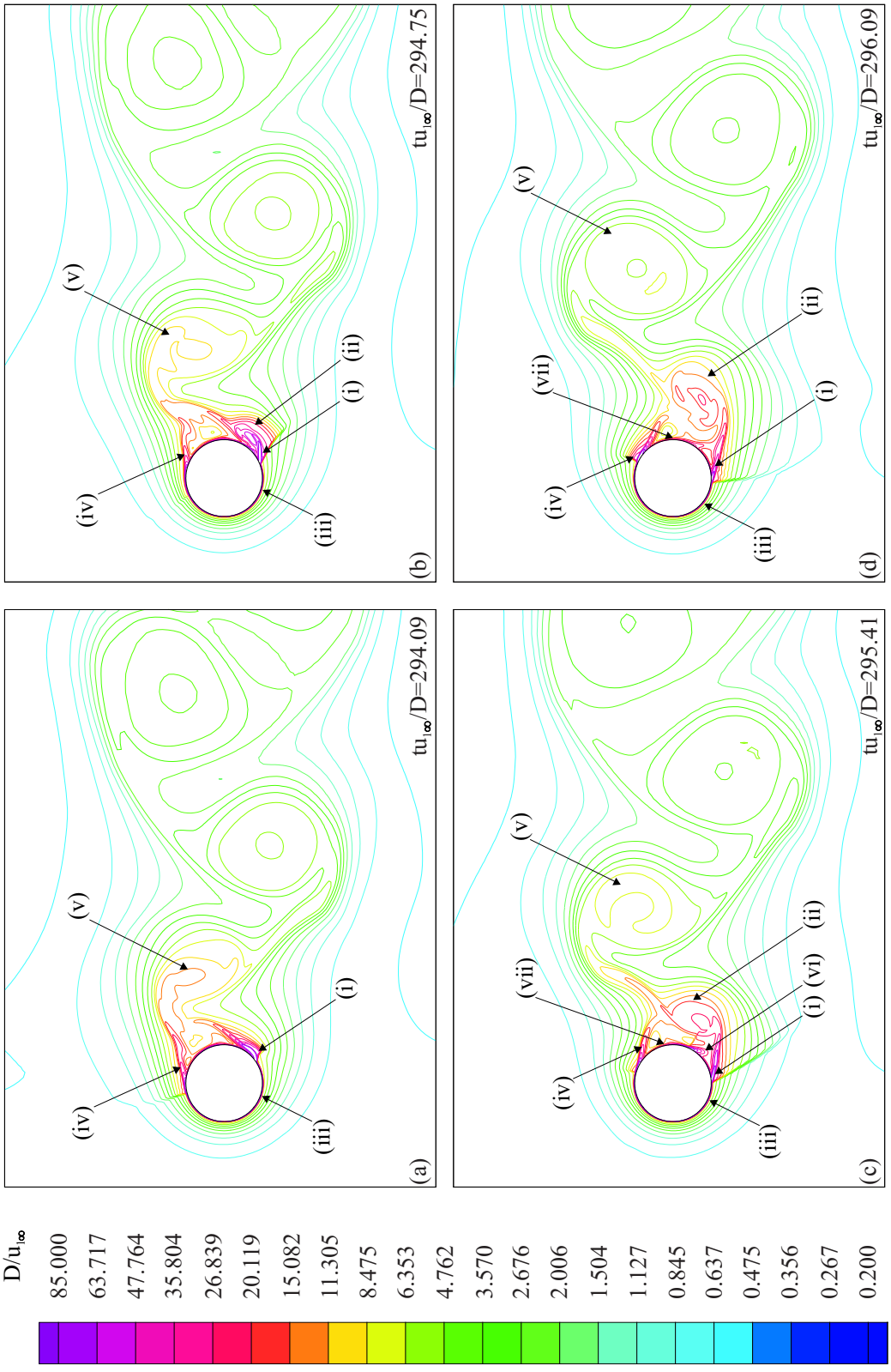

Figure 5.30: Specific turbulence kinetic energy dissipation rate ω development over the first half of the vortex shedding cycle: $294.09 \leq tu_{1\infty}/D \leq 296.09$. $\omega_{\max} = 85u_{1\infty}/D$, $\omega_{\min} = 0.2u_{1\infty}/D$, exponential contour distribution. (i)-(vii) labelled flow features.

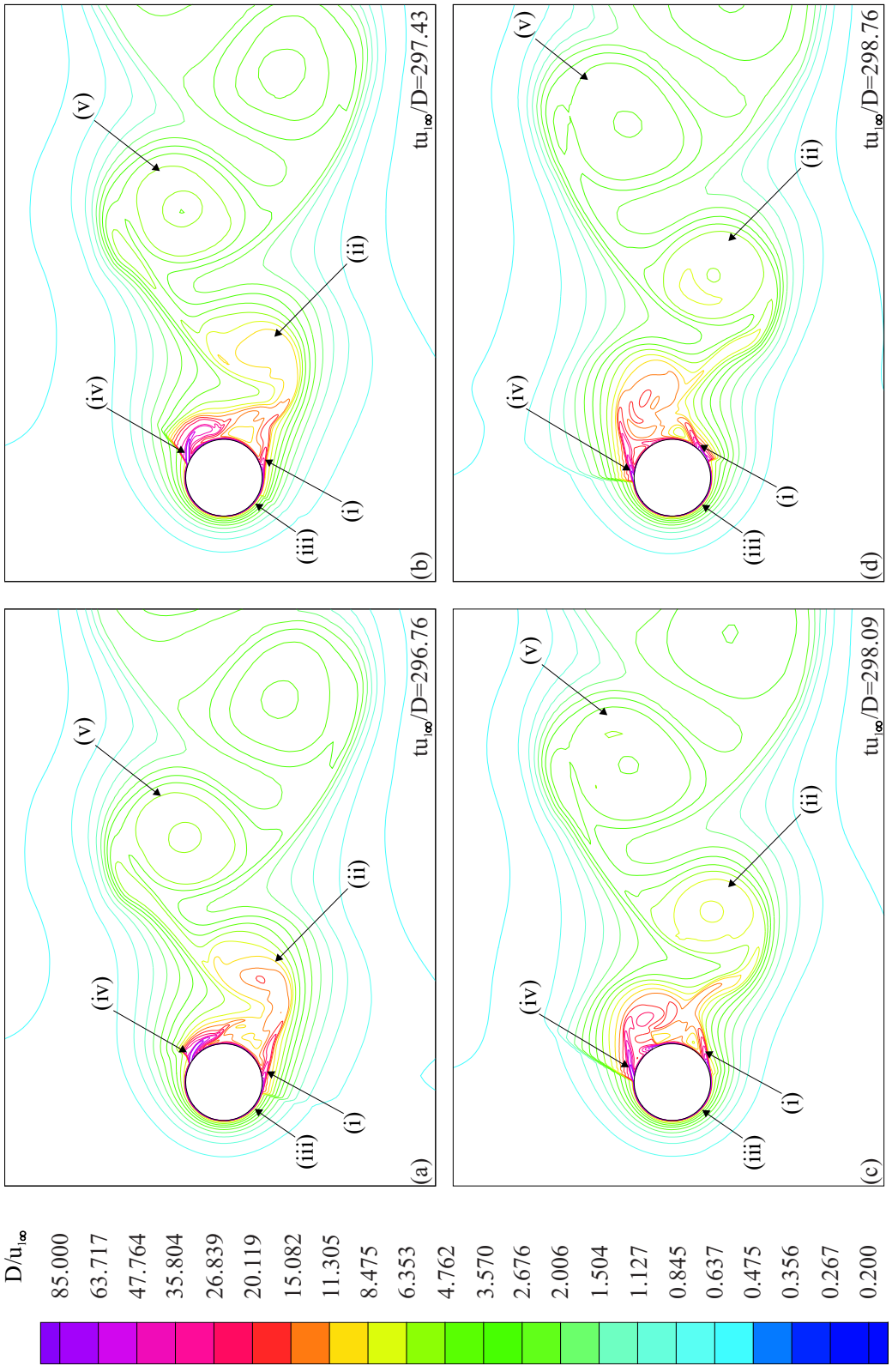

Figure 5.31: Specific turbulence kinetic energy dissipation rate ω contours over the second half of the vortex shedding cycle: $296.76 \leq tu_{1\infty}/D \leq 298.76$. $\omega_{\max} = 85u_{1\infty}/D$, $\omega_{\min} = 0.2u_{1\infty}/D$, exponential contour distribution. (i)-(v) labelled flow features.

wise velocity gradient. Approaching the wall, k decreases to an imposed value of $k = 0$ at the no-slip cylinder surface. The boundary layer is also highlighted as a region of high ω, as indicated by (iii) in Figure 5.30(a-d). As documented in Wilcox (2002), it is the balance between the production and dissipation terms in the k transport equation which models the overall effects of the onset and development of boundary layer transition in the $k - \omega$ model.

On the opposite side of the wake, a region of high k is observed along the shear layer (iv), which stretches between the clockwise rotating vortex (v) and the cylinder surface in Figure 5.28(a). This shear layer remains a region of high k as it is entrained across the wake and subsequently stretches between the contra-rotating vortices labelled (ii) and (v). An increase of k is evident immediately downstream of the upper radial shock wave at (vi) as this shock wave moves circumferentially downstream over the course of Figure 5.28(a-d). A peak in k is then observed in this shear layer at the initial formation of the clockwise rotating vortex (viii) in Figure 5.29(a-b). The entire base region of the circular cylinder constitutes a region of substantial turbulence kinetic energy over the vortex shedding cycle.

Downstream of the cylinder, the turbulence diffusion in the downstream moving vortices increases the wake width with downstream distance. The effects of turbulence diffusion are indicated by a local increase in the transverse width of flow covered by the k contours, and by an increase in spacing between each k iso-contour level at each vortex.

The development of ω over the vortex shedding cycle shows similar maxima at the precessing radial shock waves. The maximum value of ω in Figure 5.30(a) is located immediately downstream of the lower radial shock wave (i). A higher level of ω than the surrounding fluid is maintained within the growing vortex core (ii) in Figure 5.30(b-d). The transient radial shock wave that appears between the vortex (ii) and the cylinder surface constitutes an additional source of ω increase. The ω increase downstream of this shock wave is labelled (vi) in Figure 5.30(c). A higher level of ω than the surrounding fluid is also maintained at the surface of the cylinder in the base region (vii) by the no-slip condition throughout the vortex shedding

cycle. The separated shear layer (iv), downstream of the radial shock wave on the opposite side of the wake, is also indicated as a region of significant ω. The supply of fluid with high ω from the separated shear layer (iv) to the clockwise rotating vortex (v) ceases when this vortex is shed from the cylinder, as observed in Figure 5.30(a-b). The value of ω in this vortex then gradually decreases with the downstream vortex convection in Figures 5.30(b-d) and 5.31(a-d), before developing a quasi-steady level further downstream.

5.3.4 Energy Separation in the Turbulent Vortex Shedding Cycle

The $k-\omega$ turbulence model, along with the imposition of a no-slip surface condition, locally modifies the energy separation in the near wake region with respect to the inviscid prediction. The stagnation temperature field development in the near wake is documented over a typical vortex shedding cycle in Figures 5.32(a-d) and 5.33(a-d). Figure 5.32(a-d) is phase synchronous with the density, the k and the ω fields documented in Figure 5.26(a-d), Figure 5.28(a-d) and Figure 5.30(a-d) respectively. Similarly, Figure 5.33(a-d) is phase synchronous with the density, the k and the ω field predictions in Figure 5.27(a-d), Figure 5.29(a-d) and Figure 5.31(a-d) respectively. Figures 5.32(a-d) and 5.33(a-d) are also approximately phase synchronous with the inviscid stagnation temperature field predictions in Figures 5.14(a-d) and 5.15(a-d).

In the turbulent prediction, the stagnation temperature redistribution downstream of the cylinder follows a similar pattern to the inviscid prediction. Hot spots of higher stagnation temperature than the free stream condition are locally defined along the edges of the wake. Cold spots, of lower stagnation temperature than the free stream condition, are defined close to the centre of the wake. The similarity of the turbulent and inviscid stagnation temperature fields confirm that, under the current free stream conditions, the energy separation mechanism is dominated by the convective terms in the governing equations. The addition of viscosity and of the Reynolds stresses into the flow model locally modifies the magnitude and size of the hot spots at the edges of wake and the cold spots along the wake centre. Two hot spots, one located at the outer edge of the clockwise rotating vortex and

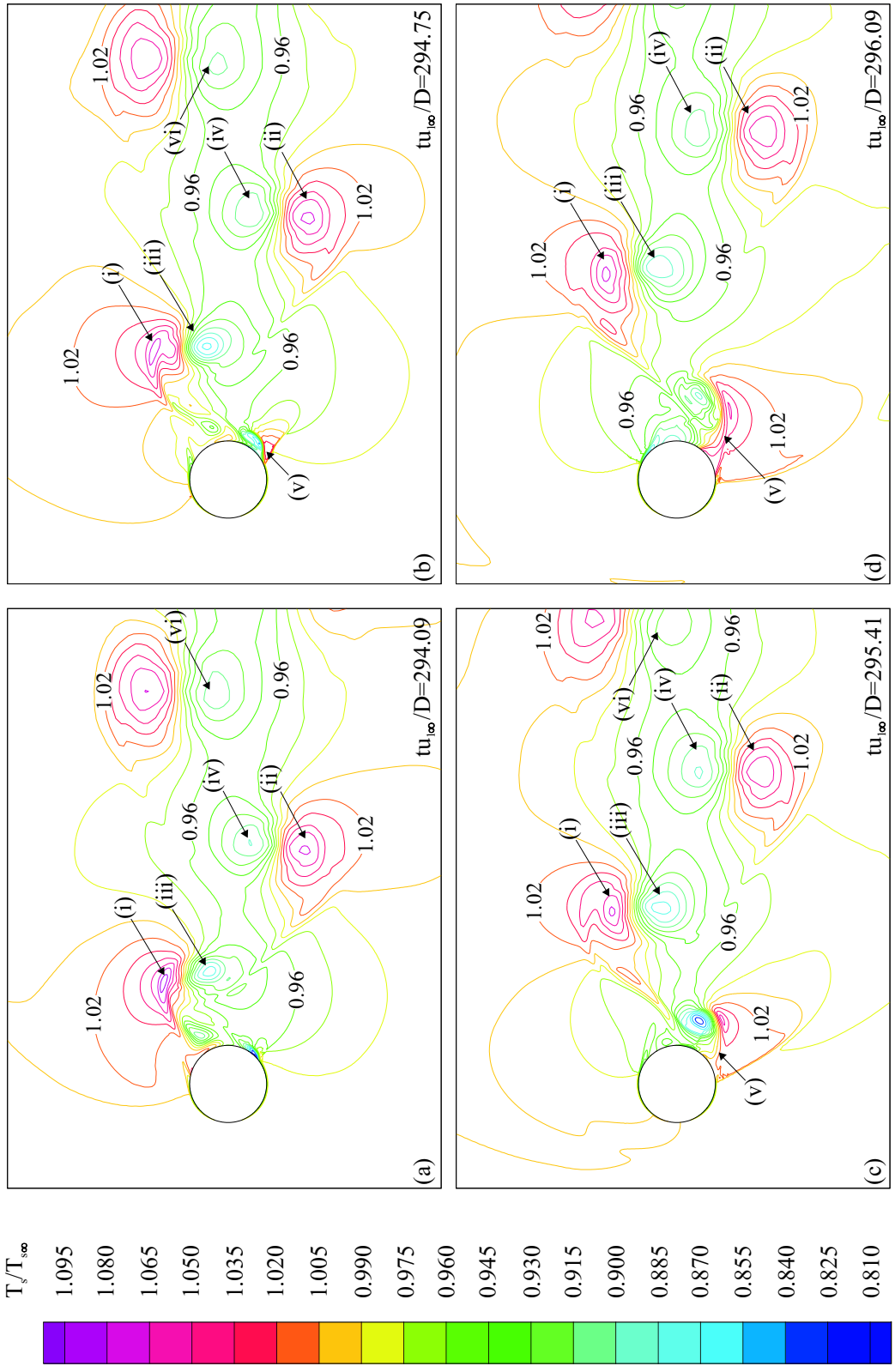

Figure 5.32: Instantaneous stagnation temperature contours over the first half of the vortex shedding cycle: $294.09 \leq tu_{1\infty}/D \leq 296.09$. $T_{s\,\max} = 1.095T_{s\infty}$, $T_{s\,\min} = 0.810T_{s\infty}$, $\Delta T_s = 0.015T_{s\infty}$. (i)-(vi) labelled flow features.

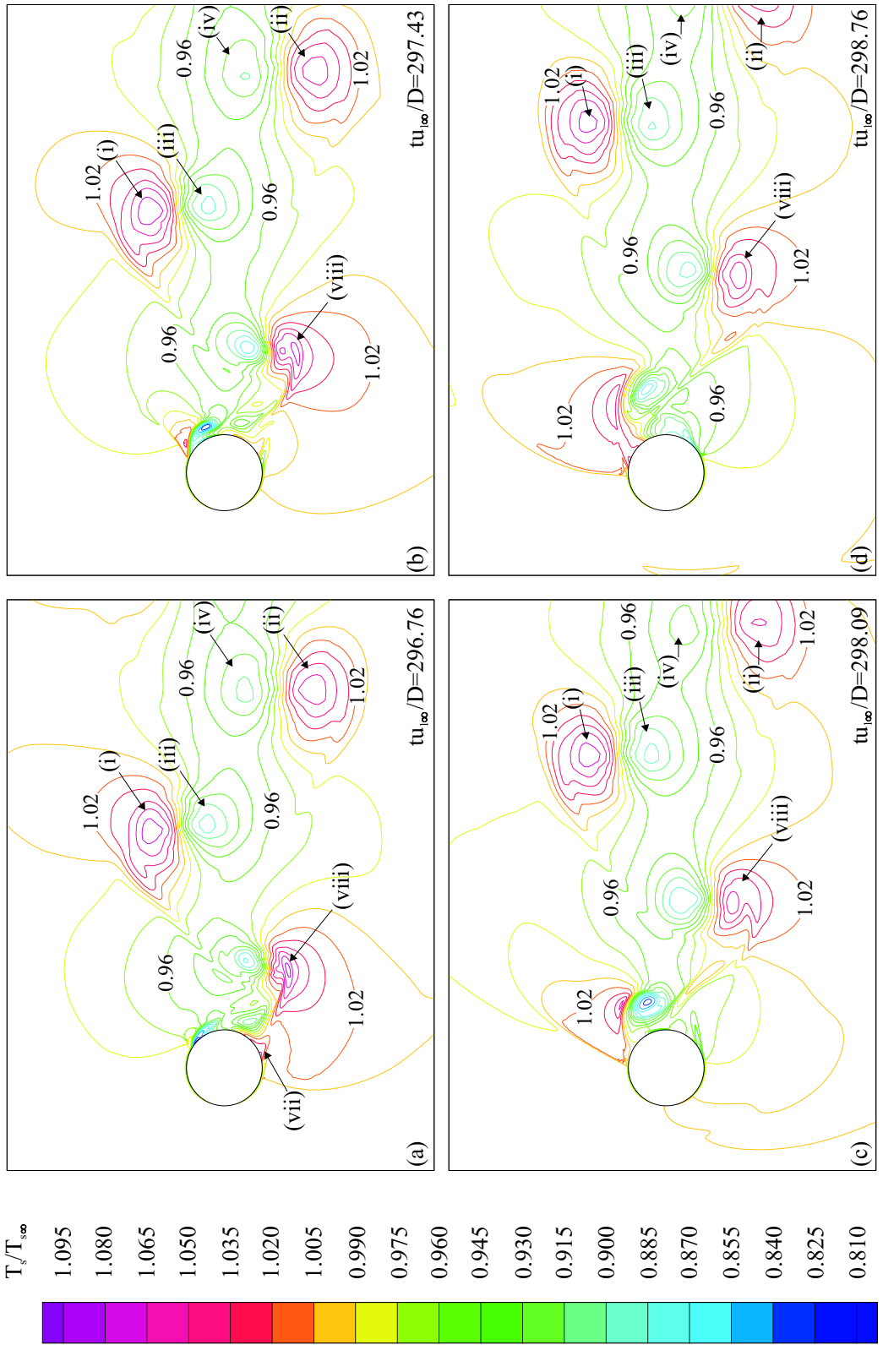

Figure 5.33: Instantaneous stagnation temperature contours over the second half of the vortex shedding cycle: $296.76 \leq tu_{1\infty}/D \leq 298.76$. $T_{s\,\max} = 1.095T_{s\infty}$, $T_{s\,\min} = 0.810T_{s\infty}$, $\Delta T_s = 0.015T_{s\infty}$. (i)-(viii) labelled flow features.

the second located at the anti-clockwise rotating vortex, are labelled (i) and (ii) in Figure 5.32(a). The two corresponding cold spots, each located on a common stream-wise alignment with the hot spots and vortex cores, are labelled (iii) and (iv) in this figure.

The turbulent prediction shows a consistent reduction in the stagnation temperature at each hot spot, with respect to the inviscid prediction. For example, the hot spot labelled (i) in Figure 5.32(a) rises to $T_s = 1.095T_{s\infty}$. The corresponding hot spot at approximately the same stage of vortex shedding in the inviscid prediction, labelled (i) in Figure 5.14(a), has a maximum stagnation temperature of $T_s = 1.105T_{s\infty}$. Similarly, the hot spot located at the anti-clockwise rotating vortex, labelled (ii) in Figure 5.32(a), rises to a local maximum of $T_s = 1.080T_{s\infty}$, compared with $T_s = 1.090T_{s\infty}$ at this vortex in Figure 5.14(a).

A similar reduction in the stagnation temperature redistribution is also observed at the cold spots labelled (iii) and (iv) in the near wake region. Specifically, the stagnation temperature minimum at the cold spot labelled (iii) in Figure 5.32(a) increases from $T_s = 0.850T_{s\infty}$ in the inviscid prediction to $T_s = 0.885T_{s\infty}$ in the turbulent flow prediction. Similarly, the cold spot labelled (iv) in Figure 5.32(a) has a minimum stagnation temperature 0.56% higher than in the inviscid prediction.

The introduction of turbulence diffusion decreases the thermal shielding of the near side shear layer by the primary and transient radial shock waves at each vortex formation event, as discussed in Section 5.2.6. For example, consider the increase in stagnation temperature in the near side shear layer labelled (v) in Figure 5.32(b-d). A significant increase in stagnation temperature is evident in the inviscid prediction at this shear layer, which is labelled (vii) in Figure 5.14(b-d). This is thought to be partially attributable to a bounding of the shear layer by the primary radial shock wave located upstream of this shear layer, and by the transient shock wave which appears in Figure 5.14(c-d) on the near side of the wake. These bounding supersonic regions on either side of the shear layer inhibit the transport of heat away from this shear layer. This effect is discussed further for the inviscid prediction in Section 5.2.6 and contributes to a local increase in stagnation temperature at the hot spots above

those documented for subsonic flow by Kurosaka et al. (1987). The introduction of turbulence diffusion into the model decreases the level of localised heating in this shear layer. The turbulent shear layer is therefore lower in stagnation temperature at the shedding of this vortex in Figure 5.33(a-d). As the near side vortex is shed, Figure 5.33(a-d), the region of high stagnation temperature in the shear layer, (v) of Figure 5.32(b-d), separates into two distinct hot spots with $T_s > T_{s\infty}$. These are labelled (vii) and (viii) in Figure 5.33(a). The hot spot (vii) remains close to the cylinder surface and rapidly loses heat to the surrounding fluid before the entrainment of this shear layer across the wake by the clockwise rotating vortex formation in Figure 5.33(b-d).

The level of heating at the outer edges of the wake and the cooling at the centre of the wake is maintained over a longer stream-wise distance in the turbulent flow prediction, even with the additional effects of turbulence diffusion and vortex dissipation. For example, a comparison of the cold spots labelled (ii) and (vi) in the inviscid prediction of Figure 5.14(a) yields a stagnation temperature increase of $\Delta T_s = 0.075 T_{s\infty}$ over this stream-wise distance. The equivalent distance in the turbulent prediction, between (iii) and (vi) in Figure 5.32(a), yields an increase in stagnation temperature of $\Delta T_s = 0.03 T_{s\infty}$. The lower stagnation temperature increase with downstream distance at the turbulent cold spots suggest an increase in the vortex shedding strength to overcome the additional turbulence diffusion and dissipation effects. Any increase in vortex strength should be accompanied by a similar increase in the stagnation pressure redistribution, discussed later in this section. This is, however, not observed. The longer duration of the cold spots in the turbulent prediction may therefore result from the convection of turbulence kinetic energy around each vortex as the vortex moves downstream.

Further downstream, the turbulent prediction is compared against the phase locked averaged stagnation temperature measurements of Ackerman (2005) at similar free stream conditions of $M_\infty = 0.6$ and $Re_D = 6.86 \times 10^5$. A stagnation temperature probe is used by Ackerman (2005) to measure the time resolved $T_s/T_{s\infty}$ distribution along a plane normal to the free stream direction at $x_1 = 6.5D$. This is

compared against the flow prediction, monitored along a fixed stream-wise plane at $x_1 = 6.5D$, over the period of one vortex shedding cycle in Figure 5.34. The normalising parameters of $T_{s\infty}$, $u_{1\infty}$ and D are taken from the prediction in Figure 5.34(a) and from the reported measurements of Ackerman (2005) in Figure 5.34(b). Dotted white circles in Figure 5.34(a,b) indicate the location of the vortices. These are estimated from the entropy field measurements and prediction, and are confirmed in the prediction from the static density contours. White crosses within these circles indicate the approximate location of the vortex centres. Figure 5.34(a,b) indicates a reasonable qualitative similarity of the experiment and prediction at $x_1 = 6.5D$. Hot spots, of similar magnitude above the free stream condition, are defined along the outer edges of the wake in both fields. Localised cold spots of stagnation temperature $T_s < T_{s\infty}$ are similarly located close to the centre of the wake ($x_2 = 0$). The stagnation temperature extrema ($T_{s\,\max}/T_{s\infty}$ and $T_{s\,\min}/T_{s\infty}$), and the average cross-stream distance from the wake centreline to these maxima $|\Delta x_2/D|_{T_{s\,\max}}$, are quantified in Table 5.8. $|\Delta x_2/D|_{T_{s\,\max}}$ gives a relative measure of the cross-stream

Source	$T_{s\,\max}/T_{s\infty}$	$T_{s\,\min}/T_{s\infty}$	$\lvert\Delta x_2/D\rvert_{T_{s\,\max}}$
Current $k-\omega$ prediction	1.054	0.928	1.144
Ackerman (2005)	1.044	0.970	1.310

Table 5.8: Stagnation temperature distribution at $x_1 = 6.5D$. Turbulent prediction comparison with the '2000 series' measurements of Ackerman (2005) at $M_\infty = 0.6$ and $Re_D = 6.86 \times 10^5$.

width of the stagnation temperature redistribution.

The measurements of Ackerman (2005) indicate a narrower stagnation temperature range of $0.970 \leq T_s/T_{s\infty} \leq 1.044$, compared with $0.928 \leq T_s/T_{s\infty} \leq 1.054$ for the current turbulent prediction. The value of $T_{s\,\max}/T_{s\infty}$ in the current prediction is, however, only 0.96% greater than the measurements of Ackerman (2005). The predicted stagnation temperature minimum $T_{s\,\min}/T_{s\infty}$ in Table 5.8(a) is 4.33% lower than the measured value. These results indicate that the computational fluid dynamics model a marginally stronger energy separation mechanism, with respect to the experiment. The cross-stream distance between the local stagnation tem-

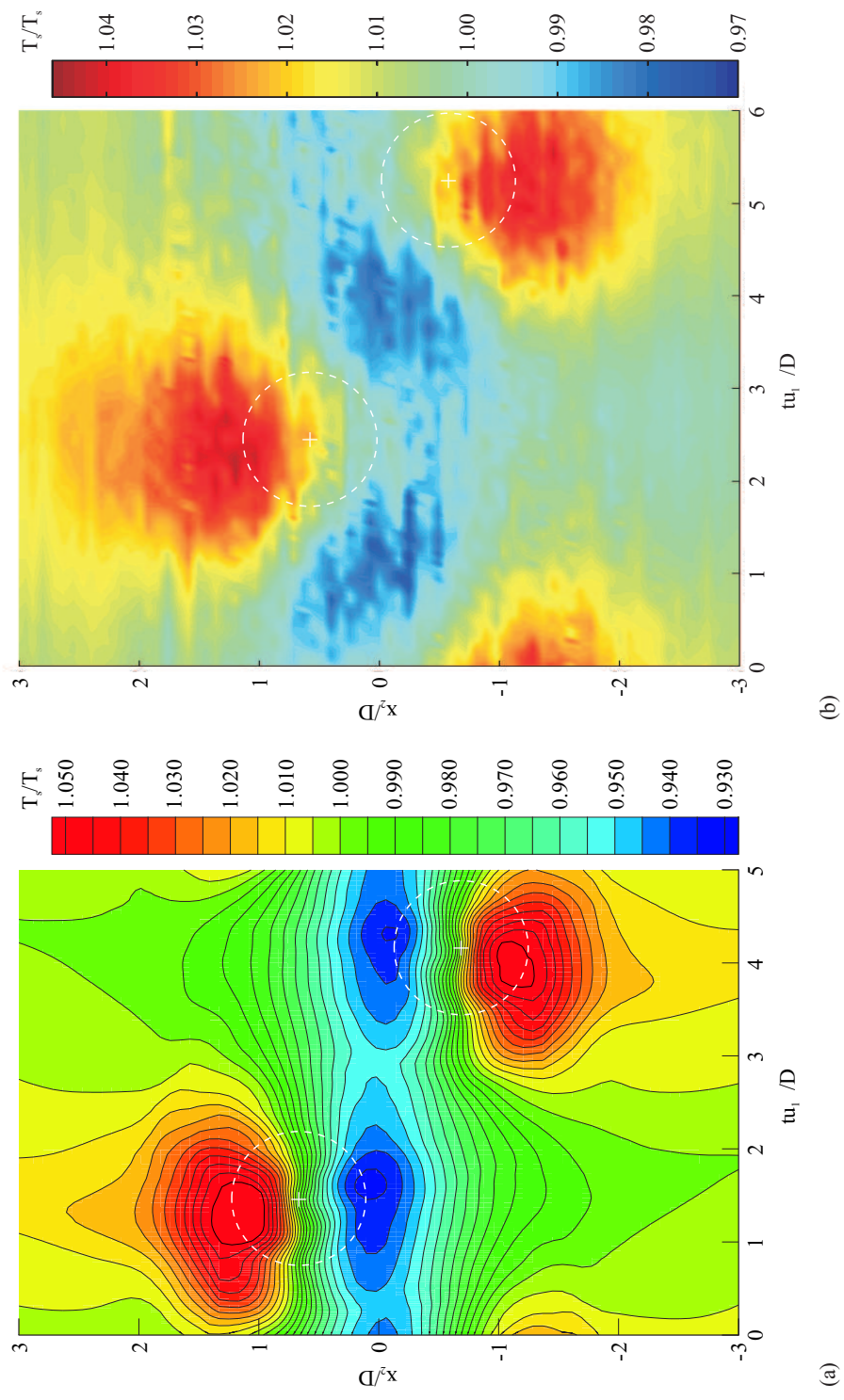

Figure 5.34: Stagnation temperature field comparison between the phase lock averaged measurements of Ackerman (2005) and the turbulent prediction at $x_1 = 6.5D$. (a) Turbulent prediction. (b) Measurements taken from the '2000 series' results of Ackerman (2005). Normalising parameters of $T_{s\infty}$, $u_{1\infty}$ and D taken from the turbulent prediction in (a) and from the reported measurements of Ackerman (2005) in (b).

perature maxima on each side of the wake is also 12.67% lower in the turbulent prediction. This implies a slightly narrower predicted wake, which may result from tighter rolling of the vortices or from a slight under-prediction in the turbulence diffusion and dissipation downstream of the cylinder. Overall, the correlation is good.

Further differences between the current turbulent prediction and the measurements of Ackerman (2005) are evident in the stream-wise alignment of the hot and cold spots. In the measurements of Ackerman (2005), the hot spots at the outer edge of the wake lie on a common temporal alignment with the vortex cores, as in the turbulent prediction. However, the measured cold spots appear between the hot spots of successive vortices. It is difficult to determine from Figure 5.34(b) whether the cold spots phase lead or phase lag the associated hot spots, but they appear out of phase with the hot spots by a quarter of a vortex shedding cycle. In contrast, the hot spot, cold spot and vortex core are approximately phase synchronous in the turbulent prediction of Figure 5.34(a). A slight phase difference is noted in the stream-wise position of each predicted maximum and minimum, with the vortex centre lying approximately between these two extrema. This is however significantly less than the one quarter phase shift in the measured distribution. A stream-wise alignment of each hot spot, cold spot and vortex core in a vortex street is similarly predicted in an analytical model of a vortex street by Kurosaka et al. (1987). A similar cross-stream alignment is also present in the inviscid prediction of Section 5.2.6.

Possible sources for this discrepancy may include the different wake vorticity distributions between the prediction and the experiment, an additional three-dimensional turbulent effect not modelled in the current two-dimensional prediction, or even a directional dependency in the stagnation temperature field measurements. Three-dimensional flow in a predominantly uniform span-wise vortex shedding is documented in a number of published measurements. Time accurate measurements downstream of a circular cylinder are reported by, for example, Cantwell & Coles (1983) and Fazle Hussain & Hayakawa (1987). Similar measurements downstream of a flat plate held normal to the free stream flow are given by

Kiya & Matsumura (1988). Three-dimensional vortex shedding is also reviewed by Williamson (1996) and by Cicatelli & Sieverding (1995). The span-wise vortices, which make up the von Kármán vortex street, are connected by 'ribs' of intensely sheared fluid. Longitudinal vortices are reported along these ribs, which rotate about an axis parallel to the direction of the shear layer. Vortex stretching along the ribs leads to locally high levels of turbulence production. This mechanism is also proposed to lead to a breakdown in the span-wise coherence of the contra-rotating vortices that characterise the vortex street. Williamson (1996) cites measurements by Szepessy & Bearman (1992), who report that the vortex shedding downstream of large aspect ratio circular cylinders is not generally in-phase along the cylinder span at high Reynolds numbers. Although the shear layers between successive vortices are highlighted in the current two-dimensional model as being regions of turbulence production, these three-dimensional effects may locally alter the stagnation temperature distribution in this region. A local increase in heat through turbulence dissipation at the saddle points between successive vortices could, for example, lead to heating of the three-dimensional wake in the region of the predicted stagnation temperature minima.

A physical explanation for the stagnation temperature discrepancy, between the prediction and the experiment, remains an open challenge. This could eventually be addressed through a three-dimensional extension to this study using a Large Eddy Simulation (LES) or Detached Eddy Simulation (DES) approach. An extension to the experimental investigation of Ackerman (2005) to include small scale turbulence measurements through a hot wire anemometry or eduction technique could also be considered, as in Cantwell & Coles (1983) and Fazle Hussain & Hayakawa (1987). The application of LES or DES models to a circular cylinder in cross-flow, at the current high Reynolds number, still represents a formidable computational challenge and is an ongoing area of turbulence modelling research at the present time. The development of LES and DES turbulence modelling for high Reynolds number circular cylinder flows is discussed, for example, in Travin et al. (1999), Breuer (2000) and Wang et al. (2001).

The importance of the pathline taken by fluid particles around each vortex to the energy separation mechanism is analysed in Appendix A.3. Figure 5.34(a,b) uses a fixed frame of reference to present the stagnation temperature of fluid flowing past a fixed plane lying normal to the free stream direction. This frame of reference is compared in Appendix A.3 with a frame of reference which moves downstream at the mean vortex convection velocity. In this relative frame of reference, the cycloidal pathline taken by fluid particles around each vortex is replaced by a tangential velocity distribution around each vortex. The choice of reference frame is shown to impact on the stagnation temperature and pressure redistribution observed in the prediction.

The resulting time averaged stagnation temperature profile at $x_1 = 6.5D$, in Figure 5.35, shows the characteristic T_s deficit at the wake centreline. At this downstream distance, the stagnation temperature falls to $T_s = 0.940T_{s\infty}$ at $x_2 = 0$. This minimum is 3% lower than the stagnation temperature at the corresponding location in the inviscid prediction. An increase in the stagnation temperature above the free stream condition is observed at the outer edges of the wake. This increase is also present in the time averaged inviscid prediction and is evident in the stagnation temperature measurements of Ackerman (2005) at $x_1 = 6.5D$. The distinctive double peaked feature at this location in the inviscid profile of Figure 5.17 is replaced in Figure 5.35 by a broad single peak due to the introduction of turbulence diffusion. The cross-stream distance covered by the stagnation temperature deficit is significantly greater in the turbulent profile of Figure 5.35, highlighting the wider wake in this prediction.

As in the inviscid prediction, the vortex induced stagnation temperature redistribution is reflected in the time resolved turbulent stagnation pressure p_s field. The development of the stagnation pressure field is documented in eight instantaneous snapshots over one typical vortex shedding cycle in Figures 5.36(a-d) and 5.37(a-d). Figure 5.36(a-d) documents the formation of a clockwise rotating vortex over the non-dimensional time interval $294.09 \leq tu_{1\infty}/D \leq 296.09$. This figure is phase synchronous with the stagnation temperature development in Figure 5.32(a-d) and

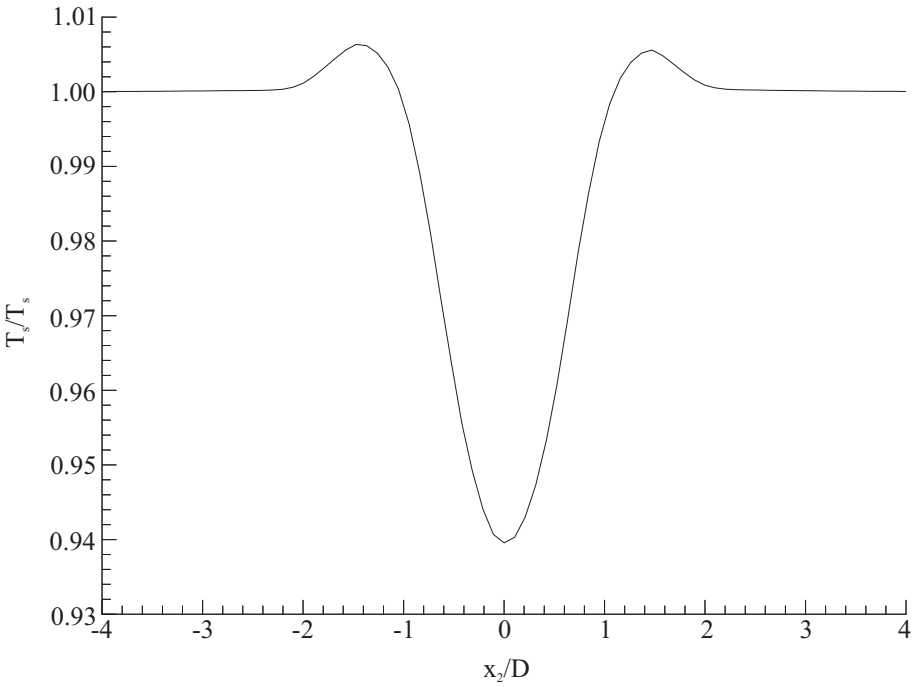

Figure 5.35: Time averaged stagnation temperature across the wake at $x_1 = 6.5D$.

the density, k and ω fields in Figures 5.26(a-d), 5.28(a-d) and 5.30(a-d) respectively. Similarly, Figure 5.37(a-d) is phase synchronous with Figures 5.33(a-d), 5.27(a-d), 5.29(a-d) and 5.31(a-d).

The turbulent stagnation pressure field shows a similar wake pattern to the inviscid prediction, with localised regions of $p_s > p_{s\infty}$ at the outer edges of the wake and localised regions of $p_s < p_{s\infty}$ close to the centre of the wake. Two local regions of $p_s > p_{s\infty}$ are labelled (i) and (ii) in Figures 5.36(a-d) and 5.37(a-d). The corresponding regions of $p_s < p_{s\infty}$, which are defined close to the low pressure vortex centres, are labelled (iii) and (iv) in these figures.

The turbulent prediction demonstrates a consistently higher stagnation pressure throughout the wake. The stagnation pressure difference between neighbouring maxima and minima in the vortex shedding stage, for example (ii) and (iv), is similar in both the inviscid and turbulent predictions. This stagnation pressure difference, between neighbouring maxima and minima, decays with downstream distance as noted in the inviscid prediction. These similarities indicate that the stagnation pressure redistribution is less influenced by turbulence production, convection and down-

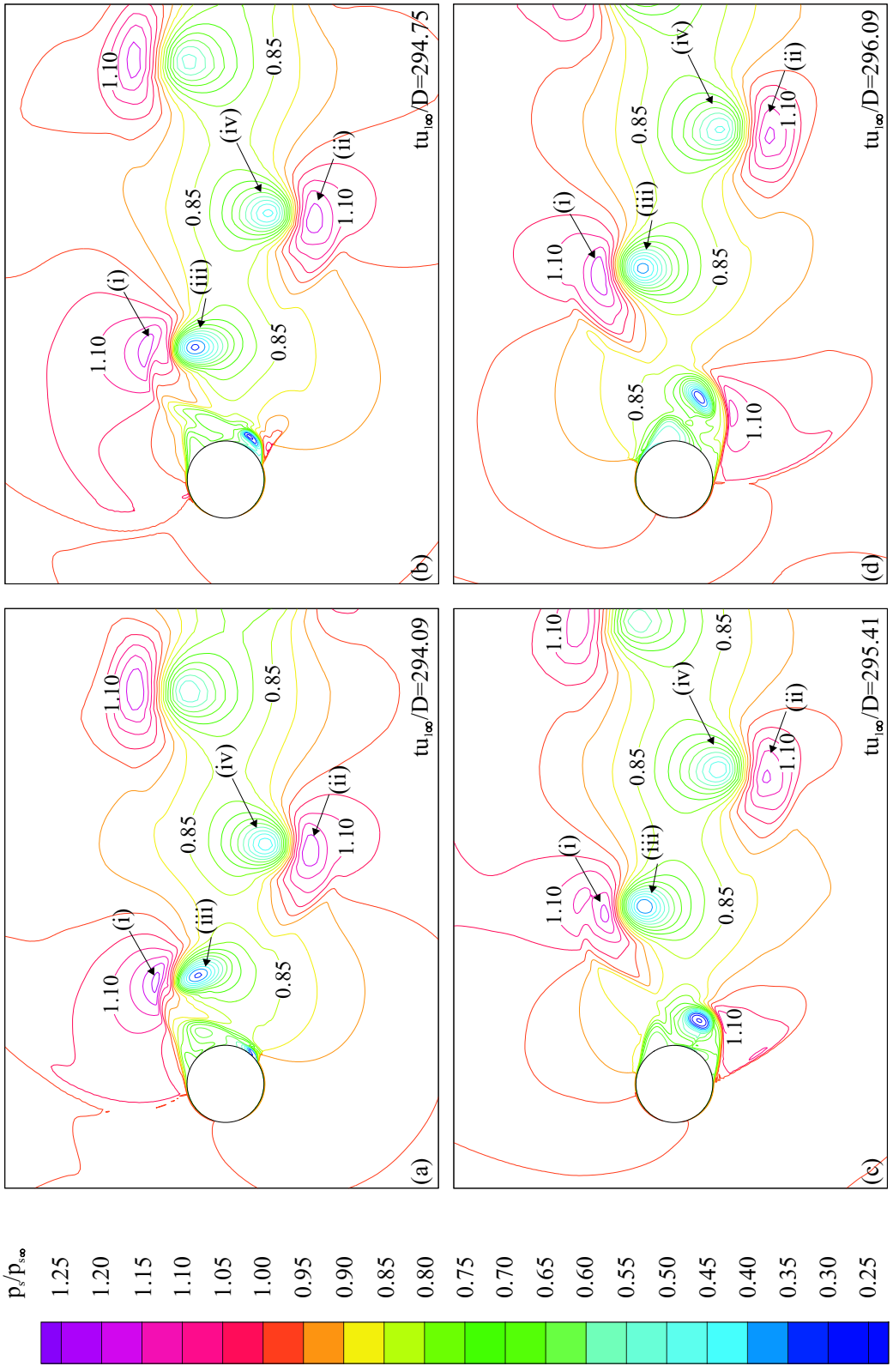

Figure 5.36: Instantaneous stagnation pressure contours over the first half of the vortex shedding cycle: $294.09 \leq tu_{1\infty}/D \leq 296.09$. $p_{s\,\max} = 1.25p_{s\infty}$, $p_{s\,\min} = 0.25p_{s\infty}$, $\Delta p_s = 0.05p_{s\infty}$. (i)-(iv) labelled flow features.

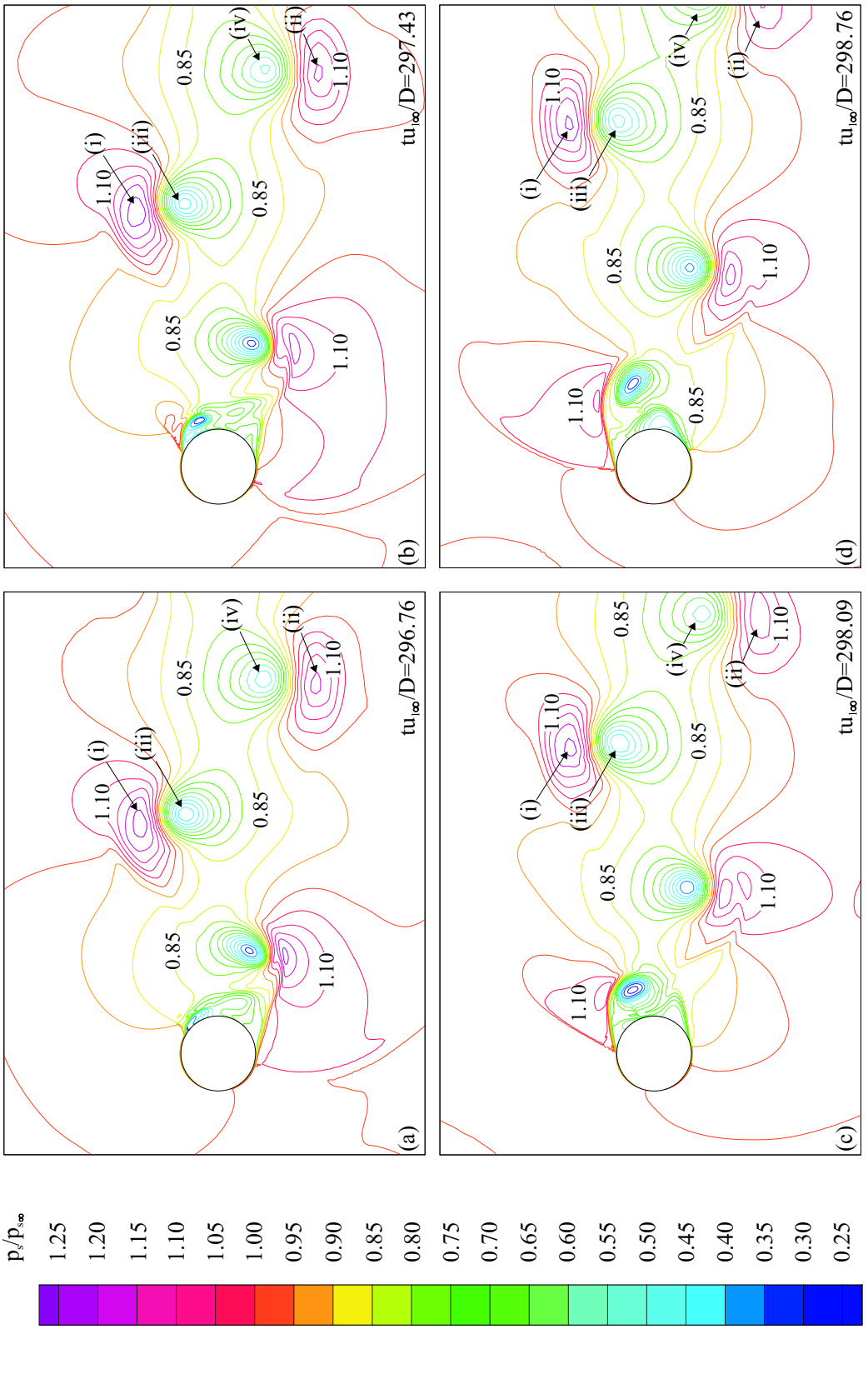

Figure 5.37: Instantaneous stagnation pressure contours over the second half of the vortex shedding cycle: $296.76 \leq tu_{1\infty}/D \leq 298.76$. $p_{s\,\max} = 1.25p_{s\infty}$, $p_{s\,\min} = 0.25p_{s\infty}$, $\Delta p_s = 0.05p_{s\infty}$. (i)-(iv) labelled flow features.

stream dissipation in the cylinder wake region than the corresponding stagnation temperature distribution.

Downstream of the cylinder, the cross-stream distribution of stagnation pressure can be compared with the measurements of Ackerman (2005) at $x_1 = 6.5D$. This comparison, along a fixed plane downstream of the circular cylinder, is given over the period of one vortex shedding cycle in Figure 5.38. Phase lock averaged stagnation pressure measurements are reported in Ackerman (2005) at the same stream-wise location as the phase lock averaged stagnation temperature measurements in Figure 5.34(b).

The stagnation pressure field in the experiment and the prediction demonstrate a good qualitative similarity. A periodic passage of localised regions with $p_s/p_{s\infty} > 1$ is observed in the prediction and the measurements at the edges of the wake. Similarly, localised regions of $p_s/p_{s\infty} < 1$ periodically occur close to the centre of the wake. The local stagnation pressure extrema, which are analogous to the hot and cold spots in the stagnation temperature distribution, lie approximately on a common x_1/D alignment in both the measured and the predicted flow fields. A phase shift in the relative location of the localised stagnation temperature and stagnation pressure extrema therefore occurs in the measurements of Ackerman (2005). This phase shift is not reflected in the turbulent prediction, which shows a similar alignment of the local stagnation temperature and stagnation pressure extrema.

The maximum $p_{s\,\max}/p_{s\infty}$ and minimum $p_{s\,\min}/p_{s\infty}$ stagnation pressures, as well as the average cross-stream distance from the wake centreline to the stagnation pressure maxima, $|\Delta x_2/D|_{p_{s\,\max}}$, are compared in Table 5.9. The measured stagnation

Source	$p_{s\,\max}/p_{s\infty}$	$p_{s\,\min}/p_{s\infty}$	$\lvert\Delta x_2/D\rvert_{p_{s\,\max}}$
Current $k-\omega$ prediction	1.124	0.610	1.340
Ackerman (2005)	1.050	0.788	2.580

Table 5.9: Stagnation pressure distribution at $x_1 = 6.5D$. Turbulent prediction comparison with the '2000 series' measurements of Ackerman (2005) at $M_\infty = 0.6$ and $Re_D = 6.86 \times 10^5$.

pressure rises to a maximum value of $p_{s\,\max} = 1.05p_{s\infty}$, which is 6.6% lower than the

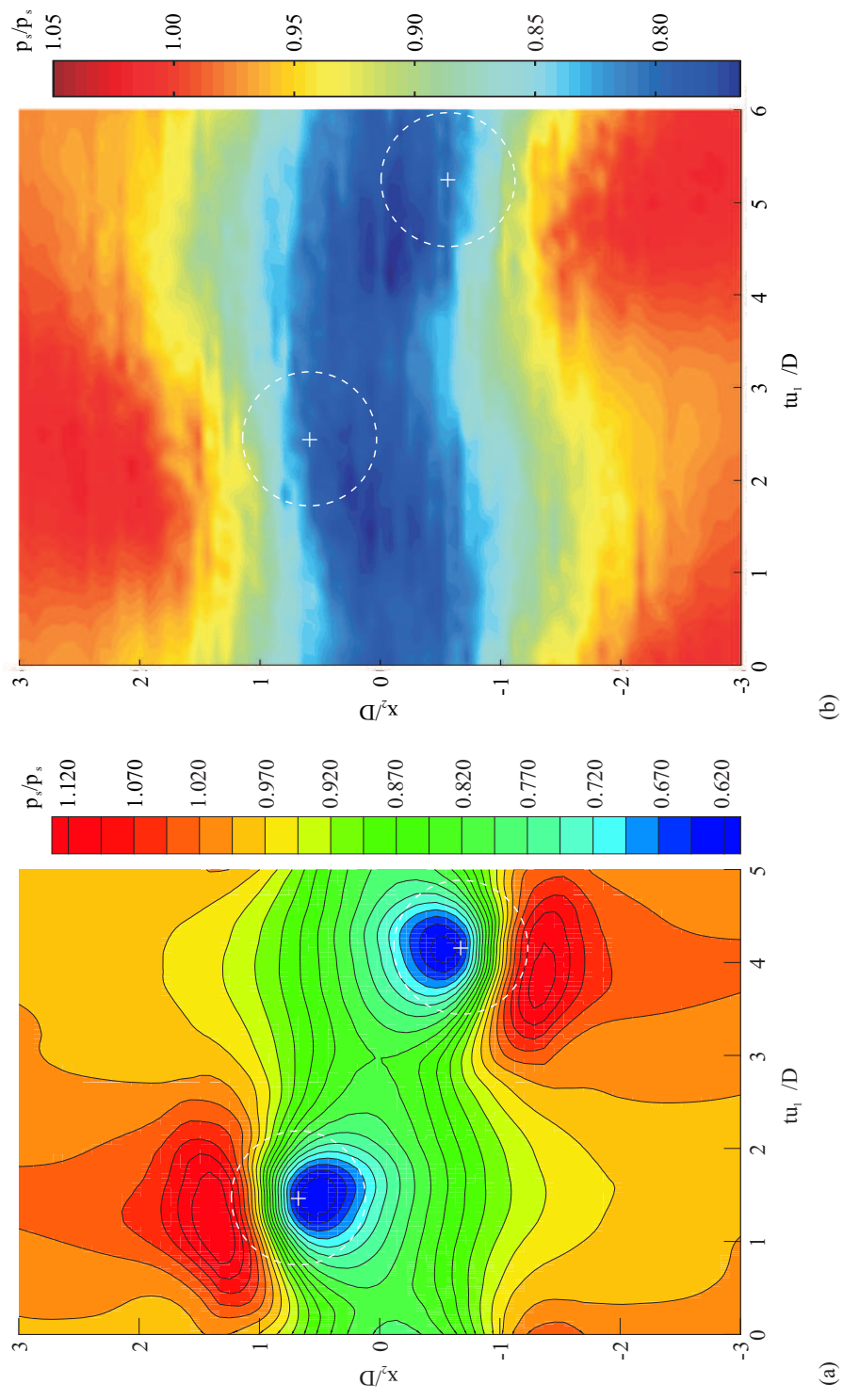

Figure 5.38: Stagnation pressure field comparison between the phase lock averaged measurements of Ackerman (2005) and the turbulent prediction at $x_1 = 6.5D$. (a) Turbulent prediction. (b) Measurements taken from the '2000 series' results of Ackerman (2005). Normalising parameters of $p_{s\infty}$, $u_{1\infty}$ and D taken from the turbulent prediction in (a) and from the reported measurements of Ackerman (2005) in (b).

turbulent prediction at the same downstream location. The average measured cross-stream distance between successive maxima is also approximately twice the distance between the predicted maxima. Specifically, $|\Delta x_2/D|_{p_s\,\max} = 2.580$ in the measurements of Ackerman (2005), compared with $|\Delta x_2/D|_{p_s\,\max} = 1.340$ in the turbulent prediction. The stagnation pressure drop at each local minimum is, however, lower in the turbulent prediction. This may partially result from the increased spatial and temporal resolution across the vortex in the turbulent prediction. These minima are located alternately above and below the wake centreline, at approximately $|\Delta x_2/D|_{p_s\,\min} = 0.585$. In contrast, the measured stagnation pressure minima are located along the wake centreline.

In isolation, the location of the stagnation pressure maxima indicate a substantial increase in the measured width of the wake at $x_1 = 6.5D$. The cross-stream distance between each successive stagnation pressure maxima in the measurements of Ackerman (2005) are, however, just under twice the cross-stream distance between the measured stagnation temperature maxima $|\Delta x_2/D|_{T_s\,\max}$ in Table 5.8. In comparison, the average cross-stream distance from the centre of the wake to the predicted stagnation pressure maxima $|\Delta x_2/D|_{p_s\,\max}$ is 17.13% greater than the predicted cross-stream distance between the centre of the wake and the stagnation temperature maxima $|\Delta x_2/D|_{T_s\,\max}$. The measurements therefore indicate a modification to the analogy between vortex induced stagnation temperature and pressure redistribution proposed for incompressible flows by Kurosaka et al. (1987). The turbulent stagnation pressure prediction at $x_1 = 6.5D$ does not reflect this modification to the same extent and remains closer in form to the predicted stagnation temperature field.

The time averaged stagnation pressure profile at $x_1 = 6.5D$ is given in Figure 5.39. The time averaged stagnation pressure in this turbulent prediction falls to $p_s = 0.75p_{s\infty}$ at the centre of the wake. The stagnation pressure drop at the centre of the wake is the same as in the inviscid prediction of Figure 5.21. The time averaged turbulent stagnation pressure minimum is however spread over a wider cross-stream distance. An increase of $p_s = 5 \times 10^{-3} p_{s\infty}$ above the free stream condition is also

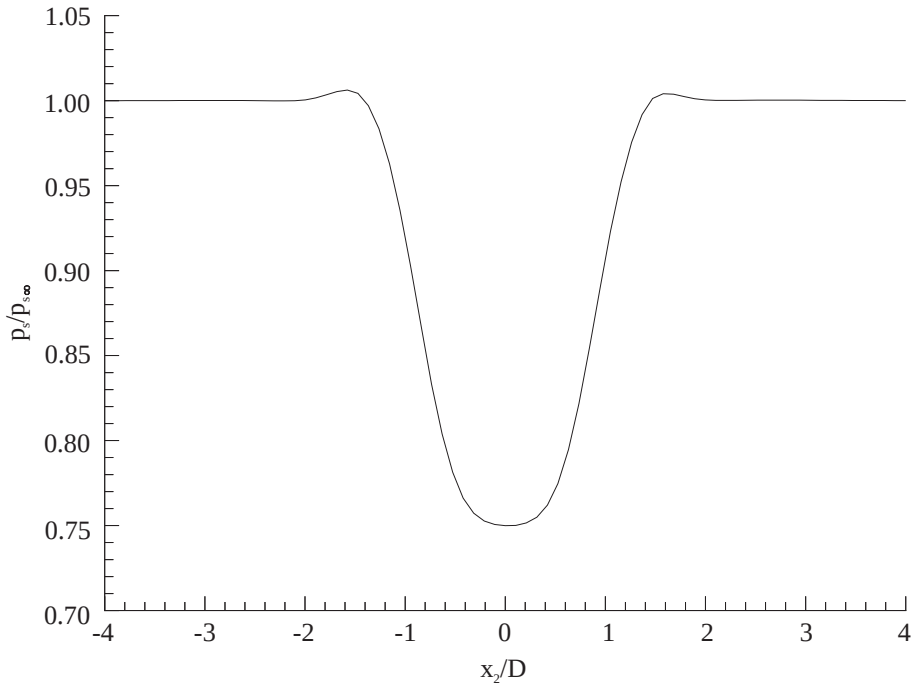

Figure 5.39: Time averaged stagnation pressure across the wake at $x_1 = 6.5D$.

predicted at $x_2 = \pm 1.6D$ in the turbulent prediction. This rise above the free stream condition, which is not predicted in the inviscid stagnation pressure profile, reflects the marginally higher stagnation pressure rise observed at each local maxima in the time resolved contours.

Variations in $T_s/T_{s\infty}$ that are not reflected in the $p_s/p_{s\infty}$ field constitute regions of entropy production. The time resolved specific entropy field is therefore computed for the turbulent prediction from Equation 5.4. The specific entropy field s, normalised by the gas constant R, is documented over the time interval $294.09 \leq tu_{1\infty}/D \leq 298.76$ in Figure 5.40(a-d) and Figure 5.41(a-d). Figure 5.40(a-d) captures the same phase of the vortex shedding cycle as the stagnation temperature time sequence in Figure 5.32(a-d) and the stagnation pressure time sequence in Figure 5.36(a-d). Similarly, Figure 5.41(a-d) is phase synchronous with Figure 5.33(a-d) and Figure 5.37(a-d). As in the inviscid prediction of Figures 5.22(a-d) and 5.23(a-d), regions of entropy production are highlighted at the centre of each vortex (i), in the shear layers extending between each successive pair of contra-rotating vortices (ii) and between the growing vortex and the cylinder surface (iii).

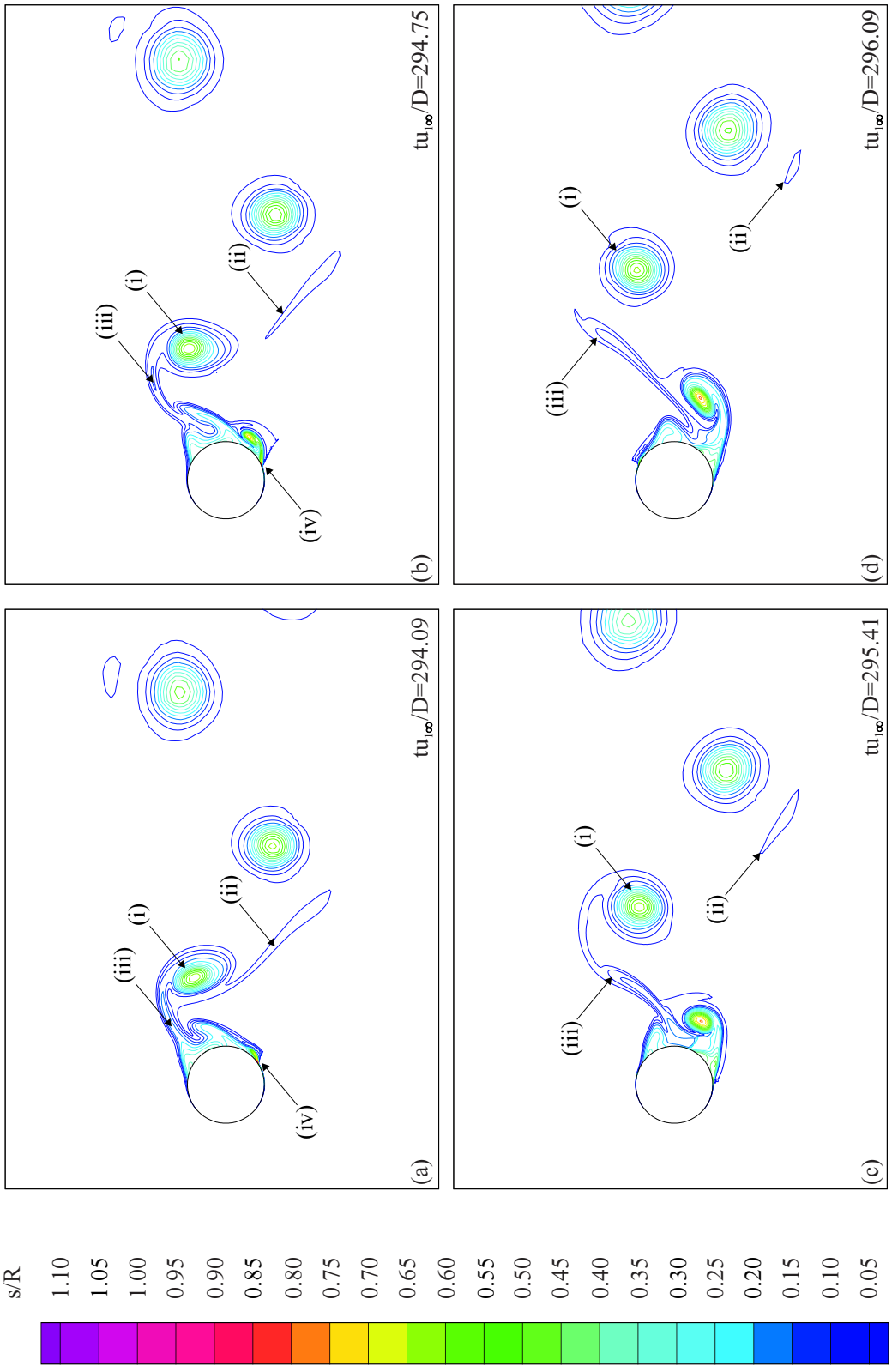

Figure 5.40: Instantaneous entropy contours over the first half of the vortex shedding cycle: $294.09 \leq tu_{1\infty}/D \leq 296.09$. $s_{\max} = 1.10R$, $s_{\min} = 0.05R$, $\Delta s = 0.05R$, $s_\infty = 0$. (i)-(iv) labelled flow features.

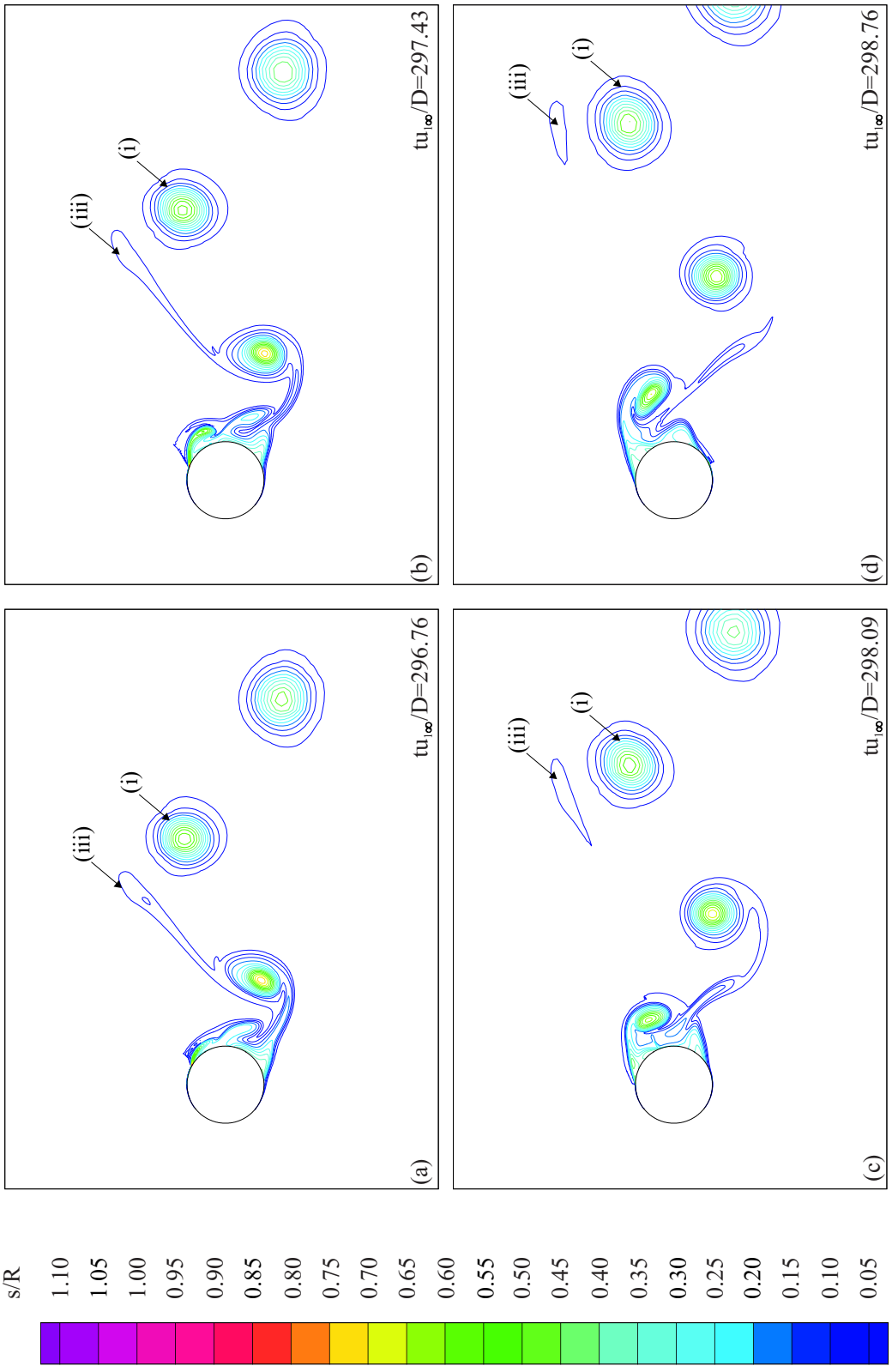

Figure 5.41: Instantaneous entropy contours over the second half of the vortex shedding cycle: $296.76 \leq tu_{1\infty}/D \leq 298.76$. $s_{\max} = 1.10R$, $s_{\min} = 0.05R$, $\Delta s = 0.05R$, $s_\infty = 0$. (i)-(iii) labelled flow features.

These downstream shear layers (ii) are reported in Fazle Hussain & Hayakawa (1987) as the location of the longitudinal vortices in the three-dimensional vortex street. It is the vortex stretching along these shear layers, along with the intense shearing between vortices on the same row, which contributes to the turbulence production in a three dimensional vortex street. In the turbulent prediction of Figure 5.40(a), an additional region of entropy production is defined upstream of the primary radial shock waves, close to the surface of the cylinder. This additional region of entropy production (iv) is caused by the surface normal stagnation temperature and pressure distribution through the developing boundary layer.

The time resolved specific entropy contours downstream of the cylinder are compared with the measurements of Ackerman (2005) at $x_1 = 6.5D$ in Figure 5.42. The turbulent prediction of Figure 5.42(a) corresponds directly to the stagnation pressure contours of Figure 5.38(a) and the stagnation temperature contours in Figure 5.34(a). Similarly, the measured entropy contours in Figure 5.42(b) correspond directly to the measured stagnation pressure contours in Figure 5.38(b) and to the stagnation temperature contours in Figure 5.34(b). At this downstream location, the main source of entropy production is highlighted as the centre of the vortices and at the rolling of the shear layers into each convecting vortex.

A quantitative summary of the specific entropy field prediction and measurements is given in Table 5.10. This table compares the specific entropy maximum $s_{\max}/R$ and the cross-stream distance of these maxima from the wake centreline, $|\Delta x_2/D|_{s_{\max}}$. The average specific entropy maximum is significantly lower in the

Source	$s_{\max}/R$	$\lvert\Delta x_2/D\rvert_{s_{\max}}$
Current $k-\omega$ prediction	0.430	0.684
Ackerman (2005)	0.315	0.554

Table 5.10: Specific entropy distribution at $x_1 = 6.5D$. Turbulent prediction comparison with the '2000 series' of Ackerman (2005), ($M_\infty = 0.6$, $Re_D = 6.86 \times 10^5$).

measurements of Ackerman (2005). This follows from the observed differences in the normalised stagnation pressure and temperature fields at this downstream location. The cross-stream distance between these entropy maxima and the wake centreline

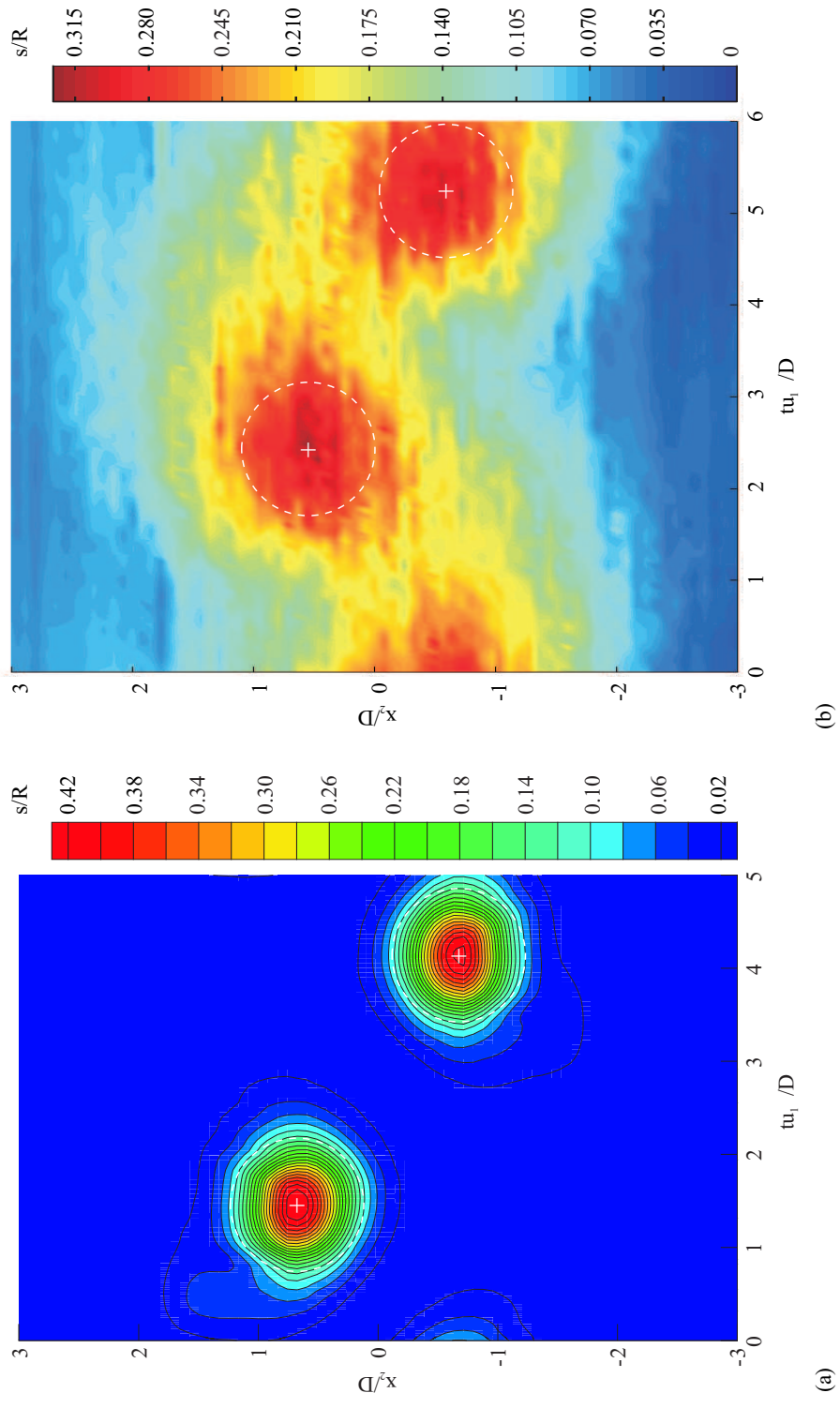

Figure 5.42: Specific entropy field comparison between the phase lock averaged measurements of Ackerman (2005) and the turbulent prediction at $x_1 = 6.5D$. (a) Turbulent prediction. (b) Measurements taken from the '2000 series' of Ackerman (2005). Normalising parameters of $u_{1\infty}$ and D are taken from the turbulent prediction in (a) and from the reported measurements of Ackerman (2005) in (b). The specific gas constant $R = 287J/(kgK)$.

is also 19% lower in the measurements of Ackerman (2005). Assuming the entropy maxima are accurate indicators of the vortex centres in both experiment and prediction, these results indicate a narrower cross-stream distance between vortex cores in the measured wake. This narrower cross-stream distance would be consistent, for a consistent vortex shedding aspect ratio, with an increase in stream-wise distance between successive vortices.

5.3.5 Summary

This section presents a turbulent prediction of the uniform compressible free stream flow past a circular cylinder at $M_\infty = 0.6$ and $Re_D = 6.87 \times 10^5$. This prediction extends the inviscid circular cylinder analysis at the same free stream Mach number in Section 5.2. A time accurate analysis of the pressure drag coefficient, lift coefficient and near wake density field are documented. A comparison of the turbulent prediction against published measurements at $M_\infty = 0.6$, and comparable free stream Reynolds numbers, demonstrates that introducing the $k-\omega$ model improves the physical wake description over the inviscid prediction in Section 5.2. Comparing the time averaged drag coefficient and Strouhal number with the published measurements indicates that the turbulent prediction more closely approximates the shock-induced separation of a turbulent boundary layer.

Energy separation leads to a localised redistribution of the stagnation temperature and stagnation pressure fields downstream of the cylinder in the turbulent prediction. The time averaged result is a stagnation temperature and pressure deficit along the wake centre, in accordance with the Eckert-Weise effect.

A high degree of similarity is evident between the stagnation temperature and pressure distributions from the inviscid and turbulent predictions, highlighting the dominant role of the convecting large scale vortical structures over the small scale turbulence effects in the energy separation mechanism. The introduction of turbulence diffusion and small-scale turbulence kinetic energy dissipation modifies the magnitude and spatial extent of the stagnation temperature and pressure redistribution in the cylinder near wake region. This is particularly evident in the stagnation

temperature rise of the near side shear layer at each vortex formation and initial shedding event.

A comparison of the predicted stagnation temperature, pressure and specific entropy fields with the time resolved measurements of Ackerman (2005) at $x_1 = 6.5D$ demonstrates a good qualitative similarity. Localised regions of higher stagnation temperature and pressure than the free stream condition are present at the outer edges of the wake in both prediction and experiment. Corresponding localised regions of stagnation temperature and pressure lower than the free stream condition occur towards the centre of the wake in both fields. Differences are however documented in the magnitude and transverse extent of the stagnation temperature and pressure redistribution. The current prediction demonstrates a consistently greater amplitude between the stagnation temperature and pressure maxima and minima. The transverse distance across the wake between the local maxima at each side of the wake is consistently lower in the turbulent prediction. The entropy field however indicates a marginally narrower distance between the measured vortex cores.

Differences are also observed in the stream-wise alignment of the hot spots, cold spots and vortex cores between the predicted and measured flow fields. The measurements of Ackerman (2005) show a phase difference between the hot and cold spots of a quarter of a vortex shedding cycle. In contrast, the predicted hot and cold spots are approximately phase synchronous with the vortex cores. This offset of the hot and cold spots is not reflected in the stagnation pressure distribution of either the prediction or the experiment. A survey of the available literature, to explain these differences, provides a possible cause from the three-dimensional vortex shedding effects reported in Williamson (1996), Fazle Hussain & Hayakawa (1987), Kiya & Matsumura (1988) and Cicatelli & Sieverding (1995). Possible improvements to the current prediction through a three-dimensional LES or DES approach are highlighted. This extension is intended to better approximate the vortex stretching that occurs along the longitudinal ribs between each vortex row, as well as the reported breakdown in span-wise uniformity of the vortex street.

Chapter 6

Turbine Cascade Prediction

6.1 Introduction

A two-dimensional time accurate numerical prediction of the flow through a turbine nozzle cascade passage at an isentropic exit Mach number of $M_e = 0.6$ is presented in this chapter. First, an inviscid flow prediction is obtained using the numerical solution procedure described in Sections 3.3, 3.5, 3.8 and 3.9. A turbulent prediction of the turbine cascade, at an exit Reynolds number of $Re_{D_t} = 7.48 \times 10^4$, is then developed using the solution procedure described in Sections 3.4-3.9. The turbulent prediction is initialised using the self-sustained inviscid vortex shedding flow field. The turbine blade modelled in this study is a cross-section of the low aspect ratio, highly loaded turbine nozzle guide vane studied by Carscallen & Oosthuizen (1989), Carscallen & Gostelow (1994), Carscallen et al. (1996, 1998, 1999), Hogg et al. (1997), Currie & Carscallen (1998) and Brooksbank (2001). This turbine blade profile is also the mean cross-section of the turbine nozzle guide vane described in Williamson et al. (1986). Surface coordinates for this mean cross-section are reported in Brooksbank (2001). Experimental oil flow visualisation by Moustapha et al. (1993) on a cascade of blades with this profile, at $M_e = 0.7$ and $M_e = 1.2$, indicates no significant span-wise flow along the surface of the blade, away from the wind tunnel side walls. These results indicate that a two-dimensional prediction may provide a reasonable physical approximation to the flow past this turbine cascade at the selected test conditions. Further details concerning past research for this turbine cascade are provided, based on the available literature, in Sections 2.2-2.4.

The present time accurate numerical study, at an isentropic exit Mach number of $M_e = 0.6$, represents a novel extension to the research concerning this turbine cascade and provides comparative asymmetric body wake data for the circular cylinder analysis of Chapter 5. Modelling details for this turbine cascade prediction, as well as results from the inviscid prediction, are discussed in Section 6.2. Improvements to the prediction, through additional physical modelling by the short-time averaged Navier-Stokes equations and the $k-\omega$ turbulence model, are discussed in Section 6.3.

6.2 Inviscid Turbine Cascade Flow Prediction

6.2.1 Numerical Model Specifications

The turbine cascade characteristic dimensions are listed in Table 6.1. The computa-

Dimension	Value
Trailing edge diameter (D_t)	$6.35 \times 10^{-3}\ m$
Throat width	$30.9 \times 10^{-3}\ m$
Chord (c)	$0.204\ m$
Pitch to chord ratio	0.7246
Inlet metal angle	$-10°$
Exit metal angle	$76°$
Stagger angle	$65.5°$

Table 6.1: Turbine blade geometry.

tional domain used to model this turbine cascade is represented diagrammatically in Figure 6.1. The computational domain extends $6.2D_t$ upstream of the turbine blade leading edge. The inlet boundary $b1$ is also an axial distance of $19.54D_t$ upstream of the turbine blade trailing edge, which represents the main source of unsteady pressure wave production. The subsonic inlet boundary condition, detailed in Section 3.9.1, is imposed at the upstream boundary ($b1$). The stagnation pressure and temperature imposed at the inlet boundary $b1$, along with the other inlet and exit conditions, are defined in Table 6.2. These inlet flow conditions are designed to approximate the wind tunnel working section in the experiments of Ackerman (2005). The periodic boundary condition described in Section 3.9.6 is specified at the pitchwise boundaries, $b2$ and $b4$. Each external (perimetrical) cell along the boundary $b2$

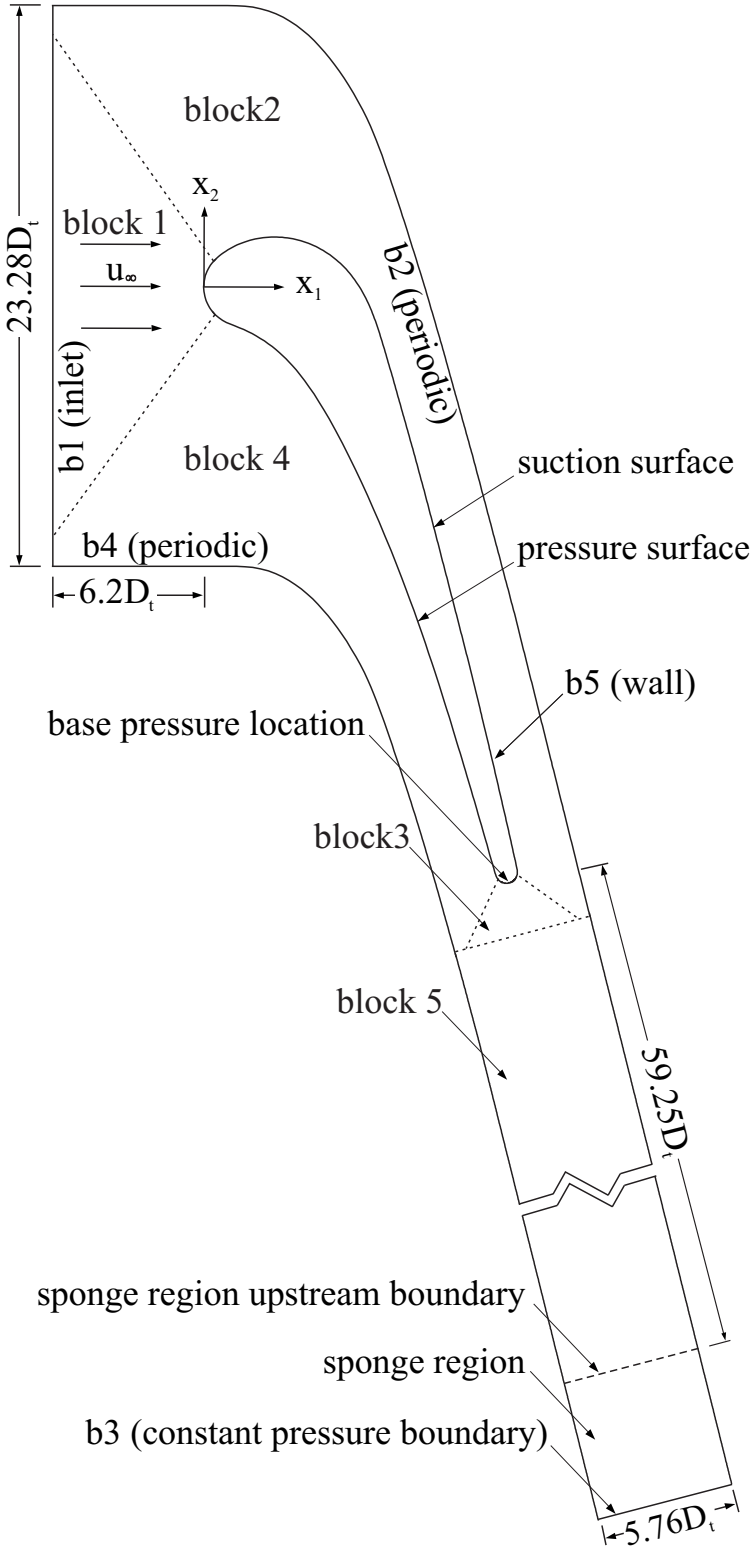

Figure 6.1: Turbine blade computational domain.

Variable	Value
M_e	0.6
M_∞	0.1025
$p_{s\infty}/p_e$	1.2755
$p_{s\infty}$	102.072 kN/m^2
p_∞	101.325 kN/m^2
$T_{s\infty}$	293.616 K
T_∞	293 K
ρ_∞	1.205 kg/m^3
u_e	199.05 m/s
u_∞	35.17 m/s

Table 6.2: Turbine blade flow conditions.

is updated by a direct copy of the flow variables stored in the interior cell, lying at the same axial location, juxtaposing the boundary $b4$. Conversely, the flow variables stored in the interior cells juxtaposing $b2$ update the perimetrical cells along $b4$. The periodic boundary condition allows a complete turbine cascade to be modelled from a prediction of the flow past a single turbine blade. The inviscid wall condition, described in Section 3.9.7, is defined along the turbine blade surface $b5$. This is replaced in the turbulent prediction by the adiabatic, no-slip surface condition described in Section 3.9.8. The constant pressure outlet boundary condition, described in Section 3.9.3, is specified at the boundary $b3$.

In a series of preliminary inviscid and turbulent predictions on this turbine blade, the definition of a constant static pressure outlet condition at $b3$ lead to significant numerical wave reflections from this boundary. These numerical wave reflections lead to the presence of a standing pressure wave, at a frequency significantly below the vortex shedding frequency. The wavelength associated with this standing wave was approximately twice the computational domain stream-wise length. These preliminary predictions, which are not documented in this study, lead directly to the implementation of a non-reflecting boundary condition at the outlet boundary $b3$. A number of non-reflecting boundary conditions are documented in the available literature. These include characteristic based approaches, which utilise the hyperbolic character of the governing equations convective terms to specify or control the in-

coming and outgoing characteristic waves. Examples of this approach are found, for example, in Thompson (1987), Giles (1990), Poinsot & Lele (1992), Colonius (1997), Rowley & Colonius (1998), Kim & Lee (1998) and Hixon (2000). An alternative approach to prevent reflected waves at the outlet is to define an absorbing 'sponge' layer of cells adjacent to the outlet boundary. This method relies on the addition of artificial viscosity to reduce the magnitude of the pressure fluctuations, upstream of the outlet boundary. The addition of artificial viscosity can be achieved in a number of ways, including the definition of additional terms in the governing equations, as described in Hu (1996), Freund (1997) and Nizampatnam et al. (1999). Alternatively, numerical dissipation can be introduced through large gradient grid stretching normal to the outlet boundary, as used in Visbal & Gaitonde (1999). This final technique is the method of choice for the present study. A sponge region of cells, stretched in the stream-wise direction, is therefore defined immediately upstream of the outlet boundary $b3$. The constant pressure outlet condition described in Section 3.9.3 is then imposed at the boundary $b3$. An extrapolation type boundary condition is defined at each pitch-wise boundary in the sponge region. The resulting prediction, documented in this section, confirms that the sponge region defined immediately upstream of the outlet boundary eliminates the numerical wave reflections from the outflow.

The computational domain is divided into five contiguous blocks. Each block is connected using the inter-domain boundary condition described in Section 3.9.5. These boundaries are shown as dashed lines in Figure 6.1. The stream-wise length of block 5 is truncated in Figure 6.1 for convenience. Block 5 is sub-divided into two regions. The first region is defined between the interface with block 3 and the long dashed line shown upstream of the boundary $b3$ in Figure 6.1, aligned in the stream-wise normal direction. This region has a constant grid spacing in the stream-wise direction. The sponge region, defined between the long dashed line in block 5 and the outlet boundary $b3$, has a significant level of stream-wise grid stretching. The interface between the two regions is defined at a distance of $59.25D_t$ downstream of the turbine blade trailing edge, as shown by the long dashed line in Figure 6.1.

The grid resolution inside each block is listed in Table 6.3. The surface of the

Block	Grid resolution ($\Sigma i \times \Sigma j$)
1	24×200 cells
2	307×204 cells
3	120×200 cells
4	115×204 cells
5	128×510 cells

Table 6.3: Grid resolution of the computational domain interior.

turbine blade is defined by 566 body-fitted cells, divided over blocks 1-4. Linear grid stretching is defined normal to the turbine blade to increase the flow field resolution close to the blade surface. Moderate linear grid stretching is also applied normal to the boundary $b2$, in blocks 3 and 5, to increase the grid resolution close to the wake centre. A Gauss-Seidel iterative smoothing method, described in Hoffman & Chiang (1995), is applied to reduce cell skewness in blocks 1-4. The sponge layer comprises of 128×20 cells. The remainder of block 5 therefore comprises of 128×490 cells. Outside of the sponge layer, the mesh in blocks 1-5 comprise of cells ranging in size from $(9.84 \times 10^{-4} D_t,\ 5.1 \times 10^{-3} D_t)$ to $(0.41 D_t,\ 0.85 D_t)$. A further frame of cells are defined around the perimeter of each block for imposing boundary conditions. The computational grid in blocks 1-4 is shown in Figure 6.2. The resolution of the grid shown in this figure is coarsened by a factor of four, normal to the surface of the blade, for clarity. A detailed view of the non-coarsened grid is given in Figure 6.3. This shows a section of the grid, close to the trailing edge, highlighting the surface normal grid stretching.

6.2.2 Time Averaged Isentropic Mach Number Distribution

The turbine blade flow field is initialised by imposing the isentropic exit flow conditions uniformly throughout the computational domain. The initial flow development approximates the inviscid circular cylinder prediction at very short times, as described in Section 5.2.2. A self-sustained vortex shedding pattern then develops at later times. The numerical prediction, within this self-sustained vortex shed-

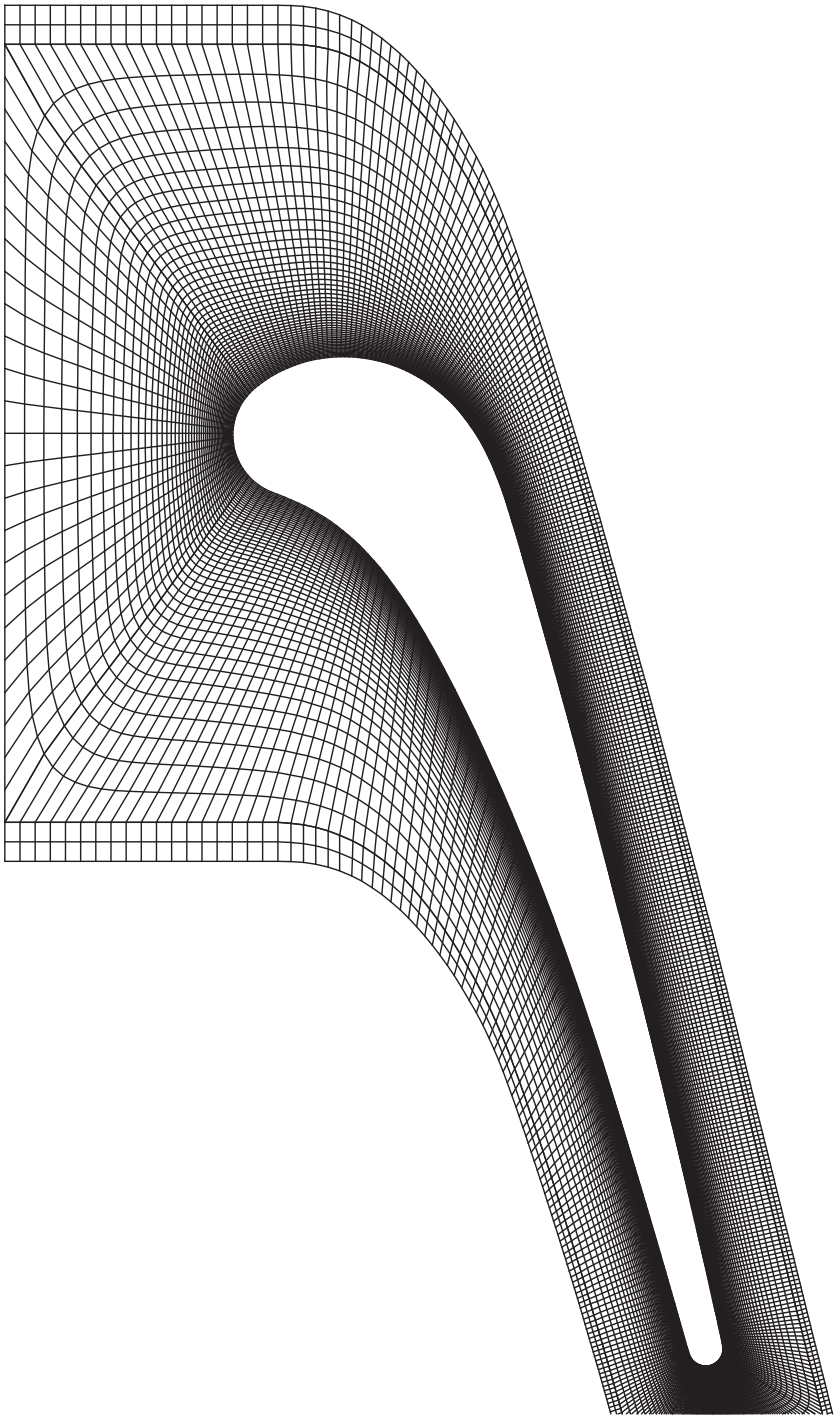

Figure 6.2: Turbine blade computational grid. Grid coarsened by factor of four normal to the blade surface.

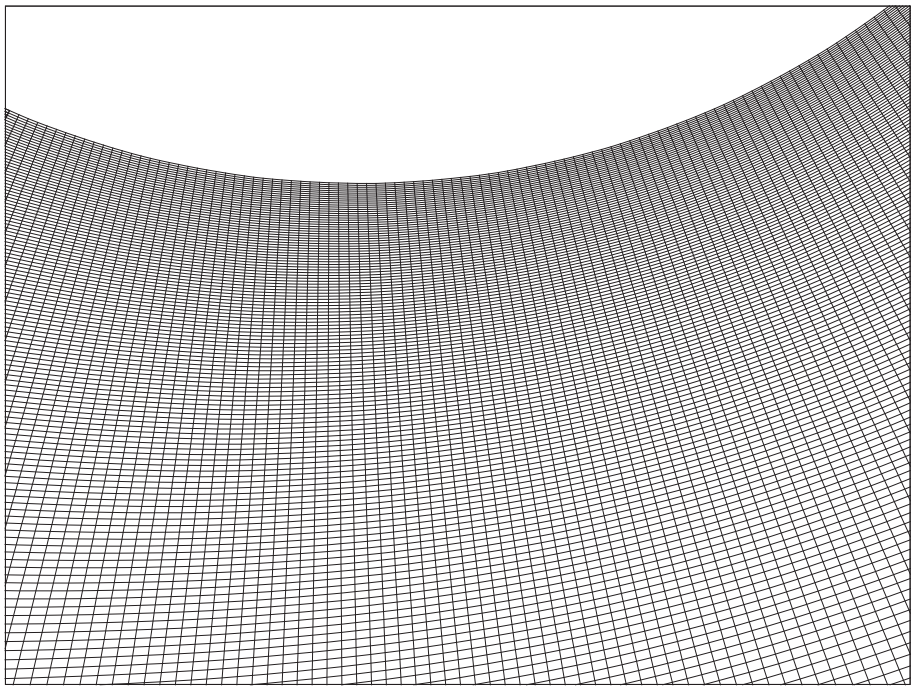

Figure 6.3: Detail of the grid resolution at the turbine blade trailing edge.

ding regime, can be verified against measurements from a concurrent experimental research program for the same turbine cascade at $M_e = 0.6$ by Ackerman (2005). Time averaged measurements of the isentropic Mach number distribution along the surface of the turbine blade are compared with the current prediction in Figure 6.4. The isentropic Mach number distribution is calculated from the surface static pressure distribution and the upstream stagnation pressure. The abscissa in Figure 6.4 is the ratio of the surface axial coordinate x_1 to the blade axial chord length c_1. The origin, $x_1 = 0$, is defined at the leading edge of the turbine blade, as shown in Figure 6.1. The leading edge stagnation point is, in fact, located along the pressure surface at $x_1/c_1 = 0.03$. The precise location of the upstream stagnation point is dependent on the pitch-wise aerodynamic loading of the turbine blade. This dependency is documented by Roberts & Denton (1996) for variable loading of a simulated turbine blade (Section 2.2). The current location for the leading edge stagnation point is consistent with the inviscid prediction of Brooksbank (2001) for the same turbine blade profile at $M_e = 1.16$.

A favourable pressure gradient is defined along the pressure surface, resulting in

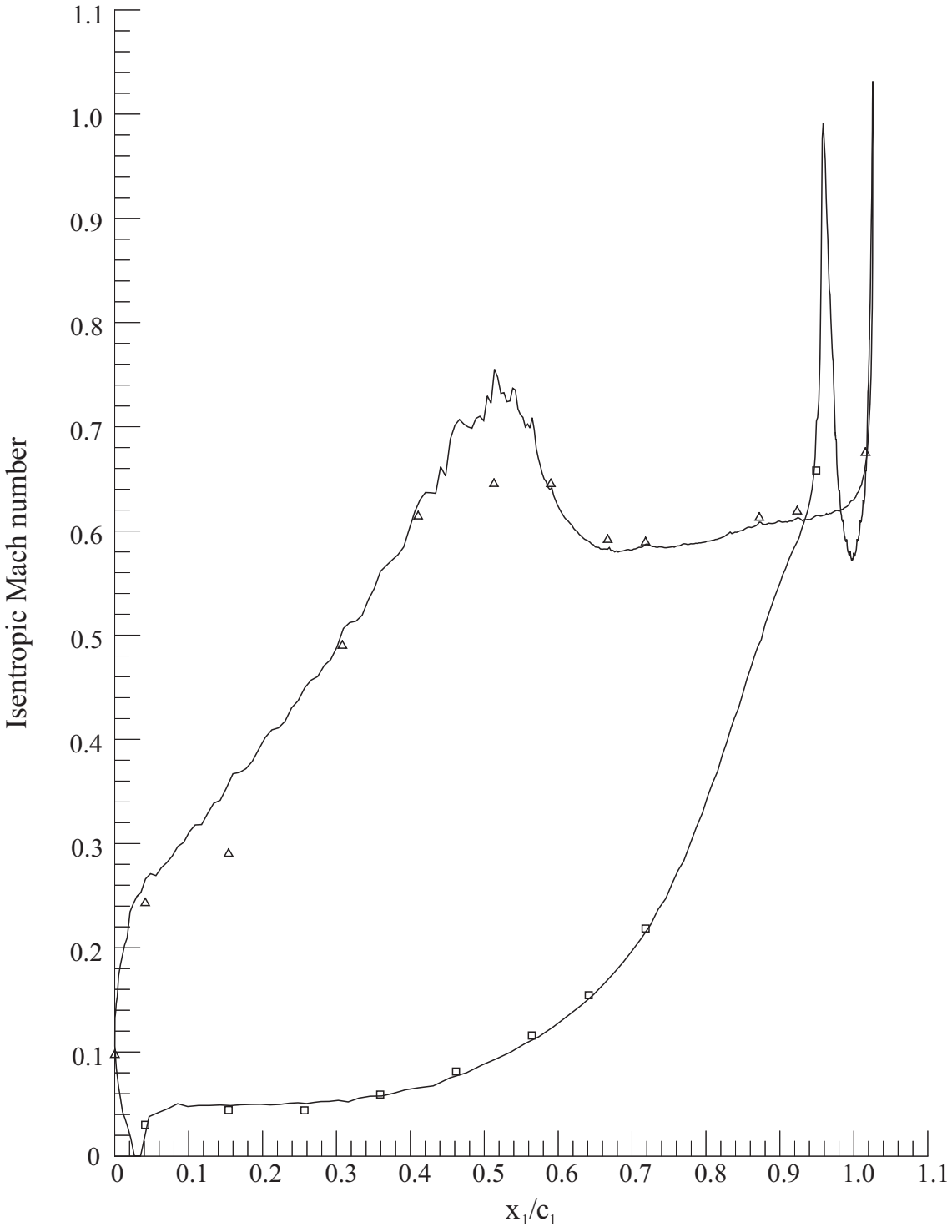

Figure 6.4: Turbine blade isentropic Mach number distribution. (—) Numerical prediction. □ Measured pressure surface distribution, Δ Measured suction surface distribution. x_1, surface axial coordinate relative to the leading edge. c_1, axial component of chord length.

an almost continuous acceleration of the fluid from the upstream stagnation point to the trailing edge. The predicted isentropic Mach number distribution demonstrates a reasonable match with the measurements, remaining within ±15% throughout the length of the pressure surface. The favourable pressure gradient around the suction surface leading edge initially results in a rapid acceleration of the fluid in this region. The numerical prediction shows an over-acceleration, between $x_1/c_1 = 0.06$ and $x_1/c_1 = 0.3$, in comparison with the measured distribution. This results in a local over-expansion of the fluid. A further over-expansion occurs along the suction surface, between $x_1/c_1 = 0.42$ and $x_1/c_1 = 0.6$, in the prediction. The plateau in the measured distribution around this region suggests the presence of a laminar separation bubble. The indication of a laminar separation bubble, which is absent in the inviscid prediction, is substantiated by Moustapha et al. (1993). Using oil flow visualisation, the presence of a laminar separation bubble is clearly visible around $x_1/c_1 = 0.5$, on the same blade profile, at $M_e = 0.7$. Furthermore, Moustapha et al. (1993) indicate a movement in the location of the laminar separation bubble further downstream at higher exit Mach numbers. In the absence of the laminar separation bubble, the prediction reaches a peak isentropic Mach number of $M = 0.76$ at $x_1/c_1 = 0.52$. The predicted isentropic Mach number distribution closely follows the measured distribution along the suction surface, after closure of the laminar separation bubble at $x_1/c_1 \approx 0.6$. The close relationship continues along the suction surface to the fluid expansion around the trailing edge at $x_1/c_1 \approx 1.02$. Overall, a satisfactory agreement is demonstrated with the measured isentropic Mach number distribution.

6.2.3 Vortex Shedding Characteristics

The time dependent base pressure, after the onset of a self-sustained vortex shedding pattern, is documented over the time interval $680 \leq tu_e/D_t \leq 880$ in Figure 6.5. The base pressure trace, which is normalised using the stagnation pressure imposed at the inlet $p_{s\infty}$, is monitored at the intersection of the exit camber line and the trailing edge surface. The approximate location of this base pressure tapping is indicated

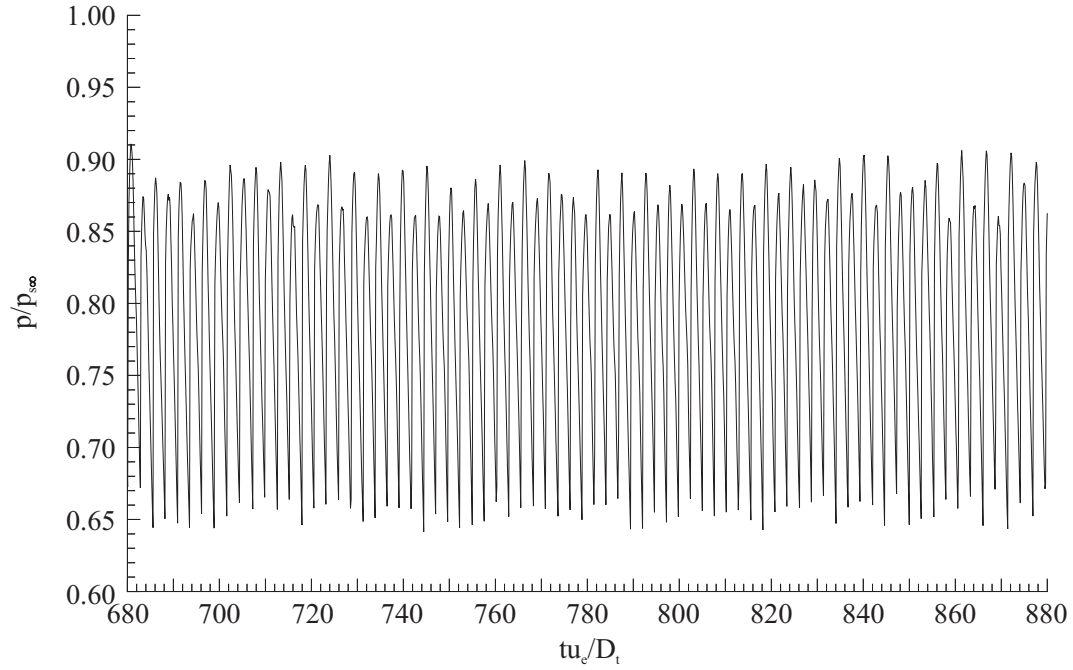

Figure 6.5: Base pressure history.

in Figure 6.1. The resulting base pressure trace has a mean value of $p = 0.79 p_{s\infty}$ and a root mean square value of $p_{rms} = 7.39 \times 10^{-2} p_{s\infty}$. A high frequency pressure oscillation, of approximately 75 cycles duration, is observed in Figure 6.5. This is associated with the formation and shedding of vortices from both sides of the trailing edge. A continuous vortex shedding is therefore predicted downstream of this turbine blade profile. The time accurate relationship, between the base pressure variation and the formation and shedding of each vortex, is documented for the circular cylinder prediction in Section 5.2.3. A similar variation is observed in the turbine blade base pressure history. The base pressure falls to a local minimum as each growing vortex at the trailing edge approaches its peak strength. This occurs immediately preceding the cessation of the circulation supply from the near side shear layer, by the cross stream entrainment of the far side shear layer. As the vortex starts to convect downstream, the base pressure rises to a local maximum, before the formation and growth of a new vortex with opposing rotation causes a subsequent decrease of the base pressure.

A Fourier analysis of the base pressure history in Figure 6.5 yields the power

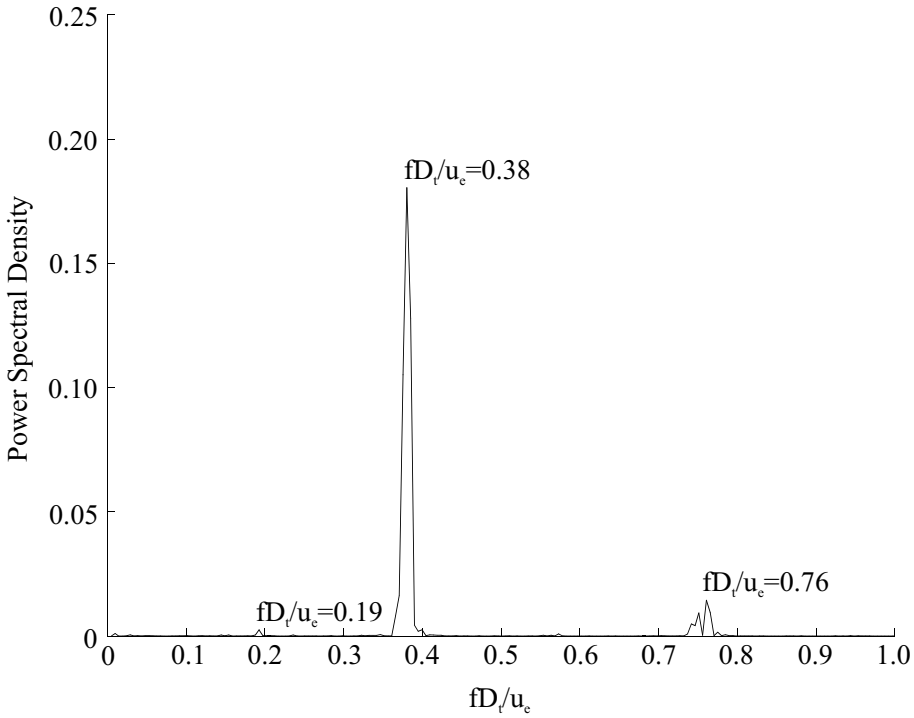

Figure 6.6: Frequency analysis of the time accurate base pressure history.

spectrum in Figure 6.6. Three isolated regions of interest are identified in Figure 6.6. These include a low magnitude tone located at $f = 0.19u_e/D_t$, a narrow-band contribution centred at $f = 0.38u_e/D_t$, and a lower magnitude (wider bandwidth) contribution, with a peak value at $f = 0.76u_e/D_t$. The narrow-band contribution at $f = 0.38u_e/D_t$, has a peak power spectral density at approximately twice the vortex shedding Strouhal number measured by Carscallen et al. (1996). This feature is associated with the fall and subsequent rise in base pressure as each vortex grows in strength and is shed from the trailing edge. The broad frequency content associated with the higher harmonic at $f = 0.76u_e/D_t$, as well as a survey of the base pressure trace, indicates that, although a dominant mode of vortex shedding is established, variations in the vortex shedding still occur on a cycle-to-cycle basis. As with the circular cylinder analysis, this cycle-to-cycle variation indicates that a phase-locking feedback of the vortex shedding remains under-developed. The low frequency peak in Figure 6.6, at $f = 0.19u_e/D_t$, is located around the vortex shedding Strouhal number in Carscallen et al. (1996), in which a Strouhal number of around $Str = 0.2$

is reported at $M_e = 0.6$. The presence of this frequency in the base pressure trace implies that the base pressure is mildly influenced by the vortex shedding events on one side of the wake. This appears consistent with the pitch-wise asymmetric vortex shedding pattern, anticipated for this turbine blade. No time resolved flow statistics for this turbine blade profile at $M_e = 0.6$ are documented in any literature available to the author. The time accurate flow analysis presented in this section therefore represents a novel contribution to the documented research on this turbine blade profile.

Figures 6.7 and 6.8 document the development of the turbine cascade near wake density field over one typical vortex shedding cycle, $853.44 \leq tu_e/D_t \leq 858.11$.

The computational domain is truncated in these figures to highlight the near wake region of one turbine blade and the suction surface of the adjacent turbine blade. Solid black lines define the turbine blade surface in Figures 6.7 and 6.8. Figure 6.7 documents the formation of an anti-clockwise rotating vortex at the pressure surface side of the trailing edge. Figure 6.8 documents the shedding and downstream convection of this vortex and the formation of a new, clockwise rotating vortex at the suction surface side of the trailing edge. This iso-density contour time sequence allows a comparison with the circular cylinder flow development over one vortex shedding cycle, as given in Figures 5.10 and 5.11.

Figure 6.7(a) shows the flow field immediately following the separation of a clockwise rotating vortex (v) from the suction side of the trailing edge. A shear layer of fluid (iv) extends between this vortex and the trailing edge surface. This is shown by local deviations in the iso-density contours near (iv) in this figure. A local expansion occurs around the curved profile of the trailing edge, along the pressure surface. This expansion is indicated by a gradual shift in the colour of the iso-density contours, immediately upstream of a short radial shock wave (i), towards the blue end of the colour spectrum. This radial shock wave (i) terminates the local supersonic region. Further regions of sharp local stream-wise compression are evident in Figure 6.7(a) along the suction surface of this blade (ii) and along the suction surface of the adjacent blade (iii). As the flow field develops from Figure 6.7(a), a new vortex

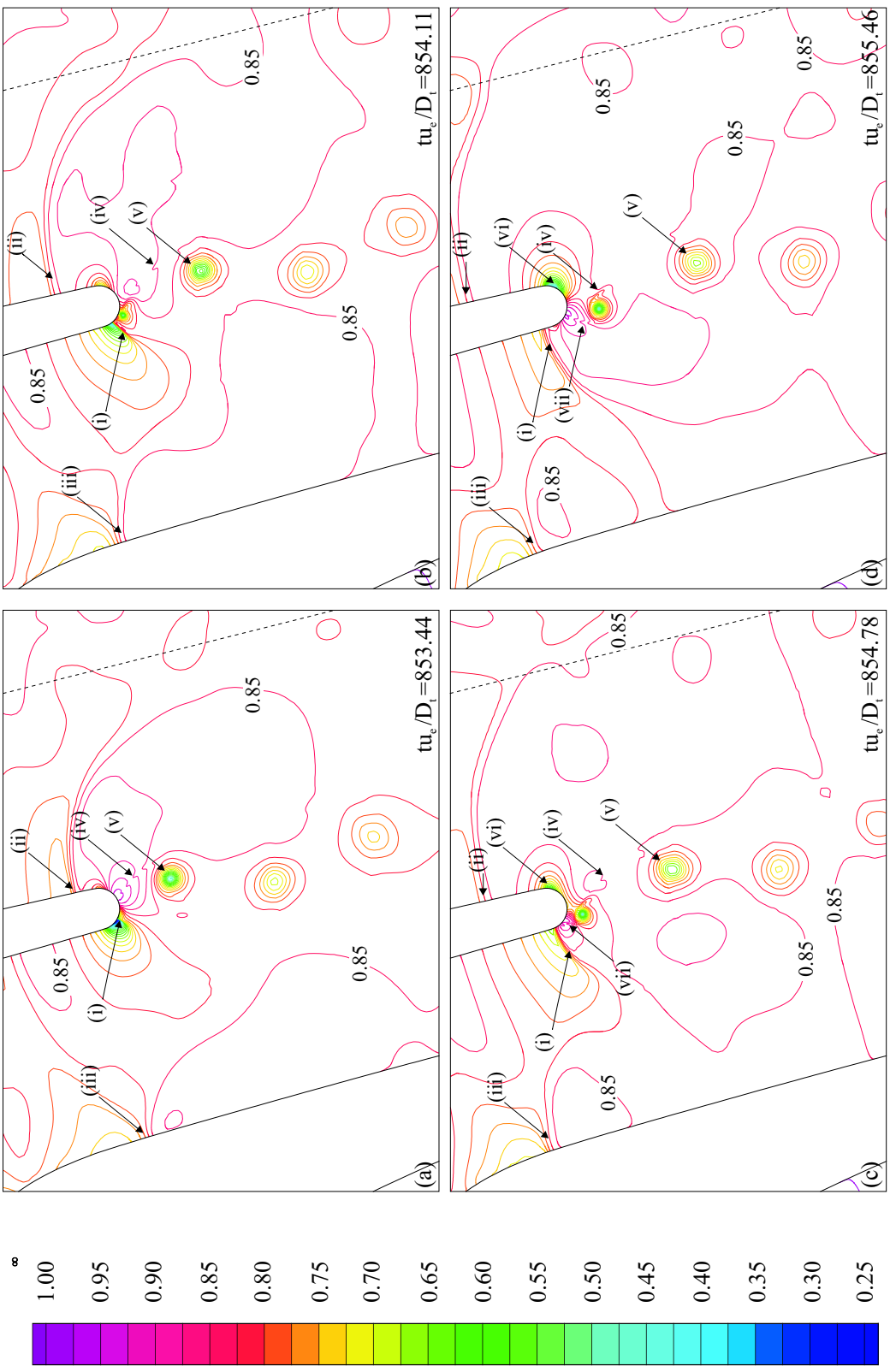

Figure 6.7: Static density contours over the first half of the vortex shedding cycle: $853.44 \leq tu_e/D_t \leq 855.46$. $\rho_{\max} = 1.0\rho_\infty$, $\rho_{\min} = 0.25\rho_\infty$, $\Delta\rho = 0.025\rho_\infty$. (i)-(vii) labelled flow features, – – – mean vortex path alignment from the adjacent blade.

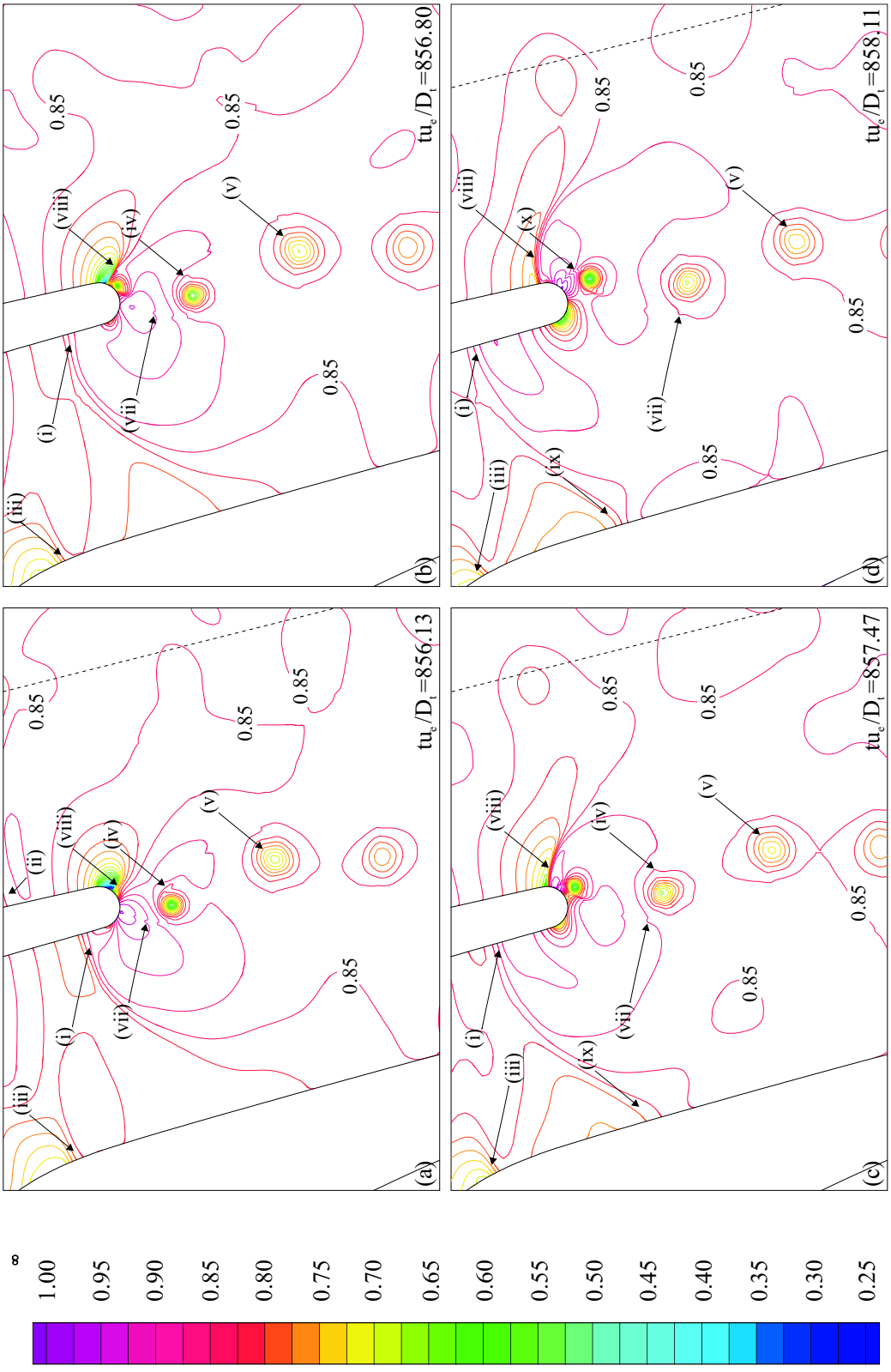

Figure 6.8: Static density contours over the second half of the vortex shedding cycle: $856.13 \leq tu_e/D_t \leq 858.11$. $\rho_{\max} = 1.0\rho_\infty$, $\rho_{\min} = 0.25\rho_\infty$, $\Delta\rho = 0.025\rho_\infty$. (i)-(x) labelled flow features, – – – mean vortex path alignment from the adjacent blade.

with anti-clockwise rotation forms at the base of the pressure surface shock wave (i). The shock wave radial extent increases, and an upstream movement follows, causing a termination of the low pressure region at lower supersonic velocities. The subsequent upstream movement of this shock wave, Figure 6.7(b-d), eventually results in a termination of the accelerated fluid at subsonic velocities. The pressure wave (i) then continues to propagate upstream, losing strength over the course of Figure 6.8(a-d). This decrease in strength and increase in dispersion is evident in Figure 6.8(a-d) as a gradual decrease in the number of iso-density contours and an increase in the contour spacing across the pressure wave (i).

The initial upstream movement of the radial shock wave in Figure 6.7(a-c), alongside the growth of a new vortex, is similar to the inviscid circular cylinder prediction documented in Section 5.2.5. However, the favourable stream-wise pressure gradient in the circular cylinder prediction, along the windward surface, forms an upstream limit to the radial shock wave movement. The radial shock wave subsequently loses strength and precesses downstream over the second half of the vortex shedding cycle. The absence of this strong favourable pressure gradient in the turbine blade prediction allows the radial pressure waves to propagate further upstream, through the turbine cascade passage. The upstream precessing pressure wave (ii) in Figure 6.7(a-d) can therefore be identified as the pressure wave that is formed during the initial growth of the clockwise rotating vortex (v). The outward propagation of this pressure wave can cause a localised interaction with the vortices shed from the adjacent blade. The location and alignment of these vortices, which are not identifiable at the present contour resolution, are indicated in Figure 6.7 and Figure 6.8 by dashed lines. The outward propagating pressure wave from the pressure surface side (i) impinges on the suction surface of the adjacent blade. This causes a localised density gradient, in the stream-wise direction, along the suction surface of this blade. This region is labelled (ix) in Figure 6.8(c-d). Similarly, the upstream moving density gradient, labelled (iii) in Figures 6.7 and 6.8, is caused by an impingement of the pressure wave formed at the conception of the previous anti-clockwise rotating vortex. This anti-clockwise rotating vortex is located imme-

diately downstream of the clockwise rotating vortex labelled (v) in Figure 6.7(a-d). In the absence of the downstream precessing shock wave, observed in the circular cylinder prediction, a region of highly expanded fluid (vi) is defined on the opposite side to the shed vortex. This expansion stretches around the trailing edge suction surface to the base pressure location in Figure 6.7(c-d). As the fluid in this region increases to supersonic velocities, a radial shock wave forms, terminating the supersonic region close to the base pressure location. This shock wave is labelled (viii) in Figure 6.8(a-d). The unperturbed upstream transport of the radial pressure waves, and the absence of a downstream pressure wave movement, represents a divergence of the vortex shedding mechanism from the inviscid circular cylinder prediction. A further divergence is the absence of a local radial shock wave, located between the growing vortex and the trailing edge surface. In the circular cylinder prediction this radial shock wave is caused by a supersonically accelerated channel of fluid, that passes between the vortex core and the cylinder surface.

As the anti-clockwise rotating vortex increases in strength over the course of Figure 6.7(b-c), fluid is increasingly entrained from the shear layer on the opposite side of the wake (iv). After sufficient fluid has been entrained from this shear layer, the circulation supply from the near side shear layer (vii) to the vortex ceases and the vortex is shed. The far side shear layer (iv) subsequently rolls up with the shed vortex, forming a region of shearing fluid between this vortex and the clockwise rotating vortex (v). These shear layers are evident as localised deviations in the iso-density contours of Figures 6.7 and 6.8, for example (iv).

A gradual decrease in the strength of each shed vortex occurs with increasing downstream distance. This decrease in strength, observed as a decrease in the radial density gradient at the centre of the vortex, is evident by following the clockwise rotating vortex (v) in Figures 6.7(a-d) and 6.8(a-d). A gradual change in the colour of the iso-density contours at the centre of each vortex, towards the red end of the colour spectrum, accompanies a decrease in the number of contours defining each vortex with downstream distance.

The unsteadiness in the static density field is further documented by the root mean

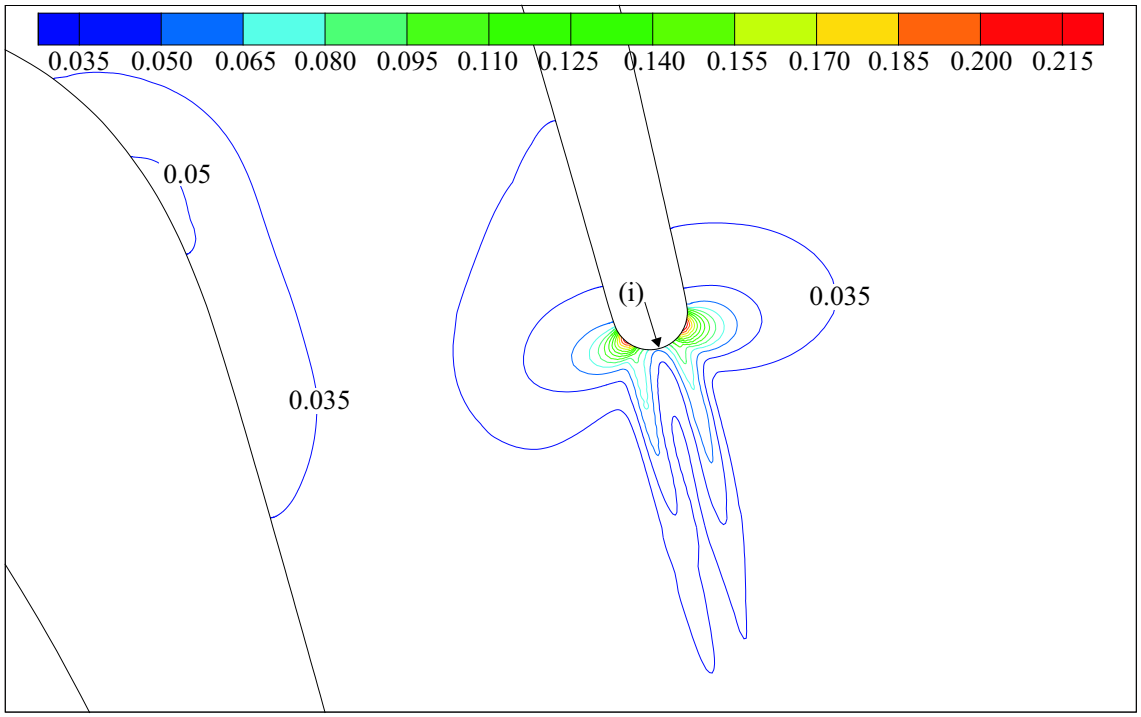

Figure 6.9: Root mean square density contours. $(\rho_{\max})_{rms} = 0.215\rho_\infty$, $(\rho_{\min})_{rms} = 0.035\rho_\infty$, $\Delta\rho = 0.015\rho_\infty$. (i) base pressure location.

square (rms) density field. This is given in Figure 6.9. Peak regions of rms density are located at approximately $\pm 60°$ around the trailing edge surface from the base pressure location (i). These regions undergo a transient change from being regions of local density minima, immediately preceding the formation of each new vortex on the near side of the wake, to regions of local density maxima, following the upstream movement of the near side shock wave. Further upstream, as the radial pressure waves decrease in strength, the rms iso-density contours intersect the turbine blade surface at increasing stream-wise intervals. These contours remain identifiable for a significant distance upstream of the trailing edge. Regions of augmented rms density are also evident in Figure 6.9, close to the suction surface of the adjacent turbine blade. These are caused by the impingement and upstream movement, along this surface, of the radial pressure waves identified in Figures 6.7(a-d) and 6.8(a-d). A short section highlighting the downstream alignment of the convecting vortices is also evident in Figure 6.9. The rms density fluctuation is shown to decrease monotonically with downstream distance along these paths. In contrast, the inviscid

circular cylinder rms iso-density contours of Figure 5.13 show an initial increase in the rms density fluctuation with downstream distance from the leeward surface. This increase is followed by a gradual decrease of the rms density fluctuation further downstream. Minor asymmetries are observed in the magnitude and distribution of the rms density fluctuation and in the location of the wake centreline, relative to the base pressure location (i) in the inviscid turbine cascade prediction. This slight asymmetry is however significantly less than the wake asymmetry reported for this turbine blade profile at higher Mach numbers by Hogg et al. (1997) and Carscallen et al. (1998, 1999). The differences highlighted in this section, between the circular cylinder and turbine blade near wake flows, may lead to associated differences in the magnitude and location of the wake stagnation temperature and pressure redistribution, as discussed in Section 6.2.4.

6.2.4 Energy Separation in the Turbine Cascade Wake

The vortex induced redistribution of stagnation enthalpy, described in Section 2.6, constitutes a significant source of entropy production downstream of each turbine blade row. This phenomenon leads to localised heating and cooling of the fluid around each vortex and results in a time averaged reduction in the stagnation pressure between successive turbine blade rows.

Figure 6.10 and Figure 6.11 document the development of the stagnation temperature in the wake of the turbine cascade over the time interval $853.44 \leq tu_e/D_t \leq 858.11$. Figure 6.10 is phase synchronous, over the vortex shedding cycle, with Figure 6.7 and is approximately phase synchronous with the inviscid circular cylinder stagnation temperature development in Figure 5.14. Similarly, Figure 6.11 is phase synchronous with Figure 6.8 and approximately phase synchronous with the inviscid cylinder prediction of Figure 5.15. The stagnation temperature T_s in Figure 6.10 and Figure 6.11 is normalised by the stagnation temperature imposed at the computational domain inlet boundary $T_{s\infty}$. Localised regions of fluid with stagnation temperatures greater than the inlet condition ($T_s > T_{s\infty}$) are located at the outer shear layer of each vortex, for example (i) in Figures 6.10 and 6.11. This 'hot spot'

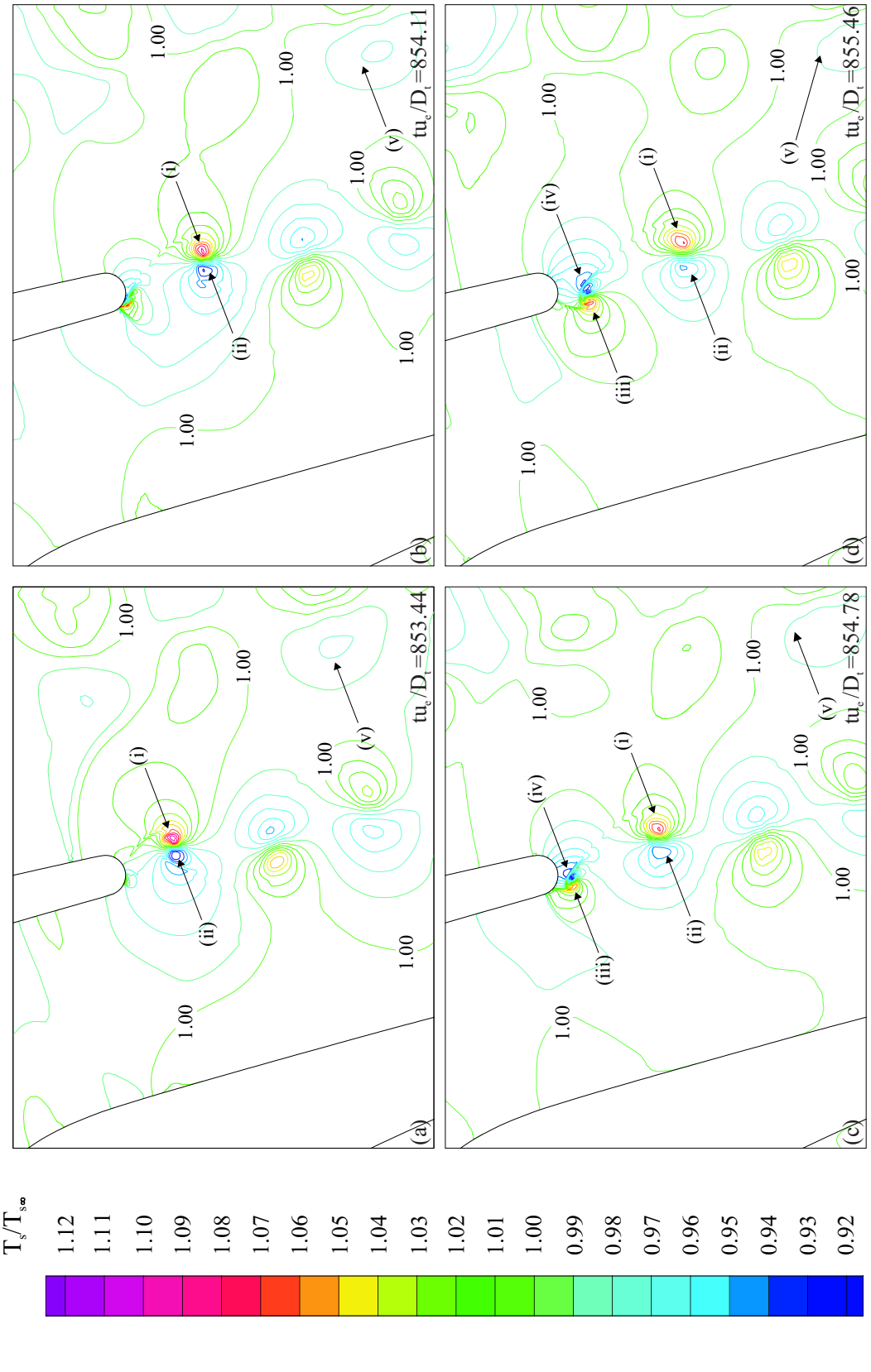

Figure 6.10: Stagnation temperature contours over the first half of the vortex shedding cycle: $853.44 \leq tu_e/D_t \leq 855.46$. $T_{s\,\max} = 1.12T_{s\infty}$, $T_{s\,\min} = 0.92T_{s\infty}$, $\Delta T_s = 0.01T_{s\infty}$. (i)-(v) labelled flow features.

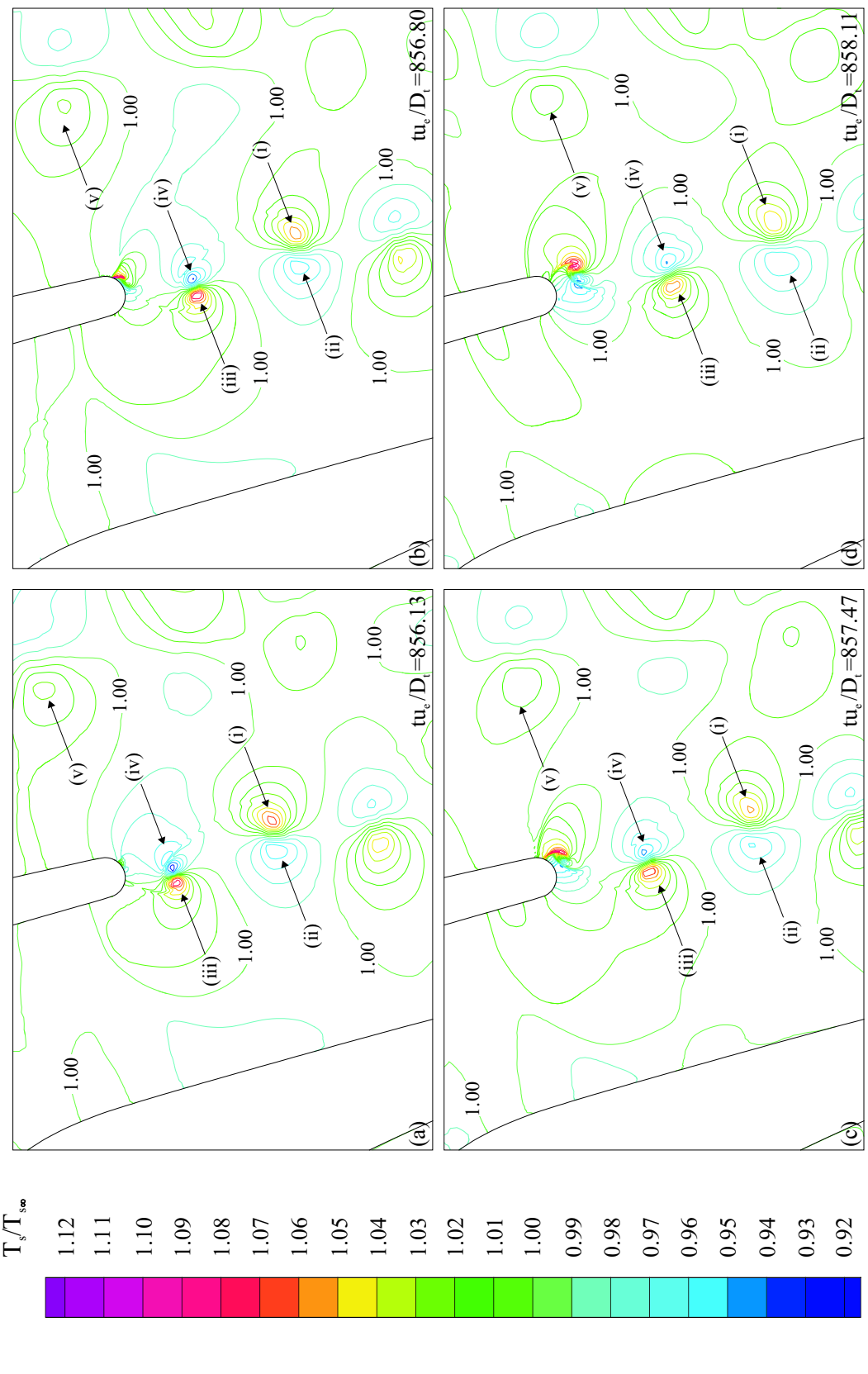

Figure 6.11: Stagnation temperature contours over the second half of the vortex shedding cycle: $856.13 \leq tu_e/D_t \leq 858.11$. $T_{s\,\max} = 1.12T_{s\infty}$, $T_{s\,\min} = 0.92T_{s\infty}$, $\Delta T_s = 0.01T_{s\infty}$. (i)-(v) labelled flow features.

(i) is paired with a localised cold spot, where $T_s < T_{s\infty}$ close to the centre of the wake (ii). Further hot spots and cold spots can be identified around each successive downstream vortex. A similar pattern of hot and cold spots are evident in the circular cylinder prediction, Figures 5.14 and 5.15.

Figure 6.10(a) documents the shedding of a vortex with clockwise rotation from the suction side of the turbine blade trailing edge. The hot (i) and cold (ii) spots surrounding this vortex have localised peak temperatures of $T_s = 1.09T_{s\infty}$ and $T_s = 0.93T_{s\infty}$ respectively. The hot spot is limited to a narrow region in the outer shear layer, along a common cross-stream alignment with the vortex centre. The phase synchronous circular cylinder prediction, in contrast, shows a larger hot spot stretching along the shear layer, between the growing vortex and the downstream surface. In addition, the local stagnation temperature about this vortex varies from $T_s = 1.105T_{s\infty}$ at the outer shear layer, to $T_s = 0.85T_{s\infty}$ on the opposite pitch-wise side of the vortex in the circular cylinder case. The decrease in magnitude and spatial area covered by the hot spot in the turbine blade prediction may be explained by analysing the initial growth of the anti-clockwise rotating vortex in Figure 6.10(b-d). A separation of the stagnation temperature around the vortex, into hot and cold regions, occurs immediately following the appearance of each vortex. This is evident close to the trailing edge surface in Figure 6.10(b). As this vortex increases in strength, Figure 6.10(c-d), an increase in the stagnation temperature occurs at the hot spot (iii). This is accompanied by a decrease in temperature at the cold spot (iv). An associated increase in the area covered by these extrema also occurs. The development of (iii) and (iv) in Figure 6.10(c-d) is compared with the inviscid cylinder development in Figure 5.14(c-d). A significantly greater area of the shear layer, extending between the growing vortex and the downstream surface, is heated above the free stream condition in the inviscid cylinder prediction. This may indicate a greater circulation of the growing vortex, causing a greater acceleration of the fluid passing in the pitch-wise direction, close to the cylinder. The resulting supersonic region is terminated in the inviscid cylinder prediction by a short radial shock wave that extends between the growing vortex and the cylinder surface. This supersonic

region may increase the stagnation temperature close to the cylinder surface by limiting the heat transport from the hot spot across the downstream surface of the cylinder. The heat transport restriction in this region is evident in Figure 5.14(c) by the large stagnation temperature gradient across the radial shock wave, extending between the anti-clockwise rotating vortex and the cylinder surface. This effect is absent from the inviscid turbine blade prediction.

The anti-clockwise rotating vortex increases to a peak strength immediately preceding the shedding of this vortex from the trailing edge, Figure 6.11(a). The localised stagnation temperature extrema, which surround each vortex, decrease in magnitude with the downstream convection of the shed vortex. This is evident by comparing the hot and cold spots surrounding the two clockwise rotating vortices in Figure 6.10(a). Specifically, a drop in temperature at the hot spot of $\Delta T_s = 0.06 T_{s\infty}$ accompanies an increase of $\Delta T_s = 0.03 T_{s\infty}$ at the cold spot, over this stream-wise distance. The gradual decay in the stagnation temperature separation with downstream distance is evident by tracking (i) and (ii) over Figures 6.10(a-d) and 6.11(a-d). The stagnation temperature separation further downstream is evident in the adjacent blade wake (v). A significant decrease in the stagnation temperature separation effect is observed at these distances.

Time averaging Figures 6.10(a-d) and 6.11(a-d) yields the Eckert-Weise effect. The time averaged stagnation temperature distribution, in the turbine blade near wake, is given in Figure 6.12. A stream-wise band of fluid, with stagnation temperatures lower than the inlet condition, is defined along the centre of the wake. This region has a minimum stagnation temperature close to the base pressure monitoring location (i). A gradual increase in the stagnation temperature occurs with downstream distance along the centre of the wake. In addition, the adjacent blade wake remains identifiable for a significant distance downstream of the turbine blade trailing edge (ii). A normalised stagnation temperature of unity is defined along the outer edges of the wake. This is the time averaged result of the alternate passing of hot spots and cool regions, along the wake edges. Two regions of fluid with $T_s/T_{s\infty} > 1$ are located upstream of the wake. These regions are labelled (iii) and

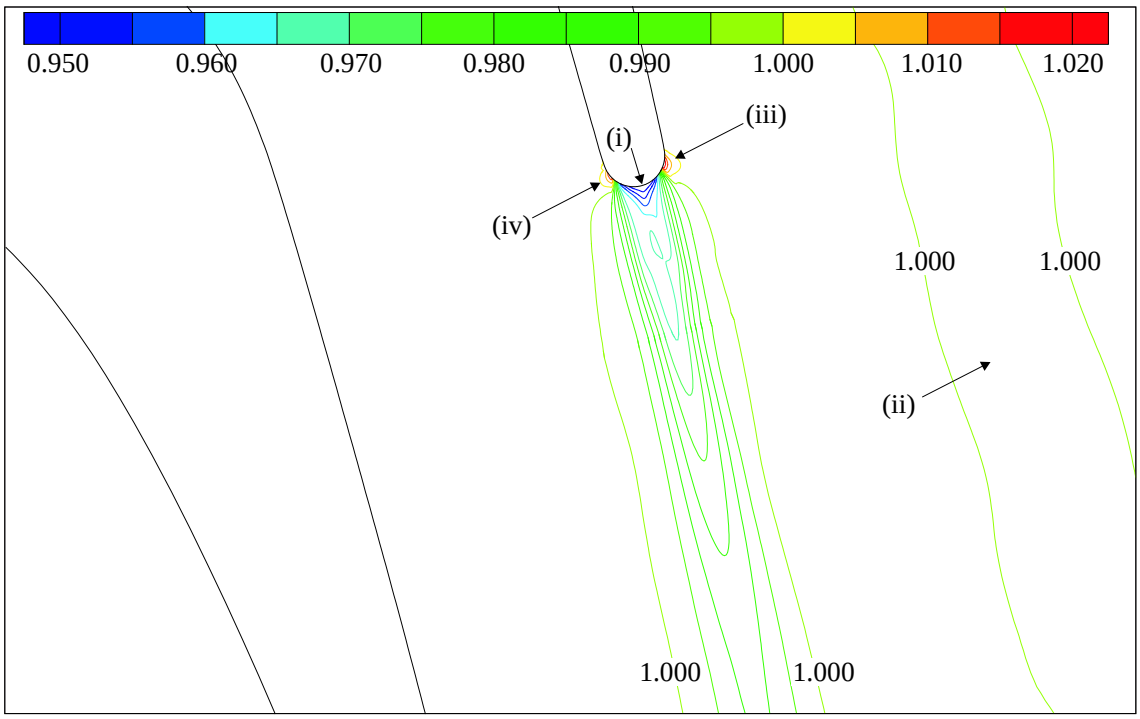

Figure 6.12: Time averaged stagnation temperature contours. $T_{s\,\max} = 1.02T_{s\infty}$, $T_{s\,\min} = 0.95T_{s\infty}$, $\Delta T_s = 0.005T_{s\infty}$. (i)-(iv) labelled flow features.

(iv) in Figure 6.12, and correspond approximately to the peak rms density locations in Figure 6.9. These hot regions of fluid are caused by the transit of the high temperature shear layers, formed as the radial shock waves move upstream at the formation of each vortex. In comparison, the time averaged stagnation temperature contours defined around the inviscid circular cylinder in Figure 5.16 show a greater increase in stagnation temperature at this location. The time averaged stagnation temperature deficit along the centre of the wake remains at a reduced temperature for a significantly greater downstream distance in the time averaged inviscid circular cylinder prediction. Specifically, the circular cylinder wake remains below $T_s = 0.96T_{s\infty}$ for approximately $3.9D$ downstream, compared with approximately $0.25D_t$ ($0.03D$) for the turbine blade prediction.

The stagnation pressure field development over one typical vortex shedding cycle is given in Figures 6.13(a-d) and 6.14(a-d). Figure 6.13(a-d) is phase synchronous over the vortex shedding cycle with Figure 6.10(a-d) and Figure 6.7(a-d). Similarly, Figure 6.14(a-d) is phase synchronous with Figure 6.11(a-d) and Figure 6.8(a-d).

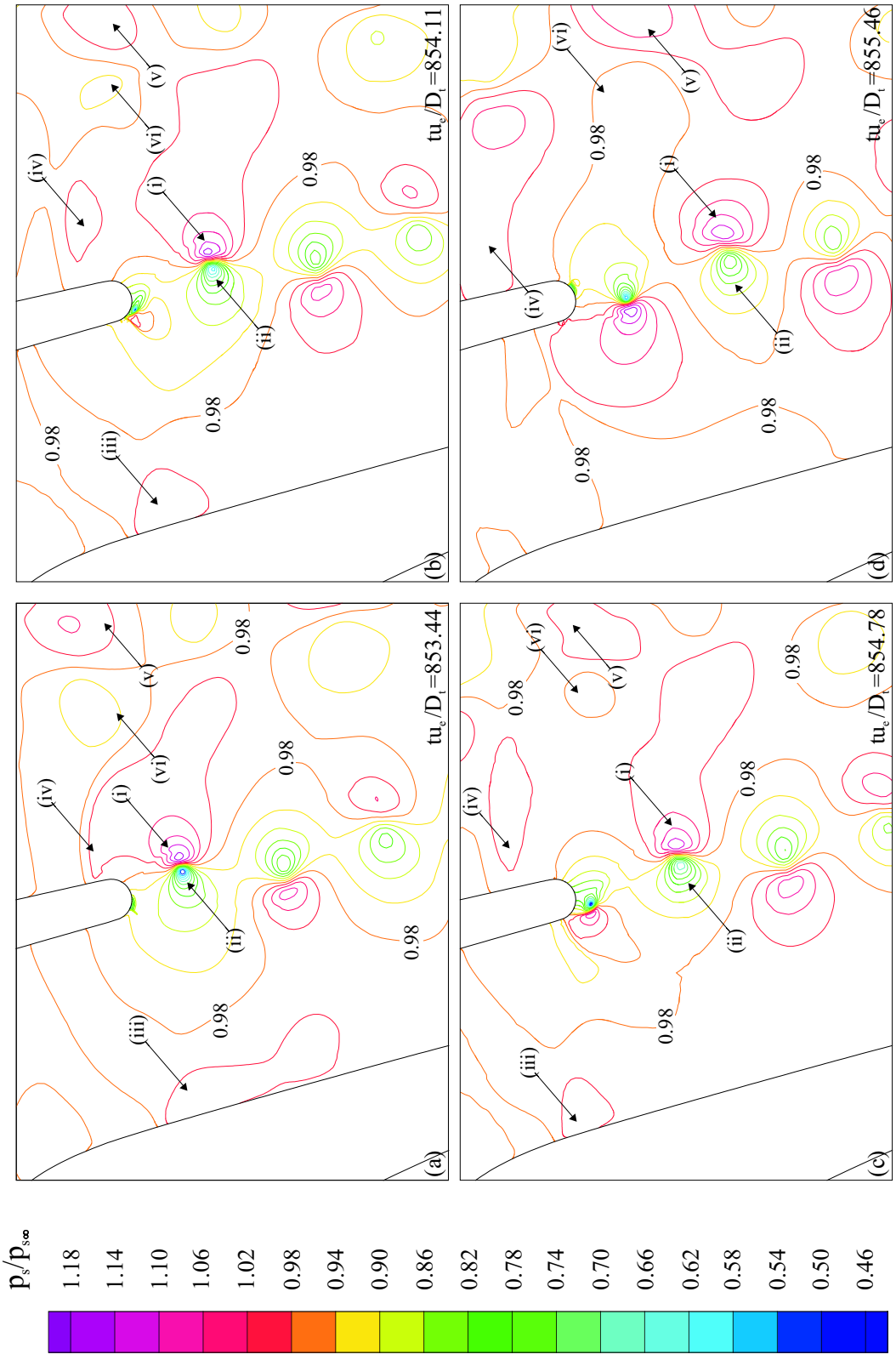

Figure 6.13: Stagnation pressure contours over the first half of the vortex shedding cycle: $853.44 \leq tu_e/D_t \leq 855.46$. $p_{s\max} = 1.18p_{s\infty}$, $p_{s\min} = 0.46p_{s\infty}$, $\Delta p_s = 0.04p_{s\infty}$. (i)-(vi) labelled flow features.

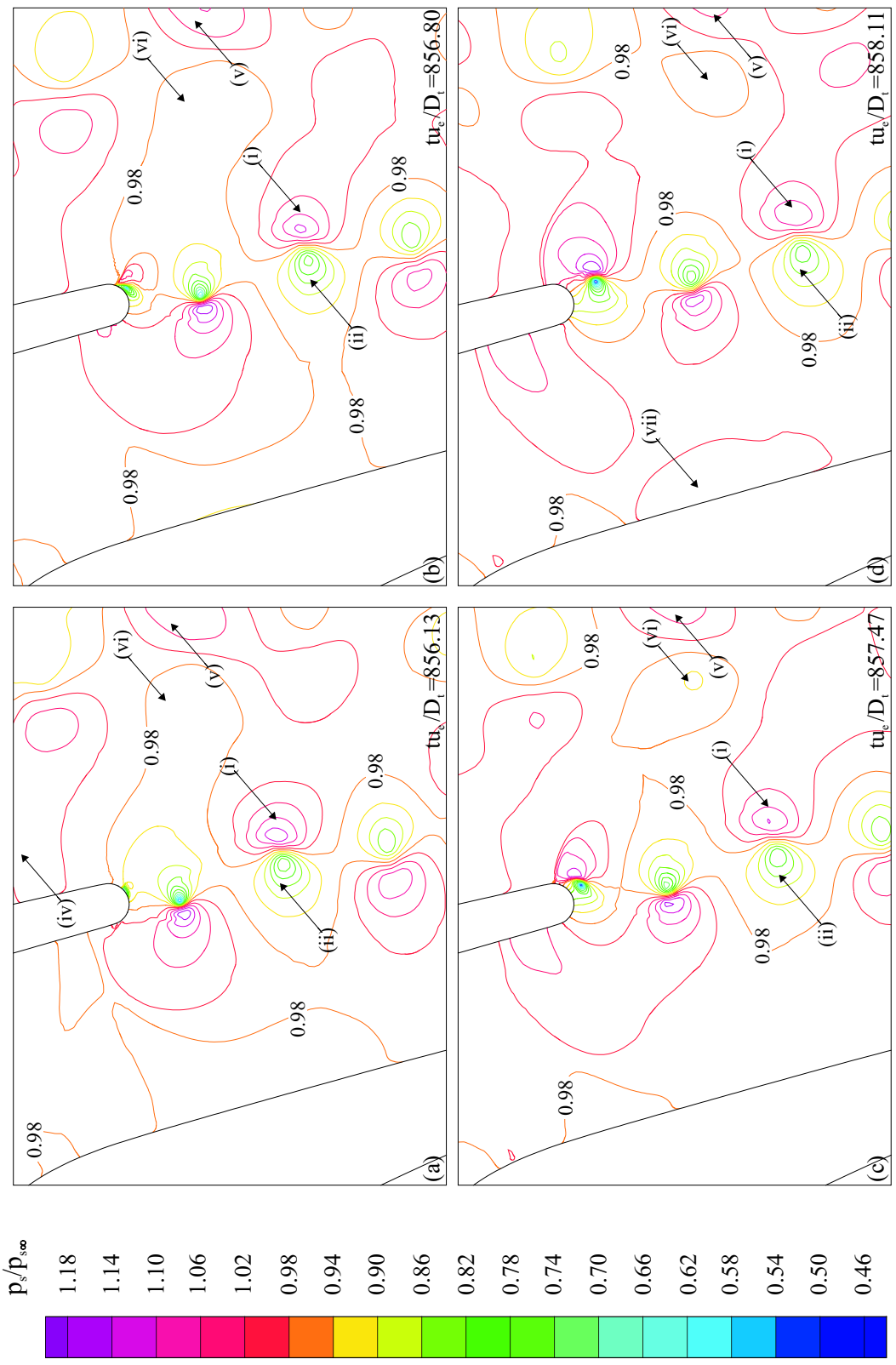

Figure 6.14: Stagnation pressure contours over the second half of the vortex shedding cycle: $856.13 \leq tu_e/D_t \leq 858.11$. $p_{s\,\max} = 1.18p_{s\infty}$, $p_{s\,\min} = 0.46p_{s\infty}$, $\Delta p_s = 0.04p_{s\infty}$. (i)-(vii) labelled flow features.

A redistribution of the normalised stagnation pressure $p_s/p_{s\infty}$ is evident. Localised regions of $p_s/p_{s\infty} > 1$ are located at the outer shear layer of each convecting vortex (i). Localised regions of $p_s/p_{s\infty} < 1$ are located along the centre of the wake (ii). The stagnation pressure field closely resembles the stagnation temperature field in Figures 6.10(a-d) and 6.11(a-d). The stagnation pressure falls to a local minimum close to the centre of each vortex. A similar distribution of stagnation pressure is identified in the circular cylinder wake, in Figures 5.18(a-d) and 5.19(a-d). The minimum stagnation pressure contour level in the inviscid circular cylinder prediction, located close to each growing vortex centre, is reduced by $\Delta p_s/p_{s\infty} = 0.26$ with respect to the turbine blade prediction. Interestingly, only a slightly higher peak stagnation pressure is evident in the inviscid circular cylinder prediction.

A similar vortex induced stagnation pressure separation is evident in the adjacent blade wake. One such region, with $p_s/p_{s\infty} > 1$ is labelled (v) in Figures 6.13(a-d) and 6.14(a-d). The corresponding region of stagnation pressure deficit, $p_s/p_{s\infty} < 1$, is labelled (vi). These extrema are significantly closer to unity than (i) and (ii), and cover a greater flow area, highlighting the downstream wake diffusion.

A further localised region of fluid with $p_s/p_{s\infty} > 1$ is evident along the suction surface of the adjacent turbine blade (iii). This region, which is located immediately downstream of the impinging pressure wave, decreases in strength and moves upstream with the upstream movement of the impinging pressure wave, Figure 6.13(a-d). A similar region is subsequently identified along this surface with the impingement of the next pressure wave, labelled (vii) in Figure 6.14(d). It is stressed that the impinging pressure wave along this surface is not a shock wave, terminating a supersonic flow region, across which a decrease in stagnation pressure would be expected.

The time averaged stagnation pressure is given in Figure 6.15. The alternate shedding of vortices from each side of the turbine blade trailing edge results in a time averaged stagnation pressure deficit along the centre of the wake. p_s is lowest close to the trailing edge surface, at either side of the base pressure location. The time averaged stagnation pressure minima in the inviscid circular cylinder prediction are

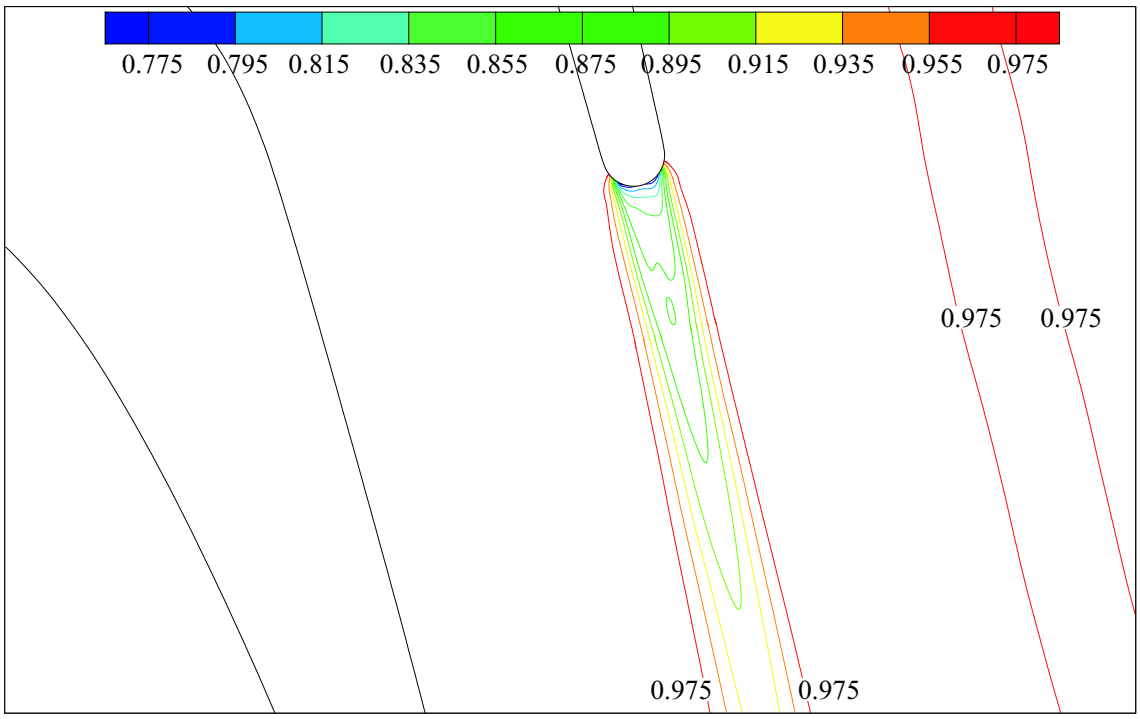

Figure 6.15: Time averaged stagnation pressure contours. $p_{s\,\max} = 0.975 p_{s\infty}$, $p_{s\,\min} = 0.775 p_{\infty}$, $\Delta p_s = 0.02 p_{s\infty}$.

correspondingly located along the leeward surface, either side of the wake centreline. The stagnation pressure minima are associated with the formation of vortices either side of the trailing edge surface. A gradual recovery of the stagnation pressure occurs along the centre of the wake with increasing downstream distance. A recovery of the stagnation pressure also occurs with cross-stream distance from the wake centreline. A cross-stream asymmetry of the stagnation pressure contours is noted in the near wake region, at $\leq 2D_t$ downstream of the trailing edge. Further downstream, the stagnation pressure contours are more symmetrical about the wake centreline. The stagnation pressure gradient, along the wake centreline in Figure 6.15, can be compared with the time averaged circular cylinder prediction in Figure 5.20. A similar stream-wise distance is required in the two predictions for an arbitrary increase of $\Delta p_s / p_{s\infty} = 0.1$ from the base pressure condition. A distance of $4.9D$ is required in the circular cylinder prediction, compared with $5.5D_t$ in the turbine blade prediction for this change in stagnation pressure. The stagnation pressure at the downstream surface of the circular cylinder is, however, significantly lower than at the turbine

blade trailing edge. Specifically, a minimum stagnation pressure of $p_{s\,\min} = 0.595 p_{s\infty}$ is defined for the circular cylinder, compared with $p_{s\,\min} = 0.775 p_{s\infty}$ in the turbine blade case. The cross-stream stagnation pressure recovery, from the wake centre to $p_s = p_{s\infty}$ also covers a greater relative distance in the circular cylinder prediction. No trace of a time averaged stagnation pressure rise above $p_{s\infty}$ is evident in either the circular cylinder or the turbine blade prediction. The local time accurate regions of $p_s/p_{s\infty} > 1$ along the edges of the wake, evident in Figures 6.13 and 6.14, are time averaged with the intervening lower stagnation pressure regions to yield an overall stagnation pressure deficit in this region.

In this section, a number of differences between the time accurate stagnation temperature and pressure fields are reported. These differences constitute localised sources of entropy production. The specific entropy s is given by Eqn. 5.4. The development, over one typical vortex shedding cycle, of the specific entropy field is given in Figures 6.16(a-d) and 6.17(a-d). Figure 6.16(a-d) is phase synchronous with Figure 6.10(a-d) and 6.13(a-d). Figure 6.17(a-d) is phase synchronous with Figure 6.11(a-d) and 6.14(a-d). The specific entropy s is normalised by the specific gas constant, $R = 287 J/kgK$. Local entropy maxima are located at each vortex centre, for example at (i) and (ii) in Figures 6.16 and 6.17. These are caused by the low stagnation pressure vortex cores, marked as regions of $p_s/p_{s\infty} < 1$ in Figures 6.13 and 6.14. As in the circular cylinder prediction, the specific entropy contours therefore highlight the formation and downstream convection of each vortex core. The maximum specific entropy produced by these vortices is greater in the circular cylinder prediction, rising to $s_{\max}/R = 1.44$, compared to $s_{\max}/R = 0.85$ in the turbine blade prediction. The higher specific entropy follows from the greater stagnation pressure deficit close to the centre of the wake in the circular cylinder prediction. The downstream convection of the vortices shed from the adjacent blade (iv) are also evident in Figures 6.16(a-d) and 6.17(a-d).

A further region of entropy increase is evident in the shear layer that extends between the growing vortex and the turbine blade trailing edge. The shear layer connecting the clockwise rotating vortex (i) with the surface is labelled (iii) in Fig-

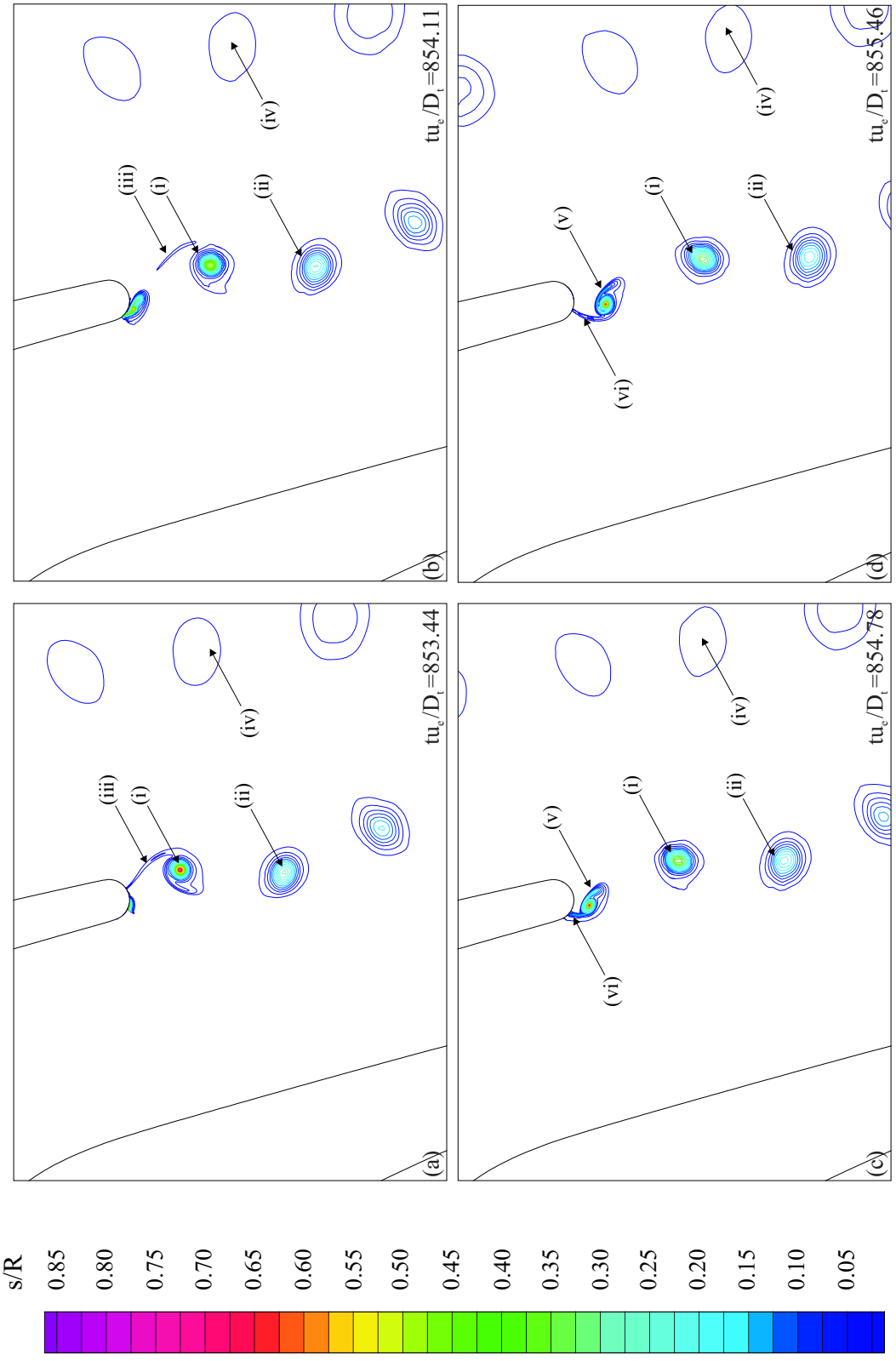

Figure 6.16: Specific entropy contours over the first half of the vortex shedding cycle: $853.44 \leq tu_e/D_t \leq 855.46$. $s_{\max} = 0.85R$, $s_{\min} = 0.025R$, $\Delta s = 0.025R$. (i)-(vi) labelled flow features.

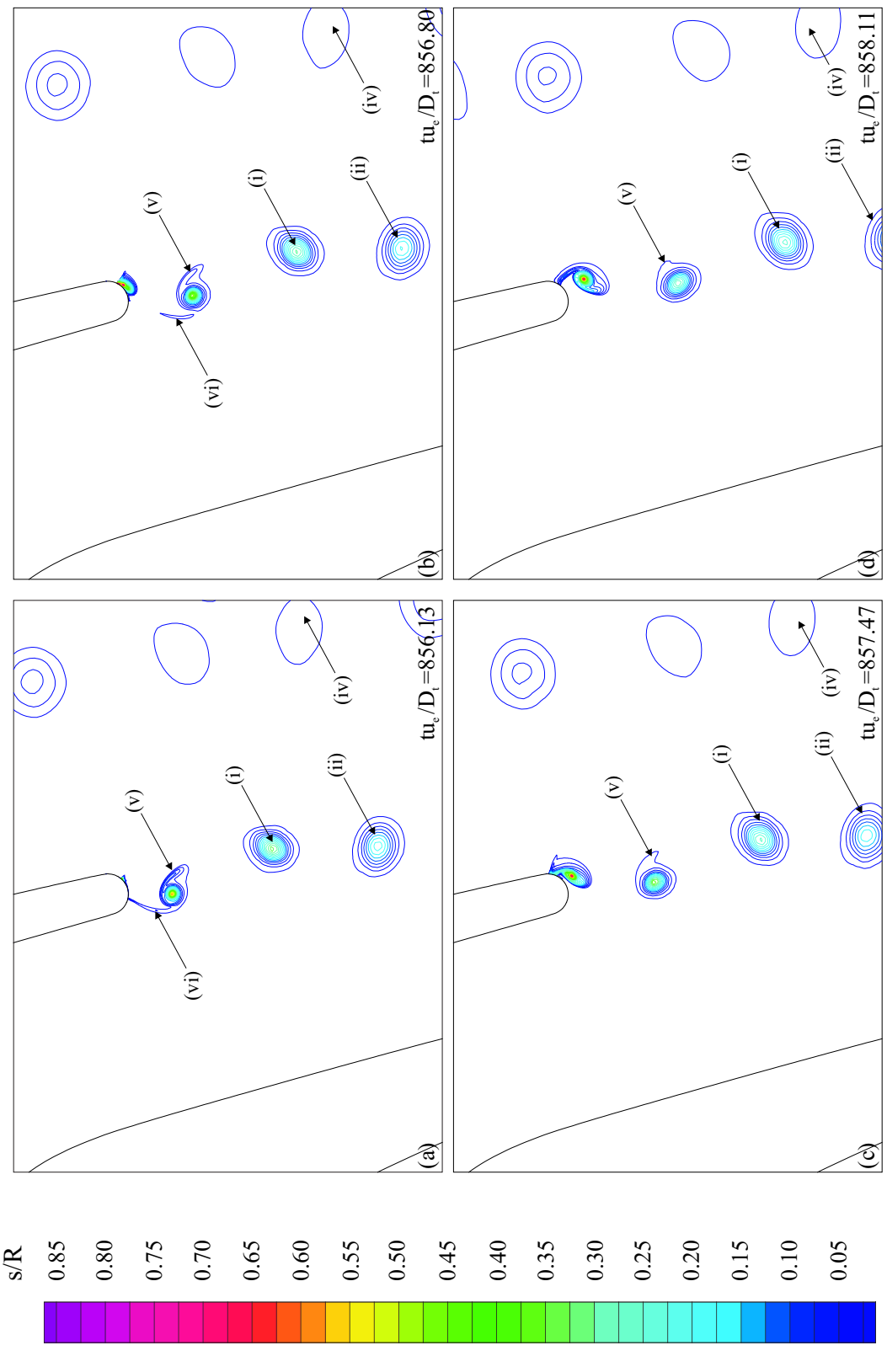

Figure 6.17: Specific entropy contours over the second half of the vortex shedding cycle: $856.13 \leq tu_e/D_t \leq 858.11$. $s_{\max} = 0.85R$, $s_{\min} = 0.025R$, $\Delta s = 0.025R$. (i)-(vi) labelled flow features.

ure 6.16(a-b). As the clockwise rotating vortex convects downstream, a new anti-clockwise rotating vortex forms at the blade trailing edge, Figure 6.16(a). The shear layer attaches to this vortex. After the shedding of this anti-clockwise rotating vortex, the shear layer continues to be stretched by the contra-rotating vortex pair. A short length of this shear layer is labelled (v) in Figure 6.16(c-d) and Figure 6.17(a-c). This short section of the shear layer is highlighted in the entropy contours due to a splitting, across the shear layer, of the cold spot labelled (iv) in Figures 6.10(c-d) and 6.11(a-d). A splitting of the corresponding minimum by the shear layer does not occur in the stagnation pressure contours of Figures 6.13(a-d) and 6.14(a-d). The overall result is a local increase in the specific entropy. A further shear layer, labelled (vi), extends between this anti-clockwise rotating vortex and the trailing edge surface in Figures 6.16(c-d) and 6.17(a-b). Differences are noted in the specific entropy produced by the shear layers labelled (iii) and (vi), against those in the inviscid cylinder prediction, Figures 5.22 and 5.23. A large region of fluid with $T_s/T_{s\infty} > 1$ develops close to the downstream surface of the cylinder during the formation of each vortex. As the vortex is shed, this hot spot is stretched along the near side shear layer and convects downstream with the vortex. This stretching of the hot spot in the outer shear layer is not reflected in the stagnation pressure field and an increase in the specific entropy along the shear layer results. The stretching of the hot spot along the near side shear layer is absent, to the same degree, downstream of the turbine cascade. The result is the observed lower rise in specific entropy along the shear layers labelled (iii) and (vi) in the turbine blade prediction.

6.2.5 Summary

This section documents an inviscid model of the flow past a low aspect ratio, highly loaded turbine cascade at an isentropic exit Mach number of $M_e = 0.6$. The turbine cascade prediction demonstrates a satisfactory agreement of the time averaged isentropic surface Mach number distribution with measurements from a concurrent experimental research program.

The thick trailing edge of each turbine blade induces an alternate shedding of

vortices from each side of the trailing edge, forming a vortex street. An essentially symmetric vortex shedding pattern is predicted downstream of the turbine blade, in contrast to published measurements for this turbine blade at higher Mach numbers. Some differences are, however, noted between the inviscid turbine blade prediction and the inviscid circular cylinder prediction. These include an absence of downstream precessing radial shock waves along the trailing edge surface. The upstream moving radial pressure waves continue through the turbine nozzle passage and interact with the suction surface and downstream wake of the neighbouring blades. Minor cross-stream asymmetries are highlighted in the rms density field and in the time averaged stagnation temperature and pressure near wake distributions. These asymmetries are, however, significantly less pronounced than for previous published measurements downstream of this turbine blade at exit Mach numbers approaching unity.

A similar vortex induced energy separation is predicted downstream of each turbine blade in the inviscid prediction. Hot spots are predicted along the edges of the wake and cold spots are predicted close to the wake centreline at each vortex in the time accurate near wake region. These hot and cold spots are paired on a cross-stream alignment around each convecting vortex, similar in form to the circular cylinder wake in Chapter 5. Differences are observed, however, in the magnitude and location of the hot region of fluid that stretches between the growing vortex and the downstream surface. A greater increase in stagnation temperature, spread over a greater area, is observed in the near side shear layer of the inviscid circular cylinder prediction.

An analogous redistribution of the stagnation pressure is predicted, providing further corroborative data for the proposed energy separation mechanism in Kurosaka et al. (1987). Localised regions of stagnation pressure greater than the inlet condition are predicted along the outer edges of the wake. Regions of stagnation pressure, lower than the inlet condition, are predicted at the wake centre, close to the centre of each convecting vortex. The resulting specific entropy field highlights the vortex centres, the shear layers between each vortex, and the radial shock waves as consti-

tuting regions of entropy production. The lower increase in stagnation temperature, above the free stream condition, in the hot spot that stretches along the near side shear layer at each vortex formation event reduces the specific entropy production in the turbine blade prediction along these shear layers.

6.3 Turbulent Turbine Cascade Flow Prediction

6.3.1 Numerical Model Specifications

This section describes the development of a turbulent turbine cascade model at exit conditions of $M_e = 0.6$ and $Re_{D_t} = 7.48 \times 10^4$, based on a turbine blade trailing edge diameter $D_t = 6.35 \times 10^{-3} m$. The turbulent cascade prediction is initialised using the inviscid turbine cascade prediction documented in Section 6.2. The turbine blade profile is a two-dimensional cross-section of the turbine blade reported in Carscallen et al. (1999). This turbine blade geometry is detailed in Table 6.1. The free stream inlet and exit conditions are listed in Table 6.2.

The computational domain is divided into five contiguous blocks. This is shown in Figure 6.1. Each block is discretised using the grid resolution listed in Table 6.3. A sponge layer region of highly stretched computational cells is defined downstream of the turbine blade to reduce numerical wave reflection from the constant pressure outlet boundary ($b3$ in Figure 6.1). The turbine blade surface condition is changed from the slip condition specified in the inviscid prediction to a condition of no-slip. The no-slip boundary condition is described in Section 3.9.8. The remaining boundary conditions are identical to those documented for the inviscid prediction.

State variables from the inviscid prediction are used to initialise the specific mass, momentum and energy state variables in the turbulent prediction. Initial estimates for the specific turbulence kinetic energy k and the specific turbulence kinetic energy dissipation rate ω are uniformly imposed throughout the computational domain at the start of the turbulent prediction. The free stream values of k and ω are based on those of Currie & Carscallen (1998) for a similar turbulent prediction of this turbine cascade at $M_e = 1.16$. Assuming a free stream turbulence intensity of $Tu = 0.1\%$, a

value of $k_\infty = 1.85 \times 10^{-3} m^2/s^2$ is uniformly imposed throughout the computational domain. Using a turbulence length scale l_c of $1 \times 10^{-3} c$, where c is the turbine blade chord length, a free stream value for ω is estimated from $\omega = \sqrt{k}/\left(\beta^\star l_c\right)$. Currie & Carscallen (1998) report that the turbine blade prediction remains insensitive to the value of ω over the range $1 \times 10^{-3} c \leq l_c \leq 0.1c$. The free stream turbulence kinetic energy dissipation rate for the current prediction is estimated as $\omega_\infty = 2346.06 Hz$. These estimates for k_∞ and ω_∞ are imposed uniformly throughout the computational domain at the start of the turbulent prediction.

6.3.2 Time Accurate Base Pressure Analysis

The turbulent prediction is time marched from these initial conditions to a self-sustained vortex shedding solution in constant time steps of $\Delta t = 8.603 \times 10^{-5} D_t/u_e$. A transient period of flow follows the onset of the turbulent prediction. As the k and ω fields develop from the uniformly imposed free stream values, the turbulent prediction eventually returns to a self-sustained vortex shedding pattern. The vortex shedding pattern that returns is, however, significantly different to the inviscid turbine cascade prediction.

The time accurate base pressure history for the turbulent cascade prediction is documented in Figure 6.18. The base pressure is recorded at the same location as in the inviscid prediction, the approximate location of which is labelled in Figure 6.1. Thirteen cycles of a high frequency fluctuation are documented in Figure 6.18 over the time interval $850 \leq tu_e/D_t \leq 910$. Each local maximum in base pressure corresponds to the shedding of a vortex from either the suction surface or the pressure surface side of the trailing edge. From the time accurate density contour sequence documented later in Section 6.3.5, the local maximum located at $t = 886.5 D_t/u_e$ can be related to the shedding of a clockwise rotating vortex from the suction surface side of the trailing edge. The subsequent decrease in base pressure to a minimum at $t = 888 D_t/u_e$, and the increase to a local maximum at $t = 889.5 D_t/u_e$, correspond to the formation and initial shedding of an anti-clockwise rotating vortex from the pressure surface side. The base pressure history over twenty six vortex shedding

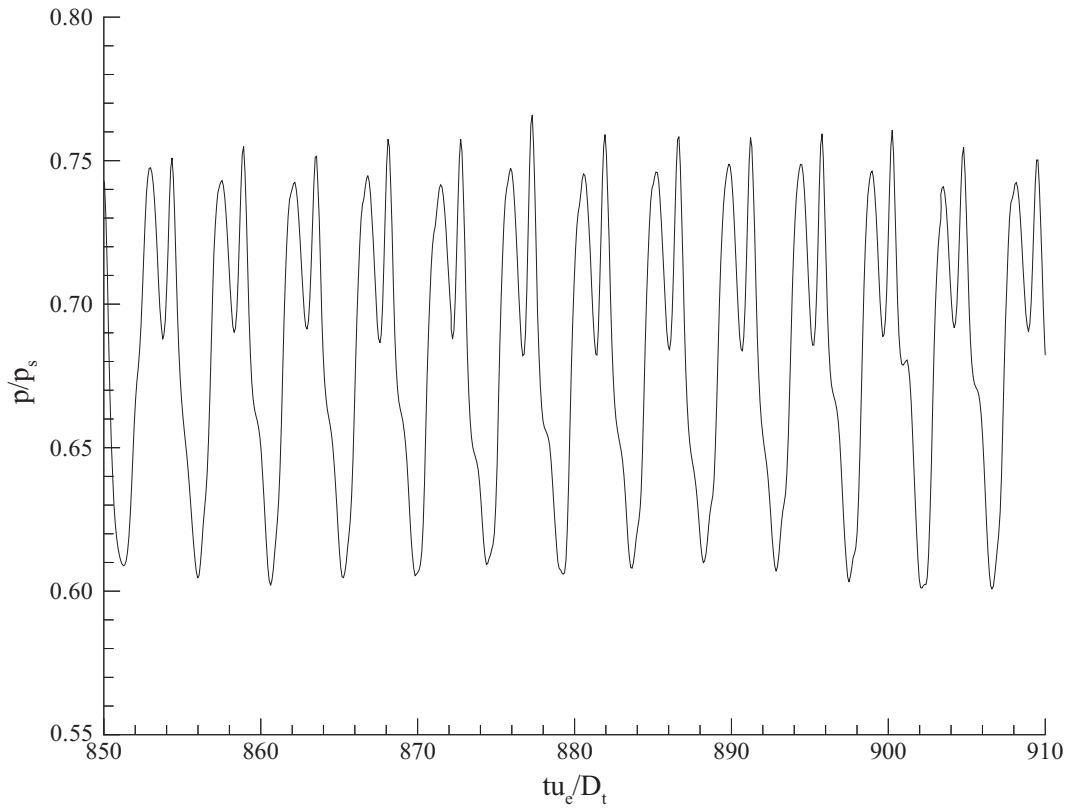

Figure 6.18: Turbulent cascade base pressure history.

events is therefore documented in Figure 6.18.

The unequal peak-to-peak amplitude between the formation and shedding of vortices from the suction and pressure sides of the trailing edge indicate an asymmetric vortex shedding pattern downstream of the turbine blade. Furthermore, the lower base pressure minima at the formation of each anti-clockwise rotating vortex from the pressure surface indicates a greater circulation of the vortices on this side of the wake. A transient drift in the base pressure amplitude is observed on a cycle-to-cycle basis in Figure 6.18. This sinuous drift modifies the base pressure trace at each vortex shedding event and is responsible for the presence of additional local extrema between vortex shedding events at, for example, $t = 901 D_t/u_e$. A similar cycle-to-cycle variation in base pressure is documented in the inviscid turbine blade prediction. Transient cycle-to-cycle fluctuations are also reported in the time accurate base pressure and drag coefficient traces for the circular cylinder predictions in Chapter 5. The base pressure trace in Figure 6.18 has a mean value of $p = 0.685 p_{s\infty}$, which is lower than the mean base pressure of $p = 0.79 p_{s\infty}$ computed for the inviscid turbine blade. The root mean square fluctuation of $p_{rms} = 4.76 \times 10^{-2} p_{s\infty}$ for the turbulent base pressure trace is also lower than the value of $p_{rms} = 7.39 \times 10^{-2} p_{s\infty}$ reported for the inviscid turbine blade prediction.

A frequency analysis of the time resolved base pressure trace in Figure 6.18 yields the power spectrum in Figure 6.19. This power spectrum highlights four dominant peaks. These are a fundamental tone at $f = 0.215 u_e/D_t$, and three associated higher harmonics at $f = 0.430 u_e/D_t$, $f = 0.645 u_e/D_t$ and $f = 0.860 u_e/D_t$. The asymmetric vortex shedding pattern from the turbine blade is associated with a decrease in the dominant frequency component, from $f = 0.380 u_e/D_t$ in the inviscid prediction to $f = 0.215 u_e/D_t$ in the turbulent prediction. This reduction is associated with a change from the equal base pressure drop at the formation of vortices on both sides of the trailing edge in the inviscid prediction, to a greater decrease in pressure at the formation of pressure surface vortices in the turbulent prediction. The power spectrum indicates a vortex shedding Strouhal number of $f = 0.215 u_e/D_t$, which constitutes an increase of 13.16% from the inviscid turbine blade prediction

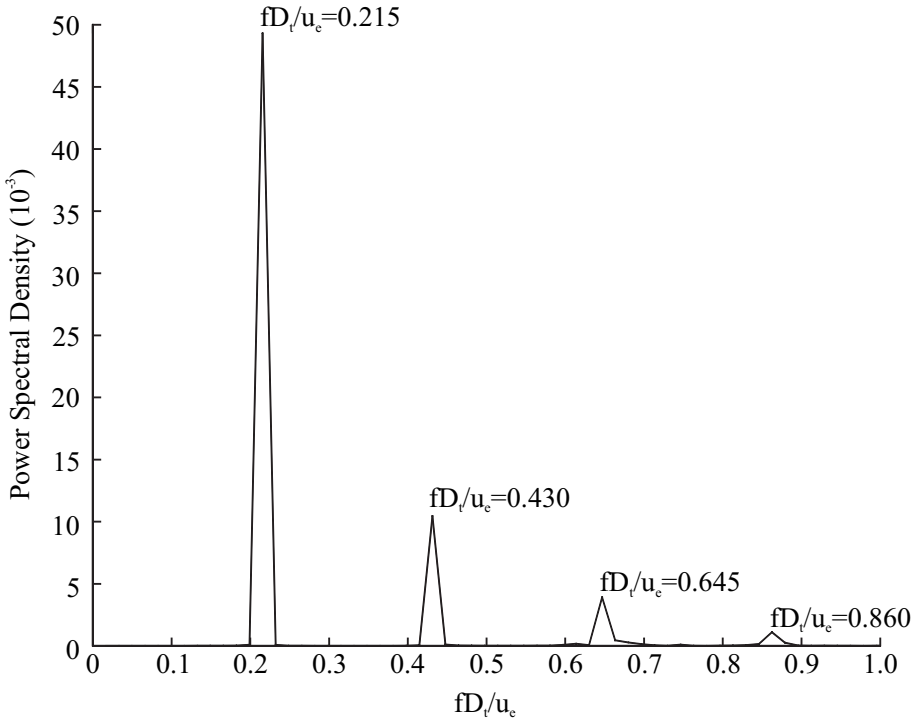

Figure 6.19: Frequency analysis of the time accurate turbulent base pressure history.

of $f = 0.190u_e/D_t$. As documented in Chapter 2, Cicatelli & Sieverding (1995) propose that Strouhal numbers below 0.23 indicate turbulent boundary layer separation from both sides of the trailing edge in turbine blade flows. This hypothesis is analysed for the current turbine cascade prediction in the following section.

6.3.3 Turbine Blade Boundary Layer Analysis

The asymmetric vortex shedding pattern in the turbulent prediction is not reflected in the inviscid prediction. This indicates an association of the asymmetry to a difference in the suction and pressure surface shear layers, downstream of the trailing edge. This proposition is based on the cited work of Sieverding & Heinemann (1989, 1990) and Cicatelli & Sieverding (1995, 1996, 1997) in the literature review of Section 2.3. From the hypothesis put forward by Gerrard (1966), that the frequency and strength of vortex shedding downstream of a cylinder is dependent on the separated shear layer thickness, Sieverding & Heinemann (1989, 1990) propose a similar influence for turbine blades with round and square trailing edges. Extending this work,

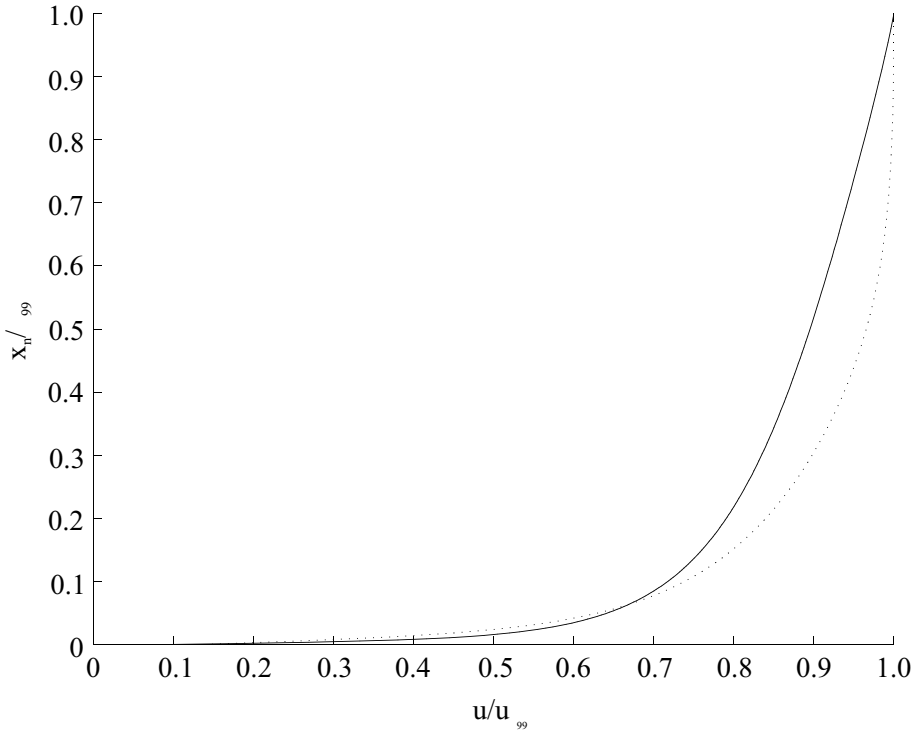

Figure 6.20: Boundary layer velocity profile at $2D_t$ upstream of the trailing edge. (—) Suction surface profile. $(\cdots)$ Pressure surface profile. x_n height normal to the local turbine blade surface. δ_{99} boundary layer thickness. Boundary layer integral parameters at this location are listed in Table 6.4.

Cicatelli & Sieverding (1995, 1996) propose that a greater shear layer thickness at the suction surface may lead to a breakdown of the vortex formation length/diffusion length balance proposed by Gerrard (1966) for circular cylinders. This breakdown is reported to be the underlying cause for the wide range of cited Strouhal numbers collated by Cicatelli & Sieverding (1995). The increase in Strouhal number between the current inviscid and turbulent cascade predictions may therefore result from a similar asymmetry of the suction and pressure surface shear layers.

The boundary layer velocity profile on the suction and pressure surfaces at a distance of $2D_t$ upstream of the trailing edge is given in Figure 6.20. The surface normal height is normalised by the boundary layer thickness δ_{99} at this location. The velocity tangential to the turbine blade surface is similarly normalised by the velocity at the edge of the boundary layer. A good overall resolution of the boundary layer is achieved at this stream-wise location by the current computational grid.

Both velocity profiles indicate that the majority of the velocity increase, from the no-slip condition at the surface to the boundary layer edge velocity, occurs within the lowest 10% of the boundary layer. The pressure surface velocity profile also shows a higher relative velocity, at surface normal heights above $x_n = 0.1\delta_{99}$. A quantitative comparison of the two boundary layers at this location is given by the integral parameters, which are listed in Table 6.4. The displacement thickness δ_1

Parameter	Suction Surface	Pressure Surface
δ_{99}/D_t	0.542	0.142
δ_1/D_t	0.073	0.014
δ_2/D_t	0.050	0.009
H_{12}	1.46	1.55

Table 6.4: Turbine blade integral parameters at $2D_t$ upstream of the trailing edge. The integral parameters correspond to the velocity profiles in Figure 6.20. δ_{99}, δ_1 and δ_2 are normalised using the turbine blade trailing edge diameter D_t. The shape Factor $H_{12} = \delta_1/\delta_2$.

and the momentum thickness δ_2 are computed from:

$$\delta_1 = \int_0^{\delta} \left(1 - \frac{\rho u}{\rho_\delta u_\delta}\right) dx_n, \tag{6.1}$$

$$\delta_2 = \int_0^{\delta} \frac{\rho u}{\rho_\delta u_\delta} \left(1 - \frac{u}{u_\delta}\right) dx_n, \tag{6.2}$$

where δ is used in Eqns. 6.1 and 6.2 to signify the boundary layer thickness δ_{99}. ρ_δ and u_δ are therefore the static density and velocity at the boundary layer edge. x_n is the local surface normal distance.

The shape factor ($H_{12} = \delta_1/\delta_2$) in Table 6.4 indicates the presence of turbulent boundary layers on the suction and pressure surfaces at this stream-wise location. This correlates well with the boundary layer/Strouhal number relationship proposed by Cicatelli & Sieverding (1995), as reported in the previous section. The displacement thickness δ_1, the momentum thickness δ_2 and the boundary layer velocity thickness δ_{99} collectively indicate a greater thickness of the boundary layer on the suction surface. Specifically, the boundary layer thickness δ_{99} is 3.82 times greater

on the suction surface at this stream-wise location. Therefore, assuming a similar relative thickness ratio of the separated shear layers, the vortex forming at the pressure surface may take longer to entrain sufficient fluid from the suction surface shear layer to cut off the circulation supply of the near side shear layer. These results correlate with the proposed increase in circulation of the vortex from the pressure surface, as indicated by the greater peak-to-peak base pressure amplitude in Figure 6.18.

The boundary layer analysis documented in this section compares well with the measurements of Sieverding et al. (2003) for a similar thick trailing edge turbine cascade at exit conditions of $M_e = 0.79$ and $Re_{D_t} = 1.487 \times 10^5$. Turbulent boundary layers are reported on both the pressure and suction surfaces at the trailing edge in Sieverding et al. (2003). The suction surface boundary layer is reported to be approximately 3.14 times greater than the pressure surface boundary layer at the trailing edge in these measurements.

The grid resolution within the boundary layer in the current study is quantified through an extension of this analysis to assess whether the laminar sublayer region is adequately resolved. This analysis indicates that at least ten points discretise the laminar sublayer on the suction side in the surface normal direction at $2D_t$ upstream of the trailing edge. Six points similarly discretise the laminar sublayer on the pressure surface at this location. This boundary layer analysis is based on the compressible momentum integral equation, as given in White (1991), and therefore assumes that at this location the turbine blade locally approximates a flat plate under a pressure gradient. The boundary layer discretisation is considered satisfactory for the purposes of the current study. The current grid resolution results from a series of preliminary turbine cascade predictions in which the surface normal grid resolution was successively increased, through either increasing the overall number of grid points or increasing the surface normal grid stretching. The final grid from this preliminary analysis is used for both the inviscid and turbulent predictions documented in this chapter.

6.3.4 Time Averaged Isentropic Mach Number Distribution

The isentropic Mach number distribution from the turbulent prediction is compared against the measurements of Ackerman (2005) in Figure 6.21. The isentropic Mach number distribution in Ackerman (2005) is measured around the same turbine blade profile modelled in this study at identical exit conditions of $M_e = 0.6$ and $Re_{D_t} = 7.48 \times 10^4$. The turbulent prediction demonstrates a reasonable approximation along both surfaces of the turbine blade. The leading edge stagnation point is located along the pressure surface at around 3% of the axial chord. A similar location for the leading edge stagnation point is predicted in the current inviscid prediction and in a similar inviscid prediction on the same turbine blade profile at $M_e = 1.16$ by Brooksbank (2001). The turbulent prediction shows a slight underprediction of the isentropic Mach number along the leading edge of the pressure surface. This may be improved by increasing the stream-wise grid resolution close to the stagnation point in order to better describe the initial onset of the boundary layer along this surface. The comparison improves further along the pressure surface and remains close to the measurements of Ackerman (2005) to separation at the trailing edge. The turbulent prediction indicates a lower expansion around the trailing edge, with respect to the inviscid prediction, on both pressure and suction surfaces. This would indicate an associated reduction in radial shock wave activity at the trailing edge and is expected to better approximate the physical situation in this region. The isentropic Mach number remains higher in the turbulent prediction at $x_1 = c_1$, compared with the inviscid prediction. This correlates with the lower mean base pressure in Figure 6.18. The turbulent prediction also provides a reasonable estimation of the isentropic Mach number distribution along the suction surface. The turbulent prediction shows an over expansion along this surface compared with the measured point at $x_1 = 0.154c_1$. A similar over expansion is observed in the inviscid prediction at this axial location. The turbulent prediction also fails to predict the short laminar separation bubble indicated in the measurements of Ackerman (2005), between $x_1 = 0.41c_1$ and $x_1 = 0.59c_1$. The current prediction does, however, maintain a good correlation with the measured isentropic Mach

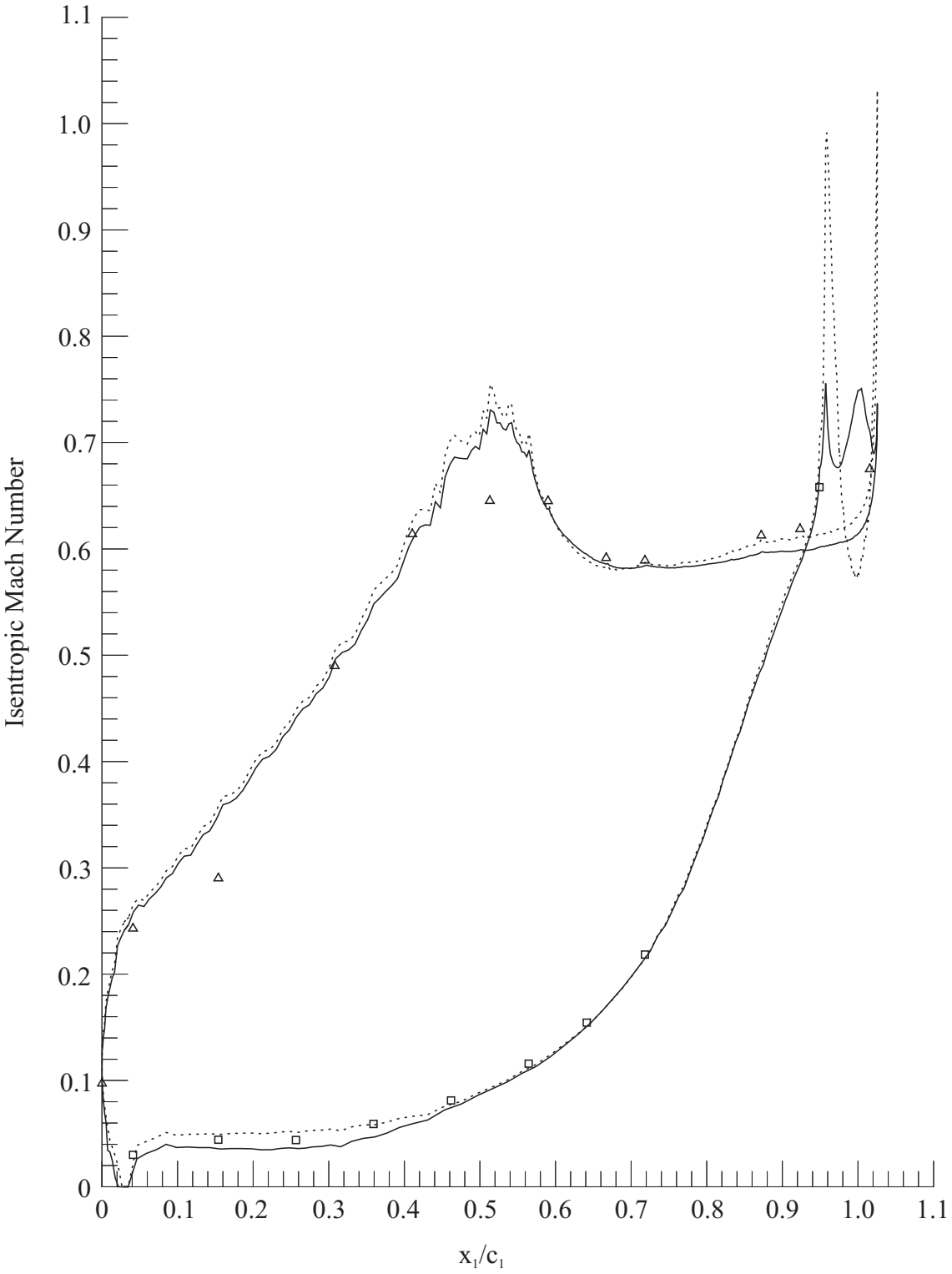

Figure 6.21: Turbine blade isentropic Mach number distribution. Comparison with the measurements of Ackerman (2005) at $M_e = 0.6$ and $Re_{D_t} = 7.48 \times 10^4$. (—) Turbulent prediction. $(\cdots)$ Inviscid prediction. □ Measured pressure surface distribution. Δ Measured suction surface distribution. x_1, surface axial coordinate relative to the leading edge. c_1, axial component of chord length.

number distribution after reattachment of the boundary layer at $x_1 \geq 0.59c_1$. Further along the suction surface, the turbulent prediction slightly under-predicts the isentropic Mach number approaching the trailing edge at $x_1 > 0.7c_1$. The turbulent prediction, however, remains within 4% of the measured isentropic Mach number over this region. Overall, the isentropic Mach number approximation is considered satisfactory for the purpose of the current study, which is an investigation into the vortex shedding and associated energy separation characteristics downstream of the turbine cascade.

6.3.5 Turbulent Vortex Shedding Characteristics

The asymmetric vortex shedding pattern indicated in the base pressure history of Figure 6.18, and the higher circulation of vortices shed from the pressure surface side of the wake, are confirmed in the time resolved static density contour sequence of Figures 6.22(a-d) and 6.23(a-d). The near wake flow development is documented in eight instantaneous snapshots over the time interval $886.68 \leq tu_e/D_t \leq 890.80$, which covers one typical vortex shedding cycle. Figure 6.22(a) corresponds to a maximum in base pressure as the clockwise rotating vortex (i) is shed from the suction surface. This vortex (i) remains close to the trailing edge as the anti-clockwise rotating vortex (ii) begins to form on the pressure surface side of the wake in this figure. Two further clockwise rotating vortices are sited downstream of this position. These are labelled (iii) and (v) respectively. Two corresponding anti-clockwise rotating vortices are defined on the pressure surface side of the wake at (iv) and (vi). These vortices (iii)-(vi) are associated with the previous two vortex shedding cycles. In contrast to the inviscid turbine blade prediction and the circular cylinder predictions, the downstream moving vortices are not equi-spaced in the stream-wise direction. This unequal stream-wise spacing is indicative of the different vortex formation characteristics. Compared with the clockwise rotating vortices (iii) and (v), the anti-clockwise rotating vortices (iv) and (vi) are also defined by a greater number of more densely packed iso-contours. The greater density gradient at the centre of the anti-clockwise rotating vortices confirm the greater circulation of these

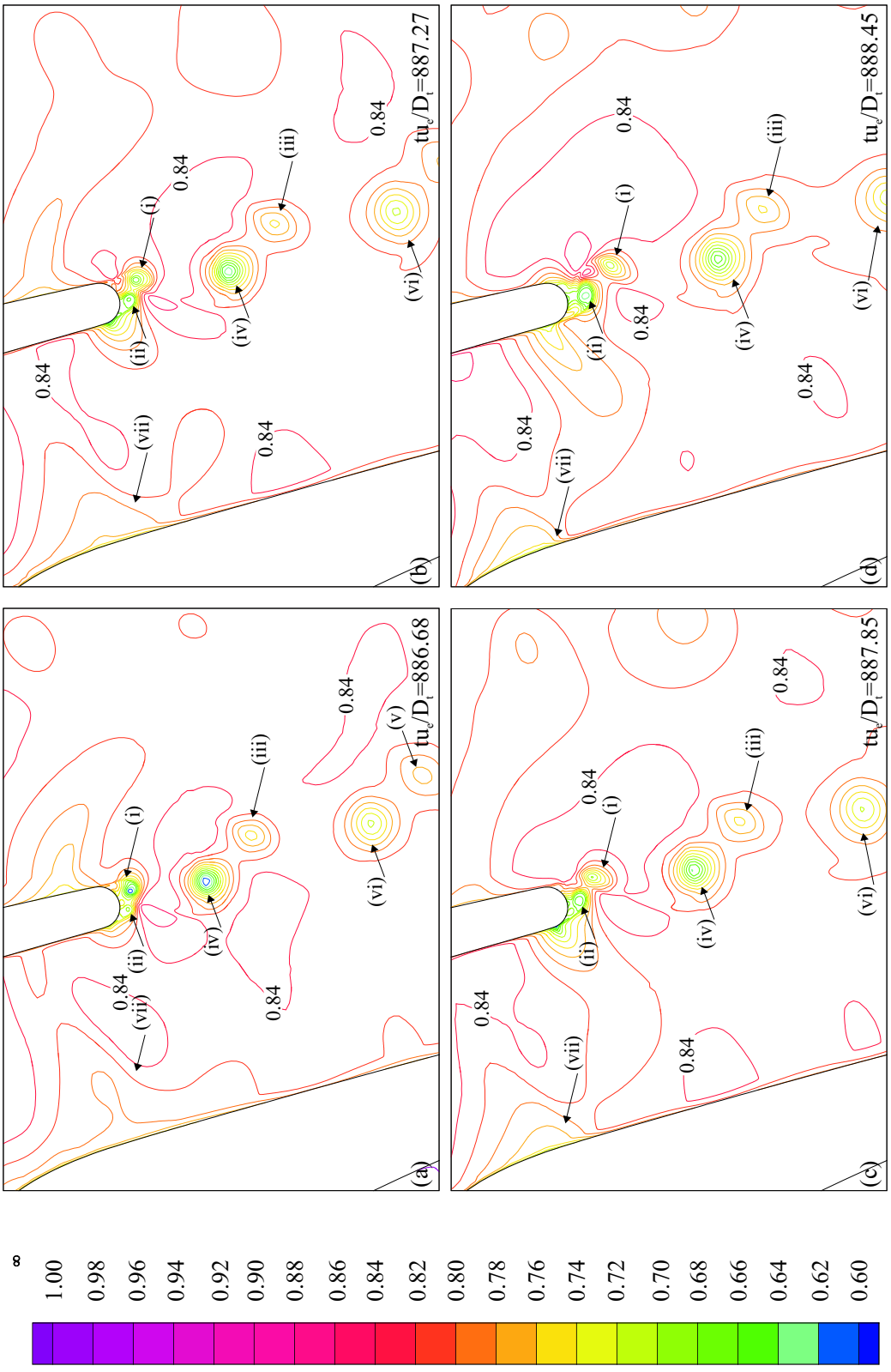

Figure 6.22: Static density contours over the first half of the turbulent vortex shedding cycle: $886.68 \leq tu_e/D_t \leq 888.45$. $\rho_{\max} = 1.00\rho_\infty$, $\rho_{\min} = 0.60\rho_\infty$, $\Delta\rho = 0.02\rho_\infty$. (i)-(vii) labelled flow features.

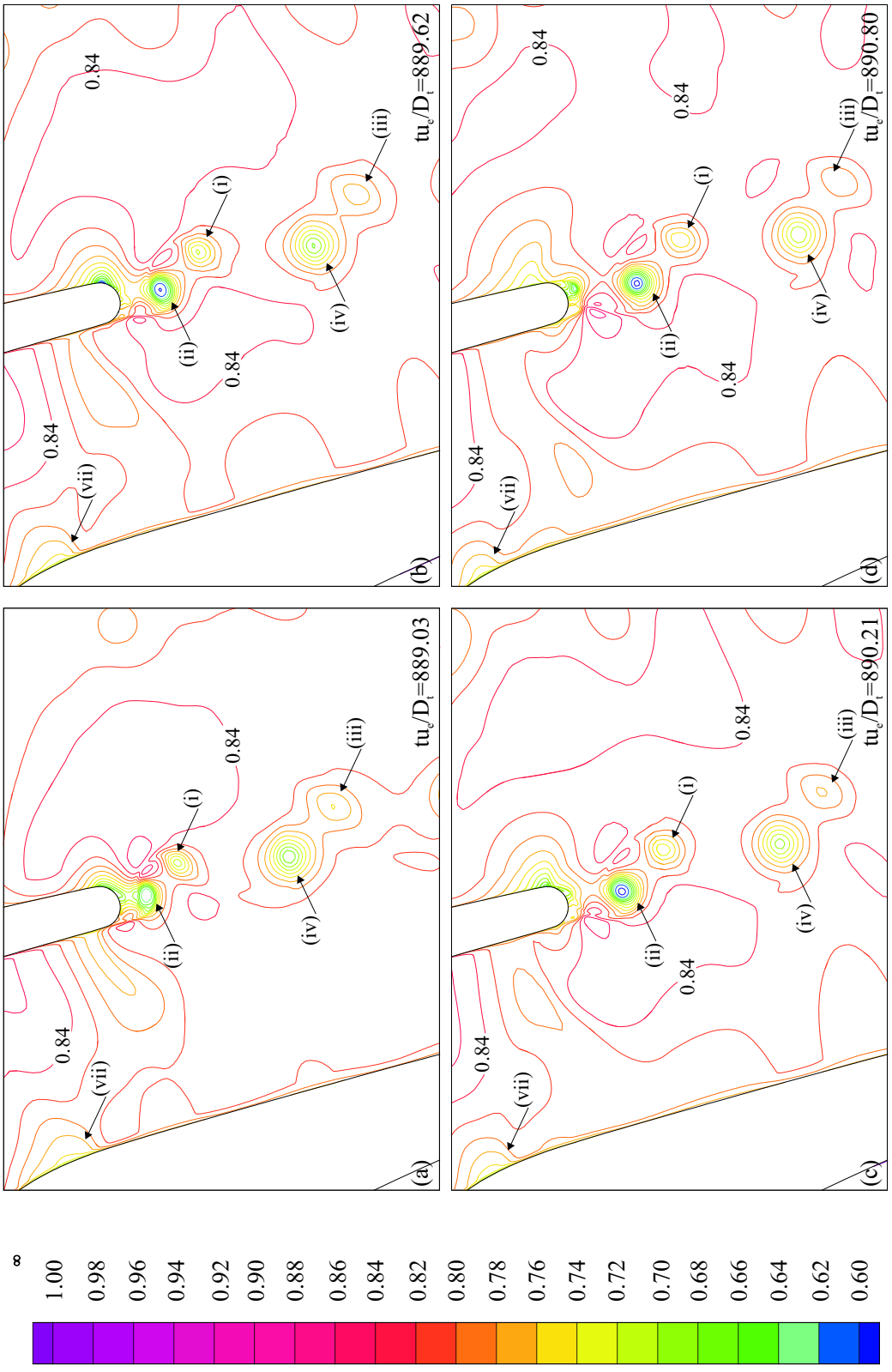

Figure 6.23: Static density contours over the second half of the turbulent vortex shedding cycle: $889.03 \leq tu_e/D_t \leq 890.80$. $\rho_{\max} = 1.00\rho_\infty$, $\rho_{\min} = 0.60\rho_\infty$, $\Delta\rho = 0.02\rho_\infty$. (i)-(vii) labelled flow features.

pressure surface vortices, as indicated in the base pressure trace of Figure 6.18. The anti-clockwise rotating vortices are also defined closer to the centre of the wake than the clockwise rotating vortices on the suction surface side.

A similar asymmetry in the wake downstream of the current turbine blade is measured in time resolved entropy contours at $6D_t$ downstream of the turbine blade by Carscallen et al. (1998, 1999) at $M_e = 0.95$. Asymmetric vortex shedding is also predicted downstream of a less highly loaded turbine blade at $M_e = 0.4$ by Arnone & Pacciani (1997) using an explicit method with an algebraic turbulence modelling approach. An asymmetric wake is further observed in smoke visualisation by Roberts & Denton (1996) downstream of a flat plate under an asymmetric pitch-wise pressure distribution. Carscallen et al. (1998, 1999) highlight two possible contributions to the asymmetric vortex shedding pattern, downstream of the turbine cascade. As well as the difference in boundary layer thickness between the suction and pressure surfaces, Carscallen et al. (1998, 1999) propose a possible contribution from the higher free stream velocity along the suction surface. This proposal is based on the work of Boldman et al. (1976), who demonstrate that increasing the velocity on one side of the wake from a symmetrical velocity distribution can significantly affect the symmetry of vortex shedding. Comparing the inviscid and turbulent turbine cascade predictions in this chapter, the symmetric vortex street predicted in the inviscid prediction is replaced in the turbulent prediction by an asymmetric vortex shedding pattern. These results imply that, for the current turbine cascade model, the relative thickness of the suction and pressure surface shear layers remains the dominant factor in the presence of the asymmetric wake. An asymmetric pitch-wise vortex shedding pattern, with non equal stream-wise vortex spacing, is also reported in Sieverding et al. (2003) from smoke visualisation and holographic/white light interferometry measurements at $M_e = 0.79$ and $Re_{D_t} = 1.487 \times 10^5$. Stronger vortices are reported on the pressure surface side of the wake, which correlate well with the reported difference in boundary layer thickness at the trailing edge. These measurements provide supporting evidence for the discussion put forward in this section. The current study corroborates the measurements of Sieverding et al. (2003), pro-

viding original time accurate numerical data of the asymmetric vortex formation and shedding development over a typical vortex shedding cycle.

No radial shock waves are observed at the turbine blade trailing edge in the turbulent prediction. Radial shock waves are, however, predicted at the trailing edge in the inviscid cascade prediction. The absence of radial shock wave recompression in the turbulent prediction follows the lower expansion around the trailing edge region in the isentropic Mach number distribution. This is also highlighted by a decrease in the static density range, from $0.25\rho_\infty \leq \rho \leq \rho_\infty$ in Figures 6.7 and 6.8 to $0.6\rho_\infty \leq \rho \leq \rho_\infty$ in Figures 6.22 and 6.23. The growing vortices still induce an outward precession of pressure waves. The upstream movement of these pressure waves onto the suction surface of the adjacent blade is evident by tracking the labelled flow feature (vii) over the course of Figures 6.22(a-d) and 6.23(a-d). The labelled flow feature (vii) is part of an upstream moving pressure wave formed at the shedding of the vortex labelled (iv). As the pressure wave moves upstream from the pressure side of the trailing edge a gradual increase in the density gradient occurs on the suction surface of the adjacent blade, close to the location of peak velocity. The increasing compression in this region is indicated by an increase in the number of contour levels at (vii) and a decrease in the spacing between successive contours at this location. The density gradient at (vii), however, remains significantly lower than the corresponding flow feature labelled (iii) in the inviscid prediction of Figures 6.7(a-d) and 6.8(a-d).

Downstream dissipation and dispersion of the vortices is documented in Figures 6.22(a-d) and 6.23(a-d) by a decrease in the number of contours at the vortex centres and by an increase in the iso-density contour spacing in this region. This is evident by tracking (iii) and (iv) over the course of Figures 6.22(a-d) and 6.23(a-d).

The asymmetric vortex shedding is expected to lead to a corresponding asymmetry in the turbulence kinetic energy characteristics. The specific turbulence kinetic energy k is documented over the same vortex shedding cycle in Figures 6.24(a-d) and 6.25(a-d). Figures 6.24(a-d) and 6.25(a-d) are therefore phase synchronous over the vortex shedding cycle with the density contour sequence in Figures 6.22(a-

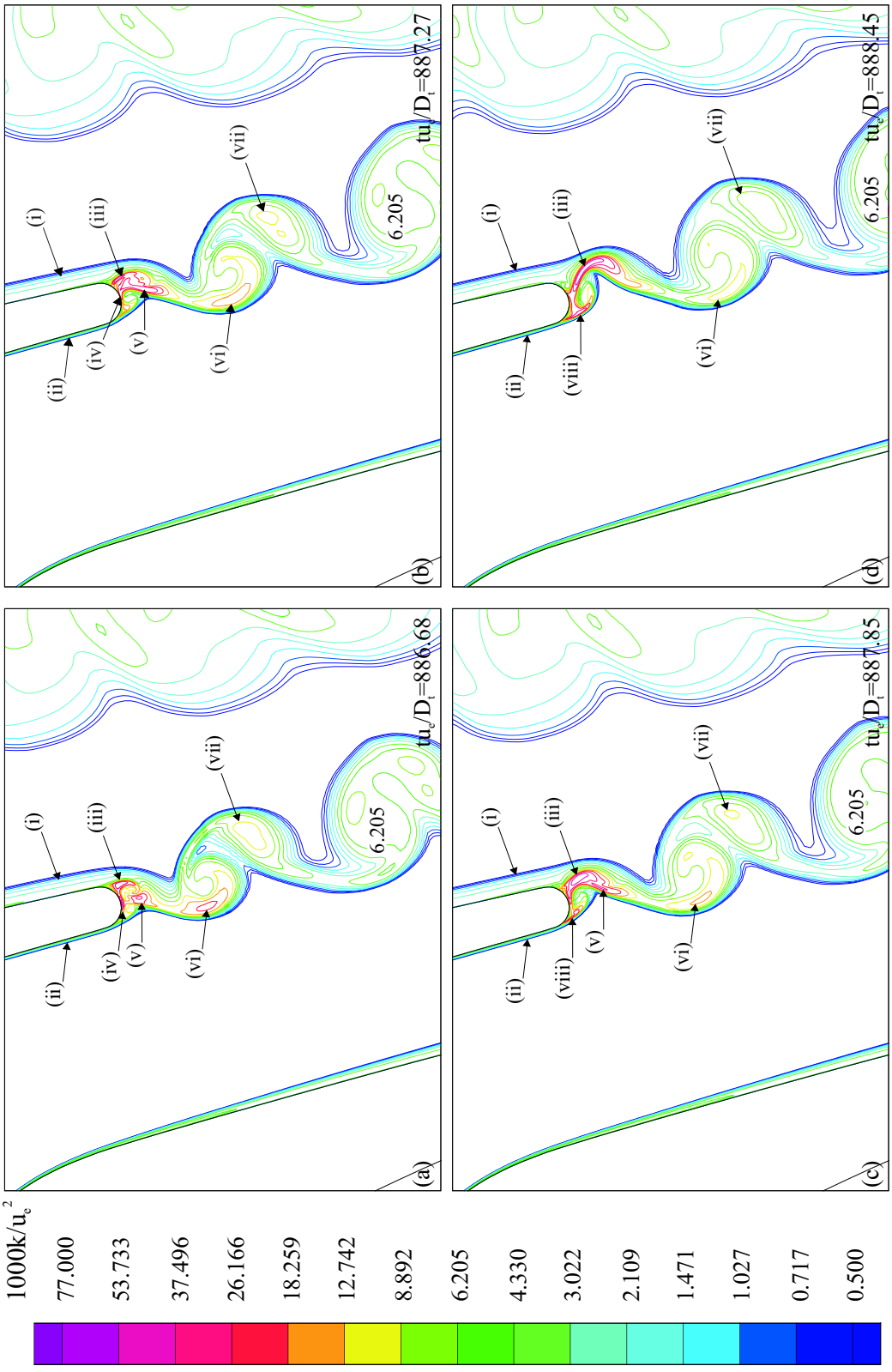

Figure 6.24: Specific turbulence kinetic energy contours over the first half of the turbulent vortex shedding cycle: $886.68 \leq tu_e/D_t \leq 888.45$. $k_{\max} = 0.077u_e^2$, $k_{\min} = 5.0 \times 10^{-4}u_e^2$, exponential distribution. (i)-(vii) labelled flow features.

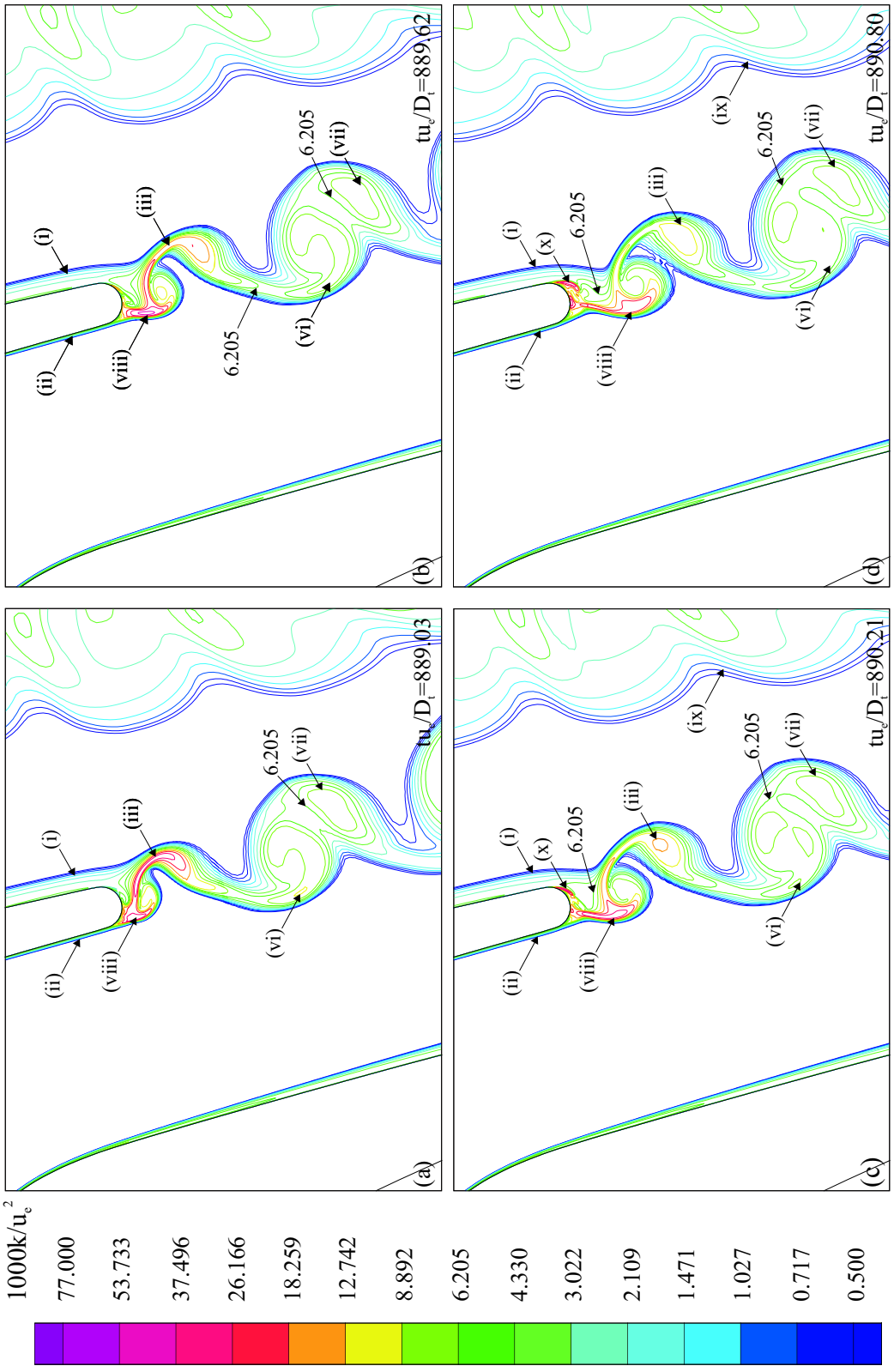

Figure 6.25: Specific turbulence kinetic energy contours over the second half of the turbulent vortex shedding cycle: $889.03 \leq tu_e/D_t \leq 890.80$. $k_{\max} = 0.077u_e^2$, $k_{\min} = 5.0 \times 10^{-4}u_e^2$, exponential distribution. (i)-(x) labelled flow features.

d) and 6.23(a-d) respectively.

The difference in boundary layer thickness between the suction side and pressure side is indicated in the k contour distribution at (i) and (ii). In the near wake region of Figure 6.24(a), localised k maxima occur in the shear layer between the clockwise rotating vortex and the trailing edge surface (iii), at the trailing edge surface (iv) and between the two contra-rotating vortices (v). Further downstream, local maxima are evident at the outer shear layer of the anti-clockwise rotating vortex (vi) and at the centre of the clockwise rotating vortex (vii). The shear layer that extends between the clockwise rotating vortex and the trailing edge (iii) remains a significant source of turbulence kinetic energy production over the course of Figure 6.24(b-d). A further region of high k then emerges at the near side shear layer of the anti-clockwise rotating vortex (viii), between this vortex and the trailing edge. Turbulence kinetic energy in the near side shear layer (viii) is augmented by convection of k from the far side shear layer (iii) as this shear layer is entrained across the wake by the growing pressure side vortex.

These shear layers remain a significant source of turbulence kinetic energy production after the shedding of each vortex. The entrainment of turbulence kinetic energy from the shear layer around the downstream anti-clockwise rotating vortex is highlighted by the contour shape bounding the local k maximum at (vi). The increase in area bounded by each k contour in the vortices downstream of the turbine blade highlight the downstream diffusion process. The wake further downstream is indicated by the wake of the adjacent turbine blade, labelled (ix) in Figure 6.25(c-d). A significant increase in the area bounded by each k contour is therefore noted between the wake at (ix) and the wake downstream of the subject blade at, for example, (vi) and (vii).

Regions of turbulence kinetic energy dissipation are highlighted over the vortex shedding cycle in the specific turbulence kinetic energy dissipation rate ω distribution of Figure 6.26(a-d) and Figure 6.27(a-d). This contour sequence is defined over the same phase of vortex shedding as the k contour sequence in Figures 6.24(a-d) and 6.25(a-d) and the static density contour sequence in Figures 6.22(a-d)

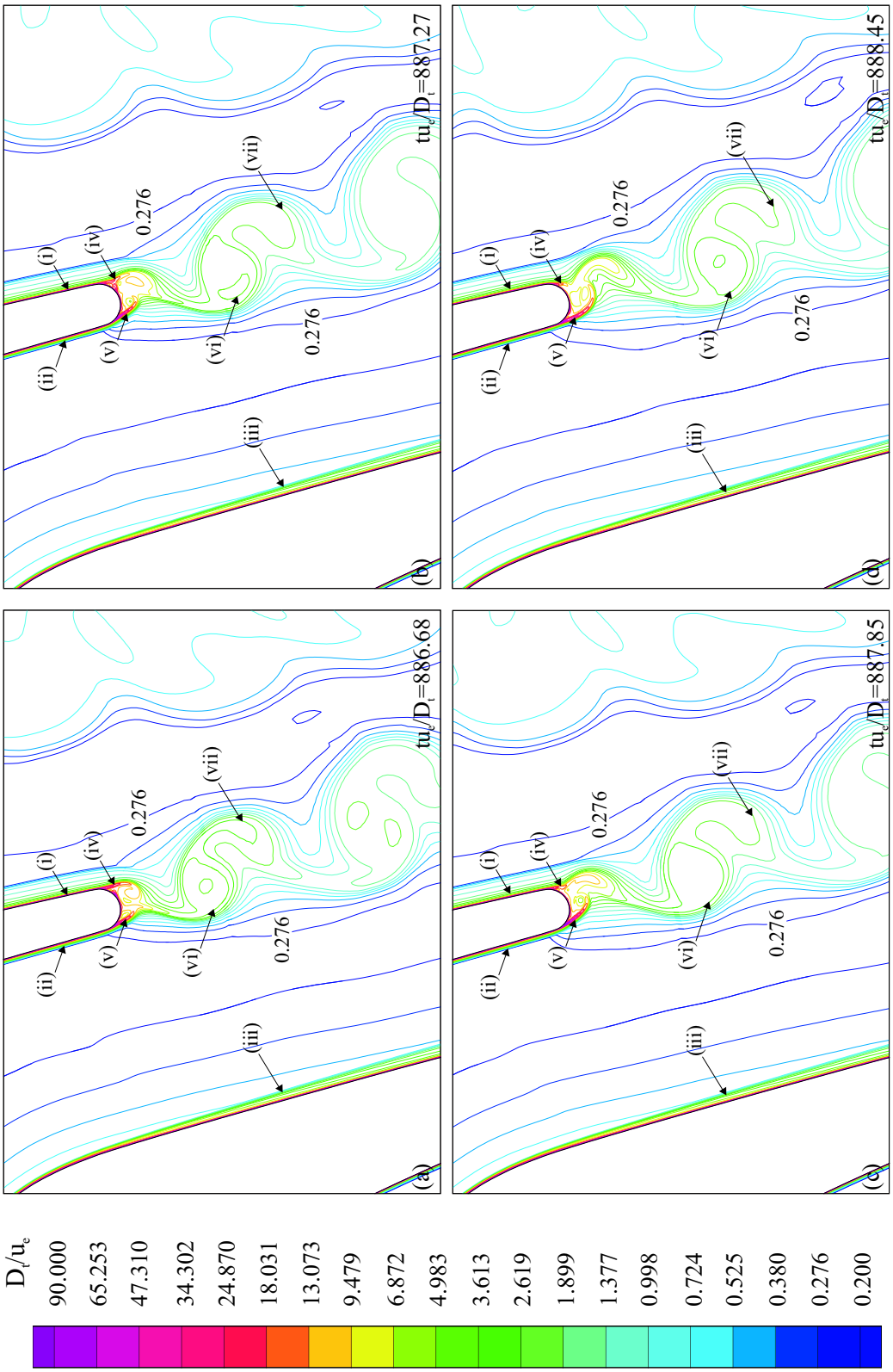

Figure 6.26: Specific turbulence kinetic energy dissipation rate contours over the first half of the turbulent vortex shedding cycle: $886.68 \leq tu_e/D_t \leq 888.45$. $\omega_{\max} = 90u_e/D_t$, $\omega_{\min} = 0.2u_e/D_t$, exponential distribution. (i)-(vii) labelled flow features.

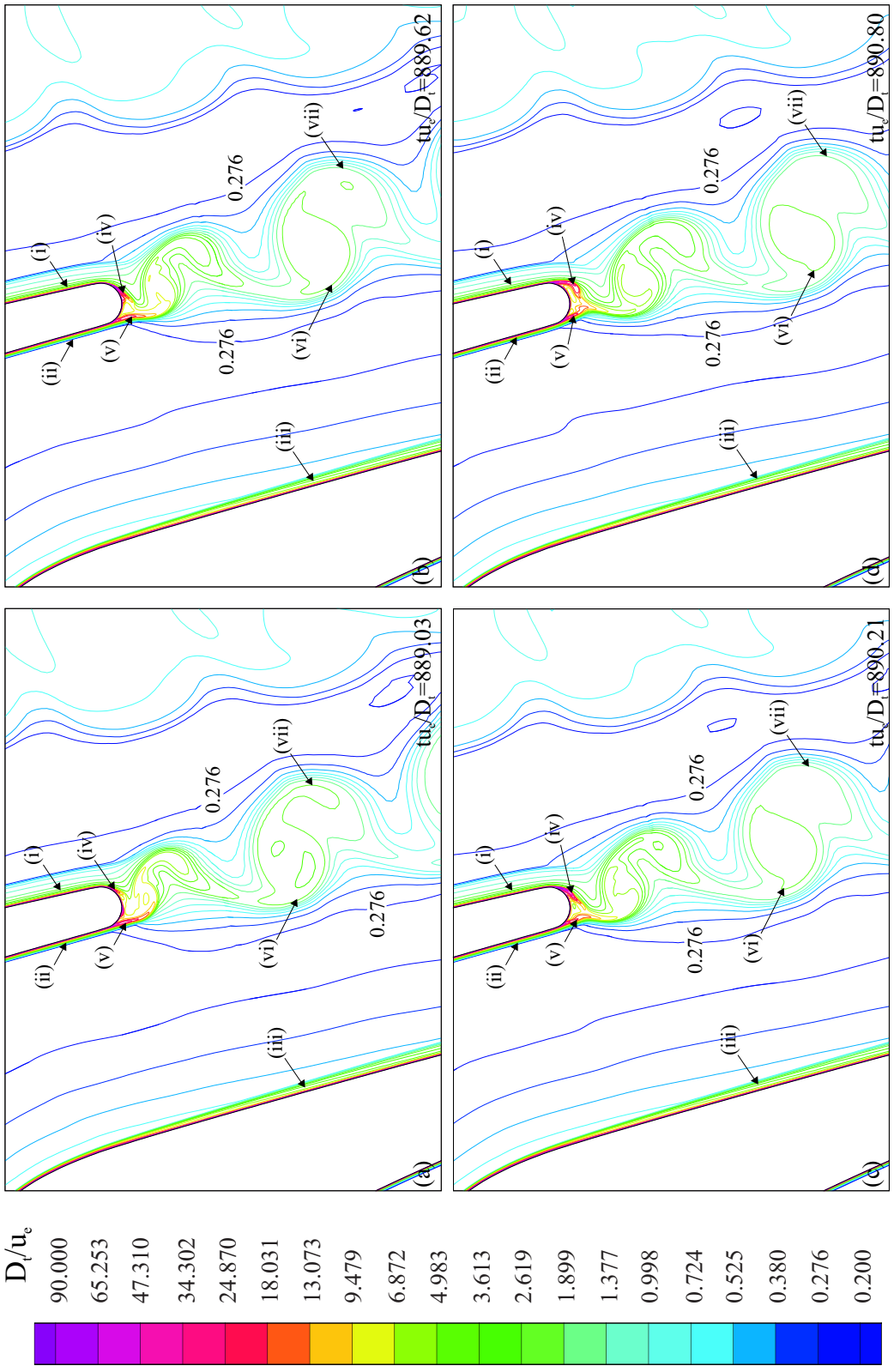

Figure 6.27: Specific turbulence kinetic energy dissipation rate contours over the second half of the turbulent vortex shedding cycle: $889.03 \leq tu_e/D_t \leq 890.80$. $\omega_{\max} = 90u_e/D_t$, $\omega_{\min} = 0.2u_e/D_t$, exponential distribution. (i)-(vii) labelled flow features.

and 6.23(a-d). A maximum in ω occurs within the viscous sublayer as turbulence kinetic energy is locally dissipated to heat. The increase in ω within the laminar sublayer is indicated by a gradual colour shift in the ω contours towards the red end of the colour spectrum at the blade surface. As in the k field, the ω contours highlight the relative increase in boundary layer thickness between the suction and pressure surfaces at (i) and (ii). The ω contours also highlight the rapid increase in boundary layer thickness with stream-wise distance on the suction surface of the adjacent turbine blade at (iii). After separation of the boundary layers, a significant dissipation rate of k remains in the separated shear layers at (iv) and (v). The region of high ω within the separated pressure surface shear layer at (v) increases in stream-wise length as the anti-clockwise rotating vortex grows in circulation over the course of Figure 6.26(a-d). The region of high ω in the opposite shear layer (iv) decreases in stream-wise length over this period, as fluid from this shear layer is entrained close to the trailing edge by the pressure surface vortex. The entrainment of fluid from this shear layer increases the turbulence kinetic energy dissipation rate in the anti-clockwise rotating vortex through convection of ω. This shear layer (iv) subsequently moves further away from the trailing edge and increases in stream-wise length as a new clockwise rotating vortex is formed on the suction surface side of the wake in Figure 6.27(c-d). Further downstream, the vortex cores are highlighted as regions of local ω maxima. Two such regions are labelled (vi) and (vii) for the anti-clockwise and clockwise rotating vortices respectively. Dissipation in these vortices decreases the strength of the vortices with downstream distance, decreasing the associated energy separation mechanism at significant distances downstream of each turbine blade.

6.3.6 Energy Separation in the Turbulent Cascade Wake

The influence of asymmetric vortex shedding on the redistribution of stagnation temperature and pressure downstream of the turbine cascade is discussed in this section. A time resolved sequence of eight contour plots document the stagnation temperature field development over a typical vortex shedding cycle. Figure 6.28(a-

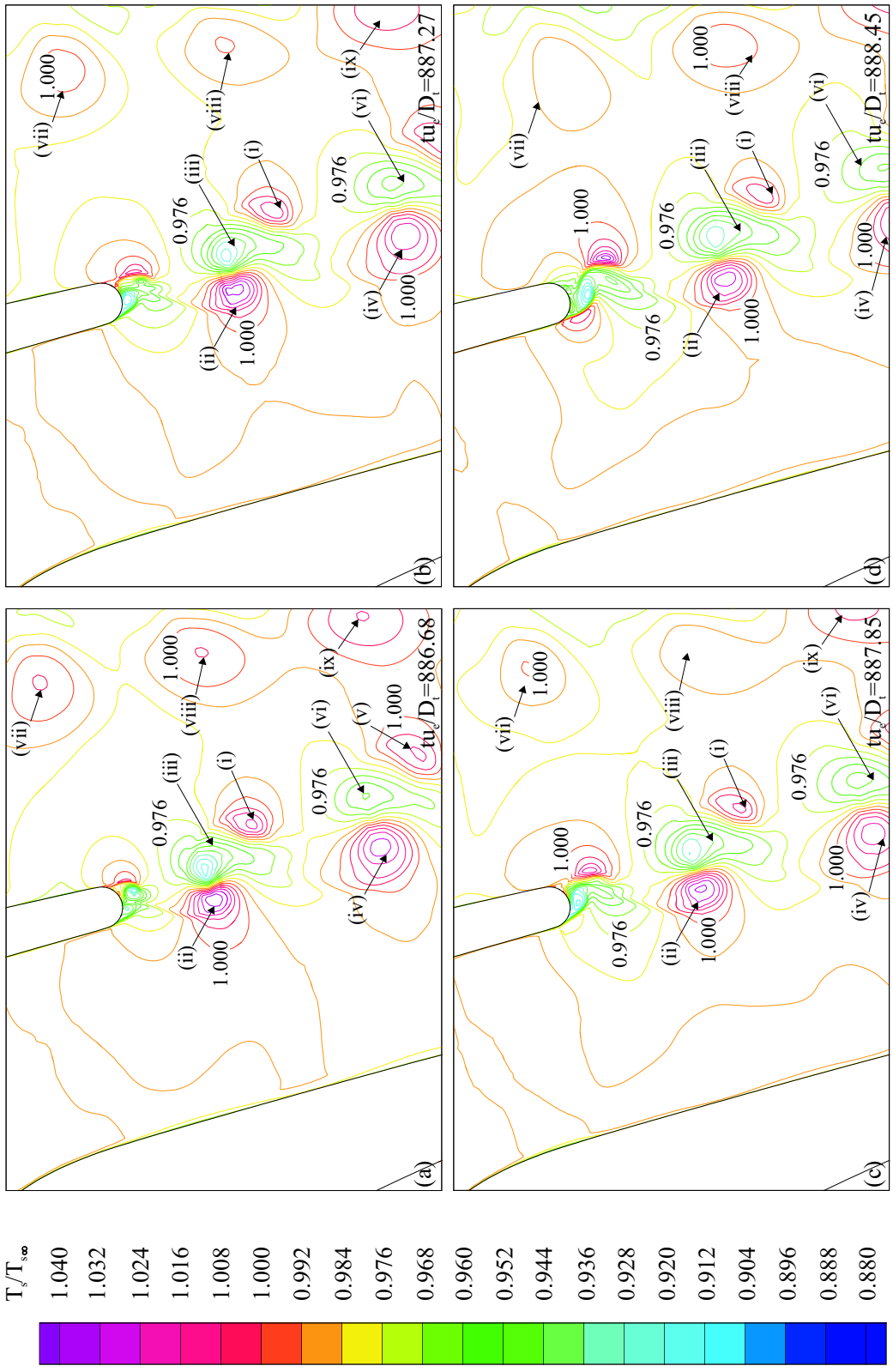

Figure 6.28: Stagnation temperature contours over the first half of the turbulent vortex shedding cycle: $886.68 \leq tu_e/D_t \leq 888.45$. $T_{s\,\max} = 1.040T_{s\infty}$, $T_{s\,\min} = 0.880T_{s\infty}$, $\Delta T_s = 0.008T_{s\infty}$. (i)-(ix) labelled flow features.

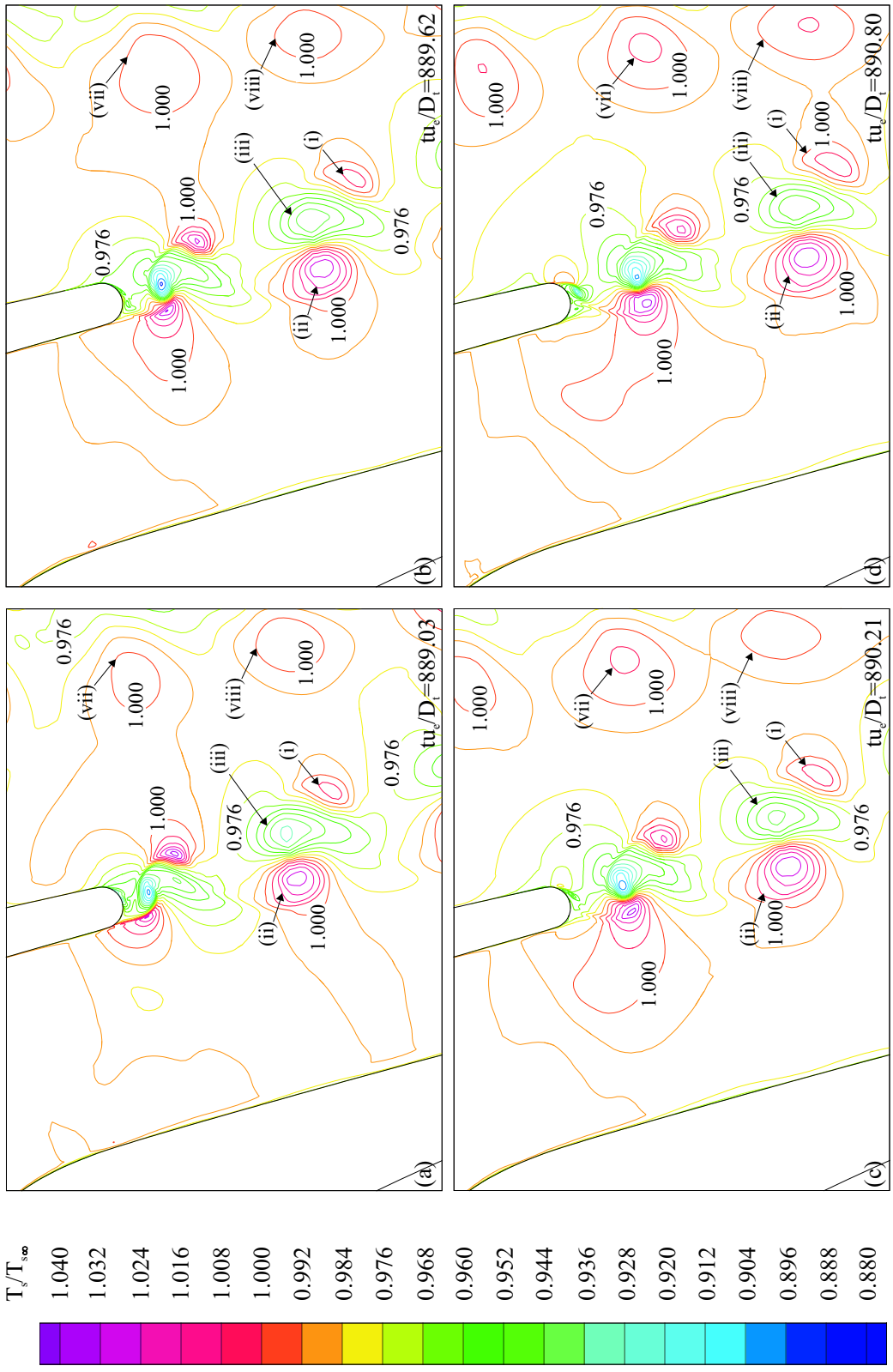

Figure 6.29: Stagnation temperature contours over the second half of the turbulent vortex shedding cycle: $889.03 \leq tu_e/D_t \leq 890.80$. $T_{s\,\max} = 1.040T_{s\infty}$, $T_{s\,\min} = 0.880T_{s\infty}$, $\Delta T_s = 0.008T_{s\infty}$. (i)-(viii) labelled flow features.

d) is phase synchronous over the vortex shedding cycle with the static density, k and ω development in Figures 6.22(a-d), 6.24(a-d) and 6.26(a-d) respectively. Figure 6.29(a-d) is therefore phase synchronous with Figures 6.23(a-d), 6.25(a-d) and 6.27(a-d) for the second half of the vortex shedding cycle. Localised regions of stagnation temperature greater than the free stream condition, hot spots, exist in the outer shear layer on the suction and pressure sides of the wake at each vortex. Localised regions of lower stagnation temperature than the free stream condition, cold spots, also exist close to the centre of the wake at each vortex. The precise form of the stagnation temperature redistribution is, however, different to the regular pattern observed downstream of the inviscid turbine cascade and in the circular cylinder predictions. Two typical hot spots are labelled (i) and (ii) in Figures 6.28(a-d) and 6.29(a-d). These two hot spots correspond respectively to the clockwise and anti-clockwise rotating vortices labelled (iii) and (iv) in Figures 6.22(a-d) and 6.23(a-d). Between these two hot spots, (i) and (ii), lies a cold region of fluid with stagnation temperature lower than the free stream condition. This cold region is labelled (iii) in Figures 6.28(a-d) and 6.29(a-d). Closer inspection of this cold region (iii) reveals its origin as two separate cold spots induced by the clockwise and anti-clockwise rotating vortices. The close proximity of these two vortices and the introduction of turbulence diffusion in the current prediction merges these two cold spots into a larger cold region which extends between the two vortices. This cold region (iii) falls to a local minimum stagnation temperature of $T_s = 0.920 T_{s\infty}$ close to the hot spot (ii) in Figure 6.28(a). An increase in stagnation temperature occurs with downstream distance from this local minimum approaching the hot spot (i) on the opposite side of the wake. The uneven stagnation temperature distribution within this cold region indicates a relative increase in the energy separation mechanism at the anti-clockwise rotating vortex. This proposition is confirmed by the higher stagnation temperature at the hot spot (ii) on this side of the wake. Specifically, the stagnation temperature rises to a local maximum of $T_s = 1.040 T_{s\infty}$ at (ii) in Figure 6.28(a), compared with $T_s = 1.024 T_{s\infty}$ at the adjacent hot spot (i) on the opposite side of the wake. The increase in the energy separation mechanism on the

pressure surface side of the wake indicates a direct correlation with vortex strength. This relationship is reconcilable with the energy separation mechanism proposed by Kurosaka et al. (1987) and extends this hypothesis to asymmetric vortex shedding. The introduction of turbulence diffusion in the current prediction reduces the stagnation temperature rise at each hot spot, relative to the inviscid prediction in Figures 6.10(a-d) and 6.11(a-d). Further downstream, a similar pattern is observed with two hot spots, (iv) and (v), located either side of a cold region (vi). A greater redistribution of stagnation temperature is again observed at the anti-clockwise rotating vortex on the pressure surface side. The hot spots on the pressure surface side of the wake remain above the free stream condition for a significant distance downstream of the turbine blade, as indicated by the precession of hot spots at (vii)-(ix).

A similar asymmetric stagnation temperature field is reported for the current turbine blade at $M_e = 0.95$ in the time resolved measurements of Hogg et al. (1997) and Carscallen et al. (1998, 1999). These measurements indicate a similar bias in the stagnation temperature redistribution towards the pressure surface side of the wake. Specifically, a 25% increase in the stagnation temperature rise above the free stream condition is measured at the hot spots on the pressure surface side of the wake. The measurements of Hogg et al. (1997) and Carscallen et al. (1998, 1999) indicate a similar coalescence of cold spots induced by each successive contra-rotating vortex pair. These measurements also indicate an uneven stream-wise spacing between successive vortices, as reported for the current prediction in Section 6.3.5. Furthermore, the stagnation temperature distributions in Hogg et al. (1997) and Carscallen et al. (1998, 1999) display a bias of the cold spots towards the suction surface side of the wake. A similar bias of the cold regions, (iii) and (vi), is predicted in Figures 6.28(a-d) and 6.29(a-d). This bias results from the location of the anti-clockwise rotating vortex cores, which move downstream along the wake centreline. The greater transverse distance of hot spots on the suction surface side from the wake centreline, documented in Figures 6.28(a-d) and 6.29(a-d), is similarly indicated in the cited measurements. The close correlation of the current prediction at

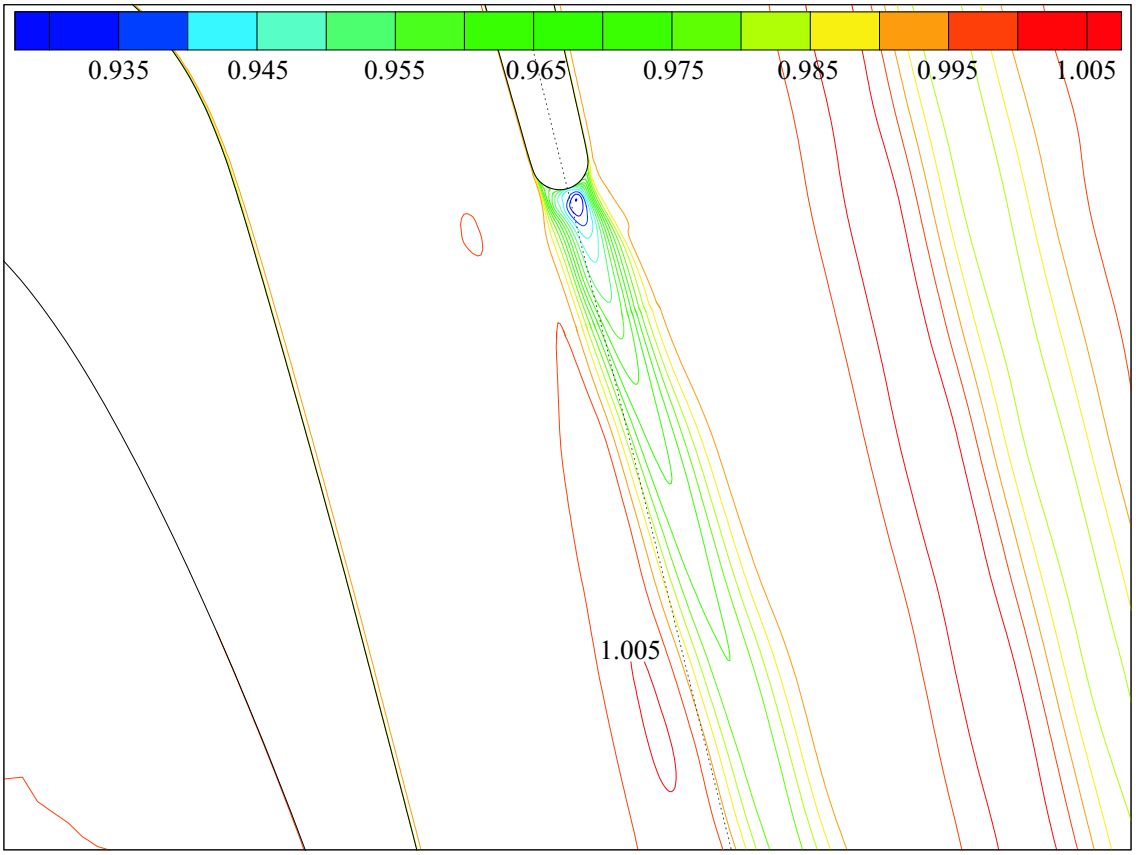

Figure 6.30: Time averaged stagnation temperature contours. $T_{s\,\max} = 1.005T_{s\infty}$, $T_{s\,\min} = 0.930T_{s\infty}$, $\Delta T_s = 0.005T_{s\infty}$. $(\cdots)$ Reference alignment of the turbine blade outlet metal angle.

$M_e = 0.6$ with the measurements of Hogg et al. (1997) and Carscallen et al. (1998, 1999) at $M_e = 0.95$ indicate that a similar vortex shedding pattern may be maintained over a significant Mach number range below $M_e = 1$ for this turbine blade profile. It is however recognised that an increase in the energy separation mechanism occurs between $M_e = 0.6$ and $M_e = 0.95$. This is associated with an increase in the vortex shedding strength over this range, as reported on a time averaged basis for this blade by Hogg et al. (1997) and Carscallen et al. (1998, 1999).

The time averaged result of the asymmetric stagnation temperature distribution represents a modification to the Eckert-Weise effect, established for circular cylinders. The time averaged stagnation temperature field for the turbulent prediction is given in Figure 6.30. The wake centreline is highlighted in this figure by a dotted black line, as determined by the turbine blade outlet metal angle. The stagnation

temperature deficit, resulting from the time averaged passage of cold spots at each vortex, is significantly biased towards the suction surface side of the wake. This bias is also evident close to the trailing edge, within the formation region, where the stagnation temperature reaches a minimum value of $T_s = 0.93T_{s\infty}$. This bias, which increases with downstream distance, is also indicated in the time averaged stagnation temperature wake profile at $6D_t$ from the trailing edge in Carscallen et al. (1998). An increase above the free stream temperature occurs further downstream on the pressure surface side of the wake in the current prediction. The absence of a similar stagnation temperature rise on the suction surface side of the wake results from a combined effect. Firstly, the stagnation temperature rise above the free stream condition is lower at the clockwise rotating vortices due to the lower circulation in these vortices. Secondly, the cold spots from the anti-clockwise rotating vortices are located on this side of the wake and reduce the influence of these hot spots on a time averaged basis.

The asymmetric wake vorticity causes a similar asymmetry in the stagnation pressure field, downstream of the turbine cascade. A sequence of eight time accurate stagnation pressure contour plots describe a typical vortex shedding cycle in Figures 6.31(a-d) and 6.32(a-d). This contour sequence is defined over the same vortex shedding cycle as the static density, k, ω and stagnation temperature contour sequence in Figures 6.22-6.29. Localised regions of $p_s > p_{s\infty}$ are labelled (i)-(iii) in Figures 6.31(a-d) and 6.32(a-d). These mark the outer shear layers of the downstream moving vortices. The stagnation pressure increase above the free stream condition at (i)-(iii) differs between the suction and pressure surface sides of the wake. The greater relative increase in stagnation pressure at (i) and (iii) correlates with the greater increase in stagnation temperature predicted in the hot spots on this side of the wake in Figures 6.28(a-d) and 6.29(a-d). The stagnation pressure deficit, below the free stream condition, on the opposite side of each vortex is also greater at these anti-clockwise rotating vortices. These regions of localised expansion are labelled (iv)-(viii) in Figures 6.31(a-d) and 6.32(a-d). The greater stagnation pressure redistribution around the anti-clockwise rotating vortices on the pressure

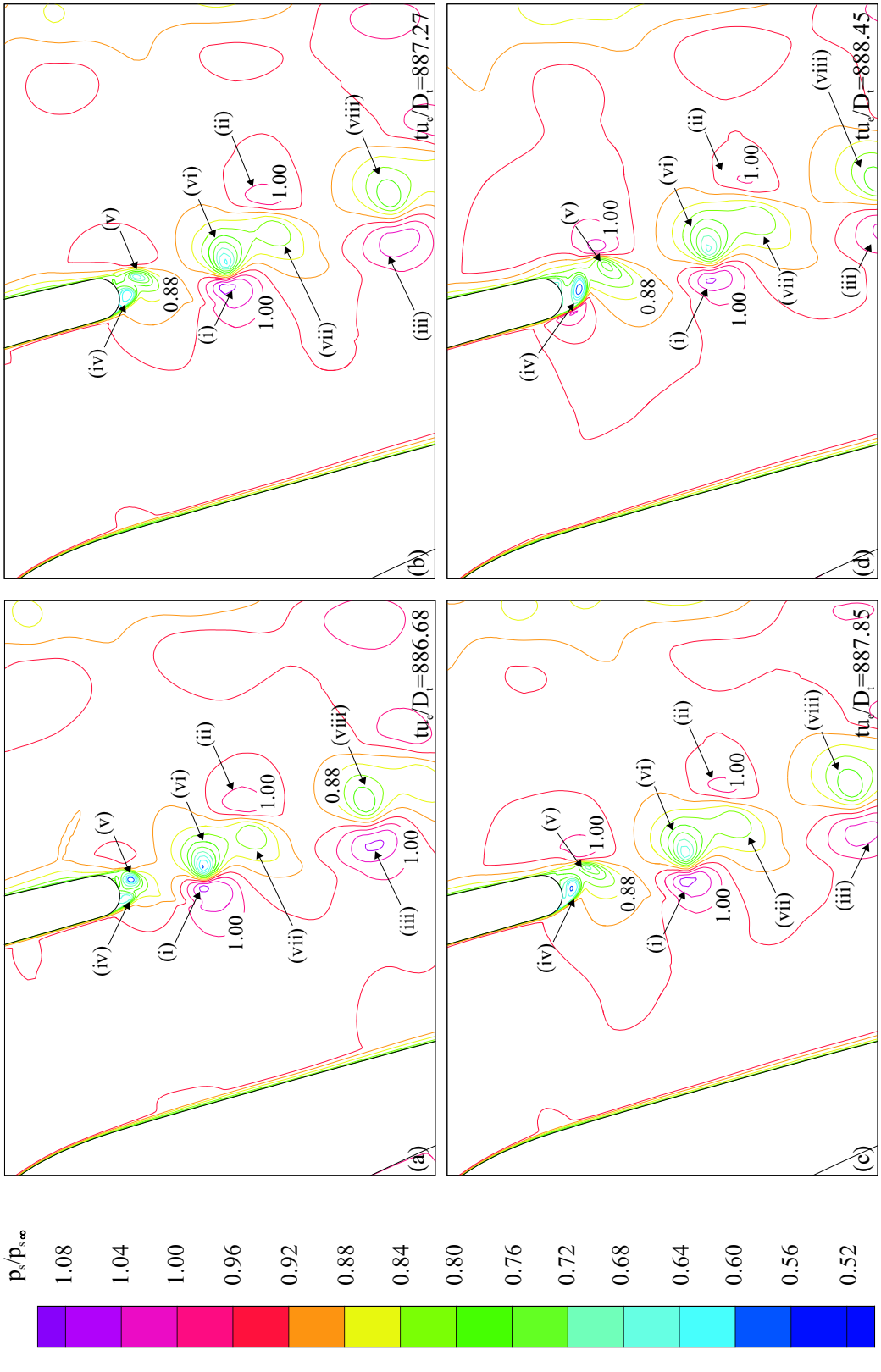

Figure 6.31: Stagnation pressure contours over the first half of the turbulent vortex shedding cycle: $886.68 \leq tu_e/D_t \leq 888.45$. $p_{s\,\max} = 1.08p_{s\infty}$, $p_{s\,\min} = 0.52p_{s\infty}$, $\Delta p_s = 0.04p_{s\infty}$. (i)-(viii) labelled flow features.

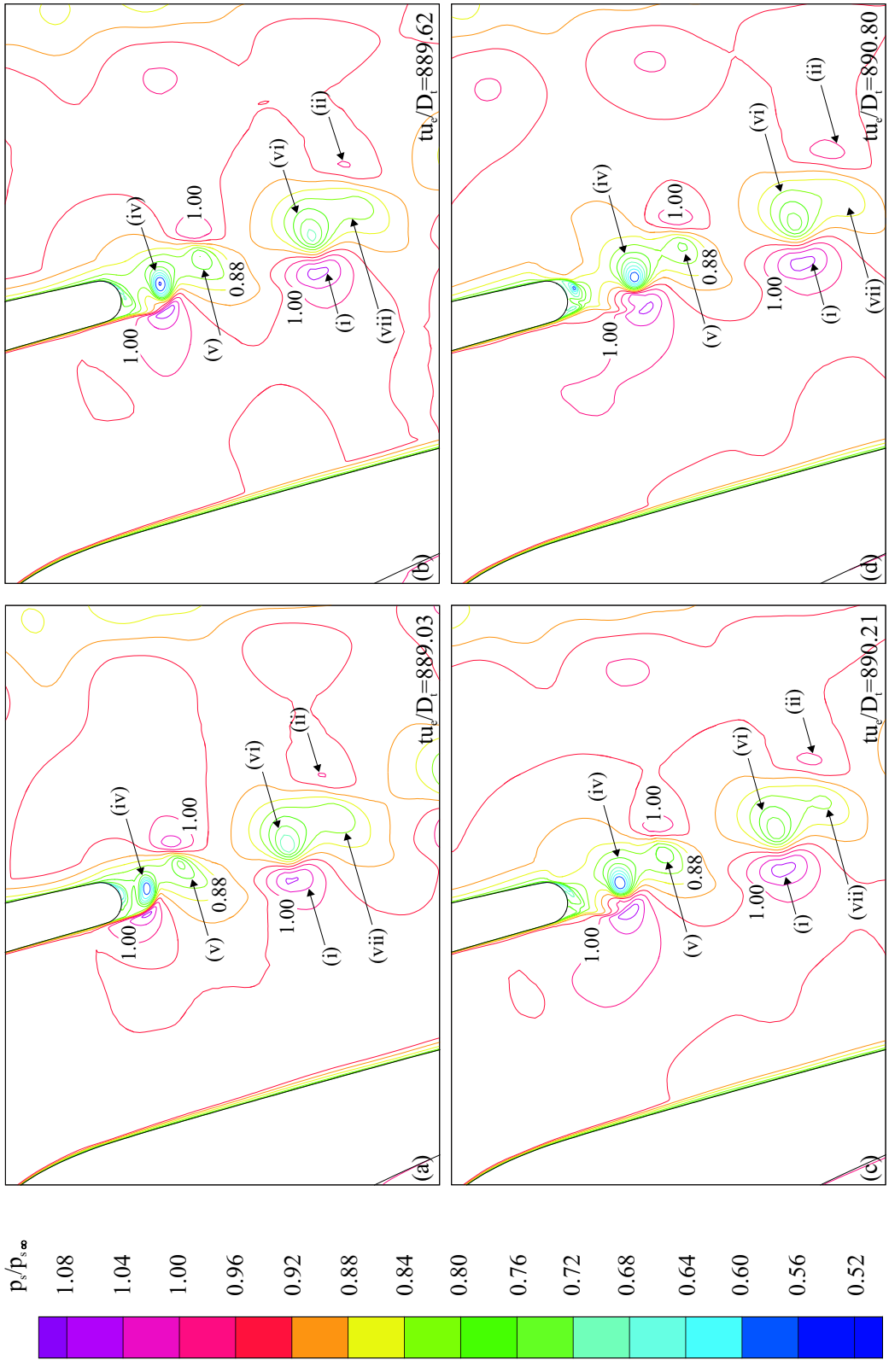

Figure 6.32: Stagnation pressure contours over the second half of the vortex shedding cycle: $889.03 \leq tu_e/D_t \leq 890.80$. $p_{s\,\max} = 1.08p_{s\infty}$, $p_{s\,\min} = 0.52p_{s\infty}$, $\Delta p_s = 0.04p_{s\infty}$. (i)-(vii) labelled flow features.

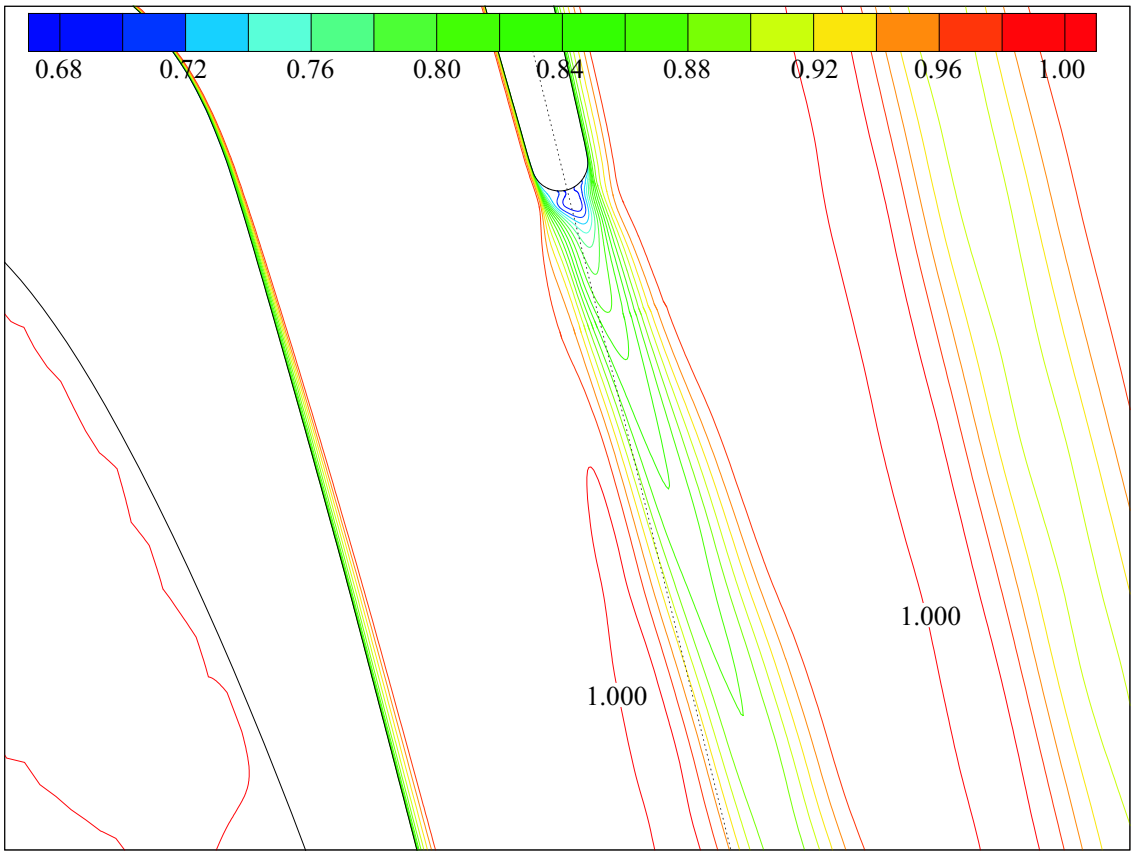

Figure 6.33: Time averaged stagnation pressure contours. $p_{s\,\max} = p_{s\infty}$, $p_{s\,\min} = 0.68p_{s\infty}$, $\Delta p_s = 0.02p_{s\infty}$. $(\cdots)$ Reference alignment of the turbine blade outlet metal angle.

surface side of the wake confirm a similar correlation with the vortex strength, as documented for the stagnation temperature field. The asymmetric stagnation pressure distribution is similarly measured downstream of the same turbine cascade at $M_e = 0.95$ by Carscallen et al. (1998, 1999). The pressure surface vortices are indicated in these measurements as inducing the greatest stagnation pressure redistribution. As in the current prediction, these measurements also indicate a bias in the stagnation pressure deficit towards the suction surface side of the wake.

The bias in stagnation pressure is also observed on a time averaged basis in Figure 6.33. For reference, the centre of the wake is defined by a black dotted line, which lies along the turbine blade metal angle. The stagnation pressure contours, which are normalised by the free stream stagnation pressure $p_{s\infty}$, clearly show a time averaged deficit on the suction surface side of the wake. The minimum stagnation

pressure occurs immediately downstream of the turbine blade, close to the location of the base pressure tapping. The downstream bias in stagnation pressure increases with downstream distance from the trailing edge as the stagnation pressure extrema spread in the transverse direction. At approximately five trailing edge diameters downstream of the turbine blade, a slight increase above the free stream stagnation pressure occurs on the pressure surface side of the wake. The stagnation pressure in this region rises to approximately $p_s = 1.008 p_{s\infty}$ at six diameters downstream of the trailing edge. The onset of this time averaged region of raised stagnation pressure, downstream of the trailing edge, results from the increasing transverse spacing between the time resolved regions of $p_s > p_{s\infty}$ and $p_s < p_{s\infty}$ across the pressure surface vortices with downstream distance. The time averaged region of $p_s/p_{s\infty} > 1$ remains significantly lower than the stagnation pressure maxima observed in the time accurate field along this side of the wake. The time averaged stagnation pressure distribution further downstream is evident at the right hand side of this figure, resulting from the wake downstream of the adjacent turbine blade.

The time accurate entropy field highlights the structure and development of the asymmetric turbine blade wake. The wake development is described over one typical vortex shedding cycle in Figures 6.34(a-d) and 6.35(a-d). These entropy contours are time matched over the interval $886.68 \leq tu_e/D_t \leq 890.80$ with the time resolved wake development in Figures 6.22-6.29 and Figures 6.31-6.32. The local entropy increase above the free stream condition is computed from the stagnation temperature and pressure fields using Equation 5.4. The resulting field highlights three main sources of entropy production in the turbulent turbine blade prediction. An entropy increase occurs along both sides of the turbine blade, as the stagnation temperature and pressure adjust through the boundary layer to the surface condition. This source of entropy production is, of course, absent in the inviscid turbine blade prediction. A similar increase in entropy is however defined close to the surface of the circular cylinder in Section 5.3.4. The thin boundary layers in the high Reynolds number circular cylinder prediction ensure that this region of entropy increase is limited to a thin strip along each side of the cylinder. In the current prediction, the entropy

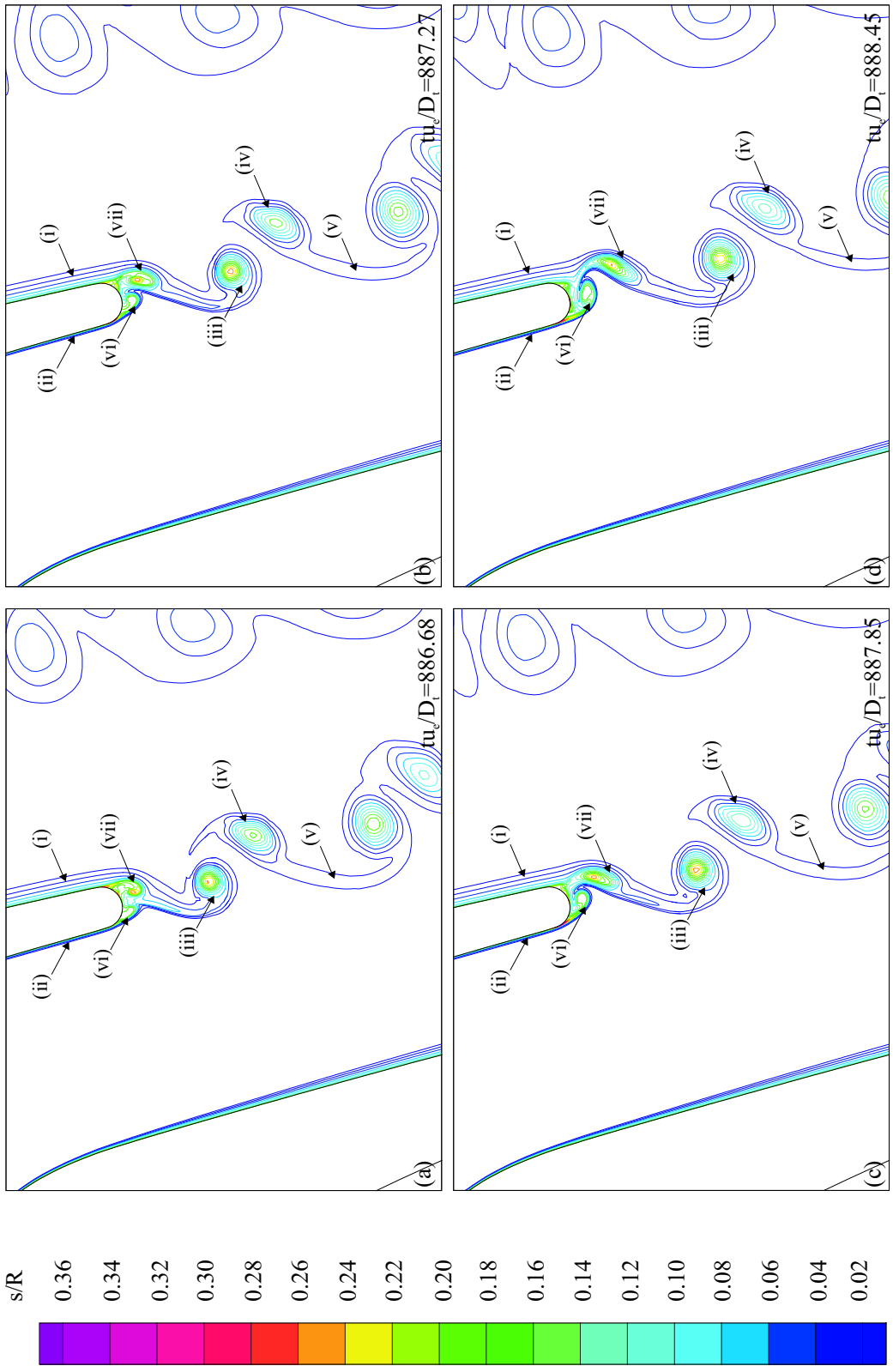

Figure 6.34: Specific entropy contours over the first half of the vortex shedding cycle: $886.68 \leq tu_e/D_t \leq 888.45$. $s_{\max} = 0.36R$, $s_{\min} = 0.02R$, $\Delta s = 0.02R$, $s_\infty = 0$. (i)-(vii) labelled flow features.

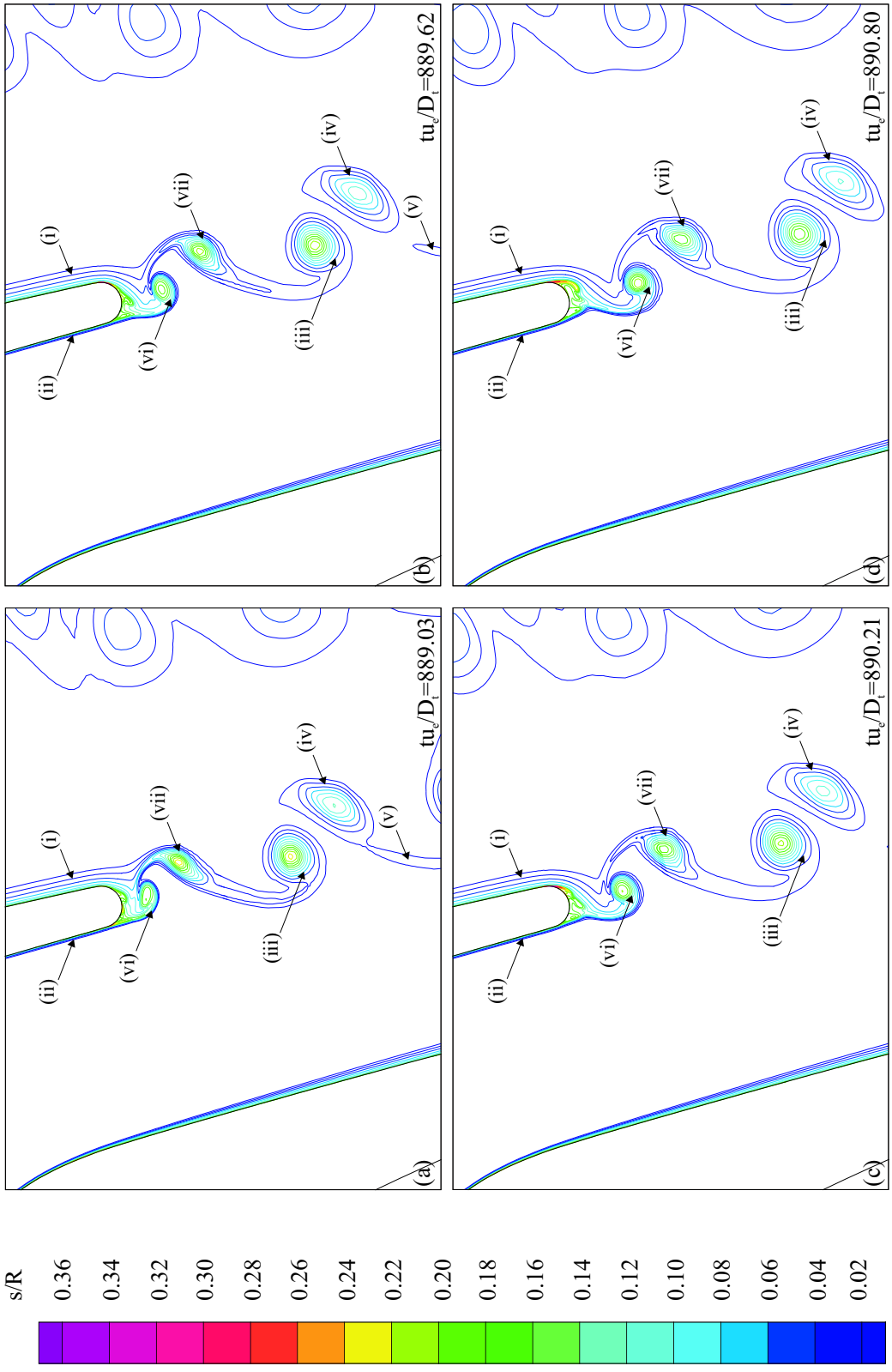

Figure 6.35: Specific entropy contours over the second half of the vortex shedding cycle: $889.03 \leq tu_e/D_t \leq 890.80$. $s_{\max} = 0.36R$, $s_{\min} = 0.02R$, $\Delta s = 0.02R$, $s_\infty = 0$. (i)-(vii) labelled flow features.

increase along the turbine blade highlights the relative thickness of the boundary layers at separation on the suction (i) and pressure (ii) surfaces. One source of entropy production absent from the turbulent cascade prediction is the increase in entropy caused by the rapid fluid recompression across the radial shock waves, as documented in the inviscid turbine blade and circular cylinder predictions. This recompression constitutes an additional source of entropy, which changes in magnitude and radial extent as the radial shock waves precess circumferentially around the downstream surface over the vortex shedding cycle. A further source of entropy production occurs at the centre of each vortex, describing the asymmetric pattern of convecting vortex cores along the pressure and suction sides of the wake. These entropy contours highlight the differences in form and strength between the vortices either side of the wake. The anti-clockwise rotating vortices, for example (iii), appear tightly rolled and well defined. The vortices on this side of the wake appear similar in form to the vortices which characterise the von Kármán vortex street in the circular cylinder prediction and the inviscid turbine blade prediction. The vortices on the suction side (iv) appear less well defined, weaker, and appear to be stretched along the direction of the shear layers that extend between adjacent vortices. These shear layers are highlighted as further regions of entropy production as fluid undergoes intense shearing between the vortices at, for example (v). The different vorticity distributions in the pressure and suction surface vortices create the previously documented uneven stream-wise distribution of vortex cores. The formation of these vortices at the trailing edge indicate that the clockwise rotating vortices are stretched along the shear layer early into the formation of the pressure surface vortex. This stretching of the suction surface vortex is evident by tracking (vi) and (vii) over the course of Figure 6.34(a-d). The downstream transport of the anti-clockwise rotating vortices along the wake centreline, and the displacement of the clockwise rotating vortices further into the suction surface side of the wake, are clearly highlighted in the entropy contours. The result of this vortex shedding pattern is the documented bias in the time averaged stagnation temperature and pressure fields, which modify the established Eckert-Weise effect in the turbine

cascade wake.

6.3.7 Summary

The turbulent flow past a highly loaded turbine nozzle cascade is predicted at exit conditions of $M_e = 0.6$ and $Re_{D_t} = 7.48{\times}10^4$. To the authors knowledge, no previous time accurate numerical predictions of this turbine cascade are published at the conditions modelled in this study, in particular with regard to the energy separation characteristics. This work therefore represents an original extension to the published measurements of Carscallen & Gostelow (1994), Carscallen et al. (1996, 1998, 1999), Hogg et al. (1997) and Ackerman (2005) for this turbine cascade. This work also extends the turbulent prediction of Currie & Carscallen (1998) at $M_e = 1.16$ to a time accurate analysis in the low transonic regime.

The turbulent prediction is developed from an inviscid prediction by imposing uniform values for the specific turbulence kinetic energy k and specific turbulence kinetic energy dissipation rate ω throughout the computational domain. A condition of no-slip is imposed at the turbine blade surface. An initial transient period of flow develops downstream of the cascade after the start of the turbulent prediction as the k and ω fields develop, and boundary layers are defined along the suction and pressure surfaces. After this short transient period, a self-sustained vortex shedding pattern resumes downstream of the turbine cascade. This pattern of alternating vortex cores is, however, asymmetric about the wake centreline.

Well defined, anti-clockwise rotating vortices are evident along the pressure surface side of the wake. Between these anti-clockwise vortices, weaker clockwise rotating vortices are defined on the opposite side of the wake. These clockwise rotating vortices appear stretched by the circulation of the anti-clockwise rotating vortices in the direction of the shear layers, which connect the adjacent vortices. The anti-clockwise rotating vortices travel along the centre of the wake, whereas, the weaker clockwise rotating vortices are displaced further onto the suction surface side of the wake. The base pressure time history confirms the greater circulation in the anti-clockwise rotating vortices on the pressure surface side of the wake. A boundary layer

analysis just upstream of the trailing edge indicates the main cause of the asymmetric wake as resulting from a difference in the 'diffusion length' of the separated shear layers. This analysis, however, indicates the presence of turbulent boundary layers on both sides of the trailing edge at separation. The boundary layer thickness on the suction surface is computed to be 3.82 times greater than the boundary layer thickness on the pressure surface at this location.

The asymmetric vortex shedding is responsible for a similar asymmetry in the time resolved redistribution of stagnation temperature and pressure across the wake. A greater redistribution of stagnation temperature is predicted at the anti-clockwise rotating vortices on the pressure surface side of the wake. The result is a greater stagnation temperature increase at the hot spots and a greater stagnation temperature deficit at the cold spots at these vortices. These results support the energy separation mechanism proposed by Kurosaka et al. (1987) and extend this theory to asymmetric, compressible turbine blade wakes. The transverse location of the pressure surface vortices at the centre of the wake, and the relative displacement of the suction surface vortices further onto the suction surface side, results in a bias of the cold spots towards this side of the wake. The time averaged result of this bias is a stagnation temperature deficit on the suction surface side of the wake and a time averaged increase above the free stream condition along the pressure surface side.

The hot and cold spots predicted in the time accurate stagnation temperature field at each vortex are analogously predicted in the stagnation pressure field. A similar transverse bias in the stagnation pressure field is observed, with a greater redistribution of stagnation pressure at the stronger anti-clockwise rotating vortices. These results further substantiate the analogy between the redistribution of stagnation temperature and pressure proposed by Kurosaka et al. (1987) and indicate a direct relationship between energy separation and vortex strength. The time averaged result is a stagnation pressure deficit close to the centre of the wake. This stream-wise band of reduced stagnation pressure is, however, displaced to the suction surface side of the wake as in the time averaged stagnation temperature field.

Similarities are highlighted between the time accurate stagnation temperature and

pressure redistribution in the turbulent prediction and the measurements of Hogg et al. (1997) and Carscallen et al. (1998, 1999). These measurements, taken at a higher exit Mach number of $M_e = 0.95$, indicate a similar transverse asymmetry in the magnitude of the hot spots, cold spots and analogous regions in the stagnation pressure distribution. These measurements indicate a similar uneven stream-wise spacing of the vortices on each side of the wake and indicate a similar displacement of the stagnation temperature and pressure extrema towards the suction surface side. The similarities documented in this section, between the turbulent prediction and these measurements, imply a similar asymmetric vortex shedding distribution remains over a significant Mach number range below unity. The current prediction provides supporting evidence for the vortex shedding mechanism proposed in the work of Hogg et al. (1997) and Carscallen et al. (1998, 1999), extending this research to lower transonic exit conditions.

Chapter 7

Conclusions & Further Research

7.1 Overview

This study documents the development and implementation of a time accurate numerical method to investigate the compressible flow past a circular cylinder and highly loaded turbine cascade at high Reynolds numbers. To the authors knowledge, no published time accurate computational fluid dynamic studies have attempted to analyse energy separation downstream of a circular cylinder at low transonic Mach numbers, within the intermittent shock wave regime. An original time accurate study of the vortex induced stagnation temperature and pressure redistribution, downstream of a circular cylinder, in compressible cross-flow is therefore presented. This is extended to a novel time accurate study of the compressible stagnation temperature and pressure redistribution in an asymmetric wake, downstream of a highly loaded turbine nozzle guide vane cascade. This is the first time accurate computational fluid dynamic study of energy separation, within the modelled turbine cascade, at low transonic Mach numbers below $M_e = 0.8$. Past research on the redistribution of stagnation temperature and pressure in a vortex street indicate that this phenomenon results from an effective exchange of work across large scale, coherent vortices. The hypothesis that energy separation is primarily a convective phenomenon is investigated through a structured sequence of numerical models to include both inviscid and turbulent predictions.

To increase the computational grid resolution close to the surface of the cylinder in the turbulent prediction, a time accurate Adaptive Mesh Refinement (AMR) al-

gorithm is implemented, based on the method of Quirk (1991). An analysis of the AMR algorithm, through a series of fundamental test cases, highlights an inherent source of numerical error. This numerical error arises from a flux limiting stage in the interpolation algorithm, which is used to prime fine levels with an initial state variable distribution from the underlying flow field. Including the flux limiting stage reduces the order of accuracy of the interpolated solution. The grid dependent wavenumber characteristics of the AMR method are examined. It is established that dispersion and dissipation in the AMR algorithm increases with the number of AMR levels used, with respect to a single level non-AMR prediction of equivalent resolution. The dispersion and dissipation error can also cover a broad wavenumber spectrum, complicating possible remedies through selective high-order filtering. This numerical error is further shown to possess both stationary and convective wavenumber characteristics. This suggests the numerical error is capable of spreading over a significant proportion of the flow domain. The numerical error highlighted in this work may therefore limit the choice of such an AMR method to predictions where the accurate modelling of small amplitude disturbance phase speeds is not required. A novel two-dimensional interpolation algorithm is also presented for use with the AMR method. This interpolation algorithm, which is based on the MUSCL (Monotone Upstream-centred Schemes for Conservation Laws) approach, preserves monotonicity and conservation for two-dimensional structured meshes of the current type. Even with the documented error, it is concluded that the implemented AMR algorithm retains sufficient accuracy to be applied to the turbulent circular cylinder prediction.

7.2 Circular Cylinder Flow

A time accurate and time mean analysis of the compressible flow past a circular cylinder at $M_\infty = 0.6$ and $Re_D = 6.87 \times 10^5$ is presented. An inviscid model is initially developed from uniformly imposed free stream conditions to a self-sustained vortex shedding solution. This model is then developed using the short-time averaged Navier Stokes equations and a $k - \omega$ turbulence model.

The inviscid prediction suggests that the circular cylinder at $M_\infty = 0.6$ is slow to develop phase-locked vortex shedding characteristics. A significant computational time is therefore necessary before an acceptable cycle-to-cycle variation in the time accurate flow is achieved.

The free stream Mach number chosen for this case places the circular cylinder in the intermittent shock wave regime. The inviscid prediction is able to capture and characterise the unsteady oscillation of these radial shock waves over the vortex shedding cycle. A circumferential oscillation of the radial shock waves is shown to occur in-phase with the vortex formation and shedding events at the near side of the wake. A good overall correlation of the drag and lift coefficient time mean and time accurate peak-to-peak values with Botta (1995) and Pandolfi & Larocca (1989) suggest the same essential flow physics are predicted in the current study.

A time accurate stagnation temperature and pressure wake analysis proves that an inviscid computation is able to predict the stagnation temperature and pressure redistribution, or 'energy separation' mechanism. The location of hot and cold spots on diametrically opposing sides of each vortex in this prediction suggest a direct association with the vortex motion, as proposed by Kurosaka et al. (1987). The redistribution of stagnation temperature is shown to occur over both the vortex formation and vortex shedding cycles. Additional compressible effects are identified in the near wake flow. These are responsible for a higher stagnation temperature maximum in the near side shear layer at each vortex formation and shedding event, with respect to the subsonic prediction of Kurosaka et al. (1987). The time averaged inviscid stagnation temperature field confirms the 'Eckert-Weise effect'. A time averaged rise in stagnation temperature, above the free stream condition, is predicted along the outer edges of the wake close to the cylinder and further downstream. This may suggest a similar compressible modification in the time averaged field, with respect to the subsonic results of Kurosaka et al. (1987). The time averaged stagnation temperature rise, however, remains significantly lower than the time accurate stagnation temperature rise at the hot spots.

The inviscid prediction substantiates the hypothesis of Kurosaka et al. (1987),

that a similar redistribution of stagnation pressure occurs across each vortex. The time accurate stagnation pressure field assumes an analogous pattern to the localised hot and cold spots observed in the time accurate stagnation temperature field. The time averaged result is a similar stagnation pressure deficit along the centreline of the wake, in analogy to the time averaged stagnation temperature field. These time averaged results demonstrate an increase in the stagnation pressure loss downstream of the circular cylinder through the energy separation mechanism.

Introducing the short-time averaged Navier Stokes equations, along with the two-equation $k - \omega$ model of Wilcox (2002), improves the correlation against published experimental work at comparable free stream conditions. The presence of a stagnation temperature and pressure redistribution in the inviscid and turbulent predictions highlight the dominance of convection over small-scale turbulent and viscous effects in the fundamental energy separation mechanism. The increase in heat transfer through turbulence diffusion reduces the stagnation temperature redistribution with respect to the inviscid wake.

A time accurate comparison of the wake distribution with measurements by Ackerman (2005) indicates an improved representation of the physical wake development in the turbulent prediction. These results suggest that, although an inviscid prediction is capable of capturing the essential mechanism underlying the vortex induced stagnation temperature and pressure redistribution, the magnitude of this redistribution is over-predicted. The introduction of a turbulence model remains essential to accurately approximate the development and diffusion of this flow phenomenon.

Differences are identified in the relative stream-wise location of the hot and cold spots, between the turbulent prediction and the measurements of Ackerman (2005). A number of possible sources for this discrepancy are suggested. These include the possibility of an additional small-scale or three-dimensional turbulent effect not predicted by the two-dimensional, short-time averaged numerical method. This discrepancy may highlight a limitation to modelling energy separation through a two-dimensional numerical method.

7.3 Turbine Cascade Flow

The circular cylinder analysis is extended to the asymmetric wake downstream of a highly loaded turbine nozzle guide vane cascade. A cross-section of the thick trailing edge turbine cascade in Carscallen (1998) is modelled at exit conditions of $M_e = 0.6$ and $Re_{D_t} = 7.48 \times 10^4$. An inviscid model of the turbine cascade is initially developed from uniformly imposed free stream conditions. The inviscid vortex shedding solution is then used to initialise the flow field for the subsequent turbulent prediction.

A symmetric vortex shedding pattern is identified in the inviscid turbine blade prediction, suggesting that the asymmetric wake documented in other work for this cascade results primarily from the separated shear layers rather than the difference in velocity at the trailing edge. A corresponding symmetry in the stagnation temperature and pressure extrema are also predicted across the wake centreline. Differences in the transient shock wave characteristics are documented with respect to the circular cylinder prediction. The upstream precession of pressure waves through the nozzle passage is shown to effect the flow development along the adjacent blade suction surface.

The turbulent cascade prediction shows a marked difference in the wake development and energy separation characteristics with respect to the inviscid prediction. Firstly, no radial shock waves are identified around the trailing edge, resulting in an absence of shock induced separation. Turbulent boundary layers are identified on the suction and pressure surfaces at separation. The suction surface boundary layer thickness is, however, 3.84 times greater on the suction surface at separation. This difference in boundary layer thickness implies a corresponding difference in separated shear layer thickness, suggesting a direct association with the asymmetric form and circulation of vortices shed from each side. This dependency of the asymmetric cascade wake on the difference in trailing edge shear layer thickness correlates well with the measurements of Sieverding et al. (2003) for a similar highly loaded turbine blade.

A greater stagnation temperature redistribution is predicted on the pressure sur-

face side of the wake, resulting in an increase in stagnation temperature at the associated hot spots and a greater cooling of the cold spots on this side of the wake. These results suggest a direct relationship between the energy separation mechanism and vortex strength. This relationship is further evident in the stagnation pressure field, yielding an increased redistribution along the pressure surface side of the wake. This relationship provides supporting evidence for the energy separation mechanism proposed by Kurosaka et al. (1987) and extends this mechanism to asymmetric vortex shedding. The current results also extend the measurements of Sieverding et al. (2003), demonstrating that the asymmetric vortex shedding pattern is responsible for a pitch-wise asymmetry in the stagnation temperature and pressure fields, downstream of the turbine blade.

The asymmetric stagnation pressure and temperature wake distribution correlates well with the time accurate measurements of Hogg et al. (1997) and Carscallen et al. (1998, 1999) for this cascade. The current prediction provides a detailed analysis of the near wake flow development upstream of the measuring plane in the cited work, for a similar asymmetric vortex shedding flow. The good qualitative agreement of the current prediction with Hogg et al. (1997) and Carscallen et al. (1998, 1999) suggest a similar asymmetric vortex shedding pattern characterises the wake downstream of the current turbine cascade over a significant Mach number range, below $M_e = 1$.

The turbine cascade results highlight the dependence of the stagnation temperature and pressure redistribution on the vortex strength, and hence on the boundary layer development and separation characteristics. Therefore, even though the inviscid model is capable of predicting the energy separation mechanism, a turbulent prediction is still necessary to accurately model the essential physics of this phenomenon.

7.4 Further Research Recommendations

One of the major numerical issues limiting the scope and accuracy of this computational study is the use of an explicit time integration method for a high Reynolds number circular cylinder flow. The restriction on time step imposed by the CFL

condition severely limits the practical grid resolution possible close to the cylinder surface. One method for relaxing this restriction is through the implementation of an implicit time integration method. Although associated increases in memory and processing overheads are reported for implicit methods, with respect to explicit methods, the beneficial effects of relaxing the CFL constraint remains an attractive alternative. Changing the current numerical source code from an explicit to an implicit method would require a significant hierarchical restructuring, rewriting and validation exercise. This was not considered feasible within the time constraints set out for this study and remains an area of crucial development for the existing numerical solution procedure. An implicit time integration method is, for example, used by Currie & Carscallen (1998) to model the flow past the current turbine cascade at $M_e = 1.16$. This implicit method has also been implemented by Brooksbank (2001) to model energy separation downstream of a simulated turbine blade. The implicit method documented in these publications may provide a sound basis for the development of an implicit time integration method into the existing numerical solution procedure.

The current AMR algorithm remains close to the original method of Quirk (1991), particularly in the cell flagging and grouping algorithms. The final implementation is capable of improvement in a number of ways. These include improving the cell 'flagging' parameter for boundary layer flows, developing more sophisticated methods for choosing the extent of refined regions and improving the interpolation method. The AMR 'flagging' parameter, used to indicate regions for dynamic refinement, is chosen as the density gradient between contiguous cells. This should provide a satisfactory flagging criterion for the refinement of shock waves and compressible shear flows. This flagging criterion could not, however, adequately resolve the initial boundary layer development close to the stagnation point on the circular cylinder. An improved flagging criterion may result from combining the density gradient with a second parameter, such as wall shear stress, to improve the resolution in developing boundary layers.

The AMR validation test cases highlight an inherent source of error in the AMR

method at the interface between levels, i.e. the fine-coarse interface. The magnitude of this error is dictated by a user-defined AMR scaling parameter b. This parameter is multiplied by the maximum density gradient between two contiguous cells to determine a criterion, above which, cells are flagged for refinement. This error increases for fine-coarse interfaces defined within regions of large flow gradient. While using a predefined AMR scaling parameter is computationally efficient for this task, the choice of the scaling parameter remains somewhat arbitrary. A more sophisticated AMR scaling parameter might be developed from an initial user-defined value, combined with a subsequent error analysis to increase the spatial extent of the refined patch in regions of significant error.

The AMR validation exercise also highlights an inherent error arising from the interpolation method used to initialise the fine AMR levels. The two-dimensional interpolation used in the current study maintains the monotonicity and conservation properties of the underlying state variable distribution. However, the necessary variable gradient limiting procedure restricts the accuracy of the flow field interpolation. The development of more sophisticated interpolation algorithms are crucial for better approximating the refined field, while maintaining the conservation and monotonicity properties of the underlying state variable distribution.

A further source of development for the numerical solution procedure is the implementation of a Large Eddy Simulation (LES) or Detached Eddy Simulation (DES) turbulence modelling procedure. A comparison of the turbulent circular cylinder prediction with measurements by Ackerman (2005) highlights differences in the stream-wise location of the time accurate hot and cold spots relative to the convecting vortices. Suggestions for this discrepancy include the possibility of a small-scale or three-dimensional effect not modelled in the current two-dimensional short-time averaged method. Extending this study to a three-dimensional study using, for example, an LES turbulence model may provide an improved estimation of the energy separation flow physics measured by Ackerman (2005).

The reported differences in stagnation temperature redistribution downstream of the circular cylinder in the current prediction, against the measurements of Acker-

man (2005), also suggest an extension to the experimental research program. An improved understanding of the interaction of turbulence with the energy separation mechanism would result from a development of the experimental program to include small-scale turbulence measurements. Fazle Hussain & Hayakawa (1987), for example, use an eduction method and a rake of cross-wire probes to study the developing turbulence downstream of a circular cylinder at a lower free stream Reynolds number. Carscallen et al. (1999) also provide promising indications that improvements to the stagnation temperature probe and associated electronics used in this work may provide an alternative method for studying the evolution of fine scale turbulent structures.

The current study also highlights a lack of validation data for the turbulent study at the modelled conditions. The experimental research program could be extended, in collaboration with the proposed extensions to the numerical model, to include further boundary layer measurements around the circular cylinder and turbine blade.

Finally, this study could be extended to place into context the predicted redistribution of stagnation temperature and pressure downstream of the cascade within a high pressure turbine stage. The turbine blade modelled in this study is the mean cross-section of a nozzle guide vane with non-uniform span-wise chord length and attack angle. The current study could be developed to better approximate the physical turbine blade through a time accurate three-dimensional extension of the complete blade. This remains a computationally intensive proposition, which may eventually be feasible through the current rapid increase in widely available high performance computing facilities. The turbine cascade model could also be extended to include a downstream row of rotor blades, to analyse the effects of the vortex induced energy separation on the downstream rotor row.

Appendices

A.1 Short-Time Averaging

Any instantaneous scalar flow variable, ζ, can be divided into a time mean component, $\tilde{\zeta}$, a fluctuating component ζ', due to large scales of motion in the flow and a stochastic component, ζ'', due to small-scale turbulence, so that

$$\zeta = \tilde{\zeta} + \zeta' + \zeta''. \tag{A.1}$$

A short-time averaged variable is defined over a time period short enough to resolve the time mean and the large scale fluctuating variables, yet not short enough to resolve the small scale stochastic turbulence component. The short-time averaged variable is therefore defined as

$$\bar{\zeta} = \tilde{\zeta} + \zeta'. \tag{A.2}$$

Each short-time averaged scalar variable, $\bar{\zeta}$, is iteratively computed on a suitable grid. The remaining small scale turbulence component, ζ'', is modelled using turbulence closure methods. The instantaneous variable is redefined as

$$\zeta = \tilde{\zeta} + \zeta' + \zeta'' = \bar{\zeta} + \zeta''. \tag{A.3}$$

Short-time averaging is a linear operator, therefore

$$\begin{aligned} \bar{\zeta}'' + \bar{\zeta}'' &= 2\bar{\zeta}'', \\ \overline{\bar{\zeta}''\zeta''} &= \bar{\zeta}'' \cdot \bar{\zeta}'', \\ \overline{\zeta''\zeta''} &\neq \bar{\zeta}'' \cdot \bar{\zeta}''. \end{aligned} \tag{A.4}$$

Short-time averaging Equation A.3 therefore yields

$$\bar{\zeta}'' = 0. \tag{A.5}$$

The instantaneous form of the Navier-Stokes equations is defined as

$$\begin{aligned}
\frac{\partial \rho}{\partial t} + \nabla \cdot (\rho \boldsymbol{u}) &= 0, && \text{(A.6)}\\
\frac{\partial}{\partial t}(\rho \boldsymbol{u}) + \nabla \cdot (\rho \boldsymbol{u} \otimes \boldsymbol{u} + p\boldsymbol{I} - \boldsymbol{\tau}) &= 0, && \text{(A.7)}\\
\frac{\partial}{\partial t}(\rho e_s) + \nabla \cdot (\rho \boldsymbol{u} h_s + \boldsymbol{q} - \boldsymbol{\tau} \cdot \boldsymbol{u}) &= 0, && \text{(A.8)}
\end{aligned}$$

where e_s, h_s, $\boldsymbol{\tau}$ and $\boldsymbol{q}$ are estimated by

$$\begin{aligned}
e_s &= \frac{p}{\rho(\gamma - 1)} + \frac{\boldsymbol{u} \cdot \boldsymbol{u}}{2}, && \text{(A.9)}\\
h_s &= e_s + \frac{p}{\rho}, && \text{(A.10)}\\
\boldsymbol{\tau} &= \mu_l \left(\nabla \boldsymbol{u} + \boldsymbol{u} \nabla - \frac{2}{3} \boldsymbol{I} \nabla \cdot \boldsymbol{u} \right), && \text{(A.11)}\\
\boldsymbol{q} &= -\frac{\mu_l c_p}{P_r} \nabla T. && \text{(A.12)}
\end{aligned}$$

The instantaneous variables of the Navier-Stokes equations, Eqns. A.6-A.8, are split into a short-time averaged component and a small-scale turbulence component according to Eqn. A.3. For the mass conservation equation, this leads to

$$\frac{\partial (\bar{\rho} + \bar{\rho}'')}{\partial t} + \nabla \cdot \left(\bar{\rho}\bar{\boldsymbol{u}} + \bar{\rho}\bar{\boldsymbol{u}}'' + \bar{\rho}''\bar{\boldsymbol{u}} + \overline{\rho''\boldsymbol{u}''} \right) = 0, \tag{A.13}$$

In the short-time averaging procedure, the contribution of the turbulent density fluctuations, ρ'', and the short-time averaged contribution of the turbulent mass fluctuations, $\overline{\rho''\boldsymbol{u}''}$, are omitted on the basis that these are negligibly small in comparison with their short time averaged contributions. Neglecting these terms and applying Eqn. A.5, the form of the short-time average mass conservation equation in Eqn. 3.29 is defined:

$$\frac{\partial \bar{\rho}}{\partial t} + \nabla \cdot (\bar{\rho}\bar{\boldsymbol{u}}) = 0. \tag{A.14}$$

After applying short-time averaging to the momentum conservation equation, Eqn. A.7, and omitting terms involving ρ'' and $\overline{\rho''\boldsymbol{u}''}$, the following form of the momentum equation is defined

$$\frac{\partial}{\partial t}\left(\bar{\rho}\bar{\boldsymbol{u}}\right) + \nabla\cdot\left(\bar{\rho}\bar{\boldsymbol{u}}\otimes\bar{\boldsymbol{u}} + \bar{\rho}\overline{\boldsymbol{u}''\otimes\boldsymbol{u}''} + \bar{p}\boldsymbol{I} - \boldsymbol{\tau}\right) \;=\; 0, \tag{A.15}$$

The additional Reynolds stress tensor in Equation A.15 results from short-time averaging of the instantaneous momentum tensor. After moving the viscous stress tensor and the Reynolds stress tensor to the right-hand side of Eqn. A.15 to leave only inviscid terms on the left-hand side expression, the form of Eqn. 3.30 is recovered:

$$\frac{\partial}{\partial t}\left(\bar{\rho}\bar{\boldsymbol{u}}\right) + \nabla\cdot\left(\bar{\rho}\bar{\boldsymbol{u}}\otimes\bar{\boldsymbol{u}} + \bar{p}\boldsymbol{I}\right) \;=\; \nabla\cdot\left(\boldsymbol{\tau} - \bar{\rho}\overline{\boldsymbol{u}''\otimes\boldsymbol{u}''}\right), \tag{A.16}$$

To allow short-time averaging of the energy conservation equation, the stagnation energy e_s and stagnation enthalpy h_s terms in Eqn. A.8 are replaced by their respective definitions in Eqns. A.9 and A.10. The heat flux $\boldsymbol{q}$ is replaced by its definition, Eqn. A.12. The resulting energy conservation equation takes the form

$$\frac{\partial}{\partial t}\left(\rho e + \rho\boldsymbol{u}\cdot\boldsymbol{u}/2\right) + \nabla\cdot\left(\rho\boldsymbol{u}h + \rho\boldsymbol{u}\otimes\boldsymbol{u}\cdot\boldsymbol{u}/2 - \frac{\mu_l c_p}{P_r}\nabla T - \boldsymbol{\tau}\cdot\boldsymbol{u}\right) \;=\; 0, \tag{A.17}$$

where, e is the specific internal energy of the flow, defined as $e = p/\left[\rho\left(\gamma-1\right)\right]$. The specific enthalpy h is defined as $h = e + p/\rho$. The short-time averaged energy conservation equation is obtained by replacing each instantaneous flow variable in Eqn. A.17 by the summation of a short-time averaged component and a small-scale turbulence component. Each component is then short-time averaged. After omitting contributions from the turbulent density fluctuations ρ'', turbulent temperature fluctuations T'' and terms involving the turbulent mass fluctuations $\overline{\rho''\boldsymbol{u}''}$, the short-

time averaged energy conservation equation becomes

$$\frac{\partial}{\partial t}\left(\bar{\rho}\bar{e}+\bar{\rho}\bar{\boldsymbol{u}}\cdot\bar{\boldsymbol{u}}/2+\bar{\rho}\overline{\boldsymbol{u}''\cdot\boldsymbol{u}''}/2\right)+\nabla\cdot\left(\bar{\rho}\bar{\boldsymbol{u}}\bar{h}+\bar{\rho}\overline{\boldsymbol{u}''h''}+\bar{\rho}\bar{\boldsymbol{u}}\otimes\bar{\boldsymbol{u}}\cdot\bar{\boldsymbol{u}}/2+\right.$$
$$\bar{\rho}\bar{\boldsymbol{u}}\otimes\overline{\boldsymbol{u}''\cdot\boldsymbol{u}''}/2+\bar{\rho}\overline{\boldsymbol{u}''\otimes\boldsymbol{u}''}\cdot\bar{\boldsymbol{u}}+\bar{\rho}\overline{\boldsymbol{u}''\otimes\boldsymbol{u}''\cdot\boldsymbol{u}''}/2-$$
$$\left.\frac{\mu_l c_p}{P_r}\nabla\bar{T}-\bar{\boldsymbol{\tau}}\cdot\bar{\boldsymbol{u}}-\overline{\boldsymbol{\tau}''\cdot\boldsymbol{u}''}\right)=0. \quad \text{(A.18)}$$

By re-introducing the stagnation energy, $e_s = e + \bar{\boldsymbol{u}}\cdot\bar{\boldsymbol{u}}/2$, the stagnation enthalpy, $h_s = h + \bar{\boldsymbol{u}}\cdot\bar{\boldsymbol{u}}/2$, and the heat flux vector, $\boldsymbol{q}$, in Eqn. A.18 and introducing the specific turbulence kinetic energy, $k = \overline{\boldsymbol{u}''\cdot\boldsymbol{u}''}/2$, the following form of the short-time averaged energy conservation equation is obtained:

$$\frac{\partial}{\partial t}\bar{\rho}\left(\bar{e}_s+\bar{k}\right)+\nabla\cdot\bar{\rho}\bar{\boldsymbol{u}}\left(\bar{h}_s+\bar{k}\right)+\nabla\cdot\left(\bar{\rho}\overline{\boldsymbol{u}''h''}+\bar{\rho}\overline{\boldsymbol{u}''\otimes\boldsymbol{u}''}\cdot\bar{\boldsymbol{u}}+\right.$$
$$\left.\bar{\rho}\overline{\boldsymbol{u}''\otimes\boldsymbol{u}''\cdot\boldsymbol{u}''}/2+\bar{\boldsymbol{q}}-\bar{\boldsymbol{\tau}}\cdot\bar{\boldsymbol{u}}-\overline{\boldsymbol{\tau}''\cdot\boldsymbol{u}''}\right)=0. \quad \text{(A.19)}$$

The short-time averaged energy conservation equation of Eqn. 3.31 is recovered by grouping inviscid terms on the left-hand side of Eqn. A.19 and grouping viscous and turbulence terms on the right-hand side, leading to

$$\begin{aligned}\frac{\partial}{\partial t}\bar{\rho}\left(\bar{e}_s+\bar{k}\right)+\nabla\cdot\bar{\rho}\bar{\boldsymbol{u}}\left(\bar{h}_s+\bar{k}\right) &= \nabla\cdot\left(-\bar{\boldsymbol{q}}-\bar{\rho}\overline{\boldsymbol{u}''h''}+\bar{\boldsymbol{\tau}}\cdot\bar{\boldsymbol{u}}+\right.\\ &\quad \overline{\boldsymbol{\tau}''\cdot\boldsymbol{u}''}-\bar{\rho}\overline{\boldsymbol{u}''\otimes\boldsymbol{u}''}\cdot\bar{\boldsymbol{u}}-\\ &\quad \left.\bar{\rho}\overline{\boldsymbol{u}''\otimes\boldsymbol{u}''\cdot\boldsymbol{u}''/2}\right). \quad \text{(A.20)}\end{aligned}$$

A.2 Circular Cylinder Laminar Sublayer Height Estimation

An estimate for the approximate height of the laminar sublayer region of a turbulent boundary layer is computed from the incompressible turbulent boundary layer measurements of Patel (1969). A circular cylinder of span-wise length $L = 1.2192m$ and diameter $D = 0.1524m$ is placed in a uniform cross-flow at $Re_D = 5.01 \times 10^5$. Trip wires of diameter $D_w = 1.016 \times 10^{-3}m$ are placed at $\Delta\theta = \pm 45^\circ$ from the upstream stagnation point to fix the location of boundary layer transition. Patel (1969) documents boundary layer integral parameters, surface normal velocity profiles and the surface pressure distribution at a number of circumferential locations along the

upstream facing (windward) side of the cylinder. An estimation for the laminar sublayer height is obtained from these results, along with the momentum integral equation, defined as

$$\frac{C_f}{2} = \frac{d\delta_2}{dx} + (2+H)\frac{\delta_2}{u_e}\frac{du_e}{dx}. \tag{A.21}$$

In this analysis x is taken circumferentially along the circular cylinder surface. The local boundary layer edge velocity u_e is computed using the incompressible surface pressure coefficient C_p, defined as $C_p = 2(p-p_\infty)/\rho_\infty u_\infty^2$, and the free stream velocity u_∞ as

$$u_e = \sqrt{u_\infty^2\,(1-C_p)}. \tag{A.22}$$

This equation uses the Bernoulli equation for an incompressible flow and assumes a constant stagnation pressure between the free stream flow and the boundary layer edge. The boundary layer edge velocity gradient du_e/dx is then estimated from the computed u_e at each stream-wise station.

The momentum thickness δ_2 is documented by Patel (1969) at each stream-wise station. The gradient $d\delta_2/dx$ is estimated from the documented values of δ_2 at each stream-wise station. The shape factor $H_{12} = \delta_1/\delta_2$ is computed from the documented values of δ_1 and δ_2. An estimate for the incompressible skin friction coefficient is then obtained from Eqn. A.21.

The second half of this analysis is concerned with applying the skin friction to the current circular cylinder model flow to obtain an estimation for the laminar sublayer height at $y^+ = 10$. In the remainder of this analysis, the turbulent boundary layer edge properties, for example $\rho_e,\ u_e$ and T_e, are obtained from the surface distribution around the current inviscid circular cylinder prediction.

A coarse approximation to the compressible skin friction coefficient is then obtained from the generic form of the van Driest II relation, according to Spalding & Chi (1964). This relation is documented in a number of standard texts including White (1991). An adiabatic wall condition is assumed in this estimation. The use

of the van Driest II relation represents one of the major assumptions in this analysis as this relation is strictly used for zero pressure gradient flows. The difference in estimated laminar sublayer height with, and without, this stage is approximately 5%.

Using the compressible skin friction coefficient estimate C_f, the wall shear stress τ_w is estimated as

$$\tau_w = \frac{C_f \rho_e u_e^2}{2}. \tag{A.23}$$

The friction velocity $u_\tau = \sqrt{\tau_w/\rho_w}$ is then computed from the wall shear stress τ_w and an estimation for the wall density ρ_w using the Crocco-Busemann relation for adiabatic walls:

$$\rho_w = \rho_e \left(1 + r\frac{(\gamma-1)}{2} M_e^2\right)^{-1}, \tag{A.24}$$

where $r \approx 0.88$ is the recovery factor and M_e is the boundary layer edge Mach number. This relation assumes a constant static pressure variation through the turbulent boundary layer. Once the friction velocity u_τ is estimated, the laminar sublayer height h_{ls} is estimated as

$$h_{ls} = \frac{y^+ \mu_w}{\rho_w u_\tau}, \tag{A.25}$$

where the laminar sublayer height is assumed to be at $y^+ = 10$. The wall viscosity μ_w is computed from Sutherlands relation with the adiabatic wall temperature $T_w = \rho_e T_e/\rho_w$. This relation again assumes a constant static pressure variation through the turbulent boundary layer.

It is recognised that the accuracy of this boundary layer analysis is limited by the assumptions made therein. However, this analysis is simply used in the context of this study to quantify the order of increase in grid resolution necessary to adequately resolve the laminar sublayer of a turbulent boundary layer at the modelled free stream conditions.

A.3 Energy Separation In The Relative Reference Frame

A fixed frame of reference is used in this thesis to study energy separation downstream of a circular cylinder and turbine cascade. In Chapter 5, a uniform free stream flow approaches a stationary circular cylinder. Vortices are shed alternately from each side of the circular cylinder and move downstream. A mean vortex velocity can be defined, which is lower in magnitude than the imposed free stream velocity. The fixed reference frame is used in Chapter 5 to describe the downstream movement of individual fluid particles around each vortex moving downstream. An alternative reference frame can be defined, in which the vortices appear steady over time. This is achieved by introducing a frame of reference which moves downstream at the mean vortex transport velocity. In this reference frame, the cylinder moves upstream with a velocity of $(u_{cyl})_r = (-u_{1v})_f$, where u_{1v} is the mean vortex velocity in the fixed frame of reference. Subscript f denotes the fixed reference frame and subscript r denotes the relative reference frame. The free stream velocity is therefore defined as $(u_{1\infty})_r = (u_{1\infty} - u_{1v})_f$.

Kurosaka et al. (1987) use a fixed Lagrangian frame of reference to provide an explanation for the redistribution of stagnation temperature and pressure around a downstream moving vortex street. This explanation is described in detail in Section 2.6 and considers the changing forces exerted on a fluid particle travelling a cycloidal pathline around a downstream moving vortex. Briefly, as the fluid particle moves from the top of the vortex to the bottom, downstream of the vortex core, the centripetal force acting on the particle in the direction of the vortex centre acts to retard the fluid particle. The result is a decrease in the stagnation temperature over the course of this movement. Conversely, as the fluid particle travels from the bottom of the vortex to the top, upstream of the vortex core, the centripetal force acts to accelerate the fluid particle along the cycloidal pathline. The result is an increase in the stagnation temperature over the course of this movement. An effective 'exchange of work' therefore occurs, from fluid particles travelling a cycloidal pathline downstream of the vortex core, to fluid particles travelling a cycloidal pathline upstream of the vortex core. This exchange of work is facilitated by the presence

of the downstream moving vortex. The overall result is a local increase in the stagnation temperature and pressure, above the free stream condition, along the outer edges of the wake. A stagnation temperature and pressure deficit, relative to the free stream condition, is generated along the wake centre.

To emphasise the role of the downstream moving vortex on the energy separation mechanism, the stagnation temperature and pressure distribution in Figures 5.34 and 5.38 are re-plotted in this appendix using a reference frame that moves downstream at the mean vortex velocity. These are compared with the dimensionless T_s and p_s fields in the fixed reference frame from Figures 5.34 and 5.38 respectively. To obtain T_s and p_s in the relative frame, the mean stream-wise vortex velocity is subtracted from the stream-wise component of velocity throughout the computational domain. The mean vortex velocity is estimated from a series of density iso-contour snapshots. The displacement of the vortex centre in the stream-wise direction in successive snapshots provides a vortex velocity u_{1v} estimate of $u_{1v} = 0.7u_{1\infty}$ at $x_1 = 6.5D$.

Figure A.1(a,b) highlights the difference in flow distribution around each vortex in the fixed (a) and relative (b) reference frames. In the relative fixed reference frame of Figure A.1(a), each vortex is shown as a deviation in the velocity vector distribution. A slowing of the fluid is observed at each vortex, towards the centre of the wake. This results from an opposition of velocity components, between the downstream directed vortex velocity and an upstream directed tangential velocity component. Figure A.1(b) highlights the tangential velocity component at each vortex. The velocity vectors in Figure A.1(b) highlight the centre of each vortex, alongside the location of the irrotational saddle points between vortices.

Figure A.2(a,b) compares the dimensionless stagnation temperature distribution in the fixed reference frame (a) with the dimensionless stagnation temperature distribution in the relative frame (b). A localised redistribution of stagnation temperature is observed in Figure A.2(a). Localised hot spots with stagnation temperature greater than the free stream condition are shown in the outer shear layer of each vortex. These are defined at (i) in Figure A.2(a). Localised cooler regions, with

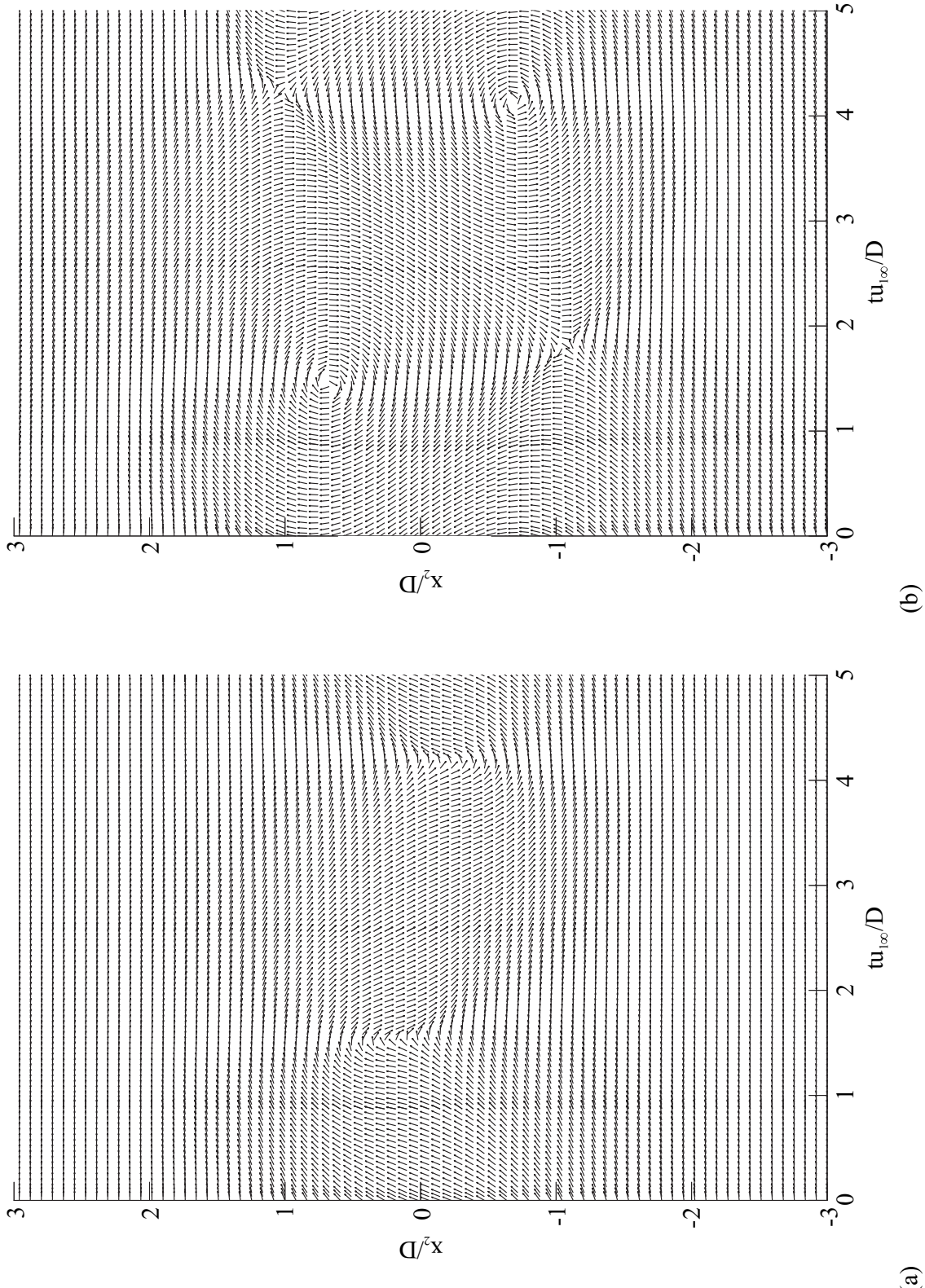

Figure A.1: Velocity vector distribution in a fixed and a relative frame of reference. All velocity vectors are of a constant length. (a) Velocity vectors in a fixed reference frame. (b) Velocity vectors in a reference frame that moves downstream at the mean vortex convection speed.

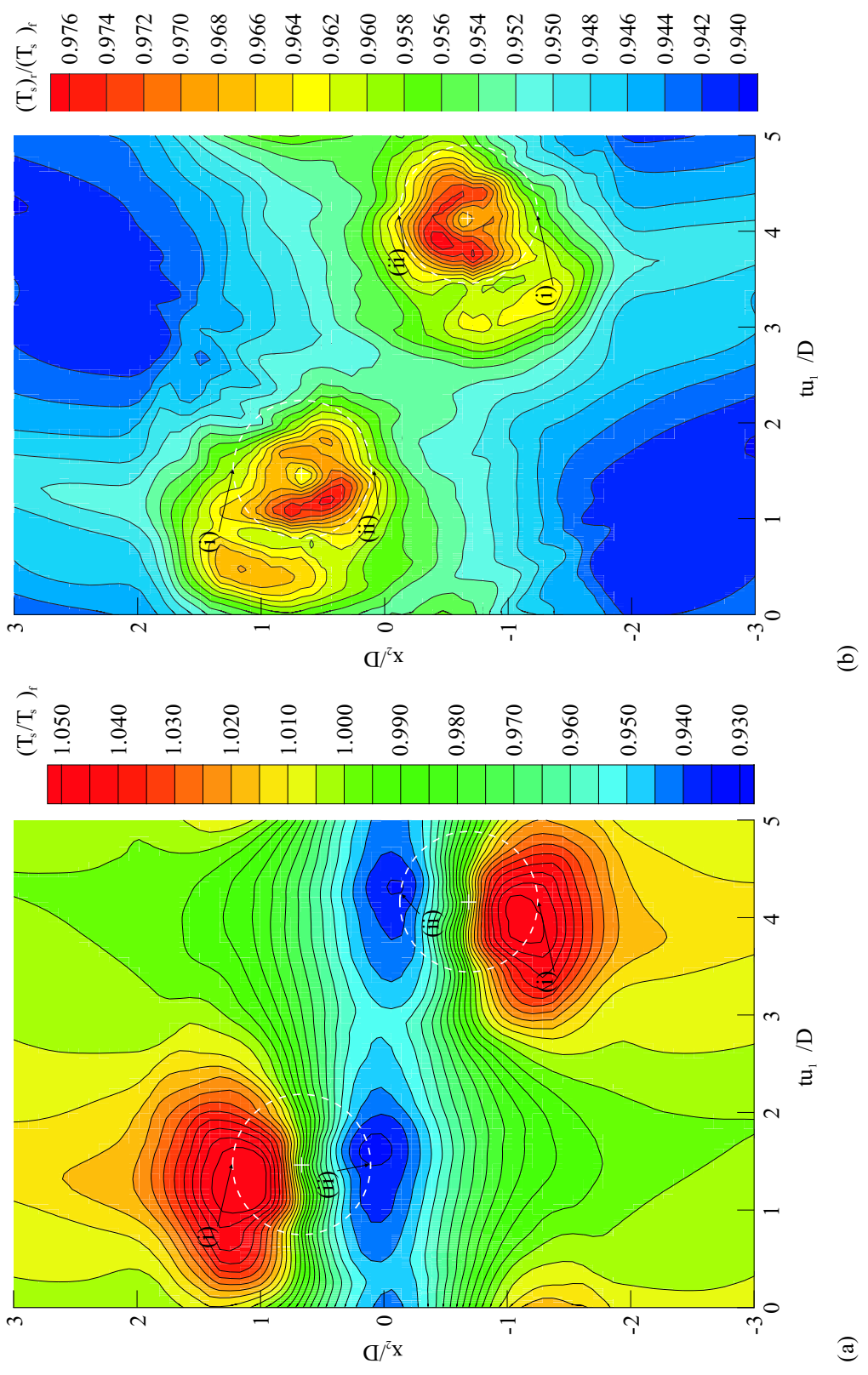

Figure A.2: Stagnation temperature distribution at $\Delta x_1 = 6.5D$ downstream of the cylinder. (a) Stagnation temperature in a fixed frame of reference, reproduced from Figure 5.34. (b) Stagnation temperature distribution in a relative frame of reference, moving at the mean vortex convection speed. The local stagnation temperature is normalised using the free stream stagnation temperature $T_{s\infty}$ in the fixed reference frame. Time is normalised using the free stream velocity $(u_{1\infty})_f$ and the cylinder diameter D.

lower than free stream stagnation temperature, occur on the opposite side of each vortex at the wake centre. These regions are marked (ii) in Figure A.2(a). In contrast, Figure A.2(b) shows a local stagnation temperature maximum close to the centre of each vortex and along its downstream outer shear layer. These differences in the T_s field are explained through the contribution of the local velocity to the stagnation temperature, which can be expressed as

$$T_s = T + \frac{(u_1^2 + u_2^2)}{2c_p} + \frac{k}{c_p}. \tag{A.26}$$

The velocity of a fluid particle travelling around the vortex in the fixed frame of reference, Figure A.2(a), is directed along a cycloidal pathline. In the relative frame of reference, Figure A.2(b), the velocity of a particle travelling around a vortex is directed tangential to the vortex. This is evident in Figure A.1(a,b). This results in a constant tangential velocity distribution, for an isolated vortex.

The difference in stagnation temperature, between the fixed frame of the reference and the relative reference frame, is most noticeable at the outer shear layer of each vortex, as well as along the wake centre. These regions are labelled (i) and (ii) respectively in Figure A.2(a,b). The instantaneous stream-wise velocity at (i) in Figure A.2(a) is a combination of the vortex velocity u_{1v} and the stream-wise component of the vortex tangential velocity. In Figure A.2(b), the instantaneous stream-wise velocity at (i) is simply the stream-wise component of the vortex tangential velocity. From Eqn. A.26, therefore, $(T_s)_f > (T_s)_r$ at (i).

On the diametrically opposite side of each vortex, labelled (ii), the difference in the instantaneous stream-wise velocity between the relative and fixed reference frames is reversed, leading to $(T_s)_f < (T_s)_r$. In fact, in Figure A.2(a) the stream-wise velocity comprises of the downstream vortex velocity in addition to the upstream oriented stream-wise component of the vortex tangential velocity. The velocity magnitude at (ii) in Figure A.2(a) is therefore significantly lower than the velocity at (i).

In Figure A.2(b), the stream-wise component of velocity at (ii) comprises of the upstream directed component of the vortex tangential velocity. The magnitude of the stream-wise velocity at (ii) in Figure A.2(b) would be equal to that at (i), for

an isolated vortex. As the square of the stream-wise velocity adds to the stagnation temperature in Eqn. A.26, the stagnation temperature does not vary significantly between (i) and (ii) in Figure A.2(b).

The stagnation temperature field in the relative frame of reference augments the static temperature distribution across the vortex. A localised region of high static temperature occurs at the centre of each vortex through a local dissipation of turbulence kinetic energy to heat. The transport of heat away from this region of raised static temperature is reduced by the absence of convection radially away from the vortex centre to the surrounding fluid. The centre of the vortex remains, therefore, a region of high static and stagnation temperature in the relative frame of reference. A further region of high stagnation temperature is evident downstream of each vortex in Figure A.2(b) and is caused by additional dissipation of the turbulence kinetic energy to heat in the shear layers that extend between successive vortices. This region would be expected to be absent in the case of a single convecting vortex. It is generated by the counter-rotation of vortex pairs in the von Kármán vortex street.

A similar difference between the fixed reference frame and the relative reference frame is evident in the stagnation pressure distribution. Figure 5.38 is reproduced in Figure A.3(a) for convenience. This is compared with the stagnation pressure distribution in the same relative frame of reference as for $(T_s)_r$ in Figure A.3(b). In Figure A.3(a), localised regions of stagnation pressure above the free stream condition ($p_s > p_{s\infty}$), are shown at the outer shear layer of each vortex. Cooler regions of fluid, lower than the free stream stagnation pressure ($p_s < p_{s\infty}$), are shown close to the wake centre. This pattern is similar to that of the stagnation temperature field. An additional contribution from each low pressure vortex centre is shown in Figure A.3(a).

Figure A.3(b), in contrast, is similar in form to the static pressure distribution with a stagnation pressure minimum sited at the centre of each vortex. The stagnation pressure in the relative frame of reference increases radially from the centre of the vortex, as shown by the almost concentrically circular contour levels in Figure A.3(b). The similarity of the relative reference frame stagnation pressure

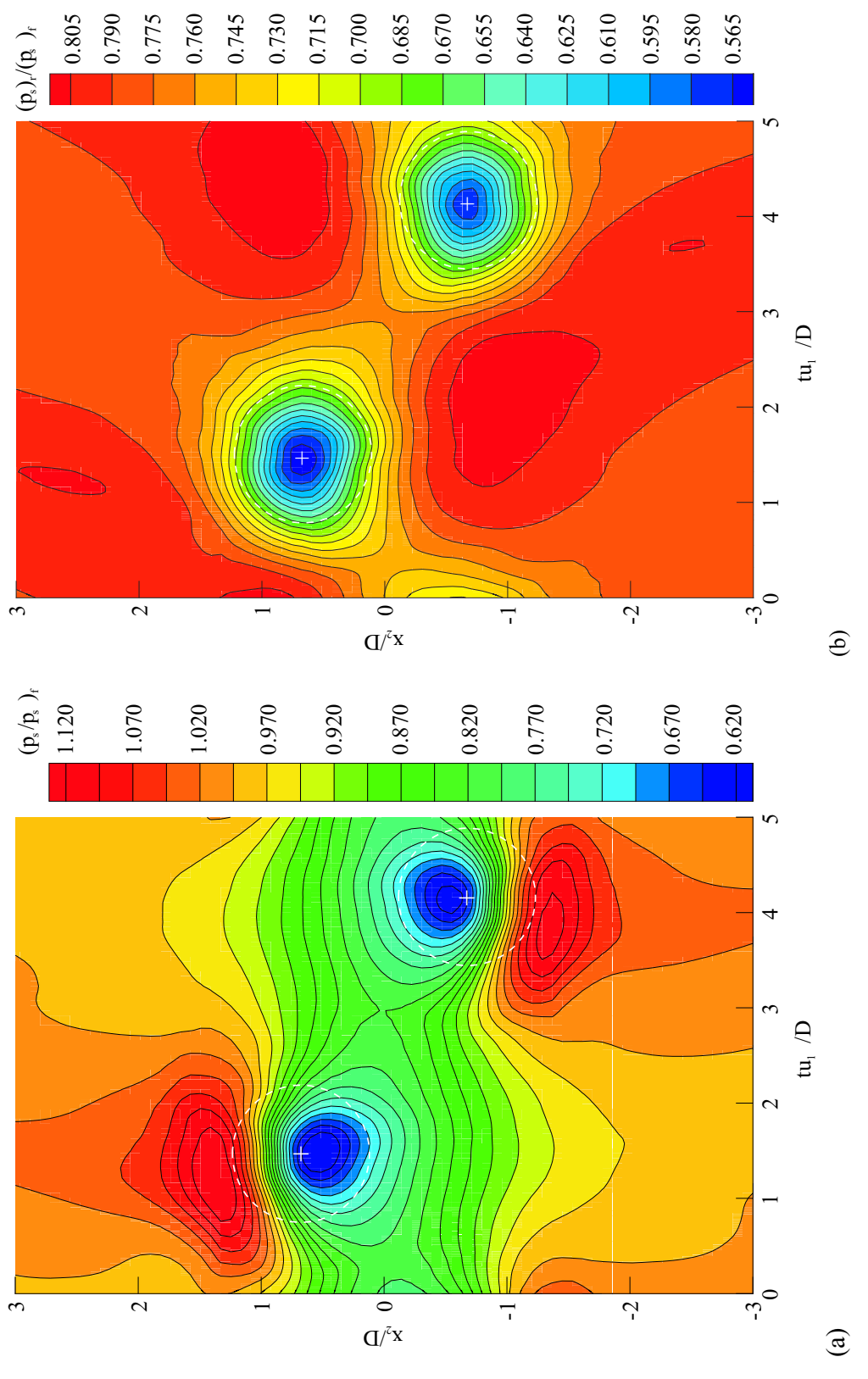

Figure A.3: Stagnation pressure distribution at $\Delta x_1 = 6.5D$ downstream of the cylinder. (a) Stagnation pressure in a fixed frame of reference, reproduced from Figure 5.38. (b) Stagnation pressure distribution in a relative frame of reference, moving at the mean vortex convection speed. The local stagnation pressure is normalised using the free stream stagnation pressure $p_{s\infty}$ in the fixed reference frame. Time is normalised using the free stream velocity $(u_{1\infty})_f$ and the cylinder diameter D.

distribution with a static pressure distribution is caused by the uniform tangential velocity distribution defined around each vortex. The low static pressure at the centre of each vortex can therefore be cited as being responsible for the low stagnation pressure in Figure A.3(b) at this location.

In summary, the analysis put forward in this appendix further serves to highlight the role of the relative downstream movement of the fluid particles and the vortices in the energy separation mechanism. This analysis also highlights the importance of a proper choice of reference frame to capture the time accurate redistribution of stagnation temperature and pressure across a vortex street.

Bibliography

Abu-Ghannam, B. J., and Shaw, R. (1980), "Natural transition of boundary layers - the effect of turbulence, pressure gradient and flow history," *J. Mech. Eng. Science*, Vol. 22, No. 5, pp. 213–228.

Achenbach, E. (1968), "Distribution of local pressure and skin friction around a circular cylinder in cross-flow up to $Re = 5 \times 10^6$," *J. Fluid Mech.*, Vol. 34, Part 4, pp. 625–639.

Ackeret, J. (1954), "Über die temperaturverteilung hinter angeströmten Zylindern", Tech. Rep. 21, ETH Inst. für Aerodynamik Mitteilungen, Zurich.

Ackerman, J. R. (2005), "Unsteady energy separation and base pressure distributions in subsonic crossflow around a circular cylinder," PhD thesis, University of Leicester.

Anderson, J. D. (1985), "Fundamentals of aerodynamics", McGraw-Hill, New York, USA.

Arnone, A., and Pacciani, R. (1989), "Numerical prediction of trailing edge wake shedding," *Paper 97-GT-89*, ASME.

Atkin, C. J., and Squire, L. C. (1992), "A study of the interaction of a normal shock wave with a turbulent boundary layer at Mach numbers between 1.3 and 1.55," *Eur. J. Mech. B/Fluids*, Vol. 11, No. 1.

Bardina, J. E., Huang, P. G., and Coakley, T. J. (1997), "Turbulence modelling validation, testing and development," *NASA Technical Memorandum 110446*.

Bearman, P. W. (1969), "On vortex shedding from a circular cylinder in the critical Reynolds number region," *J. Fluid Mech.*, Vol. 37, No. 3, pp. 577–585.

Benelmuffok, A., and Beretta-Piccoli, F. (1986), "Etude de l'ecoulements subsonique et transonique au bord de fuite epais d'un profile isole," *Rapport N., EPFL-LTT-86-31*.

Behr, M., Liou, J., Shih, R., and Tezduyar, T. E. (1991), "Vorticity-streamfunction formulation of unsteady incompressible flow past a cylinder: Sensitivity of the computed flow field to the location of the outflow boundary," *Int. J. Num. Methods in Fluids*, Vol. 12, pp. 323–342.

Boldman, D. R., Brinich, P. F., and Goldstein, M. E. (1976), "Vortex shedding from a blunt trailing edge with equal and unequal external mean velocities," *J. Fluid Mech.*, Vol. 75, Part 4, pp. 721–735.

Botta, N. (1995), "The inviscid transonic flow about a cylinder," *J. Fluid. Mech.*, Vol. 301, pp. 225–250.

Breuer, M. (1998), "Large eddy simulation of the subcritical flow past a circular cylinder: Numerical and modeling aspects," *Int. J. Num. Methods in Fluids*, Vol. 28, pp. 1281–1302.

Breuer, M. (2000), "A challenging test case for large eddy simulation: High Reynolds number circular cylinder flow," *Int. J. Heat. Fluid Flow*, Vol. 21, pp. 648–654.

Brooksbank, E. J. (2001), "A numerical investigation of time resolved flows around turbine blades," PhD thesis, University of Leicester.

Bryanston-Cross, P. J., and Camus, J. J. (1982), "Auto and cross correlation measurements in a turbine cascade using a digital correlator," *Paper 82-GT-132*, ASME.

Bryanston-Cross, P. J., Lang, T., Oldfield, M. L. G. (1981) and Norton, R. J. G., "Interferometric measurements in a turbine cascade using image-plane holography," *Trans. ASME, J. Eng. for Power*, Vol. 103, No. 1, pp. 124–130.

Cantwell, B., and Coles, D. (1983), "An experimental study of entrainment and transport in the turbulent near wake of a circular cylinder," *J. Fluid Mech.*, Vol. 136, pp. 321–374.

Carscallen, W. E., and Oosthuizen, P. H. (1989), "The effect of secondary flow on the redistribution of the total temperature field downstream of a stationary turbine cascade," AGARD CP-469.

Carscallen, W. E., and Gostelow, J. P. (1994), "Observations of vortex shedding in the wake from transonic turbine nozzle vanes," *Fifth International Symposium on*

Transport Phenomena and Dynamics of Rotating Machinery, Hawaii, USA, May 8th-11th.

Carscallen, W. E., Fleige, H. U., and Gostelow, J. P. (1996), "Transonic turbine vane wake flows," *Paper 96-GT-419*, ASME.

Carscallen, W. E., Currie, T. C., Hogg, S. I., and Gostelow, J. P. (1998), "Measurement and computation of energy separation in the vortical wake flow of a turbine nozzle cascade," *Paper 98-GT-477*, ASME.

Carscallen, W. E., Currie, T. C., Hogg, S. I., and Gostelow, J. P. (1999), "Measurement and computation of energy separation in the vortical wake flow of a turbine nozzle cascade," *Trans. ASME, J. Turbomachinery*, Vol. 121, pp. 703–708.

Chen, Y. N. (1972), "Properties of the Karman vortex street", Sulzer research, pp. 68–80.

Chima, R. V. (1996), "A $k-\omega$ turbulence model for quasi-three-dimensional turbomachinery flows," *Paper 96-0248*, AIAA.

Cicatelli, G., and Sieverding, C. H. (1995), "A review of the research on unsteady turbine blade wake characteristics," AGARD CP-571.

Cicatelli, G., and Sieverding, C. H. (1996), "The effect of vortex shedding on the unsteady pressure distribution around the trailing edge of a turbine blade," *Paper 96-GT-359*, ASME.

Cicatelli, G., and Sieverding, C. H. (1997), "The effect of vortex shedding on the unsteady pressure distribution around the trailing edge of a turbine blade," *Trans. ASME, J. Turbomachinery*, Vol. 119, pp. 810–819.

Colonius, T. (1997), "Numerically nonreflecting boundary and interface conditions for compressible flow and aeroacoustic computations," *AIAA J.*, Vol. 35, No. 7, pp. 1126–1133.

Currie, T. C., and Carscallen, W. E. (1998), "Simulation of trailing edge vortex shedding in a transonic turbine cascade," *Trans. ASME, J. Turbomachinery*, Vol. 120, No. 1, pp. 10–19.

Dawes, W. N. (1990), "A comparison of zero and one equation turbulence models for turbomachinery calculations," *Paper 90-GT-303*, ASME.

Deich, M. E., Fillipov, G. A., Saltanov, G. A., Laukhin, Y. A. (1976), "Investigation of the formation of moisture in nozzle blade cascades in turbines," *Teploenergetika*, Vol. 23, No. 3, pp. 33-36.

Délery, J. M., and Bur, R. S. (2000), "The physics of shock wave/boundary layer interaction control: last lessons learned," *Eur. Conf. on Comp. Methods in Applied Sciences and Eng., ECCOMAS 2000*, Barcelona, Spain, September 11-14.

Denton, J. D. (1993), "Loss mechanisms in turbomachines," *Trans. ASME, J. Turbomachinery*, Vol. 115, pp. 621–656.

Denton, J. D., and Xu, L. (1989), "The trailing edge loss of transonic turbine blades," *Paper 89-GT-278*, ASME.

Desse, J. M., and Pegneaux, J. C. (1991), "Whole-field measurement of gas density from two simultaneously recorded interferograms," *Exp. in Fluids*, Vol. 12, pp. 1–9.

Douglas, J. F., Gasiorek, J. M., and Swaffield, J. A. (1995), "Fluid mechanics", Longman Scientific & Technical, Essex, UK.

D'Ovidio, A., Harkins, J. A., and Gostelow, J. P. (2001a), "Turbulent spot in strong adverse pressure gradients, Part I - Spot behaviour," *Paper 2001-GT-0194*, ASME.

D'Ovidio, A., Harkins, J. A., and Gostelow, J. P. (2001b), "Turbulent spot in strong adverse pressure gradients, Part II - Spot propagation and spreading rates," *Paper 2001-GT-0406*, ASME.

Dunham, J. (1995), "Aerodynamic losses in turbomachines," AGARD CP-571.

Dyment, A., and Gryson, P. (1979), "Etude d'ecoulements turbulents subsoniques et supercritiques par visualisation ultra rapide," AGARD CP-227, Paper No. 28.

Eckert, E., and Weise, W. (1943), "Messung der temperaturverteilung auf der oberfläche schnell angeströmter unbeheizter körper," *Forsch. Geb. Ing. Wesen.*, Vol. 13, pp. 246–254.

Fazle Hussain, A. K. M., and Hayakawa, M. (1987), "Eduction of large-scale organized structures in a turbulent plane wake," *J. Fluid Mech.*, Vol. 180, pp. 193–229.

Fey, U., König, M., and Eckelmann, H. (1998), "A new Strouhal-Reynolds number relationship for the circular cylinder in the range $47 < Re < 2 \times 10^5$," *J. Phys. Fluids*, Vol. 10, No. 7, pp. 1547–1549.

Flaschbart, O. (1929), "Messungen ebenen und gewalben platten ergenbisse der aerodynamischen.," *Vers. Göttingen IV Leiferung*, Vol. 96, pp. 317.

Freund, J. B. (1997), "Proposed inflow/outflow boundary condition for direct computation of aerodynamic sound," *AIAA J.*, Vol. 35, No. 4, pp. 740–742.

Gerrard, J. H. (1966), "The mechanics of the formation region of vortices behind bluff bodies," *J. Fluid Mech.*, Vol. 25, Part 2, pp. 401–413.

Giles, M. B. (1990), "Nonreflecting boundary conditions for Euler equations calculations," *AIAA J.*, Vol. 18, No. 12, pp. 2050–2058.

Godunov, S. K. (1959), "A finite difference method for the numerical computation of discontinuous solutions of the equations of fluid dynamics," *Matematicheskii Sbornik.*, Vol. 47, pp. 357–393.

Godunov, S. K. (1976), "Numerical solution of multi-dimensional problems in gas dynamics," Nauka Press, Moscow.

Gostelow, J. P. (1984), "Cascade aerodynamics", Pergamon Press.

Gostelow, J. P., and Blunden, A. R. (1989), "Investigations of boundary layer transition in an adverse pressure gradient," *Trans. ASME, J. Turbomachinery*, Vol. 111, pp. 366–375.

Gostelow, J. P., Walker, G. J., Solomon, W. J., Hong, G., and Melwani, N. (1997), "Investigation of the calmed region behind a turbulent spot," *Trans. ASME, J. Turbomachinery*, Vol. 119, pp. 802–809.

Gostelow, J. P. (2002) enquoteUnsteady and transitional effects in turbomachinery flows, *Proc. Ninth Asian Congress of Fluid Mechanics*, Isfahan, Iran, May 27-31.

Gostelow, J. P. (2003), "On the role of intermittency in the closure of laminar separation bubbles," *Symposium on Advances in Fluid Mechanics*, Bangalor, India.

Gruschwitz, E. (1950), "Calcul approché de la couche limite laminaire en écoulement compressible sur une paroi nonconductrice de la chaleur," ONERA Pub. 47, Paris.

Han, L. S., and Cox, W. R. (1982), "A visual study of turbine blade pressure side boundary layer," *Paper 82-GT-47*, ASME.

Harten, A., and Hyman, J. M. (1983), "Self adjusting grid methods for one-dimensional hyperbolic conservation laws," *J. Comp. Phys.,* Vol. 50, pp. 235-269.

Heinemann, H. J., and Bütefisch, K. A. (1977), "Determination of the vortex shedding frequency of cascades with different trailing edge thicknesses," AGARD CP-227.

Hirsch, C. (1990), "Numerical computation of internal and external flows", Vol. 2, Wiley Series in Numerical Methods in Engineering.

Hixon, R. (1999), "Prefactored compact filters for computational aeroacoustics," *Paper 99-0358*, AIAA.

Hixon, R. (2000), "3-D characteristic-based boundary conditions for CAA," *Paper 2000-2004*, AIAA.

Hodson, H. (1985), "Boundary-layer transition and separation near the leading edge of a high-speed turbine blade," *J. Eng. for Gas Turbines and Power*, Vol. 107, pp. 127–134.

Hoffman, K. A., and Chiang, S. T. (1995), "Computational fluid dynamics for engineers, Vol. 1", Engineering Education System, Witchita, USA, 3rd Edition.

Hogg, S. I., Carscallen, W. E., Gostelow, J. P., Buttsworth, D. R. and Jones, T. V. (1997), "Wide bandwidth stagnation temperature measurements in vortical flows behind turbine vanes," ICIASF '97, Monterey.

Hu, F. Q., Hussaini, M. Y., and Manthey, J. (1995), "Application of low dissipation and dispersion Runge-Kutta schemes to benchmark problems in computational aeroacoustics," *ICASE/LaRC workshop on benchmark problems in computational aeroacoustics (CAA)*, edited by J. C. Hardin, J. R. Ristorcelli, and C. K. W. Tam, NASA Conference Publication 3300, pp. 73–98.

Hu, F. Q. (1996), "On absorbing boundary conditions for linearized Euler equations by a perfectly matched layer," *J. Comp. Phys.*, Vol. 129, No. 1, pp. 201–219.

Inger, G. R., and Mason, W. H. (1976), "Analytical theory of transonic normal shock-turbulent boundary-layer interaction," *AIAA J.*, Vol. 14, No. 9, pp. 1266–1272.

Ishii, K., Kuwahara, K., Ogawa, S., Chyu, W.J., and Kawamura T. (1985), "Computation of flow around a circular cylinder in a supercritical regime," *18th AIAA Fluid Dynamics and Plasmadynamics and Lasers Conference 85-1660*.

James, W. D., Paris, S. W., and Malcolm, G. N. (1980), "Study of viscous crossflow effects on circular cylinders at high Reynolds numbers," *AIAA J.*, Vol. 18, pp. 1066–1072.

Kato, M, and Launder, B. E. (1993), "The modelling of turbulent flow around stationary and vibrating square cylinders," *Proc. 9th symposium on turbulent shear flows*, Kyoto, Japan, pp. 10.4.1–10.4.6.

Kim, J. W, and Lee, D. J. (1989), "Generalized formulation and application of characteristic boundary conditions," *Paper 98-2222*, AIAA.

Kiya, M., Suzuki, Y., Arie, M., and Hagino, M. (1982), "A contribution to the free stream turbulence effect on the flow past a circular cylinder," *J. Fluid Mech.*, Vol. 115, pp. 151–164.

Kiya, M., and Matsumura, M. (1988), "Incoherent turbulence structure in the near wake of a normal plate," *J. Fluid Mech.*, Vol. 190, pp. 343–356.

Kok, J. C. (2000), "Resolving the dependence on freestream values for the $k-\omega$ turbulence model," *AIAA J.*, Vol. 38, No. 7, pp. 1292–1295.

Kolmogorov, A. N. (1942), "Equations of turbulent motion of an incompressible fluid," *Izvestia Academy of Sciences, USSR; Physics*, Vol. 6, Nos. 1 & 2, pp. 56–58.

Kurosaka, M., Gertz, J. B., Graham, J. E., Goodman, J. R., Sundaram, P., Riner, W. C., Kuroda, H., and Hankey, W. L. (1987), "Energy separation in a vortex street," *J. Fluid Mech.*, Vol. 178, pp. 1–29.

Larsson, J. (1997), "Turbine blade heat transfer calculations using two-equation turbulence models," *IMechE J. A, Proc. Instn. Mech. Engrs.*, Vol 211, Part A, Special turbomachinery issue, pp. 253-262.

Larsson, J. (1998), "Numerical simulation of turbulent flows for turbine blade heat transfer applications," PhD thesis, Chalmers University of Technology, Göteborg, Sweden.

Lawaczeck, O., and Heinemann, H. J. (1976), "von Kármán vortex streets in the wakes of subsonic and transonic cascades," AGARD CP-177.

Lawaczeck, O., Bütefisch, K. A., and Heinemann, H. J. (1976), "Vortex streets in the wakes of subsonic and transonic turbine cascades," *IUTAM Symposium on aeroelasticity in turbomachines*, Paris, France.

Mabey, D. G, and Sawyer, W. G. (1976), "Experimental studies of the boundary layer on a flat plate at Mach numbers from 2.5 to 4.5," *R & M No. 3784*, Aero. Res. Council.

Manna, M. (1992), "A three dimensional high resolution compressible flow solver", Ph.D. Thesis, Université Catholique de Louvain.

Mayle, R. E. (1991), "The role of laminar-turbulent transition in gas turbine engines," *Trans. ASME, J. Turbomachinery*, Vol. 113, pp. 509–537.

Mayle, R. E., and Schulz, A. (1997), "The path to predicting bypass transition," *Trans. ASME, J. Turbomachinery*, Vol. 119, No. 3, pp. 405–411.

Medic, G., and Durbin, P. A. (2002), "Toward improved prediction of heat transfer on turbine blades," *Trans. ASME, J. Turbomachinery*, Vol. 124, pp. 187–192.

Mee, D. J., Baines, N. C., Oldfield, M. L. G., and Dickens, T. E. (1992), "An examination of the contributions to loss on a transonic turbine blade in cascade," *Trans. ASME, J. Turbomachinery*, Vol. 114, pp. 155–162.

Menter, F. R. (1992), "Performance of popular turbulence models for attached and separated adverse pressure gradient flows," *AIAA J.*, Vol. 30, No. 8, pp. 2066–2072.

Menter, F. R. (1993), "Zonal two-equation $k-\omega$ turbulence models for aerodynamic flows," *Paper 93-2906*, AIAA.

Menter, F. R. (1994), "Two-equation eddy-viscosity turbulence models for engineering applications," *AIAA J.*, Vol. 32, No. 8, pp. 1598–1605.

Michel, G. W., and Kost, F. H. (1982), "The effect of coolant flow on the efficiency of a transonic HP turbine profile suitable for a small engine," *Paper 82-GT-63*, ASME.

Moustapha, S. H., Carscallen, W. E., and McGeachy, J. D. (1993), "Aerodynamic performance of a transonic low aspect ratio turbine nozzle," *Trans. ASME, J. Turbomachinery*, Vol. 115, pp. 400–408.

Morkovin, M. V. (1964), "Flow around circular cylinder - a kaleidoscope of challenging fluid phenomena," *Symposium on fully separated flows*, Vol. 15, pp. 102–118.

Murthy, V. S., and Rose, W. C. (1978), "Detailed measurements on a circular cylinder in cross flow," *AIAA J.*, Vol. 16, No. 6, pp. 549–550.

Narasimha, R. (1957), "On the distribution of intermittency in the transition region of a boundary layer," *J. Aero. Sci.*, Vol. 24, pp. 711–712.

Ng, W. F., Chakroun, W. M., and Kurosaka, M. (1990), "Time-resolved measurements of total temperature and pressure in the vortex street behind a cylinder," *Phys. Fluids A*, Vol. 2, No. 6, pp. 971–978.

Nizampatnam, L. S., Hoffmann, K. A., Papadakis, M., and Agarwal, R. K. (1992), "Investigation of boundary conditions for computational aeroacoustics," *Paper 99-0357*, AIAA, Jan. 1999.

O'Callaghan, J. J., and Kurosaka, M. (1993), "Vortex-induced energy separation in shear flows," *AIAA J.*, Vol. 31, No. 6, pp. 205–220.

Owen, P. R., and Klanfer, L. (1955), "On the laminar boundary layer separation from the leading edge of a thin aerofoil," ARC C.P. 220.

Owen, F. K., and Johnson, D. A. (1980), "Measurements of unsteady vortex flowfields," *AIAA J.*, Vol. 18, No. 10, pp. 1173–1179.

Pandolfi, M., and Larocca, F. (1989), "Transonic flow about a circular cylinder," *Computers & Fluids*, Vol. 17, No. 1, pp. 205–220.

Patel, V. C. (1969), "The effects of curvature on the turbulent boundary layer," *R & M No. 3599*, Aero. Res. Council, UK.

Pieringer, P., Gehrer, A., and Sanz, W. (2001), "Calculation of rotor-stator interaction of a transonic turbine stage using an innovative unsteady flow solver," *Fourth European Conference on Turbomachinery ATI-CST-087/01*.

Poinsot, T. J., and Lele, S. K. (1992), "Boundary conditions for direct simulations of compressible viscous flows," *J. Comp. Phys.*, Vol. 101, pp. 104–129.

Quirk, J. J. (1991), "An adaptive grid algorithm for computational shock hydrodynamics", Ph.D. thesis, Cranfield University, UK.

Reynolds, O. (1874), "On the extent and action of the heating surface for steam boilers," *Proc. Manchester Lit. Phil. Soc.*, Vol. 14, pp. 7–12.

Roe, P. L. (1981), "Approximate Riemann solvers, parameter vectors, and difference schemes," *J. Comp. Phys.*, Vol. 43, pp. 357–372.

Roe, P. L. (1986), "Characteristic-based schemes for the Euler equations," *Annual Review of Fluid Mechanics*, Vol. 18, pp. 337–365.

Roberts, Q. D., and Denton, J. D. (1996), "Loss production in the wake of a simulated subsonic turbine blade," *Paper 96-GT-421*, ASME.

Rona, A. and Bennett, W. P. (2001), "Energy separation in a compressible vortex street," *Paper 2001-0601*, AIAA.

Roshko, A. (1961), "Experiments on the flow past a circular cylinder at very high Reynolds number," *J. Fluid Mech.*, Vol. 10, pp. 345–356.

Rowley, C. W., and Colonius, T. (1998), "Numerically nonreflecting boundary conditions for multidimensional aeroacoustic computations," *Paper 98-2220*, AIAA.

Ryan, L. F. (1951), "Experiments on aerodynamic cooling", Ph.D. thesis, ETH Inst. für Aerodynamik Mitteilungen, Zurich.

Salas, M. D. (1983), "Recent developments in transonic Euler flow over a circular cylinder," *Math. and Comp. in Simulation XXV,* Elsevier Science Publishers, pp. 232–236.

Shapiro, A. H. (1953), "The dynamics and thermodynamics of compressible fluid flow - Vol. 1,", Ronald Press, New York, USA.

Schlichting, H. (1979), "Boundary layer theory", Seventh ed., McGraw-Hill, New York, USA.

Shih, W. C. L., Wang, C., Coles, D., and Roshko, A., (1992), "Experiments on flow past rough circular cylinders at large Reynolds numbers," *Proc. 2nd Int. Coll. Bluff Body Aero. Appl.*, Melbourne, Australia, December 7-10.

Schultz-Grunow, F. (1951), "Turbulenter wärmedurchgang im zentrifugalfeld," *Forsch. Geb. Ing. Wesen.*, Vol. 17.

Shang, J. S. (1982), "Oscillatory compressible flow around a cylinder," *Air Force Wright Aeronautical Laboratories Report A82-17781*.

Shobeiri, M. T., Radke, R., Read, K., Wright, L., and Chakka, P. (2002), "Advances in unsteady boundary layer transition research theory, modeling, experimental verification", *Colloqium on periodically unsteady flows in turbomachinery*, Technische Universität Berlin, Germany.

Sieverding, C. H., Stanislas, M., and Snoeck, J. (1983), "The base pressure problem in transonic turbine cascades," *Paper 83-GT-50*, ASME, 1983.

Sieverding, C. H., and Heinemann, H. (1989), "The influence of boundary layer state on vortex shedding from flat plates and turbine cascades," *Paper 89-GT-296*, ASME.

Sieverding, C. H., and Heinemann, H. (1990), "The influence of boundary layer state on vortex shedding from flat plates and turbine cascades," *Trans. ASME, J. Turbomachinery*, Vol. 112, pp. 181–187.

Sieverding, C. H., Ottolia, D., Bagnera, C., Cimadoro, A., and Desse, J. (2003), "Unsteady turbine blade wake characteristics," *Proc. ASME Turbo Expo 2003, Power for Land, Sea and Air*, ASME, Atlanta, Georgia, USA.

Simpson, R. L. (1989), "Turbulent boundary separation," *Ann. Rev. Fluid Mech.*, Vol. 21, pp. 205–234.

Simpson, R. L. (2002), "Some Reynolds number effects on separating 2-D and attached 3-D turbulent boundary layers," *Paper 2002-1107*, AIAA.

Smolny, A., and Blaszczak, J. (1995), "Boundary layer and loss studies on highly loaded turbine cascade," AGARD CP-571, 4-1.

Sod, G. A. (1978), "A survey of several finite difference methods for systems of nonlinear hyperbolic conservation laws," *J. Comp. Phys.*, Vol. 27, pp. 1–31.

Song, C. C . S., and Yuan, M. (1990), "Simulation of vortex-shedding flow about a circular cylinder at high Reynolds numbers," *Trans. ASME, J. Fluids Eng.*, Vol. 112, pp. 155–163.

Spalding, D. B., and Chi, S. W. (1964), "The drag of a compressible turbulent boundary layer on a smooth flat plate with and without heat transfer," *J. Fluid Mech.*, Vol. 18, pp. 117–143.

Stieger, R. D. (2002), "The effects of wakes on separating boundary layers in low pressure turbines," PhD thesis, Cambridge University.

Sweby, P. K. (1984), "High resolution schemes using flux limiters for hyperbolic conservation laws," *SIAM J. Num. Analysis*, Vol. 21, pp. 995–1011.

Szepessy, S., and Bearman, P. W. (1992), "Aspect ratio and end plate effects on vortex shedding from a circular cylinder," *J. Fluid Mech.*, Vol. 234, pp. 191-217.

Talan, M., and Hourmouziadis, J. (2002), "Periodically unsteady separation and transition of a boundary layer with pressure gradient", *Colloqium on periodically unsteady flows in turbomachinery*, Technische Universität Berlin, Germany.

Tam, C. K. W. and Webb, J. C. (1993), "Dispersion-relation-preserving finite difference schemes for computational acoustics," *J. of Comp. Phys.*, Vol. 107, pp. 262–281.

Tennekes, H., and Lumley, J.L. (1972), "A first course in turbulence", MIT Press, Cambridge, MA., USA.

Thomann, H. (1959), "Measurements of the recovery temperature in the wake of a cylinder and of a wedge at Mach numbers between 0.5 and 3," FFA Report 84, Flygtekniska Försöksanstalten (The Aeronautical Research Institute of Sweden), Stockholm, Sweden.

Thompson, K. W. (1987), "Time dependent boundary conditions for hyperbolic systems," *J. Comp. Phys.*, Vol. 68, pp. 1–24.

Toro, E. F. (1999), "Riemann solvers and numerical methods for fluid dynamics: a practical introduction", Springer Publications, 2nd ed.

Travin, A., Shur, M., Strelets, M., and Spalart, P. (1999), "Detached-eddy simulations past a circular cylinder," *Flow Turb. Combust.*, Vol. 63, pp. 269–291.

Truckenbrodt, E. (1952), "A method of quadrature for the calculation of laminar and turbulent boundary layers in plane and rotational symmetric flow," *NACA TM 1379*.

Ubaldi, M., and Zunino, P. (2000), "An experimental study of the unsteady characteristics of the turbulent near wake of a turbine blade," *J. Experimental Thermal and Fluid Science*, Vol. 23, pp. 23–33.

Van Leer, B. (1979), "Towards the ultimate conservative difference scheme V. A second-order sequel to Godunov's method," *J. Comp. Phys.*, Vol. 32, pp. 101–136.

Van Hest, B. F. A. (1996), "Laminar-turbulent transition in boundary layers with adverse pressure gradients", Published by Delft University of Technology, Netherlands.

Versteeg, H., and Malalasekera, W. (1995), "An introduction to computational fluid dynamics: the finite volume method ", Longman Scientific & Technical, Essex, UK.

Vicedo, J., Vilmin, S., Dawes, W. N., and Savill, A. M. (2004), "Intermittency transport modeling of separated flow transition," *Trans. ASME, J. Turbomachinery*, Vol. 126, No. 3, pp. 424–434.

Visbal, M. R., and Gaitonde, D. V. (1999), "Computation of aeroacoustic fields on general geometries using compact differencing and filtering schemes," *Paper 99-3706*, AIAA.

Wang, M., Catalano, P., and Iaccarino, G. (2001), "Prediction of high Reynolds number flow over a circular cylinder using LES with wall modeling," *Annual Research Briefs*, Center for Turbulence Research, NASA Ames/Stanford University.

White, F. M. (1991), "Viscous fluid flow", Second ed., McGraw-Hill, New York, USA.

Weiselsberger, C. (1922), "New data on the laws of fluid resistance," *NACA TN 84*.

Wilcox, D. C. (1988), "Reassessment of the scale determining equation for advanced turbulence models," *AIAA J.*, Vol. 26, No. 11, pp. 1299–1310.

Wilcox, D. C. (1992), "Dilatation-dissipation corrections for advanced turbulence models," *AIAA J.*, Vol. 30, No. 11, pp. 2639–2646.

Wilcox, D. C. (1993), "Turbulence modelling for CFD", Griffin Printing, Glendale, California, USA.

Wilcox, D. C. (1994), "Simulation of transition with a two-equation turbulence model," *AIAA J.*, Vol. 32, No. 2, pp. 247–255.

Wilcox, D. C. (2002), "Turbulence modelling for CFD", Second ed., DCW Industries Inc., California, USA.

Williamson, R. G., Moustapha, S. H., and Huot, J. P. (1986), "The effect of a downstream rotor on the measured performance of a transonic turbine nozzle," *Trans. ASME, J. Turbomachinery*, Vol. 108, pp. 269–274.

Williamson, C. H. K. (1996), "Vortex dynamics in the cylinder wake," *Ann. Rev. Fluid Mech*, Vol. 28, pp. 477–539.

de With, G., Holdo, A. E., and Huld T. A. (2003), "The use of dynamic grid adaption algorithms for the modelling of flow around a circular cylinder in sub-critical flow regime," *Int. J. Num. Methods in Fluids*, Vol. 41, pp. 789–808.

Zdravkovich, M. M. (1997), "Flow around circular cylinders, Vol. 1 - Fundamentals", Oxford University Press, New York, USA.